

**Cr (VI) REMOVAL WITH NATURAL,  
SURFACTANT MODIFIED AND BACTERIA  
LOADED ZEOLITES**

**A Thesis Submitted to the  
Graduate School of Engineering and Sciences of  
İzmir Institute of Technology  
in Partial Fulfillment of the Requirement for the Degree of**

**DOCTOR OF PHILOSOPHY  
in Chemical Engineering**

**by  
Beyhan CANSEVER ERDOĞAN**

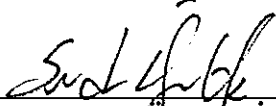
**June 2011  
İZMİR**

We approve the thesis of **Beyhan CANSEVER ERDOĞAN**



---

**Prof. Semra ÜLKÜ**  
Supervisor



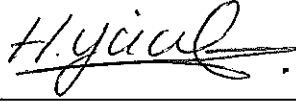
---

**Prof. Serdar ÖZÇELİK**  
Committee Member



---

**Prof. Devrim BALKÖSE**  
Committee Member



---

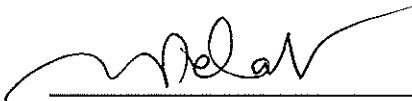
**Prof. Hayrettin YÜCEL**  
Committee Member



---

**Assoc. Prof. Öguz BAYRAKTAR**  
Committee Member

**22 June 2011**



---

**Prof. Mehmet POLAT**  
Head of the Department of  
Chemical Engineering

---

**Prof. Durmuş Ali DEMİR**  
Dean of the Graduate School of  
Engineering and Sciences

## ACKNOWLEDGEMENTS

I would like to express my sincere gratitude to my thesis advisor Prof. Semra ÜLKÜ for her guidance, thoughtful advice and continuous encouragement during the course of this work. I would also like to thank to committee members Prof. Serdar ÖZÇELİK, Assoc. Prof. Oğuz BAYRAKTAR, Prof. Devrim BALKÖSE and Prof. Hayrettin YÜCEL for their valuable discussions and contributions. I am also grateful to Prof. Hürriyet POLAT for her help in zeta potential measurements.

I would like to thank to the zeolite group members, especially Dr. Evren ALTIOK for his discussions and contributions.

I would like to thank to reseach specialists: Dr. Özlem DUVARCI, Dr. Filiz ÖMÜRLÜ and Nesrin TATLIDİL for their contributions in characterization studies. My special thanks to Nesrin GAFFAROĞLU for her contribution and support in ICP analysis.

I am also grateful to IYTE MAM reseach specialists for their help during my material characterization studies.

I would like to appreciate deeply to my friends, Pınar ARCAN, Duygu ALTIOK, Yasemin KAYA, Yılmaz OCAK, İrem ŞAHİN and Gamze KATIRCIOĞLU for their friendships.

I am grateful to my husband Gökhan ERDOĞAN for assisting me with my research and offering advice and discussion. I would like thank to my mother in law Behiye ERDOĞAN for her support and love.

Finally, I would like to express my heartfelt gratitude to my family Hüseyin CANSEVER, Güler CANSEVER, Reyhan YAZAR, Aslı YAZAR and Kaan YAZAR for their continuous support, encouragement and love, which enabled me to overcome difficulties.

## ABSTRACT

### Cr (VI) REMOVAL WITH NATURAL, SURFACTANT MODIFIED AND BACTERIA LOADED ZEOLITES

The objective of the study is to determine the bacteria removal performances of the local clinoptilolite rich mineral and its surfactant modified forms and to investigate potential applications of clinoptilolite rich mineral, surfactant modified clinoptilolite rich mineral and bacteria loaded forms in Cr (VI) sorption.

Characterizations of clinoptilolite rich mineral and its modified forms were studied. Batch sorption experiments were performed and the effects of the parameters such as pH, initial concentration, agitation speed, particle size and temperature were investigated. Sorption kinetic data were analysed by external mass transfer, intraparticle diffusion, pseudo first and second order models. Intraparticle diffusion model results indicated that sorption of Cr (VI) on the sorbents was a multi-step process, involving external and intraparticle diffusion. Effective diffusion coefficient results implied that Cr (VI) sorption process was not solely intraparticle diffusion controlled and external film diffusion was also effective. Biot number (100-3000) results indicated that Cr (VI) sorption process was mainly controlled by intraparticle diffusion. The sorption reaction model results revealed that sorption of Cr (VI) onto sorbents was well represented by the pseudo-second order kinetic model.

Sorption isotherm model results indicated that the Langmuir isotherm fitted well with the experimental data. Thermodynamic analysis, Gibbs energy change ( $<-20$  kJ/mol), entropy change of sorption ( $<-0.2$  kJ/mol K), enthalpy change ( $<-100$ kJ/mol) and activation energy ( $<40$  kJ/mol) showed that sorption process was exothermic, spontaneous and physical sorption.

## ÖZET

### DOĞAL, YÜZEY AKTİF MADDESİYLE MODİFİYE EDİLEN VE BAKTERİ YÜKLENMİŞ ZEOLİTLERLE Cr (VI) UZAKLAŞTIRILMASI

Bu çalışmanın amacı yerel klinoptilolitin ve yüzey aktif maddesiyle modifiye edilmiş formlarının bakteri giderme performanslarını hesaplamak ve klinoptilolitin, yüzey aktif maddesiyle modifiye edilen klinoptilolitin ve bakteri yüklenmiş formların krom (VI) sorpsiyonundaki potansiyel uygulamalarını araştırmaktır.

Klinoptilolitçe zengin mineralin ve modifiye edilmiş formlarının karakterizasyonu çalışılmıştır. Kesikli sorsiyon deneyleri yapılmış ve pH, başlangıç konsantrasyonu, karıştırma hızı, parçacık boyutu ve sıcaklık parametlerinin etkisi incelenmiştir. Sorpsiyon kinetik verileri dış kütle transferi ve parçacık içi difüzyon modelleriyle ve birinci ve ikinci derece yalancı kinetik modelleriyle analiz edilmiştir. Parçacık içi difüzyon modeli, tutucuların krom(VI) üzerine sorpsiyonunun dış yüzey ve parçacık içi difüzyonu da içeren çoklu proses olduğunu göstermiştir. Efektif difüzyon katsayı ( $D_{eff}$ ) sonuçları, krom(VI) sorpsiyon prosesinin yalnızca parçacık içi difüzyonun kontrolünde olmadığı, aynı zamanda dış yüzey difüzyonun da etkili olduğunu göstermiştir. Biot sayı sonuçları (100-3000), krom(VI) sorpsiyon prosesinin temelde parçacık içi difüzyonu ile kontrol edildiğini göstermiştir. Sorpsiyon reaksiyon model sonuçları, tutucuların krom (VI) üzerine sorpsiyonunun ikinci derece yalancı kinetik modeliyle çok iyi temsil edildiğini açığa çıkarmıştır.

Sorpsiyon izoterm model sonuçlarına göre Langmuir izoterm modelinin deneysel verilere daha iyi uymuştur. Termodinamik analizi, Gibbs enerji değişimi ( $<-20\text{kJ/mol}$ ), entropi değişimi ( $<-0.2\text{ kJ/mol K}$ ), entalpi değişimi ( $<-100\text{kJ/mol}$ ) ve aktivasyon enerji ( $<40\text{ kJ/mol}$ ) sorpsiyon prosesinin ekzotermik, spontane ve fiziksel sorpsiyon olduğunu göstermiştir.

# TABLE OF CONTENTS

LIST OF FIGURES .....	x
LIST OF TABLES .....	xix
CHAPTER 1. INTRODUCTION .....	1
CHAPTER 2. ZEOLITES.....	4
2.1. Zeolites.....	4
2.2. Clinoptilolite Rich Natural Zeolites.....	5
2.3. Application of Zeolites .....	7
2.4. Surfactant Modified Zeolites .....	11
2.5. Application of Surfactant Modified Zeolite.....	15
2.6. Characterization Methods of Natural and Modified Zeolites.....	18
CHAPTER 3. BACTERIA .....	23
3.1. General Information about Bacteria .....	23
3.1.1. Cell Wall Features of Gram Positive and Negative Bacteria.....	24
3.1.2. Functional Groups on the Bacteria Cell Wall.....	27
3.2. Attachment Stages of Bacteria to the Surface .....	28
3.2.1. Factors Influencing Bacteria Attachment .....	29
3.3. Previous Bacterial Adsorption Studies .....	31
CHAPTER 4. CHROMIUM REMOVAL.....	36
4.1. Chromium Ion.....	36
4.2. Sorbents Used in Hexavalent Chromium Removal .....	37
4.3. Functional Groups Related to Cr (VI) Sorption.....	44
CHAPTER 5. SORPTION.....	47
5.1. Sorption Interactions.....	49

5.2. Sorption Isotherms .....	51
5.2.1. Langmuir Isotherm Model .....	52
5.2.2. Freundlich Isotherm Model .....	53
5.2.3. Redlich-Peterson Isotherm Model .....	53
5.2.4. Temkin Isotherm Model .....	54
5.3. Sorption Kinetic .....	54
5.4. Sorption Kinetic Models .....	57
5.5. Sorption Diffusion Models .....	59
5.5.1. External Film Diffusion .....	59
5.5.2. Intraparticle Diffusion.....	64
5.5.2.1. Macropore Diffusion.....	64
5.5.2.2. Micropore Diffusion .....	69
5.5.2.3. Comparison of Micropore and Macropore Diffusion Resistance .....	73
5.5.3. Sorption Diffusion Models Based on Two-Three Resistances .....	74
5.6. Sorption Reaction Models .....	77
5.6.1. First Order Reversible Model .....	77
5.6.2. Pseudo First Order Model.....	78
5.6.3. Pseudo Second Order Model .....	79
5.6.4. Elovich Model.....	80
5.6.5. Ritchie Model .....	81
5.7. Possible Mechanisms in the Zeolite-Heavy Metal System.....	82
 CHAPTER 6. MATERIALS AND METHODS .....	 86
6.1. Zeolite Sample Preparation.....	86
6.2. Surfactant Modified Zeolite Sample Preparation .....	86
6.2.1. Surfactants .....	86
6.2.2. Preparation of Surfactant Modified Zeolite .....	86
6.3. Bacteria Loaded Zeolite Samples Preparations .....	87
6.3.1. Bacteria .....	87
6.3.2. Viable Cell Count Method.....	87
6.3.3. Preparation of Bacteria Loaded Zeolite Samples .....	88
6.4. Characterization of Natural, Surfactant Modified	

and Bacteria Loaded Zeolite Samples .....	89
6.5. Sorption Experiments .....	90
<b>CHAPTER 7. RESULTS AND DISCUSSIONS .....</b>	<b>93</b>
7.1. Characterization of Natural and Surfactant Modified Zeolites.....	93
7.1.1. Monolayer or Bilayer Formation on the Clinoptilolite Rich Mineral Surface.....	100
7.2. Results of Bacteria Removal Using Natural and Surfactant Modified Zeolites.....	104
7.2.1. Characterization of Natural and Surfactant Modified Zeolites after Bacteria Attachment .....	113
7.2.2. Proposed Mechanisms in Attachment of Bacteria to the Surface of Natural and Surfactant Modified Zeolites.....	122
7.3. Sorption of Cr (VI) onto Natural, Surfactant Modified and Bacteria Loaded Zeolites .....	124
7.3.1. Characterization Results of Natural, Surfactant Modified and Bacteria Loaded Zeolites after Cr (VI) Sorption .....	139
7.4. Effects of Experimental Parameters on Cr (VI) Sorption.....	151
7.4.1. Effect of pH on Cr (VI) Sorption.....	151
7.4.1.1. Characterization Results of Natural, Surfactant Modified and Bacteria Loaded Zeolites after Cr (VI) Sorption at pH 3 and 11 .....	166
7.4.2. Effect of Initial Concentration on Cr (VI) Sorption .....	177
7.4.3. Effect of Agitation Speed on Cr (VI) Sorption.....	182
7.4.4. Effect of Temperature on Cr (VI) Sorption .....	187
7.4.5. Effect of Particle Size on Cr (VI) Sorption.....	192
7.5. Sorption Kinetic Model Results.....	197
7.5.1. Comparison of Experimental and Model Results.....	213
7.6. Comparison of External and Internal Mass Transfer Resistance .....	227
7.7. Sorption Isotherms.....	229
7.8. Thermodynamic Parameters .....	239
7.9. Activation Energy .....	241



CHAPTER 8. CONCLUSIONS .....	243
REFERENCES .....	246
APPENDICES	
APPENDIX A. HEXAVALENT CHROMIUM SPECIATION DIAGRAM .....	263
APPENDIX B. DETERMINATION OF CHROMIUM (VI) CONCENTRATION.....	271
APPENDIX C. ORIENTATION OF SDS MOLECULE ON CLINOPTILOLITE RICH MINERAL.....	275
APPENDIX D. PORE SIZE DISTRIBUTIONS OF NATURAL SURFACTANT MODIFIED ZEOLITE SAMPLES .....	277
APPENDIX E. XRD RESULTS .....	279
APPENDIX F. SORPTION KINETIC MODEL CALCULATION .....	292
APPENDIX G. ISOTHERM MODELS.....	314
APPENDIX H. THERMODYNAMIC PARAMETERS.....	315
APPENDIX I. ACTIVATION ENERGY.....	316

## LIST OF FIGURES

<b><u>Figure</u></b>		<b><u>Page</u></b>
Figure 2.1.	Aluminosilicate tetrahedral structure and exchangeable cations within the zeolite framework.....	5
Figure 2.2.	(a) Model framework for structure of clinoptilolite. (b) Orientation of clinoptilolite structure of clinoptilolite.....	6
Figure 2.3.	Main cation positions in the clinoptilolite structure.....	7
Figure 2.4.	Molecular structure of surfactant.....	12
Figure 2.5.	Formation of a) monolayer b) bilayer on the solid surface.....	14
Figure 2.6.	Scanning electron microphotograph of the Pentalofos clinoptilolite (a) natural, (b) modified with HDTMA.....	19
Figure 2.7.	Scanning electron microphotograph of the Mexican clinoptilolite (a) natural, (b) modified with HDTMA.....	19
Figure 2.8.	XRD pattern of (a) clinoptilolite (b) HDTMA modified clinoptilolite.....	20
Figure 2.9.	XRD pattern of clinoptilolite and HDTMA modified clinoptilolite .....	20
Figure 2.10.	FTIR spectra of raw zeolite material, its Na form and zeolite samples treated by HDTMA-Br .....	21
Figure 2.11.	FTIR spectra of HDTMA modified clinoptilolite.....	22
Figure 2.12.	FTIR spectra of (A) HDTMA (B) HDTMA sorbed onto clinoptilolite samples from (a) Serbia (b) Turkey (c) Croatia....	22
Figure 2.13.	FTIR spectra of HDTMA and HDTMA modified clinoptilolite.....	22
Figure 3.1.	Structures of the peptidoglycan layer.....	25
Figure 3.2.	Gram positive bacteria cell wall structures.....	26
Figure 3.3.	Gram negative bacteria cell wall structures.....	27
Figure 3.4.	FTIR spectra of bacteria and minerals.....	34
Figure 4.1.	Cr (VI) speciation diagram as a function of pH.....	37
Figure 5.1.	Bidisperse ideal spherical particle.....	48
Figure 5.2.	Attractive forces (Keesom, Debye and London interactions)....	49

Figure 5.3.	The schematic representation of the electrical double-layer.....	50
Figure 5.4.	The variation of free energy with particle separation.....	51
Figure 5.5.	Four steps of sorption.....	55
Figure 5.6.	Sorption kinetic models based on reaction and diffusion models.....	59
Figure 5.7.	Schematic diagram of concentration profile due to external and internal mass transfer resistance.....	60
Figure 5.8.	Macropore Diffusion Mechanisms (a) Molecular (b) Knudsen (c) Surface.....	65
Figure 6.1.	Serial dilution procedure.....	88
Figure 7.1.	SEM micrographs a) CLI, b) CMCLI c) AMCLI.....	93
Figure 7.2.	X-Ray Diffraction pattern of CMCLI, HDTMA and CLI.....	95
Figure 7.3.	X-Ray Diffraction pattern of AMCLI, SDS and CLI.....	95
Figure 7.4.	FTIR results of CMCLI, HDTMA and CLI.....	96
Figure 7.5.	FTIR results of AMCLI, SDS and CLI.....	97
Figure 7.6.	The variation of the zeta potential of CLI at different pH values.....	98
Figure 7.7.	The variation of the zeta potential of CMCLI at different pH values.....	99
Figure 7.8.	The variation of the zeta potential of AMCLI at different pH values.....	99
Figure 7.9.	Illustration of the adsorption regions for surfactants adsorption on the surface.....	101
Figure 7.10.	Adsorption isotherm of clinoptilolite-HDTMA at 25 °C.....	102
Figure 7.11.	Adsorption isotherm of clinoptilolite-SDS at 25 °C.....	103
Figure 7.12.	Bilayer formation on the clinoptilolite rich mineral surface after modification with HDTMA and SDS.....	103
Figure 7.13.	Change in <i>E. coli</i> concentration before and after the addition of CLI .....	104
Figure 7.14.	Change in <i>B. subtilis</i> concentration before and after the addition of CLI.....	105
Figure 7.15	Change in <i>S. aureus</i> concentration before and after the addition	

	of CLI .....	105
Figure 7.16.	Change in <i>S. epidermidis</i> concentration before and after the addition of CLI .....	106
Figure 7.17.	Change in <i>P. aeruginosa</i> concentration before and after the addition of CLI.....	106
Figure 7.18.	Change in <i>E. coli</i> concentration before and after the addition of CMCLI.....	107
Figure 7.19.	Change in <i>B. subtilis</i> concentration before and after the addition of CMCLI.....	108
Figure 7.20.	Change in <i>S. aureus</i> concentration before and after the addition of CMCLI.....	108
Figure 7.21.	Change in <i>S. epidermidis</i> concentration before and after the addition of CMCLI.....	109
Figure 7.22.	Change in <i>P. aeruginosa</i> concentration before and after the addition of CMCLI.....	109
Figure 7.23.	Change in <i>E. coli</i> concentration before and after the addition of AMCLI.....	110
Figure 7.24.	Change in <i>B. subtilis</i> concentration before and after the addition of AMCLI.....	110
Figure 7.25.	Change in <i>S. aureus</i> concentration before and after the addition of AMCLI.....	111
Figure 7.26.	Change in <i>S. epidermidis</i> concentration before and after the addition of AMCLI.....	111
Figure 7.27.	Change in <i>P. aeruginosa</i> concentration before and after the addition of AMCLI.....	112
Figure 7.28.	SEM micrographs of a) EC-CLI b) BS-CLI c) SA-CLI d) SE-CLI e) PA-CLI.....	114
Figure 7.29.	SEM micrographs of a) EC-CMCLI b) BS-CMCLI c) SA-CMCLI d) SE-CMCLI e) PA-CMCLI.....	115
Figure 7.30.	SEM micrographs of a) EC-AMCLI b) BS-AMCLI c) SA-AMCLI d) SE-AMCLI e) PA-AMCLI.....	116
Figure 7.31.	XRD patterns of clinoptilolite rich mineral after <i>E. coli</i> attachment.....	119

Figure 7.32.	FTIR results of clinoptilolite rich mineral after <i>E. coli</i> , <i>B. subtilis</i> , <i>S. aureus</i> , <i>S. epidermidis</i> and <i>P. aeruginosa</i> attachment.....	120
Figure 7.33.	FTIR results of cationic modified clinoptilolite rich mineral after <i>E. coli</i> , <i>B. subtilis</i> , <i>S. aureus</i> , <i>S. epidermidis</i> and <i>P. aeruginosa</i> attachment.....	121
Figure 7.34.	FTIR results of anionic modified clinoptilolite rich mineral after <i>E. coli</i> , <i>B. subtilis</i> , <i>S. aureus</i> , <i>S. epidermidis</i> and <i>P. aeruginosa</i> attachment.....	122
Figure 7.35.	pH profiles clinoptilolite, anionic and cationic modified clinoptilolite rich mineral in Cr (VI) solution.....	125
Figure 7.36.	pH profiles of the bacteria loaded clinoptilolite rich mineral in Cr (VI) solution.....	125
Figure 7.37.	pH profiles of the bacteria loaded anionic modified clinoptilolite rich mineral in Cr (VI) solution.....	126
Figure 7.38.	pH profiles of the bacteria loaded cationic modified clinoptilolite rich mineral in Cr (VI) solution.....	126
Figure 7.39.	Sorption kinetic curve of Cr (VI) for CLI.....	128
Figure 7.40.	Sorption kinetic curve of Cr (VI) for AMCLI.....	129
Figure 7.41.	Sorption kinetic curve of Cr (VI) for CMCLI.....	129
Figure 7.42.	Sorption kinetic curve of Cr (VI) for EC-CLI.....	130
Figure 7.43.	Sorption kinetic curve of Cr (VI) for BS-CLI.....	131
Figure 7.44.	Sorption kinetic curve of Cr (VI) for SA-CLI.....	131
Figure 7.45.	Sorption kinetic curve of Cr (VI) for SE-CLI.....	132
Figure 7.46.	Sorption kinetic curve of Cr (VI) for PA-CLI.....	132
Figure 7.47.	Sorption kinetic curve of Cr (VI) for EC-AMCLI.....	133
Figure 7.48.	Sorption kinetic curve of Cr (VI) for BS-AMCLI.....	134
Figure 7.49.	Sorption kinetic curve of Cr (VI) for SA-AMCLI.....	134
Figure 7.50.	Sorption kinetic curve of Cr (VI) for SE-AMCLI.....	135
Figure 7.51.	Sorption kinetic curve of Cr (VI) for PA-AMCLI.....	135
Figure 7.52.	Sorption kinetic curve of Cr (VI) for EC-CMCLI.....	136
Figure 7.53.	Sorption kinetic curve of Cr (VI) for BS-CMCLI.....	137
Figure 7.54.	Sorption kinetic curve of Cr (VI) for SA-CMCLI.....	137

Figure 7.55.	Sorption kinetic curve of Cr (VI) for SE-CMCLI.....	138
Figure 7.56.	Sorption kinetic curve of Cr (VI) for PA-CMCLI.....	138
Figure 7.57.	XRD results of clinoptilolite rich mineral after Cr (VI) sorption.....	142
Figure 7.58.	FTIR results of clinoptilolite rich mineral after Cr (VI) sorption.....	143
Figure 7.59.	FTIR results of anionic modified clinoptilolite rich mineral after Cr (VI) sorption.....	144
Figure 7.60.	FTIR results of cationic modified clinoptilolite rich mineral after Cr (VI) sorption.....	144
Figure 7.61.	FTIR results of EC-CLI after Cr (VI) sorption.....	145
Figure 7.62.	FTIR results of BS-CLI after Cr (VI) sorption .....	146
Figure 7.63.	FTIR results of SA-CLI after Cr (VI) sorption .....	146
Figure 7.64.	FTIR results of SE-CLI after Cr (VI) sorption.....	146
Figure 7.65.	FTIR results of PA-CLI after Cr (VI) sorption .....	147
Figure 7.66.	FTIR results of EC-AMCLI after Cr (VI) sorption.....	147
Figure 7.67.	FTIR results of BS-AMCLI after Cr (VI) sorption.....	148
Figure 7.68.	FTIR results of SA-AMCLI after Cr (VI) sorption.....	148
Figure 7.69.	FTIR results of SE-AMCLI after Cr (VI) sorption.....	148
Figure 7.70.	FTIR results of PA-AMCLI after Cr (VI) sorption.....	149
Figure 7.71.	FTIR results of EC-CMCLI after Cr (VI) sorption.....	149
Figure 7.72.	FTIR results of BS-CMCLI after Cr (VI) sorption.....	150
Figure 7.73.	FTIR results of SA-CMCLI after Cr (VI) sorption.....	150
Figure 7.74.	FTIR results of SE-CMCLI after Cr (VI) sorption .....	150
Figure 7.75.	FTIR results of PA-CMCLI after Cr (VI) sorption .....	151
Figure 7.76.	Sorption kinetic curve of Cr (VI) at pH 3 for CLI.....	153
Figure 7.77.	Sorption kinetic curve of Cr (VI) at pH 11 for CLI.....	154
Figure 7.78.	Sorption kinetic curve of Cr (VI) at pH 3 for AMCLI.....	155
Figure 7.79.	Sorption kinetic curve of Cr (VI) at pH 11 for AMCLI.....	155
Figure 7.80.	Sorption kinetic curve of Cr (VI) at pH 3 for CMCLI.....	156
Figure 7.81.	Sorption kinetic curve of Cr (VI) at pH 11 for CMCLI.....	157
Figure 7.82.	Sorption kinetic curve of Cr (VI) at pH 3 for EC-CLI.....	158
Figure 7.83.	Sorption kinetic curve of Cr (VI) at pH 11 for EC-CLI.....	159

Figure 7.84.	Sorption kinetic curve of Cr (VI) at pH 3 for BS-CLI.....	159
Figure 7.85.	Sorption kinetic curve of Cr (VI) at pH 11 for BS-CLI.....	160
Figure 7.86.	Sorption kinetic curve of Cr (VI) at pH 3 for EC-AMCLI.....	161
Figure 7.87.	Sorption kinetic curve of Cr (VI) at pH 11 for EC-AMCLI .....	161
Figure 7.88.	Sorption kinetic curve of Cr (VI) at pH 3 for BS-AMCLI.....	162
Figure 7.89.	Sorption kinetic curve of Cr (VI) at pH 11 for BS-AMCLI.....	162
Figure 7.90.	Sorption kinetic curve of Cr (VI) at pH 3 for EC-CMCLI.....	163
Figure 7.91.	Sorption kinetic curve of Cr (VI) at pH 11 for EC-CMCLI.....	164
Figure 7.92.	Sorption kinetic curve of Cr (VI) at pH 3 for BS-CMCLI.....	164
Figure 7.93.	Sorption kinetic curve of Cr (VI) at pH 11 for BS-CMCLI.....	165
Figure 7.94.	XRD results of CLI after Cr (VI) sorption at pH 3 and 11.....	169
Figure 7.95.	XRD results of AMCLI after Cr (VI) sorption at pH 3 and 11...	170
Figure 7.96.	XRD results of CMCLI after Cr (VI) sorption at pH 3 and 11...	171
Figure 7.97.	FTIR results of CLI after Cr (VI) sorption at pH 3 and 11.....	172
Figure 7.98.	FTIR results of AMCLI after Cr (VI) sorption at pH 3 and 11...	172
Figure 7.99.	FTIR results of CMCLI after Cr (VI) sorption at pH 3 and 11...	173
Figure 7.100.	FTIR results of EC-CLI after Cr (VI) sorption at pH 3 and 11...	174
Figure 7.101.	FTIR results of BS-CLI after Cr (VI) sorption at pH 3 and 11...	174
Figure 7.102.	FTIR results of EC-AMCLI after Cr (VI) sorption at pH 3 and 11.....	175
Figure 7.103.	FTIR results of BS-AMCLI after Cr (VI) sorption at pH 3 and 11.....	175
Figure 7.104.	FTIR results of EC-CMCLI after Cr (VI) sorption at pH 3 and 11.....	176
Figure 7.105.	FTIR results of BS-CMCLI after Cr (VI) sorption at pH 3 and 11.....	177
Figure 7.106.	Effect of initial concentration on sorption of Cr (VI) with CLI.....	178
Figure 7.107.	Effect of initial concentration on sorption of Cr (VI) with AMCLI .....	178
Figure 7.108.	Effect of initial concentration on sorption of Cr (VI) with CMCLI.....	179
Figure 7.109.	Effect of initial concentration on sorption of Cr (VI) with EC-	

	CLI.....	179
Figure 7.110.	Effect of initial concentration on sorption of Cr (VI) with BS- CLI.....	180
Figure 7.111.	Effect of initial concentration on sorption of Cr (VI) with EC- AMCLI.....	180
Figure 7.112.	Effect of initial concentration on sorption of Cr (VI) with BS- AMCLI .....	181
Figure 7.113.	Effect of initial concentration on sorption of Cr (VI) with EC- CMCLI .....	181
Figure 7.114.	Effect of initial concentration on sorption of Cr (VI) with BS- CMCLI .....	182
Figure 7.115.	Effect of agitation speed on sorption of Cr (VI) with CLI.....	183
Figure 7.116.	Effect of agitation speed on sorption of Cr (VI) with AMCLI.....	183
Figure 7.117.	Effect of agitation speed on sorption of Cr (VI) with CMCLI.....	184
Figure 7.118.	Effect of agitation speed on sorption of Cr (VI) with EC- CLI.....	184
Figure 7.119.	Effect of agitation speed on sorption of Cr (VI) with BS- CLI.....	185
Figure 7.120.	Effect of agitation speed on sorption of Cr (VI) with EC- AMCLI.....	185
Figure 7.121.	Effect of agitation speed on sorption of Cr (VI) with BS- AMCLI.....	186
Figure 7.122.	Effect of agitation speed on sorption of Cr (VI) with EC- CMCLI .....	186
Figure 7.123.	Effect of agitation speed on sorption of Cr (VI) with BS- CMCLI.....	187
Figure 7.124.	Effect of temperature on sorption of Cr (VI) with CLI.....	188
Figure 7.125.	Effect of temperature on sorption of Cr (VI) with AMCLI.....	188
Figure 7.126.	Effect of temperature on sorption of Cr (VI) with	



	CMCLI.....	189
Figure 7.127.	Effect of temperature on sorption of Cr (VI) with EC- CLI.....	189
Figure 7.128.	Effect of temperature on sorption of Cr (VI) with BS- CLI.....	190
Figure 7.129.	Effect of temperature on sorption of Cr (VI) with EC- AMCLI.....	190
Figure 7.130.	Effect of temperature on sorption of Cr (VI) with BS- AMCLI.....	191
Figure 7.131.	Effect of temperature on sorption of Cr (VI) with EC- CMCLI.....	191
Figure 7.132.	Effect of temperature on sorption of Cr (VI) with BS- CMCLI.....	192
Figure 7.133.	Effect of particle size on sorption of Cr (VI) with CLI.....	193
Figure 7.134.	Effect of particle size on sorption of Cr (VI) with AMCLI.....	193
Figure 7.135.	Effect of particle size on sorption of Cr (VI) with CMCLI.....	194
Figure 7.136.	Effect of particle size on sorption of Cr (VI) with EC- CLI.....	194
Figure 7.137.	Effect of particle size on sorption of Cr (VI) with BS- CLI.....	195
Figure 7.138.	Effect of particle size on sorption of Cr (VI) with EC- AMCLI.....	195
Figure 7.139.	Effect of particle size on sorption of Cr (VI) with BS- AMCLI.....	196
Figure 7.140.	Effect of particle size on sorption of Cr (VI) with EC- CMCLI.....	196
Figure 7.141.	Effect of particle size on sorption of Cr (VI) with BS- CMCLI.....	197
Figure 7.142.	The steps in PLR model.....	199
Figure 7.143.	Comparison of theoretical and experimental concentration	

	decay curves for (a) CLI (b) AMCLI (c) CMCLI (d) ECCLI (e) BSCLI (f) ECAMCLI (g) BSAMCLI (h) ECCMCLI (i) BSCMCLI .....	213
Figure 7.144.	Comparison of theoretical and experimental Weber-Morris model results for (a) CLI (b) AMCLI (c) CMCLI (d) ECCLI (e) BSCLI (f) ECAMCLI (g) BSAMCLI (h) ECCMCLI (i) BSCMCLI .....	217
Figure 7.145.	Comparison of theoretical and experimental pseudo first order model results for (a) CLI (b) AMCLI (c) CMCLI (d) ECCLI (e) BSCLI (f) ECAMCLI (g) BSAMCLI (h) ECCMCLI (i) BSCMCLI .....	220
Figure 7.146.	Comparison of theoretical and experimental pseudo second order model results for (a) CLI (b) AMCLI (c) CMCLI (d) ECCLI (e) BSCLI (f) ECAMCLI (g) BSAMCLI (h) ECCMCLI (i) BSCMCLI.....	224
Figure 7.147.	Equilibrium isotherm for Cr (VI) sorption with CLI (a) 25 °C (b) 40 °C.....	231
Figure 7.148.	Equilibrium isotherm for Cr (VI) sorption with AMCLI (a) 25 °C (b) 40 °C.....	232
Figure 7.149.	Equilibrium isotherm for Cr (VI) sorption with CMCLI (a) 25 °C (b) 40 °C.....	233
Figure 7.150.	Equilibrium isotherm for Cr (VI) sorption with EC-CLI (a) 25 °C (b) 40 °C.....	234
Figure 7.151.	Equilibrium isotherm for Cr (VI) sorption with BS-CLI (a) 25 °C (b) 40 °C.....	235
Figure 7.152.	Equilibrium isotherm for Cr (VI) sorption with EC-AMCLI (a) 25 °C (b) 40 °C.....	236
Figure 7.153.	Equilibrium isotherm for Cr (VI) sorption with BS-AMCLI (a) 25 °C (b) 40 °C.....	237
Figure 7.154.	Equilibrium isotherm for Cr (VI) sorption with EC-CMCLI (a) 25 °C (b) 40 °C.....	238
Figure 7.155.	Equilibrium isotherm for Cr (VI) sorption with BS-CMCLI (a) 25 °C (b) 40 °C.....	239

## LIST OF TABLES

<b><u>Table</u></b>	<b><u>Page</u></b>
Table 2.1. Properties of Certain Cations.....	9
Table 2.2. Examples of the cationic, anionic, and non-ionic surfactants.....	13
Table 2.3. Critical Micelle Concentrations (CMC) values of surfactants.....	13
Table.3.1. FTIR bands observed in spectra of <i>E. coli</i> , <i>P. aeruginosa</i> , <i>B. subtilis</i> , <i>S. aureus</i> and <i>S. epidermidis</i> .....	28
Table 4.1. Natural and synthetic sorbents used for Cr (VI) removal.....	38
Table 4.2. Surfactant modified zeolites and clays used for Cr (VI) removal.....	40
Table 4.3. Bacterial sorbents used for Cr (VI) removal.....	42
Table 4.4. Algal sorbents used for Cr (VI) removal.....	42
Table 4.5. Fungal sorbents used for Cr (VI) removal.....	43
Table 4.6. Bacterial species supported materials used in Cr (VI) removal.....	44
Table 5.1. The basic characteristics of the physical and chemical sorption.....	47
Table 5.2. Empirical correlations for external mass transfer.....	64
Table 6.1. Experimental conditions of batch sorption.....	91
Table 7.1. EDS of CLI, CMCLI and AMCLI.....	94
Table 7.2. Chemical compositions of CLI, CMCLI and AMCLI.....	100
Table 7.3. EDS of CLI sample after bacteria attachment.....	117
Table 7.4. EDS of CMCLI samples after bacteria attachment.....	118
Table 7.5. EDS of AMCLI samples after bacteria attachment.....	118
Table 7.6. Zeta potential values of sorbents in 10 mg/L Cr (VI) solution at pH 5 and 6.....	127
Table 7.7. Cr(VI) removal percentage values of all sorbents.....	139
Table 7.8. EDS of CLI, AMCLI and CMCLI after Cr (VI) sorption.....	140
Table 7.9. EDS of bacteria loaded clinoptilolite rich minerals after Cr (VI) sorption.....	141
Table 7.10. EDS of bacteria loaded anionic modified clinoptilolite rich minerals after Cr (VI) sorption.....	141
Table 7.11. EDS of bacteria loaded cationic modified clinoptilolite rich minerals after Cr (VI) sorption.....	142

Table 7.12. Zeta potential values of sorbents in 10 mg/L Cr (VI) solution at pH 3 and 11.....	152
Table 7.13. Cr (VI) removal percentage values of all sorbents at pH 3 and 11.....	166
Table 7.14. EDS of clinoptilolite rich minerals after Cr (VI) sorption at pH 3 and 11.....	166
Table 7.15. EDS of anionic and cationic surfactant modified clinoptilolite rich mineral after Cr (VI) sorption at pH 3 and 11.....	167
Table 7.16. EDS of <i>E. coli</i> and <i>B. subtilis</i> loaded clinoptilolite rich mineral after Cr (VI) sorption at pH 3 and 11.....	168
Table 7.17. EDS of <i>E. coli</i> and <i>B. subtilis</i> loaded anionic surfactant modified clinoptilolite rich mineral after Cr (VI) sorption at pH 3 and 11.....	168
Table 7.18. EDS of <i>E. coli</i> and <i>B. subtilis</i> loaded cationic surfactant modified clinoptilolite rich mineral after Cr (VI) sorption at pH 3 and 11.....	169
Table 7.19. The values of model constants at different conditions for CLI.....	202
Table 7.20. The values of model constants at different conditions for AMCLI.....	203
Table 7.21. The values of model constants at different conditions for CMCLI.....	204
Table 7.22. The values of model constants at different conditions for ECCLI.....	205
Table 7.23. The values of model constants at different conditions for BSCLI.....	206
Table 7.24. The values of model constants at different conditions for ECAMCLI...	207
Table 7.25. The values of model constants at different conditions for BSAMCLI...	208
Table 7.26. The values of model constants at different conditions for ECCMCLI...	209
Table 7.27. The values of model constants at different conditions for BSCMCLI....	210
Table 7.28. Values of Biot Number for CLI, AMCLI and CMCLI.....	227
Table 7.29. Values of Biot Number for ECCLI and BSCLI.....	228
Table 7.30. Values of Biot Number for ECAMCLI and BSAMCLI.....	228
Table 7.31. Values of Biot Number for ECCMCLI and BSCMCLI.....	229
Table 7.32. Parameters of the Langmuir isotherm models.....	230
Table 7.33. Parameters of the Freundlich isotherm models.....	230
Table 7.34. Thermodynamic parameters for Cr (VI) sorption on the sorbents.....	241
Table 7.35. The activation energy values of Cr (VI) sorption onto the sorbents.....	242

# CHAPTER 1

## INTRODUCTION

Clinoptilolite rich mineral is a crystalline hydrated aluminosilicate. The framework structure is made up of  $AlO_4$  and  $SiO_4$  tetrahedra and three types of channels (A, B and C). Water and exchangeable cations such as magnesium, sodium, calcium and potassium also exist in its structure. It has high potential for separation, purification, adsorption and ion exchange depending on the type of exchangeable cations and their specific positions within the framework structure (Mumpton, 1999; Armenta et al., 2003; Ackley et al., 2003; Özkan and Ülkü, 2005). Additionally, high selective cation exchange capacity makes clinoptilolite rich mineral useful in waste water treatment especially in the removal of heavy metal and ammonium (Ülkü, 1984; Zamzow and Murphy, 1992; Alsoy, 1993; Şenatalar and Sirkecioğlu, 1995; Top, 2001; Türkmen, 2001; Inglezakis et al., 2003; Can, 2004; Cansever, 2004; Karapınar, 2009; Motsi et al., 2009; Huang et al., 2010). It is known that not only ammonium and heavy metals, but also anions and organic compounds cause in environmental pollution. Therefore, removal of anions and organic compounds is important and requires cost effective technologies. For the removal of these compounds, clinoptilolite rich mineral is not as efficient as it would be in heavy metal and ammonium removal. In order to improve its affinity toward these compounds clinoptilolite rich mineral has been modified with surfactants. The previous studies focused on using cationic surfactants. Among the cationic surfactants, Hexadecyltrimethylammonium bromide (HDTMA-Br) is widely used in the modification of clinoptilolite rich mineral (Haggerty and Bowman, 1994; Li and Bowman 1998; Armağan et al., 2003; Warchol et al., 2006; Hossein et al., 2007; Karadağ et al., 2007; Miranda and Olguin, 2007; Chutia et al., 2009; Cordoves et al., 2008; Rozic et al., 2009).

Apart from these application fields, metal exchanged clinoptilolite rich mineral and surfactant modified clinoptilolite rich mineral are also used in the removal of microorganism. Studies related to the removal of microorganism have become important since most of microorganism cause healthcare associated infections such as chronic lung infections, meningitis and urinary infections. Previous studies related to

clinoptilolite rich minerals indicated that  $\text{Cu}^{2+}$ ,  $\text{Fe}^{3+}$ ,  $\text{Ni}^{2+}$ ,  $\text{Zn}^{2+}$  and  $\text{Ag}^+$  exchanged clinoptilolite samples were effective in the removal of *S. marcescens*, *P. aeruginosa*, *E. coli* and *S. fecaecalis* and surfactant modified clinoptilolite rich mineral was promising material for the removal of *E. coli*, *B. subtilis* and *G. intestinalis* (Kallo, 2001; Milan et al., 2001; Top, 2001; Schulze, 2002; Bowman, 2003; Cansever, 2004; Lehner, 2004; Rust, 2006).

In recent years, the investigation on the chromium removal has gained much attention since it causes lung cancer, gastrointestinal disorders, dermatitis and kidney damage in humans. In addition it is toxic to other organisms. Reduction, precipitation, nano-ultrafiltration and membrane technologies are among the waste treatment methods applied for chromium (VI) removal. But due to concerns related to high energy input and large amounts of secondary wastes produced, further research on alternative methods is needed. Sorption with natural, synthetic and biologically based sorbents has been widely used as alternative method because of their high removal efficiencies and low-cost technologies. In recent years, bacteria species supported materials have been used as alternative material. Most of the studies focused on using *E. coli* supported granular activated carbon, kaolin and NaY. It has been found that the affinities of granular activated carbon, kaolin and NaY zeolite were improved by the attachment of bacteria species on the material surface (Quintelas et al., 2008, 2009; Gabr et al., 2009).

In this study, the clinoptilolite rich mineral samples were modified with cationic and anionic surfactant. Hexadecyltrimethylammonium bromide (HDTMA) was used as cationic surfactant while sodium dodecyl sulfate (SDS) was used as anionic surfactant. Various characterization methods such as Scanning Electron Microscope (SEM), X-Ray Diffraction (XRD), Fourier Transform IR (FTIR) and Zeta Potential for clinoptilolite and surfactant clinoptilolite rich mineral were investigated. Previous studies indicated that information related to the bacteria removal with clinoptilolite rich minerals is limited and thus further investigations are needed. For this reason, the potential value of clinoptilolite rich mineral in the removal of gram positive (*B. subtilis*, *S. aureus*, *S. epidermidis*) and gram negative bacteria (*E. coli*, *P. aeruginosa*) were investigated. Previous studies indicated that surfactant modified clinoptilolite rich mineral was promising material for the removal of *E. coli*, *B. subtilis* and *G. intestinalis*. 100 % *E. coli*, 75.5 % *B. subtilis* and 100 % *G. intestinalis* cysts removal was obtained with HDTMA modified clinoptilolite rich mineral (Schulze, 2002; Lehner, 2004; Rust et al., 2006). However, the removal abilities of the cationic surfactant modified clinoptilolite

rich minerals towards *S. aureus*, *S. epidermidis* and *P. aeruginosa* are unknown. For this reason, bacteria removal performances of the cationic surfactant modified clinoptilolite rich mineral towards these bacteria were determined. Moreover, there is no study related to the removal of bacteria by anionic surfactant modified clinoptilolite rich minerals. The removal performances of the anionic surfactant modified clinoptilolite rich mineral were investigated. The proposed mechanisms for the bacteria attachment were discussed. Additionally, the performance of clinoptilolite, surfactant modified clinoptilolite rich mineral, bacterial loaded forms for Cr (VI) sorption were also determined.

The effects of the parameters such as pH, initial concentration, agitation speed, particle size and temperature were investigated to understand the mechanism of the Cr (VI) sorption onto these sorbents. In order to assess the contribution from the sorption steps, sorption kinetic models based on reaction and diffusion models were used. Two methods of determining the external mass transfer coefficients were used, one based on the Mathew-Weber model and the other on the Furusawa-Smith model. Intraparticle diffusion rate constant was determined from Weber-Morris model. Pseudo first and second order rate constants were also calculated. Equilibrium data were analyzed by two isotherms, namely Langmuir and Freundlich isotherm. Various thermodynamic activation parameters such as enthalpy of sorption ( $\Delta H$ ), Gibbs energy change ( $\Delta G$ ) and entropy ( $\Delta S$ ) was estimated. Additionally, activation energy of Cr (VI) sorption was also determined.

## CHAPTER 2

### ZEOLITES

Zeolites have been recognized for more than 200 years, but only during the middle of the 20th century have attracted the attention of scientists and engineers who demonstrated the technological importance of zeolites in several fields such as adsorption, ion exchange, separation and purification. The main reason of interest for natural zeolite-bearing materials is the increasing demand of low-cost sorbents.

Zeolites are very effective sorbents in removal of heavy metal and ammonium. It is known that not only ammonium and heavy metals, but also anions and organic compounds cause in environmental pollution. Therefore, removal of anions and organic compounds is important and requires cost effective technologies. For the removal of these compounds, zeolites are not as efficient as they would be in heavy metal and ammonium removal. In order to improve their affinities toward anions and organic compounds, zeolites have been modified with surfactants. In this chapter, general information about zeolites and surfactant modified zeolites is given and their potential applications are discussed. Various characterization methods such as Scanning Electron Microscope (SEM), X-Ray Diffraction (XRD) and Fourier Transform IR (FTIR) for zeolites and surfactant modified zeolites are also investigated.

#### 2.1. Zeolites

Zeolites are composed of three dimensional frameworks of aluminosilicates tetrahedral where  $\text{AlO}_4$  and  $\text{SiO}_4$  tetrahedra are linked to each other by sharing the oxygen atoms (Mumpton, 1978). This framework contains channels and interconnected voids which are occupied by exchangeable cation and water molecules. The aluminosilicates tetrahedral structure and exchangeable cations within the zeolite framework are represented in Figure 2.1. The isomorphic substitution of silicon ( $\text{Si}^{4+}$ ) by aluminum ( $\text{Al}^{3+}$ ) causes a negative charge in the framework structure and it is balanced by exchangeable cations such as  $\text{Na}^+$ ,  $\text{K}^+$ ,  $\text{Ca}^{2+}$  and  $\text{Mg}^{2+}$ . These cations are



quite mobile and they can be exchanged by other cations. These properties enable them to be used in several applications.

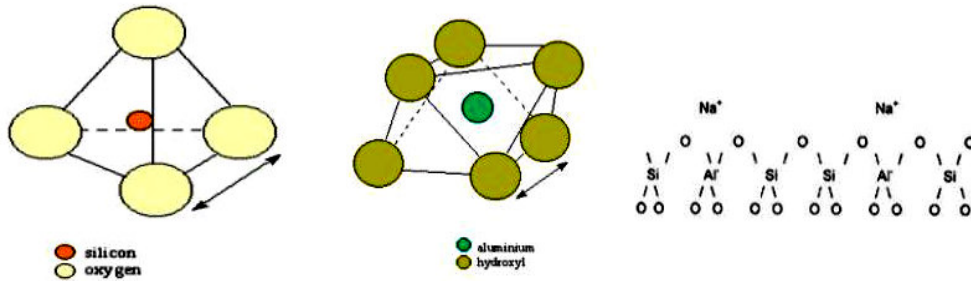


Figure 2.1. Aluminosilicates tetrahedral structure and exchangeable cations within the zeolite framework

The structural formula of a zeolite is best expressed by the idealized formula for the crystallographic unit cell as:  $M_{x/n}[(AlO_2)_x(SiO_2)_y].wH_2O$  where  $M$  is the cation of valence  $n$ ,  $w$  is the number of water molecules and the ratio  $y/x$  varies between 1 and 5 depending on the structure (Breck, 1974).

Zeolites may be either obtained from mineral deposits or synthesized. Although there have been more than 150 species of synthetic zeolite, Zeolite A, X, Y, Ferrierite, ZSM-5, MCM-41 and Beta have been widely used. There are more than 50 distinct types of zeolite mineral that occur in nature. However, only eight of them which are analcime, chabazite, clinoptilolite-heulandite, erionite, ferrierite, laumontite, mordenite and phillipsite have a considerable value as sedimentary deposits. Among these species; clinoptilolite is the most abundant natural zeolite that occurs in large sedimentary deposits.

## 2.2. Clinoptilolite Rich Natural Zeolites

Clinoptilolite is a member of the heulandite group of natural zeolites and isostructural with heulandite. Clinoptilolite preserves its crystal structure up to 700 °C whereas heulandite transforms into two phases at about 230 °C and becomes non-crystalline at about 350 °C (Tsitsishvili et al., 1992). Si/Al ratio is in the range of 4.25-5.25 for clinoptilolite whereas this ratio is in the range of 2.7-4 for heulandite.

The framework of clinoptilolite consists of three channels. Channel A (10 member ring) and channel B (8 member ring) are perpendicularly intersected by channel C (8 member ring). The approximate channel sizes are  $4.4 \times 7.2 \text{ \AA}$ ,  $4.1 \times 4.7 \text{ \AA}$  and  $4.0 \times 5.5 \text{ \AA}$  for A, B and C channels, respectively. Figure 2.2 illustrates the channel and crystal structure of clinoptilolite (Ackley and Yang, 1991).

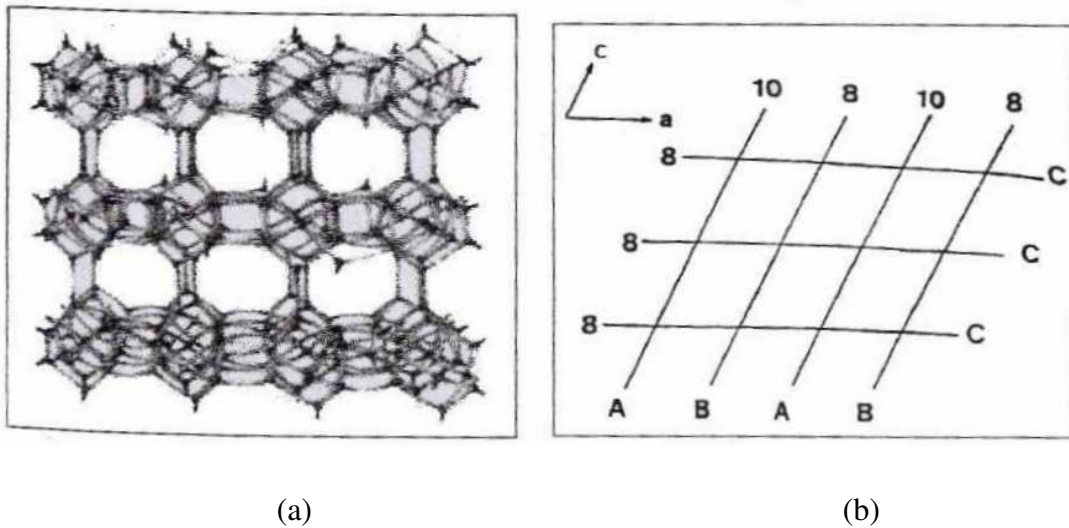


Figure 2.2. (a) Model framework for structure of clinoptilolite. (b) Orientation of clinoptilolite structure (Source: Ackley and Yang, 1991)

In these channels, there are four main sites which are shown in Figure 2.3. M1 is located in channel A and coordinated with two framework oxygen and five water molecules. Major cations in this site are  $\text{Ca}^{2+}$  and  $\text{Na}^+$ . M2 is situated in channel B and coordinated by three framework oxygen and five water molecules. Major cations in M2 are  $\text{Ca}^{2+}$  and  $\text{Na}^+$ . M3 is located in channel C coordinated by six framework oxygen atoms and three water molecule.  $\text{K}^+$  is the main cation in this site. M4 is situated in the center of channel A which differs from M1. This site is coordinated by six water molecules and  $\text{Mg}^{2+}$  is main cation in M4. Cation exchange and adsorption properties are strongly influenced by the type, number and location of the cations in these channels.

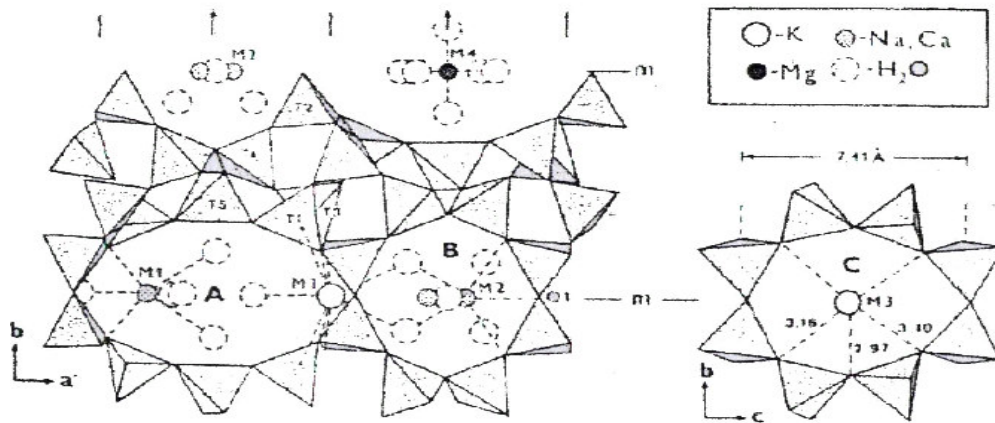


Figure 2.3. Main cation positions in the clinoptilolite structure  
(Source: Ackley and Yang, 1991)

### 2.3. Application of Zeolites

Zeolites are promising materials because of their unique adsorption, cation exchange, catalytic, hydration and dehydration properties. Therefore, they are widely used in several applications which are summarized below.

Zeolites are widely used as catalyst in the cracking, isomerization and hydrocarbon synthesis, petrochemical refining and production. Metal supported zeolites such as copper, platinum and cobalt loaded zeolites can serve as oxidation and reduction catalyst. For example, copper loaded ZSM5 and cobalt supported mordenite are widely used in  $\text{NO}_x$  reduction (Cheng and Wang, 1994; Shichi et al., 1998). Platinum loaded zeolite A and mordenite is especially used in the removal of carbon monoxide from hydrogen-rich fuels (Igarashi et al., 1997). Today, clinoptilolite and chabazite is utilized as bitumen cracking agent (Junaid et al., 2011).

High selective cation exchange capacity makes zeolites useful in several applications such as ammonium and heavy metal removal from water and wastewater. Several studies reported the effective use of natural zeolite for ammonium removal (Ülkü, 1984; Alsoy, 1993; Şenatarlar and Sirkecioğlu, 1995; Cansever, 2004; Karapınar, 2009; Huang et al., 2010) and heavy metal removal (Zamzow and Murphy, 1992; Top, 2001; Türkmen, 2001; Inglezakis et al., 2003; Can, 2004; Akdeniz, 2009; Motsi et al., 2009). The studies indicated that ammonium and heavy metal exchange capacity of

zeolites vary widely depending on the particle size of the zeolite, solid: solution ratio, initial concentration of the solution, presence of competing cation, pH of the solution, temperature and physical-chemical properties of zeolite minerals. Heavy metal exchange capacity of zeolites also strongly depends on charge of the ion, ionic radius and degree of hydration. There is a relation between ionic charge and hydration enthalpy. The higher charge shows the higher enthalpy. A large ion charge/size ratio results in an increase in the hydration energy. An increase in the ionic radius is accompanied by a decrease in the hydration enthalpy. If an ionic radius is compared with the free dimensions of the clinoptilolite channels (4.0x5.5-4.4x7.2 Å), it is apparent that all of the unhydrated ions can readily pass through the channels, but since hydrated ions are approximately the same size as the channel dimensions, they may exchange only with difficulty (Semmens et al., 1975). Eisenman's model (Eisenman, 1962) says that selectivity of exchange cations is accounted for only in terms of their hydration free energies and their energies of electrostatic interaction with the zeolite fixed anions. He separated the free energy of ion exchange reaction into two parts. The first part represents the difference between the free energy of the ions in zeolite while second part represents the free energy differences of hydration of the ions in the solution. If the electrostatic fields in zeolite are strong, then the first part dominates and small ions are preferred. Strong electrostatic fields occur in zeolites with a high framework charge and correspondingly low Si/Al ratio. However, if these electrostatic fields are weak (as in zeolites with a high Si/Al ratio), the hydration free energy is more important. So, weakly hydrated cations are preferred. The low Si/Al ratio provides a weak anionic field within the zeolite. Consideration of Eisenman's model in the case of exchange on zeolite in the presence of weakly anionic field indicates that selectivity is predominantly determined by the free energies of hydration of the competing cations. According to Eisenman's theory, the free energies of hydration listed in Table 2.1 indicate that copper with the largest hydration energy, prefers the solution phase where it may satisfy its hydration requirements, and barium, with least hydration energy, prefers the zeolite phase.

Table 2.1. Properties of Certain Cations  
(Source: Semmens et al., 1975)

Cation	Ionic Radius (Å)	Hydrated Radius (Å)	Free Energy of Hydration (kcal/gr ion)
Ba <sup>2+</sup>	1.43	4.04	-315.1
Cd <sup>2+</sup>	1.03	4.26	-430.5
Cu <sup>2+</sup>	0.82	4.19	-498.7
Pb <sup>2+</sup>	1.32	4.01	-357.8
Zn <sup>2+</sup>	0.83	4.30	-484.6
Na <sup>+</sup>	0.98	3.58	-98.2
K <sup>+</sup>	1.30	3.31	-76.67
Mg <sup>2+</sup>	0.65	4.28	-459.04
Ca <sup>2+</sup>	0.99	4.12	-380.22

The adsorption properties of the zeolites are strongly dependent on framework composition. Small ions and molecules can pass through the zeolite channels, but large ions and molecules are excluded. This ion selectivity, based on size, is known as molecular sieving which enables them to be used in gas separation applications such as ammonia, hydrogen sulfide, carbon monoxide, carbon dioxide, sulfur dioxide, water vapor, oxygen, nitrogen and ethanol vapor. Sirkecioğlu et al. (1995) studied the adsorption of H<sub>2</sub>S and SO<sub>2</sub> on cation exchanged clinoptilolite. They stated that the highest adsorption capacities for both gases were obtained with the sample in its H-form. Narin (2001) investigated the adsorption of carbon monoxide on clinoptilolite. The equilibrium constants (Henry's law constants, K) were calculated in the range of 40-952 and were found to be in good agreement with the results in the literature. Armenta et al. (2003) studied the adsorption kinetics of pure CO<sub>2</sub>, O<sub>2</sub>, N<sub>2</sub> and CH<sub>4</sub> on clinoptilolite. It has been found that the adsorption selectivity decreased in the following order: CO<sub>2</sub>>N<sub>2</sub>> CH<sub>4</sub>. The diffusion mechanisms of water vapor in clinoptilolite and acid treated clinoptilolite were investigated by Özkan and Ülkü (2005, 2008). The amount of water vapor adsorbed by the zeolite slightly increased after acid treatment. Karsheva and Ivanova (2010) investigated ethanol vapor adsorption on clinoptilolite and HCl treated clinoptilolite. Their results indicated that higher adsorption capacities were obtained with HCl treated clinoptilolite samples.

Apart from these application fields, zeolites are used as slow release fertilizers and dietary supplements. By using clinoptilolite-rich tuff as a soil conditioner, significant increases in the yields of wheat (13–15 %), eggplant (19–55 %), apples (13–

38 %), and carrots (63 %) were reported (Mumpton, 1999). The previous studies about animal nutrition indicated that the animals grew faster and their product had better quality when they fed with clinoptilolite added fodder (Mumpton, 1999). Zeolites are being used as building stone, lightweight aggregate and pozzolans in building industry (Mumpton, 1999). They are also used as inorganic fillers and stabilizers in polymer industry. Addition of zeolite into polymer causes to increase the resistance of the crack propagation which provides better mechanical properties (Erdoğan et al., 2008; Demir et al., 2008). Zeolites are used as thermal stabilizers to prevent decomposition of polyvinylchloride (PVC) (Atakul et al., 2004). Zeolite addition in PVC not only enhances the thermal stabilization of PVC but also it effects the mechanical properties of PVC. Young modulus of PVC-zeolite foams increases with increasing the concentration of zeolite in PVC foam. The addition of 20% (by weight) zeolite increases Young Modulus value from 1.53 to 8.67 N/mm (Demir, 2004).

In recent years, the usages of zeolites in biomedical fields have been gained much attention. Rodriguez-Fuentes et al. (1997) developed antidiarrheic drug based on purified clinoptilolite rich mineral. The theoretical study of metronidazole adsorption on clinoptilolite was performed by Lam et al. (2001). Metronidazole is a highly effective drug for the treatment of intestinal and extra intestinal amoebiasis, giardiasis, and trichomoniasis. It has been found that the interaction of metronidazole with clinoptilolite consisted of hydrogen bond and columbic interactions. The antacid drug was formulated as a chewing tablet allowing the direct interaction of the clinoptilolite with the gastric juice (Rodriguez-Fuentes et al., 2006). Pharmacological studies showed the neutralizing effect of clinoptilolite on the excess of HCl present in synthetic and natural gastric juices.

Pavelic et al. (2001, 2002) studied the use of finely ground clinoptilolite as a potential adjuvant in anticancer therapy. Clinoptilolite treatment of mice and dogs suffering from a variety of tumor types led to improvement in the overall health status, prolongation of life-span, and decrease in tumors size. Local application of clinoptilolite to skin cancers of dogs effectively reduced tumor formation and growth. Additionally, toxicological studies on mice and rats demonstrated that the treatment did not have negative effects. The results indicated that clinoptilolite treatment might affect cancer growth by attenuating survival signals and inducing tumor suppressor genes in treated cells. Seler and Pivac (2003) investigated the ex vivo effect of clinoptilolite on the seratogenic receptors (binding of  $^3\text{H}$ -8-OH-DPAT to  $5\text{-HT}_{1A}$  and  $^3\text{H}$ -5-HT to  $5\text{-HT}_{1B}$ ) in

the brain of mice with mammary carcinoma. The reduction in binding of  $^3\text{H}$ -8-OH-DPAT to 5-HT<sub>1A</sub> in mammary carcinoma bearing mice when compared to control mice fed with standard food was observed. The addition of clinoptilolite to the feed of mice stopped the decrease in 5-HT<sub>1A</sub> receptors binding indicating a possible beneficial effect of clinoptilolite.

Synthetic and natural zeolites have been used in the removal of microorganism. The potential of natural zeolites to remove enteric bacteria and viruses from drinking water has been studied (Kallo, 2001). The results revealed that *E. coli*, poliovirus, coxsackie virus and bacteriophages from drinking water were effectively removed by Al<sub>2</sub>(SO<sub>4</sub>)<sub>3</sub> coagulant and clinoptilolite. Efficient microorganism removal was resulted from the formation of microorganism-clinoptilolite-coagulant complexes. The study which was performed by Milan et al., 2001 indicated that highest reductions of *S. marcescens* and *P. aeruginosa* were observed with Cu<sup>2+</sup>, Fe<sup>3+</sup>, Ni<sup>2+</sup> and Zn<sup>2+</sup> exchanged natural zeolites. Cansever (2004) studied the treatment of the domestic wastewater by using natural zeolites. The results showed that microbial flocs and *G. intestinalis* attached to the surface of the clinoptilolite rich minerals indicating clinoptilolite might be used for the removal of microbiological constituents from domestic wastewater effluent. Another study which was related to the selective adsorption of bacterial cells onto synthetic zeolites was studied by Kubato et al., (2008). Their results demonstrated that Na-Beta and H-Y zeolites were useful in the separation of the bacteria mixture which was composed of *E. coli*, *B. subtilis* and *S. aureus*.

Several investigations have been carried out concerning the use of synthetic and natural zeolites: A, X, Y, Z and clinoptilolite supporting metal ions as bactericides (Rivera- Garza et al., 2000; Top, 2001; Zhang et al., 2009). These studies implied that silver exchanged natural and synthetic zeolites are promising materials due to their affinities for the most pathogens such as *E. coli*, *S. fecaecalis* and *P. aeruginosa*.

## **2.4. Surfactant Modified Zeolites**

As mentioned before, natural zeolites usually have little affinity for anions and organic compounds in aqueous solution. One of the methods for improving their affinities towards these compounds is the surfactant modification.

Surfactants are wetting agents which reduce the surface tension of liquid and the interfacial tension between two liquids. They are widely used in many industries such as petroleum, cosmetic and food industries because of their remarkable ability to influence the properties of surfaces and interfaces. Molecular structure of surfactant, which is represented in Figure 2.4, is made up of a water soluble (hydrophilic) and a water insoluble (hydrophobic) parts. The hydrophobic part consists of an uncharged carbohydrate group that can be straight, branched, cyclic or aromatic. Depending on the nature of the hydrophilic part, surfactants are classified as cationic, anionic and non-ionic. In the cationic surfactant, the hydrophilic part is positively charged while in anionic surfactant, the hydrophilic part is negatively charged. Nonionic surfactants do not have an electrical charge. Examples of the cationic, anionic, and non-ionic surfactants are listed in Table 2.2.

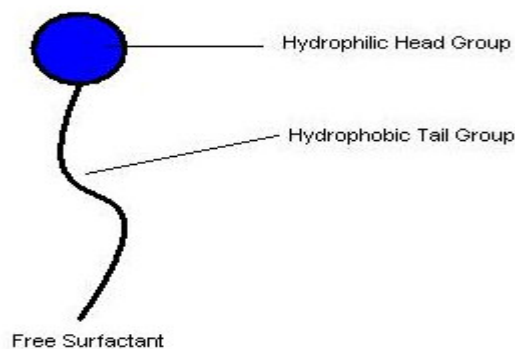
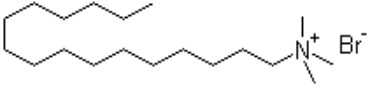


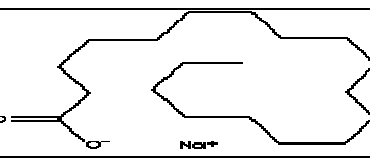
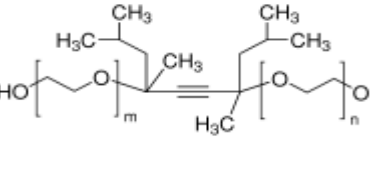


Figure 2.4. Molecular structure of surfactant



Table 2.2. Examples of the cationic, anionic, and non-ionic surfactants

Class	Examples	Structures
Cationic	Hexadecyltrimethylammonium bromide (C <sub>19</sub> H <sub>42</sub> BrN)	
	Cetylpyridinium chloride (C <sub>21</sub> H <sub>38</sub> NCl)	
Anionic	Sodium dodecyl sulfate (C <sub>12</sub> H <sub>25</sub> SO <sub>4</sub> Na)	
	Sodium stearate CH <sub>3</sub> (CH <sub>2</sub> ) <sub>16</sub> COONa	
Non-ionic	2,4,7,9-Tetramethyl-5-decyne-4,7-diol ethoxylate (C <sub>14</sub> H <sub>26</sub> O <sub>2</sub> )	

Surfactant modification is strongly influenced by the degree of surfactant adsorption on solid surface. A bilayer or monolayer is formed when the surfactant concentration is higher or less than its critical micelle concentration (CMC). The values of CMC for different types of surfactants are given in Table 2.3. If the surfactant concentration in solution exceeds CMC, the hydrophobic tails of the surfactant molecules will associate to form a bilayer. Surfactant molecules form a monolayer at the solid–aqueous interface via strong Columbic interaction below its CMC. The formation of monolayer and bilayer is represented in Figure 2.5.

Table 2.3. Critical Micelle Concentrations (CMC) values of surfactants

Surfactant	CMC
Hexadecyltrimethylammonium bromide	9.2*10 <sup>-4</sup> M
Cetylpyridinium chloride	12.4*10 <sup>-4</sup> M
Sodium Dodecyl Sulfate	8.3*10 <sup>-3</sup> M
Sodium Stearate	4*10 <sup>-4</sup> M
Polysorbate 80	0.12*10 <sup>-4</sup> M

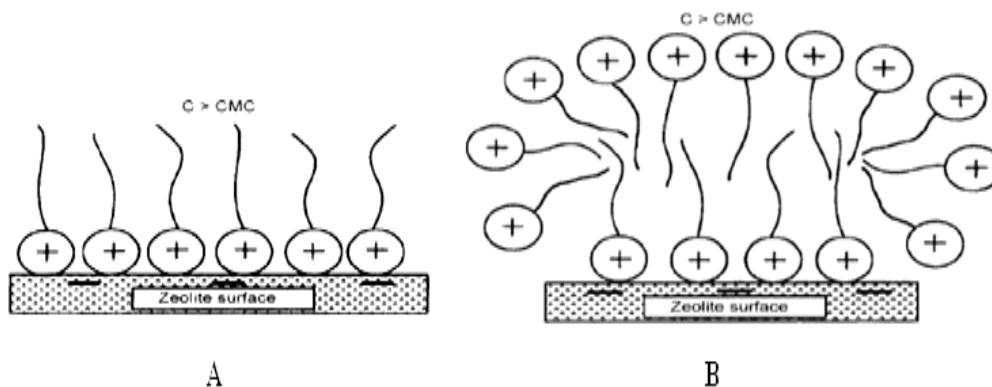


Figure 2.5. Formation of a) monolayer b) bilayer on the solid surface  
(Source: Haggerty and Bowman, 1994)

Modification of clay and zeolites by sorption of surfactant has been studied during the past years. Relatively few studies have been made for the modification of clay minerals with anionic surfactant. However, modification of zeolite with anionic surfactant has not been subject to study. Sodium dodecyl sulphate and sodium dodecyl benzene sulfonate are used as anionic surfactant in the modification step. On the other hand, there exist number of studies which focused on the usage of cationic surfactants for the modification of zeolite and clay minerals. Hexadecyltrimethylammonium bromide, Cetylpyridinium bromide and Octadecylammoniumacetate are widely used as cationic surfactants. Among these cationic surfactants, hexadecyltrimethylammonium bromide (HDTMA-Br) is widely used in the modification of natural zeolites especially clinoptilolite rich minerals. The diameter of carbohydrate chain of hexadecyltrimethylammonium cation is  $4 \text{ \AA}$ , the length is  $23 \text{ \AA}$ , and the diameter of the polar head  $-\text{N}^+(\text{CH}_3)_3$  is  $6.94 \text{ \AA}$ , which makes it too large to penetrate the largest channels of clinoptilolite. Since it is the long hydrocarbon chain, it does not enter the channels in the clinoptilolite structure. When the surfactant is adsorbed on the zeolite surface, the formations of monolayer or bilayer structure on the zeolite surface are observed depending on the surfactant concentrations to be below or above their CMC values. Under these configurations, the clinoptilolite rich mineral reverse its surface charges and behaves as anion exchangers (Haggerty and Bowman, 1994; Cordoves et al., 2008; Rozic et al., 2009).

## 2.5. Application of Surfactant Modified Zeolites

Surfactant modified zeolite (SMZ) is a promising material for the removal of anions, organic compounds and reactive dyes. It has been known that hexavalent chromium ion (VI) is highly toxic metal which is mainly found as oxyanions forms such as chromate ( $\text{CrO}_4^{2-}$ ), dichromate ( $\text{Cr}_2\text{O}_7^{2-}$ ) in the solution. A lot of investigations have been carried out to investigate the removal of Cr (VI) using surfactant modified zeolite. A former study which was performed by Li et al., (1997) showed that highest chromate removal was observed with HDTMA-Br modified clinoptilolite. Ghiaci et al. (2004) compared the performance of natural zeolite modified by surfactant hexadecyltrimethylammonium (HDTMA) and cetylpyridinium bromide (CPB) for removal of chromate from aqueous solution. Their results showed that HDTMA and CPB modified clinoptilolite exhibited higher chromate sorption than its natural form. Warchol et al. (2006) reported that HDTMA modified clinoptilolite was reliable material for the removal of chromate. Campos et al. (2007) investigated the modified-natural mordenite using (HDTMA) and ethylhexadecyldimethylammonium (EHDDMA) as adsorbents in the removal of Cr (VI) from aqueous solution. The results showed that the HDTMA modified zeolite exhibited higher adsorption for Cr (VI) than EHDDMA modified zeolite. They stated that the sorption of chromate on HDTMA-zeolite resulted from a combination of entropic, columbic and hydrophobic effects. Ramos et al. (2008) studied the adsorption of Cr (VI) form aqueous solution on HDTMA modified clinoptilolite and clinoptilolite. They stated that surfactant modified clinoptilolite adsorbed 22 times more chromium than clinoptilolite. Zeng et al. (2010) studied the adsorption of Cr (VI) by hexadecylpyridinium bromide (HDPB) modified clinoptilolite. Their results indicated that HDPB modified clinoptilolite had higher affinities toward chromate than that of natural ones.

Arsenic is strongly toxic metal which is found as arsenites [As (III)] or arsenates [As (V)] depending on the oxidation-reduction conditions. Sorption of arsenic on surfactant modified zeolite has been studied extensively in recent years. Miranda and Olguin (2007) investigated the sorption of arsenic by HDTMA modified clinoptilolite. They stated that the sorption of oxyanions form of arsenic might be resulted from the bond which was formed between the cationic head of the HDTMA and oxyanions form of arsenic. Li et al. (2007) studied the sorption of arsenic by HDTMA modified

clinoptilolite. They found that the significant increase in sorption of arsenate was achieved by modification with HDTMA. Chutia et al. (2009) compared the performance of mordenite, clinoptilolite, HDTMA modified mordenite and clinoptilolite for removal of arsenates from aqueous solution. Their results showed that HDTMA modified clinoptilolite and mordenite exhibited higher arsenates adsorption than their natural forms.

Surfactant modified zeolite are also used for the removal of dyes from wastewater. Armağan et al. (2003) studied the adsorption of three types of reactive dyes (reactive black 5, reactive red 239, and reactive yellow 176) by natural and HDTMA modified clinoptilolite. The results indicated that clinoptilolite has limited adsorption capacities of the reactive dyes. After modification with HDTMA, the dye adsorption was significantly improved. The modified zeolite adsorption capacities were found as 111, 89, and 61 mg/g for reactive red, yellow and black, respectively. Benkli et al., (2005) investigated HDTMA-modified clinoptilolite for removal of reactive azo dyes, reactive black 5, red 239 and yellow 176, in a fixed bed. The results indicated the order of dye removal by modified zeolite in the following manner: black > yellow > red. The adsorption of the dyes Basic Red 46 (BR46) and Reactive Yellow 176 (RY176) from aqueous solution onto natural, HDTMA and cetyltrimethylammonium bromide (CTAB) modified clinoptilolite was investigated by Karadağ et al., (2007). Removal of the basic dye by modified zeolite was found to have higher performance than uptake of the reactive dye by natural zeolite. Jin et al. (2008) investigated the adsorption of cationic methylene blue and anionic orange II onto ZSM5 and surfactant-modified ZSM5. Sodium dodecyl benzenesulfonate (SDBS) and sodium dodecyl sulfate (SDS) were used as anionic surfactant, while HDTMA and CPB were used as cationic surfactant in the modification steps. The results implied that SDBS and SDS modified zeolites had higher adsorption capacities for methylene blue than the unmodified zeolite, while CPB and HDTMA modified zeolites were the best adsorbents for orange II.

Apart from dyes and oxyanions, wastewater usually contains organic compounds, such as phenolics compounds, petroleum, pesticides, and pharmaceuticals, which are from various industrial sources. These organics are generally more toxic than dyes and oxyanions and thus the removal of these organic compounds is more important in water and wastewater treatment. Li and Bowman (1998) investigated the sorption of a non-polar organics, perchloroethylene (PCE), on HDTMA-modified clinoptilolite. They stated that the sorption of PCE on HDTMA-modified clinoptilolite was due to

partitioning of PCE into the organic phase formed by the surfactant on the zeolite surface. Their results revealed that surfactant-modified zeolite was an effective sorbent for removal of PCE from water. A later study by Li and Bowman (2000) indicated that surfactant modified zeolites were effective sorbent for the removal of ionisable organic compounds as well as non-polar organics. Ghiaci et al. (2004) prepared modified zeolites, ZSM-5 and clinoptilolite with HDTMA and CPB, and tested for adsorption of nonionic organic contaminants (NOCs) such as benzene, toluene, and phenol from contaminated wastewater. They found that HDTMA modified clinoptilolite exhibited higher sorption capacity of NOCs than HDTMA modified ZSM-5. The removal of polycyclic aromatic hydrocarbons (PAHs) by HDTMA-modified clinoptilolite was studied by Hossein et al., (2007). The clinoptilolite rich mineral showed small affinity toward PAHs, whereas HDTMA-modified clinoptilolite rich mineral removed more than 50 percent of the initial PAHs contents of n-paraffin. Kuleyin (2007) investigated the adsorption of phenol and 4-chlorophenol on HDTMA and benzyltetradecyl ammonium chloride (BDTDA) modified clinoptilolite. They found that phenol and 4-chlorophenol removal efficiency by the surfactant-modified clinoptilolite was higher than unmodified form. Diaz-Nava et al. (2009) studied the phenol sorption with HDTMA and benzylcetildimethylammonium chloride (BCDMACl) modified clinoptilolite rich mineral. Their results showed that the sorption of phenol depends on the quantities of surfactant in the clinoptilolite samples, the kind of surfactant, modification conditions and pH of the solutions. Sprynskyya et al. (2009) investigated adsorption of phenol on natural, NaOH and HDTMA modified clinoptilolite rich mineral. Sorption efficiency of the NaOH-treated clinoptilolite were lower than HDTMA modified clinoptilolite and highest phenol removal (>90%) was observed with HDTMA modified sample.

In recent years, the usage of surfactant modified zeolites in the pharmaceutical applications has been gained much attention. Riveria and Farias (2005) developed drug delivery system based on surfactant modified clinoptilolite rich mineral. The adsorption of surfactants of different natures (cationic, anionic and nonionic) onto clinoptilolite, and the adsorption of two model drugs (metronidazole and sulfamethoxazole) on the resulting clinoptilolite–surfactant composites were evaluated. Their results showed that cationic surfactant modified clinoptilolite composites retained a considerable amount of drugs. Lam and Riveria (2006) investigated the interaction between surfactant modified clinoptilolite and three drugs (aspirin, metronidazole and sulfamethoxazole). The results

revealed that higher sulfamethoxazole adsorption was observed surfactant modified clinoptilolite sample. The uptake of metronidazole was independent of the surfactant modification (Farias et al., 2010).

Surfactant modified zeolites are also used in the removal of microorganisms. Schulze (2002) studied the removal of viruses and bacteria with HDTMA modified clinoptilolite from ground water. He found that 99 % of the viruses and 100 % of the *E. coli* in the ground water was removed by surfactant modified clinoptilolite. The other zeolite application to adhere bacteria from water was conducted by Bowman (2003). His results indicated that the complete removal of *E. coli* and *bacteriophages MS2* was observed by HDTMA modified clinoptilolite. Another study which was performed by Lehner (2004) was related to the removal of *B. subtilis* by HDTMA modified clinoptilolite. The results showed that *B. subtilis* concentrations were reduced to 42.5% and 75.5 % by the natural and HDTMA modified clinoptilolite, respectively. Rust et al., (2006) compared the performance of surfactant modified zeolite and natural zeolite for the removal of the human pathogen *G. intestinalis* from groundwater. The results indicated that 100% of the *G. intestinalis* cysts in the ground water were removed by surfactant modified zeolite. On the contrary, 37.5 % *G. intestinalis* removal was observed with the natural zeolite. Abbaszadegan et al. (2006) investigated the antimicrobial capabilities of clinoptilolite filter modified with HDTMA. They found that the highest *E. coli* removal results were observed when HDTMA modified clinoptilolite was used as filter.

## **2.6. Characterization Methods for Natural and Modified Zeolites**

Townsend (1986) stated that the characteristics of natural zeolites depended on their origin because of variations in natural processes during the genesis. Other relevant aspect which was stated by Mumpton (1978) is that the composition, purity and water content of natural zeolites varied widely among the deposits found throughout the world. Therefore, natural zeolites should be characterized before being used in certain applications.

The surface chemistry of natural zeolite can be altered by modification with anionic and cationic surfactants. Modification is limited to the external surface of the zeolite because the molecular dimensions of the surfactant molecule are too large to penetrate the largest channels of the zeolite. After modification with surfactant, the

features of natural zeolites changes. Therefore, investigations about the characterization of zeolite have been studied to identify the features of zeolites before and after modification with surfactant.

Scanning Electron Microscopy (SEM) is used to characterize the crystalline morphologies of the natural and surfactant modified zeolites. Figure 2.6 and 2.7 show SEM micrographs of clinoptilolite and clinoptilolite after modified with HDTMA (Warchol et al., 2006; Ramos et al., 2008). The results indicated that the crystal structure of clinoptilolite was indiscernible when its surface was covered with cationic surfactant. The formation of organic layer on the clinoptilolite surface was observed after surfactant modification.

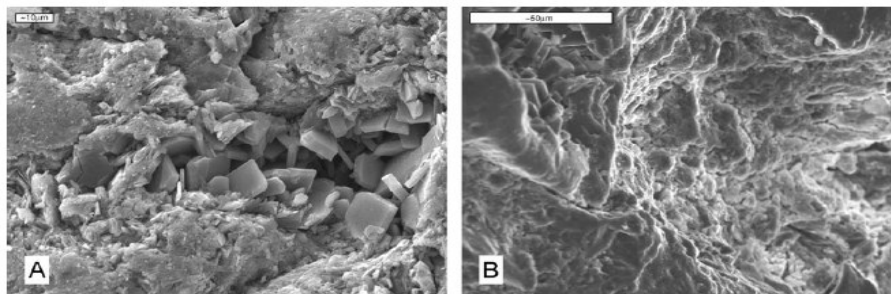


Figure 2.6. Scanning electron microphotograph of the Pentalofos clinoptilolite (a) natural, (b) modified with HDTMA (Source: Warchol et al., 2006)

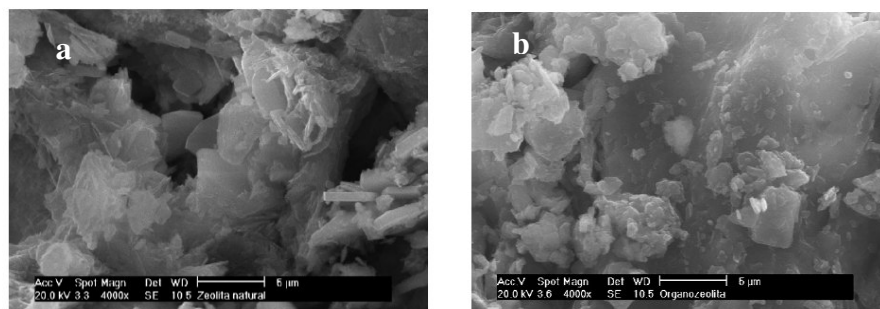


Figure 2.7. Scanning electron microphotograph of the Mexican clinoptilolite (a) natural, (b) modified with HDTMA (Source: Ramos et al., 2008)

X-Ray Diffraction (XRD) analysis is useful method for the identification of crystalline species in the material. Ramos et al. (2008) investigated XRD pattern of clinoptilolite and clinoptilolite after modification with HDTMA. Their results are presented in Figure 2.8 (a) and (b). The characteristic peaks of clinoptilolite were observed at 9.9, 22.4, 27 and 30.05. After modification, the characteristic peaks of the

clinoptilolite were unchanged and only the intensities of the peaks were decreased. The results indicated that surfactant was mainly adsorbed on the clinoptilolite phase.

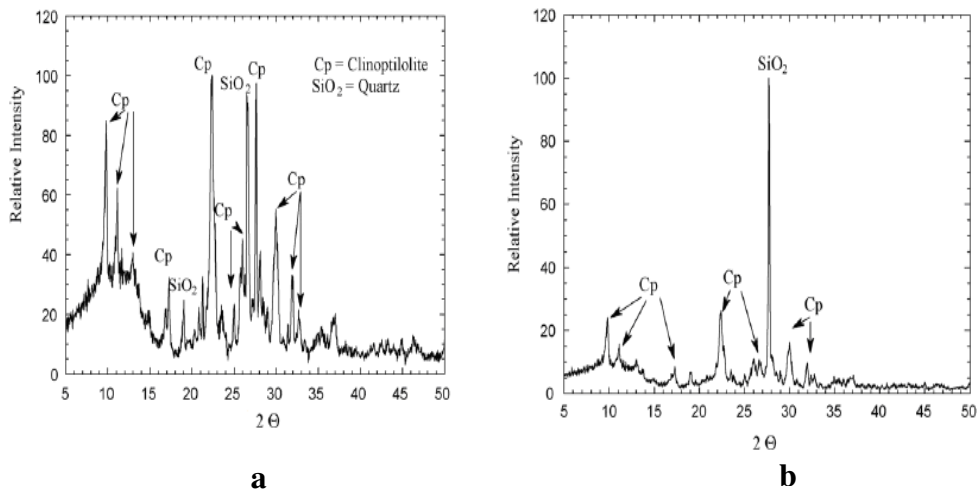


Figure 2.8. XRD pattern of (a) clinoptilolite (b) HDTMA modified clinoptilolite (Source: Ramos et al., 2008)

Chutia et al., (2009) studied XRD pattern of clinoptilolite and HDTMA modified clinoptilolite (Figure 2.9). Smaller decrease in the intensity of the major peaks of the clinoptilolite was observed.

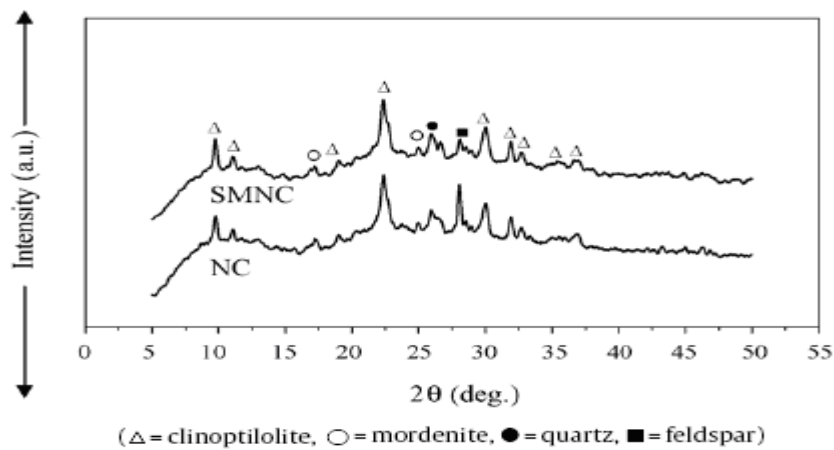


Figure 2.9. XRD pattern of clinoptilolite and HDTMA modified clinoptilolite (Source: Chutia et al., 2009)

Fourier Transform IR (FTIR) method can be useful in obtaining crucial information about the structure, channel size and cation substitution in the tetrahedral



sites of the zeolite minerals. The bands occurring in the FTIR spectra of zeolites can be characterized as follows (Breck, 1974):

- Bands due to the Si–O–Si and Si–O–Al vibrations, in the regions 1200–950  $\text{cm}^{-1}$  and 420–500  $\text{cm}^{-1}$ . In the first region (1200–950  $\text{cm}^{-1}$ ) the strongest vibration band appears. It is found in all zeolites due to the internal tetrahedron vibrations, and is assigned to a T–O stretching mode. In the second region (420–500  $\text{cm}^{-1}$ ) there is the next strongest band that is assigned to a T–O bending mode.
- Bands due to presence of zeolite water. The three typical bands observed are the broad band, characteristic of hydrogen-bonded OH to oxygen ions at about 3440  $\text{cm}^{-1}$ , the sharp band typical of isolated OH stretching vibration at 3619  $\text{cm}^{-1}$ , and the usual bending vibration of water at 1640  $\text{cm}^{-1}$ .
- Bands due to pseudo-lattice vibrations found in the region 500–800  $\text{cm}^{-1}$ . These vibrations are insensitive to the nature of the channel cations, as well as to the Si/Al ratio.

FTIR spectra of surfactant modified zeolite was investigated by Warchol et al., 2006; Karadağ et al., 2007; Rozic et al., 2009; Zeng et al., 2010. Their results are shown in Figure 2.10-2.13. The FTIR spectra of surfactant modified zeolite indicated that the spectra of modified zeolite had additional two intense bands in the region 3000-2800  $\text{cm}^{-1}$  assigned to the asymmetric and symmetric stretching of the C-CH<sub>2</sub> group of the alkyl chain.

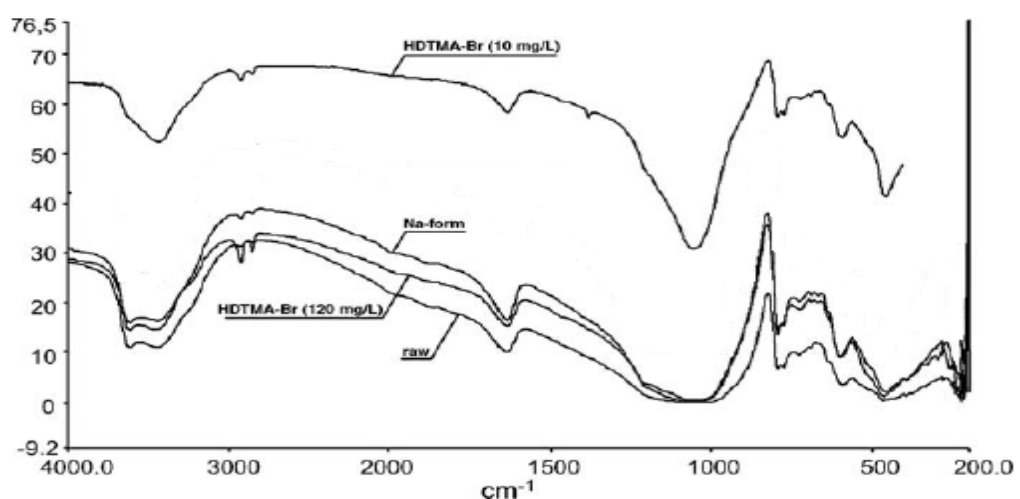


Figure 2.10. FTIR spectra of raw zeolite material, its Na form and zeolite samples treated by HDTMA-Br (Source: Warchol et al., 2006)

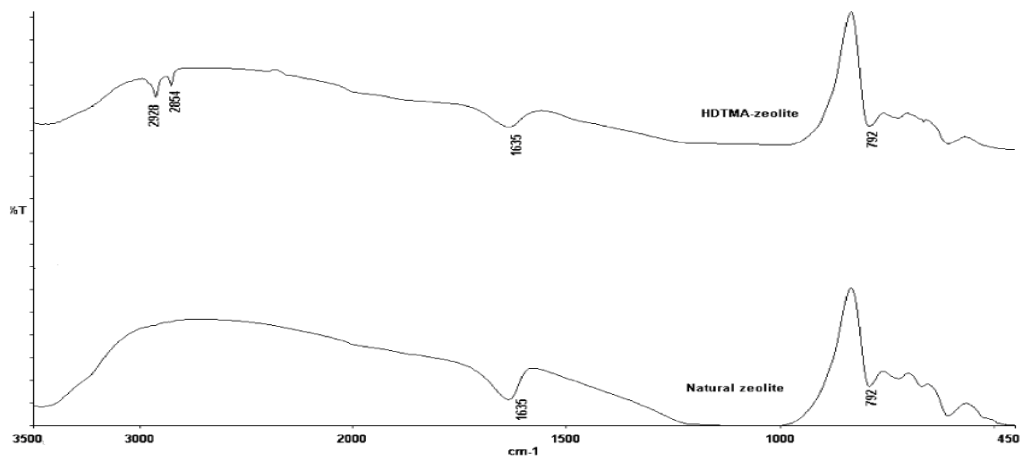


Figure 2.11. FTIR spectra of clinoptilolite and HDTMA modified clinoptilolite (Source: Karadağ et al., 2007)

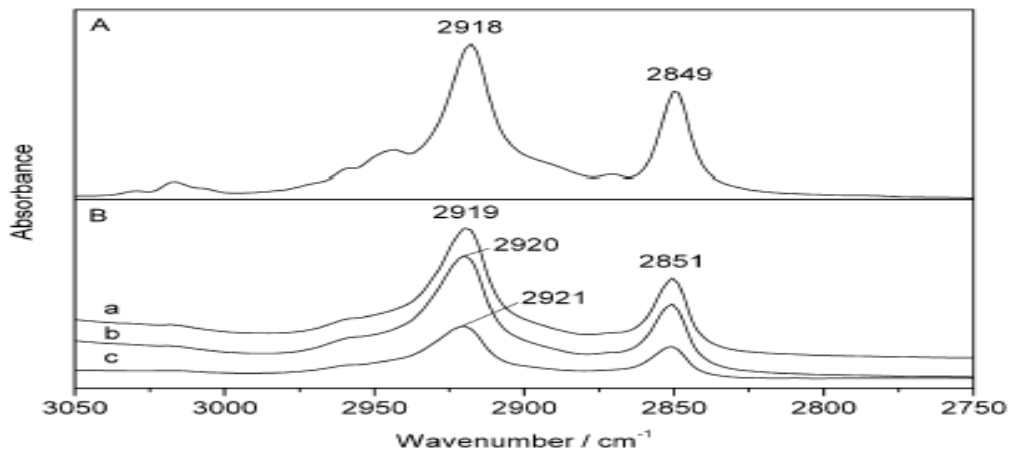


Figure 2.12. FTIR spectra of (A) HDTMA (B) HDTMA sorbed onto clinoptilolite samples from (a) Serbia (b) Turkey (c) Croatia (Source: Rozic et al., 2009)

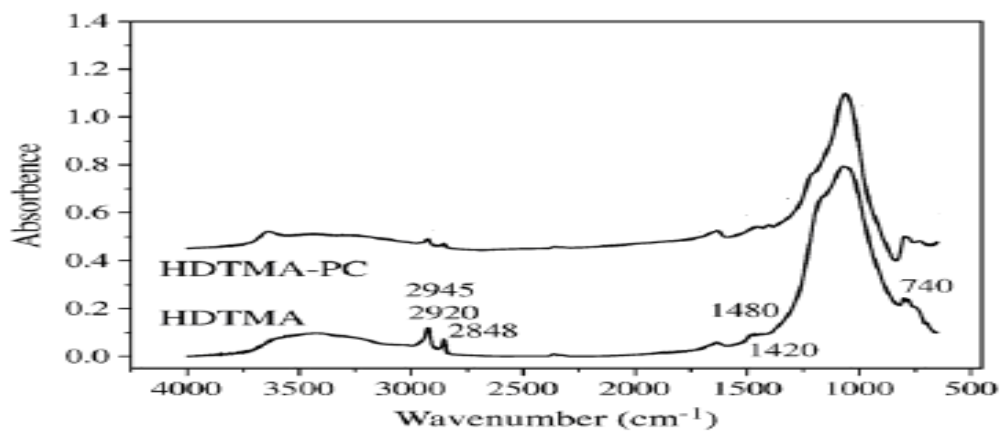


Figure 2.13. FTIR spectra of HDTMA and HDTMA modified clinoptilolite (Source: Zeng et al., 2010)

## CHAPTER 3

### BACTERIA

Bacteria are one of the most important pathogenic microorganisms and cause several disease. They are classified as “Gram Positive” and “Gram Negative” bacteria. By Gram staining method, the Gram-positive bacteria stained purple, whereas Gram-negative bacteria were colored pink or red. In this chapter, the features of the gram positive and negative bacteria are comprehensively discussed. Moreover, the functional groups on the bacteria cell wall are investigated because they are very important to understand the possible mechanisms in the attachment stages. Furthermore, the attachment stages of bacteria to the surface are explained. The effects of factors on the bacteria attachment are also discussed.

#### 3.1. General Information about Bacteria

Typically, bacteria cells are about 0.5 to 2  $\mu\text{m}$  long; however, their sizes vary from 0.1  $\mu\text{m}$  to 5  $\mu\text{m}$ . They have simple morphology. Mostly found in three distinct shapes: cocci, rod and spiral. Cocci, for instance, being spherical, become less distorted upon drying and thus can usually survive in more severe desiccation than do bacterial cells with other shapes. The cocci show different arrangement based on their division. For example, division in random planes produces a staphylococcus arrangement which is shown as grape-like clusters. Average cocci are about 0.5-1.0  $\mu\text{m}$  in diameter. Rod shaped bacteria have more surfaces exposed per unit volume than cocci shaped bacteria and thus can more readily take up nutrients form dilute solutions. Bacilli are rod-shaped bacteria. They all divide in one plane producing a bacillus, streptobacillus, or coccobacillus arrangements. An average bacillus is 0.5-1.0  $\mu\text{m}$  wide and 1.0-4.0  $\mu\text{m}$  long. Spiral shaped cells can be either rigid called spirilla or flexible called spirochaetes. Spiral-shaped bacteria are distinguished by their length, the number and size of the spirals, and direction of the coil. Spirals range in size from 1  $\mu\text{m}$  to over 100  $\mu\text{m}$  in length.

Bacteria are classified as “Gram Positive” and “Gram Negative” bacteria. Gram positive bacteria include many well-known species such as *Staphylococcus*, *Streptococcus*, *Enterococcus*, *Bacillus*, *Corynebacterium*, *Nocardia*, *Clostridium*, *Actinobacteria*, and *Listeria*. Well known species of Gram negative bacteria are *Escherichia coli*, *Salmonella*, *Shigella*, *Pseudomonas*, *Moraxella*, *Helicobacter*, *Stenotrophomonas*, *Bdellovibrio*, and *Legionella*. The features of the gram positive and negative bacteria that are used in the thesis are discussed below:

**a) *Escherichia coli* (*E. coli*):** They are gram negative, anaerobic and rod shaped bacteria which inhabit the intestine of all healthy humans and most warm-blooded animals. There are many strains of *E. coli* bacteria and most of them are harmless. Some strains such as *E. coli* O157:H7 produces a powerful toxin and can cause severe illness. Infection often causes bloody diarrhea and abdominal cramps.

**b) *Pseudomonas aeruginosa* (*P. aeruginosa*):** They are gram negative, anaerobic and rod shaped bacteria which are found in soil, water and skin flora. *P. aeruginosa* is a major cause of both healthcare-associated infections and chronic lung infections in people with cystic fibrosis.

**c) *Bacillus subtilis* (*B. subtilis*):** They are gram positive and rod-shaped bacteria which are naturally found in soil. They are non-pathogenic but they can contaminate food.

**d) *Staphylococcus aureus* (*S. aureus*):** They are spherical gram-positive bacteria, which are immobile and form grape-like clusters. They cause superficial skin lesions such as boils, styes and furuncles; more serious infections such as pneumonia, mastitis, phlebitis, meningitis, and urinary tract infections. They also cause toxic shock syndrome by release of super antigens into the blood stream.

**e) *Staphylococcus epidermidis* (*S. epidermidis*):** They are spherical gram-positive bacteria that commonly present on human skin. Infection caused by *S. epidermidis* is usually associated with medical devices, such as indwelling catheters and often occurs in people with weakened immune systems.

### **3.1.1. Cell Wall Features of Gram Positive and Negative Bacteria**

The basic distinction between gram positive and gram negative bacteria is their cell wall structure. The cell wall structure of gram negative bacteria is much more complex chemically and structurally than gram positive bacteria. The gram positive cell

wall is much thicker than a gram negative cell wall. Both gram positive and negative bacteria are composed of peptidoglycan layers. The amounts of peptidoglycan in cell walls vary with type of the bacteria. Peptidoglycan is a linear polymer of alternating units of two sugar derivatives, N-acetylglucosamine (NAG) and N-acetylmuramic acid (NAM). The structures of the peptidoglycan layer are presented in Figure 3.1. Peptidoglycan also contain several different amino acids, three of which D-glutamic acid, D-alanine and meso-diaminopimelic acid. The sugars are connected with a glycosidic bond, while the peptide chains are cross-linked by amino acids. This cross-linking occurs to different extents in different bacteria, with greater rigidity coming from more complete cross-linking.

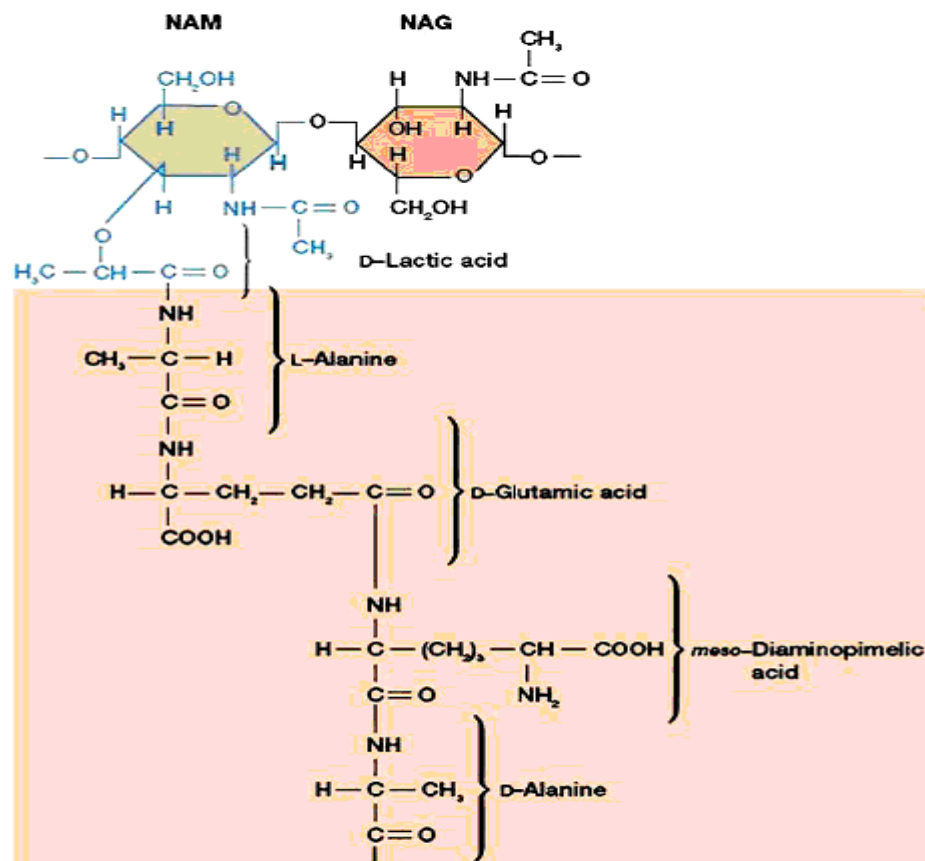


Figure 3.1. Structures of the peptidoglycan layer  
(Source: Wang and Chen, 2009)

Figure 3.2 shows the gram positive bacteria cell wall structures. Their cell wall consists of a single 20 to 80 nm thick peptidoglycan layer and it is composed of peptidoglycan and teichoic acid. The teichoic acid is connected to either peptidoglycan itself by a covalent bond with six hydroxyl of N-acetylmuramic acid (NAM) or to

plasma membrane lipids which is called as lipoteichoic acids (Wang and Chen, 2009). These acids which only present in gram positive bacteria are synthesized at the membrane surface and may extend through the peptidoglycan layer to the outer surface. Teichoic acids appear to extend to the surface of peptidoglycan layer and they also not present in the gram negative bacteria. The negative charge arises from anionic sites in the cell wall including carboxylate from the peptidoglycan and phosphate from the teichoic acids.

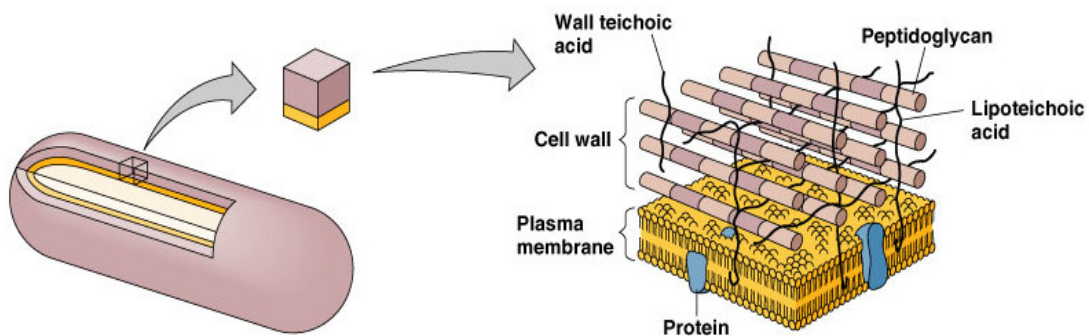


Figure 3.2. Gram positive bacteria cell wall structures  
(Source: midlanstech, 2010)

Gram negative cell wall structures are presented in Figure 3.3. They have thin cell wall which is about 5 to 10 nm. The peptidoglycan layer which is about 2 to 7 nm is surrounded by a 7 to 8 nm thick outer membrane. The outer membrane of the cell envelope is relatively permeable to small hydrophilic and hydrophobic molecules. The permeability is attributed to the presence of proteins called porins that form membrane channels. The porins are both specific and non-specific to exchange of molecules with the environment. The periplasm is between the outer and cytoplasmic membranes. It has a gel-like consistency and contains the peptidoglycan layer. Outer membrane structure is composed of phospholipids, lipopolysaccharides, enzymes and other proteins, including lipoproteins. The peptidoglycan is covalently bound to the outer membrane by lipoproteins. The outer membrane is composed of lipopolysaccharide (LPS), phospholipids and proteins. LPS consist of three parts (1) lipid A, (2) the core polysaccharides and (3) the O side chain. Lipid A is a fatty acid, commonly caproic, lauric, palmitic and stearic acids, that is at the base of the core polysaccharide and associated with phospholipids. Each LPS is held in the outer membrane by relatively weak cohesive forces (ionic and hydrophobic interactions) and can be dissociated from

cell surface with surface active agents. The net negative charges of LPS are attributed to the negative surface charge of gram negative bacteria.

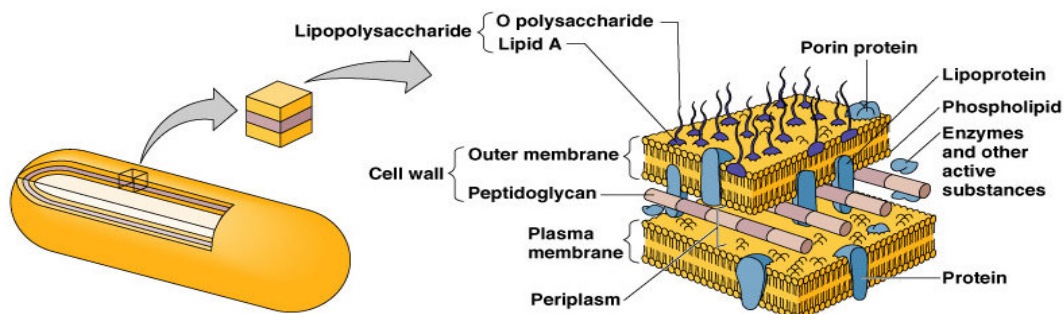


Figure 3.3. Gram negative bacteria cell wall structures  
(Source: midlanstech, 2010)

### 3.1.2. Functional Groups on the Bacteria Cell Wall

Chemical functional groups present on the bacteria cell wall are important for understanding possible mechanisms in the sorption process. The most important functional groups are summarized by Volesky (2007), including Hydroxyl, Carbonyl, Carboxyl, Sulfhydryl (thiol), Sulfonate, Thioether, Amine, Secondary amine, Amide, Imine, Imidazole, Phosphonate and Phosphodiester. Many researchers have used FTIR method to determine qualitative and preliminary analysis of the chemical functional groups. The FTIR bands observed in the spectra of *E. coli*, *P. aeruginosa*, *B. subtilis*, *S. aureus* and *S. epidermidis* are listed in Table 3.1. The region between 4000-3100  $\text{cm}^{-1}$  is resulted from  $-\text{OH}$  ( $3300 \text{ cm}^{-1}$ ). The region between 3100 and 2800  $\text{cm}^{-1}$  exhibits the C-H stretching vibrations of  $-\text{CH}_3$  and  $>\text{CH}_2$  functional groups and hence, is generally dominated by the spectral characteristics of fatty acid chains of the various membrane amphiphiles and by some amino acid side-chain vibrations. Complementary information can be deduced from the region between 1470 and 1350  $\text{cm}^{-1}$  where the various deformation modes of these functional groups are found. The region between 1800 and 1500  $\text{cm}^{-1}$  is dominated by the conformation-sensitive amide I and amide II bands, which are the most sensitive bands in the spectra of all bacterial samples. FTIR band are observed between 1300-1500  $\text{cm}^{-1}$  arising predominately from  $>\text{CH}_2$  bending mode of lipids and proteins. Characteristic symmetric stretching vibrations of  $-\text{COO}-$  functional

groups of amino acid side chains or free fatty acids are observed at these regions. Around 1250 cm<sup>-1</sup>, >P=O double bond asymmetric stretching vibrations of phosphodiester, free phosphate and monoester phosphate functional groups are observed. The spectral region between 1200 and 900 cm<sup>-1</sup> is generally dominated by the symmetric stretching vibration of PO<sub>2</sub> groups in nucleic acids and a complex sequence of peaks mainly due to C-O-C and C-O-P stretching of various oligo and polysaccharides. The region between 900-600 cm<sup>-1</sup> represent C-O-C and P-O-C bonding (phospholipids, RNA, aromatics).

Table.3.1. FTIR bands observed in spectra of *E. coli*, *P. aeruginosa*, *B. subtilis*, *S. aureus* and *S. epidermidis* (Source: Pineda, 2006)

Assignment	<i>E. coli</i>	<i>P. aeruginosa</i>	<i>B. subtilis</i>	<i>S. aureus</i>	<i>S. epidermidis</i>
O-H stretching	3305	3309	3302	3307	3311
C-H stretching (antisymmetric) of CH <sub>3</sub> in fatty acid	2974	2970	2966	2970	2966
C-H stretching (antisymmetric) of >CH <sub>2</sub>	2937	2929	2931	2933	2935
C-H stretching (symmetric) of -CH <sub>3</sub>	2873	2873	2875	2868	2877
Amide I of α-helical structures	1653	1647	1651	1656	1654
Amide II	1552	1551	1554	1552	1552
C-H deformation of >CH <sub>2</sub>	1479	1470	1468	1470	1470
C=O stretching (symmetric) of COO <sup>-</sup>	1423	1412	1404	1404	1408
P=O stretching (antisymmetric) of PO <sub>2</sub> <sup>-</sup> phosphodiester	1248	1246	1250	1252	1255
P=O stretching (symmetric) of >PO <sub>2</sub> <sup>-</sup>	1097	1093	1097	1097	1099

### 3.2. Attachment Stages of Bacteria to the Surface

The attachment of bacterial cells to the surface is an extremely complicated process which can involve a number of several mechanisms. The rates of the processes vary widely depending on the environmental conditions and the type of bacteria. One



approach used in explaining attachment, is the double layer theory (DLVO), originally devised by Derjaguin and Landau (1941) and Verwey and Overbeek (1948). The theory has been used to model the repulsive and attractive forces between the bacteria and the surface. The DLVO theory assumes that particle attraction occurs over a short distance, termed primary minimum ( $\leq 1$  nm), and a long distance, termed secondary minimum (5–10 nm). Between these two minima is a zone of maximum electrostatic repulsion which decreases with the ionic strength of the aqueous solution (Marshall et al., 1971).

Bacterial attachment to a surface is a two-step process. The first step, reversible adsorption, takes place when bacteria located in the secondary minimum overcome the secondary repulsive force between themselves and the surface, and adsorb to the surface. During the initial reversible step, attachment consists of a weak link between bacteria and the surface. The primary forces responsible for the first step are electrostatic interactions, Van Der Waals forces and hydrophobic interactions (Gilbert et al., 1991). Reversibly attached bacteria can detach from the surface because of the weak interaction between bacteria and surface. The second step, irreversible adsorption (adhesion), interaction between the bacteria and material surface becomes predominant. At the second step, the adherent bacteria begin synthesizing and producing extracellular polymeric substances (EPS). With the help of EPS, a firmer bacterial adhesion to surface can occur. The composition of EPS is complex, depending on the strain and its culture conditions. They are composed of primary polysaccharides and other macromolecules such as proteins, DNA, lipids and humic substances (Flemming and Wingender, 2001). EPS contain ionisable functional groups such as carboxyl, phosphoric, amine, and hydroxyl groups. Interactions between EPS and surfaces are caused by electrostatic attraction and hydrogen bonds (Mayer et al., 1999). These interactions play an important role in cell aggregation. After colonization of the surface, bacteria can propagate into small cells.

### **3.2.1. Factors Influencing Bacteria Attachment**

Bacterial attachment is affected by many factors including the environmental factors, the bacterial properties and the material surface characteristics. This section discusses how different factors influence bacterial adhesion.

The attachment of bacteria has been found to be effected by numerous environmental factors including temperature, pH of the solution, ionic strength and type of species. Studies of marine *Pseudomonas* showed that the proportion of bacteria attached to polystyrene was decreased at 20 °C (Fletcher, 1977). Studies of *P. putida* showed greater adsorption of *P. putida* on kaolinite was observed at 25 °C (Jiang et al., 2007). The results implied that the extent of bacteria adsorption on the surfaces was affected by temperature. The pH of the liquid phase also affects the extent of adhesion of bacteria to surfaces. The influence of pH on bacterial adhesion depends on the nature of the bacterial surfaces and ionic strength in the solution. Higher ionic strength of the aqueous solution reduces the effect of repulsive forces, and thus influences adhesion of bacteria. However, studies show that the affinity of the bacteria for the surface increases with ion strengths up to 0.1M (Marshall, 1971; Stanley, 1983; Gardon and Millero, 1984). The ionic species also affect the adhesion of bacteria to surfaces. The presence of specific cations such as Na<sup>+</sup>, Ca<sup>2+</sup> and Mg<sup>2+</sup> promotes adhesion of bacteria. Common metallic cations in solution, such as Fe<sup>3+</sup>, Cu<sup>2+</sup>, Zn<sup>2+</sup>, have been found to enhance bacterial adhesion, whereas common anions, such as Cl<sup>-</sup>, SO<sub>4</sub><sup>2-</sup>, NO<sub>3</sub><sup>-</sup>, have little influence on adhesion (Stevik et al., 2004).

Material surface characteristics such as chemical composition of the material, surface charge, hydrophobicity and surface roughness are important in bacterial adhesion. Functional groups present on the surface of the material influences hydrophobicity and surface charge and these in turn affect the bacterial adhesion. The wetting properties of a surface influence bacterial adhesion. Hydrophobicity of both material surfaces affects the overall adhesion. In general, hydrophilic materials are more resistant to bacterial adhesion than hydrophobic material. Surface roughness has been found to influence bacterial adhesion. Ortega et al. (2010) also showed that higher *S. epidermidis* adhesion was observed with rough stainless steel surface. Mei et al. (2011) stated that *Streptococcal* adhesion forces to orthodontic composite resin increased with increasing the roughness of the composite surface. Smaller particles give better adhesion results compared to coarse particles because of having more adhesion sites. The different particle sizes of the natural zeolite, magnesium-exchanged natural zeolite and quartz sand was used as natural carriers in the immobilization of *A. calcoaceticus* (Hrenovic et al., 2005). The experimental results indicated that bacteria adhesion was observed with the smallest particle sizes for all three carriers.

Bacterial properties include hydrophobicity, electrostatic charges on the cell surface, other cell surface characteristics and bacteria cell concentration. Hydrophobicity is influenced by growth phase and growth rate. Hydrophilic bacteria prefer hydrophilic surfaces, and likewise, hydrophobic bacteria prefer hydrophobic surfaces. The hydrophobic bacteria adhere to a greater extent than the hydrophilic bacteria. Electrostatic charges on the cell surface affect the adhesion of bacteria to surfaces. The dissociation of functional group such as carboxylic, amino and hydroxyl groups located on the bacterial cell wall affects the electrostatic charge on the cell surface. The magnitude of the charge on the cell surface depends on the isoelectric point of bacteria species. pH not only affects the ionization state of the functional group on the bacterial cell wall but also influence the electrostatic charges on the cell surface. If the pH of the solution is lower than isoelectric point, the surface charge on the bacteria will become positive. When pH value is higher than isoelectric point, the surface charge is negative and becomes more negative at higher pH values. Many kinds of bacteria have filamentous cell appendages, which are several to tens nanometers in diameter and hundreds to thousands of nanometers in length. These structures are associated with bacterial cell surface, can play a vital role in attachment of bacteria to the material surface. Fimbriae are cell appendages, which possess hydrophobic amino acid residues (Rosenberg and Kjelleberg, 1986). They contribute hydrophobicity to bacterial cell-surfaces and further help in attachment. The main function of fimbriae is to overcome the initial electrostatic repulsion barrier that exists between the bacteria cell and the material surface. Flagella are responsible for the motility of bacteria. Bacteria flagella are 10-20  $\mu\text{m}$  long and between 0.01 and 0.02  $\mu\text{m}$  in diameter. The concentration of the bacteria cell is important factor for the rate of adhesion. The number of bacterial collision with the surface increases with increasing cell concentration which offers an increase in possibility for adhesion (Fletcher, 1977).

### **3.3. Previous Bacterial Adsorption Studies**

As stated before, the attachment of bacterial cells to the surface is complicated process and depends on the environmental factors, the bacterial properties and the material surface characteristics. This section is important to understand the interaction between different bacteria species and material surface.

Yee et al. (2000) investigated the adsorption of *B. subtilis* onto the surfaces of two minerals, corundum and quartz, as a function of time, pH, ionic strength and bacteria: mineral mass ratio. The results indicated that *B. subtilis* displays a higher affinity for corundum surfaces than for quartz surfaces, and that the extent of bacteria adsorption onto corundum increases with decreasing pH, with increasing bacteria: mineral mass ratio, and with decreasing ionic strength. The adsorption behavior was explained by the chemical speciation of the bacterial and mineral surfaces.

Interactions between *P. polymyxa* and different minerals such as hematite, corundum and quartz were investigated by Deo et al., (2001). The results showed that bacteria were adsorbed preferentially on hematite and corundum compared to quartz. Maximum adsorption of bacterial cells on hematite and corundum occurred at a pH below the isoelectric point, whereas in the case of quartz the adsorption of bacterial cells remained almost constant in the entire pH range studied. The results implied that electrostatic interactions played significant role in bacteria adsorption. FTIR results indicated that the band shifts in water molecules were observed after bacteria adsorption. The results revealed that both electrostatic forces and hydrogen bonding were responsible in bacteria sorption.

The effect of surfactant on the removal of *P. aeruginosa* was studied by Cloete and Jacobs (2001). The results indicated that non-ionic surfactants were more efficient in removal of *P. aeruginosa* than anionic surfactants. The results implied that higher *P. aeruginosa* adhesion was observed at 6hr. After 6 hr, bacteria adhesion was remained constant. This decrease could be resulted from the removal of more loosely attached bacteria.

Ams et al. (2004) investigated the adsorption of *B. subtilis* and *P. mendocina* on Fe-oxyhydroxide- coated and uncoated quartz grains. The results indicated that neither *B. subtilis* nor *P. mendocina* exhibited significant adsorption onto dominantly negatively charged quartz surface. The results also indicated that bacteria adsorption was dramatically enhanced in the presence of Fe-oxyhydroxide-coated quartz grains relative to pure quartz grains. When the adsorption results of the gram positive and negative bacteria were compared, the gram-positive *B. subtilis* was adsorbed onto Fe-coated quartz to a greater extent than the gram-negative *P. mendocina*. The difference in adsorption behavior was explained by different structure of gram positive and negative bacteria cell walls.

Jiang et al. (2007) studied the adsorption of *P. putida* on clay minerals and iron oxide. Montmorillonite and kaolinite were used as clay minerals whereas goethite was used as iron oxide. The effects of temperature, pH and electrolyte on *P. putida* adsorption were examined. The greater adsorption of *P. putida* on minerals was observed at 25 °C. The amount of *P. putida* adsorption increased with pH from 2 to 3 and decreased with pH from 3 to 10. Different sorption behaviors at various pH values were explained by surface charges of the adsorbents. Bacteria adsorption was strongly influenced by increasing or decreasing electrostatic repulsion between *P. putida* and adsorbents. The adsorption of *P. putida* on minerals increased remarkably in the presence of 0–30mM Na<sup>+</sup> or 0–10mM Mg<sup>2+</sup> and remained constant or increased slightly with continuously increasing ionic concentrations. The extent of promotion by electrolyte for bacteria attachment on minerals studied followed the sequence of montmorillonite > kaolinite > goethite.

The adsorption of *P. putida* on kaolinite and montmorillonite was also investigated by Rong et al., (2008). Their results demonstrated that the greater bacteria adsorption was observed on kaolinite than on montmorillonite at pH 7.0. Isoelectric points of kaolinite and montmorillonite were reported as 4 and 1.8, respectively. At pH 7, the surfaces of the clays were negatively charged and the repulsive electrostatic force between bacteria and clay mineral were observed. The sorption at these conditions may be resulted from the non-electrostatic force between the bacteria and the minerals. The results implied that non-electrostatic forces might play more important roles than electrostatic force in bacterial adsorption on clay minerals. FTIR spectra of bacteria, clay minerals and bacteria-clay complexes are illustrated in Figure 3.4. The FTIR results indicated that no new band was found on the bacteria–mineral complex. However, the vibrations of water molecules sorbed on kaolinite shifted from 3450 to 3442 cm<sup>-1</sup> and from 1637 to 1647 cm<sup>-1</sup>, respectively, after the bacterial adsorption. Similar shifts were observed for the sorbed water molecules on montmorillonite after bacterial adsorption. These shifts indicated that the water molecules on the clay minerals were involved in bacterial sorption. The results also implied that hydrogen bonding was involved in bacteria sorption.

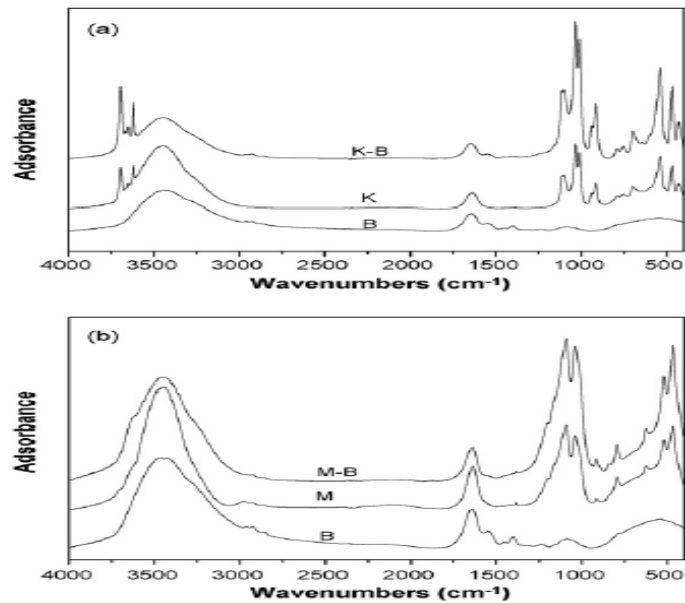


Figure 3.4. FTIR spectra of bacteria, minerals and bacteria–mineral complexes (K, kaolinite; M, montmorillonite; B, bacteria; K–B, kaolinite–bacteria M–B, montmorillonite–bacteria) (Source: Rang et al., 2008)

The adsorption of *B. thuringiensis* by clay minerals was investigated by Fu et al., (2009). Montmorillonite, kaolinite, goethite, and silicon dioxide were used as clay minerals. The results showed that the adsorption was much easier at low temperature than at high temperature at the initial concentration varying from 0 to 1000 mg/L. The Langmuir and Freundlich isotherm models fitted to the experimental data. Freundlich model was more suitable than Langmuir model. Kinetic model results revealed that the pseudo second order model was best model to describe adsorption kinetic. Thermodynamic parameters were also calculated. The negative standard free energy values of the adsorption indicated that the adsorption of *B. thuringiensis* by the minerals was spontaneous, and the changes of the standard enthalpy showed that the adsorption of *B. thuringiensis* by montmorillonite was endothermic while the adsorption by the other three minerals was exothermic.

Rong et al. (2010) studied the adsorption of *P. putida* on goethite. In that study, the isoelectric points of *P. putida* and goethite were reported as 1.9 and 7.9, respectively. The results indicated that the extent of *P. putida* adsorption on goethite was the greatest at pH 3. The reason for greater amount of bacteria adsorption was due to stronger attraction force between bacteria and goethite. At pH>8, the stronger repulsion forces between bacteria and goethite surface could occur. The marked decrease in bacteria adsorption at high pH was explained by this repulsion forces. FTIR results indicated that hydrogen bonding also showed a vital role since band shifts in

water molecule were observed after bacteria adsorption. The results implied that electrostatic forces and hydrogen bonding could be the governing factors in the sorption of bacteria on goethite.

Fang et al. (2010) studied the adsorption behavior of Cu (II) by *B. thuringiensis*, *P. putida* and their composites with minerals. The interaction of montmorillonite with bacteria increased the reactive sites and resulted in greater adsorption for Cu (II) on their composites, while decreased adsorption sites and capacities for Cu (II) were observed on goethite–bacteria composites.

The adsorption of *M. phlei* cells on the surfaces of pyrite and sphalerite was studied by Jia et al., (2011). The results indicated that a higher amount of cells adsorbing onto pyrite compared with that onto sphalerite under neutral and alkaline conditions.

Cao et al. (2011) investigated the adsorption of extracellular polymeric substances (EPS) from *B. subtilis* on montmorillonite, kaolinite and goethite. The amount of EPS-C and -N adsorbed followed the sequence of montmorillonite > goethite > kaolinite. However, EPS-P adsorption was in the order of goethite > montmorillonite > kaolinite. These results suggest that proteinaceous constituents were adsorbed preferentially on montmorillonite and kaolinite, and phosphorylated macromolecules were absorbed preferentially on goethite. Adsorption of EPS on clay minerals resulted in obvious shifts of infrared absorption bands of adsorbed water molecules, showing the importance of hydrogen bonding in EPS adsorption.

The role of extracellular polymeric substances (EPS) in Cd adsorption by *B. subtilis* and *P. putida* was investigated by Wei et al., (2011). The presence of EPS on bacterial surfaces facilitated the adsorption of Cd, and the promoting effects were more remarkable on Gram-positive (*B. subtilis*) cells than on Gram-negative (*P. putida*) cells.

Electrostatic forces and non electrostatic forces were responsible in the adsorption of bacteria on different surfaces. Repulsion and attraction forces could occur due to pH of the solution, isoelectric points of bacteria and material. During the adsorption process, the adherent bacteria begin synthesizing and producing extracellular polymeric substances (EPS). Under this condition, polymer mediated interactions such as hydrogen bonding and dipole-dipole type interaction could occur. The evidence of these types of interactions is evaluated by FTIR analysis. Band shifts in FTIR spectra give information about which polymer mediated interactions are involved in bacteria adsorption.

## CHAPTER 4

### CHROMIUM REMOVAL

Chromium (Cr), one of the most important pollutants, exists in the effluents of various industries such as leather tanning, electroplating, pigments and metal finishing. Methods for removing chromium ion from aqueous solution mainly consist of reduction, precipitation, nano-ultrafiltration and membrane technologies. But due to concerns related to high energy input and large amounts of secondary wastes produced, further research on alternative methods is needed. In recent years, investigation on sorption with natural, synthetic and biologically based sorbents has gained much attention because of its high removal efficiency and low cost of technology. In this chapter, the sorbents used in the Cr (VI) removal are investigated.

#### 4.1. Chromium Ion

Chromium (Cr) is one of the toxic metals and it can be found in water as cationic and anionic forms. Although it has oxidation states of +2, +3, +4, +5 and +6, only two states, trivalent and hexavalent chromium, are stable in the environment (Kotas and Stasicka, 2000). Chromium (III) exists in the form of cation while chromium (VI) exists in the anionic form. Cr (VI) is known to have 100-fold more toxicity than Cr (III). It is quite soluble in the aqueous phase almost in the entire pH range and mobile in the natural environment. It has been reported that Cr(VI) causes lung cancer, gastrointestinal disorders, dermatitis and kidney damage in humans and it is also toxic to other organism as well (Leonard and Lauwerys, 1980; Pellerin and Booker, 2000).

Cr (III) exists in the solution in the form of  $\text{Cr}^{3+}$ ,  $\text{Cr}(\text{OH})^{2+}$  and  $\text{Cr}(\text{OH})_2^+$  depending on the pH of the solution. Cr (VI) is found in the form of  $\text{H}_2\text{CrO}_4$ ,  $\text{HCrO}_4^-$ ,  $\text{CrO}_4^{2-}$ ,  $\text{Cr}_2\text{O}_7^{2-}$  and  $\text{HCr}_2\text{O}_7^-$  depending on the pH of the solution and total Cr (VI) concentration in the solution. Cr (VI) speciation diagram are shown in Figure 4.1. The calculation procedure that used in the speciation diagram is given in Appendix A.



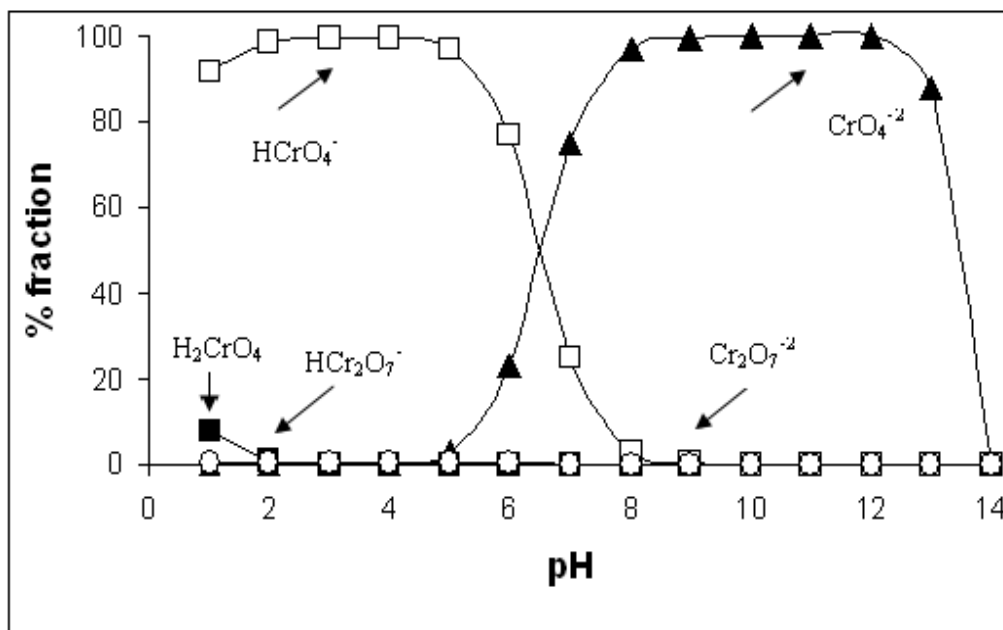


Figure 4.1. Cr (VI) speciation diagram as a function of pH

Due to environmental concern, the authorities have introduced stringent laws to restrict the limitation of chromium concentration in water. The tolerance limit for Cr (VI) for discharge into inland surface waters is 0.1 mg/L and in potable water is 0.05 mg/L (EPA, 1990).

## 4.2. Sorbents Used in Hexavalent Chromium Removal

Natural and synthetic sorbents used for the removal of hexavalent chromium from water and wastewater are activated carbon, coal, fly ash, natural zeolite, MCM 41 and ZSM 5. Previous studies related to natural and synthetic sorbents used in Cr (VI) removal are summarized in Table 4.1. Activated carbon exhibits higher chromium removal efficiency but its cost are prohibitively high. Therefore, low cost alternative materials are needed to reduce operating cost of the process. Natural zeolites are used as alternative material in heavy metal removal because of their low cost and local availability. They are low cost materials, but they have little affinity for anions. In order to improve their removal performances, natural zeolites have been modified with acid and metal exchanged cations. Natural zeolites modified in this way have better removal performance than their natural forms.

Table 4.1. Natural and synthetic sorbents used for Cr (VI) removal

Sorbents	Results	References
<b>Activated Carbon</b>	The optimum pH was found to be 2 and 3 for wood-based and coconut shell activated carbon, respectively.	Selomulya et al., 1999
	The activated carbon produced from the waste tyres was highly effective about (99% removal) at pH 2.	Hamadi et al., 2001
	KOH and H <sub>3</sub> PO <sub>4</sub> activated carbons were tested. The sorption capacity of KOH and H <sub>3</sub> PO <sub>4</sub> activated carbons were reported as 315 and 186 mg/g, respectively. Langmuir isotherm fitted well with the experimental data.	Khezami and Capart, 2005
	Adsorption of Cr (VI) is found to be effective in the lower pH range and at higher temperatures. Langmuir isotherm showed better fit than Freundlich and Temkin isotherm.	Karthikeyan et al., 2005
	The sorption capacity of activated carbons which were produced from agricultural waste materials were reported as 9-22 mg/g.	Mohan and Pittman, 2006
	H <sub>2</sub> SO <sub>4</sub> and HNO <sub>3</sub> treated activated carbon were used. The sorption capacity of H <sub>2</sub> SO <sub>4</sub> and HNO <sub>3</sub> activated carbons were reported as 7.5 and 10.9 mg/g, respectively.	Ghosh, 2009
	The activated carbon produced from algal bloom residue was used. The adsorption capacity was reported as 155.6 mg/g.	Zhang et al., 2010
<b>Coal</b>	The sorption capacity of coals has been found to lie within the range 10-30 mg/g.	Lakatos et al., 2002
	The sorption capacity of brown coal was reported as 0.98 mM/g. Maximum sorption was observed at pH 3.0. 81% Cr(VI) removal was observed at 100 mg/L.	Gode et al., 2006
	Cr (VI) adsorption on brown coals was described by Freundlich isotherm model. The sorption capacity of coals were reported as 11.2-7.4 mM/g.	Arslan and Pehlivan, 2007

(Continued on next page)

Table 4.1. (cont.)

<b>Sorbents</b>	<b>Results</b>	<b>References</b>
<b>Fly Ash</b>	The adsorption of Cr (VI) was higher at pH 3-4.	Bayat, 2002
	The adsorption capacity of fly ash was found as 1.38 mg/g. Langmuir isotherm fitted well with the experimental data.	Banerjee et al., 2004
	The sorption capacity of fly ash was reported as 23.86 mg/g. The optimum pH range for sorption of Cr (VI) was found to be between 2 and 3.	Bhattacharya et al., 2008
<b>Natural Zeolite</b>	The removal of chromium from leather industry wastewater by HNO <sub>3</sub> , H <sub>2</sub> SO <sub>4</sub> , HCl modified clinoptilolite was studied. The chromium adsorption capacities of activated clinoptilolite samples were given as following order: HNO <sub>3</sub> > H <sub>2</sub> SO <sub>4</sub> >HCl.	Toprak and Girgin, 2000
	Cr (VI) removal performance of Mexican clinoptilolite was investigated. 12 % Cr (VI) removal at pH 7 was observed.	Mier et al., 2001
	Cr (VI) uptake from simulated wastewater was studied with natural zeolite. NaCl treated zeolite had better removal capabilities (3.23 mg/g) for Cr(VI) ions than natural zeolite (1.79 mg/g) at an initial Cr concentration of 20 mg/L.	Babel and Kurniawan, 2003
	The adsorption of chromate by metal exchanged clinoptilolite was investigated. Pb-exchanged form of clinoptilolite showed the highest amount of chromate retention.	Faghihian and Bowman, 2005
	Chromium (VI) removal performances of natural and HNO <sub>3</sub> treated zeolites were tested. 70% chromium (VI) removal was observed with clinoptilolite and 79-80% chromium (VI) removal was observed with HNO <sub>3</sub> modified clinoptilolite.	Orhan and Kocaoba, 2007
<b>Synthetic Zeolites</b>	MCM-41 was more effective for removal of chromate than ZSM-5.	Ghiaci et al, 2004
	The adsorption capacity of 4A zeolite for uptake of Cr (VI) was evaluated. Highest Cr (VI) sorption was observed at pH 3.	Barakat, 2008

In recent years, surfactant modified zeolite and clay mineral have been used in the removal of Cr (VI). Literature studies about these sorbents are given in Table 4.2.

Table 4.2. Surfactant modified zeolites and clays used for Cr (VI) removal

Sorbents	Results	References
<b>Surfactant Modified Zeolites</b>	Sorption of chromate by cationic HDTMA-modified zeolites was attributed to anion exchange on exposed surfactant head groups resulting from formation of a surfactant bilayer.	Haggerty and Bowman, 1994
	The best oxyanion sorption was achieved when the initial surfactant concentration was greater than the critical micelle concentration (CMC). This was explained by the formation of surfactant bilayers; the positive charges of the bilayer were considered as adsorption sites for chromate.	Li and Bowman, 1997
	HDTMA and CPB modified clinoptilolite exhibited higher chromate adsorption than ZSM-5.	Ghiaci et al., 2004
	HDTMA modified clinoptilolite for the removal of chromates was investigated. Maximum sorption capacity was reported as 2.27 mg/g.	Warchol et al., 2006
	pH intervals for chromate sorption on surfactant modified chabazite were reported as 5-7. The sorption capacity of HDTMA-chabazite was found as 5.80 mg/g.	Majdan et al., 2006
	HDTMA modified mordenite had better removal performance than modified with EHDDMA.	Campos et al., 2007
	Cr (VI) sorption capacity of HDTMA modified zeolite decreased with increasing pH from 6 to 10 and decreasing pH from 6 to 4. The sorption capacity was reduced by increasing the temperature from 15 to 25 °C	Ramos et al., 2008
	Cr (VI) sorption was independent of the predominant species at pH range of 2 to 10. Chromium sorption capacity of HDTMA-modified clinoptilolite was reported as 7.79 mg/g.	Cordoves et al., 2008
	HDTMA modified NAY for the removal of Cr (VI) was investigated. Highest sorption efficiency was observed at pH 3.	Yusof and Malek, 2009
Chromate removal performance of clinoptilolite, chabazite and their surfactant modified forms were compared. HDPB modified samples had higher affinities toward chromate than that of natural forms.	Zeng et al., 2010	

(Continued on next page)

Table 4.2. (cont.)

Sorbents	Results	References
<b>Surfactant Modified Clays</b>	Maximum adsorption of chromates on HDTMA-modified bentonite and montmorillonite was observed at pH values below 1. Langmuir and DKR isotherm fitted well with the experimental data.	Krishna et al., 2000
	Sorption of chromate on organo-kaolinite was at least two orders of magnitude greater than its sorption on unmodified kaolinite. Optimum pH range for chromate sorption was reported as 5-9.	Li and Bowman, 2001
	Cr (VI) sorption capacities of surfactant modified, thermal and acid treated clay minerals was investigated. Adsorption capacity of modified clay with hexadecyltrimethylammonium bromide was higher than that of acid and heat treated ones.	Akar et al., 2009
	Montmorillonite was modified with cetylpyridinium bromide effectively adsorbed Cr (VI) anions over a pH range from 3 to 6.	Brum et al., 2010
	Montmorillonite was modified with hydroxyl-aluminum and cetyltrimethylammonium bromide. Higher Cr (VI) adsorption capacity was observed with hydroxyl-aluminum modified montmorillonite samples. The optimal pH for Cr (VI) removal was found as 4.	Hu and Luo, 2010

Sorption of Cr (VI) using bacterial, fungal and algae are the most productive strategies currently employed for removal of hexavalent chromium. Bacteria are used as sorbents because of their small size, ubiquity, ability to grow under controlled conditions, and their resilience to a wide range of environmental situations. Bacterial sorbents used for Cr (VI) removal are listed in Table 4.3. Both living and dead fungal cells have a remarkable ability for chromium uptake from water and wastewater. Algae are also widely used in the removal of Cr (VI). Algal sorbents used for Cr (VI) removal are given in Table 4.4. Table 4.5 represents fungal sorbents used for Cr (VI) removal.

Table 4.3. Bacterial sorbents used for Cr (VI) removal

Sorbents	Results	References
<i>B. subtilis</i>	38.8 % and 22.04% Cr(VI) removal was observed at 25 and 200 mg/L.	Kıvanç et al., 1996
	95 % and 50 % chromium removal was found at 10 and 80 µg/L.	Elangovan et al., 2006
	89.5% and 78.5% Cr (VI) removal was observed at 25 and 100 mg/L.	Parameswari et al., 2009
<i>E. coli</i>	54.62 %, 53.42%, 46.73% and 41.35 % chromium removal was achieved at 1, 2, 5 and 10 mg/L, respectively.	Abskharon et al., 2009
<i>Staph. sp</i>	The optimum pH value was found to be 3.	İlhan et al, 2004
	Cr (VI) removal was found as 90 % and 92 % at 3 and 0.3 mg/L, respectively.	Mistry et al., 2010
<i>P. aeruginosa</i>	<i>P.Aeruginosa</i> had the potential for chromium detoxification in industrial effluents if mixed with nutrient rich waste water such as sewage, which might provide the necessary energy and nutrients to the bacteria for multiplication and chromate reduction in the mixed effluent	Ganguli and Tripathi, 1999

Table 4.4. Algal sorbents used for Cr (VI) removal

Sorbents	Results	References
<i>Chlorella vulgaris</i> , <i>Scenedesmus obliquus</i> and <i>Synechocystis sp</i>	The optimum pH value was found to be 2.	Dönmez et al., 1999
<i>Sargassum wightii</i>	Optimum pH was found as 3.5–3.8. The adsorption capacity of <i>Sargassum species</i> was found as 35 mg/g.	Aravindhana et al., 2004
<i>Chlamydomonas reinhardtii</i>	Maximum Cr (VI) adsorption was obtained at pH 2.0. The biosorption capacities of native, heat and acid treated algal samples were 18.2, 25.6 and 21.2 mg/g of dry biosorbents, respectively.	Arica et al., 2005
<i>Oedogonium hatei</i>	The biosorption capacities of the raw and acid treated algae were found as 31 and 35 mg/g, respectively.	Gupta and Rastogi, 2009

Table 4.5. Fungal sorbents used for Cr (VI) removal

Sorbents	Results	References
<i>R. arrhizus</i>	Non-living free and immobilized <i>R. arrhizus</i> biomass adsorption capacities were 11 and 8.63 mg/g, respectively.	Prakasham et al., 1999
<i>Lentinus sajor-caju mycelia</i>	The maximum biosorption capacities of the untreated and heat, HCl and NaOH treated fungal biomass were 0.36, 0.61, 0.48 and 0.51 mmol/g of dry biomass, respectively.	Bayramoğlu et al., 2005
<i>Neurospora crassa</i>	Pretreatment of the raw biomass with heat, sodium hydroxide and acetic acid was studied. Acetic acid pretreatment caused the highest increase on sorption ability of <i>Neurospora crassa</i> among all pretreated methods. Sorption capacity of acetic acid pretreated biomass was found as $15.85 \pm 0.94$ mg/g.	Tunalı et al., 2005
<i>Aspergillus niger</i>	The Cr (VI) removal rate increased with a decrease in pH and with increases in Cr (VI) concentration, biomass concentration and temperature.	Park et al., 2005
	The adsorption capacity of <i>A. niger</i> was found as 117.3 mg/g.	Khambhaty et al., 2009
<i>Aspergillus flavus</i>	<i>Aspergillus flavus</i> can be used as an adsorbent for the removal of Cr (VI) from wastewaters containing low concentrations. The adsorption capacity of <i>A. flavus</i> was found as 0.335 mg/g.	Deepa et al., 2006

In recent years, the investigations for the removal of chromium with alternative material have gained much attention. Apart from the natural, synthetic and biosorbents, bacterial species supported materials have been used in the hexavalent chromium removal. Bacterial species supported materials used in Cr (VI) removal is listed in Table 4.6. Most of the studies focused on using *E. coli* supported materials.

Table 4.6. Bacterial species supported materials used in Cr (VI) removal

<b>Sorbents</b>	<b>Results</b>	<b>References</b>
<b><i>Bacillus coagulans</i>, <i>Streptococcus equisimilis</i> and <i>Escherichia coli</i> supported granular activated carbon</b>	Cr (VI) removal ranged from 46.9% to 17.2% at initial Cr (VI) concentration of 50–1000 mg/L, for <i>B. coagulans</i> , from 36.6% to 10.8%, for the <i>E. coli</i> and from 72% to 46.3%, for <i>S. equisimilis</i> supported granular activated carbon. The highest Cr (VI) removal results were obtained with <i>S. equisimilis</i> supported granular activated carbon. The results of <i>B. coagulans</i> , <i>S. equisimilis</i> and <i>E. coli</i> were comparable. The results indicated that gram positive bacteria showed higher Cr (VI) removal than gram negative bacteria.	Quintelas et al., 2008
<b><i>Arthobacter viscous</i> supported on granular activated carbon (GAC) and clinoptilolite</b>	The results indicated that 18% and 19% Cr (VI) removal was observed with zeolite and GAC. It increased to 42 % when both supports were used in series connection.	Lameiras et al., 2008
<b><i>E. coli</i> supported on kaolin</b>	The results indicated that 100% Cr (VI) removal was observed at lower concentration while percentage of chromium removal values decreased to 20 % at higher concentration.	Quintelas et al., 2009
<b><i>E. coli</i> supported on NaY</b>	30-60 % Cr (VI) removal was observed. Toth isotherm fitted well with the experimental data.	Quintelas et al., 2009
<b><i>E. coli</i> supported on granular activated carbon (GAC)</b>	The maximum biosorption capacity for hexavalent chromium using <i>E. coli</i> supported GAC, GAC and <i>E. coli</i> were 97.70, 90.70, 64.36 mg /g at pH 2.0, respectively.	Gabr et al., 2009

### 4.3. Functional Groups Related to Cr (VI) Sorption

Chemical functional groups present on the sorbents are important to understand the nature of the possible sorbent-metal ions interactions in the sorption process. Many researchers have used FTIR method to determine qualitative and preliminary analysis of the chemical functional groups on the sorbents. After metal sorption, sorbents showed some changes in the FTIR spectra pattern such as band disappearance after saturation of active sites (Mameri et al., 1999; Yun et al., 2001; Lin et al., 2005), band shifting



(Pethkar et al., 2001; Yun et al., 2001; Lin et al., 2005; Tunalı et al., 2005) and band elongation (Loukidou et al., 2004). Some researchers reported a decrease (Sheng et al., 2004; Tunalı et al., 2005) or increase (Adhiya et al., 2002; Lin et al., 2005) in certain band intensities after metal sorption. No change in the spectral pattern was observed after interaction with metal which indicated chemical reactions might not be involved in the biosorption of metal ions (Pethkar et al., 2001; Selatnia et al., 2004). The information from FTIR band should be considered to decide which functional groups are involved in Cr (VI) sorption.

A lot of studies carried out to investigate the FTIR spectra of the sorbents before and after Cr (VI) sorption. Loukidou et al. (2004) investigated the FTIR spectra of *A. caviae* before and after chromium sorption. The results indicated that 1071 and 1673  $\text{cm}^{-1}$  bands in the *A. caviae* were due to C–O and C=O stretching representing carbonyl and carboxyl groups. The group of phosphate presented certain other characteristic peaks, such as P=O stretching at 1150  $\text{cm}^{-1}$ , P–OH stretching at 1040–910  $\text{cm}^{-1}$  and P–O–C stretching at 1050–970  $\text{cm}^{-1}$ . The region between 3600 and 3100  $\text{cm}^{-1}$  indicated existence of free hydroxyl group (-OH) and N-H stretching. The region between 3100 and 2800  $\text{cm}^{-1}$  was related to the C-H stretching vibrations of -CH<sub>2</sub> groups. The region between 1250 and 1000  $\text{cm}^{-1}$  represented C–N stretching. The FTIR spectra of biomass after loaded with Cr (VI) indicated that band elongation in the carboxyl and amino groups were observed. Park et al. (2005) studied Cr (VI) sorption by brown seaweed biomass from *Ecklonia sp.* FTIR results of brown seaweed biomass revealed that the absorption peaks were observed at 3350  $\text{cm}^{-1}$  (-OH), at 2920  $\text{cm}^{-1}$  (CH stretching), at 1740  $\text{cm}^{-1}$  (C=O stretching), at 1650  $\text{cm}^{-1}$  (C=O chelate stretching and amide I), at 1530  $\text{cm}^{-1}$  (amide II), at 1160 and 1050  $\text{cm}^{-1}$  (C-N stretching). The FTIR spectrum of chromium-loaded biomass which was obtained by contacting the biomass with Cr (VI) (at pH 2) was compared with that of the biomass before Cr (VI) sorption. The peak around 1740  $\text{cm}^{-1}$  slightly disappeared and the peak around 1650  $\text{cm}^{-1}$  became larger after Cr (VI) sorption. The result indicated that the carboxyl groups (C=O) were involved in the Cr (VI) biosorption. The FTIR of *N. crassa* before and after Cr (VI) sorption was investigated by Tunalı et al., (2005). FTIR results of *N. crassa* revealed that the peaks were observed at 3346  $\text{cm}^{-1}$  (-OH), at 2908  $\text{cm}^{-1}$  (CH stretching), at 1645  $\text{cm}^{-1}$  (C=O chelate stretching and amide I), at 1549  $\text{cm}^{-1}$  (amide II), at 1408 (-SO<sub>3</sub>)  $\text{cm}^{-1}$ , at 1151 and 1077  $\text{cm}^{-1}$  (C-N stretching). After Cr (VI) sorption, band shift was observed. Additionally, the intensity of the peaks at 1645, at 1408 and at 1243  $\text{cm}^{-1}$

decreased after sorption process. The results implied that the interaction between Cr (VI) and the functional groups such as phosphate,  $\text{SO}_3$ , carboxyl and carbonyl groups should be considered in the sorption process. Gupta et al. (2009) investigated the FTIR spectra of *O. hatei* before and after Cr (VI) sorption. FTIR results of *O. hatei* indicated at  $3404\text{ cm}^{-1}$  (-OH), at  $2914\text{ cm}^{-1}$  (CH stretching), at  $1646\text{ cm}^{-1}$  (C=O chelate stretching and amide I), at  $1540\text{ cm}^{-1}$  (amide II), at  $1426\text{ cm}^{-1}$  (symmetric bending of  $\text{CH}_3$ ), at  $1243\text{ cm}^{-1}$  (-C=C-, P=O), at  $1168$  and  $1058\text{ cm}^{-1}$  (C-N stretching). After Cr (VI) sorption, there were slight changes in the peak intensities were observed. The results revealed that carboxyl and amino groups were responsible in Cr (VI) sorption process. Attia et al. (2010) studied the FTIR spectra of activated carbon which was produced from olive stones before and after Cr (VI) sorption. FTIR results of activated carbon indicated that the peaks were observed at  $3406$ ,  $2923$  and  $1627\text{ cm}^{-1}$ . The peak around  $3406\text{ cm}^{-1}$  indicated existence of free hydroxyl group. The peaks observed at  $2923\text{ cm}^{-1}$  could be attributed to the C-H stretching vibration of the  $-\text{CH}_2$  group. The peaks around  $1627\text{ cm}^{-1}$  corresponded to the carbonyl group. After Cr (VI) sorption, band shift in was observed.

All literature results revealed that hydroxyl, carbonyl, carboxyl, sulfonate, amino and phosphate groups on the sorbents are main functional groups in the Cr (VI) sorption.

## CHAPTER 5

### SORPTION

Sorption is a physical and/or chemical phenomenon in which compounds are accumulated at the interface of solid – liquid or solid-gas mixtures. In the course of a sorption process, the solid material is named as “sorbent”, whereas the species sorbed on to the solid material is called as “sorbate”. Sorption process is classified into physical and chemical sorption. Physical sorption is the results of relatively weak intermolecular forces. The forces responsible for physical sorption include both Van der Waals forces and electrostatic interactions comprising polarization, dipole and quadrupole interactions. In chemical sorption, the forces involved are much stronger and involve a considerable degree of transfer or sharing of the electrons. As a result, chemical sorption is highly specific and the adsorption energies are generally greater than those for physical sorption (Ruthven, 2006). The basic characteristics of the physical and chemical sorption are given in Table 5.1.

Table 5.1. The basic characteristics of the physical and chemical sorption  
(Source: Ruthven, 1984)

<b>Physical Sorption</b>	<b>Chemical Sorption</b>
Monolayer or multilayer	Monolayer only
Reversible	Generally irreversible
Non-specific	Highly specific
Low heat of sorption	High heat of sorption
Only significant at relatively low temperatures	Possible over a wide range of temperature

Sorbents are with pore diameter ranging from a few Å to a few hundred Å are widely used in sorption process. The sorption capacity of sorbents depend on surface area of sorbent, size of sorptive, polarity features of sorbent and sorptive, shape and size

of pores (Ülkü, 1991). According to IUPAC classification pores are divided into three categories based on their size.

- Macropores ( $>500 \text{ \AA}$ )
- Mesopores ( $20 - 500 \text{ \AA}$ )
- Micropores ( $<20 \text{ \AA}$ )

In different size ranges, different type of forces control sorption behavior. In the micropore range, surface forces are dominant and sorbed molecule never escapes from the force field of pore walls. In the mesopores, capillary forces become more important while the macropores actually contribute very little to sorption capacity (Karger and Ruthven, 1992).

Different mechanisms of diffusion occur in these different size ranges. Diffusion in micropores is dominated by interactions between the diffusing molecule and the pore wall. Diffusion within this regime is known as “intracrystalline diffusion” or “micropore diffusion”. Within the macropore range the role of surface is relatively minor. Diffusion occurs mainly by molecular diffusion mechanism. Within mesopores range Knudsen diffusion is generally more important but there may be also significant contributions from surface diffusion and capillary effects (Karger and Ruthven, 1992).

Many sorbents such as molecular sieve zeolite, carbon molecular sieve and ion exchange resins have a well defined bimodal pore size distribution since they are made from both macropore and micropore structure (Ruthven, 1984). Bidisperse ideal spherical particle is shown in Figure 5.1. Depending on the conditions, either macropore or micropore diffusion resistances may control the sorption process or both resistances may be significant.

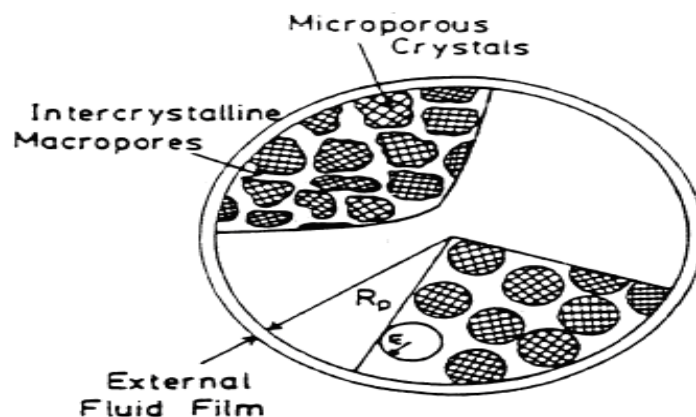


Figure 5.1. Bidisperse ideal spherical particle

## 5.1. Sorption Interactions

As a molecule approaches the solid surface, a balance is established between the intermolecular attractive and repulsive forces. Attractive forces are caused by a temporal symmetry of the charge distribution around a neutral atom or molecule due to the motion of its electron. The interaction energies between two single atoms or molecules decay as the inverse sixth power of the atom distance. The forces responsible for attractive forces include Keesom, Debye and London interactions. These interactions are shown in Figure 5.2. Keesom interactions occur between molecules exhibiting a permanent dipole. This interaction depends on the relative orientation of the two interacting dipole moments. Debye interaction describes the interaction between a molecule with a permanent dipole moment and the induced dipole moment of a polarizable molecule. London interaction arises from quantum mechanical fluctuations and describes the interaction between two induced dipoles. Of the three forces, Keesom and Debye interactions are only found between molecules which have permanent dipole moments, dominant for polar molecules. Whereas, the London interaction is always present, because it does not require existence of permanent polarity or charge-induced polarity in the molecules.

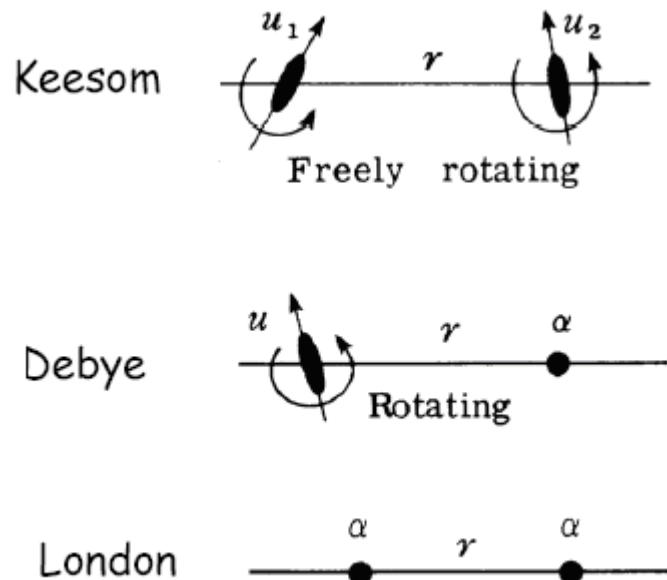


Figure 5.2. Attractive forces (Keesom, Debye and London interactions)

Electrostatic repulsive forces refer to the interaction between the molecule and the charge present on the sorbent. When a sorbent containing ionic species is placed in a liquid, the ionic groups on the surface can dissociate and dissolve in the liquid. This process creates a charge on the solid called the surface charge. Due to the separation of charge, an electric potential develops. Ions of opposite sign are attracted to the region near the surface; while ions with the same sign as the surface charge are repelled from the surface. This effect creates an electrical double layer at the proximity of the surface. The electrical double-layer consists of two layers: the Stern layer and a diffuse layer of ions. The ions within the Stern plane comprise the Stern layer and dictate the potential that governs the distribution of ions in solution. This diffuse layer is more concentrated in ions of opposite sign to the surface potential, while the ions of the same charge as the surface are depleted from the double layer. The schematic representation of the Stern and double layers is shown in Figure 5.3. As seen from the figure that the ions are strongly bound in Stern layer whereas they are less firmly attached in diffuse layer. At greater distance lesser ion concentrations are present since the electrostatic forces are weakened.

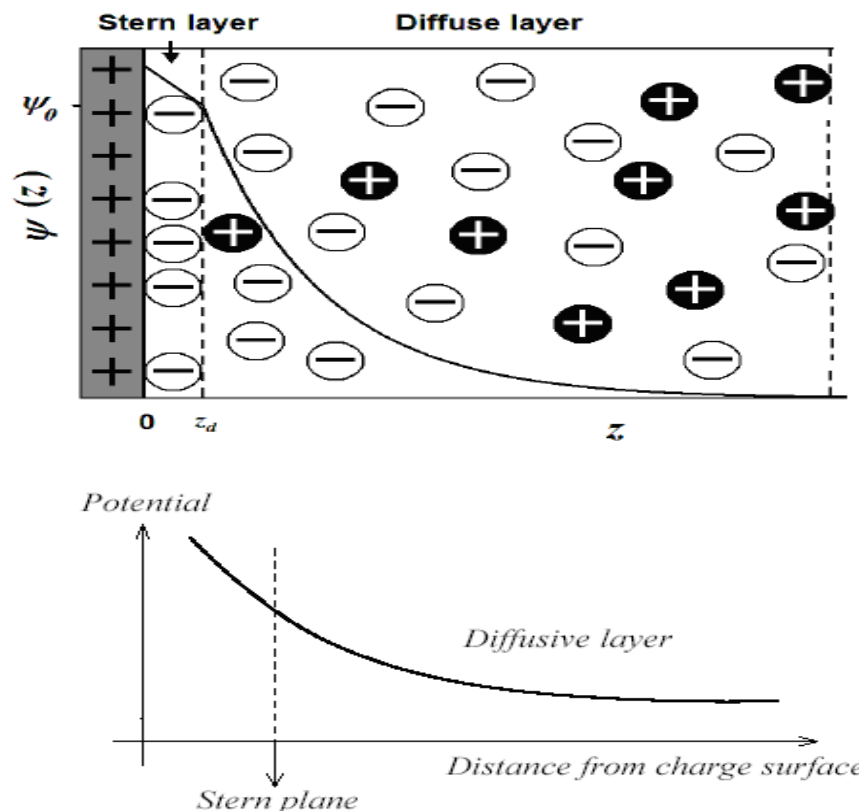


Figure 5.3. The schematic representation of the electrical double-layer

The total potential energy of the interaction between two surfaces is given by the summation of attractive and repulsive contributions (Eqn 5.1) (Hunter, 1993).

$$V_T = V_A + V_R \quad (5.1)$$

where the total interaction energy  $V_T$  is expressed in terms of the repulsive double layer interaction energy,  $V_R$ , and the attractive London–van der Waals energy,  $V_A$ . Contrary to the repulsive double layer interaction, the van der Waals interaction energy is mostly insensitive to variations in electrolyte strength and pH. Additionally, the van der Waals attraction must always be greater than the double layer repulsion at extremely small distances. A typical curve of the total interaction energy is shown in Figure 5.4.

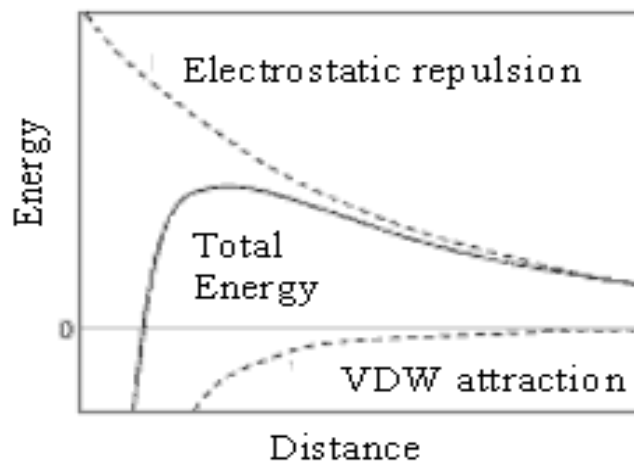


Figure 5.4. The variation of energy versus distance

## 5.2. Sorption Isotherms

Sorption isotherms are the representation of sorbed amount as a function of pressure or concentration at constant temperature. The sorption isotherms are very useful to describe the interaction between the sorbate and the sorbent. The parameters obtained from the sorption isotherm models provide important information for the sorption mechanisms, the surface properties and affinities of the sorbent. Many models such as Langmuir, Freundlich, Redlich Peterson and Temkin isotherms have been

developed to describe the equilibrium nature of sorption. Among these models, Langmuir and Freundlich are the most frequently applied isotherm models.

### 5.2.1. Langmuir Isotherm Model

Langmuir model assumes that sorption occurs at specific homogeneous sites within the adsorbents and all sites of the sorbents are identical and energetically equivalent. The Langmuir model equation and its linear form are given below:

$$q_e = \frac{bq_m C_e}{1 + bC_e} \quad (5.2)$$

$$\frac{C_e}{q_e} = \frac{1}{q_m b} + \frac{C_e}{q_m} \quad (5.3)$$

where  $q_e$  is concentration of sorbate in solid phase at equilibrium (mg/g),  $C_e$  is the concentration of sorbate in liquid phase at equilibrium (mg/L),  $q_m$  is maximum sorption capacity (mg/gr) and  $b$  is Langmuir constant (L/mg).

The Langmuir constant and maximum sorption capacity is estimated from the intercept and slope of Eq. (5.3).

The characteristics of the Langmuir isotherm can be expressed in terms of a dimensionless constant separation factor  $R_L$ . The value of  $R_L$  indicates the shape of isotherm to be either unfavorable ( $R_L > 1$ ) or linear ( $R_L = 1$ ) or favorable ( $0 < R_L < 1$ ) or irreversible ( $R_L = 0$ ).

$$R_L = \frac{1}{1 + bC_0} \quad (5.4)$$

where  $C_0$  is the highest initial concentration (mg/L) and  $b$  is Langmuir constant (L/mg).



### 5.2.2. Freundlich Isotherm Model

Freundlich isotherm is the earliest known relationship describing the non-ideal and reversible adsorption, not restricted to the formation of monolayer. This empirical model can be applied to multilayer adsorption with non-uniform distribution of adsorption heat and affinities over the heterogeneous surface. The model equation and its linear form are written as:

$$q_e = k_F \cdot C_e^{1/n} \quad (5.5)$$

$$\log q_e = \log k_F + \frac{1}{n} \log C_e \quad (5.6)$$

where  $q_e$  is concentration of sorbate in solid phase at equilibrium (mg/g),  $C_e$  is the concentration of sorbate in liquid phase at equilibrium (mg/L),  $k_F$  is Freundlich constant and  $1/n$  is heterogeneity factor. The constant  $n$  represents the deviation from linearity of adsorption as follows: if the value  $n = 1$ , the sorption is linear;  $n < 1$ , the sorption process is chemical; if  $n > 1$ , the sorption is a favorable physical process.

The slope and intercept of the linear plot of  $\log q_e$  versus  $\log C_e$  are used to determine heterogeneity factor ( $1/n$ ) and Freundlich constant ( $k_F$ ), respectively.

### 5.2.3. Redlich-Peterson Isotherm Model

Redlich–Peterson isotherm is a hybrid isotherm featuring both Langmuir and Freundlich isotherms, which incorporate three parameters into an empirical equation. In the limit, it approaches Freundlich isotherm model at high concentration (as the exponent  $b_R$  tends to zero) and is in accordance with the low concentration limit of the ideal Langmuir condition (as the values  $b_R$  are all close to one). This model is applied either in homogeneous or heterogeneous systems due to its versatility. The model equation and its linearized form is given below:

$$q_e = \frac{K_R C_e}{1 + a_R C_e^{b_R}} \quad (5.7)$$

$$\ln \frac{K_R C_e}{q_e - 1} = b_R \ln(C_e) + \ln(a_R) \quad (5.8)$$

where  $K_R$ ,  $a_R$  and  $b_R$  are Redlich–Peterson model constant.

The Redlich–Peterson model constants can not be obtained using graphical methods because of the three unknown parameters. A minimization procedure with solver add-in function of the Microsoft excel is used to calculate the model constants.

#### 5.2.4. Temkin Isotherm Model

The Temkin isotherm assumes that the heat of sorption of all the molecules in the layer decreases linearly with coverage due to sorbent–sorbate interactions, and that the sorption is characterized by a uniform distribution of the binding energies, up to some maximum binding energy. The model equation and its linear form are given in Equation 5.9 and 5.10.

$$\theta = \frac{RT}{\Delta Q} \ln K_0 C_e \quad (5.9)$$

$$\theta = \frac{RT}{\Delta Q} \ln K_0 + \frac{RT}{\Delta Q} \ln C_e \quad (5.10)$$

where  $\theta$  is the fractional coverage,  $R$  is the universal gas constant,  $T$  is the temperature,  $\Delta Q$  is the variation of sorption energy and  $K_0$  is the Temkin model constant.

The variation of sorption energy and the Temkin model constant is calculated from the slope and the intercept of the plot  $\theta$  versus  $\ln C_e$ .

### 5.3. Sorption Kinetics

Sorption equilibrium and kinetic are the basic requirements for the design of sorption process. Sorption kinetic depends on the physical and chemical properties of the sorbent, sorbent-sorbate interaction and system conditions. Several kinetic models which are based on reaction and diffusion model are used to examine the rate of sorption process. Sorption rate covers a series of resistance resulted from diffusion and

reaction steps. The relative importance of the resistance depends on the materials involved and on the specific operating conditions.

There are essentially four consecutive steps in the sorption process and these steps are shown in Figure 5.5.

- Transport of solute from bulk solution to the exterior film surrounding of the sorbent
- Diffusion of solute through the film surrounding the particle
- Diffusion of solute in the pores of the sorbent particle and/or diffusion of the solute along the sorbent surface
- Sorption of solute on the sorbent surface with surface reaction due to physical or chemical interaction.

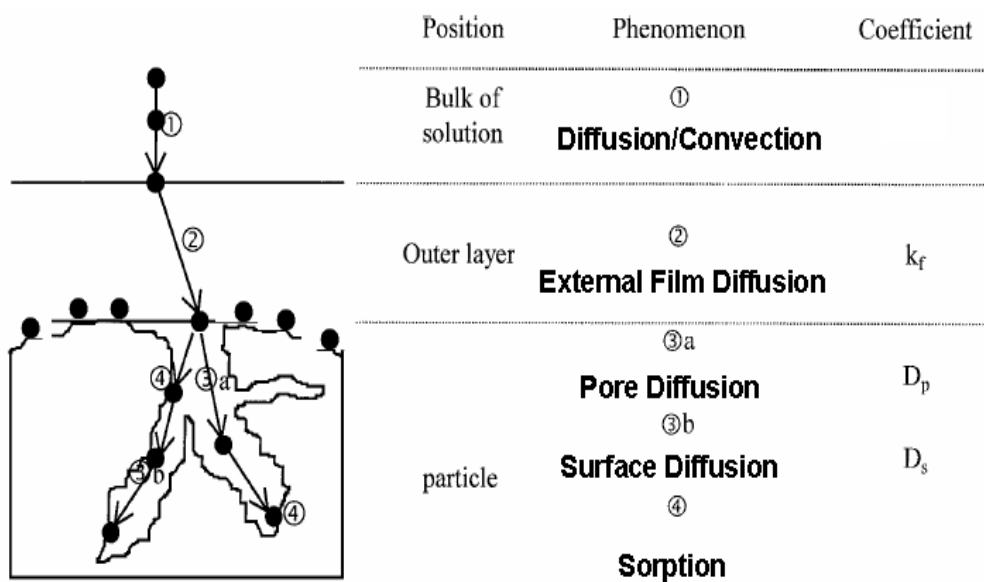


Figure 5.5. Four steps of sorption (Source: Baup et al., 2000)

The solute is transported from the bulk solution to the external layer of the sorbents in step 1. It is non-limiting when agitation is sufficient to avoid concentration gradients in the solution. Step 2 involves diffusion of solute across the external film surrounding the particle. The external film diffusion occurs by molecular diffusion through the laminar boundary layer. Step 3 is examined in two aspects which are pore and surface diffusion. Surface diffusion occurs by diffusion along the sorbent surface. Diffusion in macropores occurs by molecular diffusion. Diffusion in micropores is dominated by interactions between the diffusing molecule and pore wall. The sorption

of solute on the sorbent surface with surface reaction takes place in step 4. The rate limiting step is resulted from one or combination of these steps.

The experimental parameters such as agitation speed, particle size, initial concentration, pH and temperature should be comprehensively discussed in order to decide which mechanism are considered as rate limiting step. The best way to determine whether the external film diffusion is controlling step or not, is to carry out the series of batch kinetic experiments at different agitation speeds. The thickness of boundary layer affects the external mass transfer resistance which depends on the hydrodynamic conditions of fluid. At lower agitation speed, external mass transfer resistance becomes higher because of higher boundary layer thickness. By increasing agitation speed, the external mass resistance becomes smaller due to the reduction of the boundary layer thickness but it may be still large enough to have significant effect on the sorption process.

Particle size also affects the external and intraparticle diffusion resistance. As the particle size is decreased, the external mass transfer effect on the sorption rate becomes more and more significant. Increasing particle size yields higher intraparticle diffusion resistance. Intraparticle diffusion resistance covers both micropore and macropore resistance if the sorbent has a bi-porous structure. Depending on the conditions, either macropore or micropore diffusion resistances may control the sorption process or both resistances may be significant. If the micropore diffusion resistance is dominant, the concentration throughout the sorbent particle is considered as uniform and thus sorption rate is independent of the particle size. On the other hand, the sorption rate strongly depends on the particle size when the macropore resistance is dominant.

The initial uptake rate is significantly influenced by changing initial concentration. If the external mass transfer is the main mechanism, the initial uptake rate decreases with increasing initial concentration. If the sorption process is controlled by intraparticle mass transfer, initial uptake rate increases with increasing initial concentration. Increasing initial concentration results in steeper uptake curve.

pH of the solution affects functional groups on the sorbent surface and the properties of sorbed molecules. If the metal ion is used in sorption process, the form of the metal species should be considered to explain sorption mechanism. Sorption rate is strongly influenced by the electrostatic forces between sorbent and form of metal

species. Hence, the contribution from the electrostatic forces should be taken into account in the sorption kinetic analysis.

Change in temperature gives the idea about the nature of the sorption process. The decrease in sorption with increasing temperature indicates the weak sorption interaction between sorbents and sorbed molecule which supports the physical sorption process (Van Der Waals,  $\Pi$ - $\Pi$  and hydrogen bonding forces). The increase in sorption with increasing temperature indicates the strong sorption interaction between sorbents and sorbed molecule which supports the chemical sorption process.

All these parameters are important to understand the main controlling mechanism in the sorption process. In order to identify main controlling step, several kinetic models are investigated. The details of these kinetic models are discussed in the following part.

#### **5.4. Sorption Kinetic Models**

In order to assess the contribution from the sorption steps, kinetic models based on reaction and diffusion models are used. The kinetic models are given in Figure 5.6.

Sorption diffusion models cover single, two and three resistance models. Single resistance models are developed by assuming either external film diffusion or intraparticle diffusion as the sole rate limiting step. Analytical solutions are used to solve the mathematical models developed based on single resistance models. Single resistance models are helpful to get a quick estimate of mass transfer parameters. The single resistance models are extended to double or triple resistance mechanisms by combining external mass transfer with intraparticle diffusion. Two and three resistance models are more rigorous and allow estimation of mass transfer parameters more accurately. Film-pore, pore-surface, homogeneous surface diffusion and branched pore diffusion are such models available for the analysis of sorption kinetics and are particularly useful when both the mass transfer steps are important. However, the contribution from each mass transfer step is difficult to differentiate. Analytical solutions are very difficult for majority of these systems. Numerical methods such as Crank-Nicholson, Orthogonal and Cartesian Collocation are used to solve the set of simultaneous partial defining equations for two and three resistance models.

In reaction kinetic model, it is assumed that surface reaction step makes a significant contribution in the kinetic of a sorption process and the rate of surface reaction is considered as rate limiting step. The models include first order, pseudo-first order, pseudo-second order and Elovich model equations. Analytical methods are used to solve the reaction kinetic model.

The distinction between the diffusion and reaction controlled processes is often difficult. The diffusion-controlled systems are characterized by only a small dependence on temperature, while a reaction-controlled system is more dependent on temperature. The magnitude of the activation energy ( $E_a$ ) gives an idea about the type of sorption processes. Reaction controlled processes usually have energies greater than 25–30 kJ/mol; while diffusion controlled processes usually have energies lower than 25–30 kJ/mol.

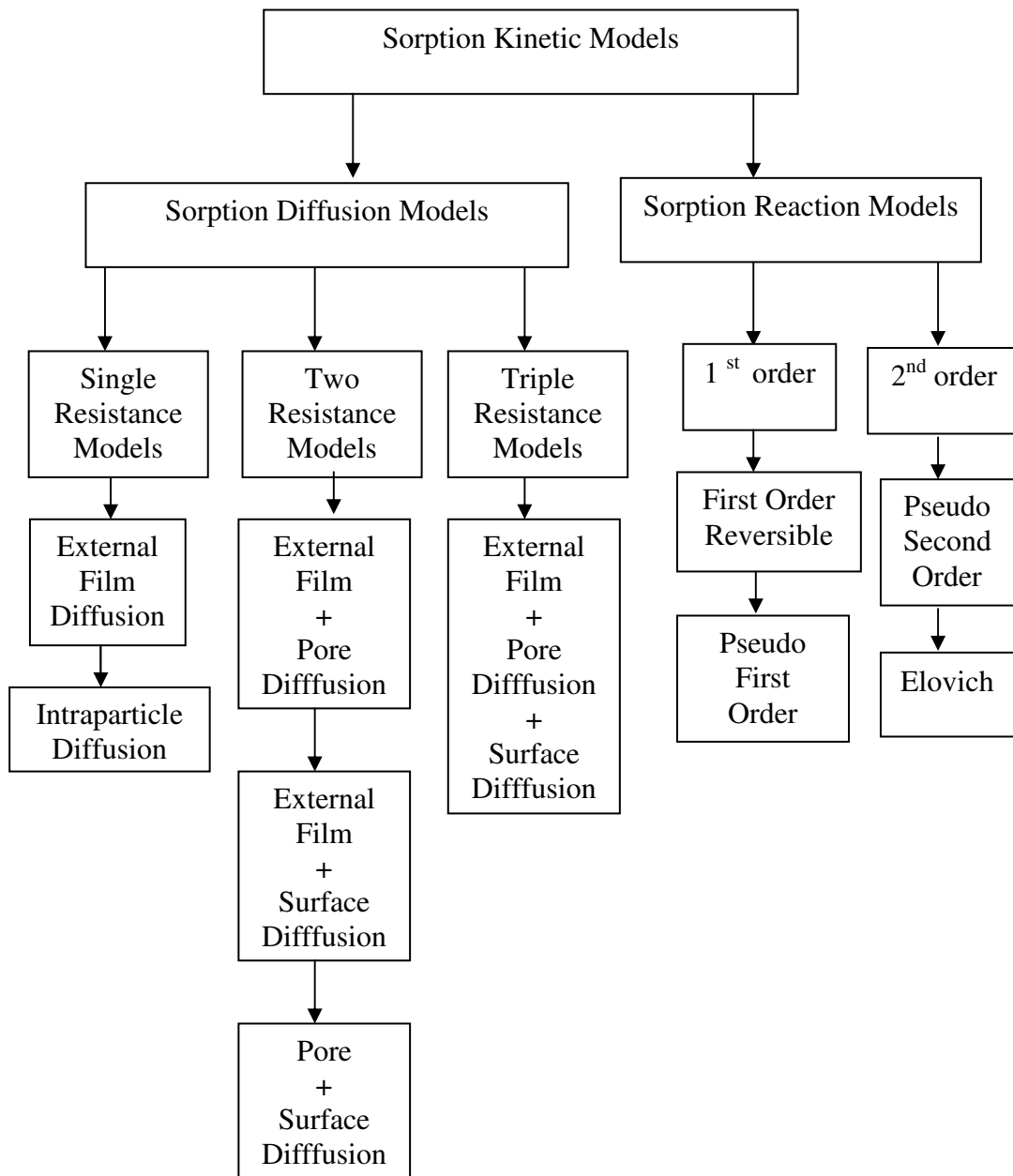


Figure 5.6. Sorption kinetic models based on reaction and diffusion models

## 5.5. Sorption Diffusion Models

### 5.5.1. External Film Diffusion

The external film diffusion occurs by molecular diffusion through the laminar boundary layer which is shown in Figure 5.7. The thickness of the boundary layer affects the external mass transfer resistance which depends on the hydrodynamic condition of the fluid. By increasing agitation speed, the external mass resistance

becomes smaller due to the reduction of the boundary layer thickness. The contribution of external resistance on the sorption process is still significant (Karger and Ruthven, 1992).

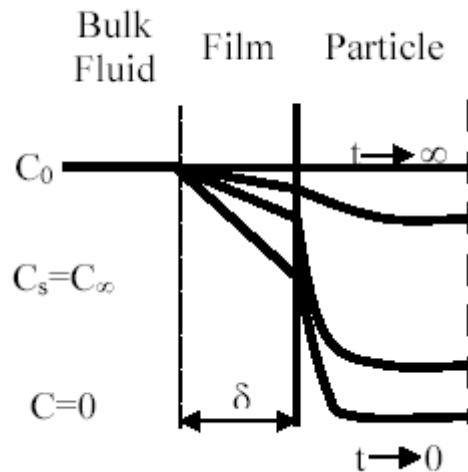


Figure 5.7. Schematic diagram of concentration profile due to external and internal mass transfer resistance (Source: Karger and Ruthven, 1992)

External mass transfer resistance is generally correlated in terms of a mass transfer coefficient ( $k_f$ ). An increase in the  $k_f$  value indicates a decrease in the external mass transfer resistance. Mathematical models for external film diffusion are developed based on single resistance model. The models assume that only external film diffusion is predominant during the initial sorption period and controls the sorption rate. External mass transfer coefficient ( $k_f$ ) is calculated by three single resistance models: (1) Mathew-Weber, (2) Furusawa-Smith and (3) Boyd models. Following assumptions are used in the development of these models.

- (a) Sorbent particles are spherical.
- (b) Mixing in the liquid phase is rapid (perfect mixing).
- (c) Isothermal system.
- (d) The rate of sorption is controlled by diffusion through the laminar fluid film surrounding the particle.

These models differ in their description of equilibrium relationship. Furusawa-Smith and Boyd Models takes into account the linear equilibrium relationship.

For Mathew-Weber model and Furusawa-Smith model, the change in fluid phase concentration,  $C$ ; with respect to time,  $t$ ; is related to the fluid phase concentration at the external surface,  $C_s$  and the external mass transfer coefficient,  $k_f$ ; by:



$$\frac{dC_t}{dt} = -k_f S(C_t - C_s) \quad (5.11)$$

The surface area for mass transfer is defined as:

$$S = \frac{6m/V}{d_p \rho_p (1 - \epsilon_p)} \quad (5.12)$$

where m is the mass of adsorbent, V is the volume of solution,  $d_p$  is the particle diameter,  $\rho_p$  is particle density and  $\epsilon_p$  is particle porosity.

For Mathew-Weber model, boundary and initial conditions are given in Equation 5.13.

$$\begin{aligned} t = 0 \quad C_s &= 0 \\ t = 0 \quad C_t &= C_0 \\ t = t \quad C_t &= C_t \end{aligned} \quad (5.13)$$

The boundary and initial conditions are substituted into Equation 5.11 and the integrated form of the equation is given in Equation 5.14.

$$\begin{aligned} \frac{dC_t}{dt} &= -k_f S(C_t) \\ \int_{C_0}^{C_t} \frac{dC_t}{C_t} &= -k_f S \int_0^t dt \\ \ln \frac{C_t}{C_0} &= -k_f S t \end{aligned} \quad (5.14)$$

The initial slope of the linear plot of  $\ln C_t/C_0$  versus t is used to determine external mass transfer coefficient ( $k_f$ ).

For Furusawa-Smith model, boundary and initial conditions are given in Equation 5.15- 5.17.

$$D_e \left( \frac{\partial C_r}{\partial r} \right)_{r=r_p} = k_f (C_t - C_s) \quad (5.15)$$

$$\frac{\partial C_r}{\partial r} = 0 \quad r = 0 \quad (5.16)$$

$$C_r = 0 \quad t = 0 \quad 0 \leq r \leq r_p$$

$$\frac{\partial q}{\partial t} = K_L \frac{dC_s}{dt} \quad \text{at } q_t = 0 \quad \text{when } t = 0 \quad (5.17)$$

The initial and boundary condition is substituted into Equation 5.11 and the integrated form of the equation is given in Equation 5.18.

$$\left( \frac{1}{1 + \frac{1}{\frac{m}{V} K_L}} \right) \ln \left( \frac{C_t}{C_0} - \frac{1}{\frac{m}{V} K_L} \left( 1 - \left( \frac{C_t}{C_0} \right) \right) \right) = -k_f S t \quad (5.18)$$

The external mass transfer coefficient for Furusawa-Smith model is determined

from the slope of  $\left( \frac{1}{1 + \frac{1}{\frac{m}{V} K_L}} \right) \ln \left( \frac{C_t}{C_0} - \frac{1}{\frac{m}{V} K_L} \left( 1 - \left( \frac{C_t}{C_0} \right) \right) \right)$  versus time.

For Boyd model, the rate of solute accumulation in the solid phase is equal to that of solute transfer across the liquid film according to the mass balance law. The equation is given in Equation 5.19.

$$\left( \frac{\partial \bar{q}}{\partial t} \right) = k_f S (C - C_s) \quad (5.19)$$

where  $\bar{q}$  is the average solute concentration in the solid,  $S$  is the surface area per unit volume of the particle,  $k_f$  is external mass transfer coefficient,  $C_s$  is the solute concentration at the particle/liquid interface,  $C$  is the bulk solute concentration.

For a linear equilibrium ( $q=K_L C$ ), the bulk solute concentration ( $C$ ) is maintained constant. Equation 5.19 becomes:

$$\left( \frac{\partial \bar{q}}{\partial t} \right) = \frac{3k_f}{K_L r_p} (q - \bar{q}) \quad (5.20)$$

Boundary conditions are given in Equation 5.21.

$$\begin{aligned} t < 0 & \quad C = q = 0 \\ t > 0 & \quad C = C_e = \frac{q_e}{K_L} \end{aligned} \quad (5.20)$$

Final form of the Boyd model equation is given below:

$$\frac{\bar{q}}{q_e} = 1 - \exp \left[ - \frac{3k_f}{K_L r_p} t \right] \quad (5.22)$$

The external mass transfer coefficient is determined from the slope of the plot  $\ln(1 - \frac{\bar{q}}{q_e})$  versus time.

The external mass transfer coefficient ( $k_f$ ) can also be calculated using empirical correlations in terms dimensionless numbers (Sherwood, Reynolds and Schmidt). Sherwood ( $Sh$ ) number is written as:

$$Sh = \frac{2k_f r_p}{D_m} \quad (5.23)$$

where  $Sh$  is Sherwood number,  $k_f$  is external mass transfer coefficient ( $k_f$ ),  $r_p$  is particle radius,  $D_m$  is molecular diffusivity.

For an isolated spherical sorbent particle in a stagnant fluid, Sherwood ( $Sh$ ) is equal 2. Under flow conditions, Sherwood ( $Sh$ ) number is function of Schmidt ( $Sc$ ) and Reynolds ( $Re$ ) number. There are several empirical correlations for Sherwood number and some of them are tabulated in Table 5.2.

Table 5.2. Empirical correlations for external mass transfer

<b>Empirical Correlations</b>	<b>Range of Validity</b>	<b>References</b>
$Sh = 2 + 0.6Sc^{1/3} Re^{1/2}$	$2 \leq ReSc^{0.67} \leq 50000$	Ranz and Marshal, 1952
$Sh = 4.58 Re^{0.33} Sc^{0.33}$	$0.4 < Re < 10$	Karabelas et al., 1971
$Sh = 1.85 \left( \frac{1-\varepsilon}{\varepsilon^2} \right)^{0.33} Re^{0.33} Sc^{0.33}$	$Re/(1-\varepsilon) < 10$	Kataoka et al., 1972
$Sh = 5.4 + Re^{1/3} Sc^{1/4}$	$0.04 < Re < 30$	Coeuret, 1976
$Sh = \frac{1.13}{\varepsilon} Re^{0.21} Sc^{0.33}$	$Re < 10$	Kumar, 1977
$Sh = 4.3 Re^{0.35} Sc^{0.25}$	$0.1 < Re < 3$	Olive and Lacoste, 1979

## 5.5.2. Intraparticle Diffusion

Intraparticle diffusion is examined in two aspects which are pore and surface diffusion. Surface diffusion occurs by diffusion along the sorbent surface. Pore diffusion covers micropore and macropore diffusion. Depending on the particular system and conditions, either macropore or micropore diffusion resistances may control the sorption process or both resistances may be significant. The details of macropore and micropore diffusion are discussed in the following part.

### 5.5.2.1. Macropore Diffusion

If the sorbent has porous structure composed of macropore and micropore, initially solute diffuses throughout macropore. Different transport mechanisms are involved in macropore diffusion, which are molecular, Knudsen and surface diffusion. The mechanisms are shown in Figure 5.8.

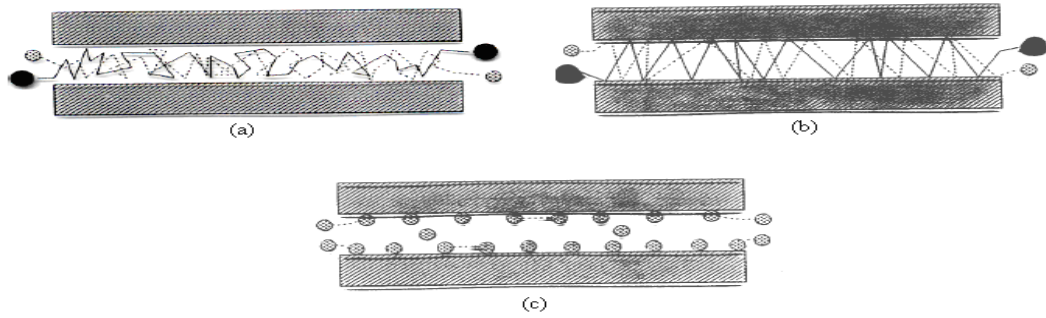


Figure 5.8. Macropore Diffusion Mechanisms (a) Molecular (b) Knudsen (c) Surface

Diffusion of a molecule in a macropore occurs through two mechanisms: molecular and Knudsen diffusion. Relative importance of molecular or Knudsen diffusivity is largely determined by the diameter of macropore and mean free path of the diffusing molecule. Molecular diffusion is the dominant mechanism if the mean free path of the diffusing molecule is smaller than the pore diameter. If the diffusion occurs only by molecular diffusion, the pore diffusivity is identical with molecular diffusivity; the pore diffusivity is given by:

$$D_p = \frac{\varepsilon_p D_m}{\tau} \quad (5.24)$$

where  $D_p$  is pore diffusivity,  $\varepsilon_p$  is porosity,  $D_m$  is molecular diffusivity and  $\tau$  is tortuosity.

Tortuosity ( $\tau$ ) is a geometric factor and thus it is independent from experimental conditions. For inert-type solids tortuosity can vary from about 1.5 to 5. For straight cylindrical pores, tortuosity is taken as 3.

Molecular diffusion for gas system is estimated from Chapman-Enskog equations. Several theoretical models such as Stokes-Einstein and Wilke-Chang correlations are used to calculate molecular diffusion for liquids.

Knudsen diffusion becomes dominant in small pores and at low pressure when collisions between the diffusing molecules and pore wall occur more frequently than collisions between the diffusing molecules themselves. The Knudsen diffusivity is estimated from the equation:

$$D_K = 9700 \bar{r} \left( \frac{T}{M} \right)^{1/2} \quad (5.25)$$

where  $D_K$  is Knudsen diffusivity,  $\bar{r}$  is the mean pore radius, T is temperature, M is molecular weight.

In transition stage, where the mean free path is comparable with the pore diameter, both Knudsen and molecular diffusion are significant. In this case, the combined effect of molecular diffusion and Knudsen diffusion is estimated by:

$$\frac{1}{\varepsilon_p D_p} = \frac{\varepsilon_p}{\tau} \left[ \frac{1}{D_K} + \frac{1}{D_m} \right] \quad (5.26)$$

Both Knudsen and molecular diffusion involve diffusion through the fluid phase in the central region of the pore. If there is significant sorption on the pore wall, there is the possibility of an additional flux due to the diffusion through the sorbed phase. This is referred as “surface diffusion”. The contribution of surface diffusion becomes significant if the adsorption equilibrium is favorable. The overall diffusivity is given by:

$$D = D_K + K \left[ \frac{1 - \varepsilon_p}{\varepsilon_p} \right] D_s \quad (5.27)$$

where  $D_K$  is Knudsen diffusivity,  $D_s$  is the surface diffusivity, K is the adsorption equilibrium constant and  $\varepsilon_p$  is the porosity.

The relative importance of surface diffusion depends on the ratio of  $K D_s / D_K$ . The temperature dependence of  $D_s$  has been usually analyzed by the Arrhenius equation by considering surface diffusion as an activated process. Surface diffusion is generally insignificant at temperatures which are high relative to the normal boiling point of the sorbate (Ruthven, 1984; Kärger and Ruthven, 1992). Surface diffusion in gas-phase adsorption systems is well documented, extensively studied. Compared to gas-phase systems, the mechanism of surface diffusion in liquid-phase adsorption systems is not well understood, and relatively little data on surface diffusivities are available. This can

be attributed to the lack of in-situ experimental techniques for determining the intrinsic surface diffusivities of solutes at solid-liquid interfaces. Most studies employ indirect methods in determining surface diffusivities in liquid systems. For example, batch-rotating basket and Wicke-Kallenbach experiments were used to estimate surface diffusivities of organic solutes in activated carbon (Komiyama and Smith, 1974; Suzuki and Takao, 1982). The estimation of surface diffusion is difficult since it varies to high degree with the combination of sorbates, sorbents and solvents.

Following assumptions are usually used in the development of the macropore diffusion model.

- (a) Micropore diffusion is rapid in the system and thus the concentration gradient within microparticles is uniform.
- (b) Macropore diffusion resistance is dominant.
- (c) Local equilibrium between the sorbed phase and fluid phase within macropore at any specified radial direction.
- (d) Pore diffusivity is independent of concentration.
- (e) Sorbent particles are spherical.
- (f) Equilibrium relationship is linear.
- (g) Isothermal system.

When diffusion within the macropore is rate controlling, the uptake rate for uniform spherical particle is expressed by the following equations.

$$(1 - \varepsilon_p) \frac{\partial q}{\partial t} + \varepsilon_p \frac{\partial C}{\partial t} = \varepsilon_p D_p \left( \frac{\partial^2 C}{\partial R^2} + \frac{2}{R} \frac{\partial C}{\partial R} \right) \quad (5.28)$$

$$\frac{\partial C}{\partial t} = \frac{\varepsilon_p D_p}{\varepsilon_p + (1 - \varepsilon_p) K} \left( \frac{\partial^2 C}{\partial R^2} + \frac{2}{R} \frac{\partial C}{\partial R} \right) \quad (5.29)$$

The boundary conditions are given as:

$$\begin{aligned} C(R,0) &= C_0 & q(R,0) &= q_0 \\ C(R_p,t) &= C_\infty & q(R_p,t) &= q_\infty \\ \frac{\partial C}{\partial R} \Big|_{R=0} &= \frac{\partial q}{\partial R} \Big|_{R=0} & &= 0 \end{aligned} \quad (5.30)$$

The solution for model equation is given below:

$$\frac{q_t}{q_\infty} = 1 - \frac{6}{\pi^2} \sum_{n=1}^{\infty} \frac{1}{n^2} \exp\left(\frac{-n^2 \pi^2 \varepsilon_p D_p \cdot t}{R_p^2 (\varepsilon_p + (1 - \varepsilon_p) K)}\right) \quad (5.31)$$

where  $\frac{D_p / R_p^2}{\left[1 + \frac{(1 - \varepsilon_p) K}{\varepsilon_p}\right]}$  is the time constant for the macropore diffusion.

The assumption of linear equilibrium and constant diffusivity is valid when the change in concentration is small. If the change in concentration is very large, the assumption of linear equilibrium and constant diffusivity is invalid. In this case, the effect of nonlinearity of the equilibrium must be considered. Pore diffusivity is assumed to be concentration dependent.

For a Langmuir isotherm,

$$\frac{q}{q_m} = \frac{bC}{1 + bC} \Rightarrow \frac{dq}{dC} = \frac{bq_m}{(1 + bC)^2} = bq_m \left(1 - \frac{q}{q_m}\right)^2 \quad (5.32)$$

Solute concentration in the pores is very small relative to in the sorbed phase and thus Equation 5.28 becomes:

$$\frac{\partial q}{\partial t} = \frac{\varepsilon_p D_p}{(1 - \varepsilon_p) bq_m} \frac{1}{R_p^2} \frac{\partial}{\partial R} \left( \frac{R^2}{\left(1 - \frac{q}{q_m}\right)^2} \frac{\partial q}{\partial R} \right) \quad (5.33)$$

The concentration dependent diffusivity is given by:

$$D_e = \frac{\varepsilon_p D_p}{(1 - \varepsilon_p) \left(1 - \frac{q}{q_m}\right)^2 bq_m} \quad (5.34)$$



### 5.5.2.2. Micropore Diffusion

If the pore size of the microparticle is close to the size of diffusing molecule, the diffusing molecules can not escape from the field of the pore walls. In this pore region, diffusion occurs by an activated process in which the molecules jump randomly between neighboring low energy sites. This diffusion regime is known as “configurational” or “intracrystalline” diffusion. The geometry of the pores, chemical composition of the sorbent (type, charge and distribution of the cations), shape, size, polarity and concentration of diffusing molecules and temperature affect diffusion in micropores (Ruthven and Karger, 1992). Micropore diffusion model generally assumes that:

- (a) Micropore diffusion resistance is dominant.
- (b) The diffusivity is independent of concentration.
- (c) Sorbent particles are spherical.
- (d) Diffusion occurs in radial direction.
- (e) The uptake of sorbate by the sorbent is small relative to the total quantity of sorbate in the solution.
- (f) Isothermal system.
- (g) Equilibrium relationship is linear.

When diffusion within the micropore is rate controlling, the uptake rate for uniform spherical particle is expressed by the following equations.

$$\frac{\partial q}{\partial t} = \frac{1}{r^2} \frac{\partial}{\partial r} \left( r^2 D_c \frac{\partial q}{\partial r} \right) \quad (5.35)$$

$$\frac{\partial q}{\partial t} = D_c \left( \frac{\partial^2 q}{\partial r^2} + \frac{2}{r} \frac{\partial q}{\partial r} \right) \quad (5.36)$$

The relevant initial and boundary condition are:

$$\begin{aligned} t < 0 \quad C = C_0 \quad q = q_0 \\ t \geq 0 \quad C = C_\infty \quad q(r_c, t) = q_\infty \\ t \rightarrow \infty \quad C = C_\infty \quad q(r, t) = q_\infty \end{aligned} \quad (5.37)$$

$$\left. \frac{\partial q}{\partial t} \right|_{r=0} = 0 \quad \text{for all } t$$

Crank (1956) gave an exact solution to Equation 5.35 for the “infinite bath” case. The solution for model equation is given below:

$$\frac{q_t}{q_\infty} = 1 - \frac{6}{\pi^2} \sum_{n=1}^{\infty} \frac{1}{n^2} \exp\left(\frac{-n^2 \pi^2 D_c \cdot t}{r_c^2}\right) \quad (5.38)$$

Equation 5.38 can be described as two periods which are short time region and long time region. The related equations for short and long time periods are given below:

$$\frac{q_t}{q_\infty} = \frac{6}{\sqrt{\pi}} \left(\frac{D_c \cdot t}{r_c^2}\right)^{1/2} \quad (q_t/q_\infty < 0.3) \quad (5.39)$$

$$1 - \frac{q_t}{q_\infty} \cong \frac{6}{\pi^2} \exp\left(-\frac{\pi^2 D_c t}{r_c^2}\right) \quad (q_t/q_\infty > 0.7) \quad (5.40)$$

Using expression in Equation 5.39 and 5.40, from the slopes of plots  $q_t/q_\infty$  versus  $\sqrt{t}$  (short time region) and  $\ln [1 - q_t/q_\infty]$  vs.  $t$  (long time region), the diffusion coefficient is calculated.

If the uptake of sorbate by the sorbent is not negligible compared to the total quantity of sorbate in the solution, the “finite bath” case is valid. The solution for the uptake curve becomes:

$$\frac{q_t}{q_\infty} = 1 - 6 \sum_{n=1}^{\infty} \frac{\exp(-D_c p_n^2 t / r_c^2)}{9\Lambda / (1-\Lambda) + (1-\Lambda) p_n^2} \quad (5.41)$$

where  $p_n$  is given by nonzero root of:

$$\tan p_n = \frac{3p_n}{3 + (1/\Lambda - 1)p_n^2} \quad (5.42)$$

$\Lambda$  is defined from the following equation:

$$\Lambda = \frac{C_0 - C_\infty}{C_0} \quad (5.43)$$

The effect of “finite bath” case becomes significant when  $\Lambda$  is greater than 0.1.

If the change in concentration is very large, the effect of nonlinearity of the equilibrium isotherm must be considered. The diffusivity is assumed to be concentration dependent.

For a Langmuir system,

$$D_c = D_o \left(1 - \frac{q}{q_s}\right)^{-1} \quad (5.44)$$

Equation 5.35 becomes:

$$\frac{\partial q}{\partial t} = \frac{D_o}{r^2} \frac{\partial}{\partial r} \left( \frac{r^2}{\left(1 - \frac{q}{q_s}\right)} \frac{\partial q}{\partial r} \right) \quad (5.45)$$

Intraparticle diffusion rate constant ( $k_d$ ) is determined from the short time solution of micropore diffusion model. In this model, boundary and initial conditions is written as  $r_p$  (particle radius) instead of  $r_c$  (crystal radius). Therefore,  $D_e$  (effective diffusivity) is replaced with  $D_c$  (intracrystalline diffusivity). The short time solution of micropore diffusion becomes:

$$\frac{q_t}{q_\infty} = \frac{6}{\sqrt{\pi}} \left( \frac{D_c \cdot t}{r_p^2} \right)^{1/2} \quad \left( \frac{q_t}{q_\infty} < 0.3 \right) \quad (5.46)$$

The intraparticle diffusion rate constant ( $k_d$ ) is expressed by the following equations.

$$q_t = \frac{6D_e^{1/2}q_\infty}{\sqrt{\pi}r_p} t^{1/2} \quad (5.47)$$

$$q_t = k_d t^{1/2} \quad (5.48)$$

Equation 5.48 is expressed as Weber Morris model. The intraparticle diffusion rate constant ( $k_d$ ) is calculated from the slope of plot of  $q_t$  versus  $t^{0.5}$ . If the plot gives a straight line through the origin, intraparticle diffusion is considered as the rate limiting step. If the plot does not pass through the origin, intraparticle diffusion is not only mechanism in the sorption process. If there are two or more mechanisms in the sorption process, the plot shows multilinearity.

An examination of the effect of initial concentration and particle size on the intraparticle diffusion rate constant ( $k_d$ ) provides additional information regarding to the sorption process. The nature of the rate-limiting step is confirmed by plotting  $k_d$  versus the first power of the initial concentration and  $k_d$  versus square of the inverse particle diameter. If these plots do not give straight lines, intraparticle diffusion is not rate limiting step.

Another intraparticle diffusion model, which was proposed by Boyd, is derived from the long time solution of micropore diffusion model. In this model, boundary and initial conditions is written as  $r_p$  (particle radius) instead of  $r_c$  (crystal radius). Therefore,  $D_e$  (effective diffusivity) is replaced with  $D_c$  (intracrystalline diffusivity). The long time solution of micropore diffusion becomes:

$$1 - \frac{q_t}{q_\infty} \cong \frac{6}{\pi^2} \exp\left(-\frac{\pi^2 D_c t}{r_p^2}\right) \quad \left(\frac{q_t}{q_\infty} > 0.7\right) \quad (5.49)$$

$$F = \frac{q_t}{q_\infty} = 1 - \frac{6}{\pi^2} \exp(-Bt) \quad (5.50)$$

where  $Bt$  is a constant and  $F$  is the fractional attainment of equilibrium at time  $t$ .

Equation 5.50 is expressed as Boyd model.  $Bt$  is calculated from following equations:

$$Bt = -0.4977 - \ln\left(1 - \frac{q_t}{q_\infty}\right) \quad F > 0.85 \quad (5.51)$$

$$Bt = \left(\sqrt{\pi} - \sqrt{\pi - \left(\frac{\pi^2 F}{3}\right)^2}\right) \quad F < 0.85 \quad (5.52)$$

The plot of  $Bt$  against  $t$  gives the idea about the existence of intraparticle diffusion. If the plot is linear and passes through the origin, intraparticle diffusion controls the rate of mass transfer. If the plot does not pass through the origin, then it is concluded that external film diffusion controls the sorption rate.

### 5.5.2.3. Comparison of Micropore and Macropore Diffusion Resistance

Depending on the particular system and the conditions, either macropore or micropore diffusion resistances may control the sorption process or both resistances may be significant. The relative dominance of the micropore diffusion in a bi-porous sorbent particle can be confirmed experimentally by varying size particle. When the sorption rate is controlled by macropore diffusion, there exists a concentration gradient within the particle. The sorption rate is dependent to the particle size. But in case of micropore diffusion controlling system, the assumption of constant concentration gradient through the particle is applicable. Thus the rate of sorption is not dependent to the particle size of sorbent (Ülkü and Mobedi, 1989).

The relative importance of the macropore and micropore diffusion resistances depends on the ratio of the time diffusional constants. The ratio of the time diffusional constant is expressed as following equation:

$$\gamma = \frac{\frac{\varepsilon_p D_p}{(\varepsilon_p + (1 - \varepsilon_p)K)}}{\frac{R_p^2}{\frac{D_c}{r_c^2}}} = \frac{\text{Time scale of macropore}}{\text{Time scale of micropore}} \quad (5.53)$$

If  $\gamma$  is less than unity, the time scale of diffusion in the crystal is greater than that in macropore, and so micropore diffusion controls the sorption process. On the other hand, if  $\gamma$  is greater than unity, macropore diffusion controls the sorption process. If the

time scales of both macropore and micropore are very close to each other, it is difficult to decide which resistance controls the sorption process. The models which includes both macropore and micropore resistance are needed to explain for the analysis of sorption process. The models are developed for intraparticle diffusion which occurs in series or in parallel. These models assume that the diffusion in the particle occurs by macropore diffusion through the voids of porous particle and diffusion in the crystals occurs by micropore diffusion.

The model equation developed for series and parallel macropore-micropore diffusion is given in Equation 5.52 and 5.53.

$$\frac{\partial C}{\partial t} + \frac{\partial q}{\partial t} = \frac{1}{R_p^2} \frac{\partial}{\partial R} \left[ (D_c \frac{\partial q}{\partial R}) + (D_p \frac{\partial C}{\partial R}) \right] \quad (5.54)$$

$$\frac{1}{R_p^2} \frac{\partial}{\partial R} (D_p \frac{\partial C}{\partial R}) = \frac{\partial C}{\partial t} + \frac{\rho(1-\varepsilon)q_0}{\varepsilon C_0} (3 \int_0^r \frac{1}{r_c^2} \frac{\partial}{\partial r} (D_c \frac{\partial q}{\partial r}) r^2 dr) \quad (5.55)$$

### 5.5.3. Sorption Diffusion Models Based on Two-Three Resistances

*Film-Pore diffusion* is based on the “unreacted shrinking core” mass transfer model proposed by Levenspiel (1972) where the reaction starts at the particle surface forming a reacted zone which moves inward with a certain velocity. Sphan and Schlunder (1975) developed the model with the following assumptions:

- (a) Sorption rate is controlled by an external mass transfer resistance and an internal pore mass transfer resistance.
- (b) Mass transfer in the pores is solely by molecular diffusion.
- (c) Internal mass transfer is measured by the effective pore diffusion coefficient ( $D_e$ )
- (d) Sorption is irreversible.
- (e) Solute concentration in the pore is very small relative to that in the sorbed phase.
- (f) Isothermal system.

The model equation is given in Equation 5.54.

$$\varepsilon_p \frac{\partial C}{\partial t} + \rho_p \frac{\partial q}{\partial t} = D_e \left( \frac{\partial C}{\partial r} + \frac{1}{r} \frac{\partial C}{\partial r} \right) \quad (5.56)$$

The initial and boundary conditions are:

$$\begin{aligned} t = 0 \quad C = 0 \quad 0 \leq r \leq r_p \\ \frac{\partial C}{\partial r} = 0 \quad r = 0 \\ k_f (C - C_s) = D_e \left. \frac{\partial C}{\partial r} \right|_{r=r_p} \end{aligned} \quad (5.57)$$

This model is solved by using finite-difference method, as approximating the spatial derivation by central difference expression.

**Homogeneous Surface Diffusion** model, which is proposed by Mathew and Weber (1977), includes the effects of external mass transfer, unsteady-state surface diffusion in the particle and non-linear sorption isotherm. The following assumptions are used to develop this model:

- (a) The sorbent particle is assumed to be a homogeneous solid in which the sorbate is transported by surface diffusion.
- (b) Pore diffusion makes a negligible contribution to mass transport.
- (c) The sorbent particles are assumed to be spherical
- (d) A linear driving force describes the liquid film transport resistance at the outer surface of the particle.
- (e) At the solid/liquid interface, there is continuity between external mass transfer and internal diffusion.
- (f) The system is isothermal.

The model equation is given in Equation 5.58.

$$\frac{\partial q}{\partial t} = \frac{D_s}{r^2} \frac{\partial}{\partial r} \left( r^2 \frac{\partial q}{\partial r} \right) \quad (5.58)$$

Initial and boundary conditions are:

$$\begin{aligned}
q(r,0) &= 0 \\
q(r_p,t) &= q_s(t) \\
\frac{\partial q}{\partial r} &= 0 \quad r = 0 \\
\rho D_s \frac{\partial q}{\partial r} &= k_f (C - C_s) \quad r = r_p \\
C(t) = C_o \quad C_s(t) &= 0 \quad t = 0
\end{aligned} \tag{5.59}$$

Orthogonal Collocation method is used to solve this model equation.

**Pore-Surface Diffusion** model are mainly based on the diffusional step inside the porous particle (Mijangos et al., 2001). General assumptions for this model are:

- (a) External resistance is negligible
- (b) The concentration outside the particle is constant.
- (c) Surface concentration is constant assuming that the equilibrium value corresponds to fluid phase concentration.
- (d) Pore and surface diffusion coefficients are constant.
- (e) Diffusion takes place only in radial direction.
- (f) The sorbent particles are assumed to be spherical.
- (g) Temperature is constant.
- (h) Equilibrium relationship is linear.

According to these assumptions and considering surface and pore diffusion through the macropore, the model is described by Equation 5.60.

$$\varepsilon_p \frac{\partial C}{\partial t} + \rho \frac{\partial q}{\partial t} = \frac{1}{r^2} \frac{\partial}{\partial r} \left( \varepsilon_p r^2 D_p \frac{\partial C}{\partial r} + \rho r^2 D_s \frac{\partial q}{\partial r} \right) \tag{5.60}$$

Initial and boundary conditions are:

$$\begin{aligned}
t = 0 \quad r = r_p \quad C &= C_o \quad q = q_o \\
t = 0 \quad 0 < r < r_p \quad C &= 0 \quad q = 0 \\
t > 0 \quad r = 0 \quad \frac{\partial C}{\partial r} &= 0 \quad \frac{\partial q}{\partial r} = 0
\end{aligned} \tag{5.61}$$



**Branched pore diffusion model** covers three resistances which are external, macropore and micropore diffusion resistances. Diffusion through macropores is mainly described by solid diffusion, while in micropores multidirectional interactions between pore walls and solute molecule are significant. Model equations are:

$$\begin{aligned}
 f \frac{\partial q_{mac}}{\partial t} &= f \frac{D_{emac}}{r^2} \frac{\partial}{\partial r} \left( r^2 \frac{\partial q_{mac}}{\partial r} \right) - R_b \\
 (1-f) \frac{\partial q_{mic}}{\partial t} &= (1-f) \frac{D_{emic}}{r^2} \frac{\partial}{\partial r} \left( r^2 \frac{\partial q_{mic}}{\partial r} \right) + R_b \\
 q &= f q_{mac} + (1-f) q_{mic}
 \end{aligned} \tag{5.62}$$

where  $f$  is the volume fraction occupied by macropore region and  $R_b$  is the rate transfer of the diffusing species from the macropore to micropore region.

Initial and boundary conditions are:

$$\begin{aligned}
 q_{mac}(r,0) &= 0 \\
 q_{mic}(r,0) &= 0 \\
 q_{mac}(r_p,t) &= q_s(t) \\
 \frac{\partial q_{mac}}{\partial r} &= 0 \quad r=0 \\
 f\rho D_s \frac{\partial q_{mac}}{\partial r} &= k_f (C - C_s) \quad r=r_p
 \end{aligned} \tag{5.63}$$

The model equations are solved using Crank- Nicholson finite difference techniques.

## 5.6. Sorption Reaction Models

### 5.6.1. First Order Reversible Model

The first order reversible kinetic model is based on a reversible reaction with equilibrium state being established between two phases and is expressed as: (Bhattacharya and Venkobachar, 1984)

$$\begin{aligned}\frac{dC_B}{dt} &= -\frac{dC_A}{dt} = C_A \frac{dX_A}{dt} = k_1 C_A - k_2 C_B \\ &= k_1(C_{A0} - C_{A0} X_A) - k_2(C_{B0} - C_A X_A)\end{aligned}\quad (5.64)$$

where  $C_A$  (mg/l) is the concentration of solute on the adsorbent and  $C_B$  (mg/l) is the concentration of solute in solution at time  $t$ ,  $C_{A0}$  and  $C_{B0}$  are the initial concentrations of solute on sorbent and solution, respectively.  $X_A$  is the conversion of solute;  $k_1$  and  $k_2$  are the first order rate constants.

Initial and boundary conditions are given in Equation 5.65.

$$\begin{aligned}t = 0 \quad C_t &= 0 \\ t = t \quad C_t &= C_t \\ \frac{dC_B}{dt} &= -\frac{dC_A}{dt} = 0\end{aligned}\quad (5.65)$$

The final form of the equation is given in Equation 5.66.

$$\begin{aligned}\ln\left[\frac{(C_t - C_e)}{(C_t - C_0)}\right] &= -k^* t \\ k^* &= k_1\left(1 + \frac{1}{K_c}\right) = k_1 + k_2 \\ K_c &= \frac{k_1}{k_2}\end{aligned}\quad (5.66)$$

The first order rate constant is determined from the plot of  $\ln\left[\frac{(C_t - C_e)}{(C_t - C_0)}\right]$  versus time.

### 5.6.2. Pseudo First Order Model

Lagergren's pseudo first order model equation is the earliest known one describing the sorption rate based on the sorption capacity. The model assumes that the rate of change of solute uptake with time is directly proportional to the difference in saturation concentration and the amount of solid uptake with time. Its differential form is explained from the following equation:

$$\frac{dq_t}{dt} = k_1(q_e - q_t) \quad (5.67)$$

where  $q_e$  and  $q_t$  (mg/g) are the sorption capacities at equilibrium and at time  $t$  (min), respectively.  $k_1$  ( $\text{min}^{-1}$ ) is the pseudo first order rate constant.

After integration and applying boundary conditions  $t = 0$  to  $t = t$  and  $q_t = 0$  to  $q_t = q_t$ , the integrated form of equation becomes;

$$\log(q_e - q_t) = \log q_e - \frac{k_1}{2.303} t \quad (5.68)$$

The pseudo first order rate constant  $k_1$  ( $\text{min}^{-1}$ ) and the calculated  $q_e$  values are determined from the plots of slopes and intercepts of  $\log(q_e - q_t)$  versus  $t$  respectively.

The pseudo first order model differs from a classical first order reaction in two aspects: the expression of  $k(q_e - q_t)$  does not represent the number of available sites and the parameter  $\log q_e$  is an adjustable parameter whose value is not equal to the intercept of the  $\log(q_e - q_t)$  versus  $t$  (Ho and McKay, 1998).

The pseudo first order equation of Lagergren does not fit well for the whole range of contact time and is generally applicable over the initial 20 to 30 minutes of the sorption process. Therefore, it is difficult to predict true  $q_e$  values by using this model since it is valid at the initial period of sorption time.

The pseudo first order model is based on the assumption that the rate-limiting step is a physical sorption involving adsorption force through van der Waals force,  $\Pi$ - $\Pi$  force and hydrogen bonding between sorbent and sorbate (Wang et al., 2009).

### 5.6.3. Pseudo Second Order Model

The pseudo second order model assumes that the sorption process is a pseudo-chemical reaction process with the driving force being the difference between the average solid concentration and the equilibrium concentration with the overall sorption rate proportional to the square of the driving force (Yang and Al-Duri, 2005). Ho and McKay (1998) assumed that the sorption capacity is proportional to the number of active sites occupied in the sorbent and expressed the rate equation accordingly:

$$\frac{dq_t}{dt} = k_2(q_e - q_t)^2 \quad (5.69)$$

where  $q_e$  and  $q_t$  (mg/g) are the sorption capacities at equilibrium and at time  $t$  (min), respectively.  $k_2$  ( $\text{g mg}^{-1} \text{min}^{-1}$ ) is the pseudo second order rate constant.

For the initial conditions  $t=0$  to  $t=t$  and  $q_t=0$  to  $q_t= q_t$  the integrated form of Equation 5.69 becomes:

$$\left( \frac{t}{q_t} \right) = \frac{1}{k_2 q_e^2} + \frac{1}{q_e} (t) \quad (5.70)$$

The calculated  $q_e$  and pseudo second order rate constant ( $k_2$ ) are determined from the plots of slopes and intercepts of  $t/q_t$  versus  $t$ , respectively.

The pseudo-second-order equation has the following advantages: it allows the evaluation of effective sorption capacity, initial sorption rate and the rate constant of the pseudo-second-order kinetic model without knowing any parameter beforehand (Ho and Mckay, 1998; Ho and Ofomaja, 2006).

The pseudo second order model is based on the assumption that the rate-limiting is a chemical sorption involving sorption force through sharing or exchange of electrons between sorbent and sorbate (Wang et al., 2009).

#### 5.6.4. Elovich Model

The Elovich equation is often valid for heterogeneous surface. This model is expressed as:

$$\frac{dq_t}{dt} = \alpha \exp(-\beta q_t) \quad (5.71)$$

where  $\alpha$  is the initial adsorption rate ( $\text{mg g}^{-1} \text{min}^{-1}$ ) and  $\beta$  is the desorption constant ( $\text{gmg}^{-1}$ ).

It is simplified by assuming  $\alpha\beta t \gg 1$  and by applying the boundary conditions  $q_t = 0$  at  $t = 0$  and  $q_t = q_t$  at  $t = t$  Eq. (5.71) becomes form as followed:

$$q_t = \frac{1}{\beta} \ln(\alpha\beta) + \frac{1}{\beta} \ln(t) \quad (5.72)$$

The parameter is obtained from the slope of intercept of the linear plot of  $q_t$  versus  $\ln(t)$ .

### 5.6.5. Ritchie Model

Ritchie model was developed originally to describe the kinetics of gas–solid sorption, but its use was extended to liquid-solid sorption .The basic assumption of Ritchie model is: the rate of sorption depends solely on the fraction of sites which are unoccupied at time t. The model equation is given as:

$$\frac{d\theta}{dt} = \alpha(1-\theta)^n \quad (5.73)$$

where  $\theta$  is the fraction of surface, n is the number of surface sites and  $\alpha$  is the rate constant.

After integration, for the boundary conditions  $\theta=\theta_0$  at  $t=t_0$  and  $\theta=\theta$  at  $t=t$ , Equation 5.73 becomes:

$$\frac{1}{(1-\theta)^{n-1}} = (n-1)\alpha t + \frac{1}{(1-\theta_0)^{n-1}} \quad (5.74)$$

It is assumed that no site is occupied at  $t=0$ . Equation 5.74 becomes:

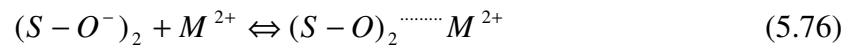
$$\frac{q_\infty^{n-1}}{(q_\infty - q)^{n-1}} = (n-1)\alpha t + 1 \quad (5.75)$$

## 5.7. Possible Mechanisms in the Zeolite-Heavy Metal System

Sorption, surface precipitation and dissolution are possible mechanisms in zeolite–heavy metal systems. Investigation of these interactions is important to understand the mechanism throughout the process.

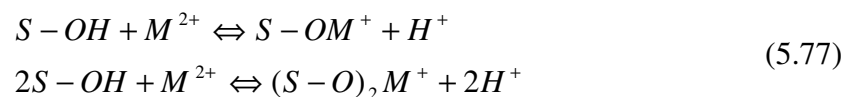
Sorption is one of the most important processes in heavy metal removal. The forces involved in sorption can range from weak, physical, Van der Waals forces and electrostatic outer-sphere complexes to chemical interactions. Chemical interactions can include inner-sphere complexation that involves a ligand exchange mechanism, covalent bonding, hydrogen bridges, and steric or orientation effects (Doula and Ioannou, 2003).

In general, the process of sorption begins as soon as outer-sphere complexes are formed on external surface sites of the adsorbent. The outer-sphere complexation involves the ion-exchange reactions between metal ions and surface counterbalance cations. The outer-sphere mechanism in sorbent metal system is shown in the following reaction (Doula and Ioannou, 2003). Outer-sphere complexation is usually rapid and reversible. This kind of complexation leads to less stable surface groups due to the formation of weak forces.



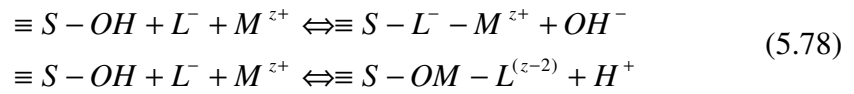
where S corresponds to surface central atom and M represents metal cation.

The increase in metal concentration forces metal ions into internal surface sites cause formation of inner-sphere complexes. Inner-sphere complexation involves covalent bonding. Inner-sphere complexation is slower and irreversible. This kind of complexation leads to more stable surface groups due to the formation of covalent bonding.



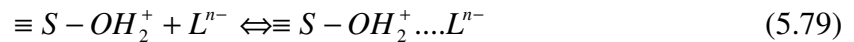
When the metal is sorbed by surface, both outer and inner sphere complex coexist. Therefore, they affect the rate and reversibility of sorption process (Scheidegger and Sparks, 1996).

During metal sorption, the metals often exist in the aqueous phase as complexes with inorganic and organic ligands. These complexing ligands have a significant effect on metal ion behavior (Doula and Ioannou, 2003). Interactions between metal ions and complexing ligands is described by following reaction: (Stumm and James, 1990)



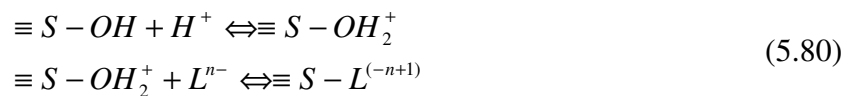
Metal-ligand complexes may form in solution. They compete with surface complexes and sorption is decreased because of the competition. By altering the surface electrical properties, the metal-ligand complexes may interact directly at the surface. The metal-ligand complexes may adsorb strongly. In this case, removal of metal is enhanced by these complexes (Stumm and James, 1990).

Anionic ligands can be sorbed to solids by both inner and outer sphere complexation mechanisms. The following reaction can describe anion-ligand complexes: (Goldberg, 1992)



Outer sphere complexation is the coordination of anion ( $L^{n-}$ ) to a protonated hydroxyl. Anions complexes in the outer sphere of the sorbent are readily exchangeable and free to move in solution because there is no complex formed with surface functional groups, but also neutralization of surface charge (Doula and Ioannou, 2003).

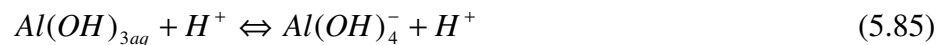
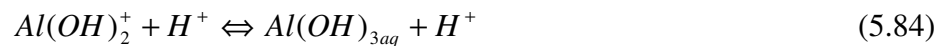
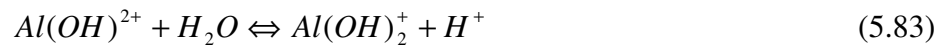
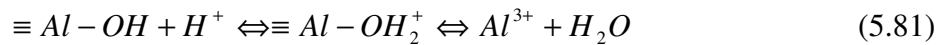
Inner sphere complexation of anionic ligands involves two steps. Initially, the protonation of surface occurs. After protonation, hydroxyl ligand exchange occurs.



At higher surface coverage, surface precipitation can form due to the increase in metal cation or anion sorbed on a surface. At low surface coverage, complexation is dominant mechanism. The formation of aggregates occurs when the surface coverage increases. At higher surface coverage, surface precipitation becomes the dominant mechanism. Metal uptake by sorbent reduced by the formation of precipitates in sorbent which causes to pore clogging in the sorbent (Inglezakis et al., 1999). Therefore, the controlling pH of solution is important in order to prevent precipitation during the sorption process (Doula and Ioannou, 2003).

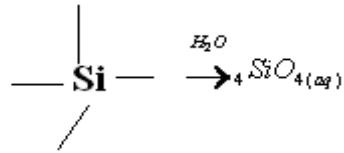
In addition to sorption and surface precipitation, dissolution also takes place in a heavy metal solution-zeolite system. Metal ions and ligand can impact on surface and cause dissolution of  $Al^{3+}$  or  $Si^{4+}$ . The dissolution of sorbent is strongly influenced by the type of surface species that forms inner surface complexes. For example,  $Cl^-$  ions enhances dissolution because it makes detachment of central atom easier. This is due to the electron density shift from ligands towards the central metal ion at the surface (Doula and Ioannou, 2003). The dissolution increases with increasing protonation and decreasing surface protonation. Surface protonation leads to highly polarized interatomic bonds in the immediate proximity of the surface central ions and therefore enhances the detachment of cationic surface group into the solution (Doula and Ioannou, 2003).

The dissolution of Al as a function pH is represented in following reactions:



The dissolution of Si does not involve  $H^+$  or  $OH^-$  and its dissolution reaction is represented below:





(5.86)

The dissolution of Si only depends on pH of the solution. Generally, it appears under acidic and basic conditions while the minimum dissolution occurs at pH of the solution equal to the isoelectric point value (Stumm, 1991).

## CHAPTER 6

### MATERIALS AND METHODS

#### 6.1. Zeolite Sample Preparation

Clinoptilolite rich mineral (CLI) was obtained from mineral deposits located in Manisa Gördes region. The clinoptilolite rich mineral sample was crushed in Fritsch jaw crusher and sieved into different particle size ranges. Each particle size ranges were wet sieved to remove soluble impurities. After wet sieving, the clinoptilolite rich mineral sample was dried overnight at 105°C and then it was kept in desiccator which was filled with saturated NH<sub>4</sub>Cl solution.

#### 6.2. Surfactant Modified Zeolite Sample Preparation

##### 6.2.1. Surfactants

In order to modify the clinoptilolite rich mineral samples, cationic and anionic surfactants were used. A quaternary amine, hexadecyltrimethylammonium bromide (C<sub>19</sub>H<sub>42</sub>BrN) purchased from Alfa (99.9 %) was used as cationic surfactant. Sodium dodecyl sulfate (C<sub>12</sub>H<sub>25</sub>SO<sub>4</sub>Na) purchased from Merck (99 %) was used as anionic surfactant.

##### 6.2.2. Preparation of Surfactant Modified Zeolite

In the preparation of HDTMA modified clinoptilolite rich mineral samples, the following procedure was applied. Fifty milliliters of HDTMA solution with concentration of 0.02 mol/L was placed in a flask and 0.5 g of clinoptilolite rich mineral sample was added into the solution. Then, the sample was placed into a shaker and was shaken at 400 rpm and 25 °C for 3 hours. The mixture was centrifuged at 1000 rpm for 10 min. After centrifugation, the liquid part was removed and the solid part was washed

three times with deionized water to remove the excess cationic surfactant on the zeolite surface. The centrifugation procedure was repeated for three times under the same conditions. Finally, HDTMA modified clinoptilolite sample was dried in an oven at 40 °C for 24 hours and stored in desiccators for further studies.

Similar modification steps were applied for anionic surfactant modified clinoptilolite rich minerals by using 0.03 mol/L SDS.

After modification step, cationic and anionic surfactant modified clinoptilolite rich mineral samples were abbreviated as CMCLI and AMCLI, respectively.

### **6.3. Bacteria Loaded Zeolite Samples Preparations**

#### **6.3.1. Bacteria**

*Escherichia coli* (NRLL-B-3008) and *Pseudomonas aeruginosa* (ATCC- 27853) were chosen as Gram negative bacteria whereas *Bacillus subtilis* (NRLL-B-4378), *Staphylococcus aureus* (ATCC-29213) and *Staphylococcus epidermidis* (ATCC-12228) were chosen as Gram positive bacteria.

Stock bacteria cultures were stored at -80°C. Bacteria cell cultures were grown in 8 mL Mueller Hinton Broth (Oxoid) at 37 °C for 24 hr.

#### **6.3.2. Viable Cell Count Method**

Serial dilution was used for the quantitative estimation of bacteria cells in a known volume of samples. Peptone-water solution was used in serial dilution method. In order to prepare peptone-water solution, 1 g peptone (Oxoid) was put into 1 L deionized water. After that, peptone-water solution was mixed in a stirrer to obtain homogeneous solution and then 1 mL from each sample was added to 9 ml peptone water solution. Serial dilution procedure is given in Figure 6.1.

After serial dilution step, 1 mL sample was added to a sterile petri dish and then melted Mueller Hinton agar (Merck) was poured in and mixed with sample. After drying of agar, the petri dishes were placed into incubator at 37°C. Within two or three

days, the bacteria colonies were grown in the petri dishes. The numbers of colonies were counted to calculate the bacteria concentration.

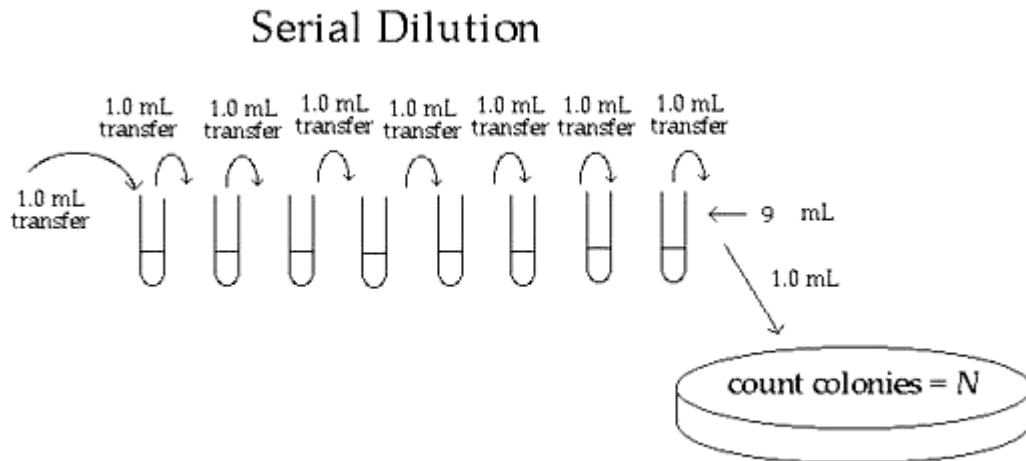


Figure 6.1. Serial dilution procedure

### 6.3.3. Preparation of Bacteria Loaded Zeolite Samples

Phosphate buffer solution (5 mM PBS, pH 7.4) was used as medium in the preparation of the zeolite samples. 5 mM disodiumhydrogen phosphate ( $\text{Na}_2\text{HPO}_4$ ) (Riedel-de Häen, 304271), 5 mM sodiumhydrogen phosphate monohydrate ( $\text{NaH}_2\text{PO}_4 \cdot \text{H}_2\text{O}$ ) (Sigma S071) and 150 mM NaCl (Riedel-de Häen, 31434) were used to prepare the phosphate buffer solution.

At the end of 24 hr, bacteria cell cultures were centrifuged at 5000 rpm for 10 min. After centrifugation, Mueller Hinton broth was removed from cell cultures. Then, the cell cultures were suspended in 10 mL PBS solution. In order to obtain homogeneous solution, PBS solution was vortexed with Yellowline TTS 2 for 3 seconds.

In order to investigate the effect of parent and modified clinoptilolite rich mineral samples on the bacteria concentration, two groups were studied. One group contained only bacteria cell culture whereas other group contained parent mineral sample-bacteria cell culture and surfactant modified clinoptilolite rich mineral samples-bacteria cell culture. Bacteria concentrations of the two groups were measured against time and calculated by using Viable Cell Count method.

0.1 g parent and surfactant modified clinoptilolite rich mineral samples were added into 10 mL PBS solution and then the two groups were placed in incubator at 37 °C for 1 hr. After that, PBS solution was refreshed to eliminate loosely bound bacteria to zeolite surfaces. After PBS refreshing, the two groups were placed in thermostat shaker (37 °C, 2 hr). This procedure was repeated for three times under the same conditions. In each experiment, bacteria concentrations of two groups were measured before refreshing PBS solution. Finally, solid phase was dried at 37 °C for 24 hr.

After bacteria loading, *Escherichia coli*, *Pseudomonas aeruginosa*, *Bacillus subtilis*, *Staphylococcus aureus* and *Staphylococcus epidermidis* loaded clinoptilolite and modified clinoptilolite samples were abbreviated as ECCLI, PACLI, BSCLI, SACLI, SECLI, ECAMCLI, PAAMCLI, BAAMCLI, SAAMCLI, SEAMCLI, ECCMCLI, PACMCLI, BSCMCLI, SACMCLI and SECMCLI, respectively.

#### **6.4. Characterization of Natural, Surfactant Modified and Bacteria Loaded Zeolite Samples**

Identifications of the crystalline species present in the zeolite samples were investigated using a Philips X'Pert Pro Diffractometer with Ni-filtered CuK $\alpha$  radiation in the range of 2 $\theta$  values 5 to 80°.

For quantitative phase purity analysis, the clinoptilolite references with >95% clinoptilolite content (27031, Castle Creek, Idaho) was used. The quantitative analysis method which was proposed by Nakamura et al. (1992) was applied. This method is based on the ratio of the summation of intensities of the seven characteristic peaks belong to clinoptilolite in the 2 $\theta$  range of 9.82°–19.02° (2 $\theta$  = 9.82°, 11.15°, 13.07°, 14.89°, 16.91°, 17.28°, and 19.02°). By comprising of summation of clinoptilolite peaks and reference Idaho sample (27031, Castle Creek, Idaho) (>95%), the purity of the sample was calculated.

The crystalline morphology of the zeolite samples was determined by Philips XL30S model Scanning Electron Microscope. The chemical compositions of the elements within the mineral were determined by EDAX EDS (Energy Dispersive X-Ray). An average elemental composition of the sample was obtained by a data collection at five different regions of samples.

FTIR characterizations were carried out between 400 and 4000  $\text{cm}^{-1}$  with Shimadzu FTIR-8201 using KBr pellet technique. In this analysis, the pellet samples were mixed with 1-2 wt % KBr.

Thermogravimetric analyses of the zeolites were performed on a thermal gravimetric analyzer (Shimadzu TGA-51, Shimadzu) up to 1000  $^{\circ}\text{C}$  at a heating rate of 10  $^{\circ}\text{C}/\text{min}$ , under 40 mL/min  $\text{N}_2$  flow.

The surface properties were determined by Micromeritics ASAP 2010 model static volumetric adsorption instrument. The samples were first degassed at 350  $^{\circ}\text{C}$  for 24 hours. The analysis was carried out with liquid  $\text{N}_2$  at its normal boiling temperatures of 77K.

Chemical compositions of the samples were determined by Varian ICP-AES 96 Inductively Coupled Plasma Atomic Emission Spectrometer. The lithium borate fusion method was used in the determination of the major elements within the zeolite samples such as sodium, calcium, magnesium, potassium, iron, aluminum, and silicon. 0.1 gr sample was mixed with 1g lithium tetraborate until homogeneity was obtained. Then it was placed in furnace (1000  $^{\circ}\text{C}$ ) for about 1 hr. The glass bead formed was dissolved in 70 mL 1.6 M  $\text{HNO}_3$  and the volume was completed to 250 mL with deionized water.

Zeta potentials of the samples in deionized water, PBS and Cr (VI) solution were measured by zeta potential measurement instruments (Zeta meter 3.0). In the analysis, the samples were dispersed in 20 mL solution. pH of the solution was adjusted by using 0.1 M NaOH and 0.1 M  $\text{HNO}_3$ .

## **6.5. Sorption Experiments**

Hexavalent chromium solution was prepared by dissolving  $\text{K}_2\text{Cr}_2\text{O}_7$  (Sigma, 99.9% pure) in deionized water. All working solutions of varying concentrations were obtained by diluting the stock solution with deionized water.

Batch sorption studies were performed at different initial concentrations, agitation speeds, temperatures, particle sizes and pH values. The experimental conditions are tabulated in Table 6.1. The details of experimental procedure of the batch studies were discussed below.

Table 6.1. Experimental conditions of batch sorption

Sorbents	Parameters	pH	Initial Concentration (mg/L)	Agitation Speed (rpm)	Particle Size ( $\mu\text{m}$ )	Temperature ( $^{\circ}\text{C}$ )
CLI	pH	3	10	140	25-106	25
		11				25
AMCLI	Initial Concentration (mg/L)	3	10	140	25-106	25
CMCLI		50				
ECCLI		100				
BSCLI		200				
		300				
ECAMCLI	Agitation Speed (rpm)	3	10	60	25-106	25
BSAMCLI				100		
ECCMCLI				140		
BSCMCLI	Temperature ( $^{\circ}\text{C}$ )	3	10	140	25-106	25
						40
	Particle Size ( $\mu\text{m}$ )	3	10	140	25-106 106-425	25

In order to understand the effect of pH on the sorption kinetic, two different pH values were studied. pH of the solution was adjusted to 3 and 11 using 0.1 M NaOH and 0.1 M HNO<sub>3</sub> solutions. 0.5 gr zeolite samples were added into 50 mL solution containing Cr (VI) 10 mg/L. The flasks were agitated for 4 days with a constant agitation speed of 140 rpm at 25 °C.

The effect of initial concentration of Cr (VI) was examined by studying different initial concentrations changing from 10 to 300 mg/L. 0.5 gr zeolite samples were added into 50 mL solution containing Cr (VI) with the initial concentrations varying from 10 to 300 mg/L. The flasks were agitated at 140 rpm and 25°C for 4 days.

In order to find out the effect of agitation speed, a series of experiments were carried out with 50 mL solution containing 10 mg/L of Cr (VI) and 0.5 g of zeolite samples by varying the speed of agitation from 60 to 140 rpm. The flasks were agitated for 4 days at 60, 100, 140 rpm and 25°C.

The effect of temperature on adsorption was examined by operating at various temperatures; 25 °C and 40°C in a constant temperature water bath. 0.5 gr zeolite samples were added into 50 mL solution containing 10 mg/L Cr (VI). The samples were agitated at 140 rpm for 4 days.

Two different particle size ranges were studied. 0.5 gr zeolite samples were added into 50 mL solution containing 10 mg/L Cr (VI). The samples were agitated at 140 rpm and 25°C for 4 days.

Equilibrium experiments were carried out by contacting 0.5 g zeolite samples with 50 mL of Cr (VI) solution of different initial Cr (VI) concentrations 10, 50, 100, 200 and 300 mg/L. The stirring speed was kept constant at 140 rpm. The temperatures examined were 25 and 40 °C.

All sorption experiments were repeated three times and the average values of three replicates were used in the calculation part.

The methods used in determination of Cr (VI) concentration were given in Appendix B.1. The values of amount of exchangeable cations in the liquid phase are tabulated in Appendix B.2.



# CHAPTER 7

## RESULTS AND DISCUSSION

### 7.1. Characterization of Natural and Surfactant Modified Zeolites

SEM micrographs of clinoptilolite rich mineral and surfactant modified clinoptilolite rich mineral are presented in Figure 7.1 (a), (b) and (c). Thin platy crystals which belong to the clinoptilolite mineral were observed in Figure 7.1 (a). The SEM micrographs of surfactant modified clinoptilolite rich mineral indicated that the clinoptilolite crystal structure was covered with cationic and anionic surfactants after modification and organic layer was formed on the clinoptilolite rich mineral surface.

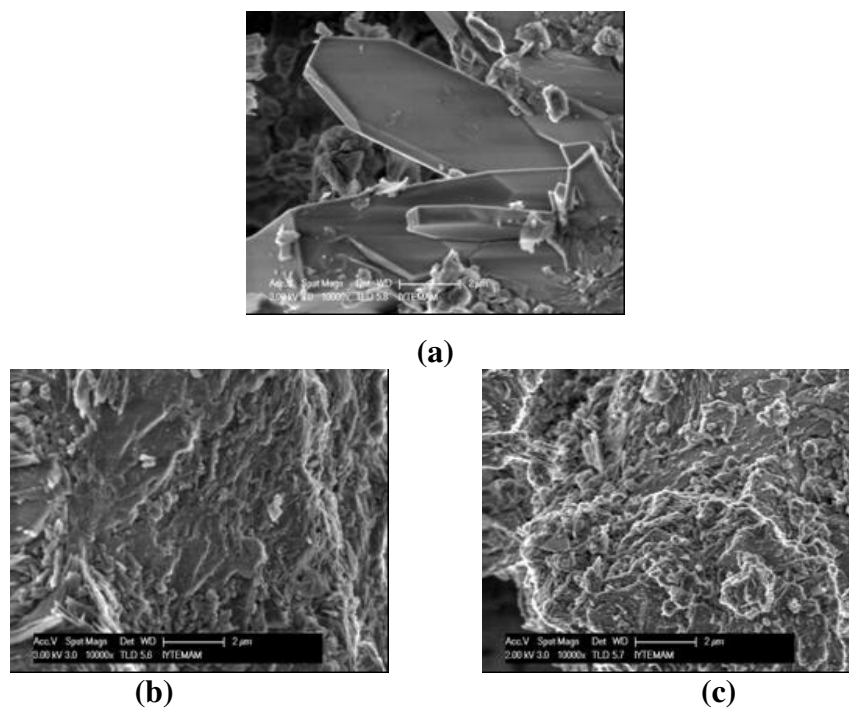


Figure 7.1. SEM micrographs a) CLI, b) CMCLI c) AMCLI

EDS of clinoptilolite rich mineral and surfactant modified clinoptilolite rich mineral are tabulated in Table 7.1. An average elemental composition of the samples was obtained by data collection at five different regions of the samples. The values of standard deviation were calculated from five measurements. EDS results of

clinoptilolite rich mineral showed that the main exchangeable cations (Na, K, Ca and Mg) present in the structure and potassium has the highest amount. EDS results of surfactant modified clinoptilolite mineral showed that weight percent values of exchangeable cations in the clinoptilolite structure decreased whereas weight percent values of C and S in the structure increased after modification with cationic and anionic surfactant.

Table 7.1. EDS of CLI, CMCLI and AMCLI

Element %	CLI	CMCLI	AMCLI
C	0	14.62±0.153	7.94±0.185
O	47.86±0.44	36.09±0.35	41.25±0.24
Na	0.714±0.022	0.54±0.045	0.77±0.029
Mg	0.95±0.027	0.82±0.021	0.83±0.017
Al	7.51±0.052	7.26±0.023	7.46±0.047
Si	36.74±0.38	35.3±0.158	35.88±0.35
K	3.35±0.078	2.92±0.034	2.8±0.068
Ca	2.88±0.038	2.55±0.057	2.51±0.091
S	0	0	0.57±0.027
TOTAL	100	100	100

\*±Standard deviation values

The crystalline species present in the clinoptilolite rich minerals and surfactant modified clinoptilolite rich minerals was identified by X-Ray diffraction. The zeolite samples is identified as clinoptilolite and its characteristic peaks are recognized at  $2\theta = 9.76^\circ$ ,  $22.23^\circ$ , and  $30.05^\circ$ . Qualitative mineralogical analysis revealed that sample contained predominantly clinoptilolite and quartz as mineral impurities. Quantitative analysis was performed to calculate the purity of the clinoptilolite rich mineral samples. The purity of the clinoptilolite rich mineral sample was found 90 %. Figure 7.2 shows XRD patterns of cationic surfactant and cationic modified clinoptilolite rich mineral. The cationic surfactant results indicated that the major peaks were observed at  $6.78^\circ$ ,  $17.05^\circ$ ,  $20.45^\circ$ ,  $21.4^\circ$  and  $23.94^\circ$ . XRD results of cationic modified clinoptilolite rich mineral revealed that the major peaks of clinoptilolite mineral were unchanged and only the intensities of these peaks were decreased after modification with cationic surfactant.

The results showed that cationic surfactant was mainly adsorbed on the clinoptilolite phase. XRD patterns of anionic surfactant and anionic modified clinoptilolite rich mineral are given in Figure 7.3. The anionic surfactant results indicated that the major peaks were observed at 6.3 °. XRD results of anionic modified clinoptilolite rich mineral revealed that two new peaks were observed at 5.6 and 8.7 °. The orientation of SDS molecule on the clinoptilolite rich mineral surface was determined from Bragg's Law. The details of the calculation procedure are given in Appendix C.

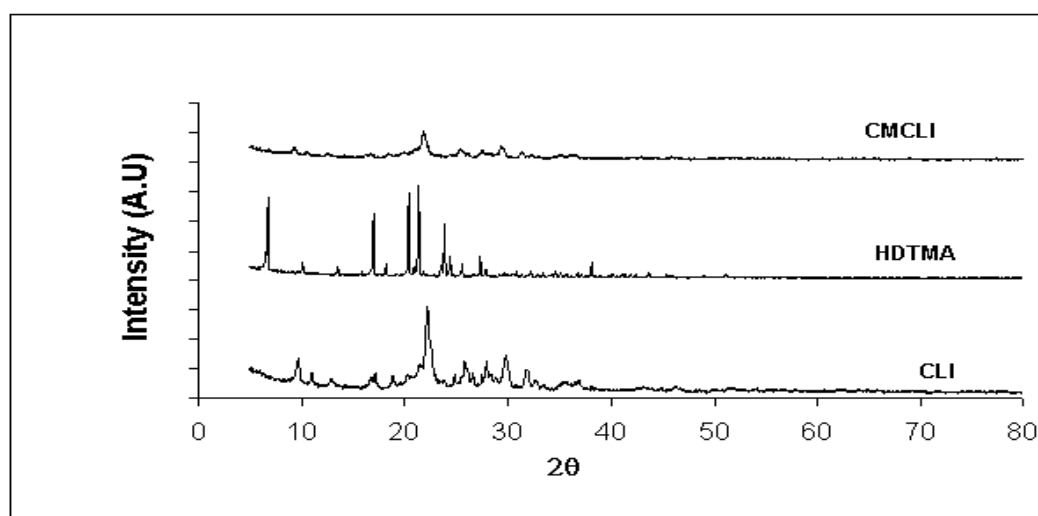


Figure 7.2. X-Ray Diffraction pattern of CMCLI, HDTMA and CLI

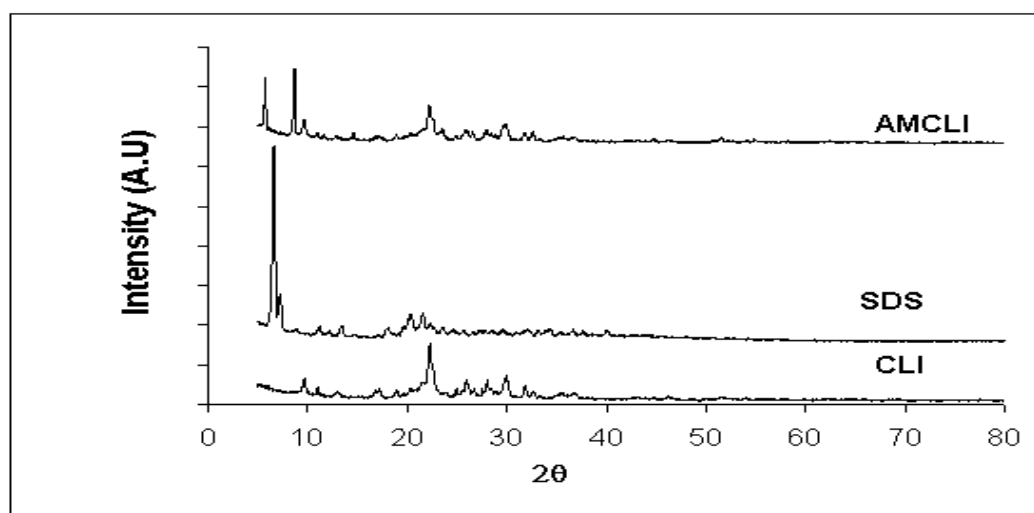


Figure 7.3. X-Ray Diffraction pattern of AMCLI, SDS and CLI

FTIR results of clinoptilolite rich minerals and surfactant modified clinoptilolite rich minerals are shown in Figure 7.4 and 7.5. The characteristic bands of clinoptilolite

rich mineral were at  $1085\text{ cm}^{-1}$  and  $476\text{ cm}^{-1}$  due to T-O stretching and T-O bending mode, respectively. Bands related to isolated OH stretching at  $3672\text{ cm}^{-1}$ , hydrogen bonding of water at  $3477\text{ cm}^{-1}$  and water bending at  $1672\text{ cm}^{-1}$  were seen in Figure 7.4. FTIR results of HDTMA indicated that HDTMA exhibited two bands at  $2918$  and  $2847\text{ cm}^{-1}$  due to antisymmetric and symmetric C-H stretching of methylene groups. For the all trans-alkyl chain, the positions of the antisymmetric and symmetric C-H stretching are around  $2918$  and  $2847\text{ cm}^{-1}$ , respectively. If the conformational disorder is included, the positions of the band shift to higher wave number depending on the average content of gauge conformers. FTIR results of cationic surfactant modified clinoptilolite mineral revealed that two new bands appeared at  $2937$  and  $2860\text{ cm}^{-1}$ . FTIR results also indicated that the chains were highly ordered (all-trans conformation). The results revealed the evidence of successful modification with cationic surfactant. After modification with surfactant, the characteristic bands of clinoptilolite rich mineral were observed at  $1076\text{ cm}^{-1}$  and  $470\text{ cm}^{-1}$ . Bands related to isolated OH stretching at  $3651\text{ cm}^{-1}$ , hydrogen bonding of water at  $3458\text{ cm}^{-1}$  and water bending at  $1660\text{ cm}^{-1}$  were seen in Figure 7.4. The band shift in the characteristic bands of clinoptilolite rich mineral after modification pointed out the presence of cationic surfactant on the clinoptilolite surface.

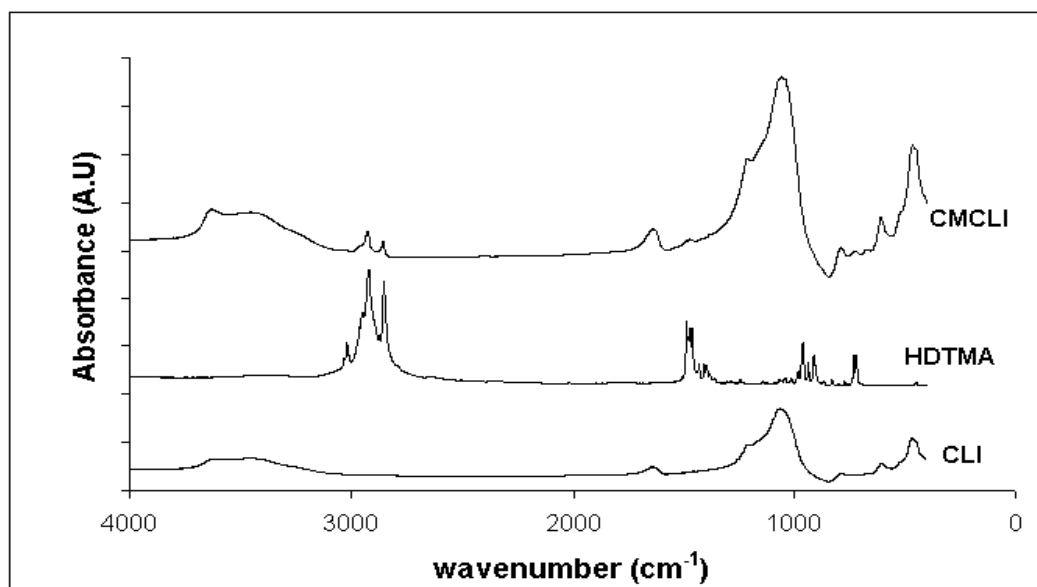


Figure 7.4. FTIR results of CLI, HDTMA and CLI

Figure 7.5 shows FTIR results of anionic surfactant and anionic surfactant modified clinoptilolite rich mineral. FTIR results of anionic surfactant indicated that

SDS exhibited three main bands. Bands due to the symmetric and asymmetric stretching of methylene groups were observed at 2853 and 2924  $\text{cm}^{-1}$ , respectively. The other band were attributed to the  $-\text{S}=\text{O}$  stretching which was observed at 1219  $\text{cm}^{-1}$  (Mehta et al., 2007; Gaikar et al., 2008). FTIR results of anionic surfactant modified clinoptilolite mineral showed that four additional bands were observed after modified with anionic surfactant. Bands observed at 2924, 2855, 1214 and 1467  $\text{cm}^{-1}$  were assigned to the asymmetric and symmetric stretching of methylene groups, stretching modes of sulphonic acid group present in SDS and C-H bending in  $\text{CH}_3$ . The existence of four new bands after modification gave a clue about the success of the modification steps. After modification with anionic surfactant, T-O stretching and T-O bending mode shifted from the 1085  $\text{cm}^{-1}$  to 1043  $\text{cm}^{-1}$  and 476  $\text{cm}^{-1}$  to 455  $\text{cm}^{-1}$ , respectively. In addition, bands due to the OH stretching, hydrogen bonding of water and water bending were observed at 3620, 3423 and 1616  $\text{cm}^{-1}$ , respectively. The band shift in the characteristic bands of clinoptilolite rich mineral after modification of SDS pointed out the presence of anionic surfactant on the clinoptilolite surface.

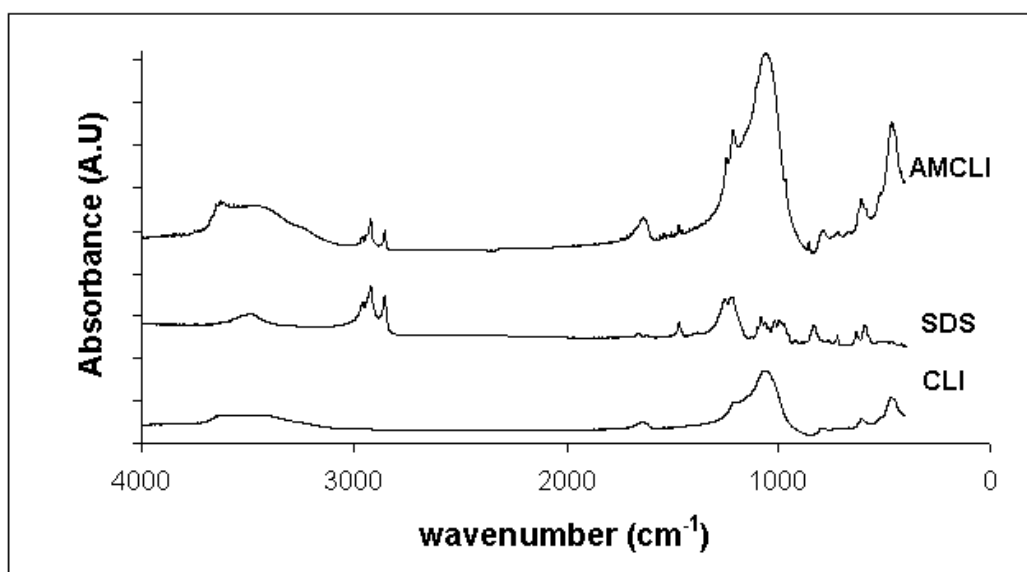


Figure 7.5. FTIR results of AMCLI, SDS and CLI

The surface areas of clinoptilolite rich mineral, cationic surfactant modified clinoptilolite rich mineral and anionic surfactant modified clinoptilolite rich mineral are determined by Micromeritics ASAP 2010. The values of surface area were found as 71.2, 51.2 and 48.8  $\text{m}^2/\text{g}$  for clinoptilolite rich mineral, cationic surfactant modified clinoptilolite rich mineral and anionic surfactant modified clinoptilolite rich mineral,

respectively. The results indicated that the surface area of the clinoptilolite decreased when it was modified with the surfactants. These surfactant molecules are composed of large hydrocarbon chains and they do not enter the largest channels of clinoptilolite. The channels of the zeolites were obstructed by these surfactants and the diffusion of  $N_2$  throughout these channels was impeded by them. The decrease in the surface area was due to obstruction of the channels of the zeolite. The pore size distributions of the natural and surfactant modified zeolite samples are given in Appendix D.

Figure 7.6 shows the variation of zeta potential of clinoptilolite versus pH. As seen in this figure, clinoptilolite rich mineral surface has a negative surface charge and it preserves its negative surface charge in the pH range of 2-12. The increase of pH solution resulted in negative charge of the clinoptilolite rich mineral sample. The results could be explained by the deprotonation or protonation of aluminol Al-OH and silanol Si-OH groups.

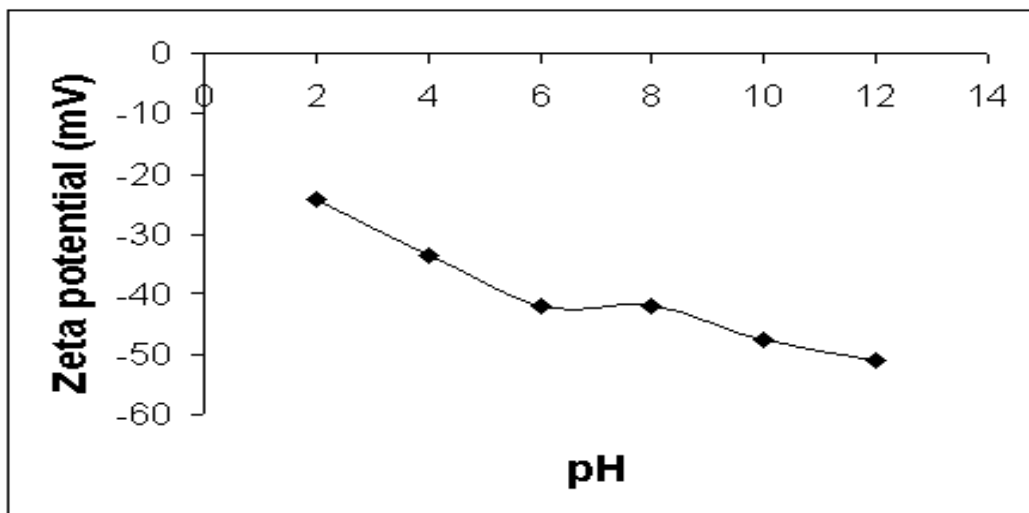


Figure 7.6. The variation of the zeta potential of CLI at different pH values

Figure 7.7 represents the variation of zeta potential of cationic surfactant modified clinoptilolite rich mineral versus pH. As shown in this figure, the isoelectric point of cationic surfactant modified clinoptilolite rich mineral is found as  $\approx 8.2$ . This means that the cationic surfactant modified clinoptilolite rich mineral is positively charged at  $pH < 8.2$  while it is negatively charged at  $pH > 8.2$ . The results revealed that the surface of clinoptilolite rich minerals acquired a positive charge after modification with cationic surfactant.

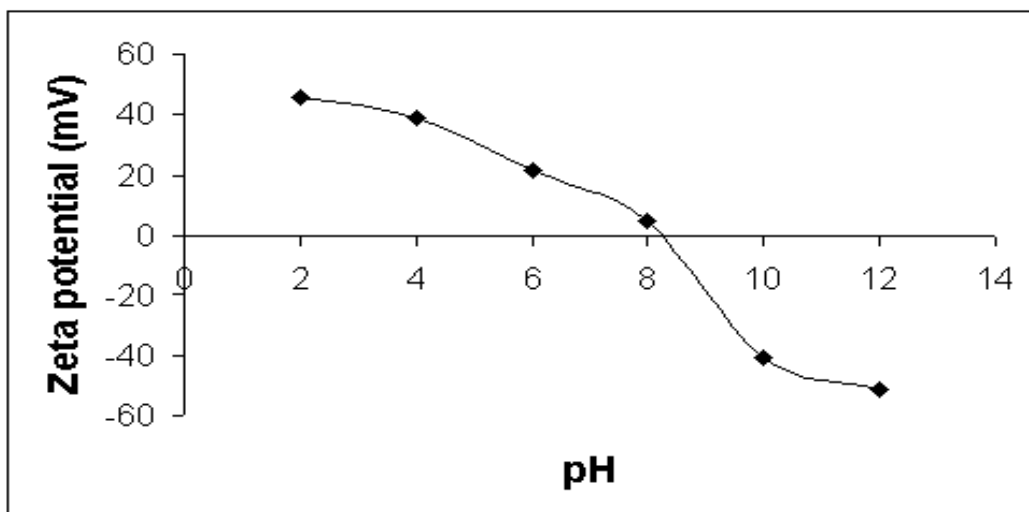


Figure 7.7. The variation of the zeta potential of CMCLI at different pH values

The variation of zeta potential of anionic modified clinoptilolite versus pH graph is shown in Figure 7.8. The results indicated anionic modified clinoptilolite rich mineral exhibited a negative surface charge like clinoptilolite rich mineral and it preserved its negative surface charge in the pH range of 2-12. When the zeta potential values of clinoptilolite and anionic modified clinoptilolite rich mineral were compared, higher negative zeta potential values were observed with anionic modified clinoptilolite rich mineral. The results revealed that clinoptilolite rich mineral gained much more negative surface charge after modification with anionic surfactant.

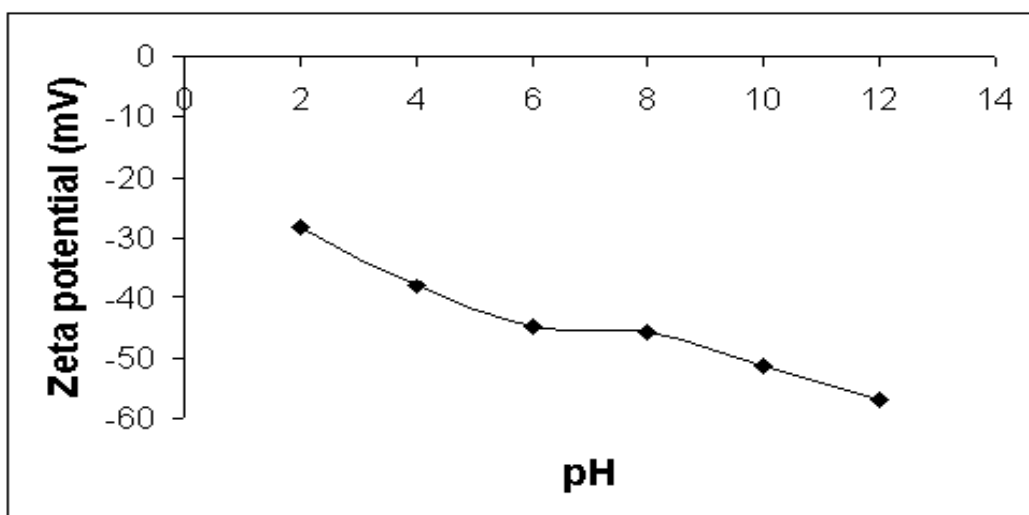


Figure 7.8. The variation of the zeta potential of AMCLI at different pH values

The chemical compositions of clinoptilolite rich mineral, anionic and cationic surfactant modified clinoptilolite rich mineral are presented in Table 7.2. As shown in

this table, clinoptilolite rich mineral sample was identified as potassium clinoptilolite rich mineral because of its highest potassium content. Si/Al ratio of the clinoptilolite rich mineral sample was found as 5.16 which agreed well with Si/Al ratio of the clinoptilolite rich mineral in the literature. Chemical composition results of anionic and cationic surfactant modified clinoptilolite rich mineral showed that the weight percent values of oxide forms of exchangeable cations ( $K_2O$ ,  $Na_2O$ ,  $CaO$  and  $MgO$ ) were decreased after modification with cationic and anionic surfactant. Si/Al ratios of the modified clinoptilolite rich mineral were calculated as 5.21 and 5.29 for cationic surfactant modified clinoptilolite rich mineral and anionic surfactant modified clinoptilolite rich mineral, respectively.

Table 7.2. Chemical compositions of CLI, CMCLI and AMCLI

Oxides %	CLI	AMCLI	CMCLI
$SiO_2$	65.1	66.7	67.7
$Al_2O_3$	12.6	12.8	12.8
$Fe_2O_3$	1.42	0.89	0.62
$K_2O$	3.93	0.99	0.8
$Na_2O$	0.92	2.88	2.4
$CaO$	1.92	0.88	0.7
$MgO$	0.85	0.68	0.52
$H_2O$	13.4	14.4	14.6

### 7.1.1. Monolayer or Bilayer Formation on the Clinoptilolite Rich Mineral Surface

As mentioned before, surfactant modification is strongly influenced by the degree of surfactant adsorption on solid surface. A bilayer or monolayer is formed when the surfactant concentration is higher or less than its critical micelle concentration (CMC). If the surfactant concentration in solution exceeds CMC, the hydrophobic tails of the surfactant molecules will associate to form a bilayer. Surfactant molecules form a monolayer at the solid–aqueous interface via strong Columbic interaction below its CMC.

Figure 7.9 shows adsorption isotherm regions for surfactants. Region I adsorption occurs at low equilibrium surfactant concentrations and low levels of adsorption, and is frequently called the Henry’s Law adsorption region. Surfactant



adsorption occurs in this region primarily due to the electrostatic attraction between the surfactant head groups and the oppositely charged surface, and to a lesser extent, the interaction of the surfactant tail groups with the surface. There is little interaction between the tail groups of the adsorbed surfactant molecules in this adsorption region (Scamehorn et al., 1982). Region I-Region II transition occurs when the surfactant aggregates are formed more quickly. In Region II, the slope of the adsorption isotherm increases sharply with increasing equilibrium surfactant concentration. In region III, the curve slope is lower than in region II. This decrease is attributed to the electrostatic repulsion between the unimers (i.e. surfactant monomers) and to the lower availability of high energy patches for adsorption. The transition between regions III and IV occurs near or at the CMC of the surfactant, when the adsorption patches become saturated. Therefore, region IV corresponds to the adsorption plateau and is characterized by a near zero slope. The adsorbed surfactant configurations for each region are schematically illustrated in Figure 7.9.

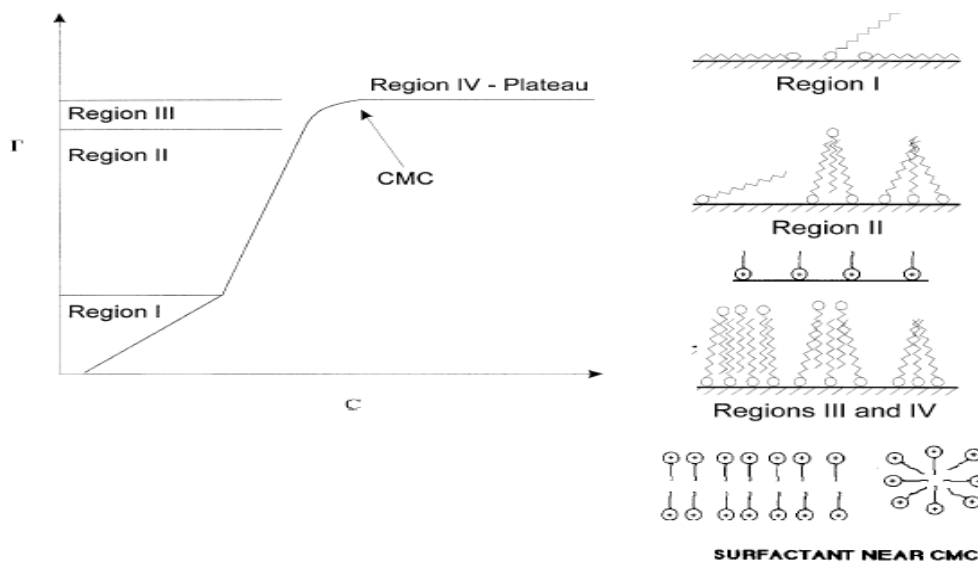


Figure 7.9. Illustration of the adsorption regions for surfactants adsorption on the Surface

In order to draw the adsorption isotherm of clinoptilolite-HDTMA system, the adsorption density was calculated from the following equation:

$$\Gamma = \frac{(C_i - C_r) * V}{mS * 1000} \quad (7.1)$$

where  $C_i$  and  $C_r$  represents the initial and residual concentrations in mol/L,  $m$  the amount of solid in grams,  $V$  the volume of solution in mL,  $S$  the specific area of clinoptilolite rich mineral ( $m^2/g$ ) and  $\Gamma$  the adsorption density in  $mol/m^2$ .

The concentration of HDTMA and SDS were determined spectrophotometrically using UV spectrophotometer (at 287 and 266 nm).

The adsorption isotherm of clinoptilolite-HDTMA system at 25 °C is shown in Figure 7.10. The results indicated that plateau adsorption density for clinoptilolite-HDTMA system was found as  $1 \times 10^{-4}$  mole/ $m^2$ .

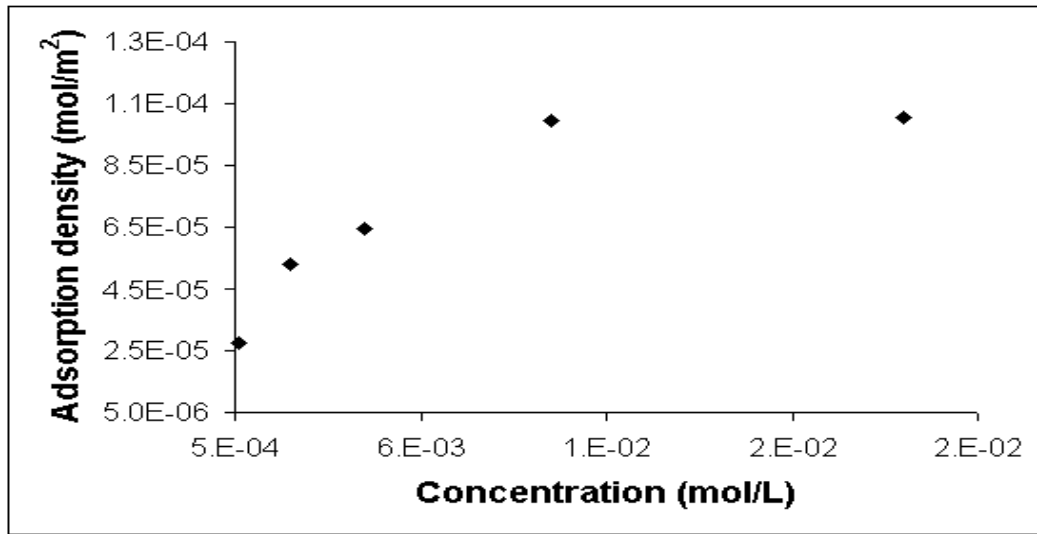


Figure 7.10. Adsorption isotherm of clinoptilolite-HDTMA at 25 °C

Using the value of adsorption density at plateau region, packing area for the HDTMA onto clinoptilolite rich mineral was calculated as:

$$Parking\ Area = \frac{10^{20}}{\Gamma_{max} A} \quad (7.2)$$

where  $\Gamma_{max}$  is the adsorption capacity at the plateau region ( $1 \times 10^{-4}$  mole/ $m^2$ ), and  $A$  is the Avogadro Number ( $6.02 \times 10^{23}$ ).

The parking area of HDTMA on the clinoptilolite rich mineral was found to be 16.61  $\text{Å}^2/\text{molecule}$ . The cross sectional area of HDTMA molecule was reported as 37.82  $\text{Å}^2/\text{molecule}$  (Sullivan et al., 1997). The surface coverage ( $\theta$ ) was found to be  $\sim 2.0$ .

The adsorption isotherm of clinoptilolite-SDS system at 25 °C is given in Figure 7.11. The results indicated that plateau adsorption density for clinoptilolite-SDS system was found as  $7 \cdot 10^{-5}$  mole/m<sup>2</sup>.

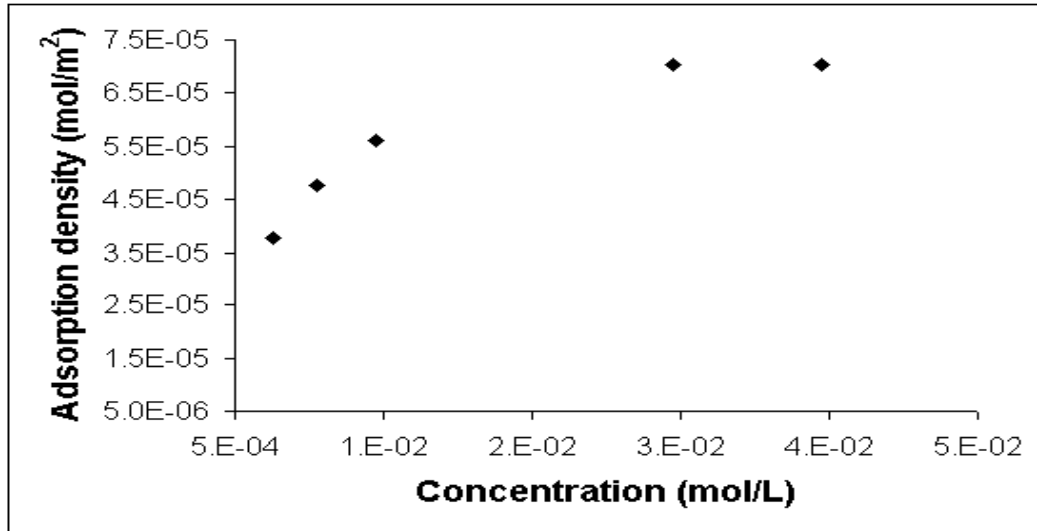


Figure 7.11. Adsorption isotherm of clinoptilolite-SDS at 25 °C

Packing area for the SDS onto clinoptilolite rich mineral was calculated from Equation 7.2 and found as 23 Å<sup>2</sup>/molecule. The cross sectional area of SDS molecule was reported as 30 Å<sup>2</sup>/molecule (Çelik and Somasundaran, 1987). The surface coverage ( $\theta$ ) was found to be  $\sim 2.0$ .

The results indicated that a bilayer configuration was formed on the clinoptilolite rich mineral surface after modification with HDTMA and SDS which is shown in Figure 7.12.

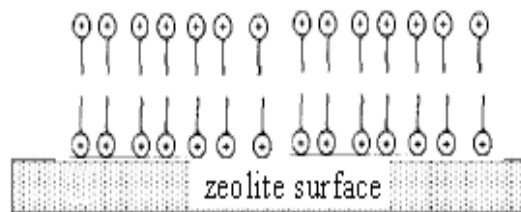


Figure 7.12. Bilayer formation on the clinoptilolite rich mineral surface after modification with HDTMA and SDS

## 7.2. Results of Bacteria Removal Using Natural and Surfactant Modified Zeolites

The changes in the concentrations of the gram positive and gram negative bacteria before and after the addition of the clinoptilolite rich mineral are given in the Figures 7.13-7.17. As it is seen from the figures, the values of bacteria concentration with and without clinoptilolite rich mineral were very close to each other for a given specific period of time. The results indicated that bacteria concentration did not significantly change with the addition of the clinoptilolite rich mineral. The removal performances with clinoptilolite rich mineral were found in the following order: *S. aureus* > *S. epidermidis* > *B. subtilis* > *E. coli* > *P. aeruginosa*.

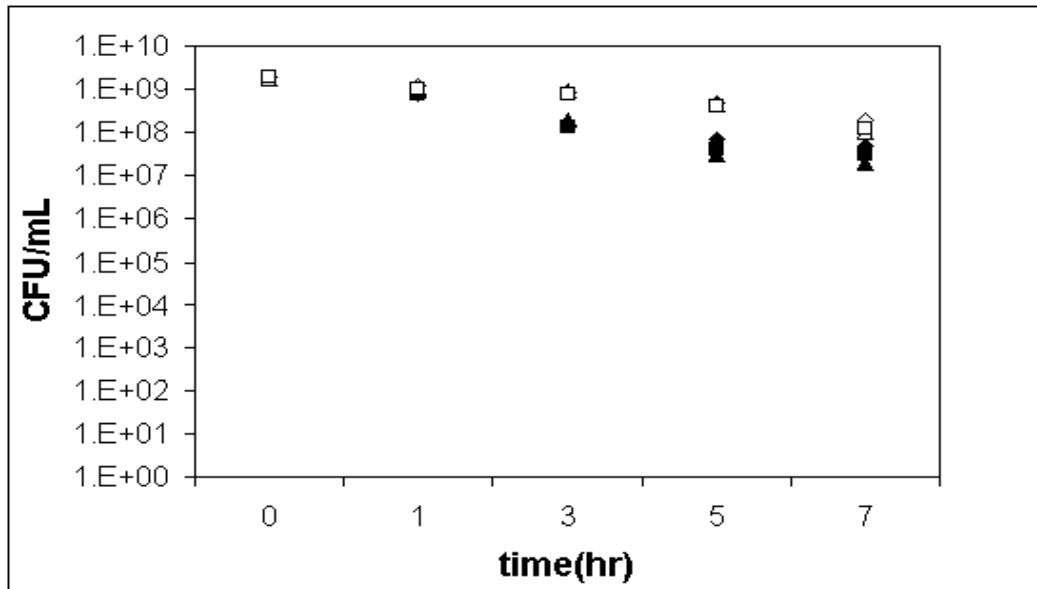


Figure 7.13. Change in *E. coli* concentration before and after the addition of CLI  
(◇, △, □ : without CLI; ◆, ▲, ■ : with CLI)

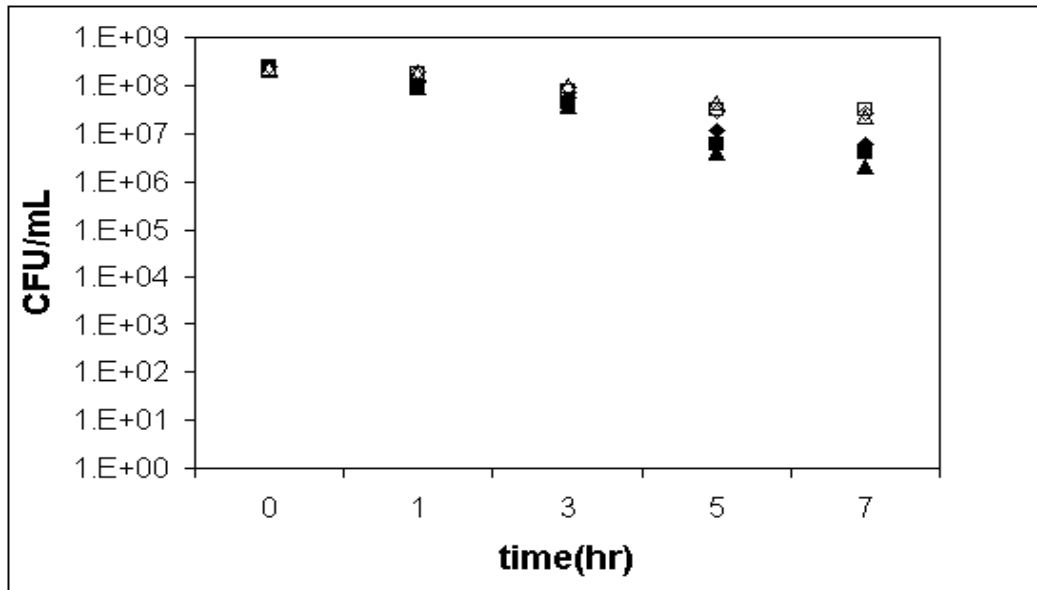


Figure 7.14. Change in *B. subtilis* concentration before and after the addition of CLI ( $\diamond, \triangle, \square$  : without CLI;  $\blacklozenge, \blacktriangle, \blacksquare$  : with CLI)

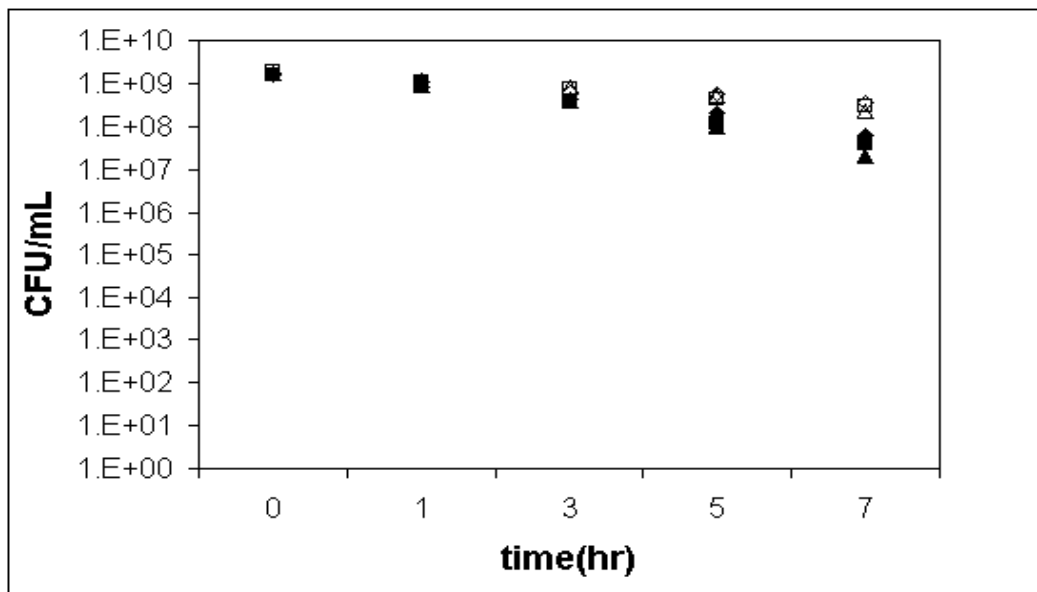


Figure 7.15. Change in *S. aureus* concentration before and after the addition of CLI ( $\diamond, \triangle, \square$  : without CLI;  $\blacklozenge, \blacktriangle, \blacksquare$  : with CLI)

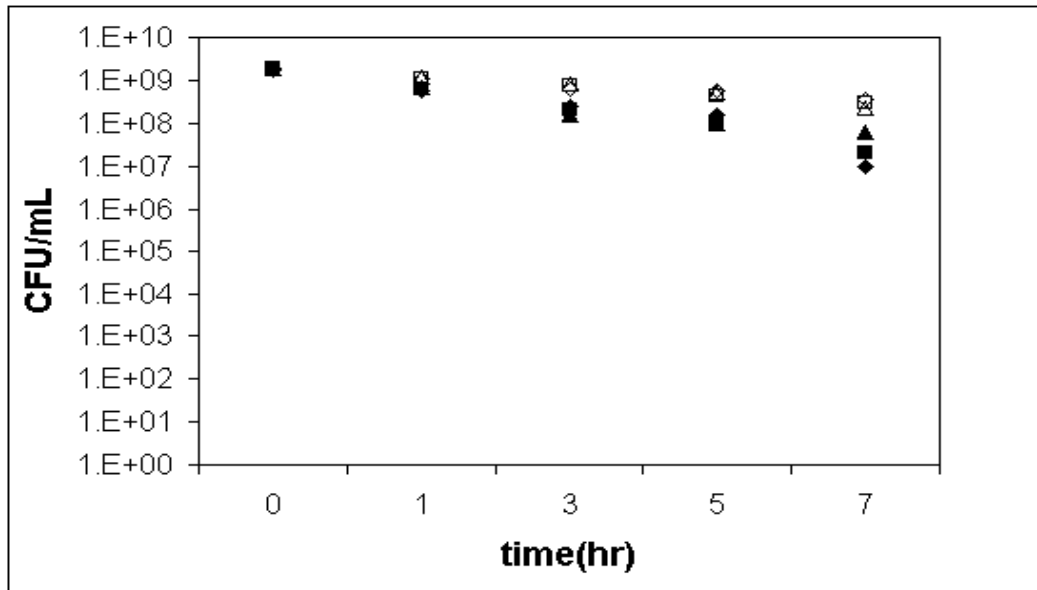


Figure 7.16. Change in *S. epidermidis* concentration before and after the addition of CLI ( $\diamond, \triangle, \square$  : without CLI;  $\blacklozenge, \blacktriangle, \blacksquare$  : with CLI)

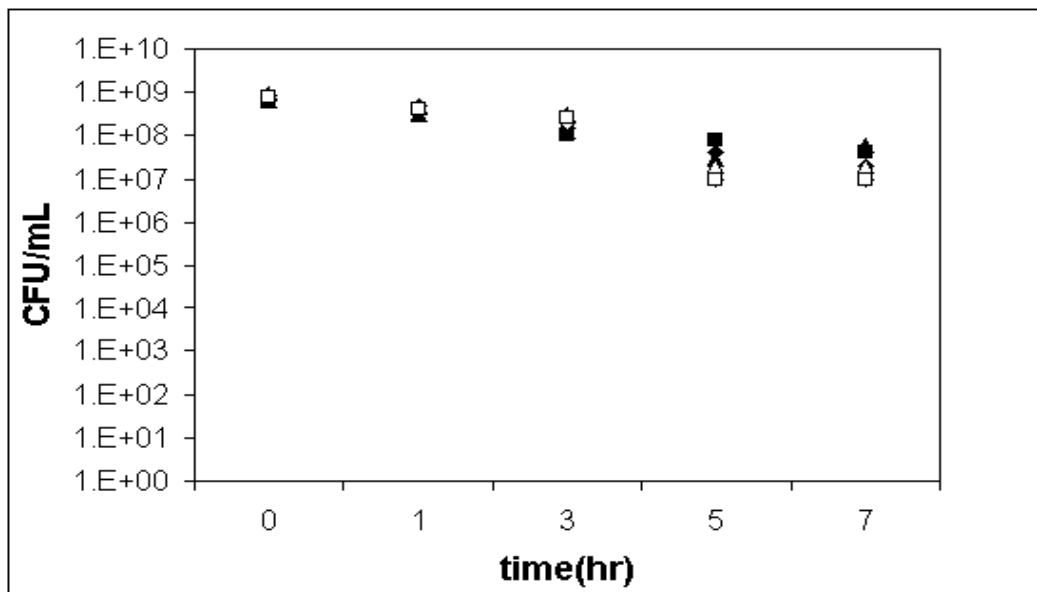


Figure 7.17. Change in *P. aeruginosa* concentration before and after the addition of CLI ( $\diamond, \triangle, \square$  : without CLI;  $\blacklozenge, \blacktriangle, \blacksquare$  : with CLI)

Surfactants prevent microbial adhesion (Cloete et al., 1992; Whitekettle, 1991) and there is no evidence that surfactants will have any mutagenic effects on bacteria (Russel et al., 1990). McDonnell and Russell (1999) stated that cationic surfactant's mode of action was attributed to its positive charge, which formed an electrostatic bond with negatively charged sites on bacteria cell walls. Those electrostatic bonds created stresses in the bacteria cell wall, leading to cell lysis and disruption of cell-wall permeability. Previous studies related to bacteria removal indicated that surfactant

modified clinoptilolite rich mineral was promising material for the removal of *E. coli*, *B. subtilis* and *G. intestinalis*. 100% *E.Coli*, 75.5 % *B.Subtilis* and 100% *G. intestinalis* cysts removal was obtained with HDTMA modified clinoptilolite rich mineral (Schulze, 2002; Lehner, 2004; Rust et al., 2006). However, there is no information about the ability of HDTMA modified clinoptilolite rich mineral for the removal of other bacteria such as *S. aureus*, *S. epidermidis* and *P. aeruginosa*. For this reason, the removal abilities of the cationic surfactant modified clinoptilolite rich minerals towards *E. coli*, *B. subtilis*, *S. aureus*, *S. epidermidis* and *P. aeruginosa* were investigated. The changes in the concentrations of the gram positive and gram negative bacteria before and after the addition of the cationic surfactant modified clinoptilolite rich mineral are represented in the Figures 7.18-7.22. The results revealed that bacteria concentration significantly changed with the addition of cationic surfactant modified clinoptilolite rich mineral. Higher bacteria removal results were observed with gram positive bacteria whereas lower bacteria removal results were observed with gram negative bacteria. The order of removal performances were found as: *S. aureus* > *S. epidermidis* > *B. subtilis* > *E. coli* > *P. aeruginosa*. When the bacteria removal performances of clinoptilolite and cationic surfactant modified clinoptilolite rich mineral were compared, cationic surfactant modified clinoptilolite rich mineral was much more effective than clinoptilolite rich mineral.

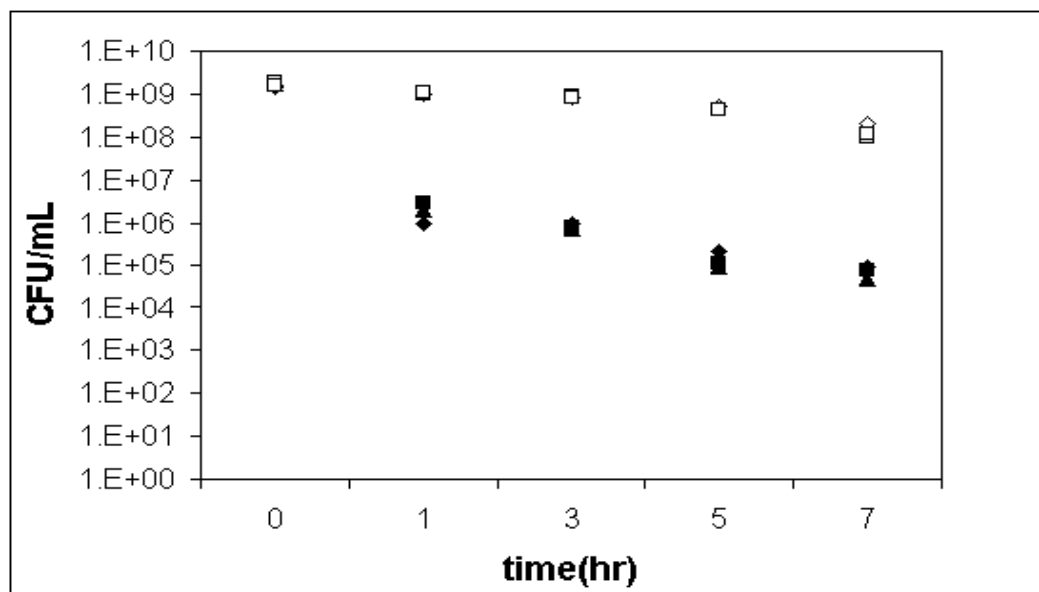


Figure 7.18. Change in *E. coli* concentration before and after the addition of CMCLI ( $\diamond$ ,  $\triangle$ ,  $\square$  : without CMCLI;  $\blacklozenge$ ,  $\blacktriangle$ ,  $\blacksquare$  : with CMCLI)

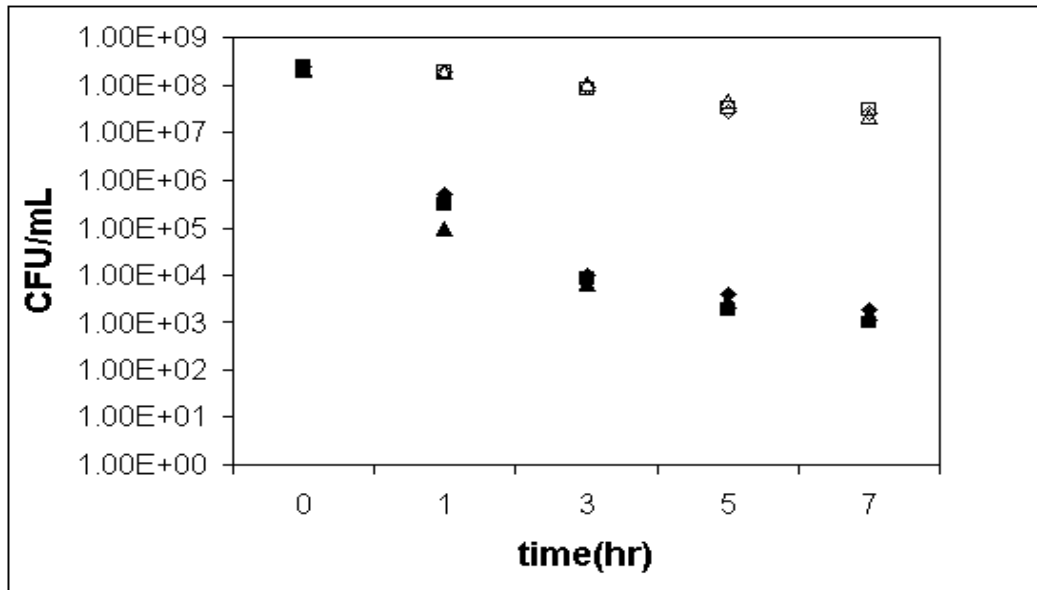


Figure 7.19. Change in *B. subtilis* concentration before and after the addition of CMCLI ( $\diamond, \triangle, \square$  : without CMCLI;  $\blacklozenge, \blacktriangle, \blacksquare$  : with CMCLI)

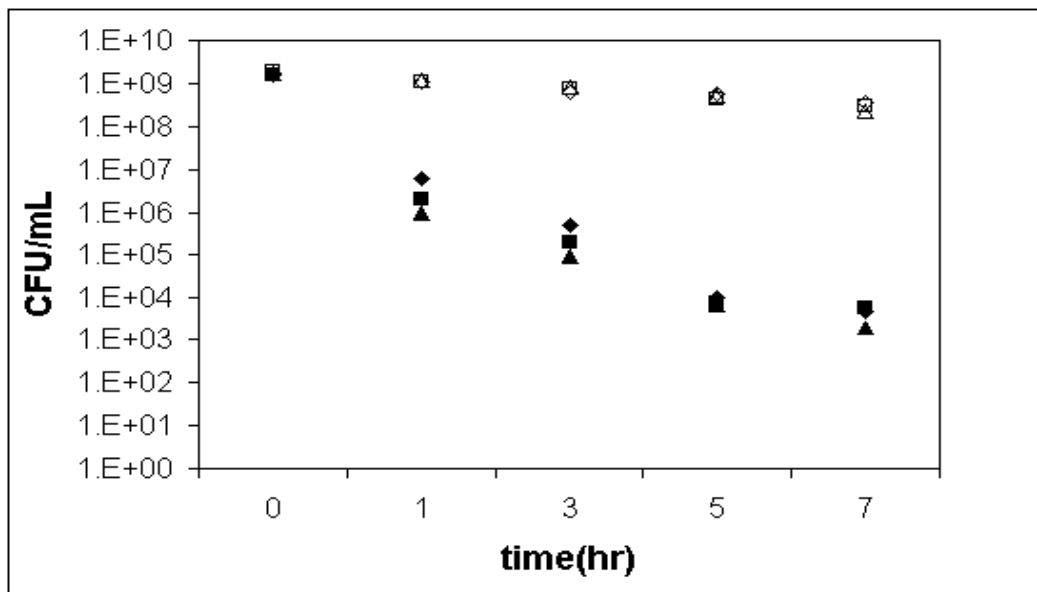


Figure 7.20. Change in *S. aureus* concentration before and after the addition of CMCLI ( $\diamond, \triangle, \square$  : without CMCLI;  $\blacklozenge, \blacktriangle, \blacksquare$  : with CMCLI)



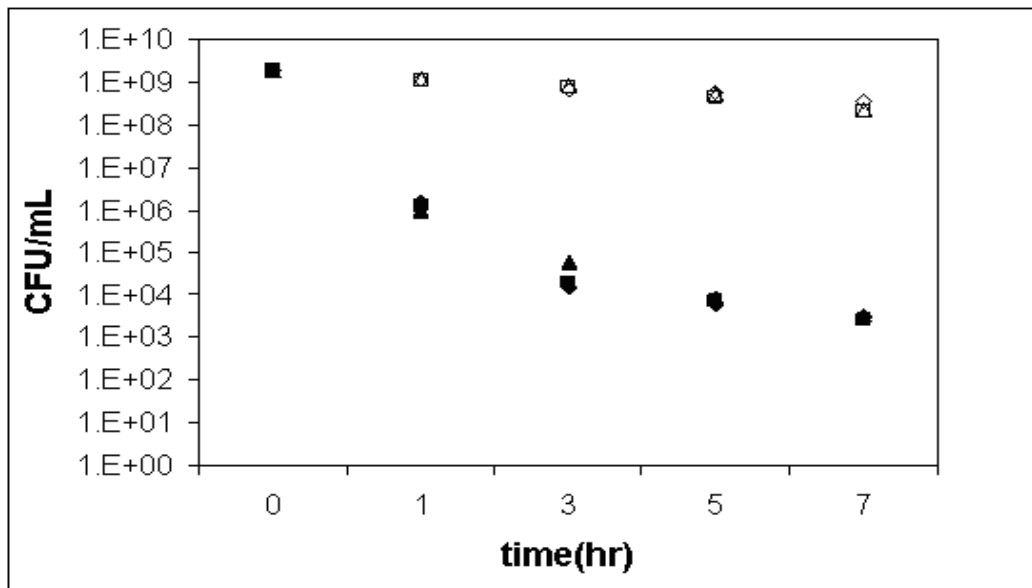


Figure 7.21. Change in *S. epidermidis* concentration before and after the addition of CMCLI ( $\diamond, \triangle, \square$  : without CMCLI;  $\blacklozenge, \blacktriangle, \blacksquare$  : with CMCLI)

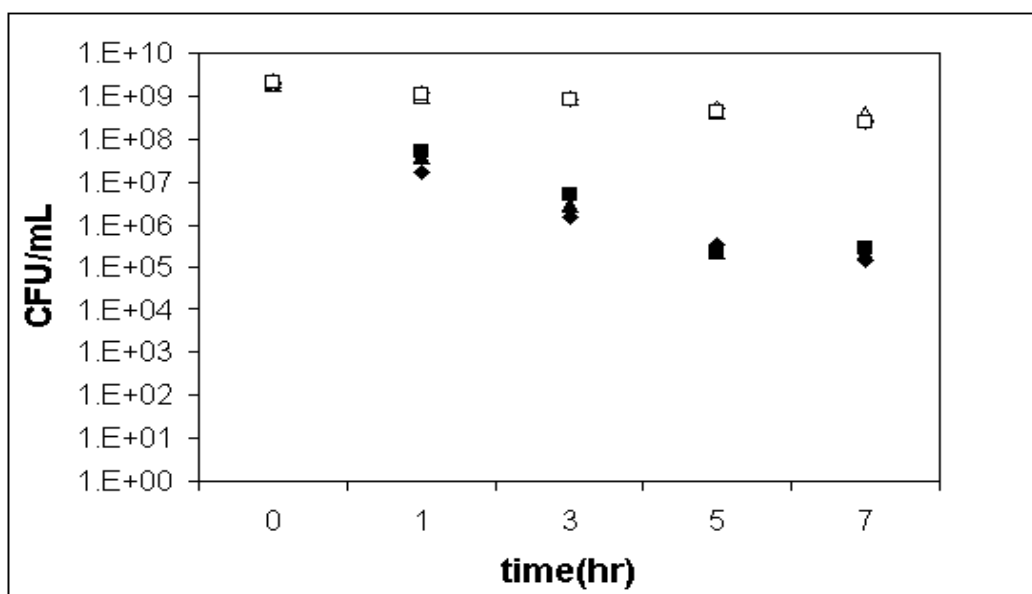


Figure 7.22. Change in *P. aeruginosa* concentration before and after the addition of CMCLI ( $\diamond, \triangle, \square$  : without CMCLI;  $\blacklozenge, \blacktriangle, \blacksquare$  : with CMCLI)

There is no study related to the removal of gram negative and positive bacteria using anionic surfactant modified clinoptilolite rich mineral. For this reason, bacteria removal performances of the anionic surfactant modified clinoptilolite rich mineral were determined. The changes in the concentrations of the gram positive and gram negative bacteria before and after the addition of anionic surfactant modified clinoptilolite rich mineral are shown in the Figures 7.23-7.27. The results indicated that bacteria concentration was significantly influenced by the addition of the anionic

surfactant modified clinoptilolite rich mineral. Highest bacteria removal results were obtained with *S. aureus* while lowest bacteria removal results were obtained with *P. aeruginosa*.

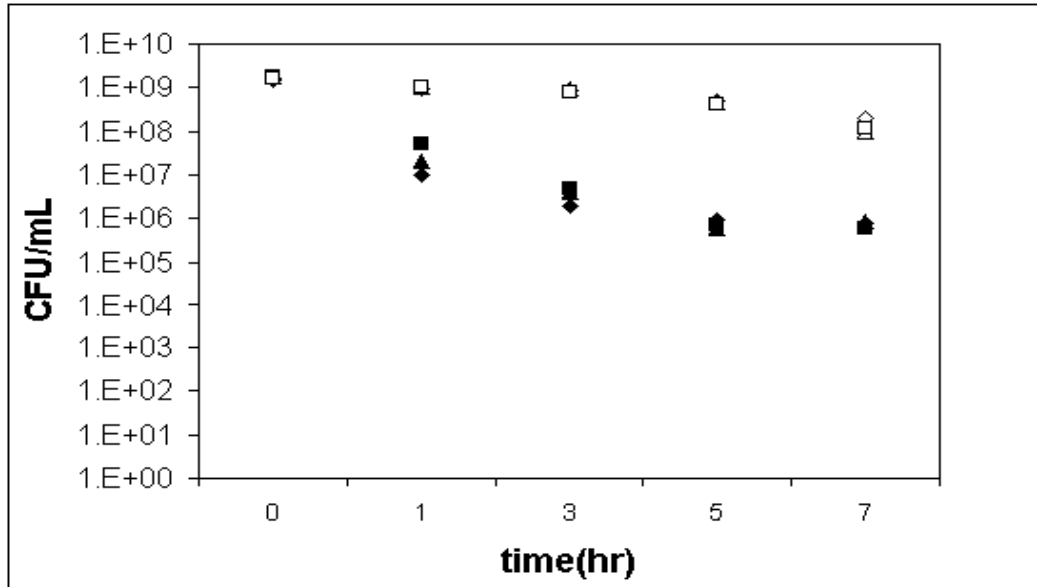


Figure 7.23. Change in *E. coli* concentration before and after the addition of AMCLI ( $\diamond, \triangle, \square$  : without AMCLI;  $\blacklozenge, \blacktriangle, \blacksquare$  : with AMCLI)

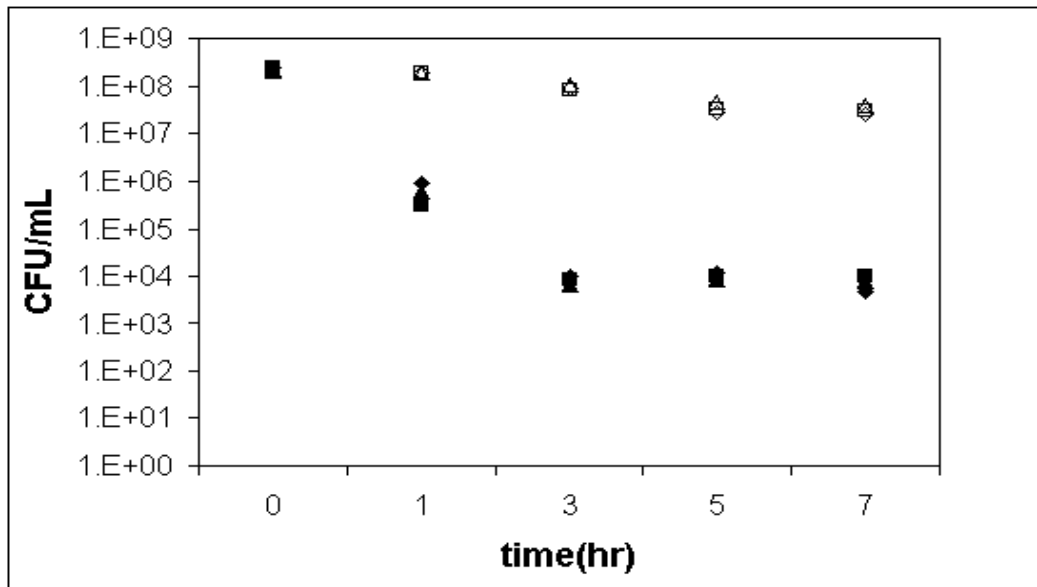


Figure 7.24. Change in *B. subtilis* concentration before and after the addition of AMCLI ( $\diamond, \triangle, \square$  : without AMCLI;  $\blacklozenge, \blacktriangle, \blacksquare$  : with AMCLI)

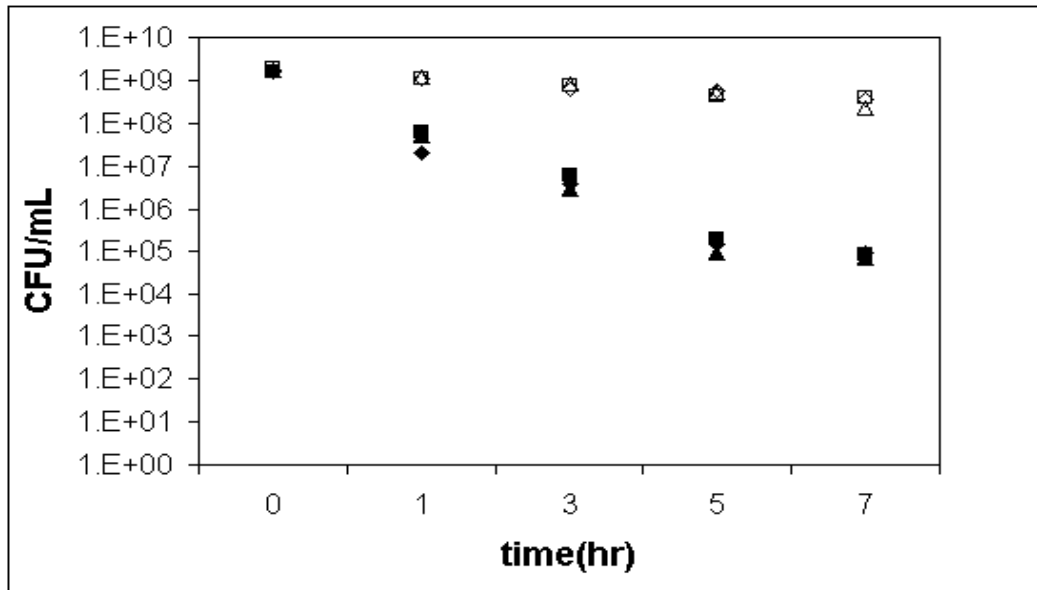


Figure 7.25. Change in *S. aureus* concentration before and after the addition of AMCLI ( $\diamond, \triangle, \square$  : without AMCLI;  $\blacklozenge, \blacktriangle, \blacksquare$  : with AMCLI)

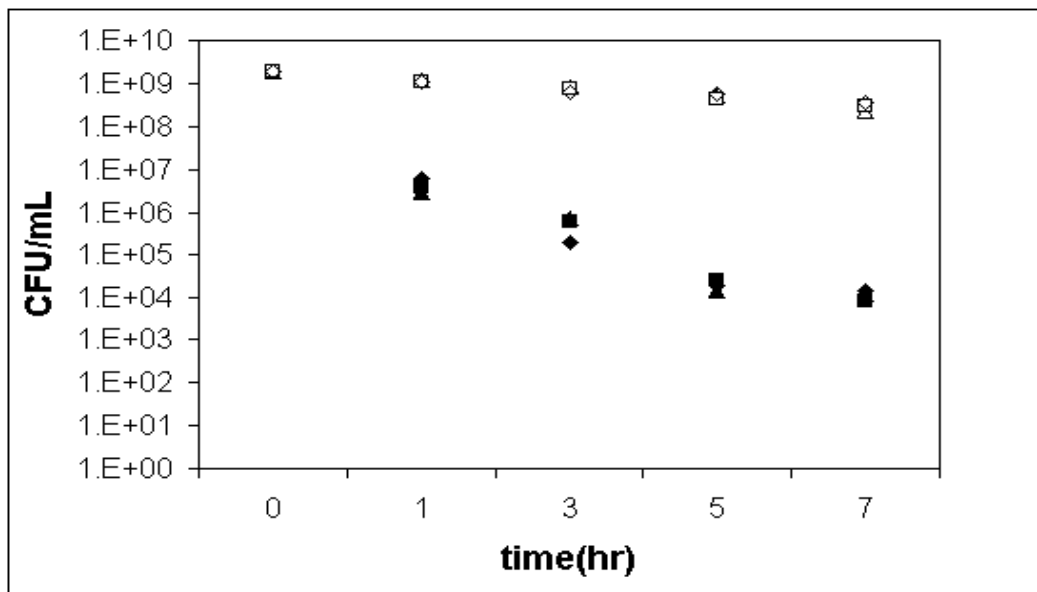


Figure 7.26. Change in *S. epidermidis* concentration before and after the addition of AMCLI ( $\diamond, \triangle, \square$  : without AMCLI;  $\blacklozenge, \blacktriangle, \blacksquare$  : with AMCLI)

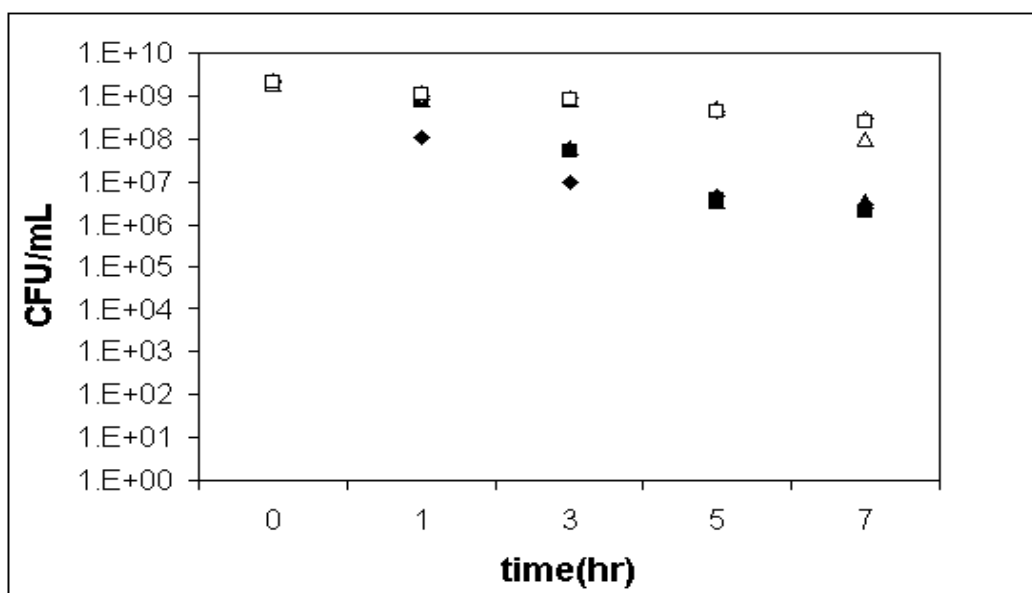


Figure 7.27. Change in *P. aeruginosa* concentration before and after the addition of AMCLI ( $\diamond$ ,  $\triangle$ ,  $\square$  : without AMCLI;  $\blacklozenge$ ,  $\blacktriangle$ ,  $\blacksquare$  : with AMCLI)

The removal performances of clinoptilolite rich mineral, cationic and anionic surfactant clinoptilolite rich mineral were found to be in the following order: *S. aureus* > *S. epidermidis* > *B. subtilis* > *E. coli* > *P. aeruginosa*. By comparing removal degrees against control, decrease levels in bacteria concentrations were found as in the order of  $1\text{-}10^2$  for clinoptilolite rich mineral,  $10^2\text{-}10^4$  for anionic surfactant modified clinoptilolite rich mineral and  $10^3\text{-}10^5$  for cationic surfactant modified clinoptilolite rich mineral. The results implied that cationic and anionic surfactant modified clinoptilolite rich mineral were promising materials for the removal of gram positive and negative bacteria. The extent of gram positive bacteria removal was significantly greater than gram negative bacteria removal. The difference between gram positive and negative bacteria behavior was explained by their cell wall structures. The outer surface of gram positive cell is characterized by a thick layer of peptidoglycan layer. Secondary polymers such as teichoic acid are often present and introduced more functional groups into the peptidoglycan layer. On the other hand, the outer surface of gram negative bacteria cell consists of a thin layer of peptidoglycan layer surrounded by an outer lipid bilayer which contains lipopolysaccharide (LPS). Outer cell membrane structure only present in the gram negative bacteria whereas secondary polymers such as teichoic acids do not present in the gram negative bacteria. The reason for higher bacteria removal might be attributed to secondary polymers on the gram positive bacteria cell wall which may enhance the chemical reactivity of the functional groups.

### **7.2.1. Characterization of Natural and Surfactant Modified Zeolites after Bacteria Attachment**

Figure 7.28 shows SEM micrographs of clinoptilolite rich mineral after *E. coli*, *B. subtilis*, *S. aureus*, *S. epidermidis* and *P. aeruginosa* attachment. The results indicated that some parts of the clinoptilolite rich mineral which had a higher surface roughness were covered by gram positive and negative bacteria. SEM micrographs of cationic and anionic surfactant modified clinoptilolite rich mineral after *E. coli*, *B. subtilis*, *S. aureus*, *S. epidermidis* and *P. aeruginosa* attachment are given in Figure 7.29 and 7.30. The results showed that bacteria were especially attached to the organic layers which were formed on the surface of the clinoptilolite after cationic and anionic surfactant modification. When SEM results of clinoptilolite rich mineral after bacteria attachment were compared with those of cationic and anionic surfactant modified clinoptilolite rich mineral after bacteria attachment, higher bacteria attachment were observed with cationic and anionic surfactant modified clinoptilolite rich mineral. The experimental results indicated that higher bacteria removal results were observed with surfactant modified clinoptilolite rich mineral. The reason for higher bacteria removal with surfactant modified clinoptilolite rich mineral was due to existence of organic layer which enhanced bacteria attachment to the surfactant modified clinoptilolite rich mineral surface.

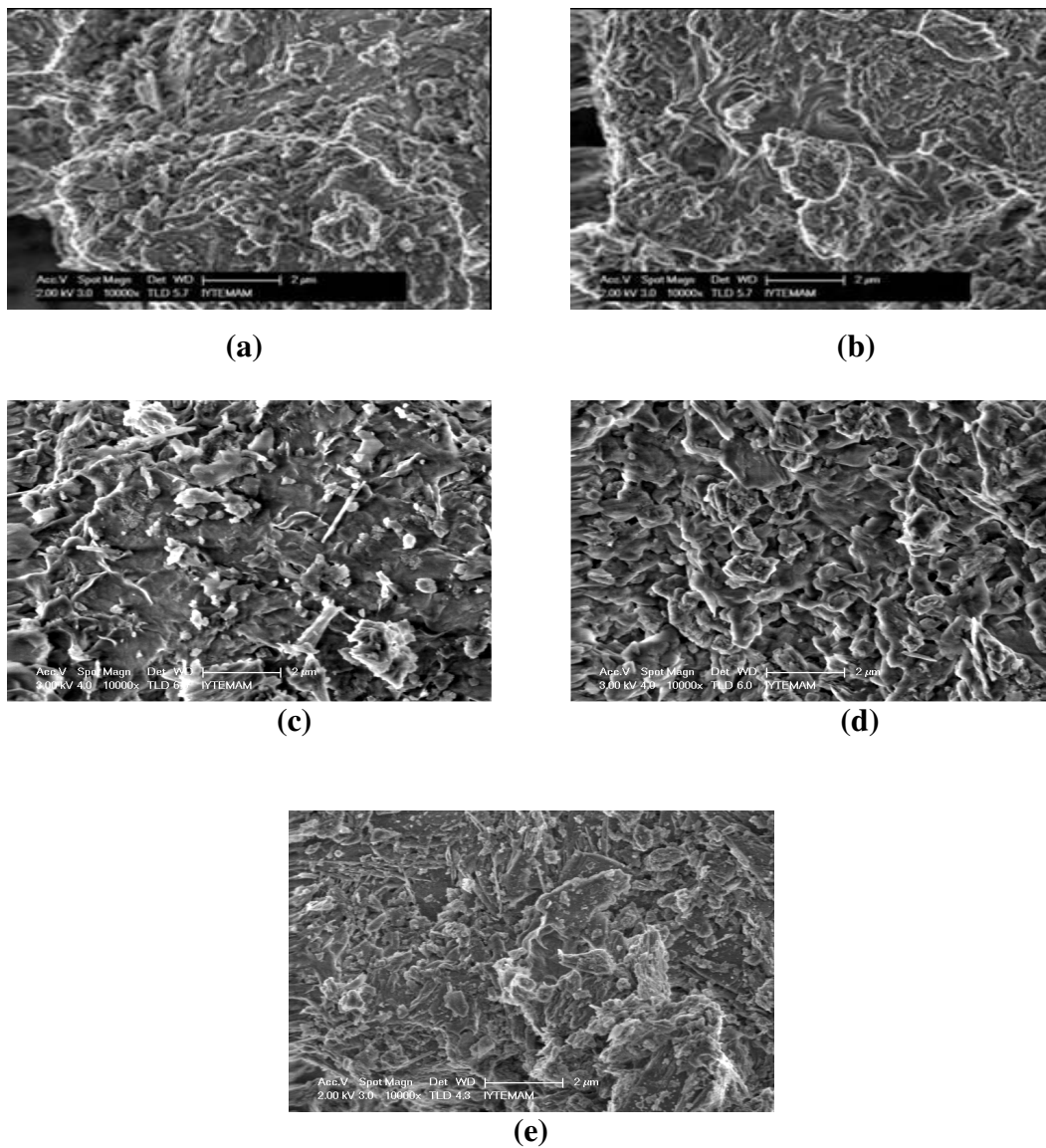
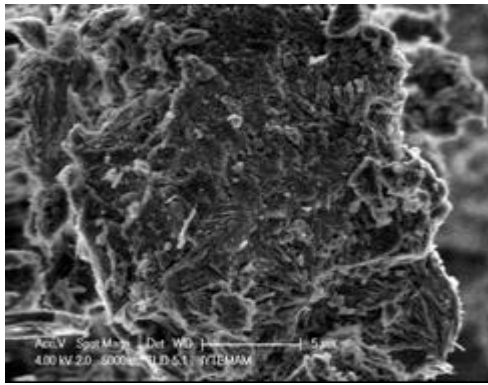
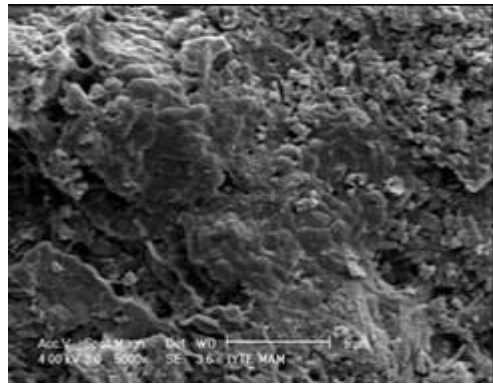


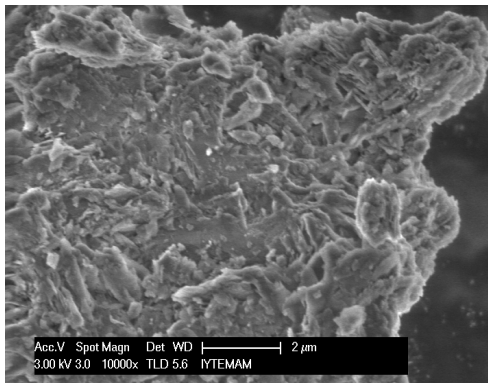
Figure 7.28. SEM micrographs of a) EC-CLI b) BS-CLI c) SA-CLI d) SE-CLI e) PA-CLI



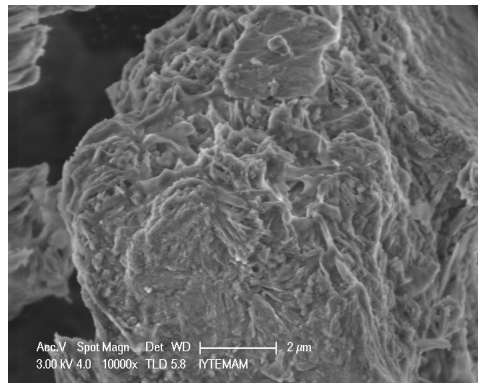
(a)



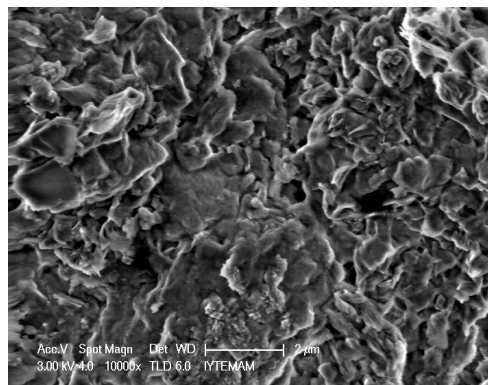
(b)



(c)



(d)



(e)

Figure 7.29. SEM micrographs of a) EC-CMCLI b) BS-CMCLI c) SA-CMCLI d) SE-CMCLI e) PA-CMCLI

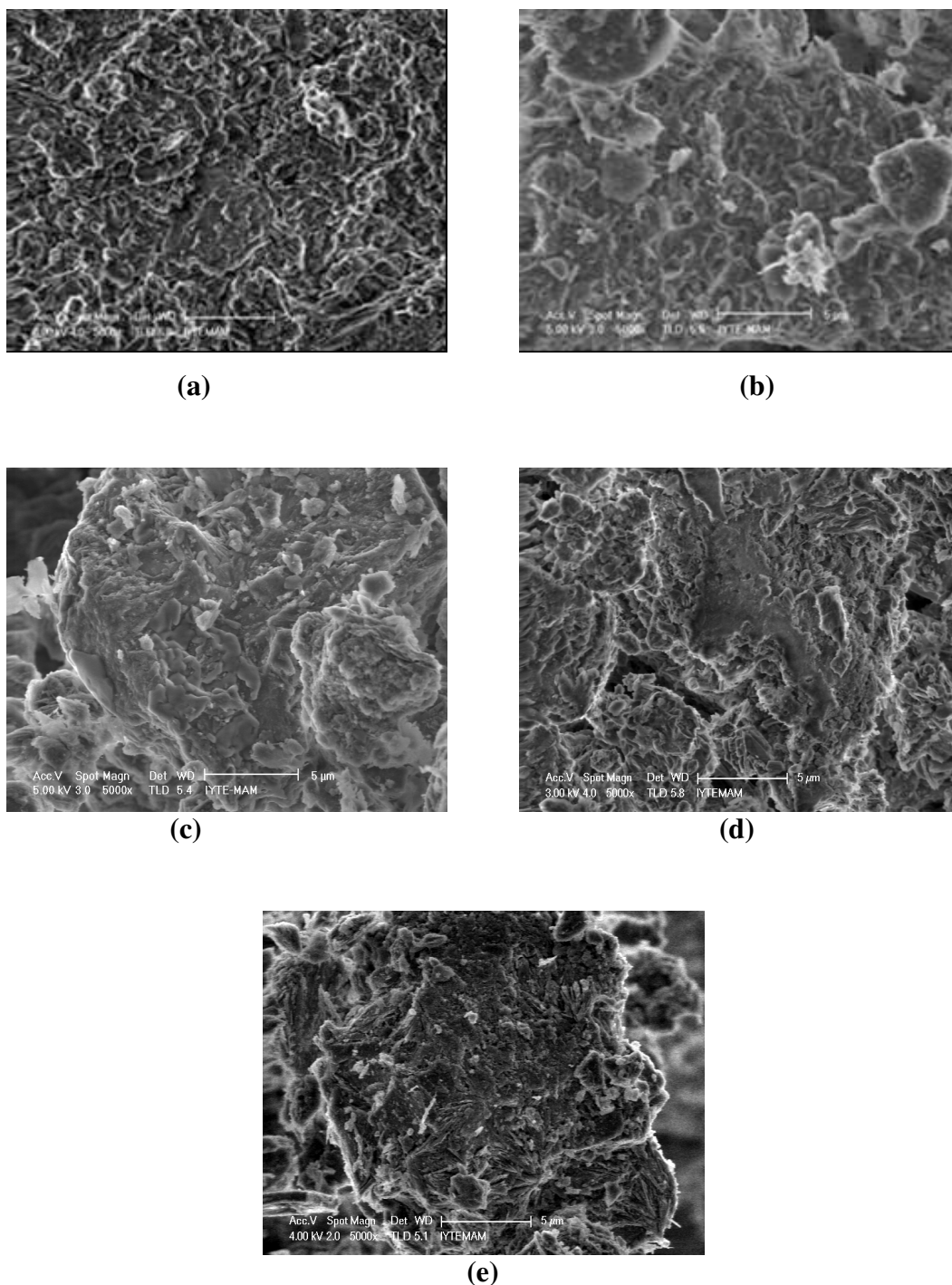


Figure 7.30. SEM micrographs of a) EC-AMCLI b) BS-AMCLI c) SA-AMCLI d) SE-AMCLI e) PA-AMCLI

EDS can provide information regarding the elemental composition of clinoptilolite and surfactant modified clinoptilolite rich mineral samples after bacteria attachment. An average elemental composition of the samples was obtained by data collection at five different regions of the samples. The values of standard deviation were calculated from five measurements. EDS results are tabulated in Table 7.3-7.5. The results indicated that C and S content in the clinoptilolite rich mineral increased after



bacteria attachment. Elemental composition of bacteria is mainly composed of carbon and sulphur. The increase in C and S content in the clinoptilolite rich mineral could be attributed to the attachment of bacteria on the clinoptilolite rich mineral surface. Similar EDS results were obtained with surfactant modified clinoptilolite rich mineral samples.

Table 7.3. EDS of CLI sample after bacteria attachment

<b>Element %</b>	<b>EC-CLI</b>	<b>BS-CLI</b>	<b>SA-CLI</b>	<b>SE-CLI</b>	<b>PA-CLI</b>
C	4.3±0.4	5.2±0.4	4.6±0.2	4.8±0.4	3.8±0.3
O	45.6±0.4	45.6±0.1	45.65±0.2	45.8±0.3	46.3±0.2
Na	0.7±0.02	0.7±0.02	0.7±0.1	0.6±0.2	0.6±0.01
Mg	0.9±0.03	0.9±0.01	0.9±0.01	0.9±0.07	0.8±0.03
Al	7.7±0.06	7.7±0.04	7.6±0.2	7.6±0.1	7.7±0.3
Si	34.7±0.4	33.7±0.1	34.4±0.05	34.4±0.1	35.1±0.2
K	3.1±0.08	3.1±0.02	3.1±0.1	2.9±0.02	2.8±0.1
Ca	2.7±0.04	2.7±0.02	2.7±0.07	2.6±0.05	2.6±0.2
S	0.3±0.5	0.4±0.3	0.4±0.4	0.4±0.3	0.3±0.4
<b>TOTAL</b>	<b>100</b>	<b>100</b>	<b>100</b>	<b>100</b>	<b>100</b>

\*±Standard deviation values

Table 7.4. EDS of CMCLI samples after bacteria attachment

%	EC-CMCLI	BS-CMCLI	SA-CMCLI	SE-CMCLI	PA-CMCLI
C	16.8±0.4	18.1±0.01	17.4±0.3	17.9±0.02	15.6±0.2
O	35.3±0.2	34.7±0.5	35.2±0.07	34.8±0.01	35.9±0.1
Na	0.5±0.01	0.5±0.1	0.5±0.1	0.5±0.06	0.5±0.02
Mg	0.8±0.08	0.7±0.02	0.7±0.05	0.7±0.08	0.8±0.01
Al	7.1±0.1	7.1±0.1	7.1±0.1	7.1±0.04	7.2±0.1
Si	34.6±0.03	34.15±0.02	34.4±0.1	34.1±0.6	34.8±0.2
K	2.4±0.1	2.3±0.1	2.4±0.08	2.3±0.2	2.6±0.2
Ca	2.1±0.1	2.1±0.1	1.9±0.1	2.2±0.6	2.2±0.1
S	0.4±0.05	0.4±0.09	0.3±0.02	0.4±0.03	0.4±0.02
	100	100	100	100	100

\*±Standard deviation values

Table 7.5. EDS of AMCLI samples after bacteria attachment

%	EC-AMCLI	BS-AMCLI	SA-AMCLI	SE-AMCLI	PA-AMCLI
C	10.1±0.2	13.8±0.01	13.2±0.1	13.6±0.05	10.7±0.1
O	40.3±0.06	38.3±0.01	38.8±0.5	38.6±0.3	40.7±0.1
Na	0.7±0.1	0.7±0.2	0.7±0.2	0.7±0.1	0.7±0.2
Mg	0.7±0.05	0.7±0.3	0.7±0.2	0.7±0.2	0.7±0.3
Al	7.3±0.06	7.2±0.1	7.1±0.03	7.1±0.2	7.2±0.1
Si	34.3±0.1	34.1±0.2	34.1±0.1	34±0.08	34.5±0.3
K	2.4±0.03	2.2±0.05	2.4±0.02	2.3±0.03	2.5±0.06
Ca	2.2±0.05	2.1±0.1	2.1±0.1	2.2±0.1	2.3±0.09
S	0.9±0.03	0.9±0.1	0.8±0.08	0.8±0.04	0.7±0.3
	100	100	100	100	100

\*±Standard deviation values

XRD patterns of clinoptilolite rich mineral after *E. coli* attachment is shown in Figure 7.31. The results revealed that the major peaks of the clinoptilolite were

unchanged and only the intensities of the major peaks were decreased after bacteria loading. The same XRD patterns were observed with clinoptilolite rich mineral after *B. subtilis*, *S. aureus*, *S. epidermidis* and *P. aeruginosa* attachment. The results also indicated that XRD results of clinoptilolite rich mineral after bacteria attachment showed similar trend with the XRD results of anionic and cationic surfactant modified clinoptilolite rich mineral after bacteria attachment. Their results are given in Appendix E.1.

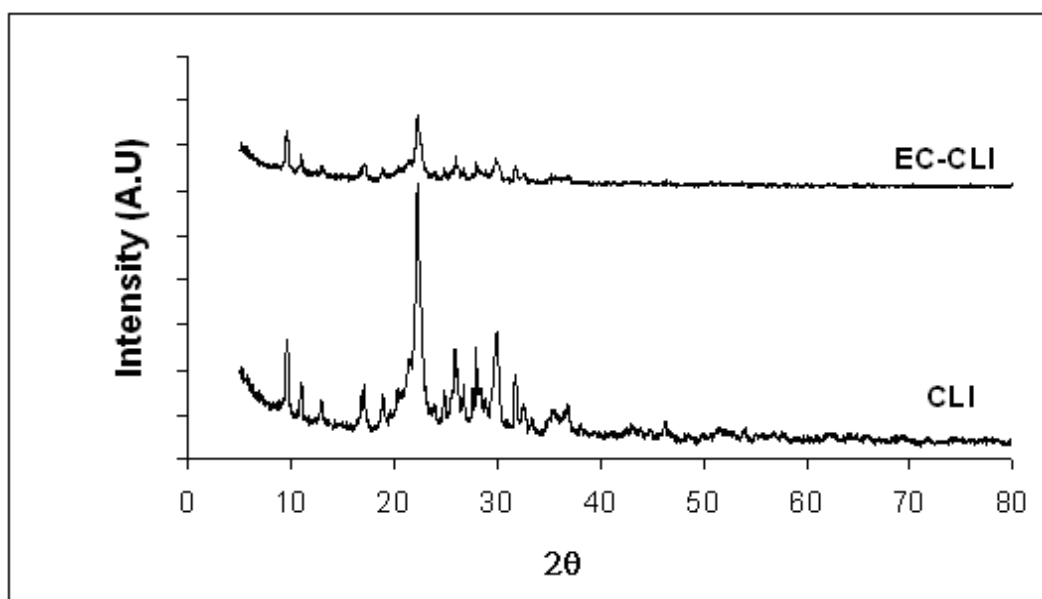


Figure 7.31. XRD patterns of clinoptilolite rich mineral after *E. coli* attachment

FTIR results of the clinoptilolite rich mineral after *E. coli*, *B. subtilis*, *S. aureus*, *S. epidermidis* and *P. aeruginosa* attachment are given in Figure 7.32. After bacteria attachment, no new band was found on the bacteria-clinoptilolite rich mineral samples. Only, the band shift in the water molecules was observed after bacteria attachment. For example, the vibrations of water molecules on clinoptilolite rich mineral shifted from  $3672\text{ cm}^{-1}$  to  $3655\text{ cm}^{-1}$  and from  $1672\text{ cm}^{-1}$  to  $1649\text{ cm}^{-1}$  after *E. coli* attachment. In the case of *B. subtilis* attachment, the sorbed water molecules on clinoptilolite rich mineral shifted from  $3672\text{ cm}^{-1}$  to  $3649\text{ cm}^{-1}$  and from  $1672\text{ cm}^{-1}$  to  $1654\text{ cm}^{-1}$ . Similar shift was observed for sorbed water molecules on clinoptilolite rich mineral after *S. aureus*, *S. epidermidis* and *P. aeruginosa* attachment. The shift in water molecules on the clinoptilolite rich mineral was indication of the existence of hydrogen bonding.

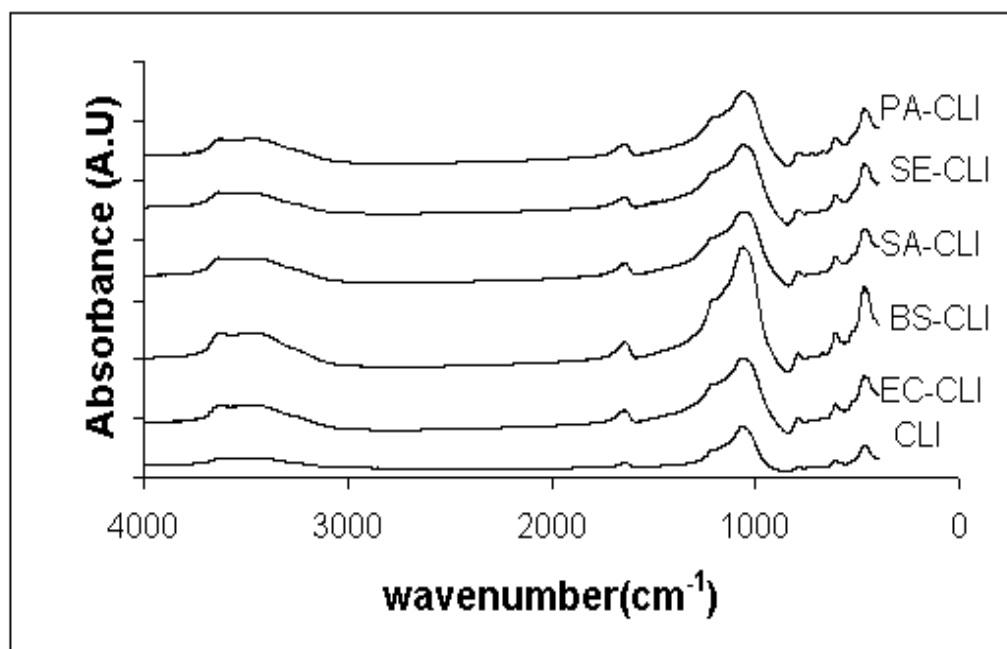


Figure 7.32. FTIR results of clinoptilolite rich mineral after *E. coli*, *B. subtilis*, *S. aureus*, *S. epidermidis* and *P. aeruginosa* attachment

FTIR results of the cationic modified clinoptilolite rich mineral after *E. coli*, *B. subtilis*, *S. aureus*, *S. epidermidis* and *P. aeruginosa* attachment are shown in Figure 7.33. The results implied that the band shift in the water molecules and methylene groups on the cationic modified clinoptilolite rich mineral was observed after bacteria attachment. After *E. coli* attachment, the vibrations of water molecules on cationic modified clinoptilolite rich mineral shifted from  $3651\text{ cm}^{-1}$  to  $3647\text{ cm}^{-1}$  and from  $1660\text{ cm}^{-1}$  to  $1651\text{ cm}^{-1}$ . Moreover, methylene groups on the cationic modified clinoptilolite rich mineral shifted from  $2937\text{ cm}^{-1}$  to  $2953\text{ cm}^{-1}$  and from  $2860\text{ cm}^{-1}$  to  $2872\text{ cm}^{-1}$ . Similar shift was observed for water molecules and methylene groups on cationic modified clinoptilolite rich mineral after *B. subtilis*, *S. aureus*, *S. epidermidis* and *P. aeruginosa* attachment. The shift in water and methylene groups on the cationic modified clinoptilolite rich mineral was indication of existence of hydrogen bonding. As stated before, higher bacteria removal results were observed with cationic modified clinoptilolite rich mineral whereas lower bacteria removal results were observed with clinoptilolite rich mineral. The reason for higher bacteria removal with cationic modified clinoptilolite rich mineral was due to the existence of additional hydrogen bonding coming from the methylene groups on the cationic modified clinoptilolite rich mineral.

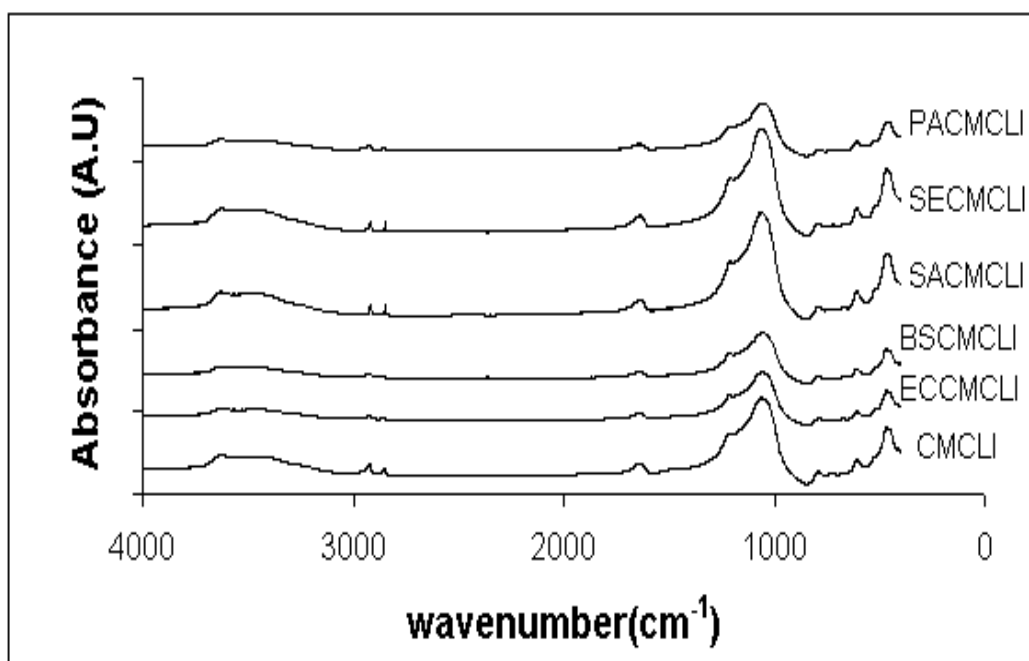


Figure 7.33. FTIR results of cationic modified clinoptilolite rich mineral after *E. coli*, *B. subtilis*, *S. aureus*, *S. epidermidis* and *P. aeruginosa* attachment

Figure 7.34 shows FTIR results of anionic surfactant modified clinoptilolite rich mineral after *E. coli*, *B. subtilis*, *S. aureus*, *S. epidermidis* and *P. aeruginosa* attachment. After bacteria attachment, band shift and disappearance was observed. The band disappearance ( $1467\text{ cm}^{-1}$ ) in FTIR spectra implied that CH interaction was involved in attachment of bacteria on the surface of the anionic modified clinoptilolite rich mineral. Band disappearance in the bending of C-H and band shift in water molecules and methylene groups on the anionic modified clinoptilolite rich mineral pointed out the existence of hydrogen bonding. The reason for higher bacteria removal with anionic surfactant modified clinoptilolite rich mineral was explained by hydrogen bonding coming from CH bending, water molecules and methylene groups.

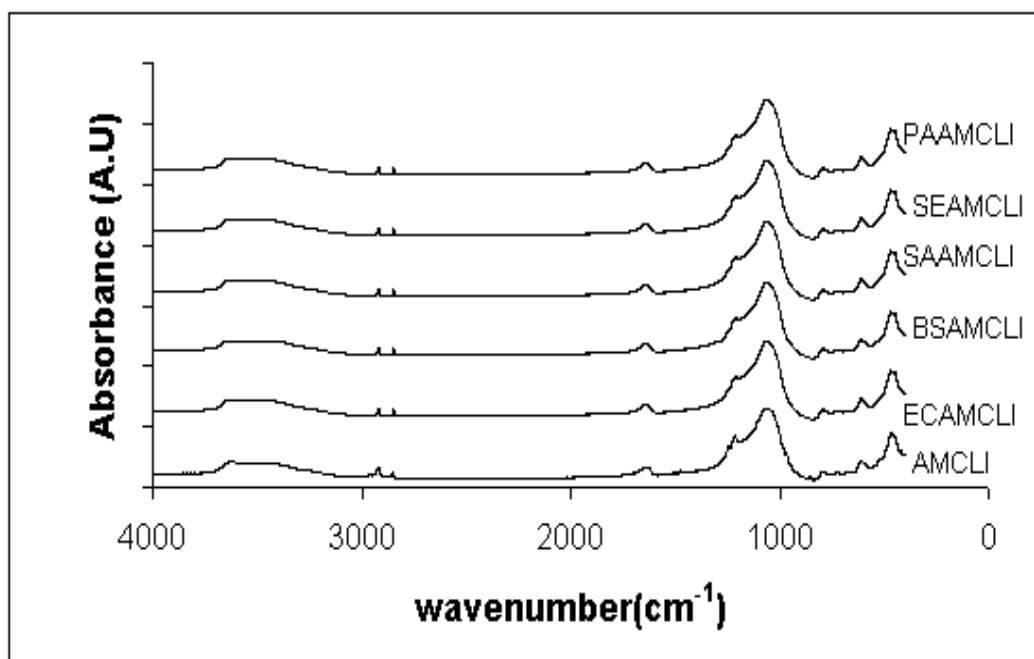


Figure 7.34. FTIR results of anionic modified clinoptilolite rich mineral after *E. coli*, *B. subtilis*, *S. aureus*, *S. epidermidis* and *P. aeruginosa* attachment

### 7.2.2. Proposed Mechanisms in Attachment of Bacteria to the Surface of Natural and Surfactant Modified Zeolites

Previous studies indicated that electrostatic forces and non electrostatic forces were responsible in bacteria removal with clay minerals (Jiang et al., 2007; Rong et al., 2008; Fu et al., 2009; Fang et al., 2010; Rong et al., 2010; Cao et al., 2011). The electrostatic force originates from the Columbic interaction between two charged entities whereas the non-electrostatic ones come from the hydrogen bonding, van der Waals force and hydrophobic interactions. Repulsive and attractive electrostatic forces between bacteria and surface of the material are resulted from the negative or positive surface charge on the bacteria and mineral surface. The surface charge on bacteria and material surface depend on the pH of the solution.

In the literature, there is no information about bacteria removal mechanism with clinoptilolite rich mineral and surfactant modified clinoptilolite rich mineral. The main reason for the lack of data on attachment of bacteria to the surface of the clinoptilolite and surfactant modified clinoptilolite rich mineral was the complicated nature of the attachment process. In this part, the proposed mechanisms for the bacteria attachment are explained by taking into account electrostatic and non electrostatic forces.

In order to understand electrostatic interactions between the bacteria and the clinoptilolite and the bacteria and the surfactant modified clinoptilolite rich mineral, the zeta potentials of the clinoptilolite and surfactant modified clinoptilolite rich mineral in PBS solution (pH 7.4) were measured. At pH 7.4, the surfaces of the gram positive and negative bacteria were negatively charged (Li and Logan, 2004; Kinnari et al., 2009). The zeta potential values were found as -49.4, -58.5 and 17.8 for clinoptilolite rich mineral, anionic surfactant modified clinoptilolite rich mineral and cationic surfactant modified clinoptilolite rich mineral samples, respectively.

Since bacteria, clinoptilolite rich mineral surface and anionic surfactant modified clinoptilolite mineral had negative surface charges, the repulsive electrostatic forces between bacteria-clinoptilolite mineral and bacteria-anionic modified clinoptilolite mineral could occur at pH 7.4. Although repulsive electrostatic forces were dominant, bacteria removal with clinoptilolite and anionic surfactant modified clinoptilolite mineral was observed. The results revealed that non electrostatic forces (hydrogen bonding) might play more important roles than the electrostatic forces in bacteria removal. The existence of hydrogen bonding was supported by FTIR band shift in the water molecules on the parent clinoptilolite rich mineral and on the anionic surfactant modified forms. Moreover, band disappearance in bending of C-H group and band shift in methylene groups on the anionic surfactant modified clinoptilolite rich mineral also pointed out the existence of hydrogen bonding.

Cationic surfactant modified clinoptilolite rich mineral was positively charged at pH 7.4 and thus there were attractive electrostatic forces between bacteria and cationic surfactant modified clinoptilolite rich mineral. In addition to attractive electrostatic forces, non electrostatic forces also play an important role in the bacteria attachment. The evidence of hydrogen bonding was supported by the FTIR results. The experimental results demonstrated that the extent of bacteria removal with cationic surfactant modified clinoptilolite rich mineral was the greatest. The reason was explained by attractive electrostatic forces and hydrogen bonding which comes from band shift in the water molecules and methylene groups on the cationic surfactant modified clinoptilolite rich mineral.

The results implied that hydrogen bonding was the significant mechanism in the bacteria removal with clinoptilolite rich mineral and anionic surfactant modified clinoptilolite rich mineral whereas both attractive electrostatic forces and hydrogen bonding were responsible in the bacteria removal with cationic surfactant modified

clinoptilolite rich mineral. The highest bacteria removal results with cationic surfactant modified clinoptilolite rich mineral was attributed to the summation of electrostatic and non electrostatic forces which enhanced the attachment of bacteria to the surface of the cationic surfactant modified clinoptilolite rich mineral.

### **7.3. Sorption of Cr (VI) onto Natural, Surfactant Modified and Bacteria Loaded Zeolites**

In this part, the potential applications of clinoptilolite, surfactant modified clinoptilolite and bacteria loaded clinoptilolite and surfactant modified clinoptilolite in Cr (VI) sorption were investigated.

pH of the solution affects not only the form of Cr (VI) ions but also surface charge of the sorbents. Cr (VI) is found in the form of  $\text{H}_2\text{CrO}_4$ ,  $\text{HCrO}_4^-$ ,  $\text{CrO}_4^{2-}$ ,  $\text{Cr}_2\text{O}_7^{2-}$  and  $\text{HCr}_2\text{O}_7^-$  depending on the pH of the solution. Cr (VI) is mainly found as  $\text{HCrO}_4^-$  in the pH range 1 to 5 while it exists in the form of  $\text{CrO}_4^{2-}$  at pH 8 to 14. At pH 6 to 7,  $\text{HCrO}_4^-$  and  $\text{CrO}_4^{2-}$  forms of Cr (VI) species exist in the solution.

pH profiles of the sorbents in Cr (VI) solutions were measured to understand which Cr (VI) species interacted with sorbents. pH results of the sorbents in Cr (VI) solution are given in Figure 7.35-7.38. pH values of sorbents in Cr(VI) solution were between 5.1 and 6.5. At these pH ranges, all the sorbents interacted with two Cr (VI) species.



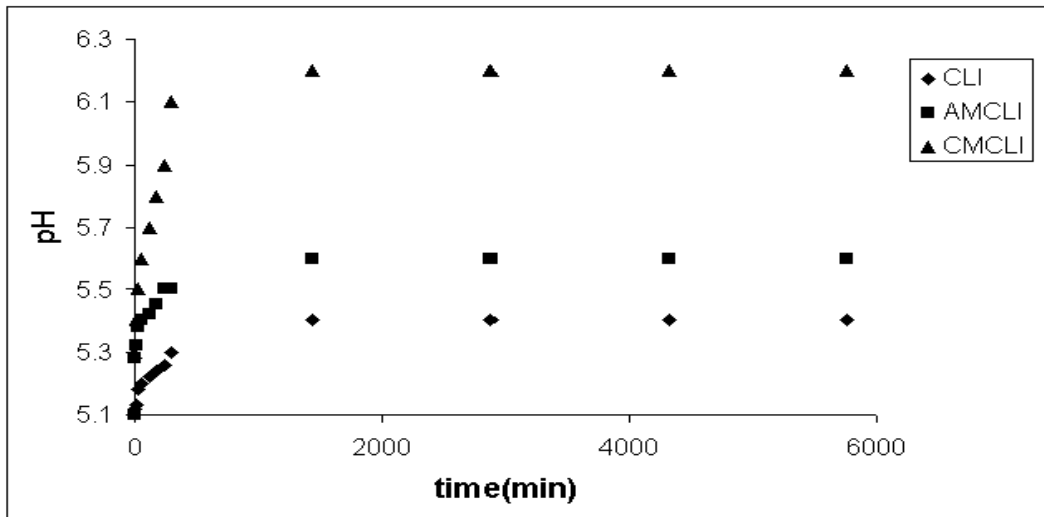


Figure 7.35. pH profiles of clinoptilolite, anionic and cationic surfactant modified clinoptilolite rich mineral in Cr(VI) solution

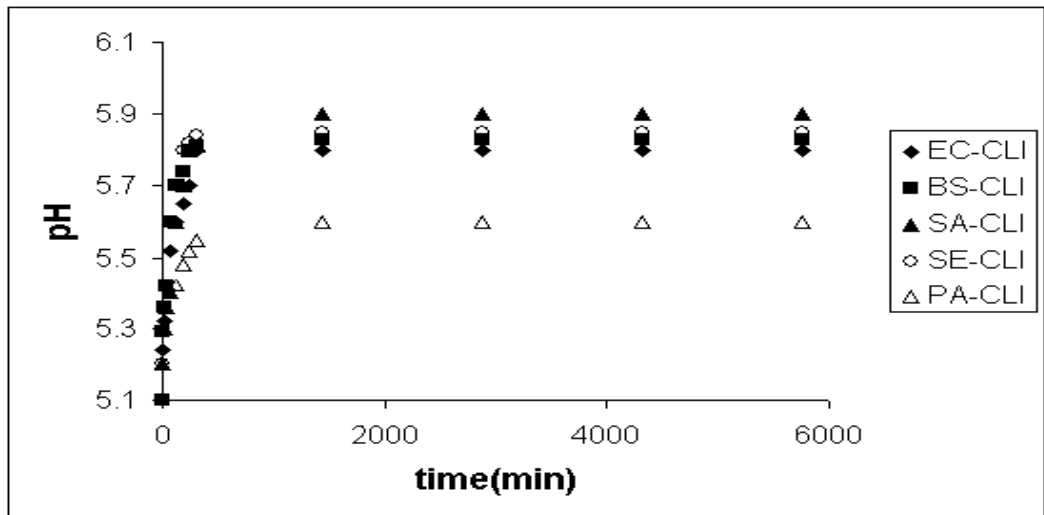


Figure 7.36. pH profiles of the bacteria loaded clinoptilolite rich mineral in Cr(VI) solution

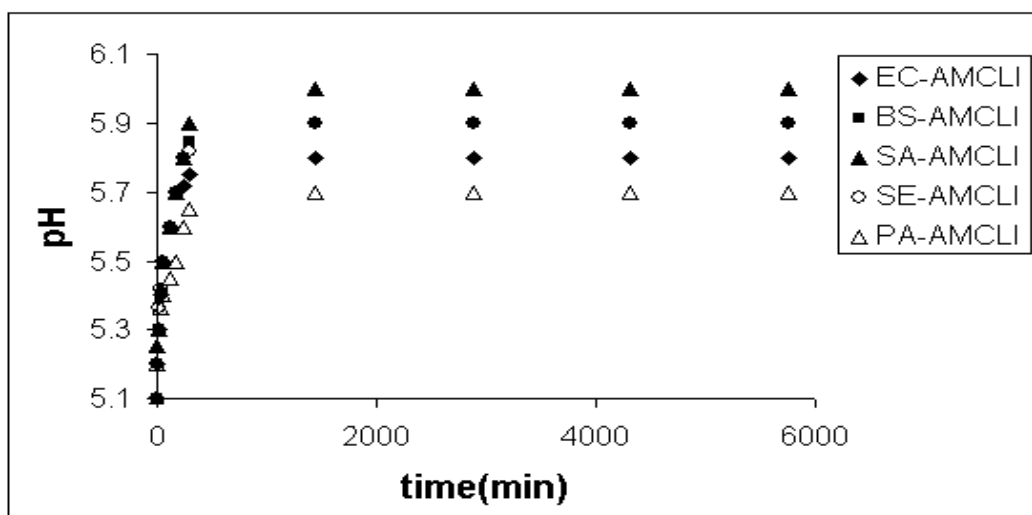


Figure 7.37. pH profiles of the bacteria loaded anionic surfactant modified clinoptilolite rich mineral in Cr(VI) solution

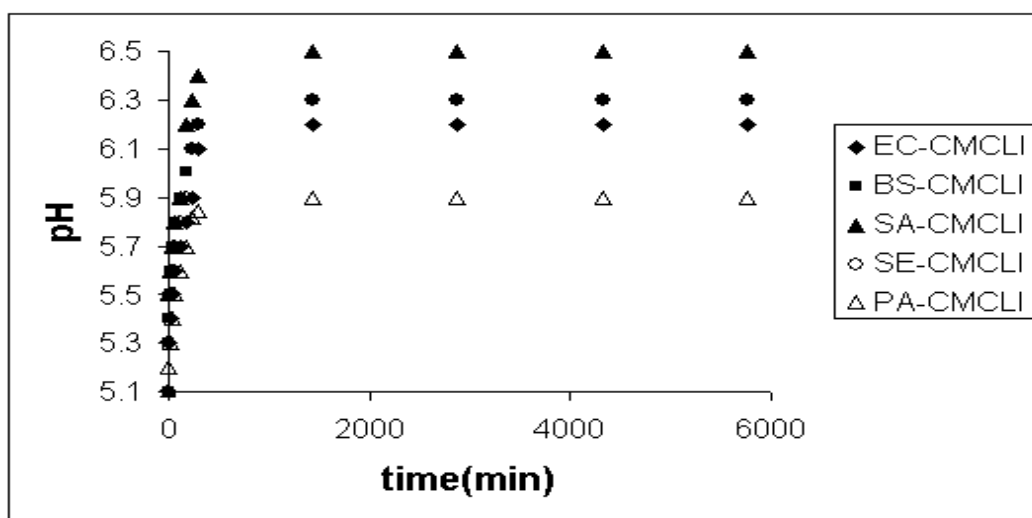


Figure 7.38. pH profiles of the bacteria loaded cationic modified clinoptilolite rich mineral in Cr(VI) solution

After pH measurements, zeta potential analysis was performed to understand the electrostatic interactions between sorbents and Cr (VI) species. Zeta potentials of the sorbents in Cr (VI) solution at pH 5 and 6 were measured and their values are tabulated in Table 7.6. The results indicated that there were repulsive and attractive electrostatic forces between Cr (VI) species and sorbents. The results implied that the surfaces of the clinoptilolite and anionic modified clinoptilolite rich mineral were negatively charged; and thus repulsive electrostatic forces could exist between the clinoptilolite rich mineral-Cr (VI) species and anionic surfactant modified clinoptilolite rich mineral-Cr (VI) species. Since the surfaces of bacteria loaded clinoptilolite rich mineral and anionic

surfactant modified clinoptilolite rich mineral samples were negatively charged, there were repulsive electrostatic forces between bacteria loaded clinoptilolite rich mineral-Cr (VI) species and bacteria loaded anionic surfactant modified clinoptilolite rich mineral-Cr (VI) species. Cationic surfactant modified clinoptilolite rich mineral and bacteria loaded cationic surfactant modified clinoptilolite had positive surface charge and thus the attractive electrostatic forces between cationic surfactant modified clinoptilolite rich mineral-Cr (VI) species and bacteria loaded cationic surfactant modified clinoptilolite-Cr (VI) species could occur.

Table 7.6. Zeta potential values of sorbents in 10 mg/L Cr (VI) solution at pH 5 and 6.

<b>Samples</b>	<b>pH 5</b>	<b>pH 6</b>
	<b>Zeta Potential (mV)</b>	<b>Zeta Potential (mV)</b>
<b>CLI</b>	-28.9	-31.9
<b>AMCLI</b>	-37.6	-40.1
<b>CMCLI</b>	29.3	33.5
<b>EC-CLI</b>	-32.4	-33.4
<b>BS-CLI</b>	-31.9	-32.8
<b>SE-CLI</b>	-28.4	-29.2
<b>SA-CLI</b>	-27.2	-28.6
<b>PA-CLI</b>	-29.4	-30.6
<b>EC-AMCLI</b>	-38.8	-40.4
<b>BS-AMCLI</b>	-35.1	-36.2
<b>SE-AMCLI</b>	-37.4	-38.2
<b>SA-AMCLI</b>	-39.6	-40.5
<b>PA-AMCLI</b>	-41.3	-42.5
<b>EC-CMCLI</b>	22.7	14.4
<b>BS-CMCLI</b>	24.6	16.3
<b>SE-CMCLI</b>	22.5	13.5
<b>SA-CMCLI</b>	21.3	12.8
<b>PA-CMCLI</b>	17.7	10.4

The sorption kinetic curves of Cr (VI) for clinoptilolite, anionic and cationic surfactant modified clinoptilolite rich mineral are given in Figure 7.39-7.41. At equilibrium, the sorbed amounts of Cr (VI) values were found as 0.48, 0.51 and 0.82 mg/g for clinoptilolite, anionic surfactant modified clinoptilolite and cationic surfactant modified clinoptilolite rich mineral, respectively. The results indicated that there was no significant difference between sorption values of clinoptilolite rich mineral and anionic surfactant modified clinoptilolite rich mineral. Higher Cr (VI) sorption value was

obtained with cationic surfactant modified clinoptilolite rich mineral. The reason for higher Cr (VI) sorption with cationic surfactant modified clinoptilolite rich mineral was explained by repulsive and attractive forces between sorbents and Cr (VI) species. Because of having attractive electrostatic forces, higher Cr (VI) sorption was observed with cationic surfactant modified clinoptilolite rich mineral. Although repulsive electrostatic forces between the clinoptilolite rich mineral-Cr (VI) species and anionic surfactant modified clinoptilolite rich mineral-Cr (VI) species were dominant, Cr (VI) sorption with clinoptilolite and anionic surfactant modified clinoptilolite mineral was observed. The results revealed that non electrostatic forces played more important roles than the electrostatic forces in Cr (VI) sorption with clinoptilolite and anionic surfactant modified clinoptilolite mineral.

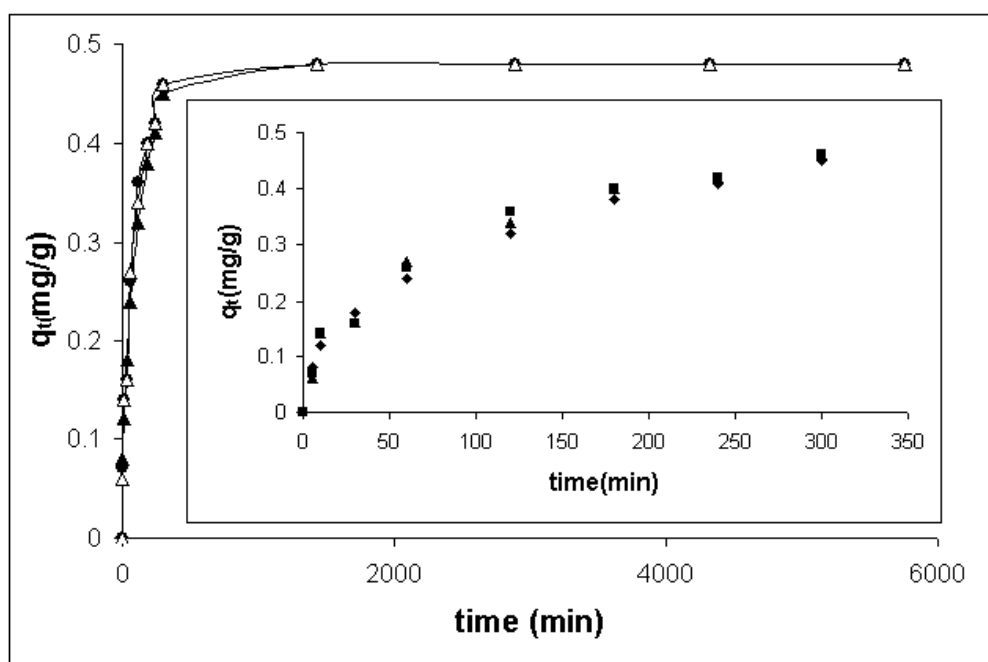


Figure 7.39. Sorption kinetic curve of Cr (VI) for CLI (Conditions: 10 mg/L, 25 °C, 140 rpm, 25–106 μm)

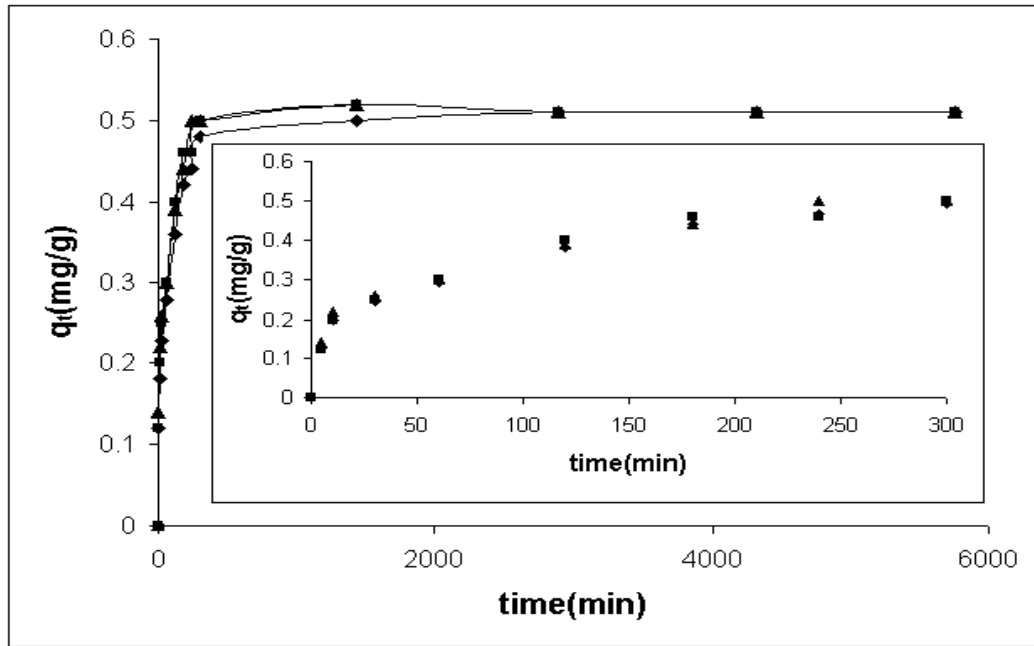


Figure 7.40. Sorption kinetic curve of Cr (VI) for AMCLI (Conditions: 10 mg/L, 25 °C, 140 rpm, 25–106  $\mu\text{m}$ )

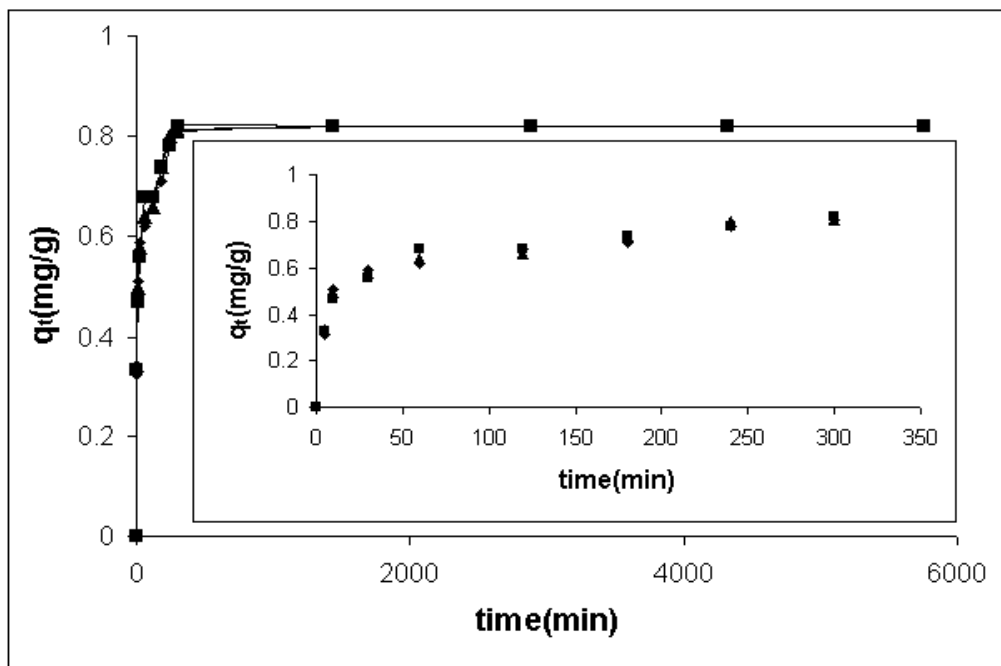


Figure 7.41. Sorption kinetic curve of Cr (VI) for CMCLI (Conditions: 10 mg/L, 25 °C, 140 rpm, 25–106  $\mu\text{m}$ )

The sorption kinetic curves of Cr (VI) for bacteria loaded clinoptilolite rich mineral are shown in Figure 7.42-7.46. At equilibrium, the sorbed amounts of Cr (VI) values were determined as 0.54, 0.58, 0.55, 0.56 and 0.50 mg/g for EC-CLI, BS-CLI, SA-CLI, SE-CLI and PA-CLI, respectively. When Cr (VI) sorption values of

clinoptilolite and bacteria loaded clinoptilolite rich mineral samples were compared, bacteria loaded clinoptilolite rich mineral samples were much more effective than clinoptilolite rich mineral. Functional groups on the bacteria species enhanced the interaction between Cr (VI) species and the clinoptilolite rich mineral samples. The results also indicated that Cr (VI) sorption with gram positive bacteria loaded clinoptilolite rich mineral samples were slightly higher than gram negative bacteria loaded samples. Secondary polymers which only present on the gram positive cell wall structure enhanced the interaction between Cr (VI) species and the sorbents and thus higher Cr (VI) sorption values were observed with gram positive bacteria loaded clinoptilolite rich mineral samples.

As stated before, the repulsive electrostatic forces could exist between bacteria loaded clinoptilolite rich mineral and Cr (VI) species. Although there were repulsive electrostatic forces, the existence of Cr (VI) sorption indicates a significant role of the non electrostatic forces in Cr (VI) sorption with bacteria loaded clinoptilolite rich mineral.

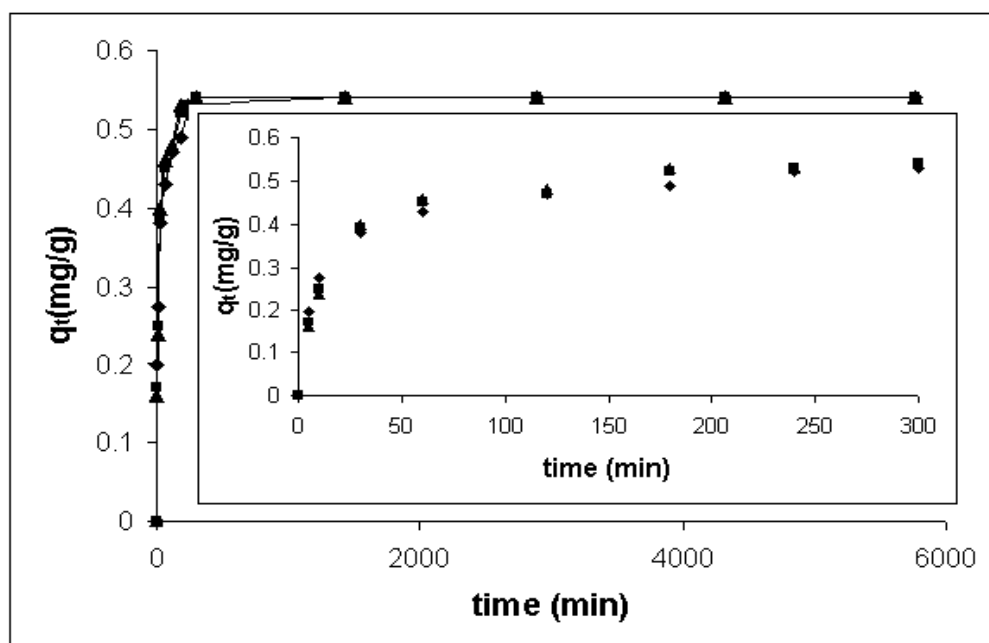


Figure 7.42. Sorption kinetic curve of Cr (VI) for EC-CLI (Conditions: 10 mg/L, 25 °C, 140 rpm, 25–106 μm)

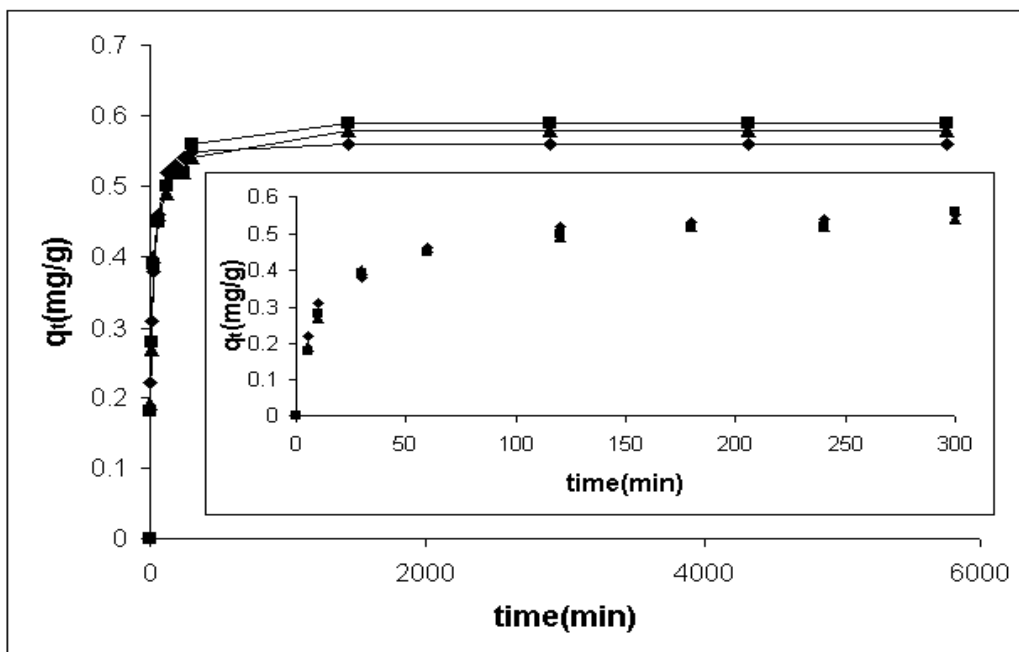


Figure 7.43. Sorption kinetic curve of Cr (VI) for BS-CLI (Conditions: 10 mg/L, 25 °C, 140 rpm, 25–106  $\mu$ m)

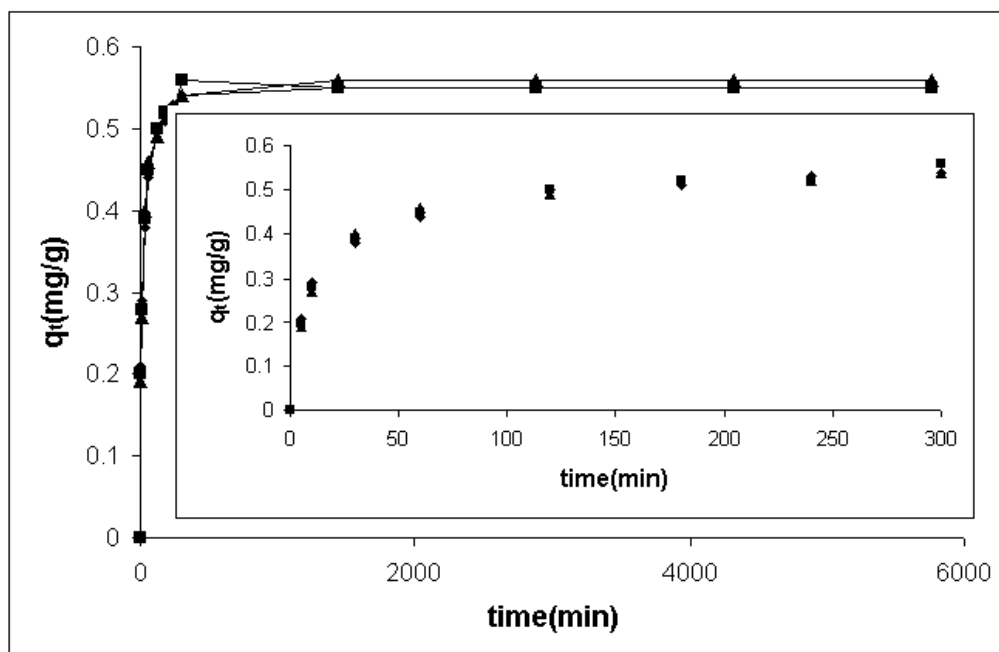


Figure 7.44. Sorption kinetic curve of Cr (VI) for SA-CLI (Conditions: 10 mg/L, 25 °C, 140 rpm, 25–106  $\mu$ m)

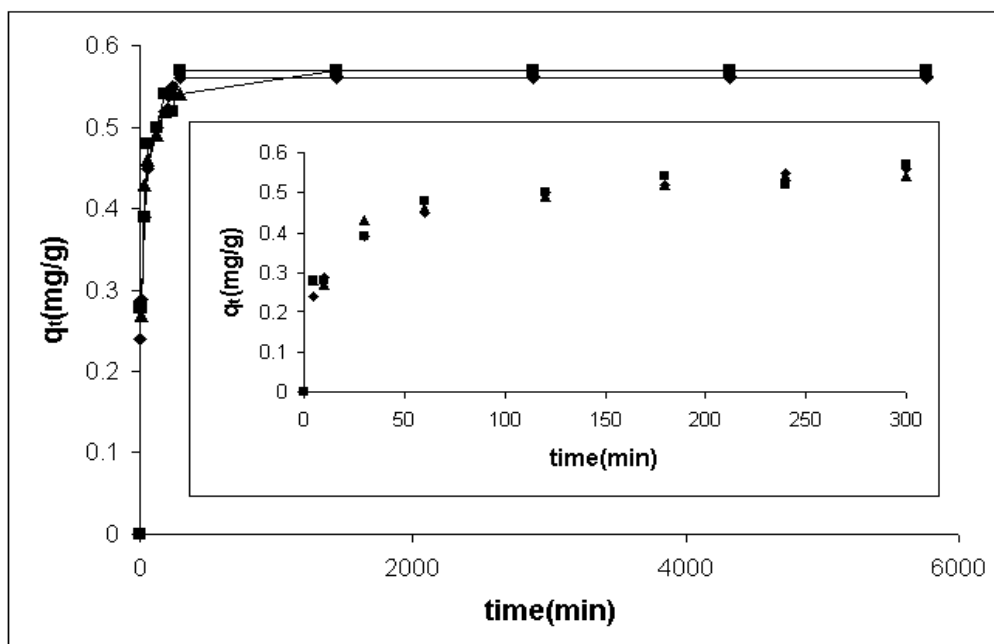


Figure 7.45. Sorption kinetic curve of Cr (VI) for SE-CLI (Conditions: 10 mg/L, 25 °C, 140 rpm, 25–106  $\mu\text{m}$ )

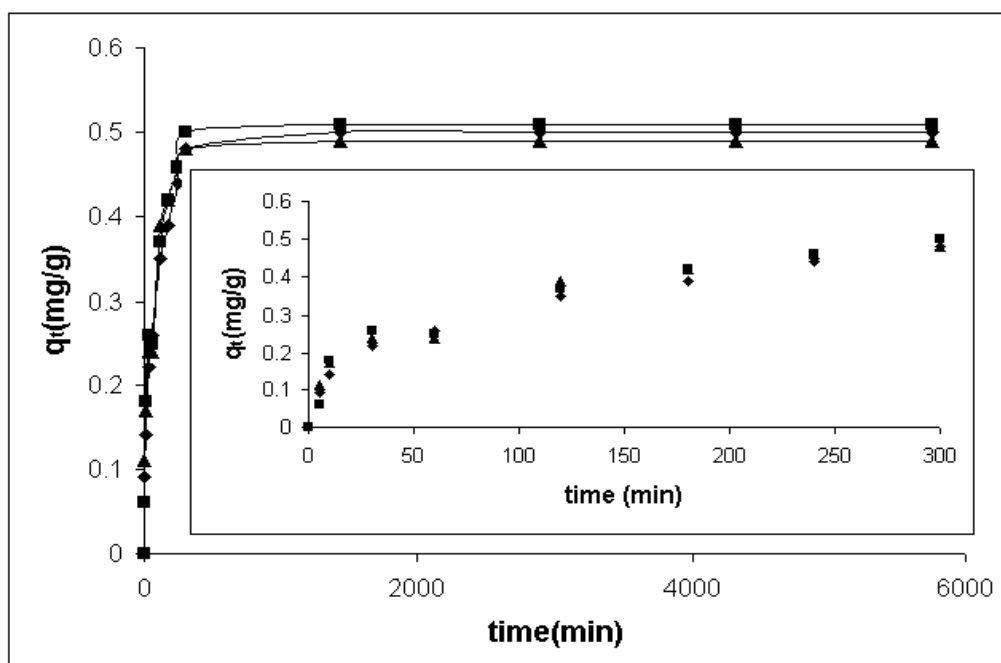


Figure 7.46. Sorption kinetic curve of Cr (VI) for PA-CLI (Conditions: 10 mg/L, 25 °C, 140 rpm, 25–106  $\mu\text{m}$ )

The sorption kinetic curves of Cr (VI) for bacteria loaded anionic surfactant modified clinoptilolite rich mineral are given in Figure 7.47-7.51. At equilibrium, the sorbed amounts of Cr (VI) values were found as 0.61, 0.65, 0.62, 0.63 and 0.56 mg/g for EC-AMCLI, BS-AMCLI, SA-AMCLI, SE-AMCLI and PA-AMCLI, respectively.



After bacteria loading, anionic surfactant modified clinoptilolite rich mineral had higher Cr (VI) sorption values. The results indicated that Cr (VI) sorption performances of gram positive bacteria were slightly higher than those of gram negative bacteria. The reason was explained by secondary polymers in gram positive cell wall structure which might enhance the interaction between Cr (VI) and gram positive bacteria loaded anionic surfactant modified clinoptilolite rich mineral.

As stated before, there were repulsive electrostatic forces between Cr (VI) species and bacteria loaded anionic surfactant modified samples. Although repulsive electrostatic forces were dominant, the extent of Cr (VI) sorption with bacteria loaded anionic surfactant modified clinoptilolite rich mineral was greater. The results revealed that non electrostatic forces played a significant role rather than the electrostatic forces in Cr (VI) sorption with bacteria loaded anionic surfactant modified clinoptilolite rich mineral.

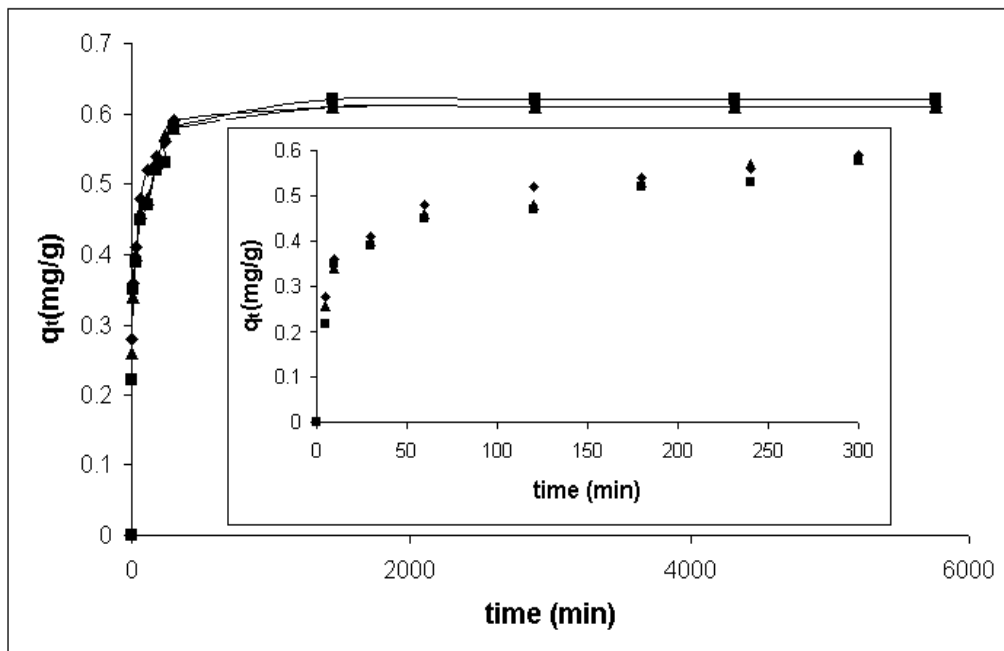


Figure 7.47. Sorption kinetic curve of Cr (VI) for EC-AMCLI (Conditions: 10 mg/L, 25 °C, 140 rpm, 25–106  $\mu$ m)

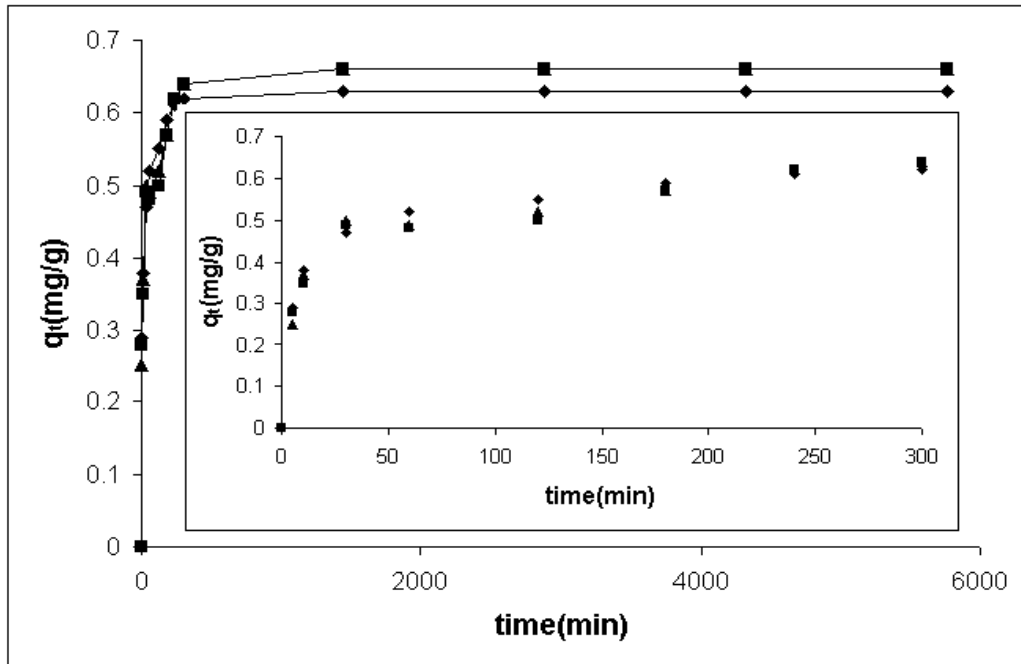


Figure 7.48. Sorption kinetic curve of Cr (VI) for BS-AMCLI (Conditions: 10 mg/L, 25 °C, 140 rpm, 25–106  $\mu$ m)

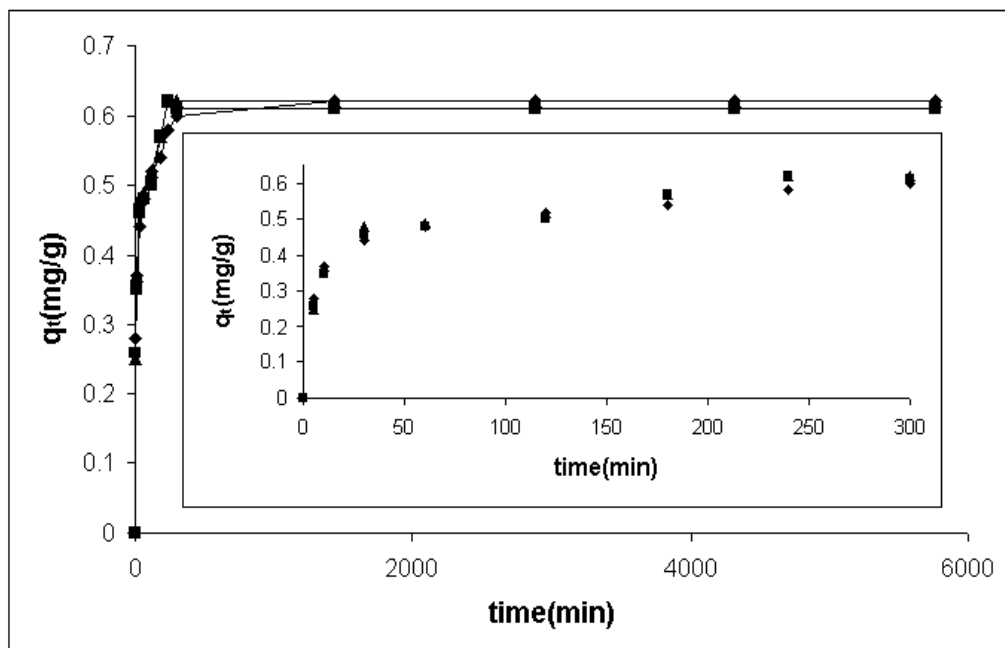


Figure 7.49. Sorption kinetic curve of Cr (VI) for SA-AMCLI (Conditions: 10 mg/L, 25 °C, 140 rpm, 25–106  $\mu$ m)

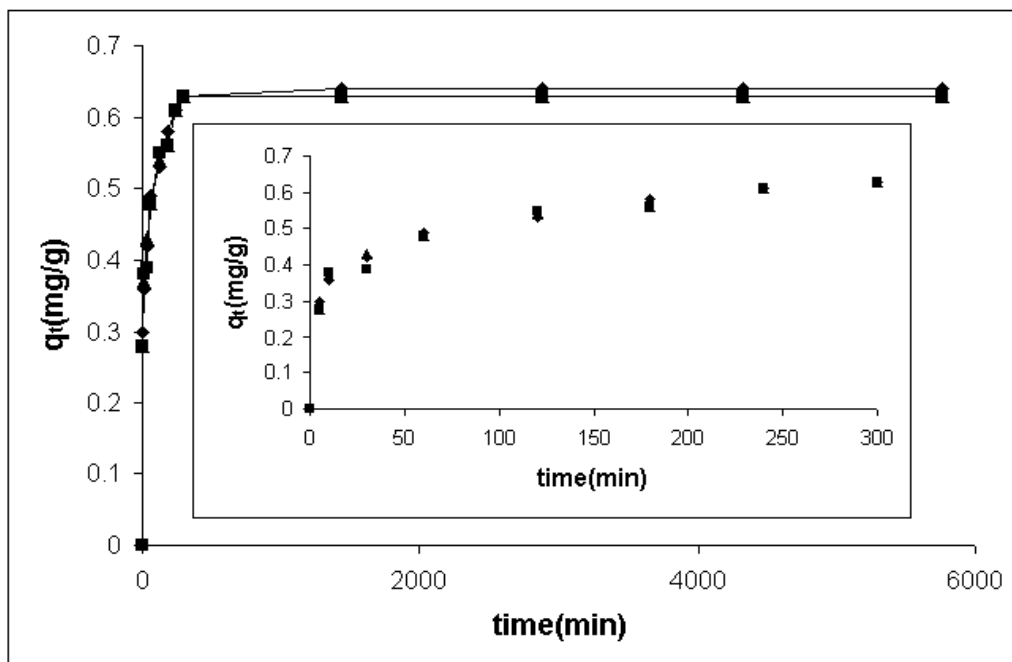


Figure 7.50. Sorption kinetic curve of Cr (VI) for SE-AMCLI (Conditions: 10 mg/L, 25 °C, 140 rpm, 25–106  $\mu\text{m}$ )

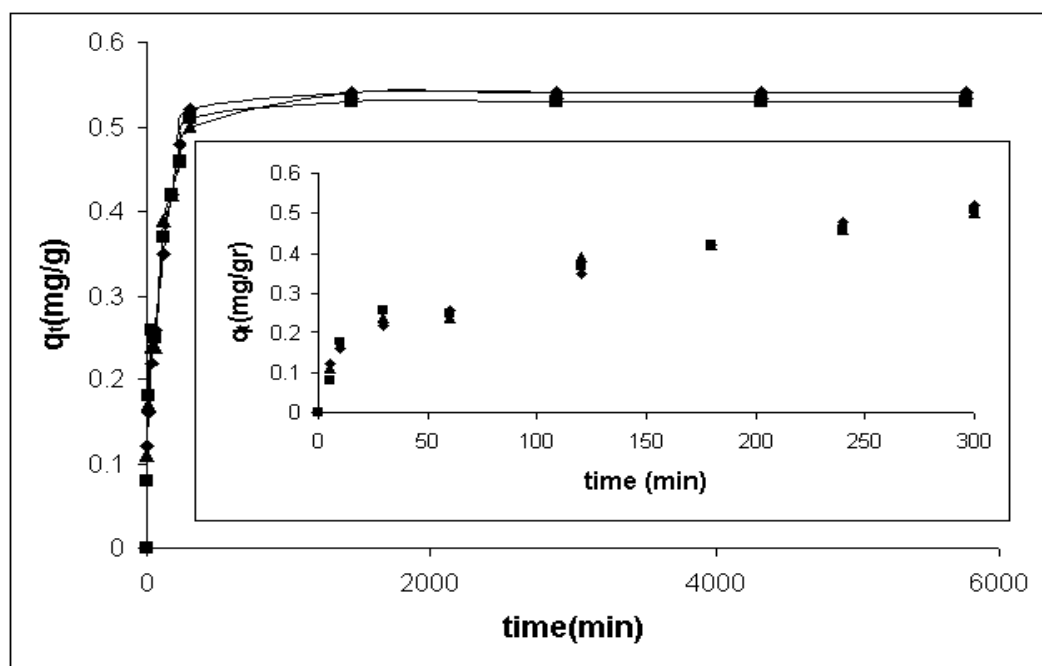


Figure 7.51. Sorption kinetic curve of Cr (VI) for PA-AMCLI (Conditions: 10 mg/L, 25 °C, 140 rpm, 25–106  $\mu\text{m}$ )

The sorption kinetic curves of Cr (VI) for bacteria loaded cationic surfactant modified clinoptilolite rich mineral are given in Figure 7.52-7.56. The results revealed that the sorbed amounts of Cr (VI) values were found in the following order: BS-CMCLI > SE-CMCLI > SA-CMCLI > EC-CMCLI > PA-CMCLI. The results indicated that

Cr (VI) sorption capacities of the cationic surfactant modified clinoptilolite rich mineral samples were increased after bacteria loading. Higher Cr (VI) sorption values were observed with gram positive bacteria loaded cationic surfactant modified clinoptilolite rich mineral due to the existence of secondary polymers on the gram positive cell wall structure.

As stated before, there were attractive electrostatic forces between bacteria loaded cationic surfactant modified clinoptilolite rich mineral and Cr (VI) species since the surfaces of the bacteria loaded samples were positively charged. The results implied that electrostatic forces played an important role in the Cr (VI) sorption with these samples.

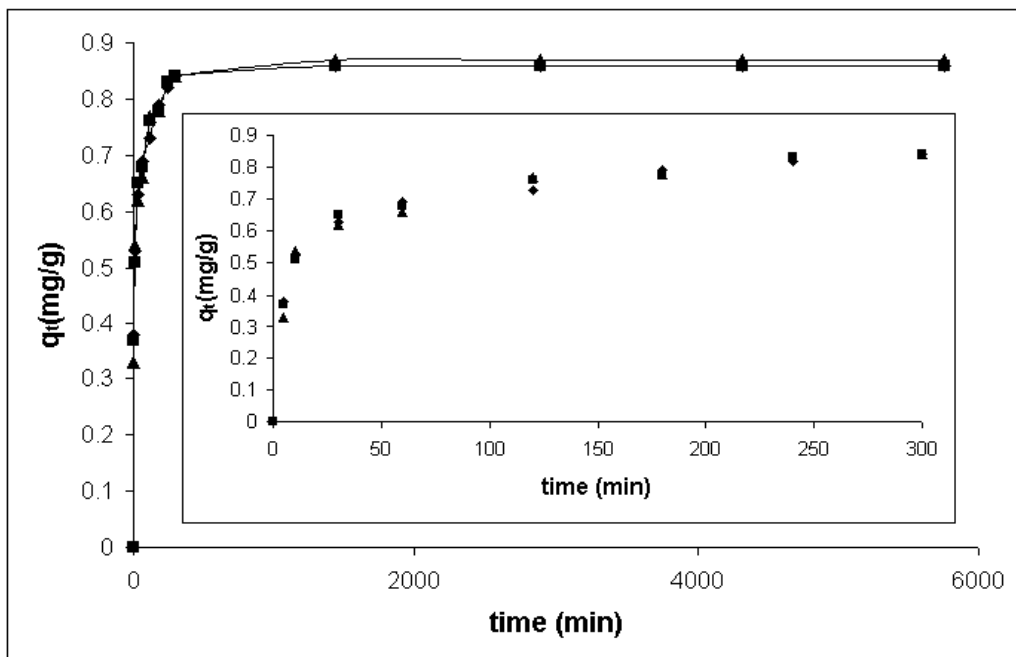


Figure 7.52. Sorption kinetic curve of Cr (VI) for EC-CMCLI (Conditions: 10 mg/L, 25 °C, 140 rpm, 25–106  $\mu$ m)

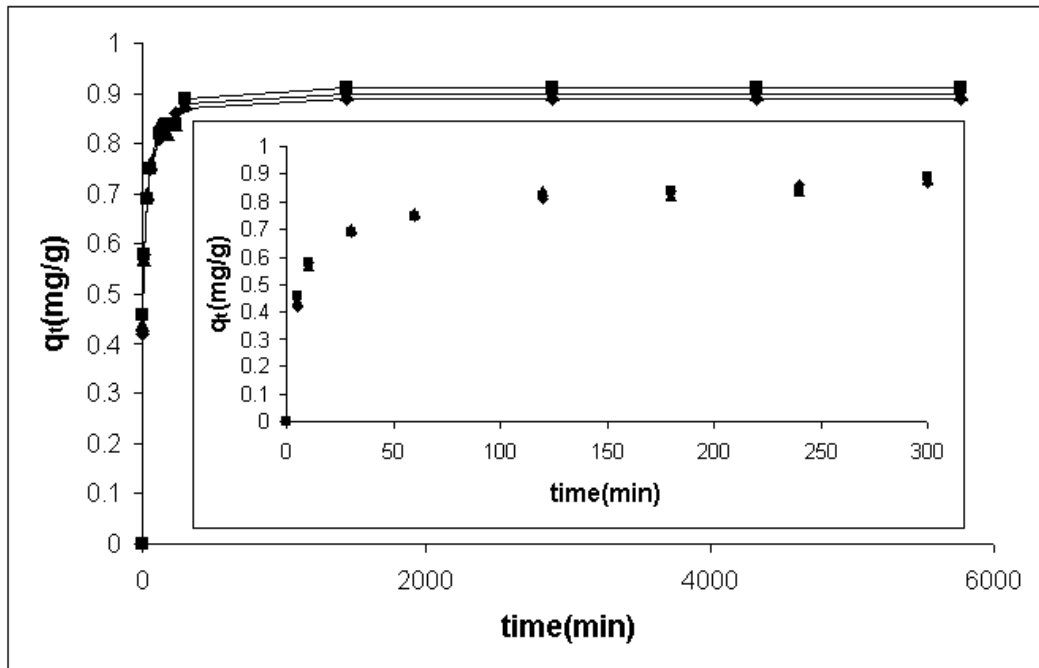


Figure 7.53. Sorption kinetic curve of Cr (VI) for BS-CMCLI (Conditions: 10 mg/L, 25 °C, 140 rpm, 25–106  $\mu$ m)

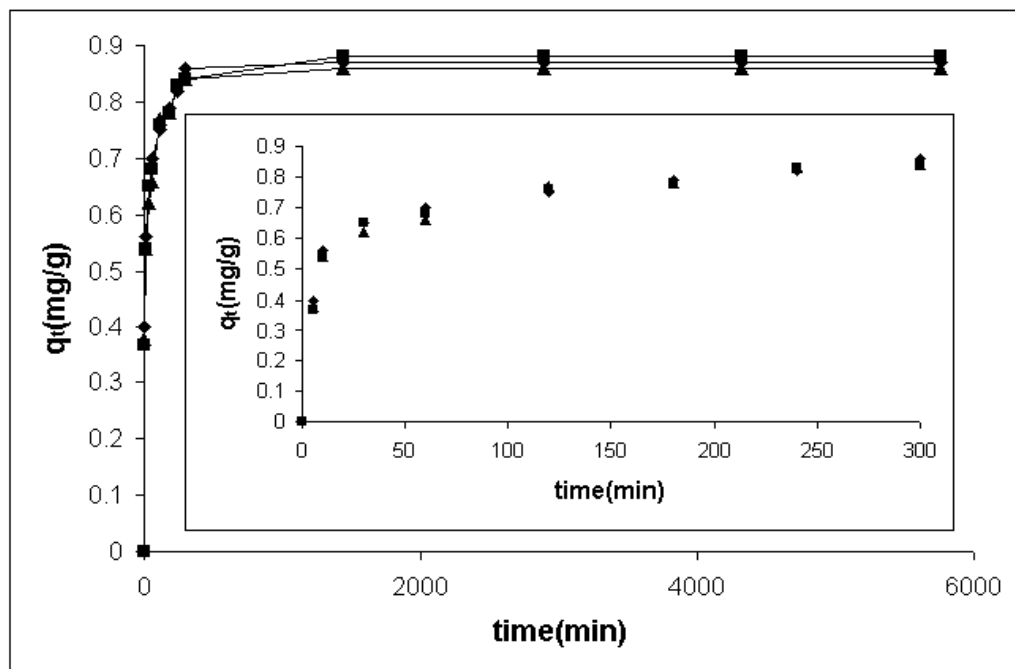


Figure 7.54. Sorption kinetic curve of Cr (VI) for SA-CMCLI (Conditions: 10 mg/L, 25 °C, 140 rpm, 25–106  $\mu$ m)

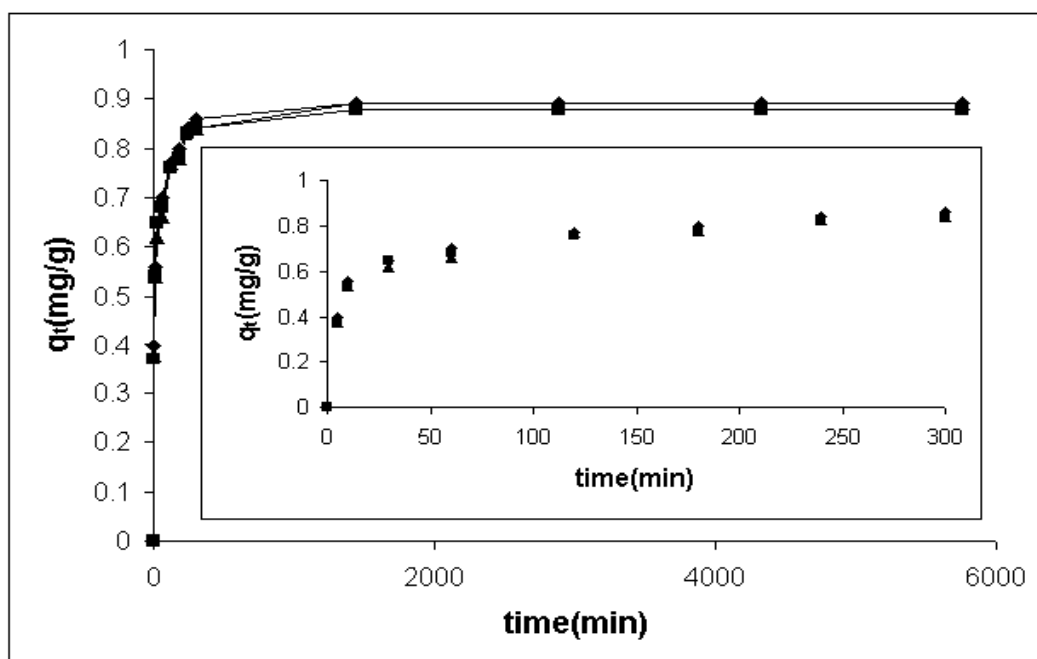


Figure 7.55. Sorption kinetic curve of Cr (VI) for SE-CMCLI (Conditions: 10 mg/L, 25 °C, 140 rpm, 25–106  $\mu$ m)

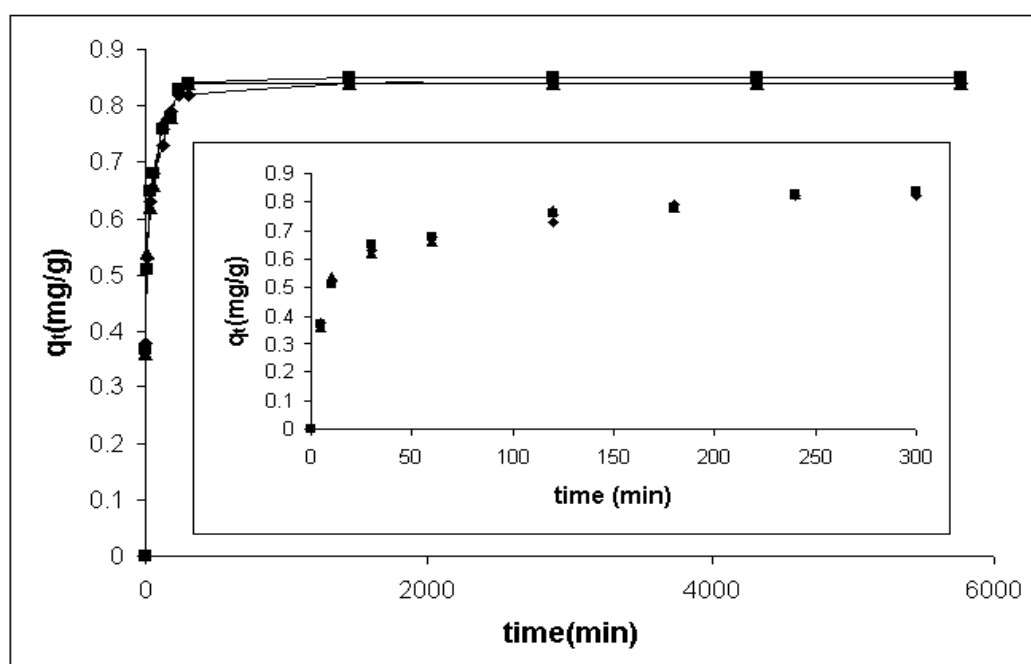


Figure 7.56. Sorption kinetic curve of Cr (VI) for PA-CMCLI (Conditions: 10 mg/L, 25 °C, 140 rpm, 25–106  $\mu$ m)

Cr (VI) removal percentage values of all the sorbents are tabulated in Table 7.7. The results implied that Cr (VI) removal percentage value of clinoptilolite rich mineral increased after modification with cationic surfactant. As indicated in Table 7.7, Cr (VI) removal percentage value of the clinoptilolite rich mineral was slightly increased after

the attachment of bacteria to its surface. Similar results were obtained with bacteria loaded anionic and cationic surfactant modified clinoptilolite rich mineral. The results also indicated that gram positive bacteria loaded clinoptilolite and surfactant modified clinoptilolite rich mineral samples showed higher Cr (VI) removal than gram negative bacteria loaded samples. Gram positive bacteria loaded cationic surfactant modified clinoptilolite rich mineral, especially *B. subtilis*, is promising materials in Cr (VI) removal.

Table 7.7. Cr(VI) removal percentage values of all sorbents

Sorbents	% Cr(VI) removal
CLI	48
AMCLI	51
CMCLI	82
EC-CLI	54
BS-CLI	58
SE-CLI	56
SA-CLI	55
PA-CLI	50
EC-AMCLI	61
BS-AMCLI	65
SE-AMCLI	63
SA-AMCLI	62
PA-AMCLI	56
EC-CMCLI	86
BS-CMCLI	90
SE-CMCLI	89
SA-CMCLI	87
PA-CMCLI	84

### 7.3.1. Characterization of Natural, Surfactant Modified and Bacteria Loaded Zeolites after Cr (VI) Sorption

EDS of clinoptilolite rich mineral and surfactant modified clinoptilolite rich mineral after Cr (VI) sorption are tabulated in Table 7.8. The results showed that cationic modified clinoptilolite rich mineral had higher weight percent of chromium values than clinoptilolite and anionic modified clinoptilolite rich mineral.

Table 7.8. EDS of CLI, AMCLI and CMCLI after Cr (VI) sorption

Element %	CLI-Cr	AMCLI-Cr	CMCLI-Cr
C	0	7.9±0.2	14.6±0.2
O	47.4±0.7	41.2±0.2	35.5±0.3
Na	0.7±0.03	0.7±0.01	0.5±0.01
Mg	0.9±0.01	0.8±0.01	0.8±0.02
Al	7.5±0.05	7.4±0.04	7.2±0.03
Si	36.6±0.6	35.8±0.3	35.3±0.2
K	3.3±0.04	2.8±0.06	2.8±0.08
Ca	2.9±0.04	2.5±0.8	2.6±0.06
S	0	0.6±0.018	0
Cr	0.1±0.01	0.2±0.01	0.7±0.03
TOTAL	100	100	100

\*±Standard deviation values

EDS of bacteria loaded clinoptilolite rich mineral are given in Table 7.9. The results indicated that *B. subtilis* loaded clinoptilolite rich mineral had higher weight percent of chromium values than other bacteria loaded clinoptilolite rich mineral samples. Table 7.10 and 7.11 show EDS results of bacteria loaded anionic and cationic modified clinoptilolite rich mineral. The results showed that higher weight percent of chromium values were observed with *B. subtilis* loaded anionic and cationic modified clinoptilolite rich mineral samples.



Table 7.9. EDS of bacteria loaded clinoptilolite rich minerals after Cr (VI) sorption

%	<b>EC-CLI-Cr</b>	<b>BS-CLI-Cr</b>	<b>SA-CLI-Cr</b>	<b>SE-CLI-Cr</b>	<b>PA-CLI-Cr</b>
C	4.3±0.1	5.2±0.3	4.6±0.2	4.8±0.1	3.8±0.2
O	45.6±0.3	45.4±0.1	45.6±0.09	45.6±0.05	46.1±0.06
Na	0.6±0.1	0.7±0.20	0.7±0.1	0.6±0.3	0.6±0.2
Mg	0.9±0.1	0.9±0.2	0.9±0.2	0.8±0.1	0.8±0.1
Al	7.6±0.1	7.7±0.05	7.6±0.1	7.6±0.2	7.7±0.1
Si	34.7±0.2	33.6±0.1	34.3±0.1	34.4±0.2	35.1±0.1
K	3.1±0.01	3.1±0.03	3.1±0.02	2.9±0.05	2.8±0.06
Ca	2.7±0.02	2.7±0.2	2.7±0.3	2.6±0.1	2.6±0.3
S	0.3±0.08	0.4±0.14	0.3±0.2	0.3±0.4	0.3±0.2
Cr	0.24±0.4	0.3±0.01	0.25±0.2	0.27±0.03	0.2±0.04
	100	100	100	100	100

\*±Standard deviation values

Table 7.10. EDS of bacteria loaded anionic modified clinoptilolite rich minerals after Cr (VI) sorption

%	<b>EC-AMCLI-Cr</b>	<b>BS-AMCLI-Cr</b>	<b>SA-AMCLI-Cr</b>	<b>SE-AMCLI-Cr</b>	<b>PA-AMCLI-Cr</b>
C	11.2±0.1	13.8±0.2	13.2±0.2	13.6±0.2	10.7±0.1
O	40.2±0.1	38.1±0.1	38.1±0.2	38.3±0.1	40.4±0.1
Na	0.7±0.2	0.7±0.1	0.6±0.2	0.7±0.2	0.7±0.1
Mg	0.7±0.2	0.7±0.1	0.7±0.2	0.7±0.2	0.7±0.1
Al	7.2±0.08	7.1±0.1	7.1±0.06	7.1±0.06	7.2±0.08
Si	34.3±0.2	34.0±0.2	33.7±0.2	34±0.2	34.5±0.2
K	2.4±0.2	2.2±0.2	2.4±0.2	2.3±0.2	2.5±0.2
Ca	2.2±0.3	2.1±0.1	2.3±0.3	2.2±0.3	2.3±0.1
S	0.9±0.1	0.9±0.2	0.8±0.2	0.8±0.1	0.7±0.2
Cr	0.32±0.09	0.36±0.22	0.34±0.22	0.35±0.11	0.28±0.18
	100	100	100	100	100

\*±Standard deviation values

Table 7.11. EDS of bacteria loaded cationic modified clinoptilolite rich minerals after Cr (VI) sorption

%	EC-CMCLI-Cr	BS-CMCLI-Cr	SA-CMCLI-Cr	SE-CMCLI-Cr	PA-CMCLI-Cr
C	16.8±0.2	18.1±0.08	17.4±0.2	17.9±0.2	15.6±0.1
O	35.0±0.1	34.2±0.1	34.9±0.2	34.0±0.1	35.4±0.1
Na	0.4±0.2	0.4±0.1	0.4±0.2	0.5±0.2	0.5±0.1
Mg	0.7±0.1	0.6±0.08	0.6±0.08	0.7±0.07	0.7±0.09
Al	7.1±0.1	7.1±0.07	7.1±0.08	7.1±0.09	7.2±0.1
Si	34.2±0.3	34.1±0.2	34.1±0.1	34.1±0.1	34.8±0.1
K	2.4±0.3	2.2±0.2	2.4±0.1	2.3±0.2	2.6±0.1
Ca	2.1±0.2	2.1±0.2	1.9±0.1	2.2±0.2	2.2±0.2
S	0.4±0.3	0.4±0.2	0.3±0.1	0.4±0.1	0.4±0.09
Cr	0.82±0.2	0.86±0.2	0.84±0.2	0.84±0.2	0.6±0.2
	100	100	100	100	100

\*±Standard deviation values

XRD result of clinoptilolite after Cr (VI) sorption is shown in Figure 7.57. After Cr (VI) sorption, major peaks of clinoptilolite rich mineral were unchanged and only the intensities of these peaks were slightly decreased. Similar XRD results were obtained with surfactant modified clinoptilolite rich mineral and bacteria loaded samples. Their XRD results are shown in Appendix E.2.

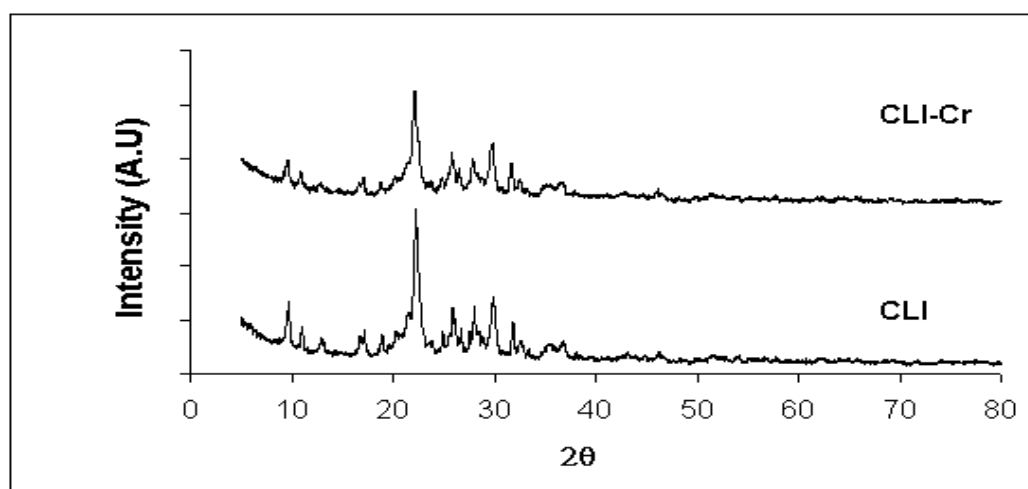


Figure 7.57. XRD results of clinoptilolite rich mineral after Cr (VI) sorption

FTIR results of clinoptilolite rich mineral after Cr (VI) sorption are given in Figure 7.58. Band shift in the water molecules on clinoptilolite rich mineral, which was an indication of existence of hydrogen bonding, was observed after Cr (VI) sorption. The results revealed that non electrostatic forces (hydrogen bonding) played a significant role rather than electrostatic forces in Cr (VI) sorption with clinoptilolite rich mineral.

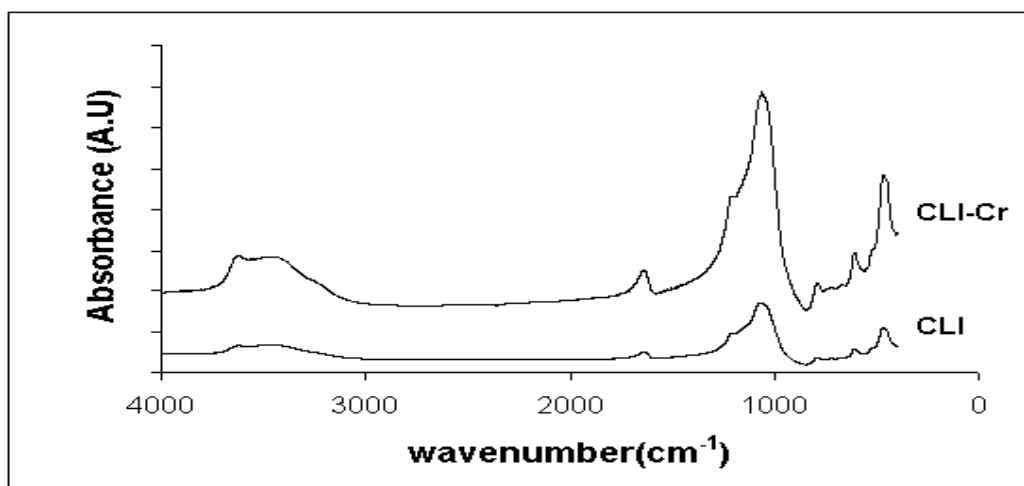


Figure 7.58. FTIR results of clinoptilolite rich mineral after Cr (VI) sorption (CLI-Cr)

FTIR results of anionic surfactant modified clinoptilolite rich mineral after Cr (VI) sorption are shown in Figure 7.59.  $1467\text{ cm}^{-1}$  which are assigned to the bending of C-H in  $\text{CH}_3$  was disappeared after Cr (VI) sorption. In addition to band disappearance, band shift in water molecules and methylene groups on the anionic surfactant modified clinoptilolite rich mineral were observed after Cr (VI) sorption. The results implied that the hydrogen bonding coming from CH bending, water molecules and methylene groups was responsible for Cr (VI) sorption with anionic surfactant modified clinoptilolite rich mineral. The experimental results indicated that anionic surfactant modified clinoptilolite rich mineral showed higher Cr (VI) sorption values than clinoptilolite rich mineral. The reason for higher Cr (VI) sorption with anionic surfactant modified clinoptilolite rich was due to the existence of additional hydrogen bonding coming from the CH bending and methylene groups on the anionic surfactant modified clinoptilolite rich mineral.

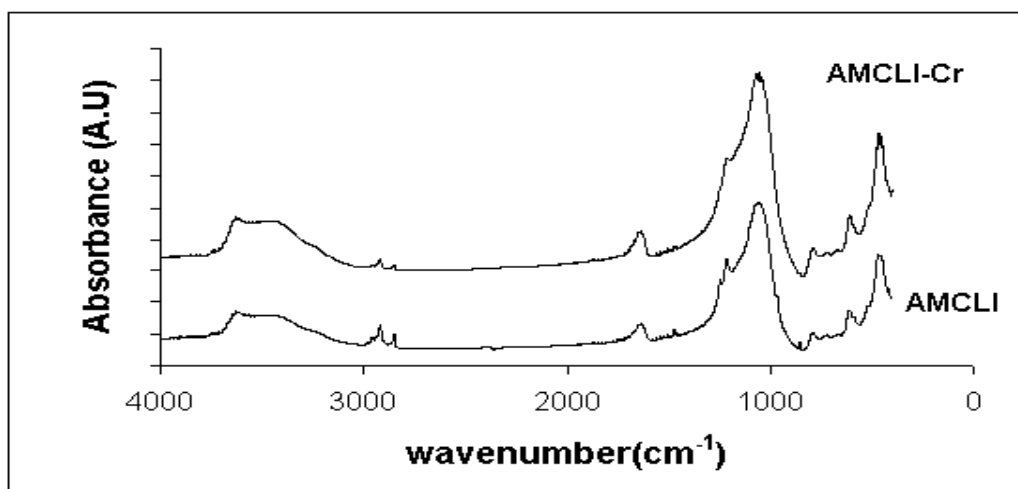


Figure 7.59. FTIR results of anionic modified clinoptilolite rich mineral after Cr (VI) sorption (AMCLI-Cr)

Figure 7.60 shows the FTIR results of cationic modified clinoptilolite rich mineral after Cr (VI) sorption. The results implied that the band shift in the water molecules and methylene groups on the cationic modified clinoptilolite rich mineral was observed after Cr (VI) sorption. The results inferred that hydrogen bonding coming from methylene group and water molecule on the cationic modified clinoptilolite rich mineral were involved in Cr (VI) sorption with cationic modified clinoptilolite rich mineral. The experimental results indicated that higher Cr (VI) sorption was observed with cationic modified clinoptilolite rich mineral. Higher Cr (VI) sorption results with cationic modified clinoptilolite rich mineral was attributed to the summation of the attractive electrostatic forces and non electrostatic forces (hydrogen bonding).

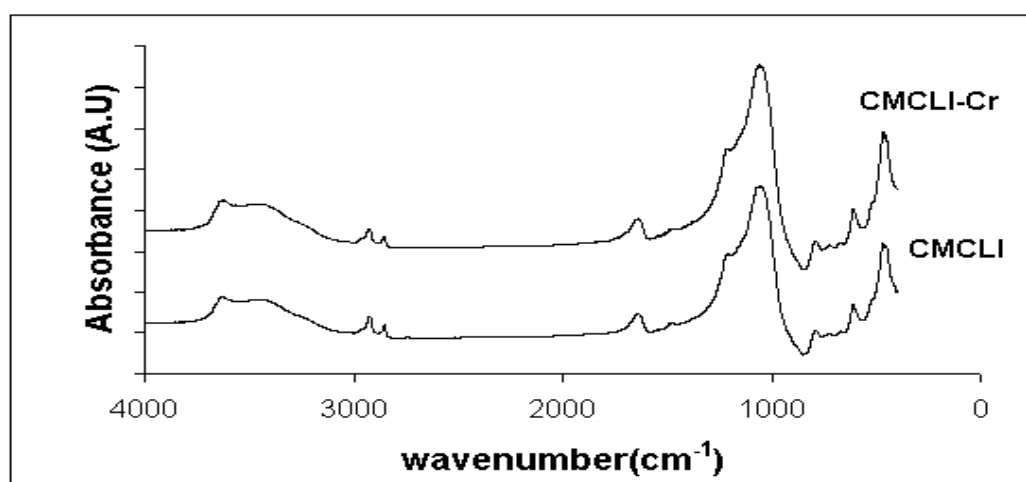


Figure 7.60. FTIR results of cationic modified clinoptilolite rich mineral after Cr (VI) sorption (CMCLI-Cr)

FTIR results of bacteria loaded clinoptilolite rich mineral after Cr (VI) sorption are given in Figure 7.61-7.65. After Cr (VI) sorption, no new band was found on the bacteria-clinoptilolite rich mineral samples. Only, the band shift in the water molecules on the bacteria loaded clinoptilolite rich mineral, which was an indication of existence of hydrogen bonding, was observed after Cr (VI) sorption. For example, the vibrations of water molecules on *E.Coli* loaded clinoptilolite rich mineral shifted from  $3655\text{ cm}^{-1}$  to  $3607\text{ cm}^{-1}$  and from  $1649\text{ cm}^{-1}$  to  $1622\text{ cm}^{-1}$  after Cr (VI) sorption. In the case of the sorption of Cr (VI) onto *B.Subtilis* loaded clinoptilolite rich mineral, the sorbed water molecules on *B.Subtilis* loaded clinoptilolite rich mineral shifted from  $3647\text{ cm}^{-1}$  to  $3639\text{ cm}^{-1}$  and from  $1654\text{ cm}^{-1}$  to  $1639\text{ cm}^{-1}$ . Similar shift was observed for sorbed water molecules on bacteria loaded clinoptilolite rich mineral after Cr (VI) sorption. The results revealed that hydrogen bonding was significant mechanism in Cr (VI) sorption with bacteria loaded clinoptilolite rich mineral.

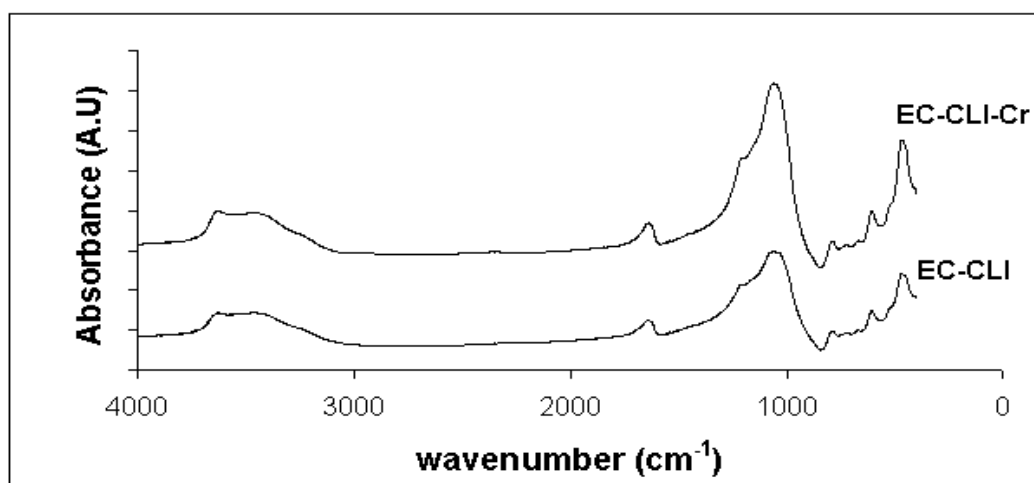


Figure 7.61. FTIR results of EC-CLI after Cr (VI) sorption (EC-CLI-Cr)

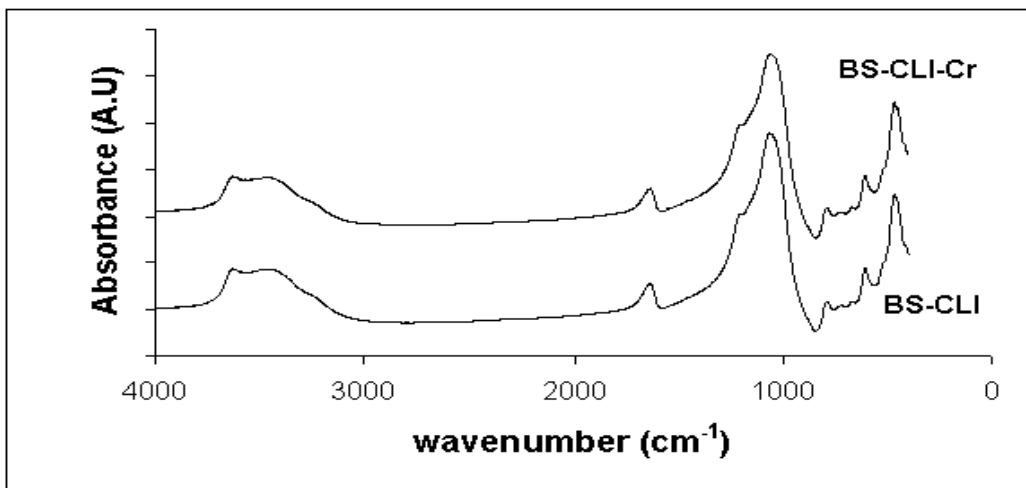


Figure 7.62. FTIR results of BS-CLI after Cr (VI) sorption (BS-CLI-Cr)

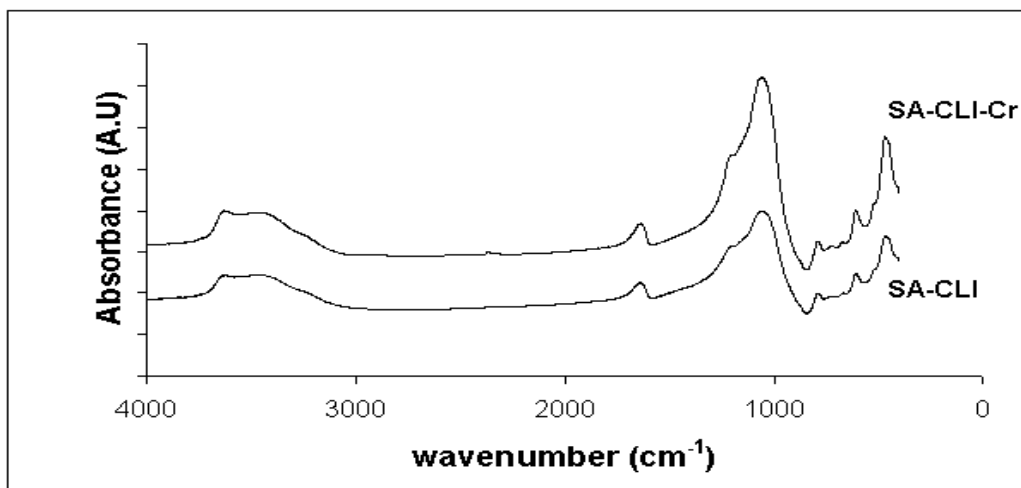


Figure 7.63. FTIR results of SA-CLI after Cr (VI) sorption (SA-CLI-Cr)

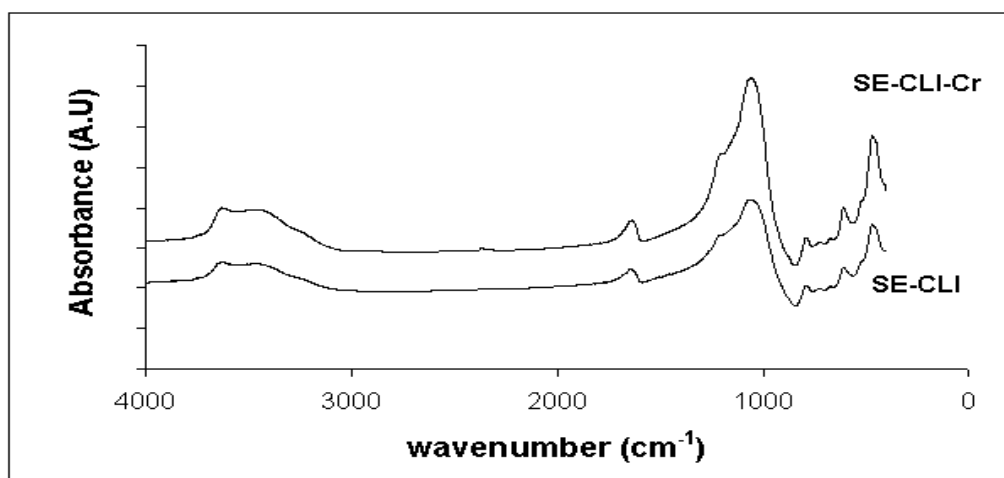


Figure 7.64. FTIR results of SE-CLI after Cr (VI) sorption (SE-CLI-Cr)

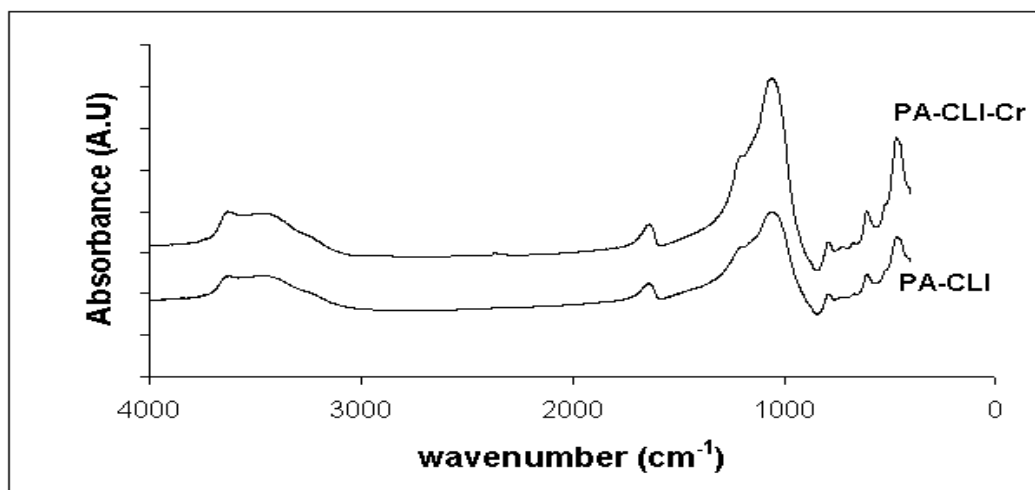


Figure 7.65. FTIR results of PA-CLI after Cr (VI) sorption (PA-CLI-Cr)

FTIR results of bacteria loaded anionic surfactant modified clinoptilolite rich mineral after Cr (VI) sorption are given in Figure 7.66-7.70. After Cr (VI) sorption, band disappearance and shift was observed in FTIR results of bacteria loaded surfactant anionic modified clinoptilolite rich mineral samples. Band disappearance in methylene groups and bands shift in water molecules on the bacteria loaded anionic surfactant modified clinoptilolite rich mineral pointed out the existence of hydrogen bonding. The results revealed that non electrostatic forces (hydrogen bonding) played a significant role in Cr (VI) sorption with bacteria loaded anionic surfactant modified clinoptilolite rich mineral.

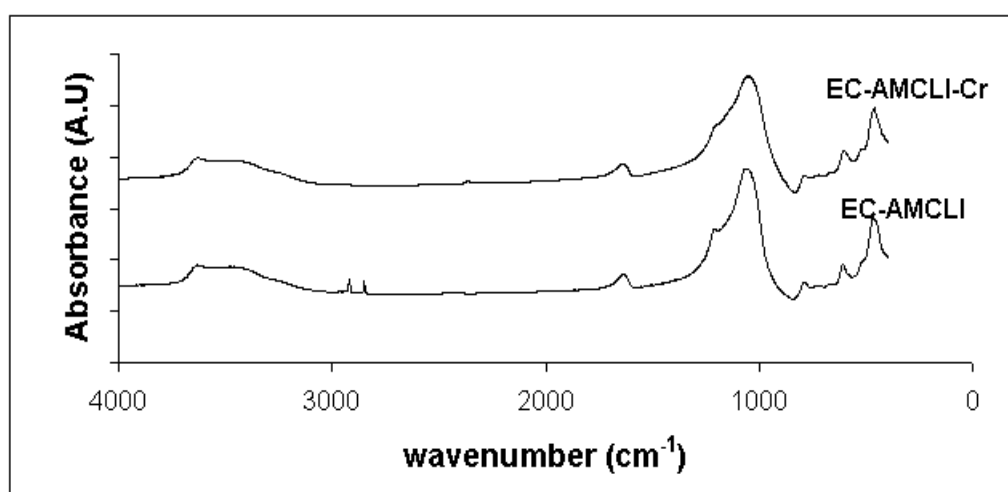


Figure 7.66. FTIR results of EC-AMCLI after Cr (VI) sorption (EC-AMCLI-Cr)

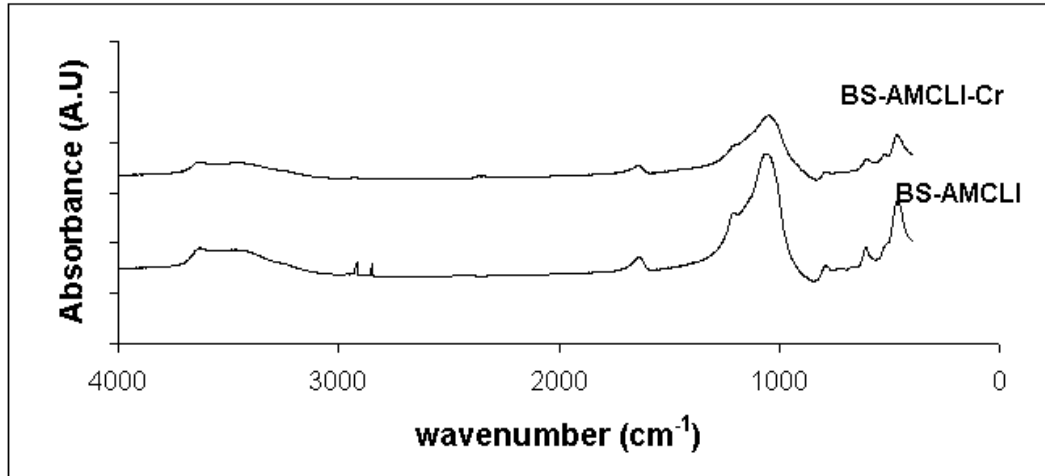


Figure 7.67. FTIR results of BS-AMCLI after Cr (VI) sorption (BS-AMCLI-Cr)

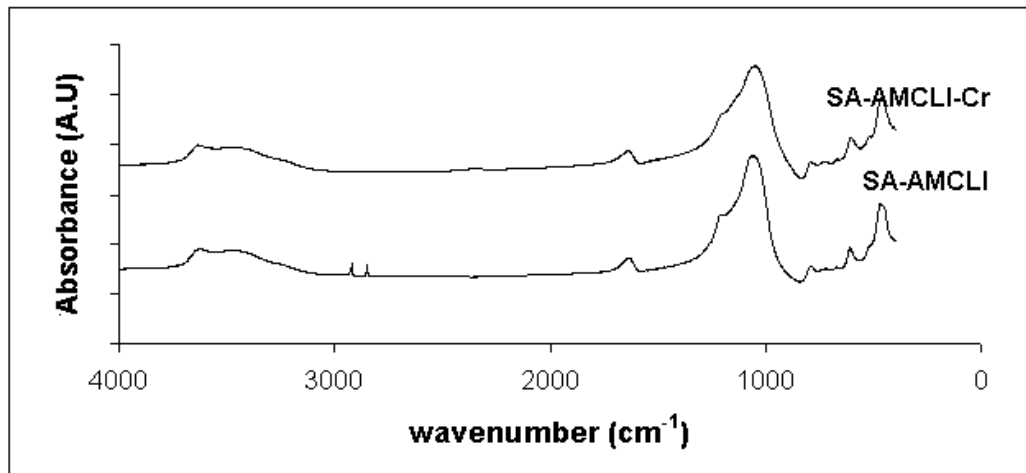


Figure 7.68. FTIR results of SA-AMCLI after Cr (VI) sorption (SA-AMCLI-Cr)

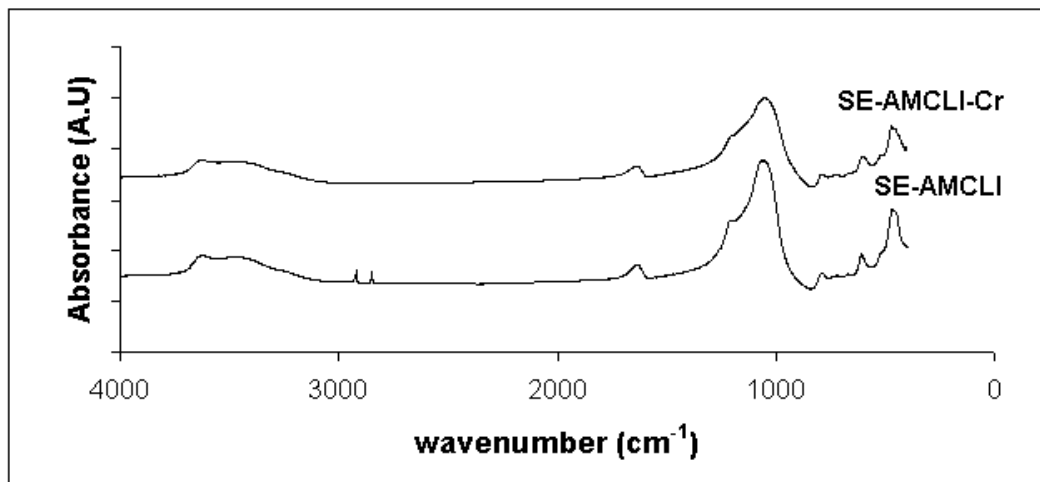


Figure 7.69. FTIR results of SE-AMCLI after Cr (VI) sorption (SE-AMCLI-Cr)



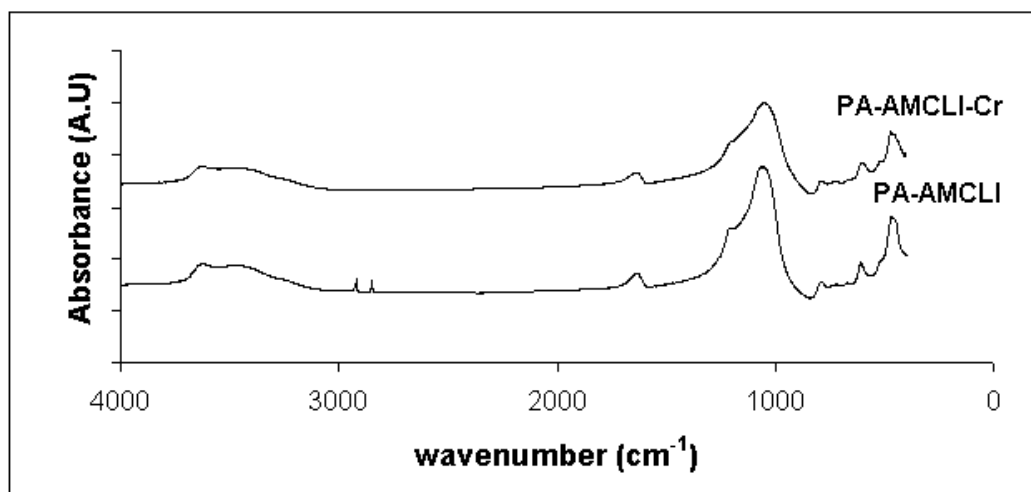


Figure 7.70. FTIR results of PA-AMCLI after Cr (VI) sorption (PA-AMCLI-Cr)

Figure 7.71-7.75 show FTIR results of bacteria loaded cationic surfactant modified clinoptilolite rich mineral after Cr (VI) sorption. The band shift in the water molecules and band disappearance in methylene group on the bacteria loaded cationic surfactant modified clinoptilolite rich mineral, which was an indication of existence of hydrogen bonding, was observed after Cr (VI) sorption. In addition to hydrogen bonding, attractive electrostatic forces were responsible in Cr (VI) sorption with bacteria loaded cationic surfactant modified clinoptilolite rich mineral. The highest Cr (VI) sorption results with bacteria loaded cationic surfactant modified clinoptilolite rich mineral was attributed to the summation of electrostatic and non electrostatic forces which enhanced the interaction between Cr (VI) species and bacteria loaded cationic surfactant modified clinoptilolite rich mineral samples.

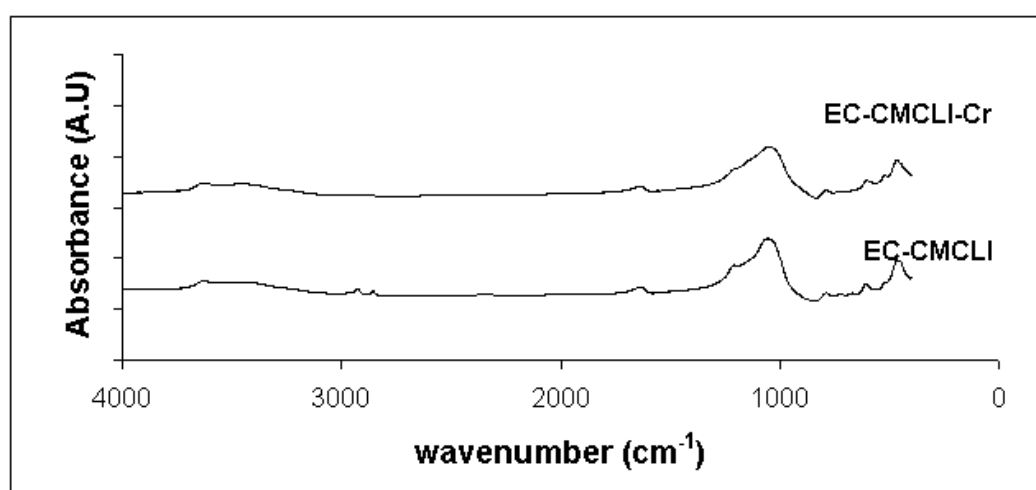


Figure 7.71. FTIR results of EC-CMCLI after Cr (VI) sorption (EC-CMCLI-Cr)

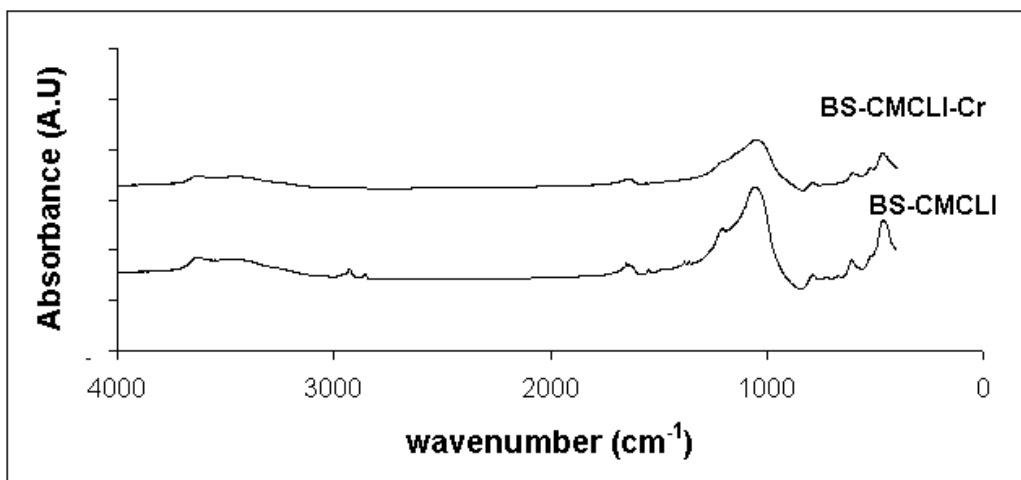


Figure 7.72. FTIR results of BS-CMCLI after Cr (VI) sorption (BS-CMCLI-Cr)

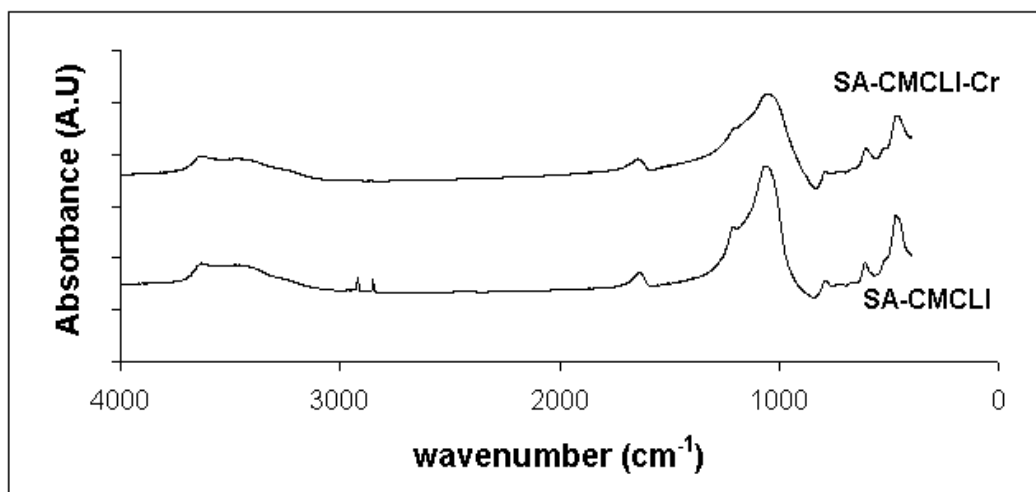


Figure 7.73. FTIR results of SA-CMCLI after Cr (VI) sorption (SA-CMCLI-Cr)

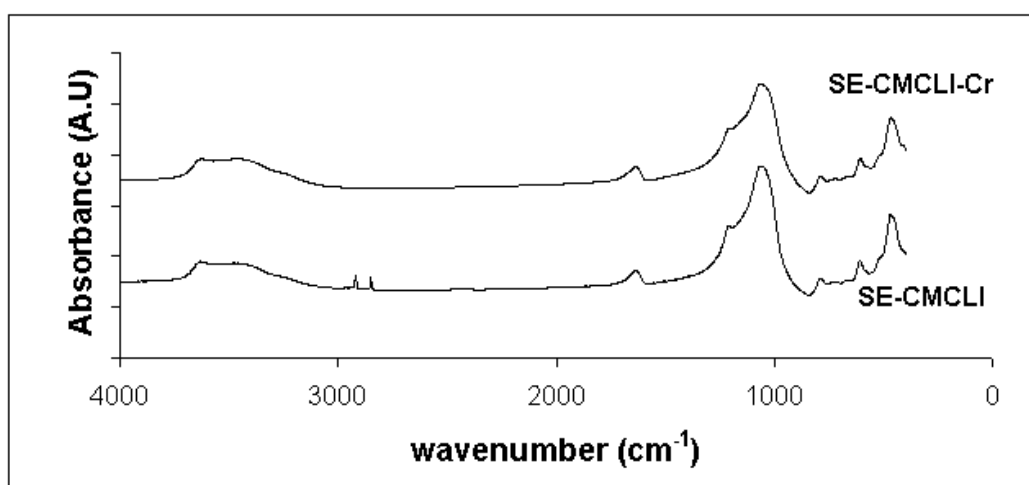


Figure 7.74. FTIR results of SE-CMCLI after Cr (VI) sorption (SE-CMCLI-Cr)

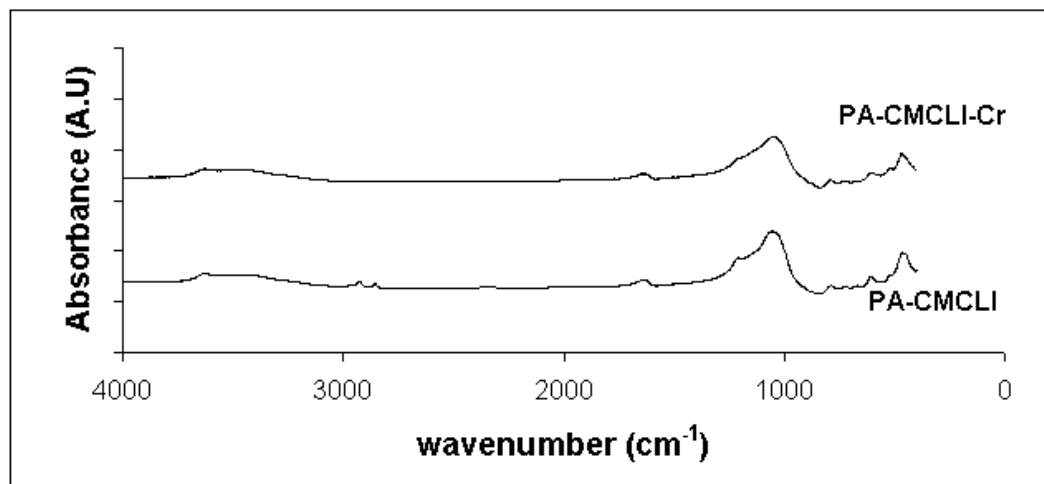


Figure 7.75. FTIR results of PA-CMCLI after Cr (VI) sorption (PA-CMCLI-Cr)

## 7.4. Effects of Experimental Parameters on Cr (VI) Sorption

There are several factors affecting sorption of metals such as pH, initial concentration, agitation speed, temperature and particle size. These effects are important to understand the mechanism of the sorption process. In this part, effects of the parameters on the sorption of Cr(VI) onto clinoptilolite rich mineral, surfactant modified clinoptilolite rich mineral, bacteria loaded clinoptilolite rich mineral and surfactant modified clinoptilolite rich mineral were investigated and their results were discussed.

### 7.4.1. Effect of pH on Cr (VI) Sorption

pH of the solution affects the form of metal ions and also surface charge of the sorbents. The forms of metal ions exist in the solution either cationic or anionic forms depending on the pH of the solution. Both cationic and anionic forms show different sorption behavior in the same pH range. As a result, it is necessary to determine form of metal ions to explain sorption mechanism between sorbents and metal.

In the previous studies, pH results of the sorbents in Cr (VI) solution were reported as 5.1 to 6.5. At this pH range,  $\text{HCrO}_4^-$  and  $\text{CrO}_4^{2-}$  forms of Cr (VI) species exist in the solution. Most of the sorbents interacted with both Cr (VI) species and thus competition could happen during the sorption process between two Cr (VI) species. Because of this competition, it was difficult to decide which Cr (VI) form was dominant

during the sorption. In order to differentiate Cr (VI) forms, it was necessary to carry out the experiments at adjusted pH values. The pH values were selected as 3 and 11. Cr (VI) was mainly found as  $\text{HCrO}_4^-$  (99.6 %) at pH=3 whereas at pH 11 it was predominantly formed as  $\text{CrO}_4^{2-}$  (99.99 %).

In order to understand electrostatic interactions between Cr (VI) species and the sorbents at these pH values, the zeta potentials of the sorbents were measured and their values are tabulated in Table 7.12. The results demonstrated that there were repulsive and attractive electrostatic forces between Cr (VI) species and the sorbents.

Table 7.12. Zeta potential values of sorbents in Cr (VI) solution at pH 3 and 11

	<b>pH 3</b>	<b>pH 11</b>
<b>Samples</b>	<b>Zeta Potential (mV)</b>	<b>Zeta Potential (mV)</b>
<b>CLI</b>	-22.4	-42.9
<b>AMCLI</b>	-32.6	-49.1
<b>CMCLI</b>	44.3	-27.5
<b>EC-CLI</b>	17.9	-40.4
<b>BS-CLI</b>	14.9	-40.8
<b>SE-CLI</b>	-11.7	-39.2
<b>SA-CLI</b>	-12.2	-38.6
<b>PA-CLI</b>	-12.4	-40.6
<b>EC-AMCLI</b>	12.4	-42.4
<b>BS-AMCLI</b>	15.1	-41.2
<b>SE-AMCLI</b>	-10.4	-40.2
<b>SA-AMCLI</b>	-11.6	-42.5
<b>PA-AMCLI</b>	-14.3	-47.5
<b>EC-CMCLI</b>	33.7	-44.4
<b>BS-CMCLI</b>	34	-36.3
<b>SE-CMCLI</b>	28.5	-32.5
<b>SA-CMCLI</b>	24.3	-32.8
<b>PA-CMCLI</b>	22.7	-39.4

The sorption kinetic curves of Cr (VI) at pH 3 and 11 for clinoptilolite rich mineral are shown in Figure 7.76 and 7.77. At equilibrium, the sorbed amounts of Cr (VI) values at pH 3 and 11 were found as 0.43 and 0.38 mg/g, respectively. When Cr (VI) sorption values of clinoptilolite rich mineral at pH 3 and 11 were compared with values without any pH adjustment, lower Cr (VI) sorption results were observed at pH 3 and 11. Lower Cr (VI) sorption values at pH 3 were explained by the competition between  $\text{HCrO}_4^-$  and  $\text{NO}_3^-$  which was introduced in the form of nitric acid to maintain the pH of the solution at 3 (Bhattacharya and Gupta, 2006). Lower sorption values at

pH 11 were resulted from the formation of hydroxyl complexes of chromium ion which hindered the diffusion of Cr (VI) into the clinoptilolite rich mineral surface (Bhattacharyya and Gupta, 2006). Zeta potential results implied that clinoptilolite rich mineral was negatively charged at pH 3 and 11 and thus there were repulsive electrostatic forces between Cr (VI) species and clinoptilolite rich mineral. Although there were repulsive electrostatic forces, the existence of Cr (VI) sorption indicates a significant role of the non electrostatic forces in Cr (VI) sorption with clinoptilolite rich mineral at pH 3 and 11.

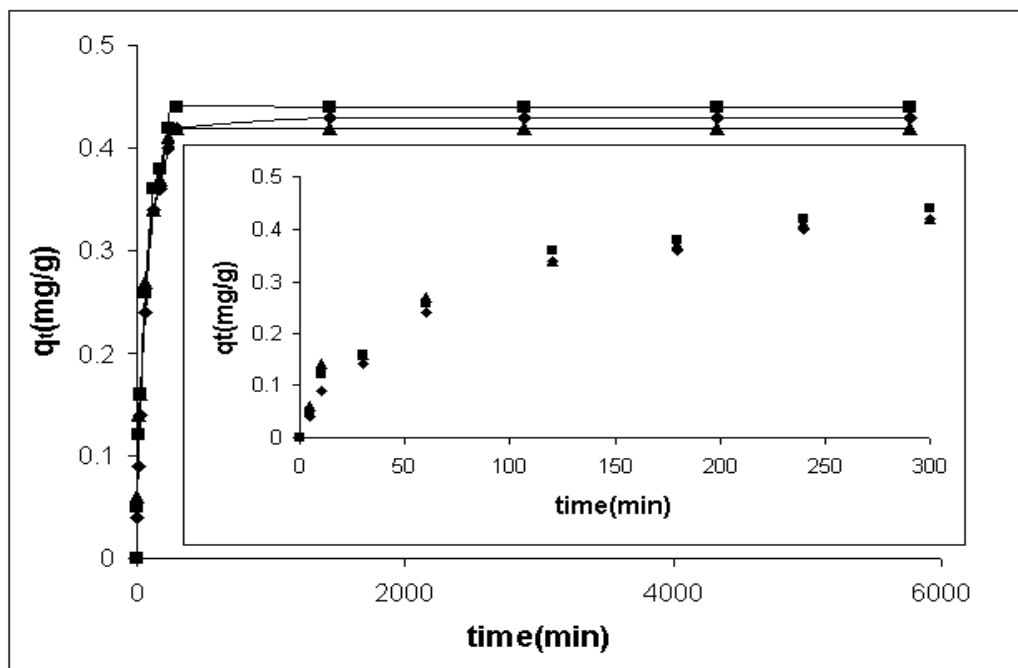


Figure 7.76. Sorption kinetic curve of Cr (VI) at pH 3 for CLI (Conditions: 10 mg/L, 25 °C, 140 rpm, 25–106  $\mu$ m)

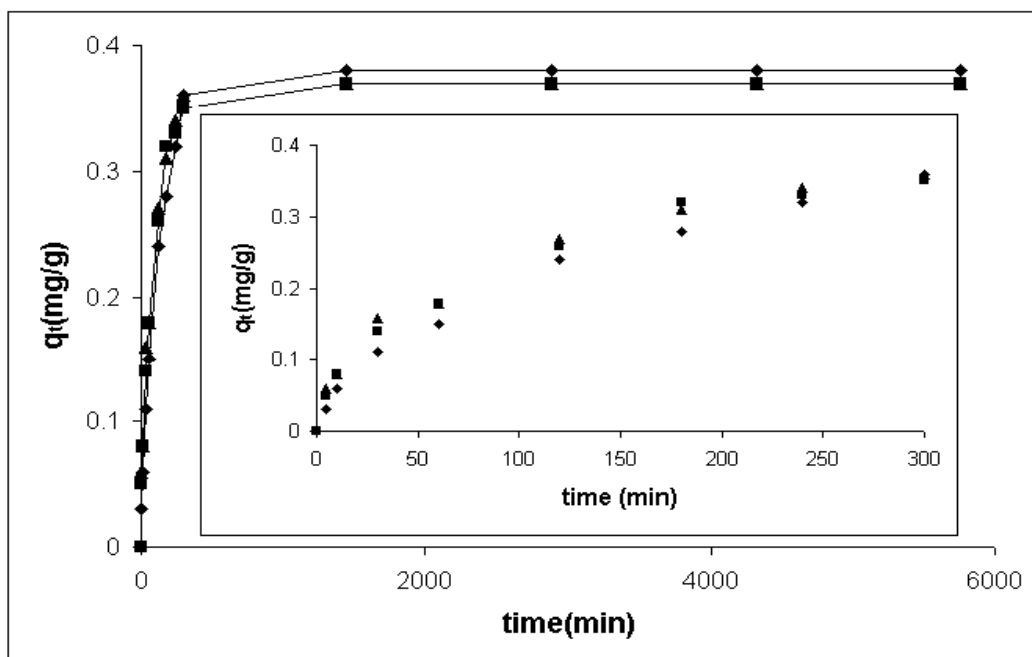


Figure 7.77. Sorption kinetic curve of Cr (VI) at pH 11 for CLI (Conditions: 10 mg/L, 25 °C, 140 rpm, 25–106  $\mu\text{m}$ )

The sorption kinetic curves of Cr (VI) at pH 3 and 11 for anionic surfactant modified clinoptilolite rich mineral are given in Figure 7.78 and 7.79. At equilibrium, the sorbed amounts of Cr (VI) values at pH 3 and 11 were found as 0.47 and 0.41 mg/g, respectively. The results indicated that Cr (VI) sorption with anionic surfactant modified clinoptilolite rich mineral showed similar trend with Cr (VI) sorption with clinoptilolite rich mineral. Zeta potential results showed that anionic surfactant modified clinoptilolite rich mineral like clinoptilolite rich mineral exhibited negative surface charges at pH 3 and 11. The reasons for lower Cr (VI) sorption values at pH 3 and 11 that were discussed above were valid since anionic surfactant modified clinoptilolite rich mineral and clinoptilolite rich mineral had similar surface charge properties. The results also indicated that there were repulsive forces between Cr (VI) species and negatively charged anionic surfactant modified clinoptilolite rich mineral. Cr (VI) sorption with anionic surfactant modified clinoptilolite rich mineral was observed at these pH values indicating the existence of non electrostatic forces.

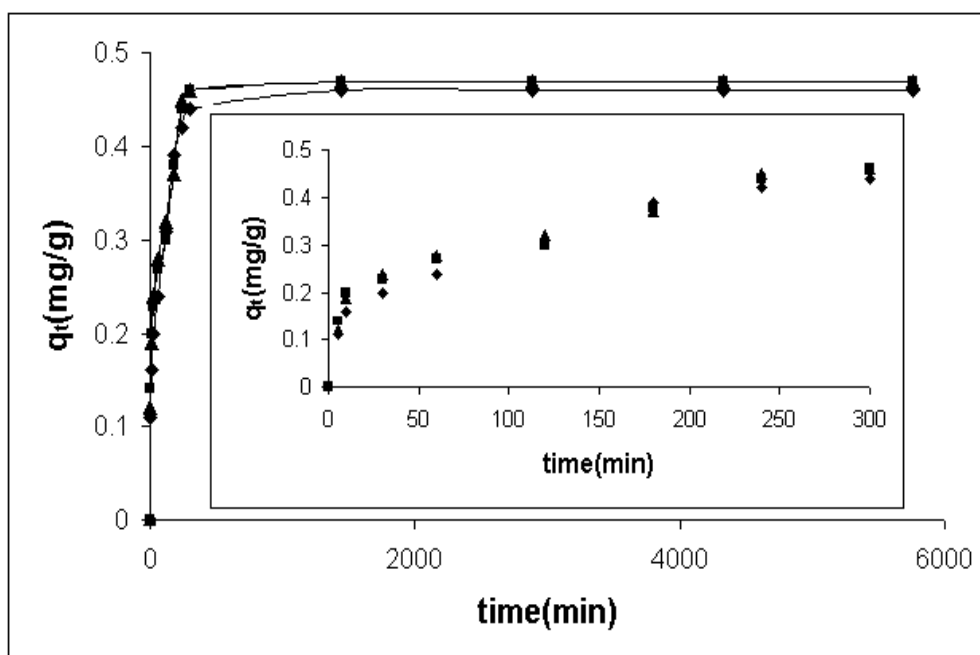


Figure 7.78. Sorption kinetic curve of Cr(VI) at pH 3 for AMCLI (Conditions: 10 mg/L, 25 °C, 140 rpm, 25–106  $\mu\text{m}$ )

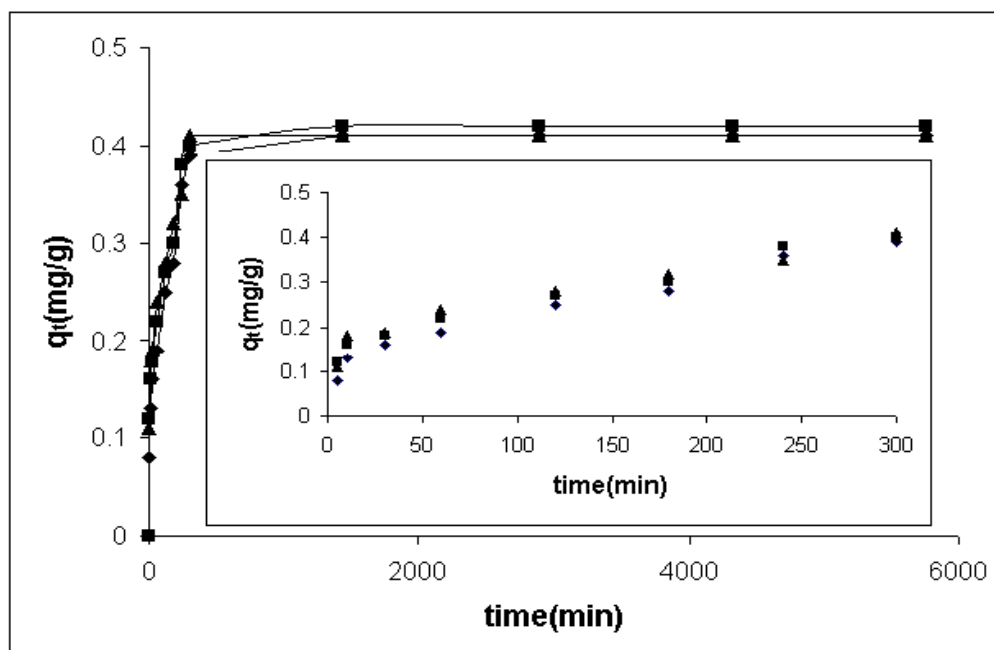


Figure 7.79. Sorption kinetic curve of Cr(VI) at pH 11 for AMCLI (Conditions: 10 mg/L, 25 °C, 140 rpm, 25–106  $\mu\text{m}$ )

Figure 7.80 and 7.81 show sorption kinetic curves of Cr(VI) at pH 3 and 11 for cationic surfactant modified clinoptilolite rich mineral. At equilibrium, the sorbed amounts of Cr(VI) values at pH 3 and 11 were determined as 0.87 and 0.49 mg/g, respectively. The results showed that higher Cr(VI) sorption values were observed at

pH 3 and Cr (VI) sorption values were decreased by increasing pH up to 11. When Cr (VI) sorption values of cationic surfactant modified clinoptilolite rich mineral at pH 3 were compared with values without any pH adjustment, lower Cr (VI) sorption results were observed without any pH adjustment. The reason for lower Cr (VI) sorption was explained by the existence of Cr (VI) species. Cr (VI) was mainly found as  $\text{HCrO}_4^-$  at pH 3 and thus the cationic surfactant modified clinoptilolite rich mineral only interacted with  $\text{HCrO}_4^-$ . On the other hand, both  $\text{HCrO}_4^-$  and  $\text{CrO}_4^{2-}$  forms of Cr (VI) species could exist in the solution and therefore the cationic surfactant modified clinoptilolite rich mineral interacted with both  $\text{HCrO}_4^-$  and  $\text{CrO}_4^{2-}$ . Because of existing two Cr (VI) species, the competition could happen during Cr (VI) sorption. As a result, lower Cr (VI) sorption was observed. Zeta potential results showed that cationic surfactant modified clinoptilolite rich mineral was positively charged at pH 3 while it was negatively charged at pH 11. Therefore, there were attractive and repulsive electrostatic forces between Cr (VI) species and cationic surfactant modified clinoptilolite rich mineral at pH 3 and 11. The results revealed that attractive electrostatic forces were significant mechanism in Cr (VI) sorption with cationic surfactant modified clinoptilolite rich mineral at pH 3 whereas non electrostatic forces were responsible for Cr (VI) sorption with cationic surfactant modified clinoptilolite rich mineral at pH 11.

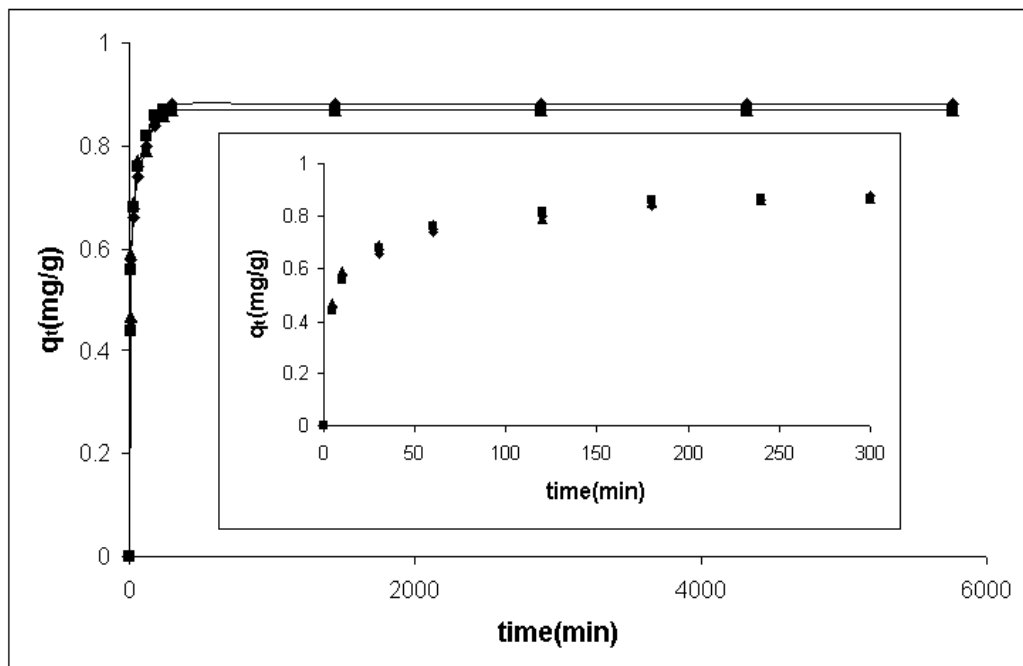


Figure 7.80. Sorption kinetic curve of Cr (VI) at pH 3 for CMCLI (Conditions: 10 mg/L, 25 °C, 140 rpm, 25–106  $\mu\text{m}$ )



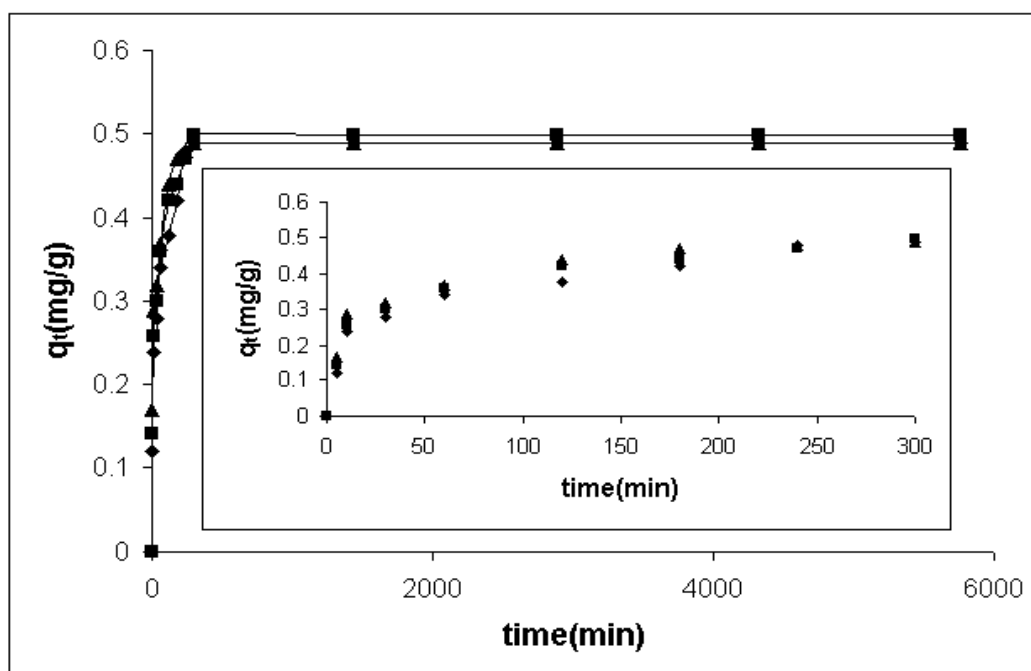


Figure 7.81. Sorption kinetic curve of Cr (VI) at pH 11 for CMCLI (Conditions: 10 mg/L, 25 °C, 140 rpm, 25–106  $\mu\text{m}$ )

Previous bacteria loaded clinoptilolite rich mineral results indicated that gram negative bacteria *E. coli* and gram positive bacteria *B. subtilis* loaded samples showed higher Cr (VI) sorption values. Zeta potential results showed that the surfaces of *E. coli* and *B. subtilis* loaded clinoptilolite rich mineral samples were positively charged whereas the surfaces of *S. aureus*, *S. epidermidis* and *P. aeruginosa* loaded clinoptilolite rich mineral samples were negatively charged at pH 3. In the selection of bacteria, their Cr (VI) sorption affinities and their surface charges was taken into account. *S. aureus*, *S. epidermidis* and *P. aeruginosa* loaded clinoptilolite rich mineral was eliminated since their Cr (VI) sorption values were lower than *E. coli* and *B. subtilis* loaded clinoptilolite. Moreover, they had negative surface charges at pH 3. Taking all the results into account that have discussed, *E. coli* and *B. subtilis* loaded clinoptilolite rich mineral was chosen.

The sorption kinetic curves of Cr (VI) at pH 3 and 11 for *E. coli* and *B. subtilis* loaded clinoptilolite rich mineral are shown in Figure 7.82-7.85. At equilibrium, the sorbed amounts of Cr (VI) values for *E. coli* and *B. subtilis* loaded clinoptilolite rich mineral at pH 3 and 11 were found as 0.74, 0.82, 0.41 and 0.42 mg/g, respectively. Zeta potential results showed that *E. coli* and *B. subtilis* loaded clinoptilolite rich mineral samples were positively charged at pH 3 while their surface charges were negative at pH 11. Therefore, there were attractive and repulsive electrostatic forces between Cr

(VI) species and bacteria loaded clinoptilolite rich mineral at pH 3 and 11. The results indicated that higher Cr (VI) sorption values were observed at pH 3 whereas Cr (VI) sorption values decreased with increasing pH up to 11. When Cr (VI) sorption values of *E. coli* and *B. subtilis* loaded clinoptilolite rich mineral at pH 3 were compared with values without any pH adjustment, lower Cr (VI) sorption results were observed without any pH adjustment. Lower Cr (VI) sorption values were resulted from the competition between  $\text{HCrO}_4^-$  and  $\text{CrO}_4^{2-}$  species of Cr (VI) and repulsive electrostatic forces between Cr (VI) species and *E. coli* and *B. subtilis* loaded clinoptilolite rich mineral. The reason for higher Cr (VI) sorption with *E. coli* and *B. subtilis* loaded clinoptilolite rich mineral at pH 3 was due to the existence of attractive electrostatic forces between  $\text{HCrO}_4^-$  and bacteria loaded samples.

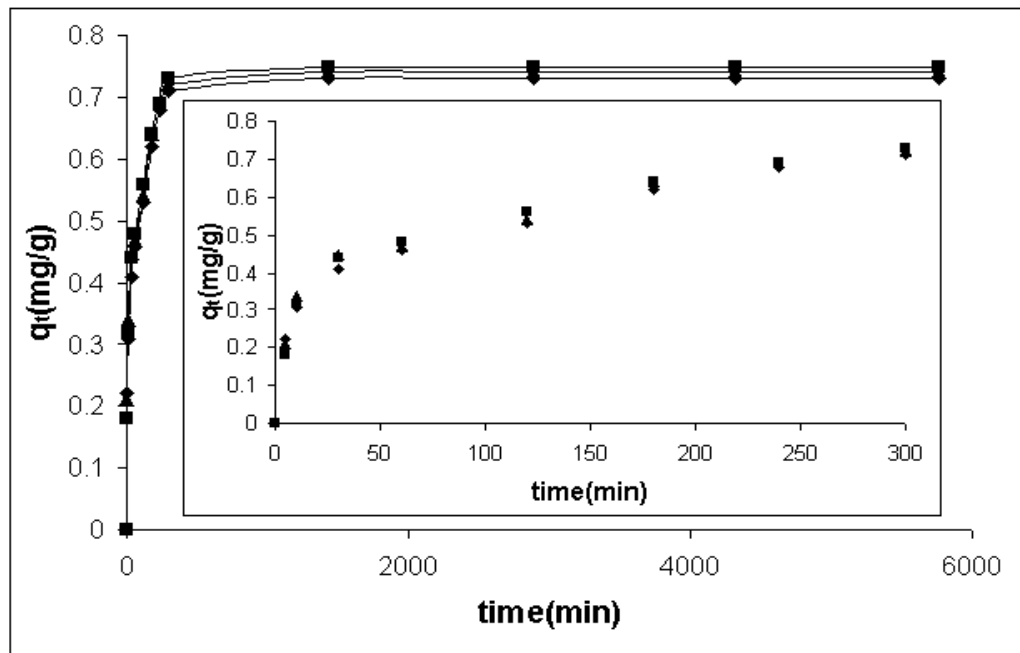


Figure 7.82. Sorption kinetic curve of Cr (VI) at pH 3 for EC-CLI (Conditions: 10 mg/L, 25 °C, 140 rpm, 25–106  $\mu\text{m}$ )

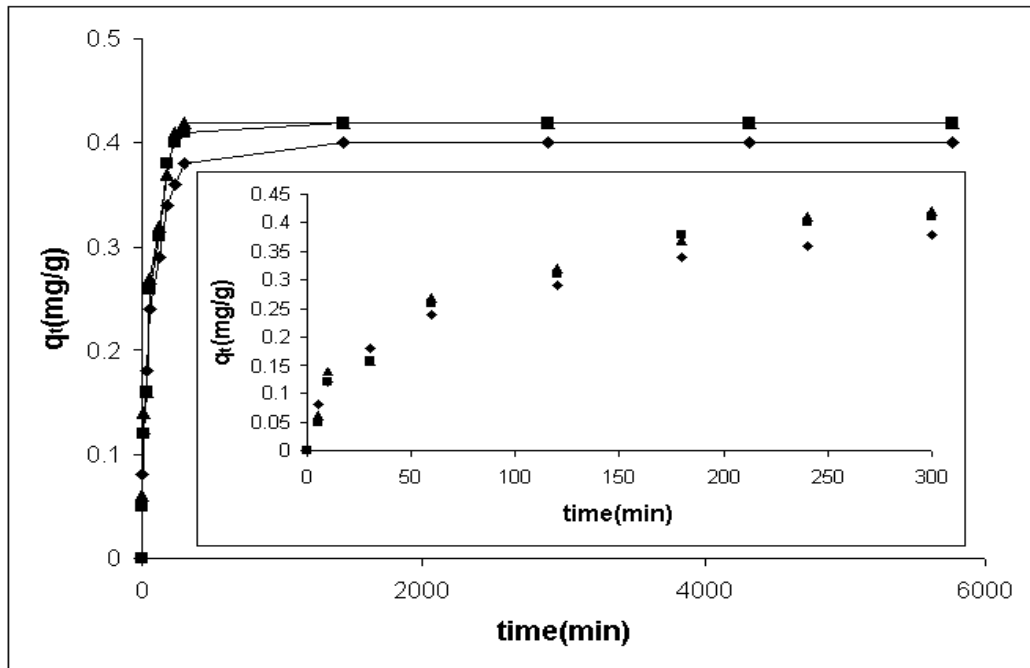


Figure 7.83. Sorption kinetic curve of Cr (VI) at pH 11 for EC-CLI (Conditions: 10 mg/L, 25 °C, 140 rpm, 25–106  $\mu\text{m}$ )

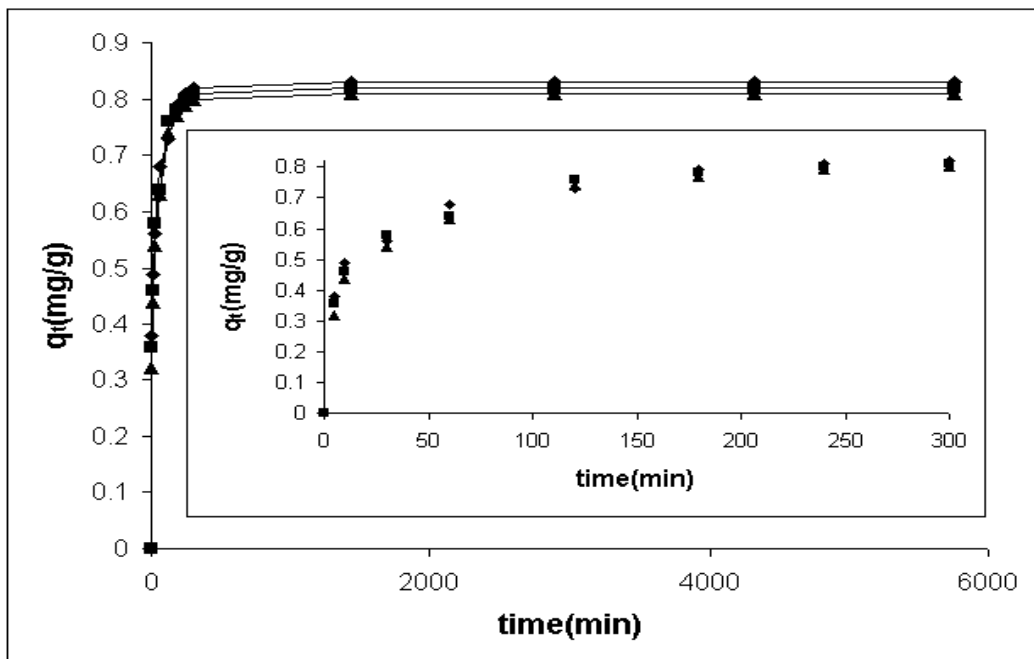


Figure 7.84. Sorption kinetic curve of Cr (VI) at pH 3 for BS-CLI (Conditions: 10 mg/L, 25 °C, 140 rpm, 25–106  $\mu\text{m}$ )

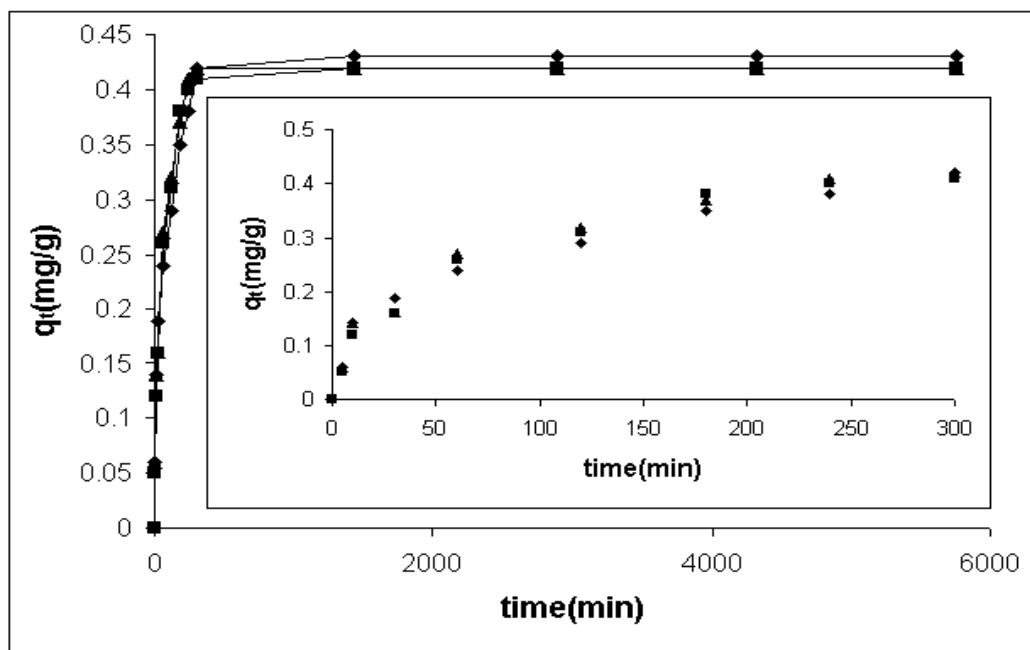


Figure 7.85. Sorption kinetic curve of Cr (VI) at pH 11 for BS-CLI (Conditions: 10 mg/L, 25 °C, 140 rpm, 25–106  $\mu\text{m}$ )

The previous results about bacteria loaded anionic surfactant modified clinoptilolite rich mineral indicated that Cr (VI) sorption with bacteria loaded anionic surfactant modified clinoptilolite rich mineral showed similar trend with Cr (VI) sorption with bacteria loaded clinoptilolite rich mineral. Because of similar trend, *E. coli* and *B. subtilis* loaded anionic modified clinoptilolite rich mineral were selected. The sorption kinetic curves of Cr (VI) at pH 3 and 11 for *E. coli* and *B. subtilis* loaded anionic surfactant modified clinoptilolite rich mineral are given in Figure 7.86-7.89. At equilibrium, the sorbed amounts of Cr (VI) values for *E. coli* loaded anionic surfactant modified clinoptilolite rich mineral at pH 3 and 11 were determined as 0.84 and 0.41 mg/g, respectively. At equilibrium, the sorbed amounts of Cr (VI) values for *B. subtilis* loaded anionic surfactant modified clinoptilolite rich mineral at pH 3 and 11 were found as 0.88 and 0.42 mg/g, respectively. The results indicated that higher Cr (VI) sorption values were observed at pH 3 whereas lower Cr (VI) sorption values were observed without pH adjustment and at pH 11. Since *E. coli* and *B. subtilis* loaded anionic surfactant modified clinoptilolite rich mineral had positive surface charges at pH 3, the attractive electrostatic forces between bacteria loaded anionic surfactant modified clinoptilolite rich mineral and Cr (VI) species played a significant role in Cr (VI) sorption. On the other hand, surfaces of the bacteria loaded samples were negatively

charged without pH adjustment and at pH 11; and thus repulsive electrostatic forces could exist between the sorbents and anionic Cr (VI) species.

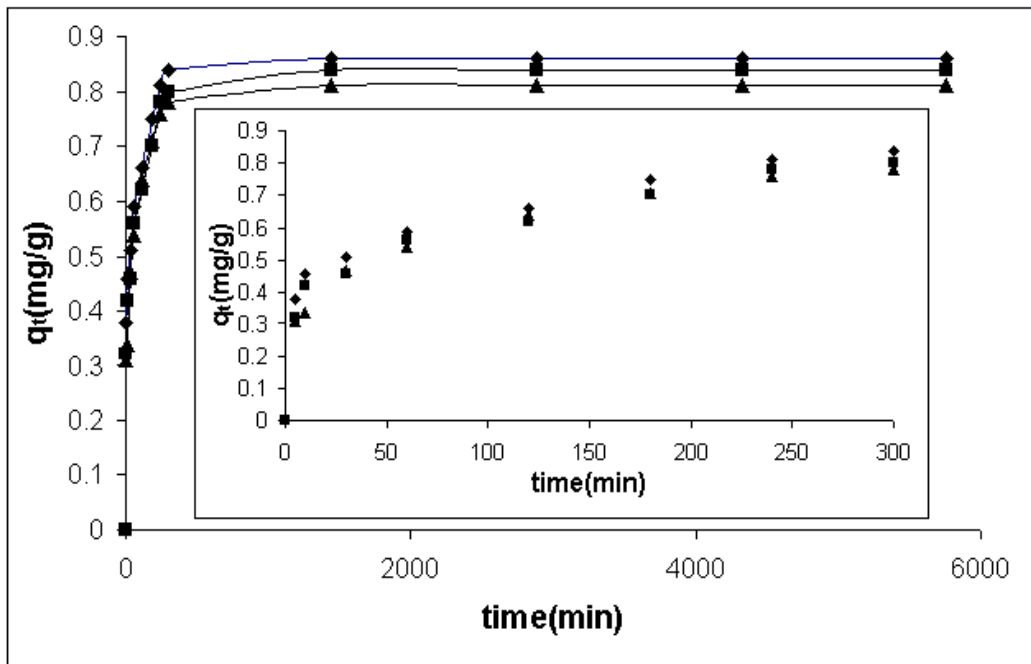


Figure 7.86. Sorption kinetic curve of Cr (VI) at pH 3 for EC-AMCLI (Conditions: 10 mg/L, 25 °C, 140 rpm, 25–106  $\mu$ m)

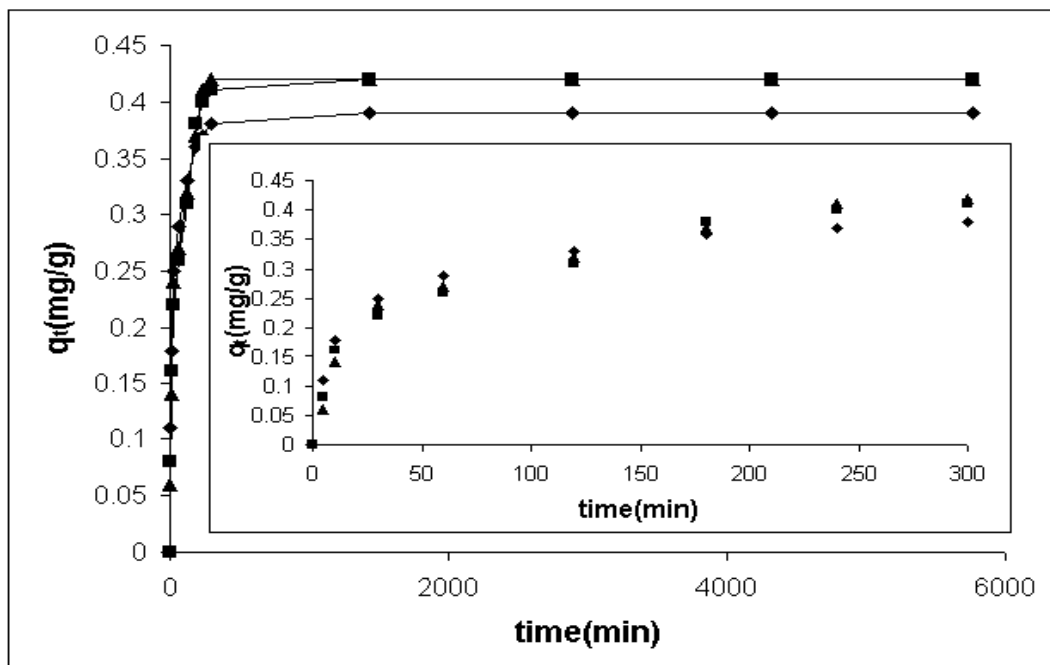


Figure 7.87. Sorption kinetic curve of Cr (VI) at pH 11 for EC-AMCLI (Conditions: 10 mg/L, 25 °C, 140 rpm, 25–106  $\mu$ m)

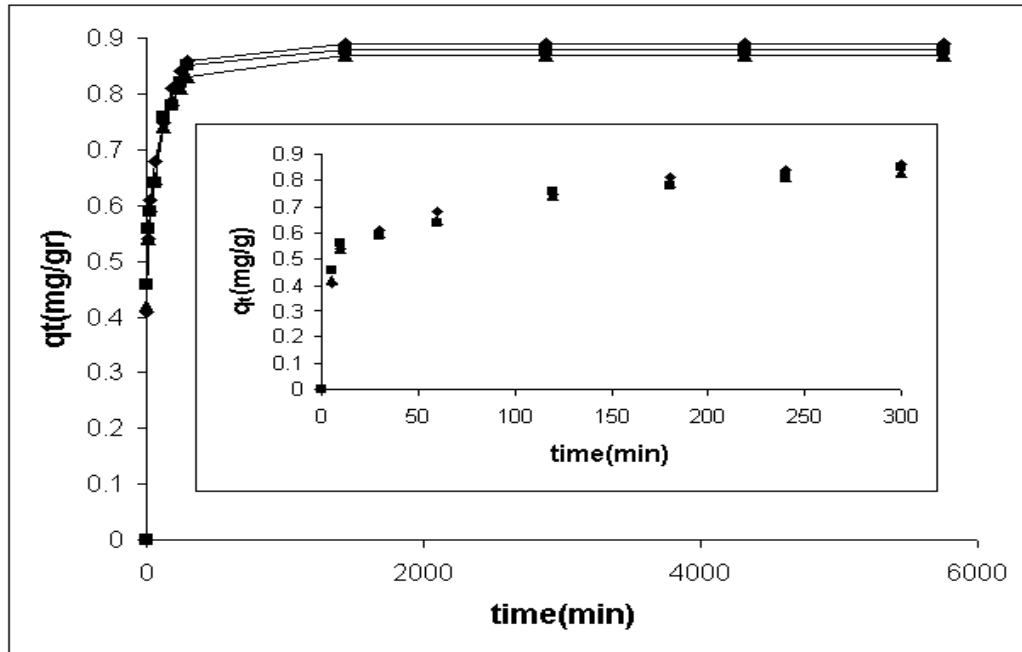


Figure 7.88. Sorption kinetic curve of Cr (VI) at pH 3 for BS-AMCLI (Conditions: 10 mg/L, 25 °C, 140 rpm, 25–106  $\mu\text{m}$ )

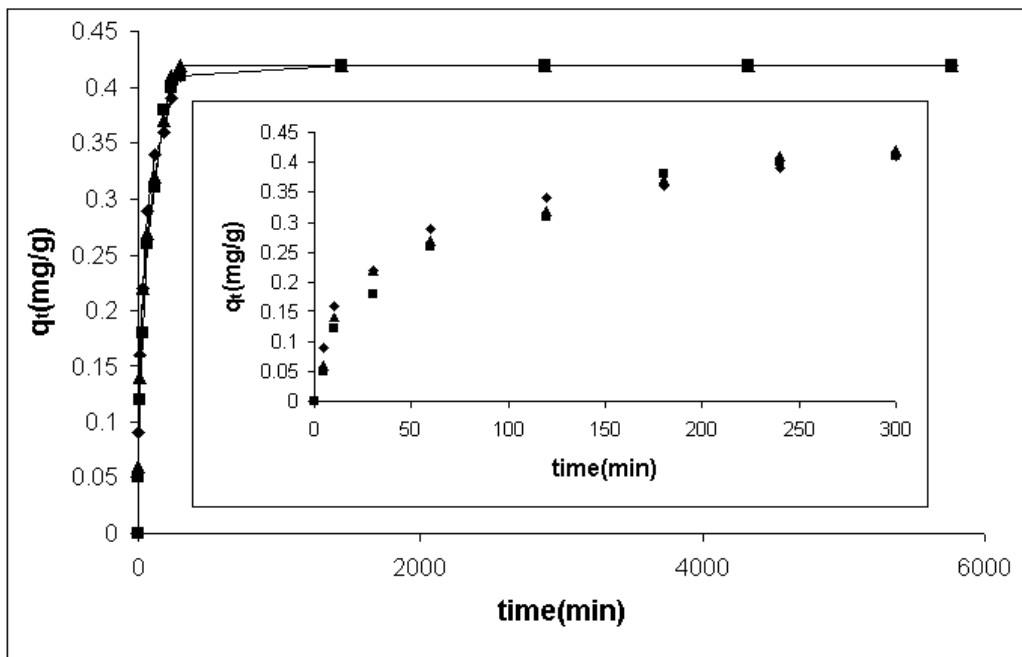


Figure 7.89. Sorption kinetic curve of Cr (VI) at pH 11 for BS-AMCLI (Conditions: 10 mg/L, 25 °C, 140 rpm, 25–106  $\mu\text{m}$ )

The previous results about bacteria loaded cationic surfactant modified clinoptilolite rich mineral indicated that higher Cr (VI) sorption values were observed with *E. coli* (gram negative) and *B. subtilis* (gram positive) loaded cationic surfactant modified clinoptilolite rich mineral samples. The sorption kinetic curves of Cr (VI) at

pH 3 and 11 for *E. coli* and *B. subtilis* loaded cationic surfactant modified clinoptilolite rich mineral are shown in Figure 7.90-7.93. At equilibrium, the sorbed amounts of Cr (VI) values for *E. coli* loaded cationic surfactant modified clinoptilolite rich mineral at pH 3 and 11 were found as 0.94 and 0.42 mg/g, respectively. At equilibrium, the amount of Cr (VI) sorbed values for *B. subtilis* loaded cationic surfactant modified clinoptilolite rich mineral at pH 3 and 11 were found as 0.98 and 0.44 mg/g, respectively. Higher Cr (VI) sorption values at pH 3 were resulted from the attractive forces between Cr (VI) species and bacteria loaded cationic surfactant modified clinoptilolite rich mineral samples. Lower Cr (VI) results were obtained at pH 11 and without pH adjustment. The decrease in Cr (VI) sorption values at pH 11 were resulted from repulsive force between bacteria loaded cationic surfactant modified clinoptilolite rich mineral and Cr (VI) species. Lower Cr (VI) sorption values without pH adjustment was observed due to the competition between  $\text{HCrO}_4^-$  and  $\text{CrO}_4^{2-}$  species of Cr (VI).

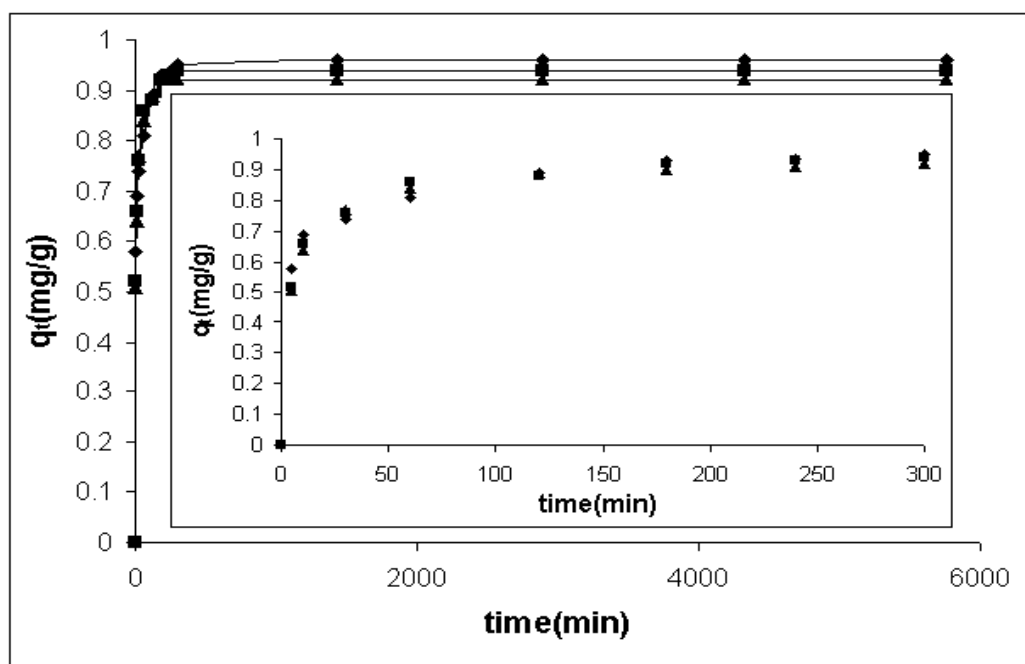


Figure 7.90. Sorption kinetic curve of Cr (VI) at pH 3 for EC-CMCLI (Conditions: 10 mg/L, 25 °C, 140 rpm, 25–106 μm)

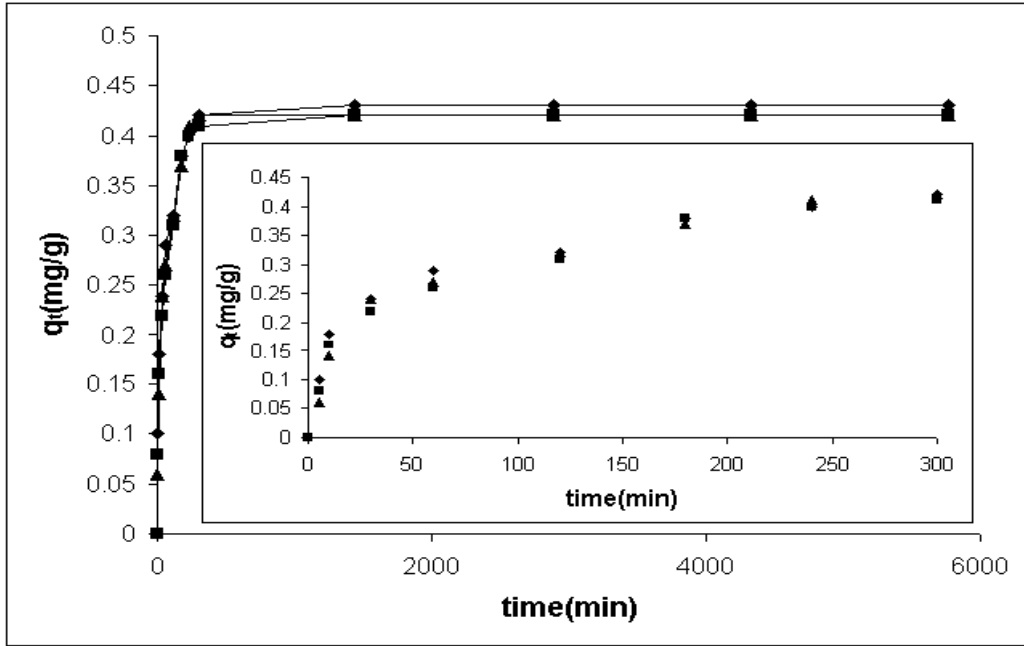


Figure 7.91. Sorption kinetic curve of Cr (VI) at pH 11 for EC-CMCLI (Conditions: 10 mg/L, 25 °C, 140 rpm, 25–106  $\mu$ m)

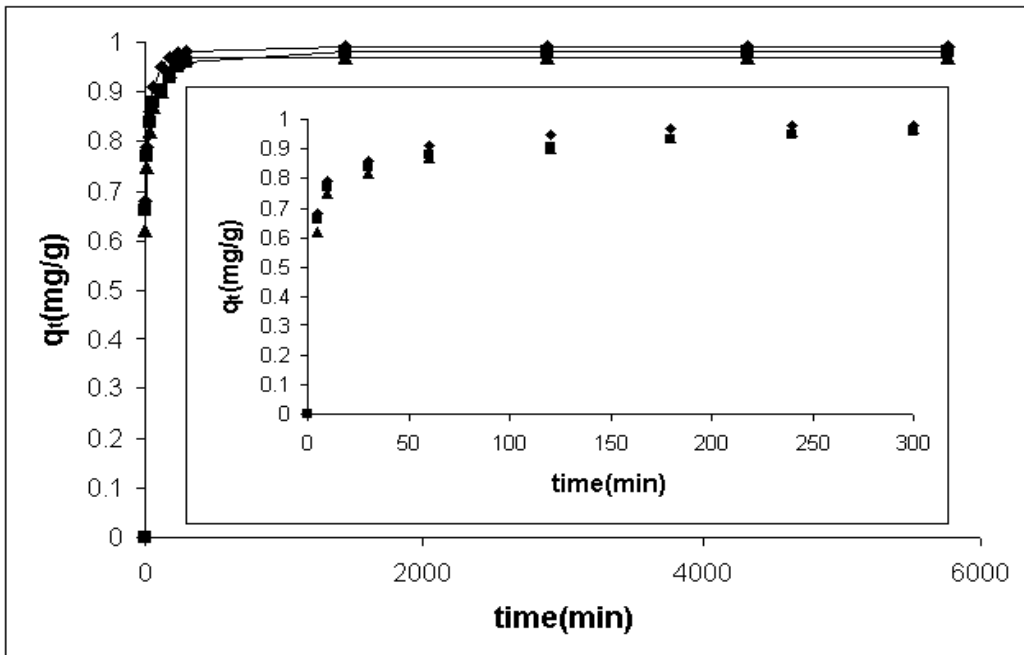


Figure 7.92. Sorption kinetic curve of Cr (VI) at pH 3 for BS-CMCLI (Conditions: 10 mg/L, 25 °C, 140 rpm, 25–106  $\mu$ m)



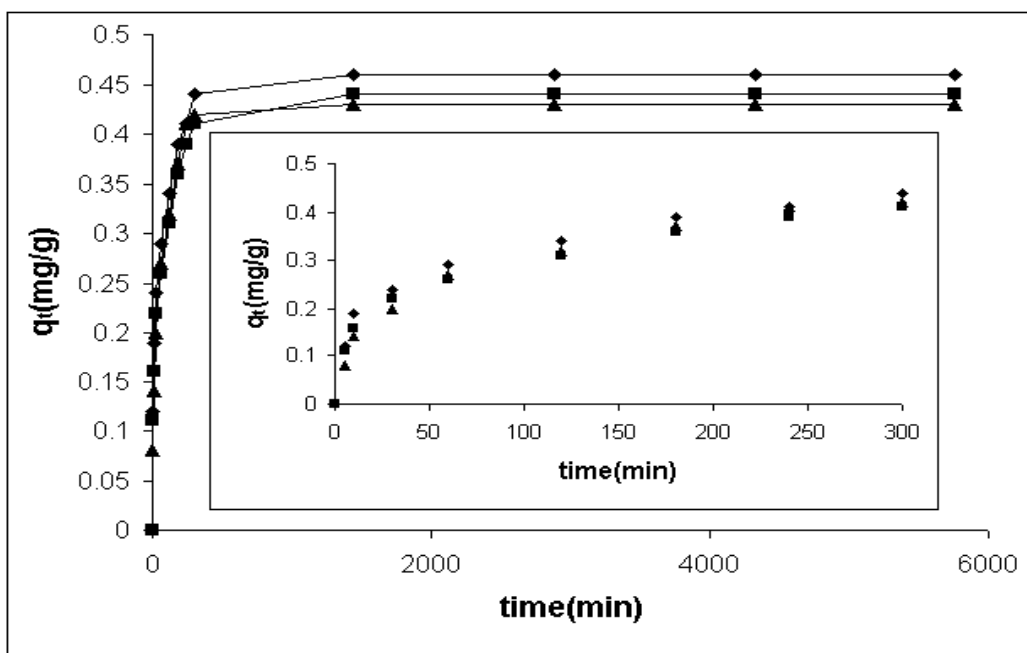


Figure 7.93. Sorption kinetic curve of Cr (VI) at pH 11 for BS-CMCLI (Conditions: 10 mg/L, 25 °C, 140 rpm, 25–106  $\mu\text{m}$ )

Cr (VI) removal percentage values of all sorbents at pH 3 and 11 are shown in Table 7.13. The results implied that higher Cr (VI) removal values were obtained at pH 3 whereas lower Cr (VI) removal values were observed at pH 11. The results also indicated that that Cr (VI) removal percentage value of clinoptilolite rich mineral increased after modification with cationic surfactant. As indicated in Table 7.13, Cr (VI) removal percentage value of the clinoptilolite rich mineral was increased after the attachment of bacteria to its surface. Similar results were obtained with bacteria loaded anionic and cationic surfactant modified clinoptilolite rich mineral. Bacteria on the clinoptilolite and surfactant modified clinoptilolite enhanced the interaction between Cr (VI) species and the sorbents and thus higher Cr (VI) removal was observed. Highest Cr (VI) removal results were observed with *E. coli* and *B. subtilis* loaded cationic surfactant modified zeolite at pH 3.

Table 7.13. Cr (VI) removal percentage values of all sorbents at pH 3 and 11

Sorbent	%Cr(VI) removal	
	pH 3	pH 11
CLI	43	38
AMCLI	47	41
CMCLI	88	49
EC-CLI	74	41
BS-CLI	83	42
EC-AMCLI	84	41
BS-AMCLI	89	42
EC-CMCLI	94	42
BS-CMCLI	98	44

#### 7.4.1.1. Characterization of Natural, Surfactant Modified and Bacteria Loaded Zeolites after Cr (VI) Sorption at pH 3 and 11

EDS of clinoptilolite rich mineral after Cr (VI) sorption at pH 3 and 11 are tabulated in Table 7.14. The results showed that clinoptilolite rich mineral without any pH adjustment had higher weight percent of chromium than clinoptilolite rich mineral at pH 3 and 11.

Table 7.14. EDS of clinoptilolite rich minerals after Cr (VI) sorption at pH 3 and 11.

Element %	CLI-Cr pH 3	CLI-Cr pH 11
C	0	0
O	47.9±0.7	47.9±0.7
Na	0.6±0.03	0.6±0.03
Mg	0.9±0.01	0.9±0.01
Al	7.5±0.04	7.5±0.04
Si	36.7±0.6	36.7±0.6
K	3.3±0.08	3.3±0.08
Ca	2.9±0.05	2.9±0.04
S	0	0
Cr	0.1±0.02	0.1±0.02
TOTAL	100	100

\*±Standard deviation values

EDS of anionic and cationic surfactant modified clinoptilolite rich mineral after Cr (VI) sorption at pH 3 and 11 are given in Table 7.15. The results indicated that anionic surfactant modified clinoptilolite rich mineral without any pH adjustment had higher weight percent of chromium than anionic surfactant modified clinoptilolite rich mineral at pH 3 and 11. The results also demonstrated that cationic surfactant modified clinoptilolite rich mineral at pH 3 had higher weight percent of chromium than cationic surfactant modified clinoptilolite rich mineral without any pH adjustment and at pH 11.

Table 7.15. EDS of anionic and cationic surfactant modified clinoptilolite rich mineral after Cr (VI) sorption at pH 3 and 11

Element %	AMCLI-Cr pH 3	AMCLI-Cr pH 11	CMCLI-Cr pH 3	CMCLI-Cr pH 11
C	7.9±0.2	7.9±0.2	14.6±0.1	14.6±0.1
O	41.3±0.22	41.3±0.2	35.2±0.14	35.6±0.04
Na	0.7±0.01	0.7±0.01	0.5±0.01	0.5±0.03
Mg	0.8±0.01	0.8±0.01	0.7±0.03	0.7±0.02
Al	7.4±0.04	7.4±0.03	7.2±0.03	7.2±0.06
Si	35.9±0.3	35.9±0.3	35.4±0.2	35.7±0.1
K	2.8±0.05	2.8±0.05	2.8±0.08	2.8±0.05
Ca	2.5±0.08	2.5±0.05	2.6±0.06	2.6±0.05
S	0.6±0.02	0.6±0.01	0	0
Cr	0.12±0.02	0.12±0.01	0.89±0.05	0.17±0.02
TOTAL	100	100	100	100

\*±Standard deviation values

EDS of *E. coli* and *B. subtilis* loaded clinoptilolite rich mineral after Cr (VI) sorption at pH 3 and 11 are represented in Table 7.16. As shown in Table 7.16, *E. coli* and *B. subtilis* loaded clinoptilolite rich mineral at pH 3 had the highest weight percent of chromium. Similar results were obtained with *E. coli* and *B. subtilis* loaded anionic and cationic modified clinoptilolite rich mineral and their results are shown in Table 7.17-7.18.

Table 7.16. EDS of *E. coli* and *B. subtilis* loaded clinoptilolite rich mineral after Cr (VI) sorption at pH 3 and 11

Element %	EC-CLI-Cr pH 3	BS-CLI-Cr pH 3	EC-CLI-Cr pH 11	BS-CLI-Cr pH 11
C	4.3±0.1	5.2±0.2	4.3±0.1	5.2±0.2
O	45.5±0.2	45.4±0.1	45.7±0.1	45.4±0.1
Na	0.6±0.1	0.6±0.2	0.6±0.1	0.7±0.2
Mg	0.9±0.1	0.9±0.2	0.9±0.1	0.9±0.2
Al	7.7±0.01	7.7±0.02	7.7±0.06	7.7±0.02
Si	34.7±0.2	33.6±0.2	34.6±0.08	33.6±0.3
K	3.0±0.01	3.1±0.09	3.0±0.01	3.1±0.1
Ca	2.7±0.02	2.7±0.1	2.7±0.02	2.7±0.2
S	0.3±0.08	0.4±0.06	0.3±0.1	0.4±0.05
Cr	0.26±0.02	0.32±0.08	0.20±0.04	0.22±0.1
TOTAL	100	100	100	100

\*±Standard deviation values

Table 7.17. EDS of *E. coli* and *B. subtilis* loaded anionic surfactant modified clinoptilolite rich mineral after Cr (VI) sorption at pH 3 and 11.

%	EC-AMCLI-Cr pH 3	BS-AMCLI-Cr pH 3	EC-AMCLI-Cr pH 11	BS-AMCLI-Cr pH 11
C	11.2±0.1	13.8±0.2	11.2±0.1	13.8±0.2
O	40.1±0.1	38.1±0.1	40.1±0.04	38.2±0.1
Na	0.6±0.3	0.6±0.1	0.6±0.6	0.7±0.08
Mg	0.7±0.2	0.6±0.1	0.7±0.1	0.7±0.1
Al	7.2±0.08	7.1±0.08	7.2±0.1	7.1±0.1
Si	34.2±0.2	34.0±0.2	34.6±0.1	34.0±0.2
K	2.4±0.2	2.2±0.2	2.4±0.02	2.2±0.2
Ca	2.2±0.3	2.1±0.1	2.2±0.1	2.1±0.1
S	0.9±0.1	0.9±0.2	0.9±0.1	0.9±0.2
Cr	0.46±0.09	0.54±0.06	0.22±0.04	0.3±0.22
	100	100	100	100

\*±Standard deviation values

Table 7.18. EDS of *E. coli* and *B. subtilis* loaded cationic surfactant modified clinoptilolite rich mineral after Cr (VI) sorption at pH 3 and 11

%	EC-CMCLI-Cr pH 3	BS-CMCLI-Cr pH 3	EC-CMCLI-Cr pH 11	BS-CMCLI-Cr pH 11
C	16.8±0.2	18.1±0.08	16.8±0.2	18.1±0.06
O	34.8±0.1	34.05±0.1	35.2±0.09	34.4±0.1
Na	0.5±0.2	0.4±0.1	0.4±0.1	0.4±0.1
Mg	0.7±0.1	0.6±0.08	0.7±0.06	0.7±0.06
Al	7.1±0.1	7.0±0.07	7.1±0.1	7.1±0.1
Si	34.2±0.3	34.1±0.2	34.4±0.2	34.2±0.2
K	2.4±0.3	2.2±0.2	2.4±0.3	2.2±0.2
Ca	2.1±0.2	2.1±0.2	2.1±0.2	2.2±0.2
S	0.4±0.3	0.43±0.2	0.4±0.3	0.43±0.2
Cr	0.98±0.2	1.1±0.2	0.4±0.2	0.4±0.2
	100	100	100	100

\*±Standard deviation values

XRD results of clinoptilolite rich mineral after Cr (VI) sorption at pH 3 and 11 are shown in Figure 7.94. After Cr (VI) sorption at pH 3 and 11, relative intensity of one characteristic peak which was observed at 30.05° was considerably reduced. Moreover, relative intensities of the other characteristic peaks which were observed at 9.76° and 22.23° were slightly decreased after Cr (VI) sorption at pH 3 and 11.

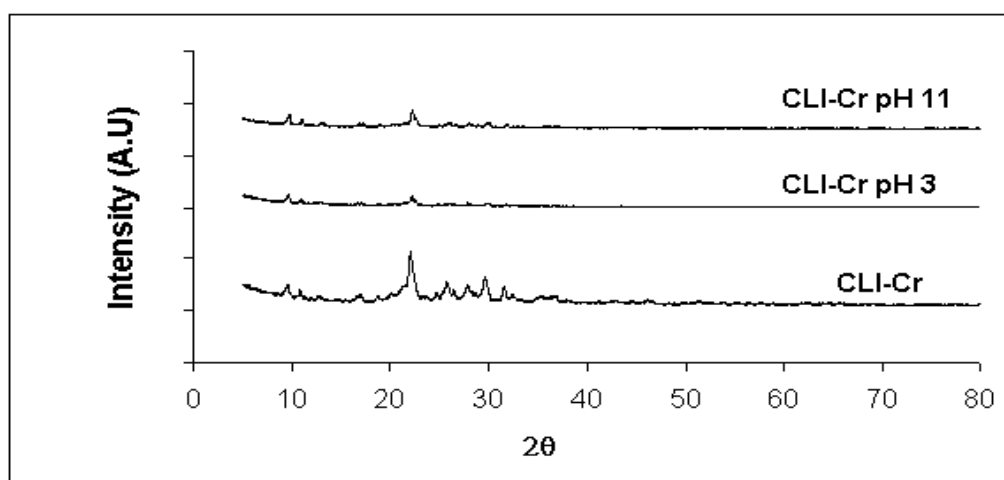


Figure 7.94. XRD results of CLI after Cr (VI) sorption at pH 3 and 11

XRD results of anionic surfactant modified clinoptilolite rich mineral after Cr (VI) sorption at pH 3 and 11 are given in Figure 7.95. At pH 3, relative intensity of one characteristic peak which was observed at  $8.7^\circ$  was considerably reduced. The characteristic peaks which were observed at  $5.6$  and  $8.7^\circ$  were disappeared at pH 11. The results implied that the organic layer was preserved at acidic pH whereas the dissolution of the organic layer was observed at basic pH.

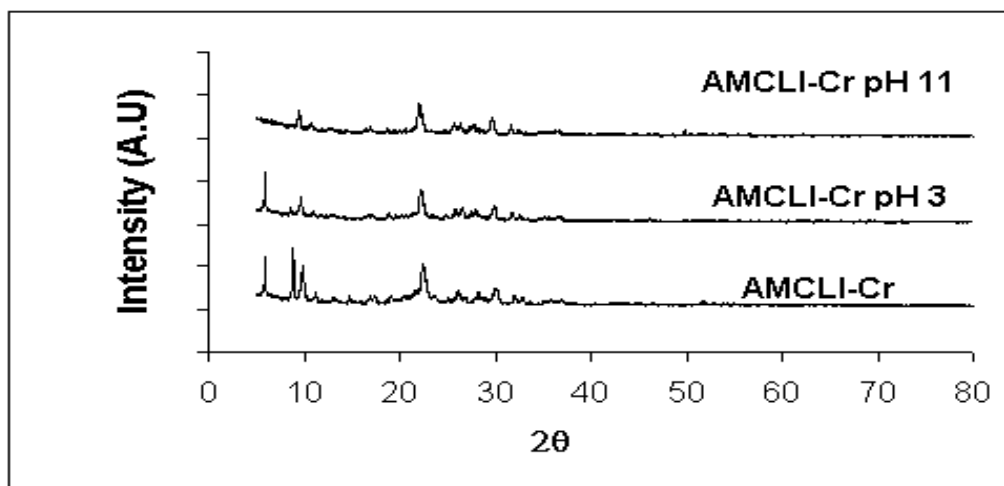


Figure 7.95. XRD results of AMCLI after Cr (VI) sorption at pH 3 and 11

Figure 7.96 shows XRD results of cationic surfactant modified clinoptilolite rich mineral after Cr (VI) sorption at pH 3 and 11. At pH 3, the intensity of major peaks of cationic surfactant modified clinoptilolite rich mineral decreased after Cr (VI) sorption whereas the intensities of major peaks increased after Cr (VI) at pH 11. The increase in intensities of these peaks was indication of dissolution of organic layer on the clinoptilolite rich mineral. Cationic surfactant modified clinoptilolite rich mineral like anionic surfactant modified clinoptilolite rich mineral did not preserve its organic layer at basic pH.

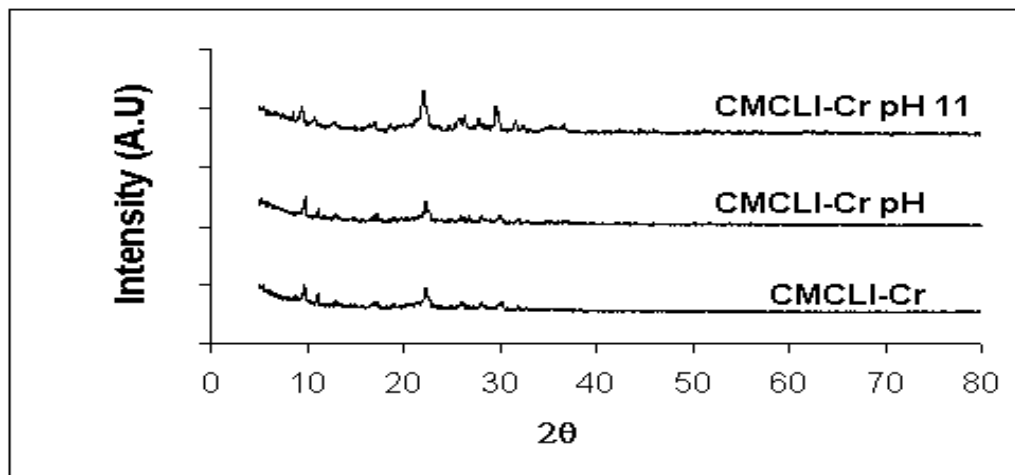


Figure 7.96. XRD results of CMCLI after Cr (VI) sorption at pH 3 and 11

XRD results of bacteria loaded clinoptilolite, anionic and cationic surfactant modified rich mineral after Cr (VI) sorption at pH 3 and 11 are shown in Figure Appendix E.3. Smallest changes in the relative intensities of major peaks were observed after Cr (VI) sorption at pH 3 and 11.

FTIR results of clinoptilolite rich mineral after Cr (VI) sorption at pH 3 and 11 are shown in Figure 7.97. The results indicated that band shift in the water molecules on the clinoptilolite rich mineral was observed after Cr (VI) sorption at pH 3. On the other hand, there was no band shift in the water molecule on the clinoptilolite rich mineral after Cr (VI) sorption at 11. The band shift in the water molecules after Cr (VI) sorption at pH 3 indicated the existence of hydrogen bonding. Zeta potential results implied that repulsive electrostatic forces were dominant between Cr (VI) species and clinoptilolite rich mineral at pH 3. Cr (VI) sorption was observed with clinoptilolite rich mineral at this pH value due to the existence of non electrostatic forces (hydrogen bonding).

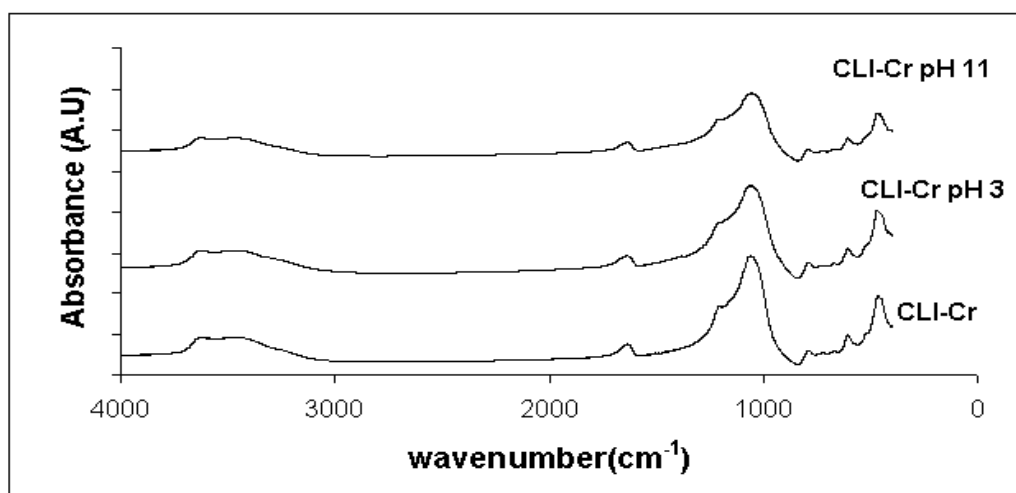


Figure 7.97. FTIR results of CLI after Cr (VI) sorption at pH 3 and 11

Figure 7.98 shows FTIR results of anionic surfactant modified clinoptilolite rich mineral after Cr (VI) sorption at pH 3 and 11. As shown in Figure 7.98, neither band shift or band disappearance on FTIR spectra was observed at pH 11. The results inferred that band shift in methylene groups and water molecules were observed at pH 3. Zeta potential results showed that anionic surfactant modified clinoptilolite rich mineral was negatively charged at pH 3. Although there were repulsive electrostatic forces, the existence of Cr (VI) sorption indicates a significant role of the non electrostatic forces in Cr (VI) sorption with anionic surfactant modified clinoptilolite rich mineral at pH 3. The existence of non electrostatic forces was confirmed by the FTIR results.

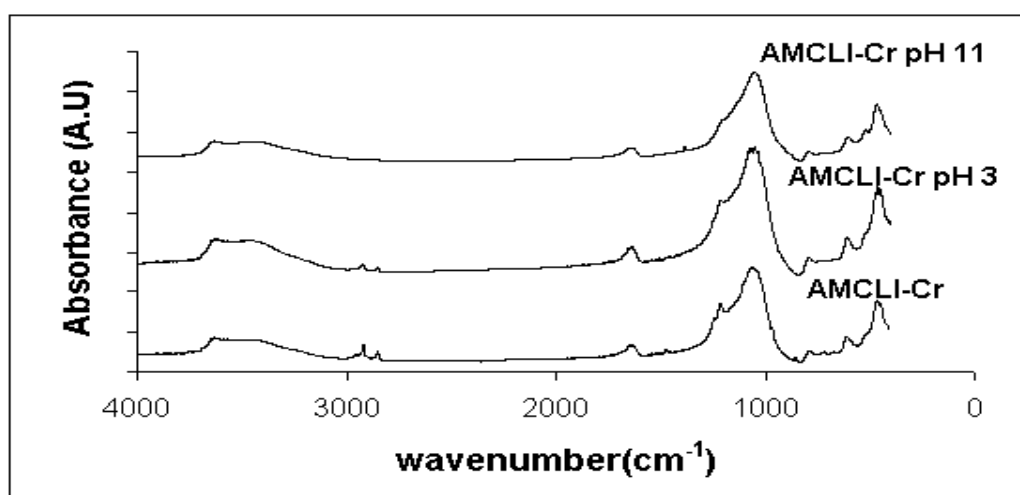


Figure 7.98. FTIR results of AMCLI after Cr (VI) sorption at pH 3 and 11

FTIR results of cationic surfactant modified clinoptilolite rich mineral after Cr (VI) sorption at pH 3 and 11 is shown in Figure 7.99. At pH 3, only band shift in



methylene groups on the cationic surfactant modified clinoptilolite rich mineral was observed after Cr (VI) sorption. At pH 11, there was no band shift in methylene groups after Cr (VI) sorption. Zeta potential results showed that cationic surfactant modified clinoptilolite rich mineral was positively charged at pH 3 and thus attractive electrostatic forces were dominant between Cr (VI) species and cationic surfactant modified clinoptilolite rich mineral. The highest Cr (VI) sorption results with cationic surfactant modified clinoptilolite rich mineral at pH 3 was attributed to the summation of electrostatic and non electrostatic forces coming from band shift in methylene group.

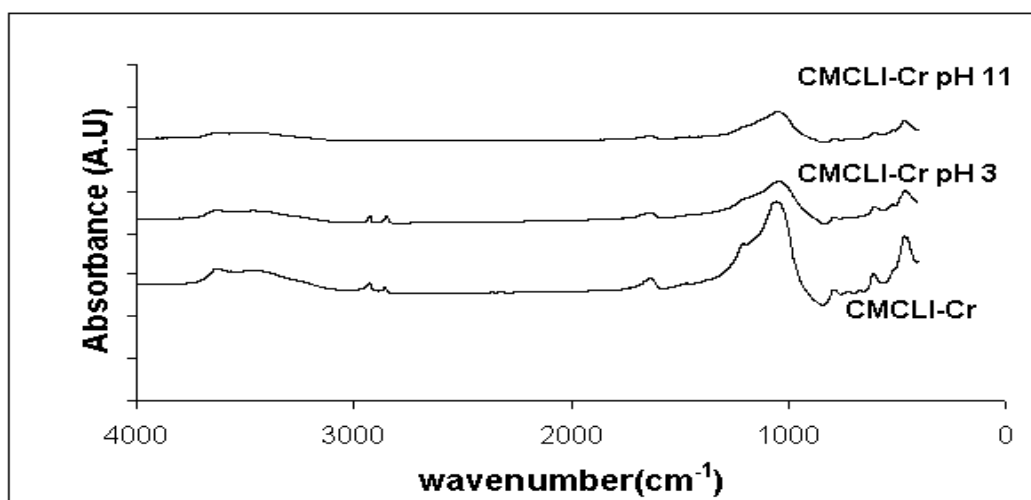


Figure 7.99. FTIR results of CMCLI after Cr (VI) sorption at pH 3 and 11

FTIR results of *E. coli* and *B. subtilis* loaded clinoptilolite rich mineral after Cr (VI) sorption at pH 3 and 11 are given in Figure 7.100 and 7.101. The results indicated that the new bands were observed after Cr (VI) sorption at pH 3 whereas no new band was observed at pH 11. Bands observed in 1626 and 1525  $\text{cm}^{-1}$  were assigned to the amide I and amide II. These amide groups on *E. coli* loaded clinoptilolite rich mineral were involved in Cr (VI) sorption. Bands observed in 2951, 1649 and 1523  $\text{cm}^{-1}$  were assigned to the asymmetric stretching of C–H bond of the  $-\text{CH}_2$  groups, amide I and amide II, respectively. The results inferred that both C–H bonds and amide groups were responsible in the Cr (VI) sorption with *B. subtilis* loaded clinoptilolite rich mineral. Zeta potential results indicated that *E. coli* and *B. subtilis* loaded clinoptilolite rich mineral samples were positively charged at pH 3 and thus there were attractive electrostatic forces between Cr (VI) species and bacteria loaded clinoptilolite rich samples. Attractive electrostatic forces, C–H bonds and amide groups were responsible

for Cr (VI) sorption with *E. coli* and *B. subtilis* loaded clinoptilolite rich mineral at pH 3.

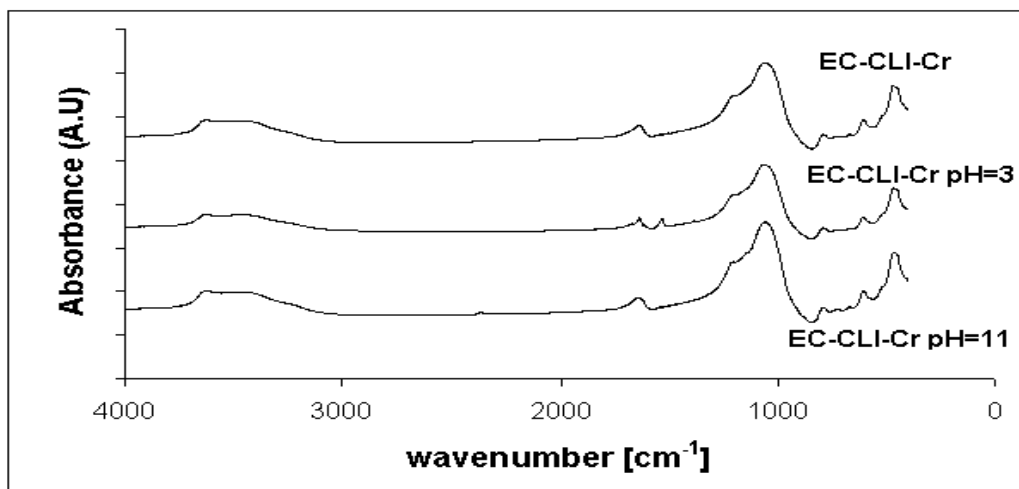


Figure 7.100. FTIR results of EC-CLI after Cr (VI) sorption at pH 3 and 11

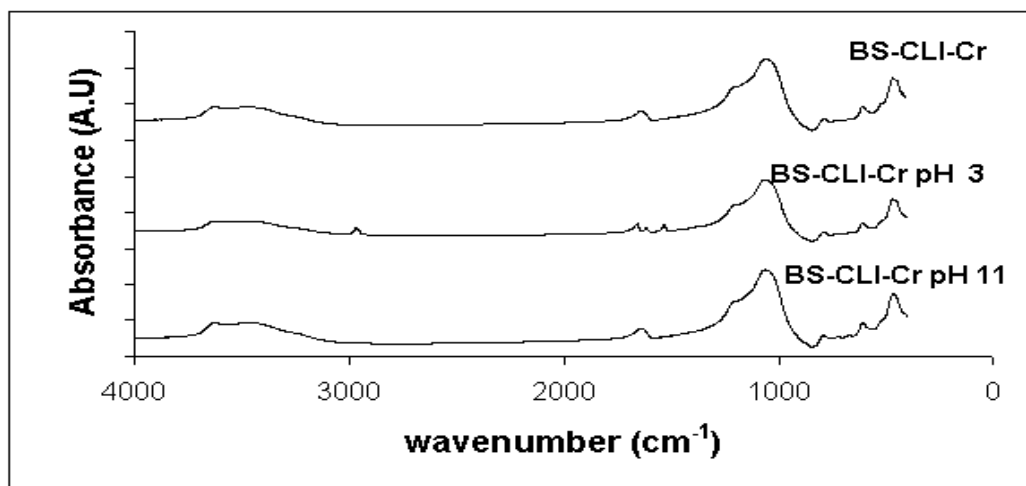


Figure 7.101. FTIR results of BS-CLI after Cr (VI) sorption at pH 3 and 11

FTIR results of *E. coli* and *B. subtilis* loaded anionic surfactant modified clinoptilolite rich mineral after Cr (VI) sorption at pH 3 and 11 are given in Figure 7.102 and 7.103. At pH 3, the four new bands were appeared on *E. coli* loaded anionic surfactant modified clinoptilolite rich mineral samples. Bands observed at 1624 and 1529 cm<sup>-1</sup> were related to amide I and amide II whereas bands observed at 1402 and 1359 cm<sup>-1</sup> were related to C-O bending from carboxylate. These amide and carboxylate groups on *E. coli* loaded anionic surfactant modified clinoptilolite rich mineral were involved in Cr (VI) sorption. FTIR result of *B. subtilis* loaded anionic surfactant modified clinoptilolite showed that four new bands were observed at pH 3 after Cr (VI)

sorption. Bands observed in 2872, 1624, 1523 and 1357  $\text{cm}^{-1}$  were assigned to the asymmetric stretching of C–H bond of the  $-\text{CH}_2$  groups, amide I, amide II and C–O bending from carboxylate, respectively. All groups were involved in the Cr (VI) sorption with *B. subtilis* loaded anionic surfactant modified clinoptilolite. No new band was observed after Cr (VI) sorption with *E. coli* and *B. subtilis* loaded anionic surfactant modified clinoptilolite rich mineral at pH 11. Zeta potential results indicated that there were attractive electrostatic forces between Cr (VI) species and bacteria loaded anionic surfactant modified clinoptilolite rich mineral at pH 3. The results revealed that attractive electrostatic forces, C–H,  $-\text{CH}_2$ , amide and carboxylate groups were involved in Cr (VI) sorption with bacteria loaded anionic surfactant modified clinoptilolite rich mineral at pH 3.

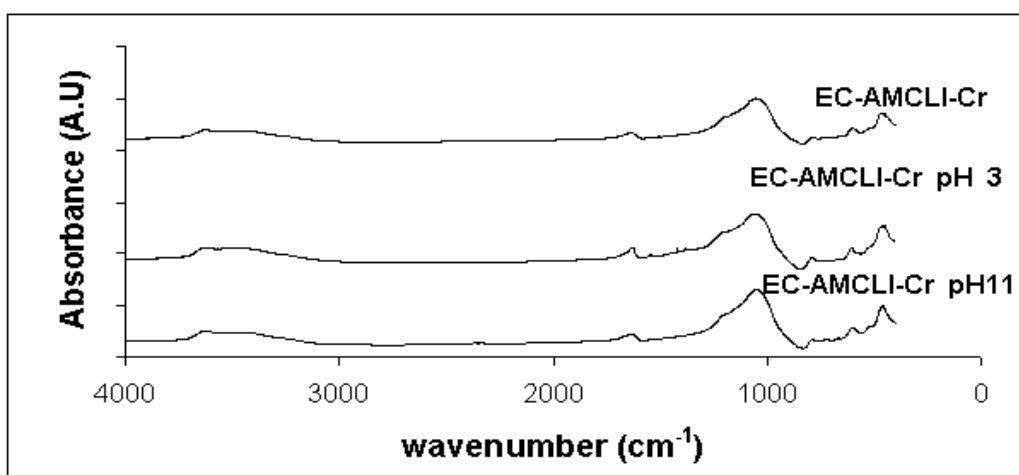


Figure 7.102. FTIR results of EC-AMCLI after Cr (VI) sorption at pH 3 and 11

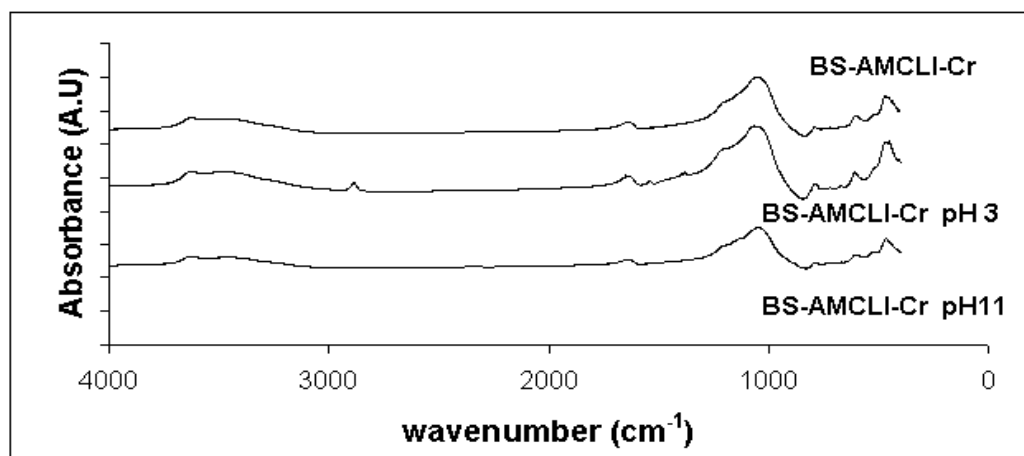


Figure 7.103. FTIR results of BS-AMCLI after Cr (VI) sorption at pH 3 and 11

FTIR results of *E. coli* and *B. subtilis* loaded cationic surfactant modified clinoptilolite rich mineral after Cr (VI) sorption at pH 3 and 11 are shown in Figure 7.104 and 7.105. At pH 3, the four new bands were appeared on *E. coli* loaded cationic surfactant modified clinoptilolite rich mineral samples. Bands observed at 2883 and 2820  $\text{cm}^{-1}$  were related to the asymmetric stretching of C–H bond of the  $-\text{CH}_2$  groups whereas bands observed at 1614 and 1510  $\text{cm}^{-1}$  were related to amide I and amide II group. These groups on *E. coli* loaded cationic surfactant modified clinoptilolite rich mineral could interact with Cr (VI). FTIR result of *B. subtilis* loaded cationic surfactant modified clinoptilolite showed that six new bands were observed at pH 3 after Cr (VI) sorption. Bands observed in 2910 and 2845  $\text{cm}^{-1}$  were related to the asymmetric stretching of C–H bond of the  $-\text{CH}_2$  groups. The other bands were observed at 1618, 1518, 1361 and 1222  $\text{cm}^{-1}$  which were assigned to the amide I, amide II, C–O bending from carboxylate and P=O double bond asymmetric stretching vibrations of phosphodiester, respectively. All groups were involved in the Cr (VI) sorption with *B. subtilis* loaded cationic surfactant modified clinoptilolite. Zeta potential results indicated that there were attractive electrostatic forces between Cr (VI) species and bacteria loaded cationic surfactant modified clinoptilolite rich mineral at pH 3. In addition to attractive electrostatic forces,  $-\text{CH}_2$ , amide, carboxylate and phosphodiester groups were responsible for Cr (VI) sorption with bacteria loaded cationic surfactant modified clinoptilolite rich mineral.

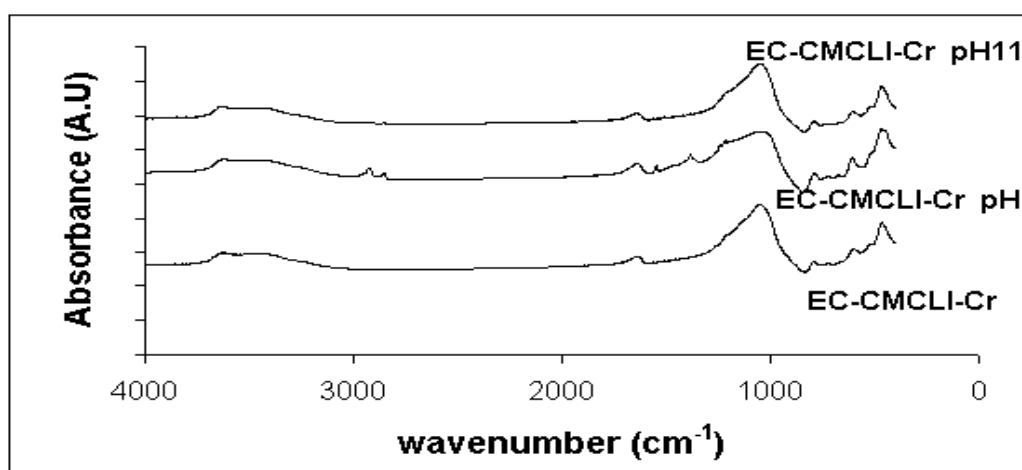


Figure 7.104. FTIR results of EC-CMCLI after Cr (VI) sorption at pH 3 and 11

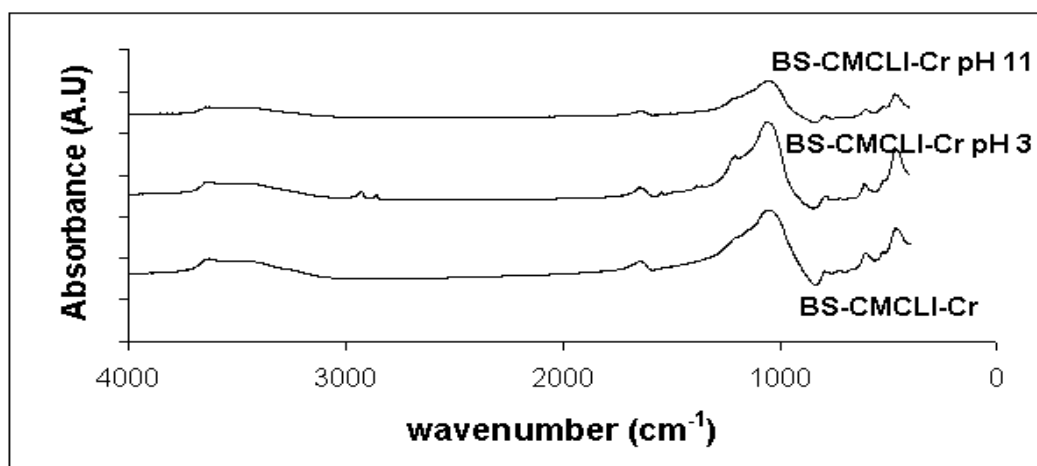


Figure 7.105. FTIR results of BS-CMCLI after Cr (VI) sorption at pH 3 and 11

#### 7.4.2. Effect of Initial Concentration on Cr (VI) Sorption

The experimental studies were carried out with varying initial metal ion concentrations of Cr (VI), ranging from 10 to 300 mg/L at 25°C and 140 rpm; the results are shown in Figures 7.106-7.114. As shown in these figures, uptake rate of Cr (VI) was rapid at the beginning of the sorption process since there were available unoccupied sites in the sorbents. As sorption time progressed, Cr (VI) uptake rate gradually slowed down because sites in the sorbents were occupied and fewer available sites involved in the sorption process. At equilibrium, the uptake rate approached zero. The results indicated that at equilibrium the amount of Cr (VI) sorbed on the sorbents increased with increasing initial concentration. The results also revealed that the initial uptake rate decreased with increasing initial concentration.

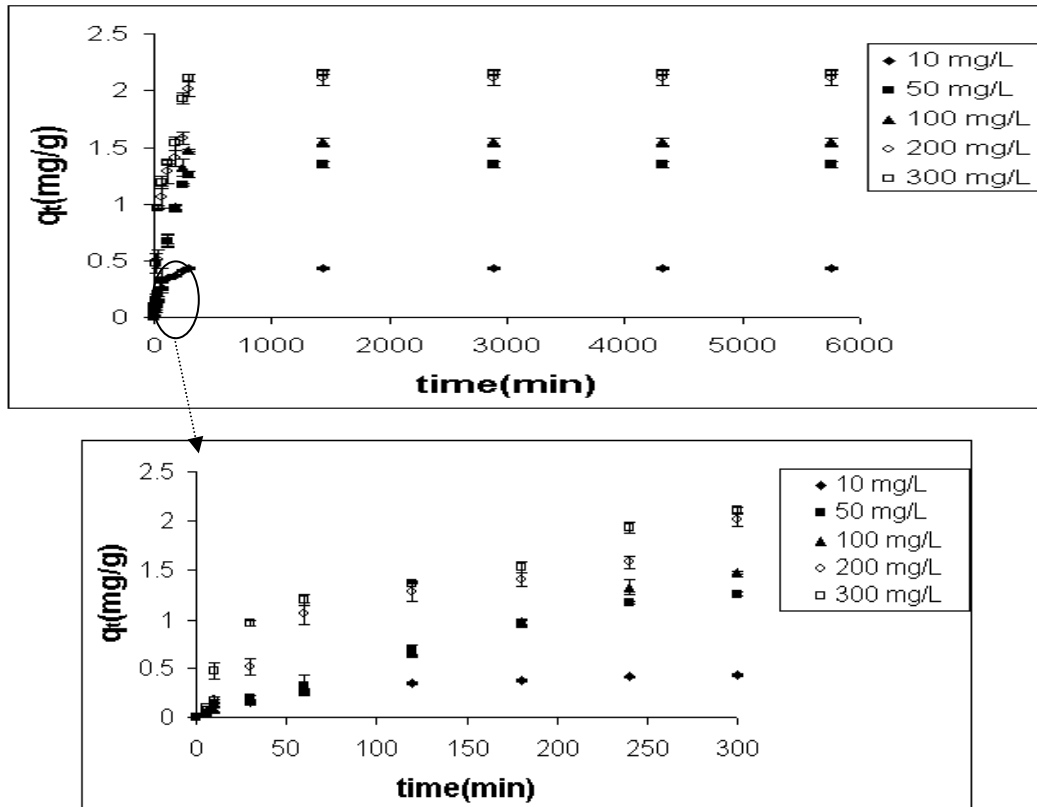


Figure 7.106. Effect of initial concentration on sorption of Cr (VI) with CLI (Conditions: pH: 3, 25 °C, 140 rpm, 25–106  $\mu$ m)

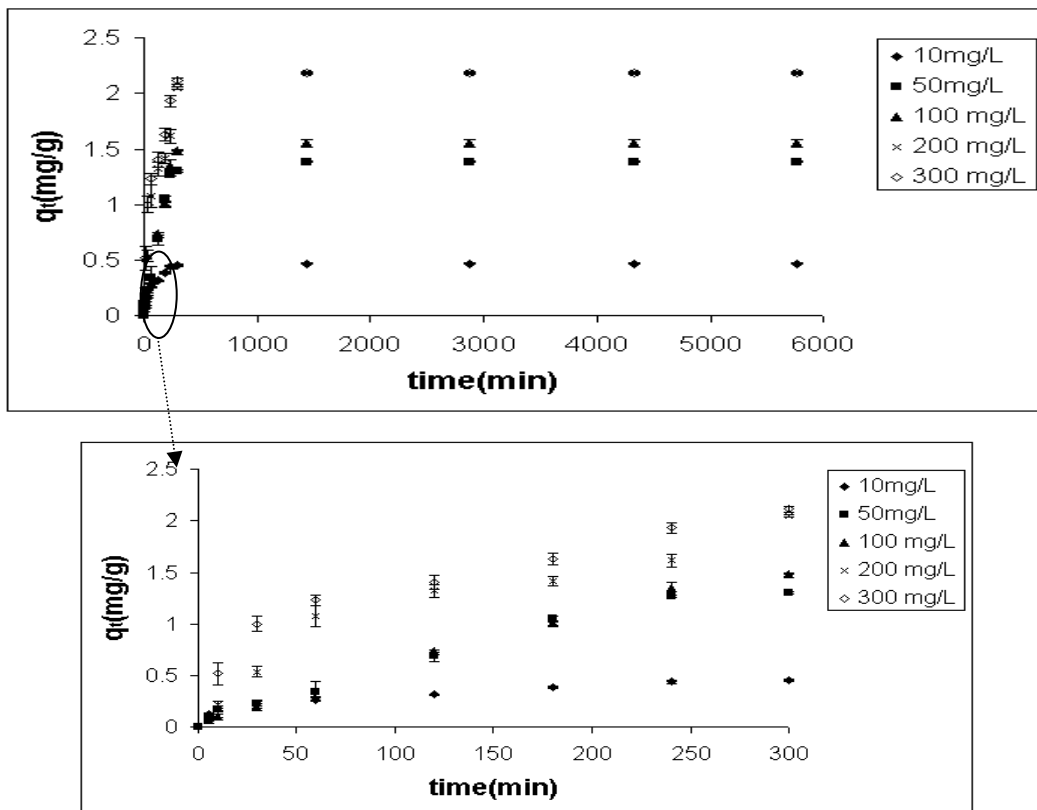


Figure 7.107. Effect of initial concentration on sorption of Cr (VI) with AMCLI (Conditions: pH: 3, 25 °C, 140 rpm, 25–106  $\mu$ m)

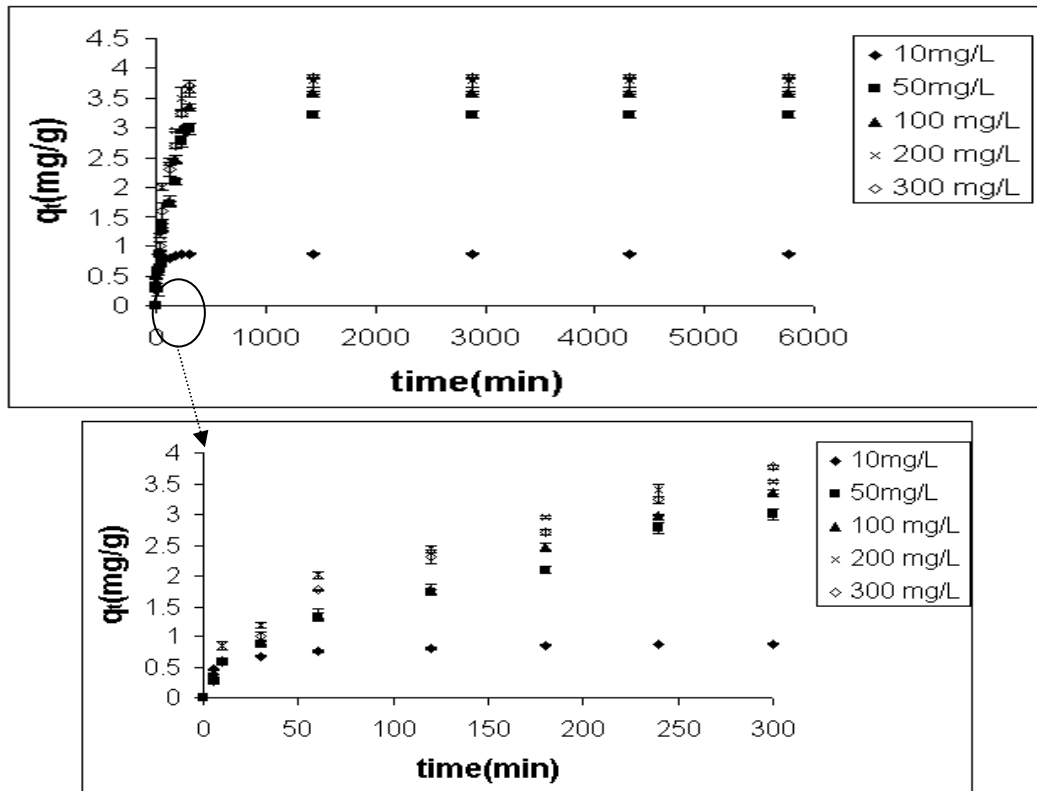


Figure 7.108. Effect of initial concentration on sorption of Cr (VI) with CMCLI (Conditions: pH: 3, 25 °C, 140 rpm, 25–106  $\mu\text{m}$ )

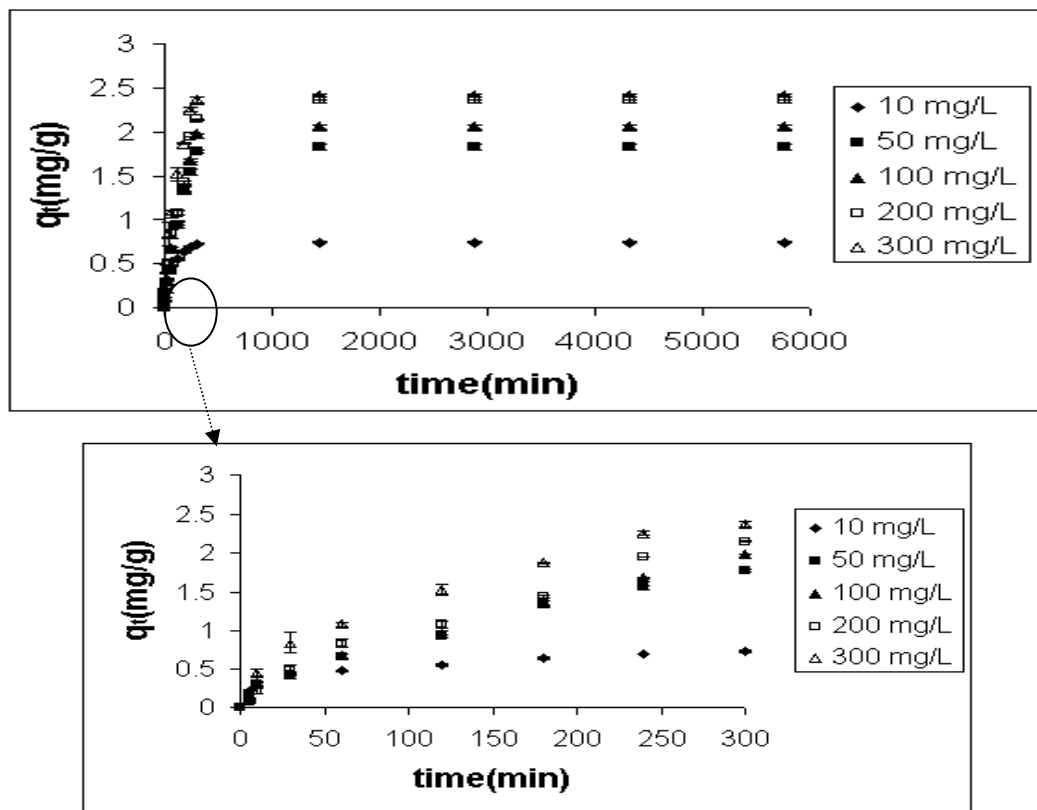


Figure 7.109. Effect of initial concentration on sorption of Cr (VI) with EC-CLI (Conditions: pH: 3, 25 °C, 140 rpm, 25–106  $\mu\text{m}$ )

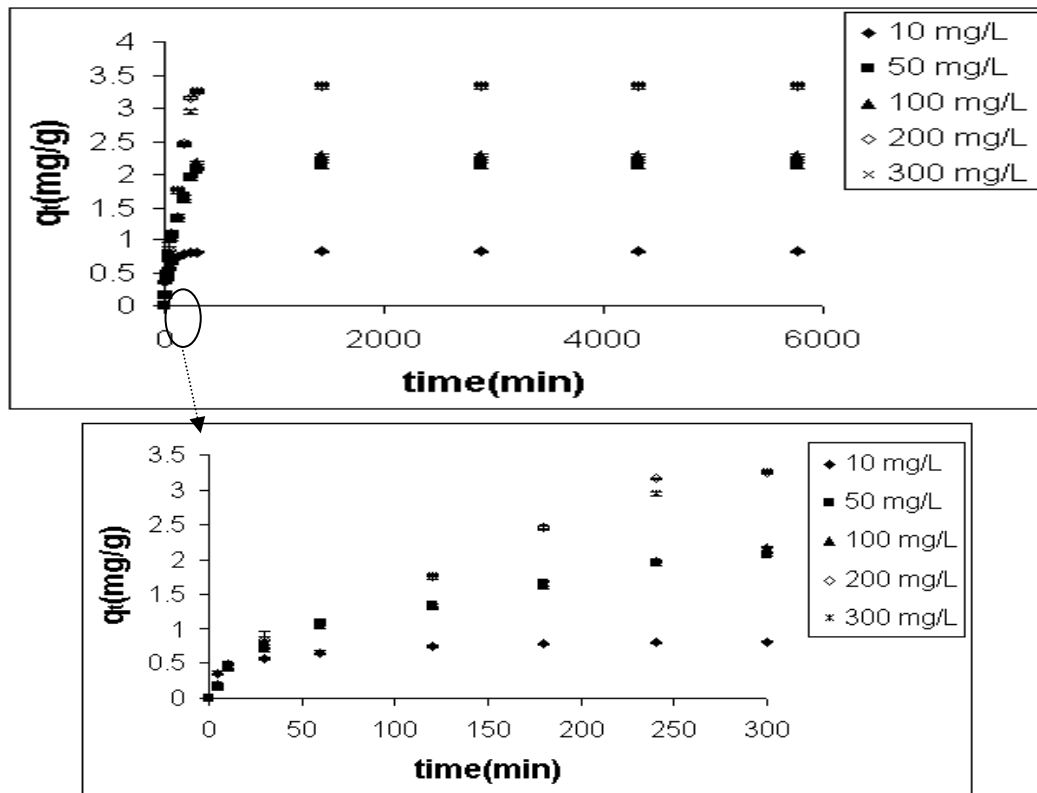


Figure 7.110. Effect of initial concentration on sorption of Cr (VI) with BS-CLI (Conditions: pH: 3, 25 °C, 140 rpm, 25–106  $\mu$ m)

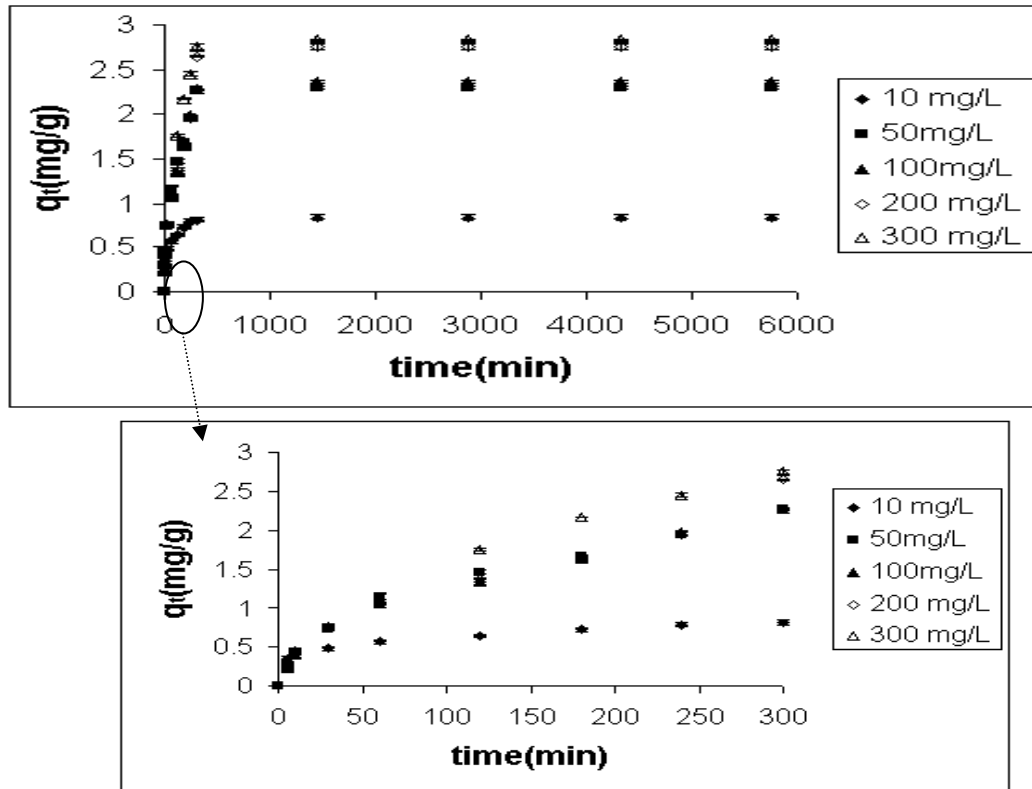


Figure 7.111. Effect of initial concentration on sorption of Cr (VI) with EC-AMCLI (Conditions: pH: 3, 25 °C, 140 rpm, 25–106  $\mu$ m)



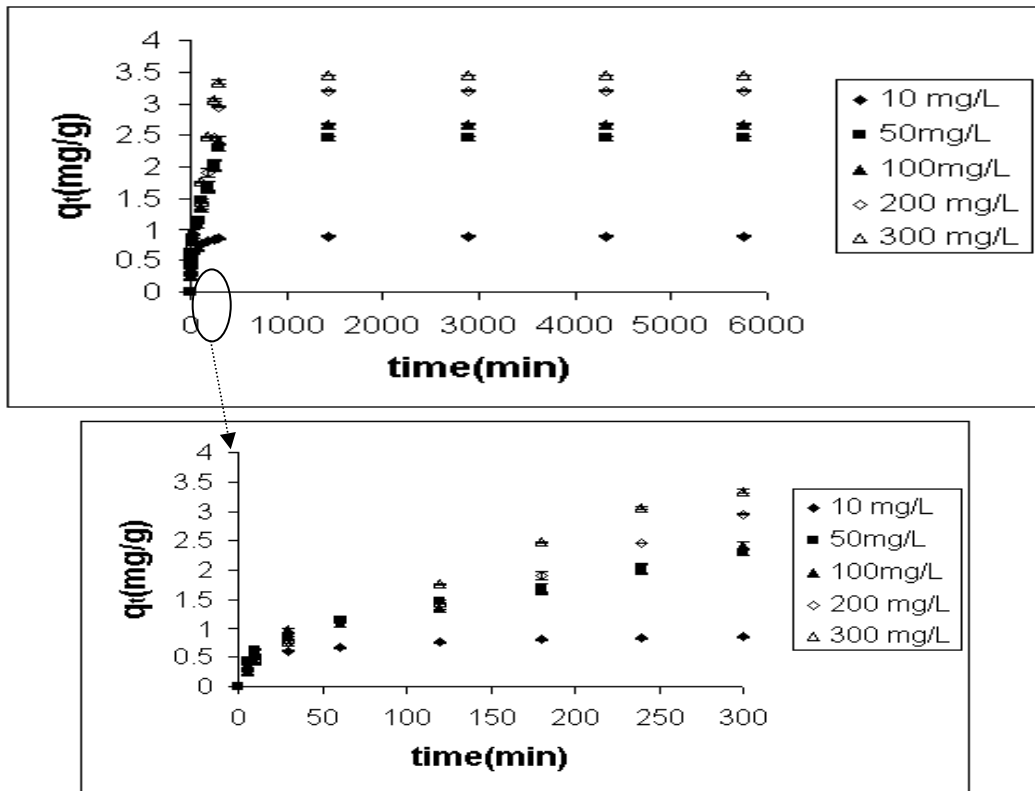


Figure 7.112. Effect of initial concentration on sorption of Cr (VI) with BS-AMCLI (Conditions: pH: 3, 25 °C, 140 rpm, 25–106  $\mu$ m)

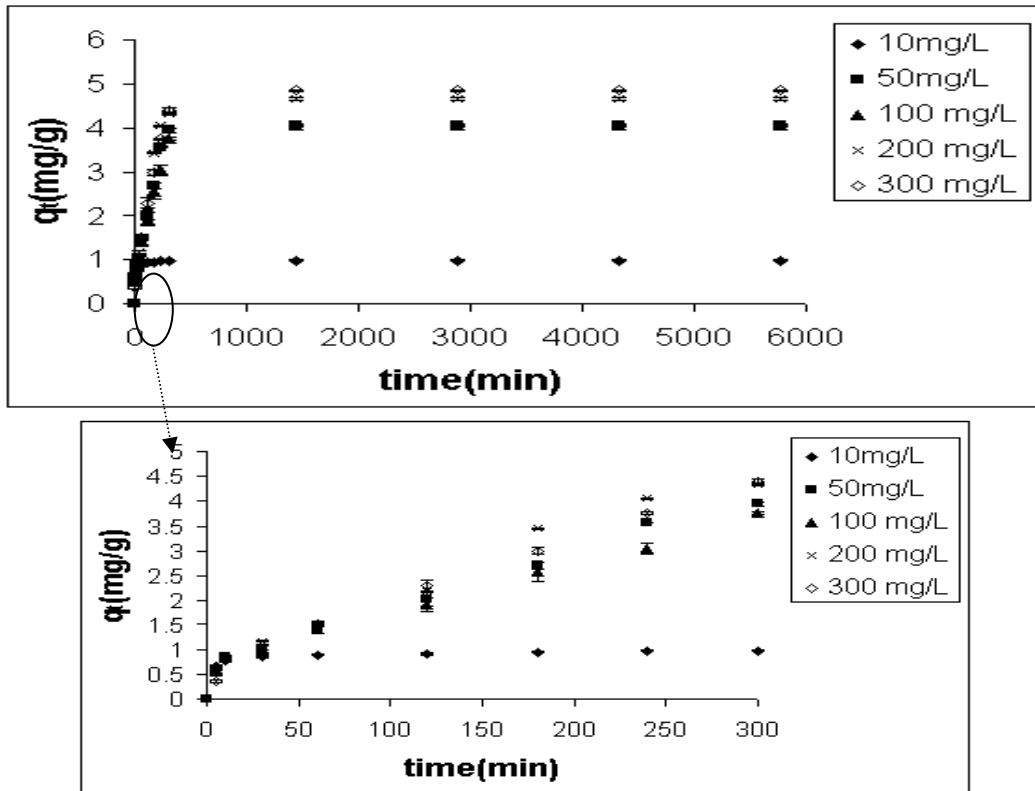


Figure 7.113. Effect of initial concentration on sorption of Cr (VI) with EC-CMCLI (Conditions: pH: 3, 25 °C, 140 rpm, 25–106  $\mu$ m)

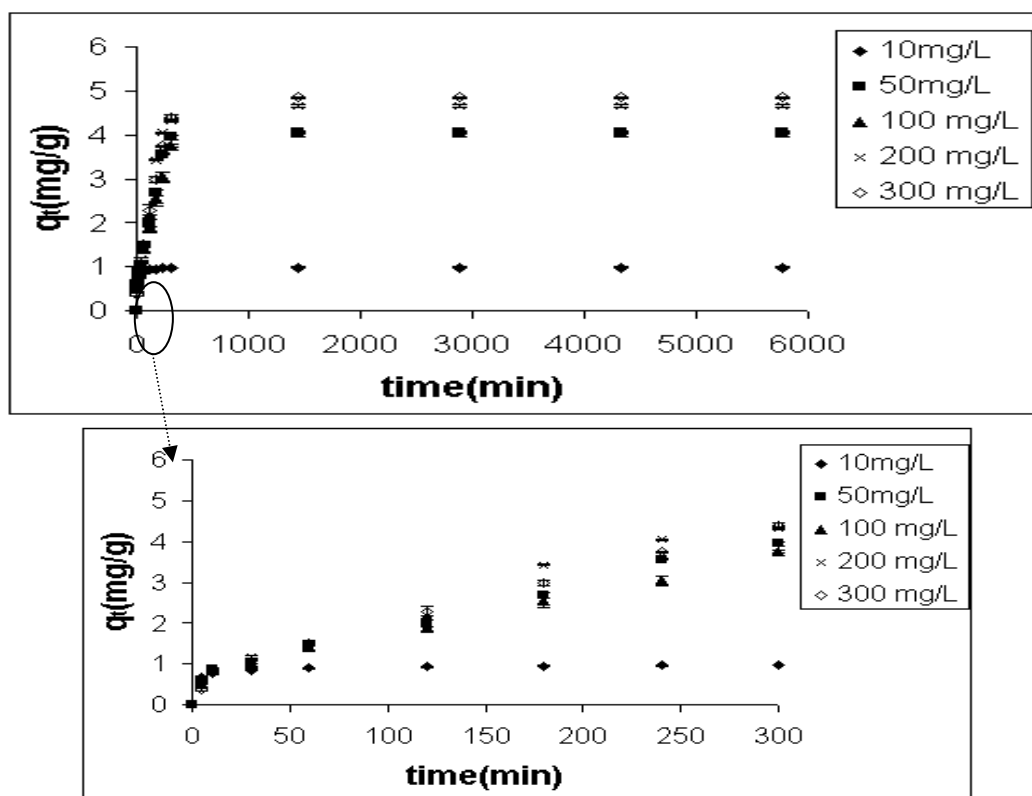


Figure 7.114. Effect of initial concentration on sorption of Cr (VI) with BS-CMCLI (Conditions: pH: 3, 25 °C, 140 rpm, 25–106  $\mu$ m)

### 7.4.3. Effect of Agitation Speed on Cr (VI) Sorption

Agitation speed influences in the distribution of the solute molecules in the bulk solution but can also act on the formation of the external boundary film. By increasing agitation speed, the external mass resistance becomes smaller due to the reduction of the boundary layer thickness.

The effects of stirring speed on Cr (VI) sorption by sorbents at different stirring speeds, ranging from 60 to 140 rpm, are shown in 7.115-7.123. As seen in figures, initial uptake rate increased with increasing agitation speed. The results indicated that at equilibrium the amount of Cr (VI) sorbed on the sorbents almost remained constant as the agitation speed increased.

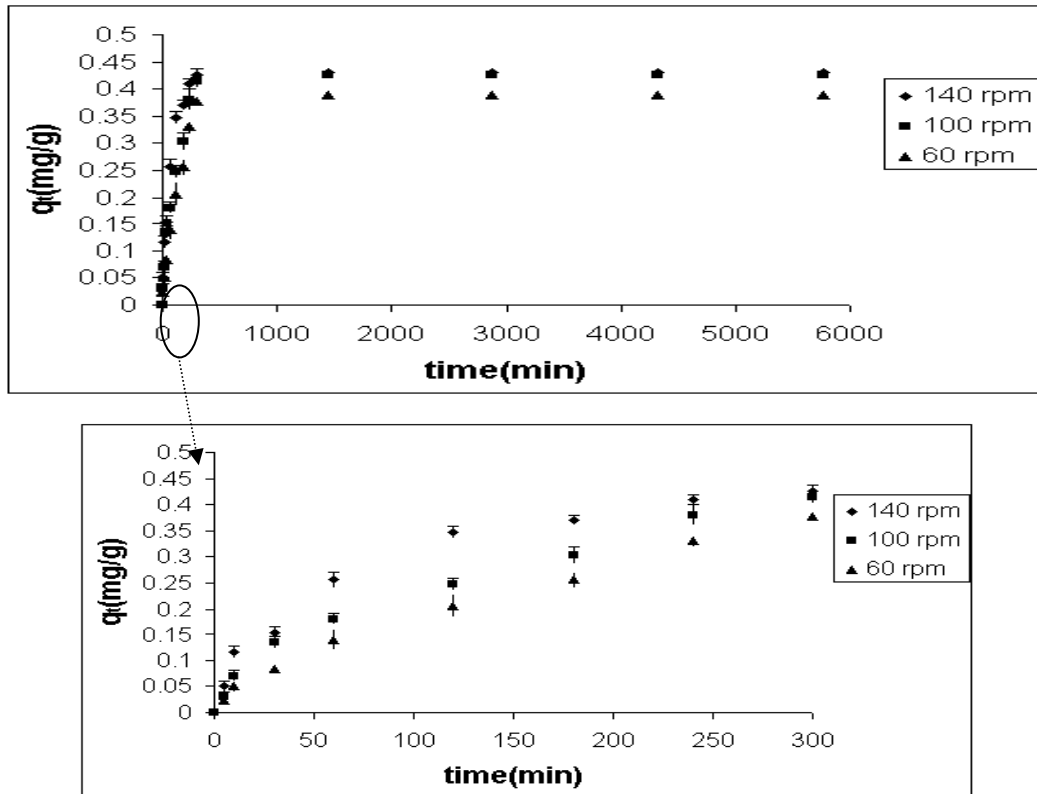


Figure 7.115. Effect of agitation speed on sorption of Cr (VI) with CLI  
 (Conditions: pH: 3, 10 mg/L, 25 °C, 25–106  $\mu\text{m}$ )

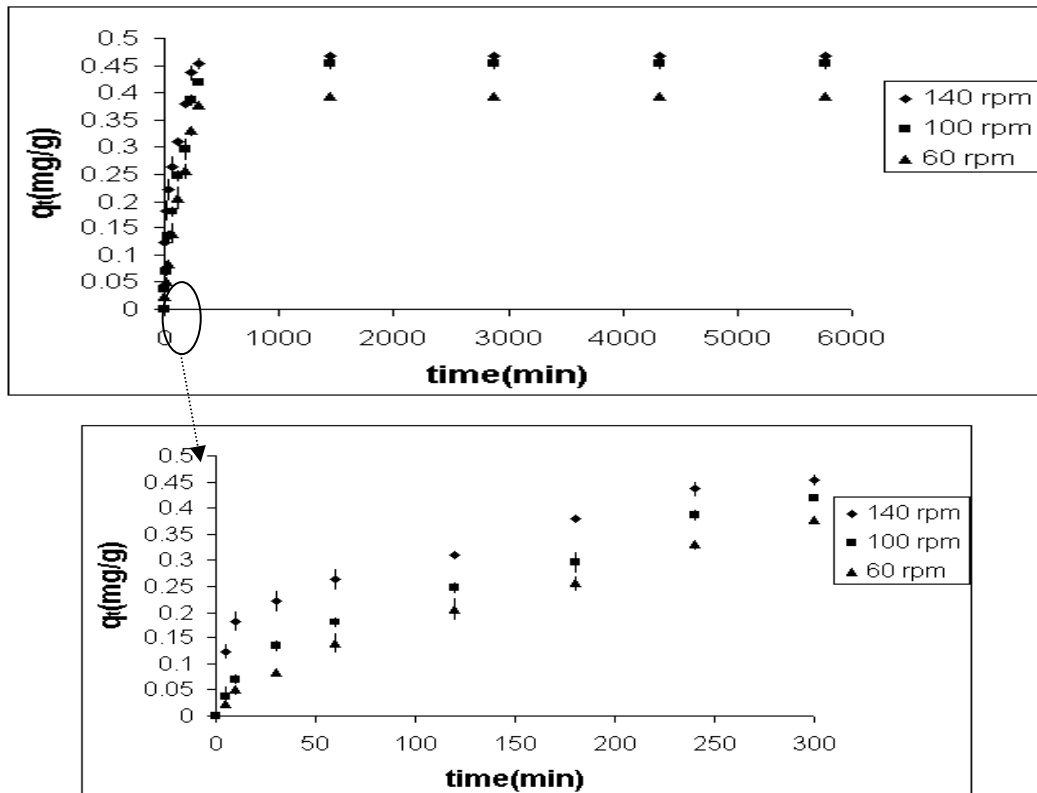


Figure 7.116. Effect of agitation speed on sorption of Cr (VI) with AMCLI  
 (Conditions: pH: 3, 10 mg/L, 25 °C, 25–106  $\mu\text{m}$ )

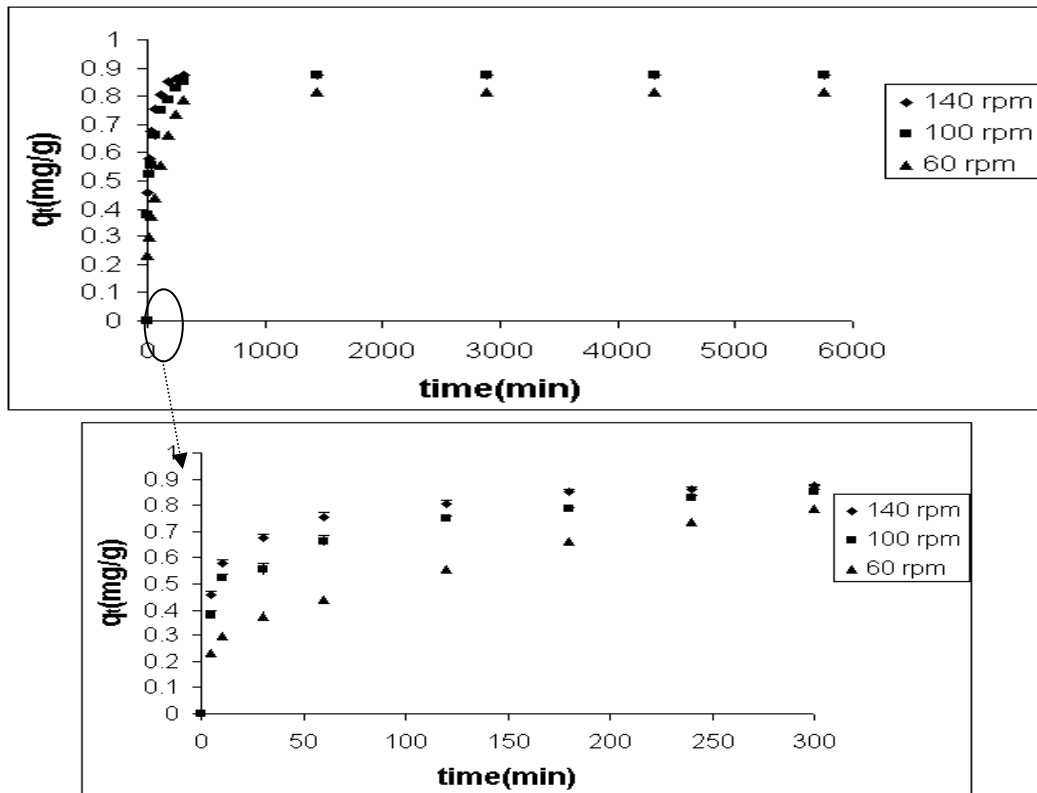


Figure 7.117. Effect of agitation speed on sorption of Cr (VI) with CMCLI (Conditions: pH: 3, 10 mg/L, 25 °C, 25–106  $\mu\text{m}$ )

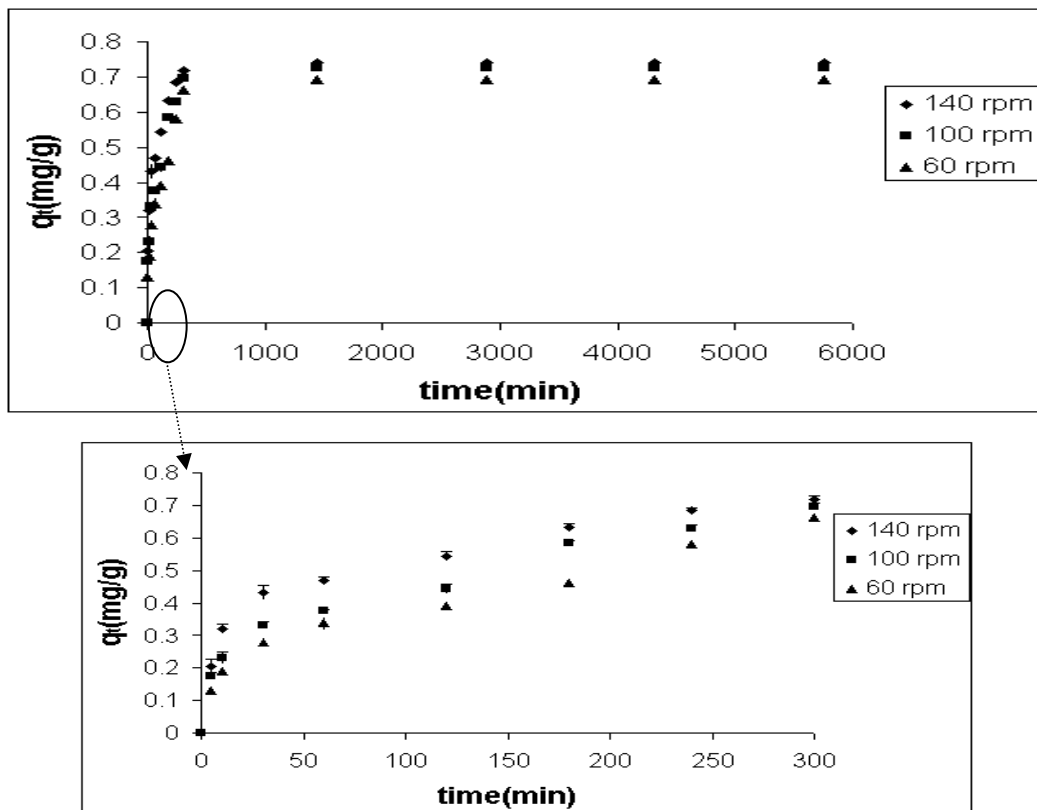


Figure 7.118. Effect of agitation speed on sorption of Cr (VI) with EC-CLI (Conditions: pH: 3, 10 mg/L, 25 °C, 25–106  $\mu\text{m}$ )

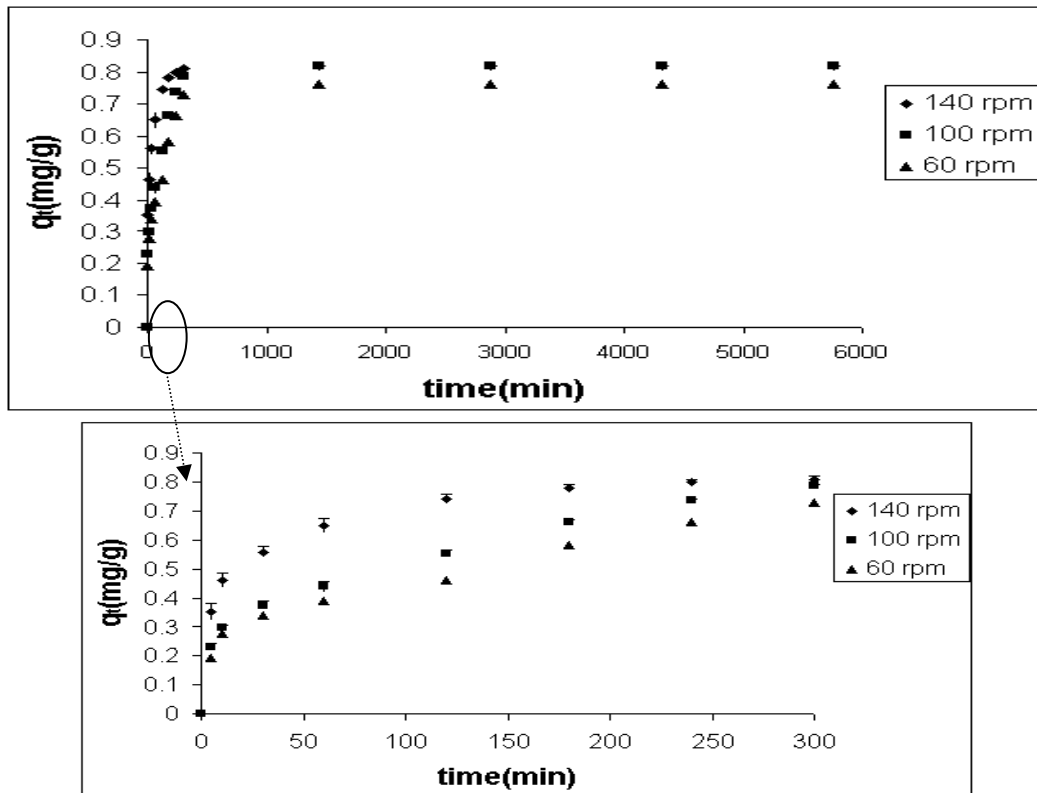


Figure 7.119. Effect of agitation speed on sorption of Cr (VI) with BS-CLI  
(Conditions: pH: 3, 10 mg/L, 25 °C, 25–106  $\mu\text{m}$ )

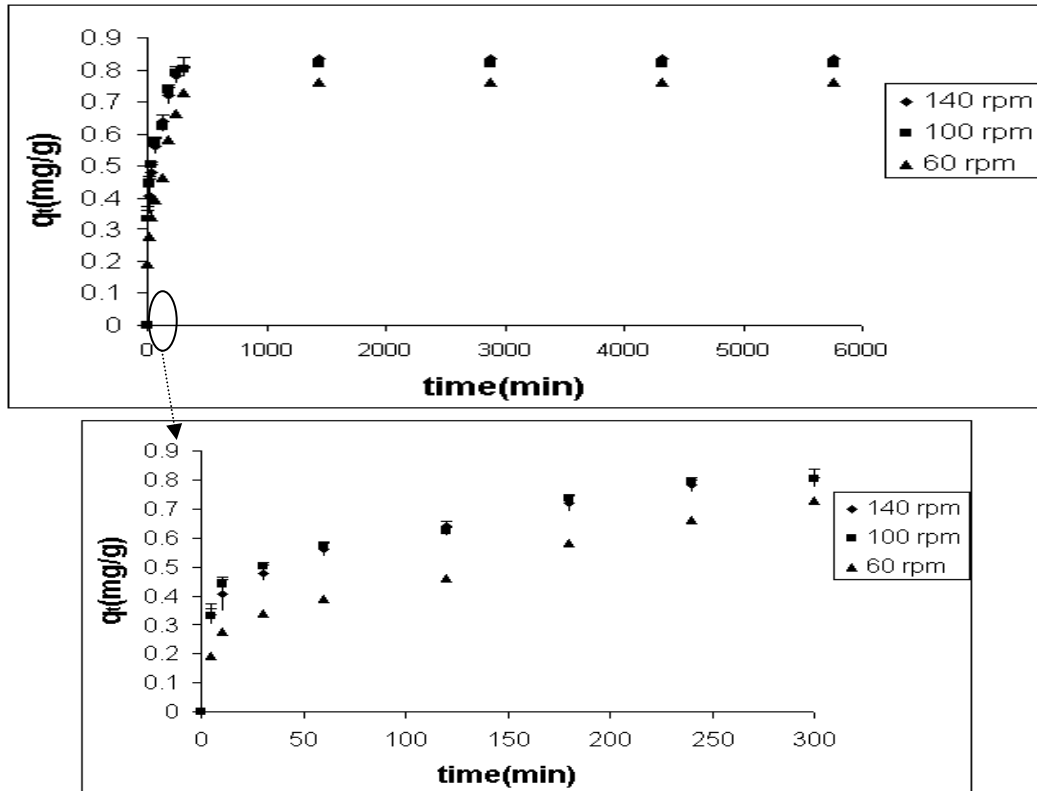


Figure 7.120. Effect of agitation speed on sorption of Cr (VI) with EC-AMCLI  
(Conditions: pH: 3, 10 mg/L, 25 °C, 25–106  $\mu\text{m}$ )

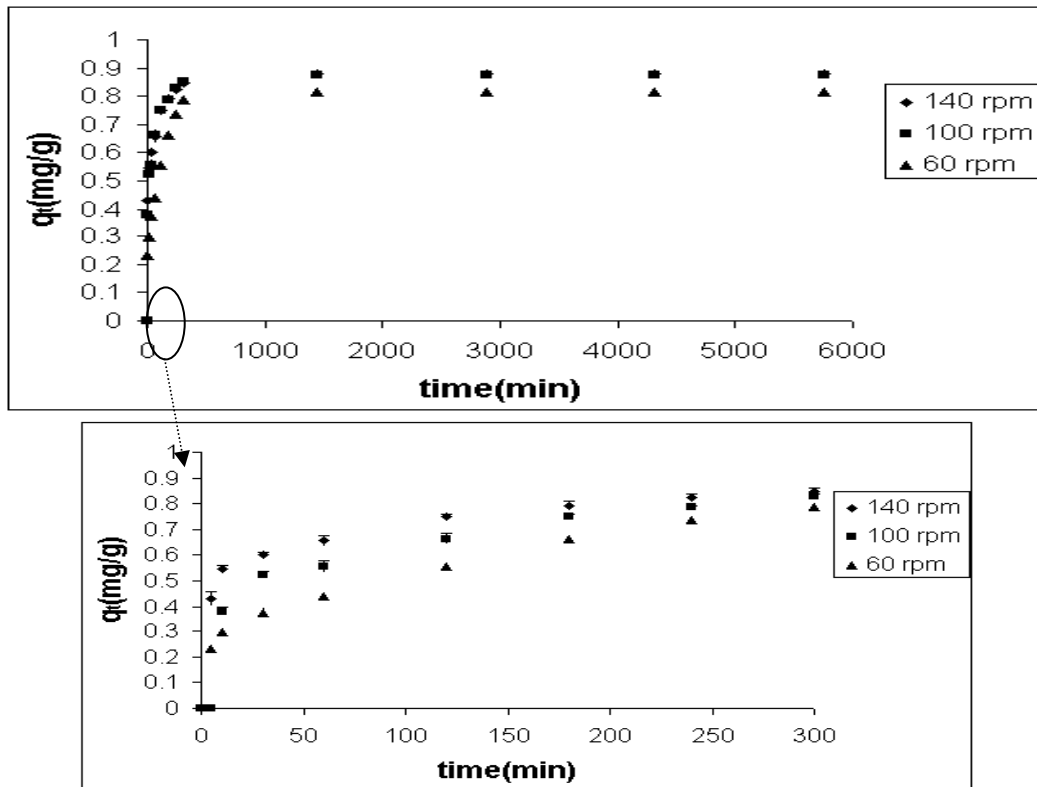


Figure 7.121. Effect of agitation speed on sorption of Cr (VI) with BS-AMCLI (Conditions: pH: 3, 10 mg/L, 25 °C, 25–106  $\mu\text{m}$ )

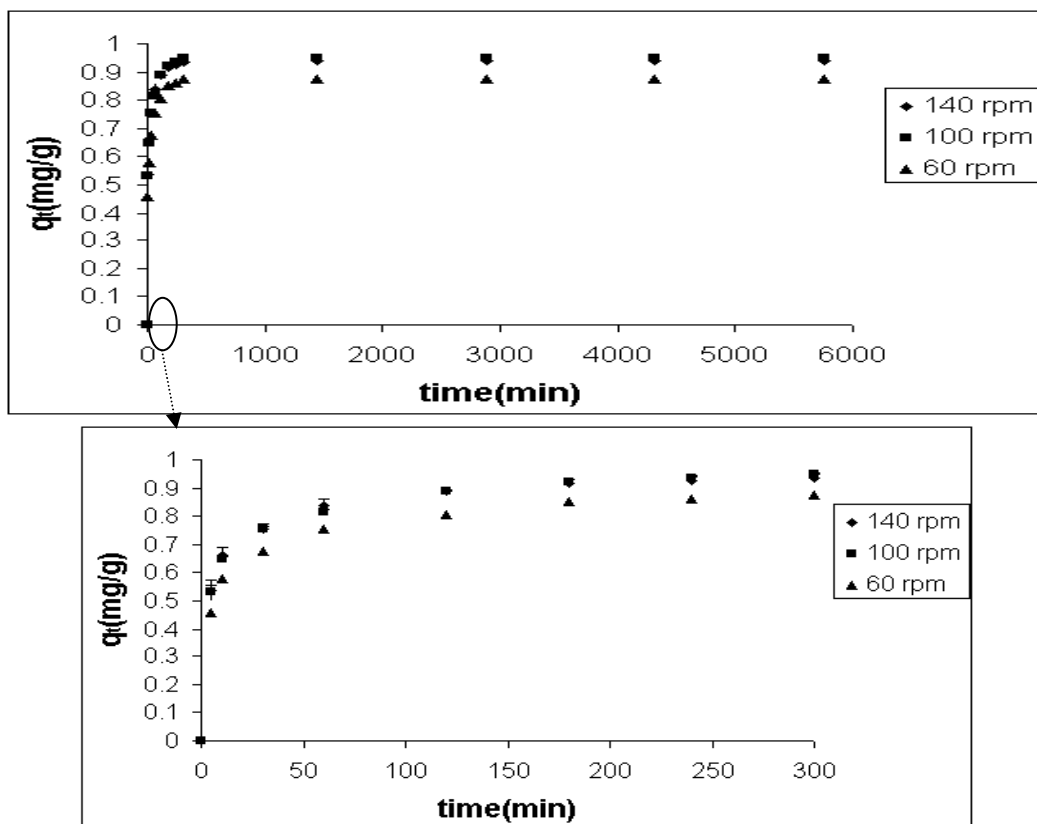


Figure 7.122. Effect of agitation speed on sorption of Cr (VI) with EC-CMCLI (Conditions: pH: 3, 10 mg/L, 25 °C, 25–106  $\mu\text{m}$ )

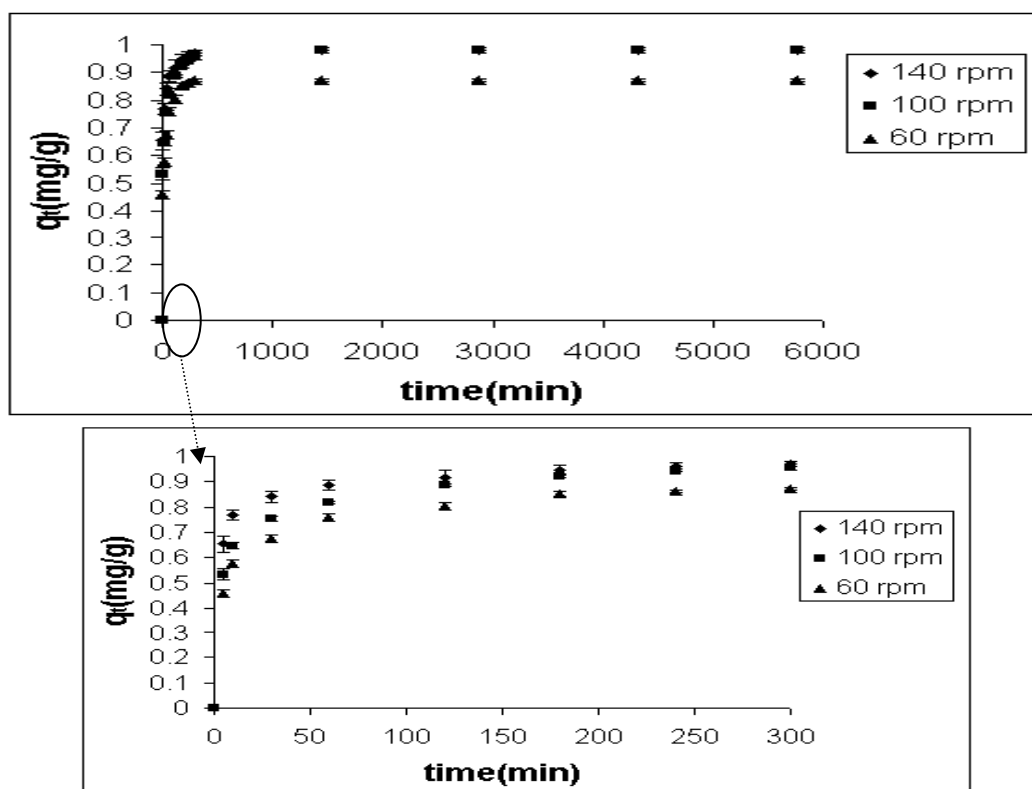


Figure 7.123. Effect of agitation speed on sorption of Cr (VI) with BS-CMCLI (Conditions: pH: 3, 10 mg/L, 25 °C, 25–106  $\mu\text{m}$ )

#### 7.4.4. Effect of Temperature on Cr (VI) Sorption

The temperature dependence of Cr (VI) sorption by different sorbents was studied with a constant initial Cr (VI) concentration of 10 mg/L at 140 rpm at various temperatures and their results are illustrated in Figure 7.124-7.132. The results indicated that the amount of Cr (VI) sorbed at equilibrium decreased when the temperature increased from 25 to 40°C. The decrease in Cr (VI) sorption with increasing temperature indicated the weak interaction between sorbents and Cr (VI) species. Moreover, the decrease in Cr (VI) sorption with increasing temperature revealed that Cr (VI) sorption was an exothermic process and thus it was favored at low temperature.

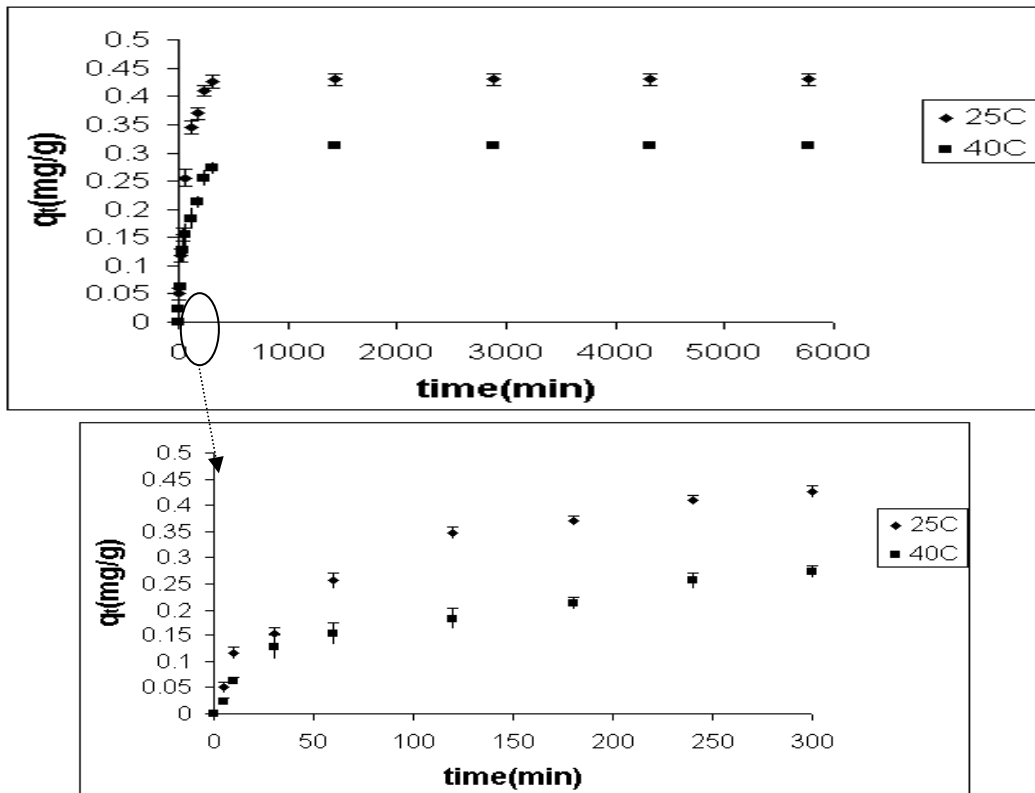


Figure 7.124. Effect of temperature on sorption of Cr (VI) with CLI  
(Conditions: pH: 3, 10 mg/L, 140 rpm, 25–106  $\mu$ m)

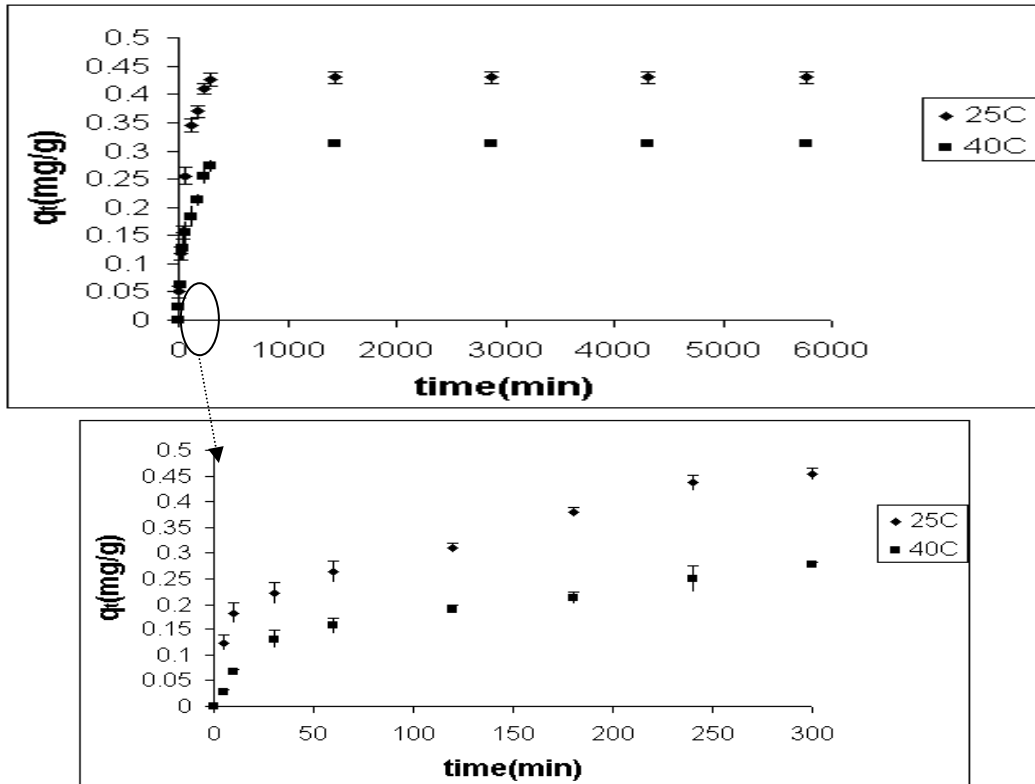


Figure 7.125. Effect of temperature on sorption of Cr (VI) with AMCLI  
(Conditions: pH: 3, 10 mg/L, 140 rpm, 25–106  $\mu$ m)



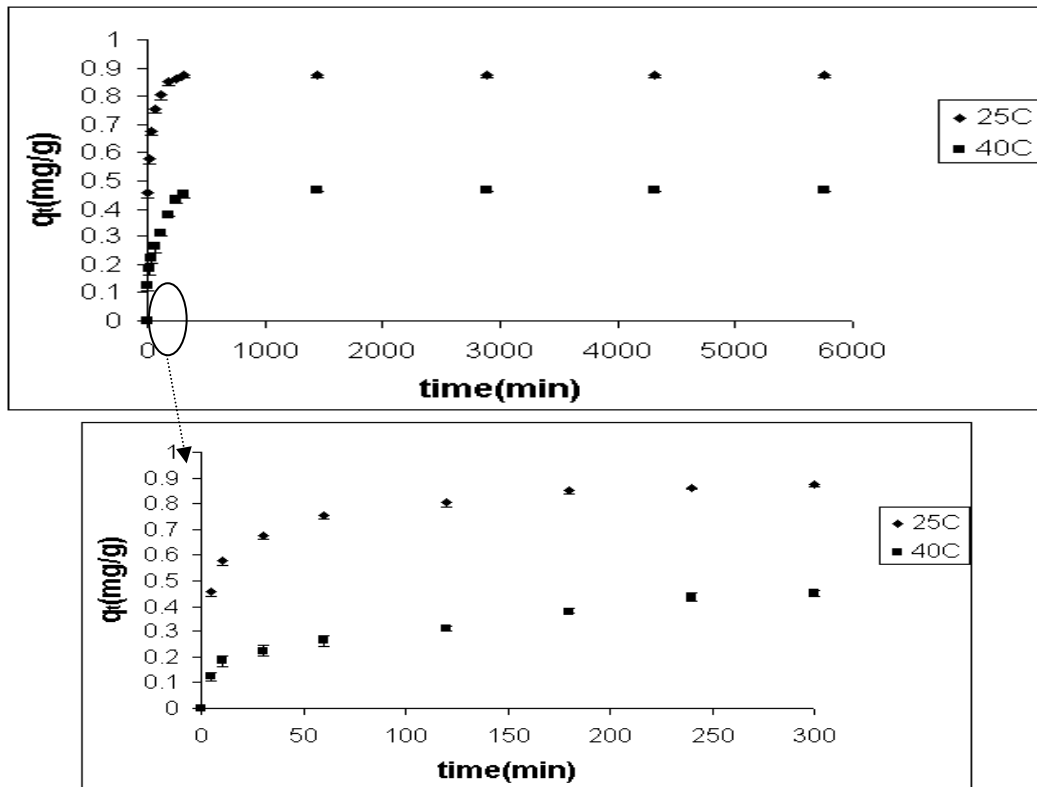


Figure 7.126. Effect of temperature on sorption of Cr (VI) with CMCLI (Conditions: pH: 3, 10 mg/L, 140 rpm, 25–106  $\mu\text{m}$ )

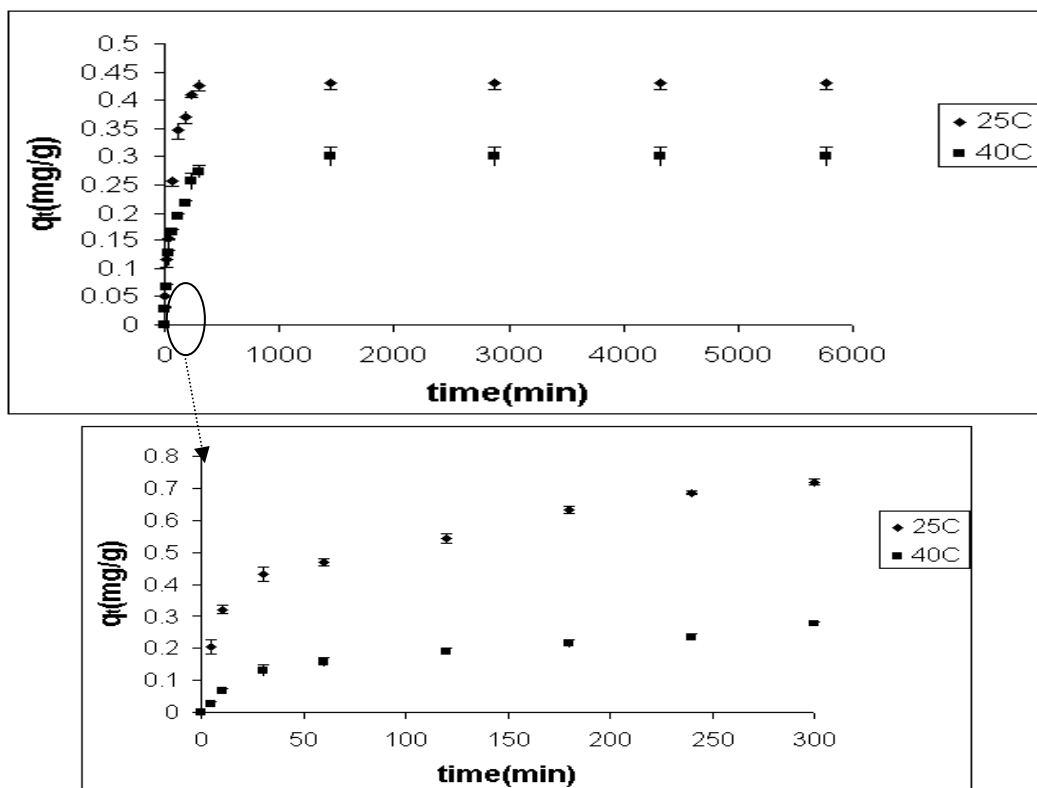


Figure 7.127. Effect of temperature on sorption of Cr (VI) with EC-CLI (Conditions: pH: 3, 10 mg/L, 140 rpm, 25–106  $\mu\text{m}$ )

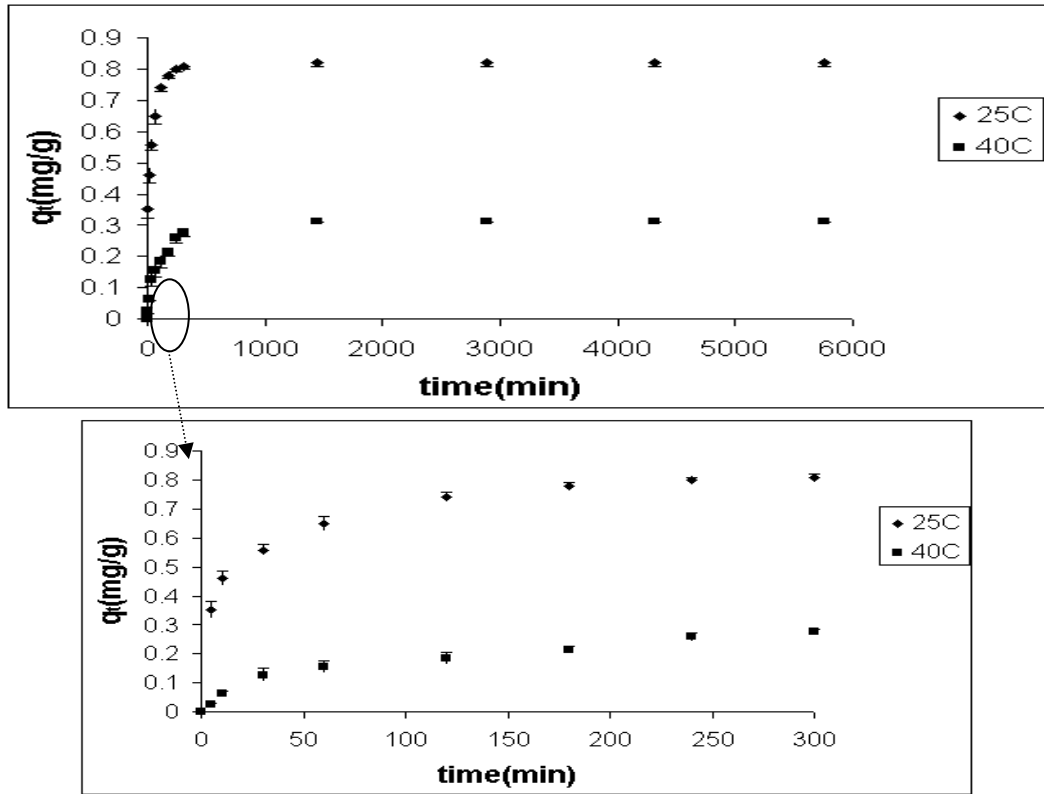


Figure 7.128. Effect of temperature on sorption of Cr (VI) with BS-CLI  
(Conditions: pH: 3, 10 mg/L, 140 rpm, 25–106  $\mu\text{m}$ )

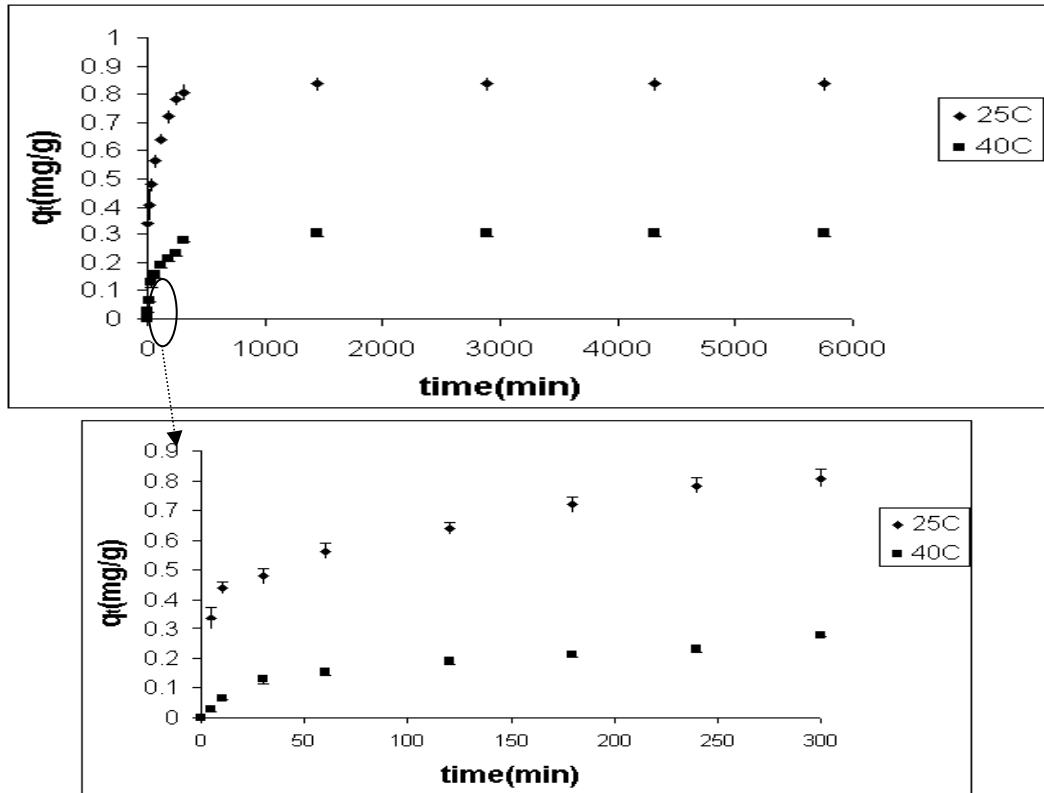


Figure 7.129. Effect of temperature on sorption of Cr (VI) with EC-AMCLI  
(Conditions: pH: 3, 10 mg/L, 140 rpm, 25–106  $\mu\text{m}$ )

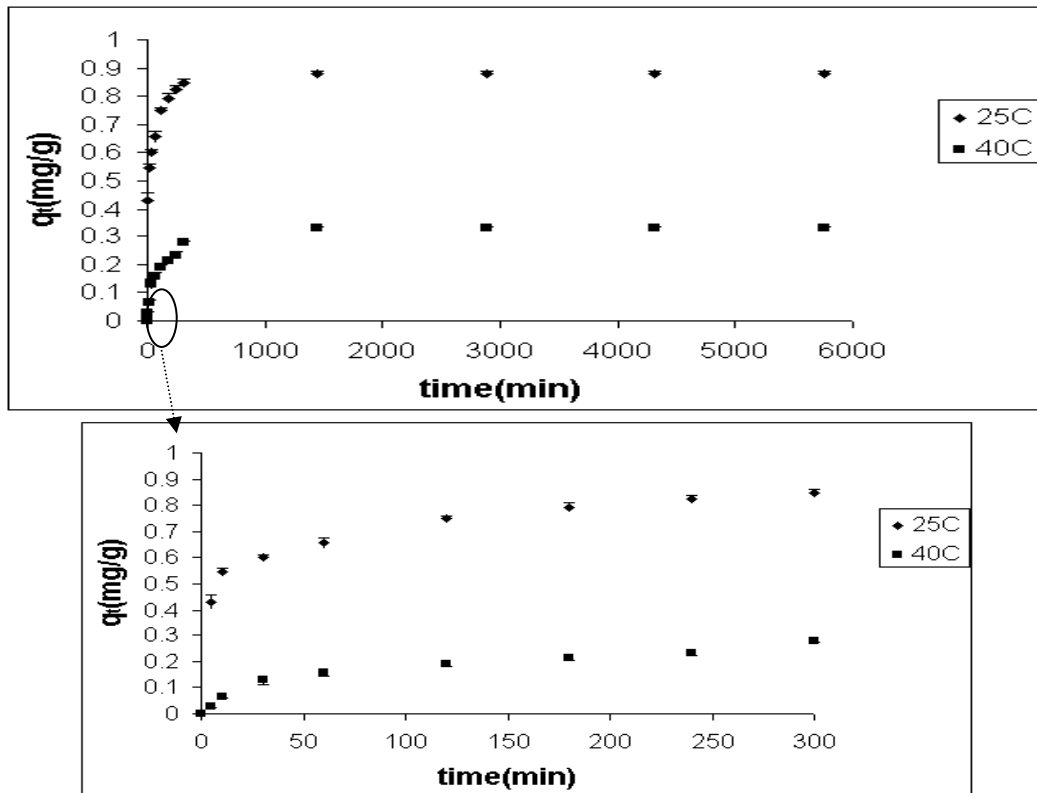


Figure 7.130. Effect of temperature on sorption of Cr (VI) with BS-AMCLI (Conditions: pH: 3, 10 mg/L, 140 rpm, 25–106  $\mu\text{m}$ )

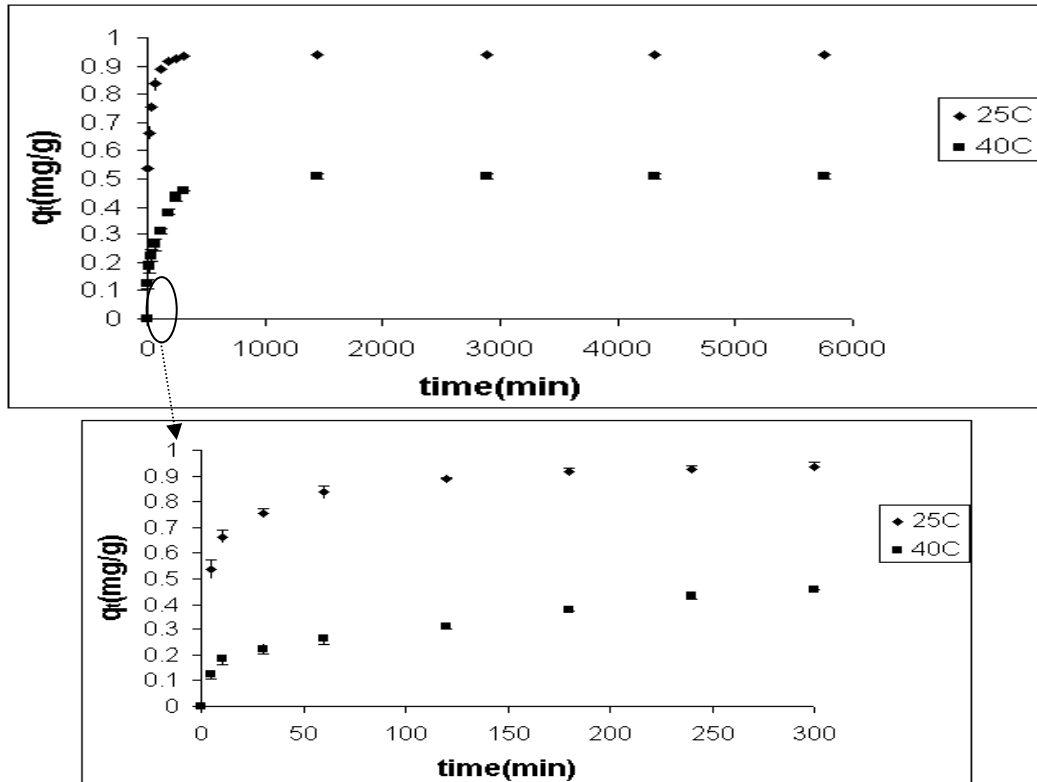


Figure 7.131. Effect of temperature on sorption of Cr (VI) with EC-CMCLI (Conditions: pH: 3, 10 mg/L, 140 rpm, 25–106  $\mu\text{m}$ )

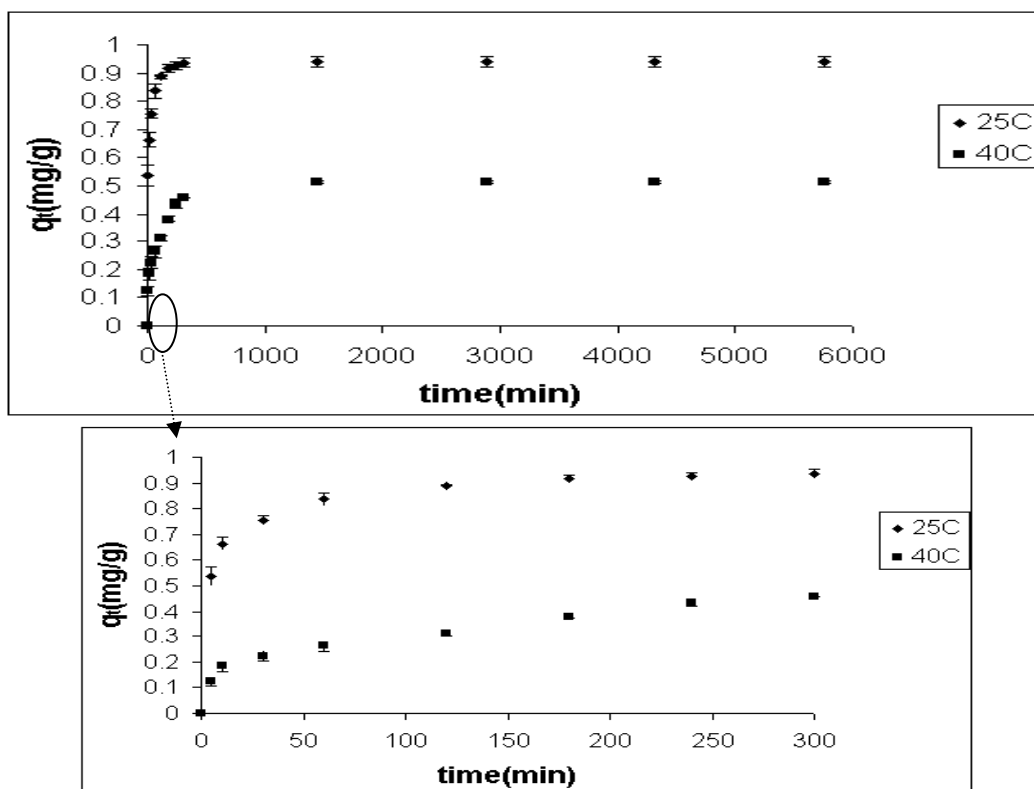


Figure 7.132. Effect of temperature on sorption of Cr (VI) with BS-CMCLI (Conditions: pH: 3, 10 mg/L, 140 rpm, 25–106  $\mu\text{m}$ )

#### 7.4.5. Effect of Particle Size on Cr (VI) Sorption

To understand the effect of the particle size on Cr (VI) sorption, two ranges of particle size distribution (25-106 and 106-425  $\mu\text{m}$ ) were studied. The results are shown in Figure 7.133-7.141. The results indicated that initial uptake rate increased with decreasing particle size. The results also revealed that at equilibrium the amount of Cr (VI) sorbed on the clinoptilolite and bacteria loaded clinoptilolite rich mineral samples did not change with changing of particle size whereas at equilibrium the amount of Cr (VI) sorbed on the surfactant modified clinoptilolite and bacteria loaded surfactant modified clinoptilolite rich mineral samples slightly increased with decreasing particle size. The reason for slightly higher amount of Cr (VI) might be explained by their surfactant amounts. Surfactant amount on the samples increased with decreasing particle size. As the particle size is decreased, the external surface area of the sorbents increases. For smaller particle, a larger external surface area is presented to the surfactant molecule and thus surfactant amount on the samples increases.

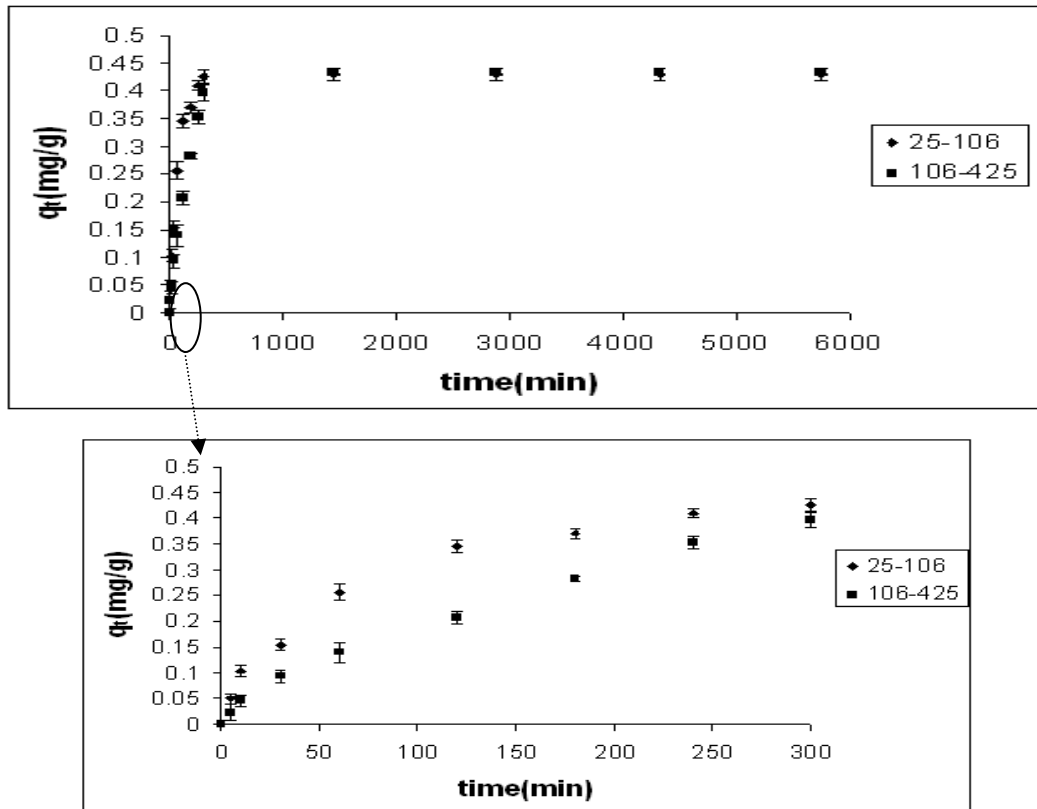


Figure 7.133. Effect of particle size on sorption of Cr (VI) with CLI  
(Conditions: pH: 3, 10 mg/L, 140 rpm, 25°C)

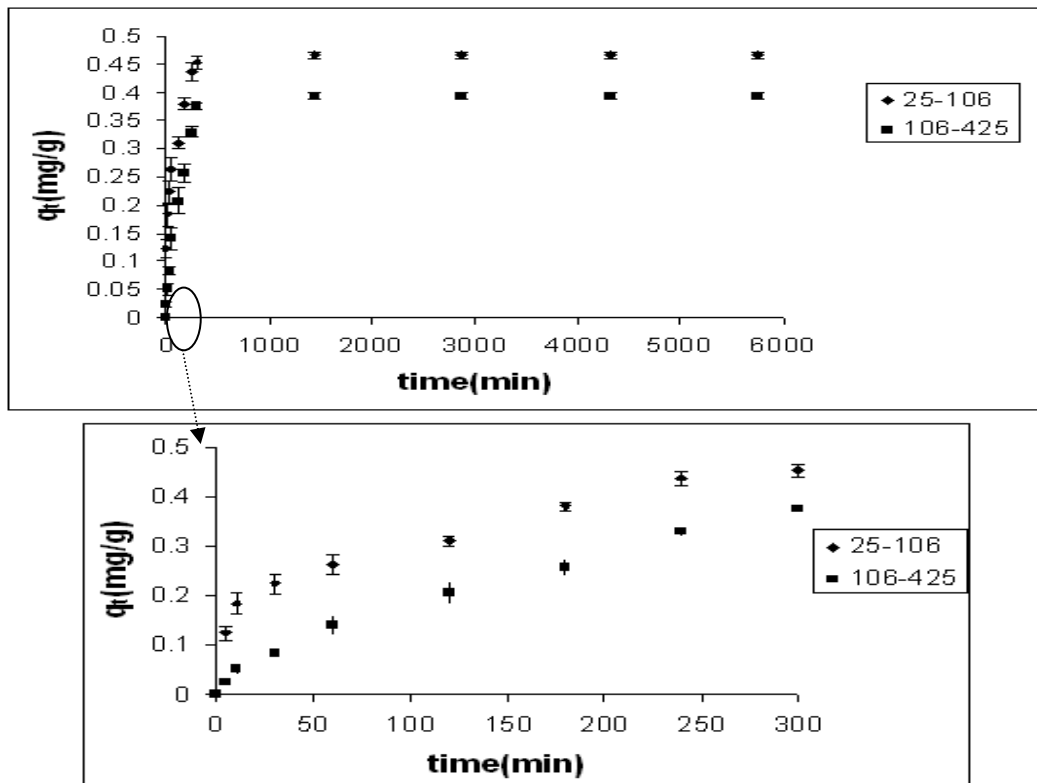


Figure 7.134. Effect of particle size on sorption of Cr (VI) with AMCLI  
(Conditions: pH: 3, 10 mg/L, 140 rpm, 25–106  $\mu\text{m}$ )

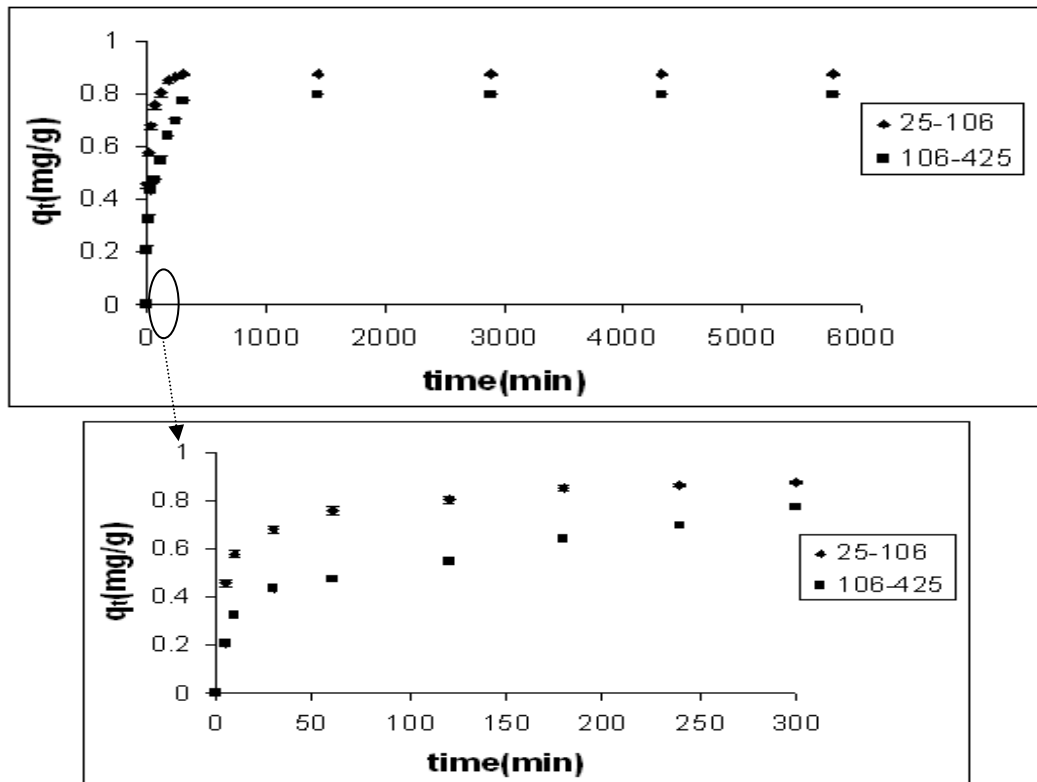


Figure 7.135. Effect of particle size on sorption of Cr (VI) with CMCLI  
(Conditions: pH: 3, 10 mg/L, 140 rpm, 25–106  $\mu\text{m}$ )

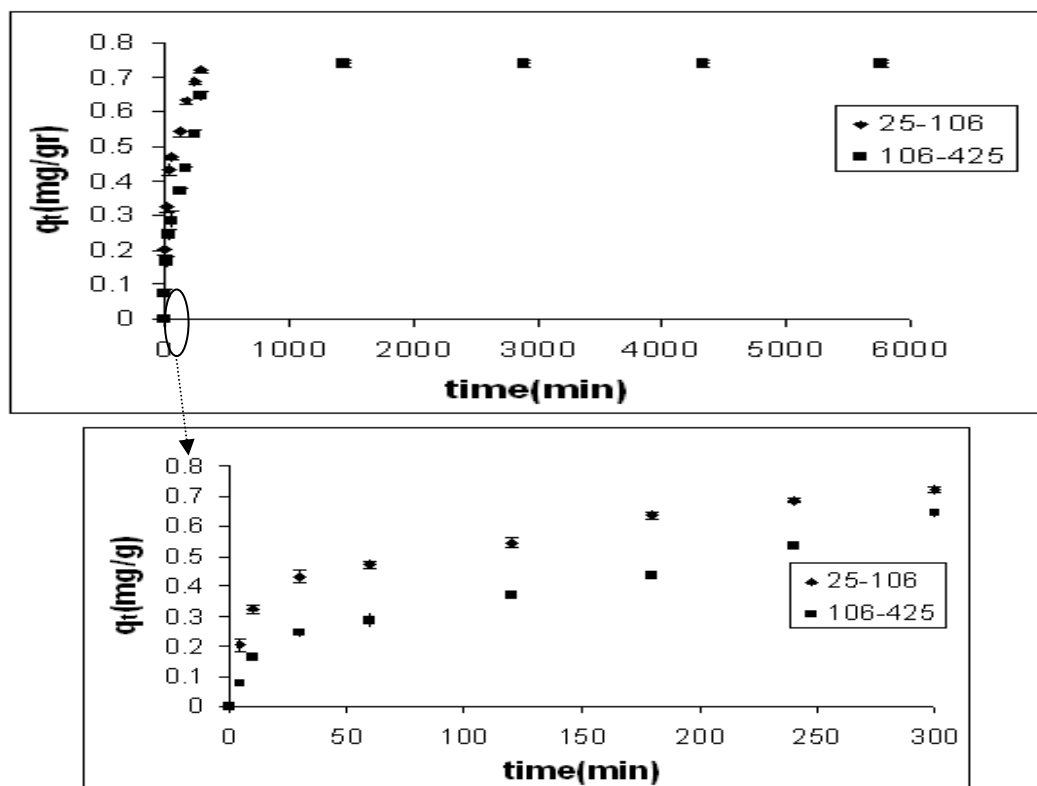


Figure 7.136. Effect of particle size on sorption of Cr (VI) with EC-CLI  
(Conditions: pH: 3, 10 mg/L, 140 rpm, 25–106  $\mu\text{m}$ )

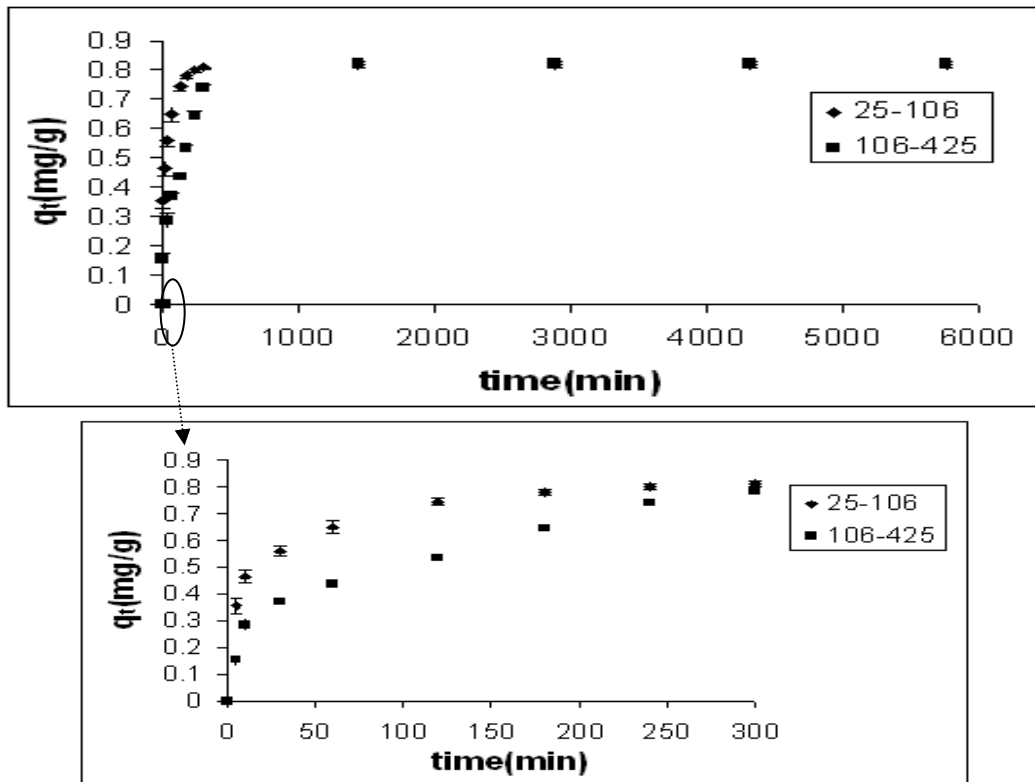


Figure 7.137. Effect of particle size on sorption of Cr (VI) with BS-CLI  
(Conditions: pH: 3, 10 mg/L, 140 rpm, 25–106  $\mu\text{m}$ )

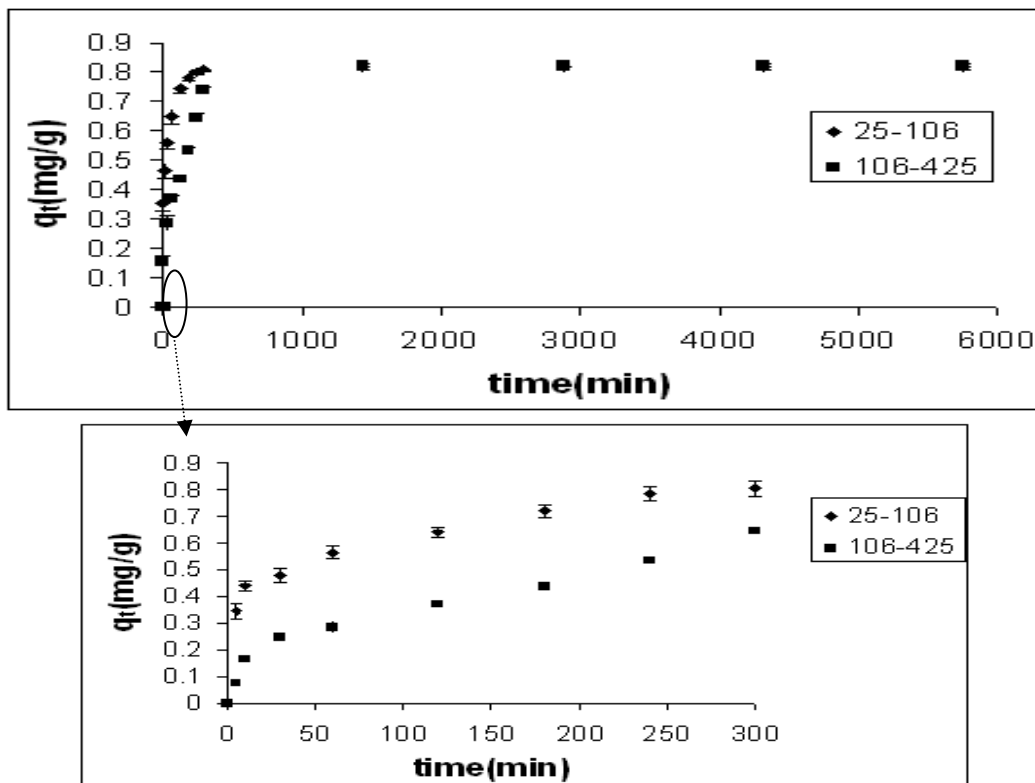


Figure 7.138. Effect of particle size on sorption of Cr (VI) with EC-AMCLI  
(Conditions: pH: 3, 10 mg/L, 140 rpm, 25–106  $\mu\text{m}$ )

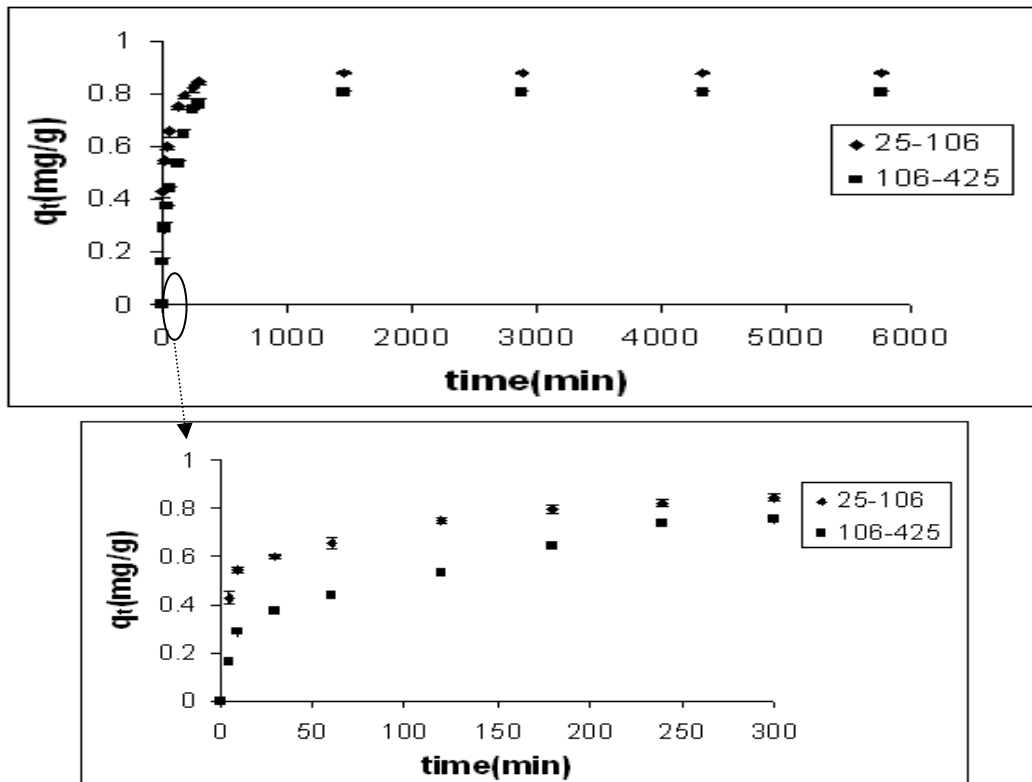


Figure 7.139. Effect of particle size on sorption of Cr (VI) with BS-AMCLI (Conditions: pH: 3, 10 mg/L, 140 rpm, 25–106  $\mu\text{m}$ )

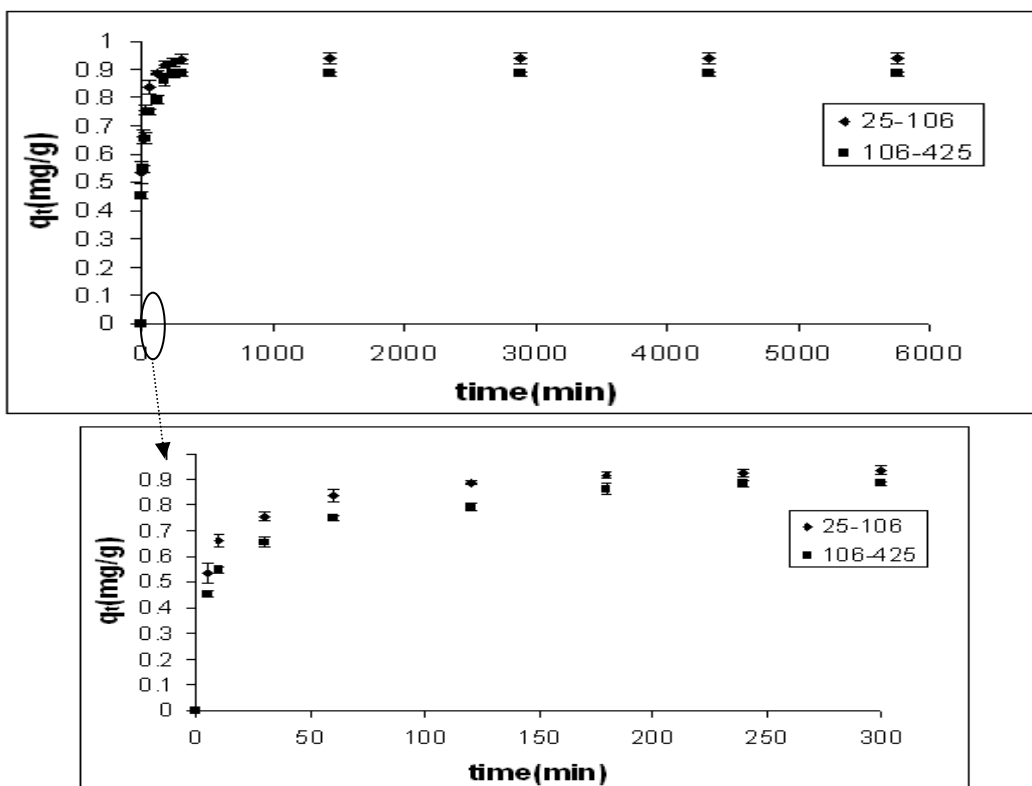


Figure 7.140. Effect of particle size on sorption of Cr (VI) with EC-CMCLI (Conditions: pH: 3, 10 mg/L, 140 rpm, 25–106  $\mu\text{m}$ )



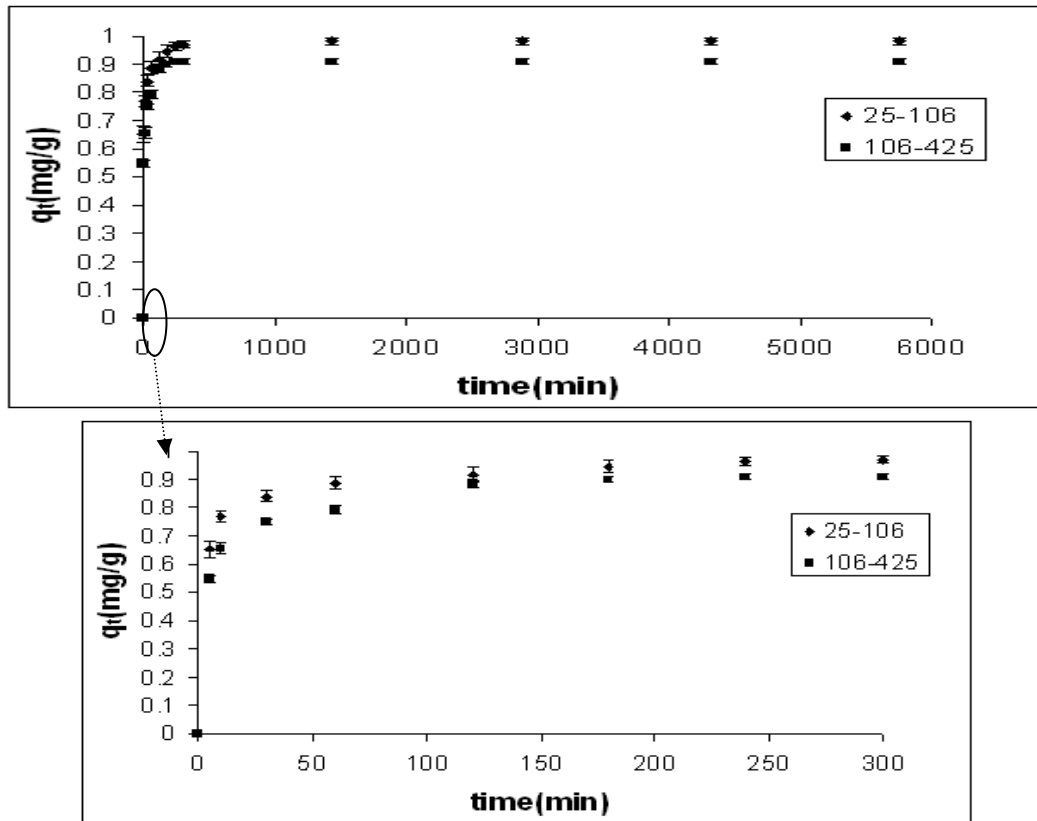


Figure 7.141. Effect of particle size on sorption of Cr (VI) with BS-CMCLI (Conditions: pH: 3, 10 mg/L, 140 rpm, 25–106  $\mu\text{m}$ )

## 7. 5. Sorption Kinetic Model Results

Sorption diffusion models were used to evaluate the contribution of external and internal mass transfer during sorption of Cr (VI) onto natural, surfactant modified and bacteria loaded forms.

External mass transfer coefficient was calculated by two models: (1) Mathew-Weber and (2) Furusawa-Smith. Both model assumed that only external diffusion resistance was predominant during the initial sorption period and controlled the sorption rate. The external mass transfer coefficient for Mathew-Weber model was calculated from the slope of plot of  $\ln C/C_0$  vs. time. In Furusawa-Smith model, the external mass-transfer coefficient was determined by incorporating the linear region of the isotherm. The external mass transfer coefficient for this model was determined from the slope of

$$\left( \frac{1}{1 + \frac{1}{\frac{m}{V}K_L}} \right) \ln \left( \frac{C_t}{C_0} - \frac{1}{\frac{m}{V}K_L} \left( 1 - \frac{C_t}{C_0} \right) \right) \text{ versus time. (Appendix F.1)}$$

Weber-Morris model was used to calculate the intraparticle diffusion rate constant ( $k_d$ ). This model assumed that the external mass transfer resistance was not significant or only significant during the initial sorption period. The intraparticle diffusion rate constant ( $k_d$ ) was calculated from the slope of plot of  $q_t$  versus  $t^{0.5}$ . According to Weber and Morris (1963), if the rate-limiting step is intraparticle diffusion, a plot of  $q_t$  versus  $t^{0.5}$  should yield a straight line passing through the origin. If the plot  $q_t$  versus  $t^{0.5}$  shows multi linearity, two or more steps are involved in the sorption process. Allen et al. (1989) stated the multi-linearity of the intraparticle diffusion plots may due to two or more steps occurring. The first sharp section is instant or the external mass transfer. The second section is the gradual sorption where intraparticle diffusion is rate limiting. The third section is the final equilibrium stage where intra-particle diffusion starts to slow down. McKay and Poots (1980) identified three linear sections on the  $q_t$  versus  $t^{0.5}$  plot by extending the model over longer periods. The authors explained the three sections in terms of pore diameters: macropores, mesopores and micropores. Walker et al., (2003) stated four regions on the  $q_t$  versus  $t^{0.5}$  plot. The initial stage represents external mass transfer, with the following three stages representing intra-particle diffusion in the macro, meso and micropore structure of the sorbent.

Weber-Morris plot often show multilinearity coming from several linear segments. The misuse of choosing of the linear segments is the most common error in Weber-Morris model analysis. The uncertainty in determining linear segments leads to uncertainties in calculating their slopes and intercepts, and consequently uncertainties in estimating intraparticle diffusion rate constant. The linear segments can be either chosen visually or determined numerically. In some cases, boundaries between linear segments are obvious and linear segments can be chosen from breakpoints which are obtained from boundaries between linear segments. However, in some cases, boundaries between linear segments are hidden and thus the linear segments are determined numerically. Malash and El-Khaiary (2010) developed piecewise linear regression method (PLR) to solve the linear segments numerically. In this method, each of linear segments and its points is identified and then linear regression method is applied to these points and the corresponding intraparticle diffusion rate constant is estimated. The steps in PLR model is shown in Figure 7.142.

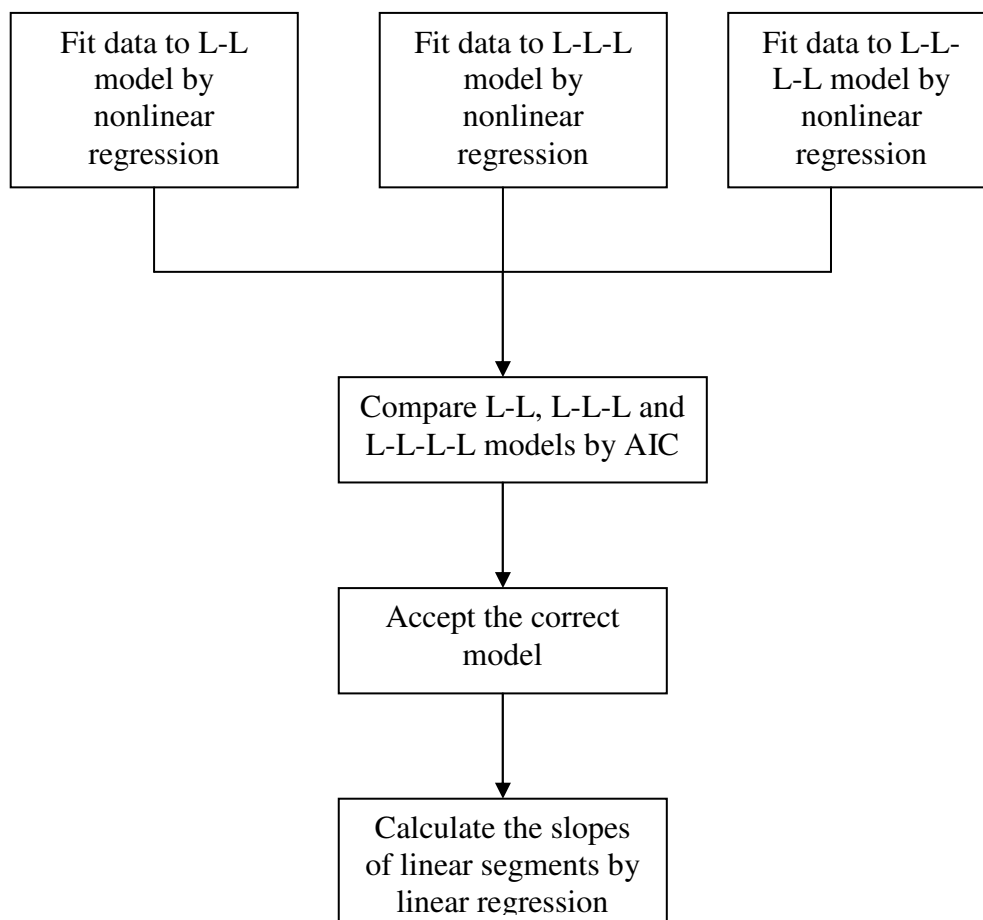


Figure 7.142. The steps in PLR model

Firstly, statistical methods are applied to fit experimental data and the regression analysis is performed separately for linear segments. The common equation of piecewise regression for linear segments is expressed as:

$$Y = a_1 + b_1X \quad X \leq J_1 \quad (7.3)$$

$$Y = a_2 + b_2X \quad J_2 \geq X \geq J_1 \quad (7.4)$$

$$Y = a_n + b_nX \quad X \geq J_n \quad (7.5)$$

where Y is the dependent variable, X is the independent variable,  $J_1$  to  $J_n$  are the breakpoints,  $a_1$  to  $a_n$  are the slopes of the linear segments,  $b_1$  to  $b_n$  are the intercepts of linear segments.

The nonlinear regression is calculated by minimizing the sum of squared deviations, (SSE) and performed using the Solver Method. The objective function for minimization is given as:

$$SSE = \sum_{i=1}^N (Y_{\text{exp}} - Y_{\text{est}})^2 \quad (7.6)$$

The regression parameters for two (L-L), three (L-L-L) and four (L-L-L-L) linear segments are calculated minimizing the sum of squared deviations. After determination of regression parameters, breakpoints of the linear segments are identified and then model data is divided into linear segments based on the values of breakpoints. The slopes and intercepts of linear segments are accurately determined.

The values of Akaike's Information Criterion (AIC) are helpful to decide which linear segments are statistically significant. The value of AIC can be positive or negative and its sign has no significance. When AIC values for two (L-L), three (L-L-L) and four (L-L-L-L) linear segments models are compared, it is seen that their absolute values should be taken into account. The correct model is chosen by considering lower AIC values. AIC values are calculated from the following equations:

$$AIC = N \ln \frac{SSE}{N} + 2N_p + \frac{2N_p(N_p + 1)}{N - N_p - 1} \quad (7.7)$$

where  $N$  is the number of data points and  $N_p$  is the number of parameters in the model.

The model results of PLR method are given in Appendix F.2-F.3. The results indicated that three linear segments (L-L-L) had lower AIC values than two linear segments (L-L). For this reason, three linear segments (L-L-L) was statistically significant than two (L-L) linear segments and thus three linear segments (L-L-L) model was used in the calculation of intraparticle diffusion rate constant.

The effective diffusion coefficient ( $D_{\text{eff}}$ ) for short and long time period was determined from the slope of the plot of  $q_t/q_e$  versus  $\sqrt{t}$  and  $\ln [1 - q_t/q_e]$  versus  $t$ , respectively (Appendix F.4). The values of effective diffusion coefficient give the idea about the rate limiting step. According to Michelson et al., (1975) for external film diffusion to be rate limiting step, the value of diffusion coefficient should be in range between  $10^{-6}$  and  $10^{-8}$   $\text{cm}^2/\text{s}$ , and for intraparticle diffusion to be rate limiting step, the value of diffusion coefficient should be in range between  $10^{-11}$  and  $10^{-13}$   $\text{cm}^2/\text{s}$ .

Sorption reaction models include pseudo-first and second order model. The pseudo first order rate constant ( $k_1$ ) was determined using Lagergren kinetic model. This model assumed that the rate of change of solute uptake with time was directly proportional to the difference in saturation concentration and the amount of solid uptake with time. The pseudo first order rate constant ( $k_1$ ) is determined from the slope of plot of the  $\log (q_e - q_t)$  versus  $t$  (Appendix F.5).

Pseudo second order rate constant ( $k_2$ ) was determined using Ho and McKay model. This model assumed that the sorption process was a pseudo-chemical reaction process with the driving force being the difference between the average solid concentration and the equilibrium concentration with the overall sorption rate proportional to the square of the driving force. The pseudo second-order rate constant ( $k_2$ ) values were determined from intercepts of the plots of  $t/q_t$  versus  $t$  (Appendix F.5).

External mass transfer coefficient ( $k_f$ ), intraparticle diffusion rate constant ( $k_d$ ), pseudo first ( $k_1$ ) and second order ( $k_2$ ) rate constant, effective diffusion coefficient ( $D_{eff}$ ) for short and long term were determined for each experimental parameters including initial concentration, agitation speed, temperature, pH and particle size. Their values are tabulated in Table 7.19-7.27.

The values of correlation coefficient of models for all sorbents were given in Appendix F.6. The correlation coefficients of Mathew-Weber and Furusawa-Smith model for different sorbents were in the range of 0.91- 0.99. The correlation coefficient ( $R^2$ ) values of Weber-Morris model were higher than 0.94. For the pseudo first order kinetic model, the obtained  $R^2$  values were between 0.70 and 0.91. The values of  $R^2$  for the pseudo second-order model were always greater than 0.98. The results indicated that pseudo-second order kinetic model and Weber-Morris model fitted well with the experimental data more accurately than the pseudo first order kinetic model and Mathew-Weber and Furusawa-Smith model.

Table 7.19. The values of model constants at different conditions for CLI

Parameters	MW	FS	WM	Effective Diffusion Coefficient		PFO	PSO	
	$k_f \cdot 10^6$ (m/min)	$k_f \cdot 10^6$ (m/min)	$k_d \cdot 10^3$ (mg/grmin <sup>0.5</sup> )	$De \cdot 10^{14}$ (m <sup>2</sup> /s) short time	$De \cdot 10^{14}$ (m <sup>2</sup> /s) long time	$k_1 \cdot 10^3$ (min <sup>-1</sup> )	$k_2 \cdot 10^3$ (gr/mgmin)	
Initial Concentration (mg/L)	10	15.1	14.2	34.8	0.99	2.2	13.6	82.9
	50	3.6	3.5	52.9	0.57	1.1	9.4	9.4
	100	1.9	2	96.5	0.31	1.1	5.1	7.0
	200	1.1	1.1	137.3	0.15	1.1	3.5	5.7
	300	1.0	0.9	158.7	0.08	1.1	2.5	4.1
Agitation Speed (rpm)	60	6.2	6	17.7	0.25	1.1	7.6	33.1
	100	8.9	8.5	22.4	0.36	1.1	12.2	41.1
	140	15.1	14.2	34.8	0.99	2.2	13.6	82.9
Temperature (°C)	25	15.1	14.2	34.8	0.99	2.2	13.6	82.9
	40	7.9	7.6	22.8	0.53	0.9	11.2	52.6
pH	3	15.1	14.2	34.8	0.99	2.2	13.6	82.9
	11	9.3	8.9	27.7	0.58	1.1	11.2	63.8
Particle size (µm)	25-106	15.1	14.2	34.8	0.99	2.2	13.6	82.9
	106-425	41.2	39.6	20.5	4.2	17.8	7.8	26.4

MW: Mathew-Weber, FS: Furusawa-Smith, WM: Weber-Morris, PFO: Pseudo-first order model, PSO: Pseudo-second order model

Table 7.20. The values of model constants at different conditions for AMCLI

Parameters	MW	FS	WM	Effective Diffusion Coefficient		PFO	PSO
	$k_f \cdot 10^6$ (m/min)	$k_f \cdot 10^6$ (m/min)	$k_d \cdot 10^3$ (mg/grmin <sup>0.5</sup> )	$De \cdot 10^{14}$ (m <sup>2</sup> /s) short time	$De \cdot 10^{14}$ (m <sup>2</sup> /s) long time	$k_1 \cdot 10^3$ (min <sup>-1</sup> )	$k_2 \cdot 10^3$ (gr/mgmin)
Initial Concentration (mg/L)	10	24	37.5	2.2	2.2	18.7	75.8
	50	4.3	50	0.64	1.1	9.4	9.6
	100	2.1	100.6	0.32	1.1	5.5	8.1
	200	1.4	137.9	0.16	1.1	3.9	5.8
	300	1.3	157.3	0.08	1.1	2.1	5.1
Agitation Speed (rpm)	60	6.6	17.7	0.76	1.1	7.6	33.2
	100	9.2	31	1.2	1.1	13.1	44.2
Temperature (°C)	140	24	37.5	2.2	2.2	18.7	75.8
	25	24	37.5	2.2	2.2	18.7	75.8
pH	40	8.3	27	0.64	1.0	16.4	53
	3	24	37.5	2.2	2.2	18.7	75.8
Particle size (µm)	11	9.6	17.7	0.25	1.1	14.2	62.1
	25-106	24	37.5	2.2	2.2	18.7	75.8
	106-425	42.1	20.9	4.2	18.1	7.6	32.8

MW: Mathew-Weber, FS: Furusawa-Smith, WM: Weber-Morris, PFO: Pseudo-first order model, PSO: Pseudo-second order model

Table 7.21. The values of model constants at different conditions for CMCLI

Parameters	MW	FS	WM	Effective Diffusion Coefficient		PFO	PSO
	$k_f \cdot 10^6$ (m/min)	$k_f \cdot 10^6$ (m/min)	$k_d \cdot 10^3$ (mg/grmin <sup>0.5</sup> )	$De \cdot 10^{14}$ (m <sup>2</sup> /s) short time	$De \cdot 10^{14}$ (m <sup>2</sup> /s) long time	$k_1 \cdot 10^3$ (min <sup>-1</sup> )	$k_2 \cdot 10^3$ (gr/mgmin)
Initial Concentration (mg/L)	10	115	100	63.1	3.3	42.4	209.3
	50	16.6	15.6	154	1.1	11.7	5.7
	100	8.2	7.8	176.8	0.37	1.1	5.1
	200	5.8	5.6	216.3	0.34	1.1	4.4
	300	2.7	2.6	223.1	0.27	1.1	4.1
Agitation Speed (rpm)	60	47.1	39.7	38.2	1.1	17.2	40.7
	100	99.6	84.1	45.7	2.2	27.1	87.1
	140	115	100	63.1	3.3	42.4	209.3
Temperature (°C)	25	115	100	63.1	3.3	42.4	209.3
	40	27.1	24.5	33	2.2	18.7	107.1
pH	3	115	100	63.1	3.3	42.4	209.3
	11	41	35.1	42.1	2.2	27.9	147.2
Particle size (µm)	25-106	115	100	63.1	3.3	42.4	209.3
	106-425	209	187.3	47.5	17.9	23.5	44.1

MW: Mathev-Weber, FS: Furusawa-Smith, WM: Weber-Morris, PFO: Pseudo-first order model, PSO: Pseudo-second order model

\*:  $q/q_{\infty} > 0.3$



Table 7.22. The values of model constants at different conditions for ECCLI

Parameters	MW	FS	WM	Effective Diffusion Coefficient		PFO	PSO	
	$k_f \cdot 10^6$ (m/min)	$k_f \cdot 10^6$ (m/min)	$k_d \cdot 10^3$ (mg/grmin <sup>0.5</sup> )	$De \cdot 10^{14}$ (m <sup>2</sup> /s) short time	$De \cdot 10^{14}$ (m <sup>2</sup> /s) long time	$k_1 \cdot 10^3$ (min <sup>-1</sup> )	$k_2 \cdot 10^3$ (gr/mgmin)	
Initial Concentration (mg/L)	10	49.3	40.7	47.5	2.4	2.2	26.5	62.7
	50	7.6	7.3	84.5	0.41	1.1	14.1	8.1
	100	3.8	3.6	96.4	0.28	1.1	8.1	7.8
	200	1.9	1.9	123.5	0.24	1.1	7.4	5.7
	300	1.4	1.3	167.4	0.22	1.1	6.6	4.1
Agitation Speed (rpm)	60	26.7	23.9	32.6	1.1	1.1	15.2	30.4
	100	32.9	30.6	41.5	1.8	1.1	18	38.7
	140	49.3	40.7	47.5	2.4	1.1	26.5	62.7
Temperature (°C)	25	49.3	40.7	47.5	2.4	2.2	26.5	62.7
	40	8.7	8.4	24.1	0.65	1.1	20.3	31.1
pH	3	49.3	40.7	47.5	2.4	2.2	26.5	62.7
	11	17.1	16.1	21.4	0.72	1.1	14.5	42.8
Particle size (µm)	25-106	49.3	40.7	47.5	2.4	2.2	26.5	62.7
	106-425	89.7	82.2	27.2	5.1	12.5	12.2	21.2

MW: Mathew-Weber, FS: Furusawa-Smith, WM: Weber-Morris, PFO: Pseudo-first order model, PSO: Pseudo-second order model

\*:  $q_t/q_{\infty} > 0.3$

Table 7.23. The values of model constants at different conditions for BSCLI

Parameters	MW	FS	WM	Effective Diffusion Coefficient		PFO	PSO
	$k_f \cdot 10^6$ (m/min)	$k_f \cdot 10^6$ (m/min)	$k_d \cdot 10^3$ (mg/grmin <sup>0.5</sup> )	$De \cdot 10^{14}$ (m <sup>2</sup> /s) short time	$De \cdot 10^{14}$ (m <sup>2</sup> /s) long time	$k_1 \cdot 10^3$ (min <sup>-1</sup> )	$k_2 \cdot 10^3$ (gr/mgmin)
Initial Concentration (mg/L)	10	78.2	68.2	59.5	2.2	32.7	136.6
	50	12.2	11.6	119.4	0.6	13.8	10.6
	100	5.7	5.5	139.6	0.5	12.4	8.2
	200	3.2	3.0	158.4	0.4	9.7	4.5
	300	1.9	1.9	163.7	0.34	9.4	4.1
Agitation Speed (rpm)	60	40.8	35.8	42.6	1.1	16.8	35.7
	100	44.3	39.4	51.5	1.1	17.3	40.7
	140	78.2	68.2	59.5	1.1	32.7	136.6
Temperature (°C)	25	78.2	68.2	59.5	2.2	32.7	136.6
	40	21.2	19.4	36	0.53	17.3	78.2
pH	3	78.2	68.2	59.5	2.2	32.7	136.6
	11	18	15.9	26.7	1.1	15.9	82.9
Particle size (µm)	25-106	78.2	68.2	59.5	2.2	32.7	136.6
	106-425	170	164.4	24	17.9	18	58.2

MW: Mathew-Weber, FS: Furusawa-Smith, WM: Weber-Morris, PFO: Pseudo-first order model, PSO: Pseudo-second order model

\*:  $q_t/q_\infty > 0.3$

Table 7.24. The values of model constants at different conditions for ECAMCLI

Parameters	MW	FS	WM	Effective Diffusion Coefficient		PFO	PSO
	$k_f \cdot 10^6$ (m/min)	$k_f \cdot 10^6$ (m/min)	$k_d \cdot 10^3$ (mg/grmin <sup>0.5</sup> )	$De \cdot 10^{14}$ (m <sup>2</sup> /s) short time	$De \cdot 10^{14}$ (m <sup>2</sup> /s) long time	$k_1 \cdot 10^3$ (min <sup>-1</sup> )	$k_2 \cdot 10^3$ (gr/mgmin)
Initial Concentration (mg/L)	10	71.8	64.5	75.6	-	23.1	61.7
	50	11.8	11.4	133.2	0.51	11.5	9.3
	100	5.9	5.7	152.3	0.46	10.2	7.7
	200	3.1	3.0	174.5	0.41	9.9	6.3
	300	2.1	2.1	188.4	0.39	8.9	4.7
Agitation Speed (rpm)	60	44.6	38.1	46.7	1.94	16.8	35.7
	100	62.6	60.9	58.4	-	19.2	46.9
	140	71.8	64.5	75.6	-	23.1	61.7
Temperature (°C)	25	71.8	64.5	75.6	-	23.1	61.7
	40	19.5	19.2	38.1	0.65	18.4	29.7
pH	3	71.8	64.5	75.6	-	23.1	61.7
	11	18.6	17.5	31.2	1.3	15.9	41.7
Particle size (µm)	25-106	71.8	64.5	75.6	-	23.1	61.7
	106-425	97.9	89.7	37.2	5	12.7	18.1

MW: Mathew-Weber, FS: Furusawa-Smith, WM: Weber-Morris, PFO: Pseudo-first order model, PSO: Pseudo-second order model

\*:  $q_t/q_\infty > 0.3$

Table 7.25. The values of model constants at different conditions for BSAMCLI

Parameters	MW	FS	WM	Effective Diffusion Coefficient		PFO	PSO	
	$k_f \cdot 10^6$ (m/min)	$k_f \cdot 10^6$ (m/min)	$k_d \cdot 10^3$ (mg/grmin <sup>0.5</sup> )	$De \cdot 10^{14}$ (m <sup>2</sup> /s) short time	$De \cdot 10^{14}$ (m <sup>2</sup> /s) long time	$k_1 \cdot 10^3$ (min <sup>-1</sup> )	$k_2 \cdot 10^3$ (gr/mgmin)	
Initial Concentration (mg/L)	10	105.4	92.8	84	-*	2.2	31.1	84.4
	50	17.8	16.6	146.9	0.99	0.9	13.8	8.3
	100	7.2	6.9	188.6	0.60	0.9	11.7	5.6
	200	2.9	3	206.5	0.30	0.9	8.3	4.1
	300	2	2	221.8	0.26	0.9	7.8	3.6
Agitation Speed (rpm)	60	46.9	39.5	62.4	2.49	1.1	17.3	40.7
	100	98.7	89.6	76.2	-*	1.1	24.5	78.1
	140	105.4	92.8	84	-*	2.2	31.1	84.4
Temperature (°C)	25	105.4	92.8	84	-*	2.2	31.1	84.4
	40	29.2	29.2	43.6	0.56	0.8	16.8	43.2
pH	3	105.4	92.8	84	-*	2.2	31.1	84.4
	11	20.1	17.9	38.4	0.55	0.7	21.4	47.4
Particle size (µm)	25-106	105.4	92.8	84	-*	2.2	31.1	84.4
	106-425	180	168.4	43.2	21.1	18	18.4	37.2

MW: Mathew-Weber, FS: Furusawa-Smith, WM: Weber-Morris, PFO: Pseudo-first order model, PSO: Pseudo-second order model

\*:  $q/q_{\infty} > 0.3$

Table 7.26. The values of model constants at different conditions for ECCMCLI

Parameters	MW	FS	WM	Effective Diffusion Coefficient		PFO	PSO
	$k_f \cdot 10^6$ (m/min)	$k_f \cdot 10^6$ (m/min)	$k_d \cdot 10^3$ (mg/grmin <sup>0.5</sup> )	$De \cdot 10^{14}$ (m <sup>2</sup> /s) short time	$De \cdot 10^{14}$ (m <sup>2</sup> /s) long time	$k_1 \cdot 10^3$ (min <sup>-1</sup> )	$k_2 \cdot 10^3$ (gr/mgmin)
Initial Concentration (mg/L)	10	147.6	117.7	-*	3.3	46.1	227.5
	50	22.1	20.1	0.35	1.1	9.2	4.6
	100	8.9	8.7	151.9	0.29	1.1	8.3
	200	4.5	4.4	179.7	0.25	1.1	7.8
	300	2.7	2.6	199.1	0.24	1.1	7.4
Agitation Speed (rpm)	60	116.4	105.8	-*	1.1	42.4	200.7
	100	140.7	127.5	-*	2.2	44.2	209.3
	140	147.6	117.7	-*	3.3	46.1	227.5
Temperature (°C)	25	147.6	117.7	-*	3.3	46.1	227.5
	40	27.5	26.4	32.1	1.8	1.1	16.5
pH	3	147.6	117.7	62.6	-*	46.1	227.5
	11	23.5	21.2	28.4	1.1	2.2	112.9
Particle size (µm)	25-106	147.6	117.7	62.6	-*	46.1	227.5
	106-425	182.8	176.4	43.2	22.4	17.9	84.4

MW: Mathew-Weber, FS: Furusawa-Smith, WM: Weber-Morris, PFO: Pseudo-first order model, PSO: Pseudo-second order model

\*:  $q/q_{\infty} > 0.3$

Table 7.27. The values of model constants at different conditions for BSCMCLI

Parameters	MW	FS	WM	Effective Diffusion Coefficient		PFO	PSO
	$k_f \cdot 10^6$ (m/min)	$k_f \cdot 10^6$ (m/min)	$k_d \cdot 10^3$ (mg/grmin <sup>0.5</sup> )	$De \cdot 10^{14}$ (m <sup>2</sup> /s) short time	$De \cdot 10^{14}$ (m <sup>2</sup> /s) long time	$k_1 \cdot 10^3$ (min <sup>-1</sup> )	$k_2 \cdot 10^3$ (gr/mgmin)
Initial Concentration (mg/L)	10	195.7	182.4	106	3.3	53.4	225.6
	50	24.8	20.4	125.6	1.1	8.6	3.9
	100	11.7	10.7	183.7	0.33	7.8	3.4
	200	5.9	5.2	192.4	0.28	7.6	3.2
	300	3.7	3.6	201.6	0.24	6.9	2.4
Agitation Speed (rpm)	60	114.5	101.4	82.4	1.1	40.8	119.9
	100	138.5	129.6	92.6	2.2	42.3	202.5
	140	195.7	182.4	106	3.3	53.4	225.6
Temperature (°C)	25	195.7	182.4	106	3.3	53.4	225.6
	40	27	25.3	51.2	0.9	16.4	105.2
pH	3	195.7	182.4	106	3.3	53.4	225.6
	11	23.7	20.6	42.4	1.1	20.5	85.2
Particle size (µm)	25-106	195.7	182.4	106	3.3	53.4	225.6
	106-425	221	204.6	69.4	18	14.9	80.4

MW: Mathew-Weber, FS: Furusawa-Smith, WM: Weber-Morris, PFO: Pseudo-first order model, PSO: Pseudo-second order model

\*:  $q/q_{\infty} > 0.3$

As seen from the tables, the effects of initial concentration, agitation speed, temperature, pH and particle size are similar for all the sorbents (clinoptilolite, surfactant modified clinoptilolite and bacteria loaded forms).

The sorption diffusion model results implied that an increase in the initial concentration in solution caused an increase in the external mass transfer resistance and consequently a decrease in the initial rate of sorption. This can be attributed to the molecular interaction between solute molecules and greater competition between solute molecules for the available sorption sites, which appears to have more influence on the initial sorption rate than driving force of diffusion. The intraparticle diffusion rate constant increased with increasing initial concentration. The increase of Cr (VI) concentration resulted in an increase in the driving force and thus diffusion rate of Cr (VI) into the pores increased. The values of  $D_{\text{eff}}$  for short and long time period decreased with increasing initial concentration. The sorption kinetic model results indicated that the values of pseudo first ( $k_1$ ) and second order ( $k_2$ ) decreased with increasing initial concentration.

Increasing agitation speed caused to decrease in the thickness of the boundary layer resistance surrounding the particle and thus external mass transfer resistance decreased with increasing agitation speed. Intraparticle diffusion rate constants ( $k_d$ ) increased with increasing agitation speed. High agitation rate could overcome the boundary layer resistance and subsequently increased the intraparticle diffusion rate constant. The values of  $D_{\text{eff}}$  for short and long time period increased with increasing agitation speed. The diffusion rate of molecule increases with increasing agitation speed and thus the molecule reach the sorbent surface more rapidly. The sorption kinetic model results indicated that the values of pseudo first and second order rate constant increased with increasing agitation speed.

Increasing temperature served to increase external mass transfer resistance and intraparticle diffusion resistance. The values of  $D_{\text{eff}}$  for short and long time period decreased with increasing temperature. The sorption kinetic model results indicated that the values of pseudo first ( $k_1$ ) and second order ( $k_2$ ) decreased with increasing temperature.

An increase in pH of the solution caused an increase in the external and intraparticle mass transfer resistance. At high pH values, the repulsive electrostatic forces between the sorbents and Cr (VI) species got stronger. Diffusion rate decreased with increasing pH value because of existence of repulsive electrostatic forces. Effective

diffusion coefficient values for short and long time period decreased with increasing pH. The sorption kinetic model results indicated that the values of pseudo first ( $k_1$ ) and second order ( $k_2$ ) decreased with increasing pH.

As the particle size decreased, the external mass transfer effect on the sorption rate became more and more significant. Increasing the particle size resulted in a greater time to reach equilibrium. As the particle size increased, the distance for diffusion of solute molecule in the particle become longer and thus the solute required more time to diffuse to the interior of the particle. Increasing particle size yielded higher intraparticle diffusion resistance. The values of  $D_{\text{eff}}$  for short and long time period increased with increasing particle size. The sorption kinetic model results indicated that the values of pseudo first ( $k_1$ ) and second order ( $k_2$ ) decreased with increasing particle size.

The comparison of experimental and models with three (L-L-L) linear segments for all sorbents are shown in Appendix F.3. It is evident from the figures that the plots consisted of three regions. The three stages in these plots revealed that more than one step was involved in the sorption process. Cr (VI) sorption onto all sorbents at different conditions had the same patterns and Cr (VI) sorption tended to follow three stages. The values of the intraparticle diffusion rate constant were determined from the slope of the second linear portion of the  $q_t$  versus  $t^{0.5}$ . The plot of  $q_t$  versus  $t^{0.5}$  for all sorbents did not pass through the origin. The results implied that although intraparticle diffusion was involved in Cr (VI) sorption process, it was not the sole rate limiting steps. This results also confirmed that sorption of Cr (VI) on the sorbents was a multi-step process, involving external and intraparticle diffusion.

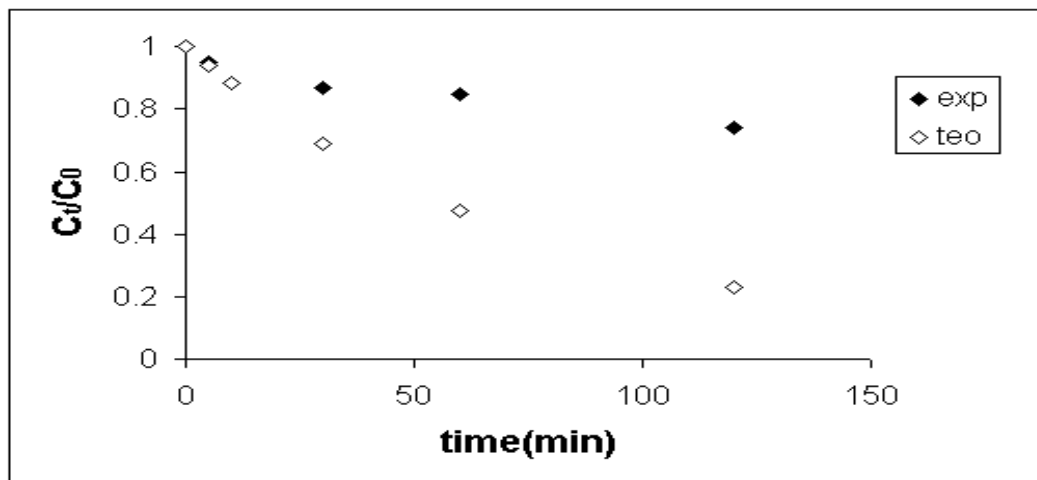
The calculated effective diffusion ( $D_{\text{eff}}$ ) values for all sorbents were in the order of  $10^{-10}$  and higher than  $10^{-11}$ . The results implied that Cr (VI) sorption process was not solely intraparticle diffusion controlled and external film diffusion was also effective. The results were also confirmed from the plots of  $q_t$  versus  $t^{0.5}$ .



### 7.5.1. Comparison of Experimental and Model Results

Comparison of correlation coefficient values that obtained from models is not enough to choose the “best model”. The best way to decide which model is fitted well is the comparison of the experimental and theoretical model results. Comparison results are shown in Figure 7.143-7.146.

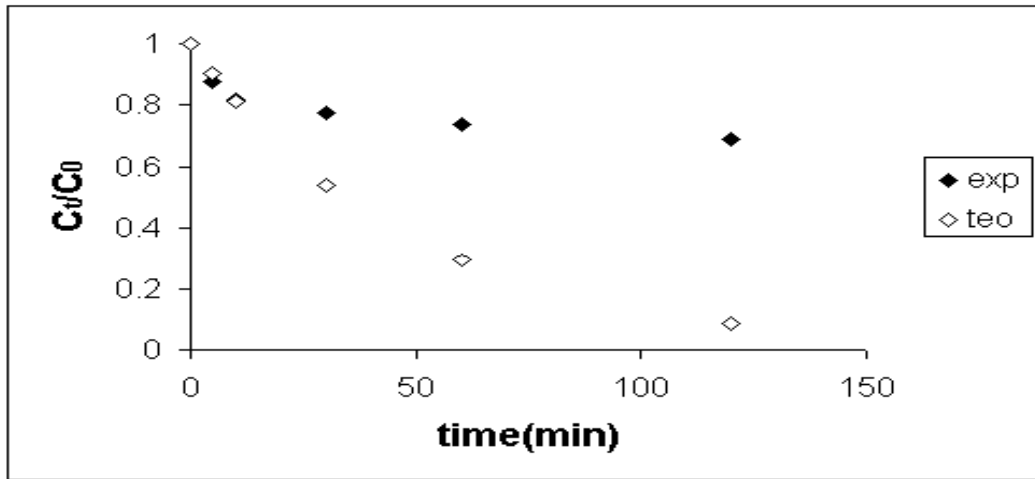
Using the external mass transfer coefficient obtained from Mathew and Weber, it was possible to draw experimental and theoretical concentration decay curves. Figure 7.143 (a)-(i) show the comparison of theoretical and experimental concentration decay curves for all sorbents. The results indicated that the experimental and theoretical data were much close during the first 10 min of sorption period. After 10 min, a noticeable deviation was observed between experimental and theoretical data. After approximately 10 min contact time, deviation between experimental and predicted results showed the effect of a second mass transfer resistance. In order to asses the contribution from second mass transfer resistance, the further analysis are needed.



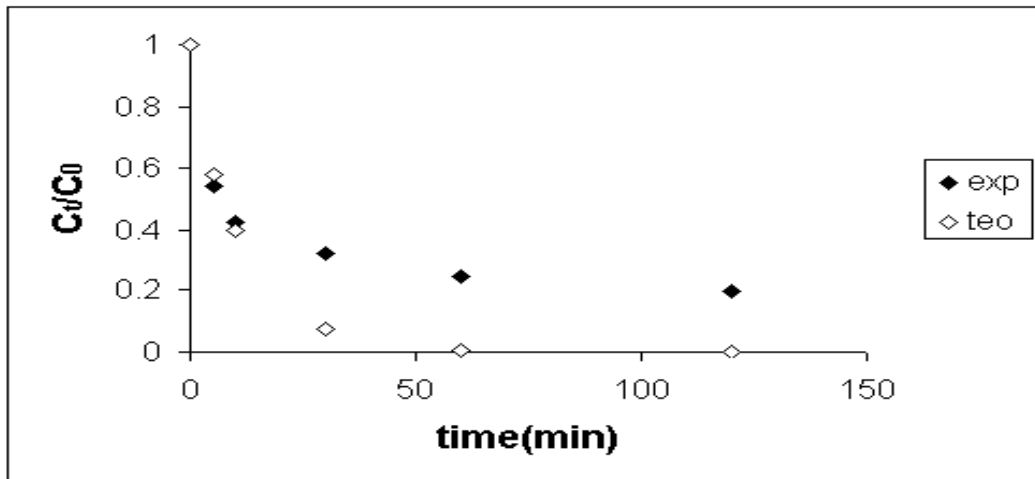
(a)

Figure 7.143. Comparison of theoretical and experimental concentration decay curves for (a) CLI (b) AMCLI (c) CMCLI (d) ECCLI (e) BSCLI (f) ECAMCLI (g) BSAMCLI (h) ECCMCLI (i) BSCMCLI (Conditions: 10 mg/L, 140 rpm, 25 °C, pH: 3, 25–106 μm)

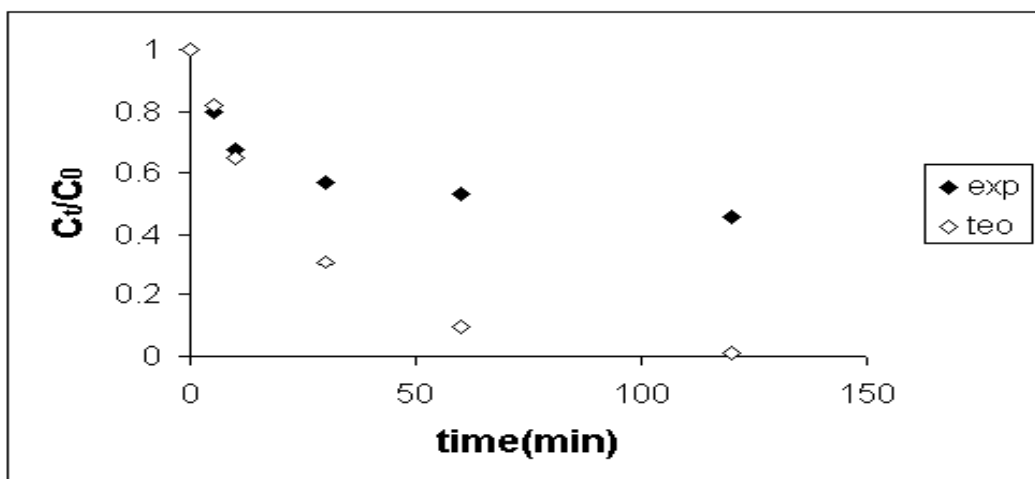
(Continued on next page)



(b)



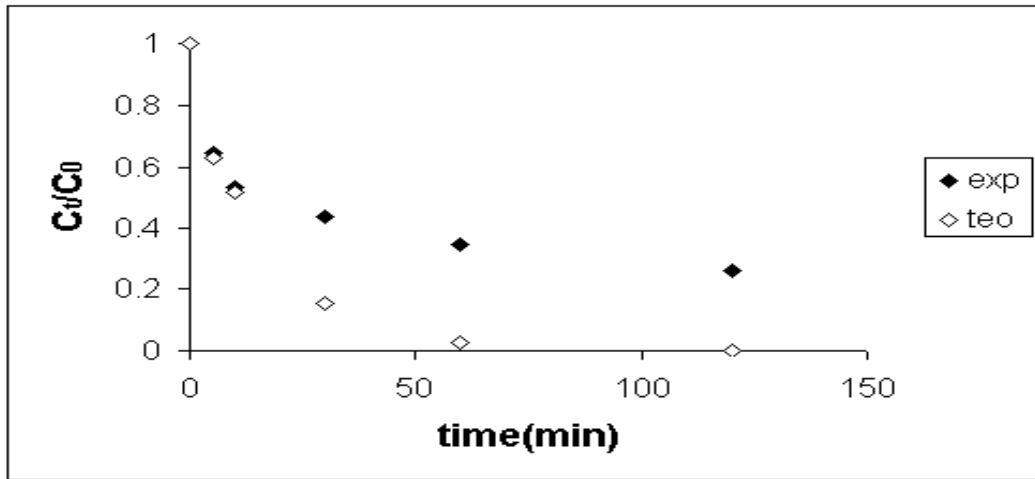
(c)



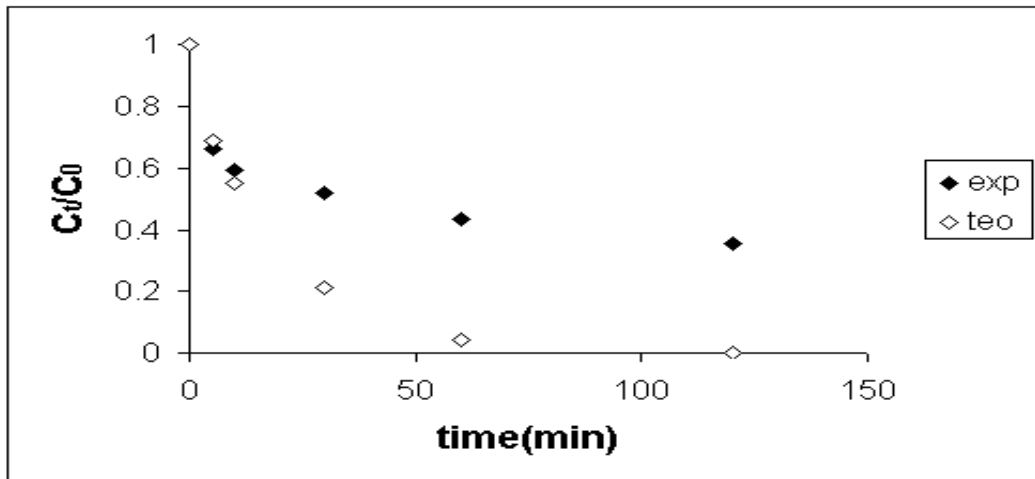
(d)

Figure 7.143 (cont)

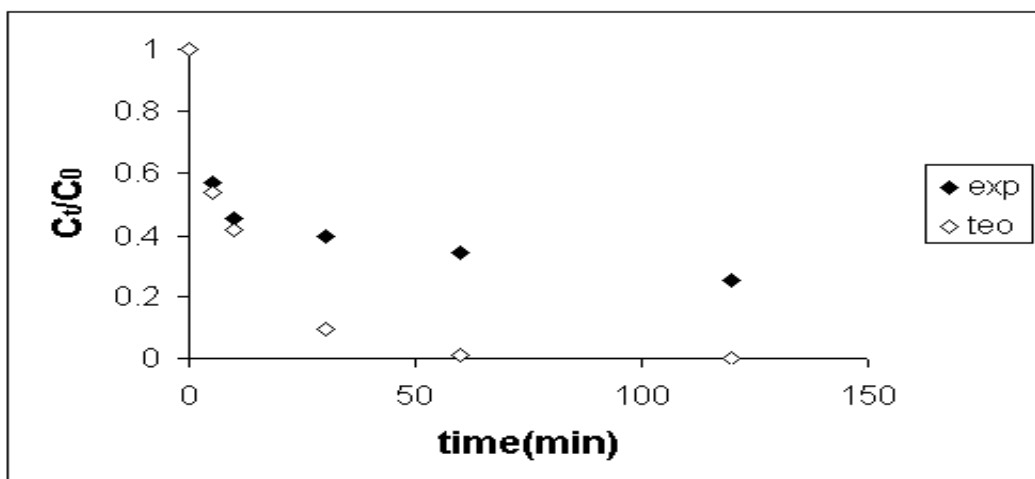
(Continued on next page)



(e)



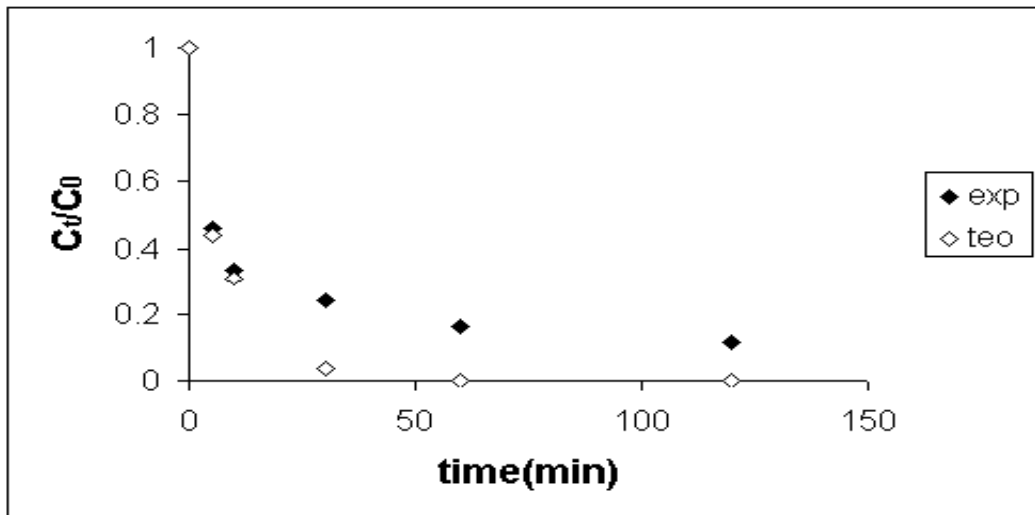
(f)



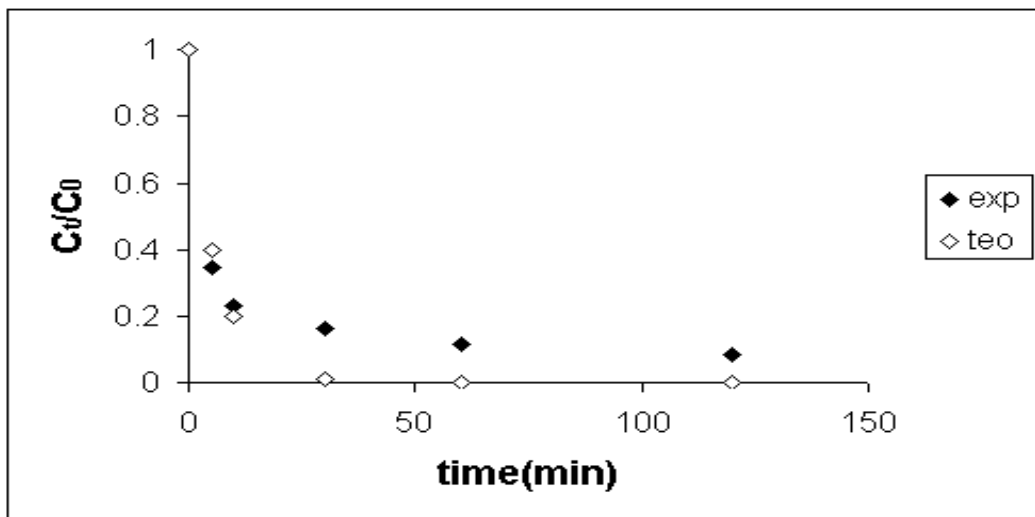
(g)

Figure 7.143 (cont)

(Continued on next page)



(h)



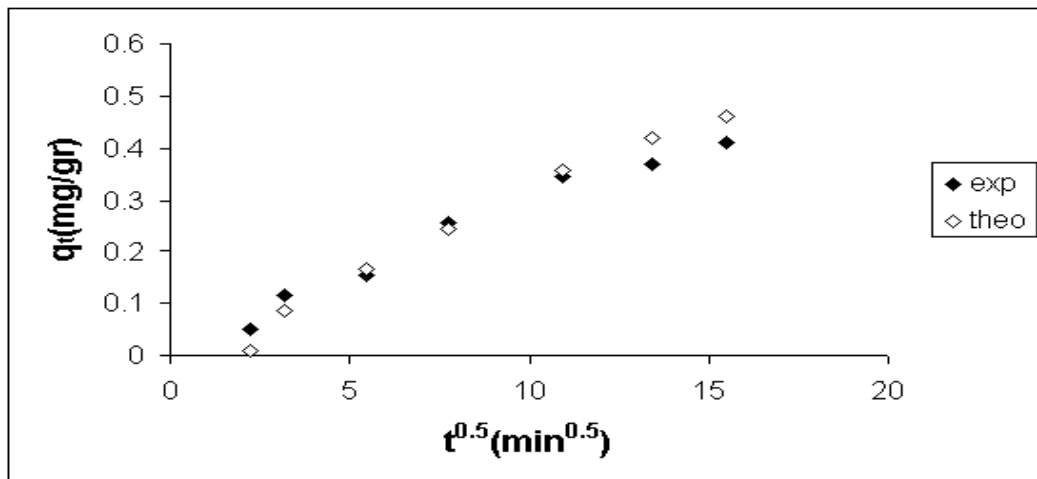
(i)

**Figure 7.143 (cont)**

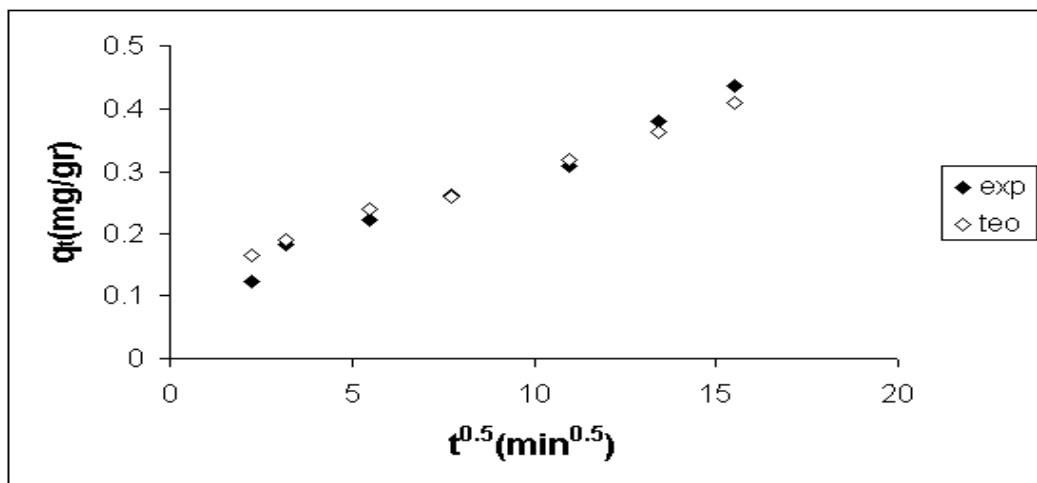
Figure 144 (a)-(i) show the comparison of theoretical and experimental results of Weber-Morris model. During the first 10 min, experimental data for clinoptilolite rich mineral deviated from theoretical data and noticeable difference was observed. After 10 min, experimental and theoretical data were much close to each other. The deviation between experimental and theoretical data during 10 min showed the effect of external mass transfer resistance. The results implied that external mass transfer controlled the sorption process during 10 min. After 10 min, intraparticle diffusion governed the sorption process.

The results also indicated that experimental data for surfactant modified clinoptilolite rich mineral deviated from theoretical data during 5 min. After 5 min,

experimental and theoretical data were much close to each other. The deviation between experimental and theoretical data during 5 min showed the effect of external mass transfer resistance. After this time, intraparticle diffusion controlled the sorption process. Similar results were obtained with bacteria loaded clinoptilolite rich mineral samples.

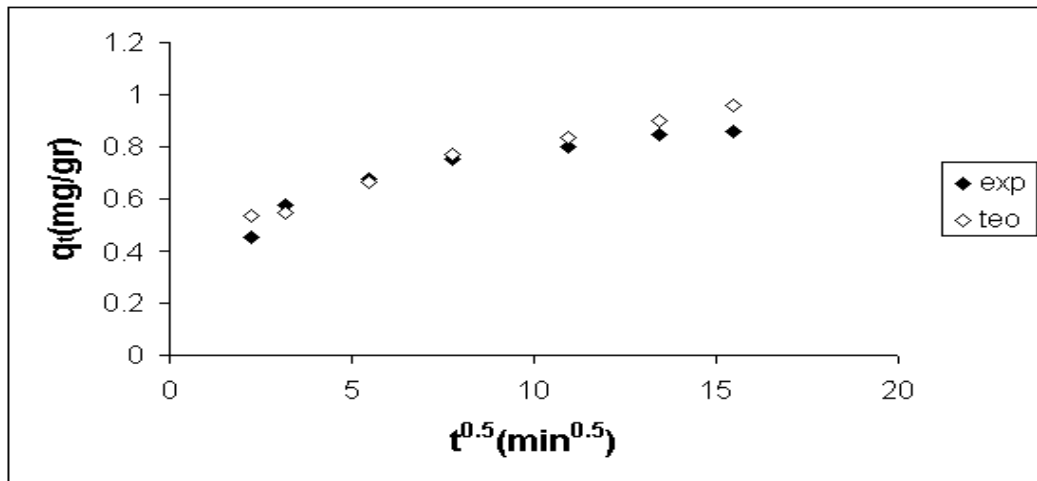


(a)

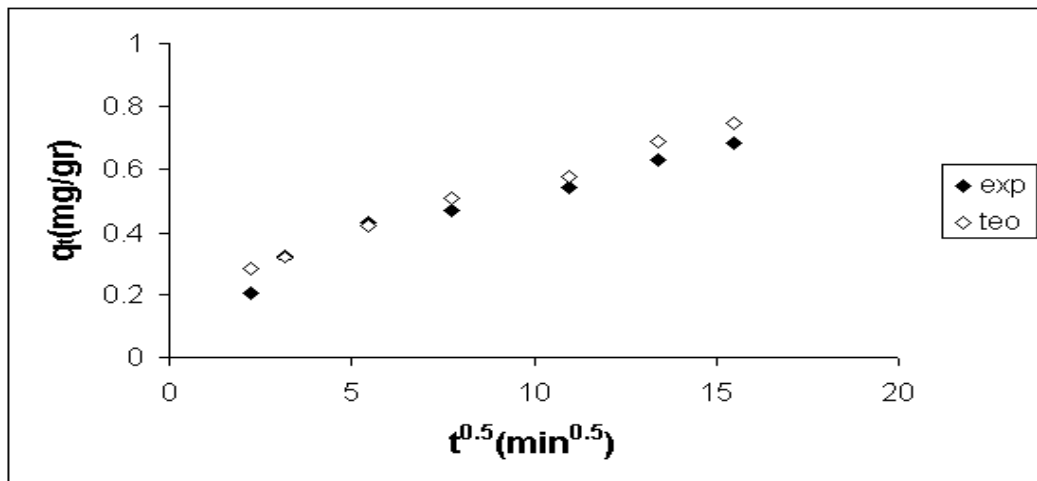


(b)

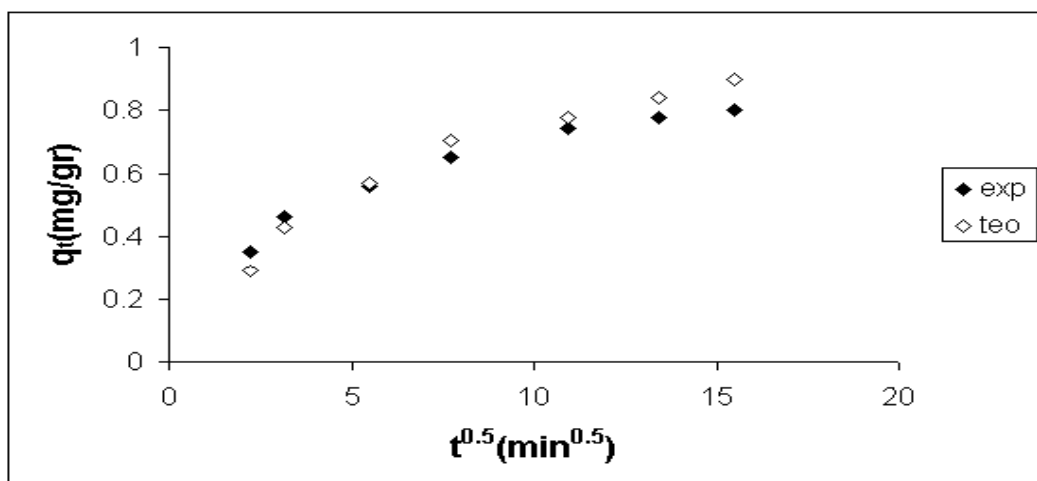
Figure 7.144. Comparison of theoretical and experimental Weber-Morris model results for (a) CLI (b) AMCLI (c) CMCLI (d) ECCLI (e) BSCLI (f) ECAMCLI (g) BSAMCLI (h) ECCMCLI (i) BSCMCLI (Conditions: 10 mg/L, 140 rpm, 25 °C, pH: 3, 25–106  $\mu\text{m}$ )



(c)



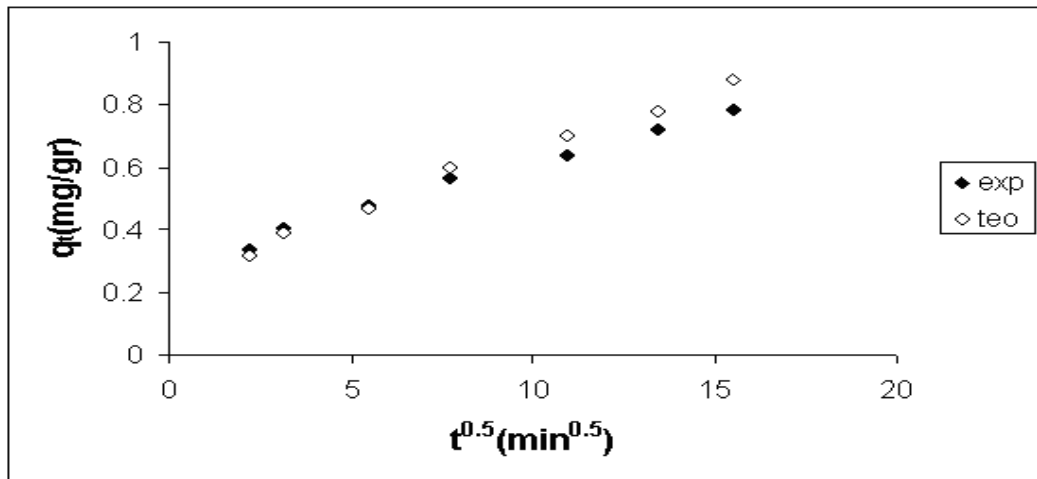
(d)



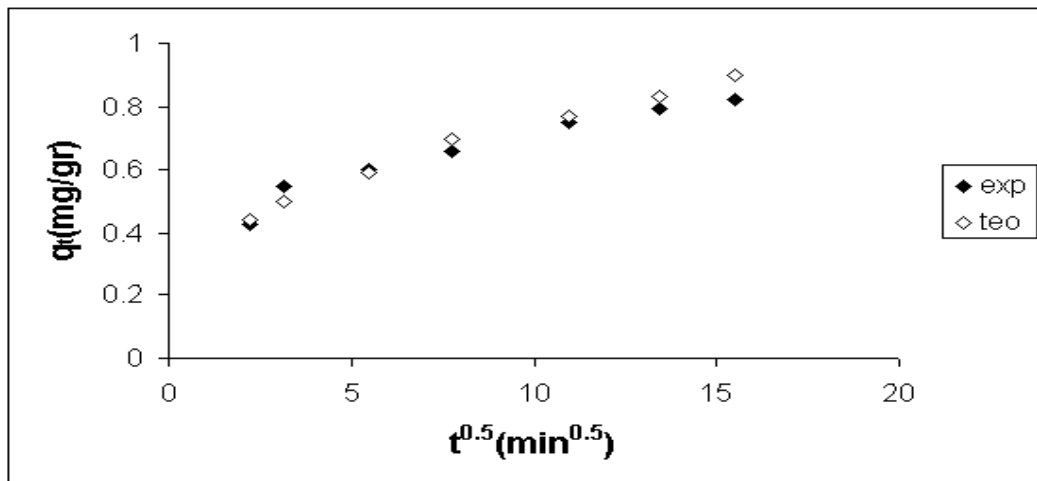
(e)

Figure 7.144 (cont)

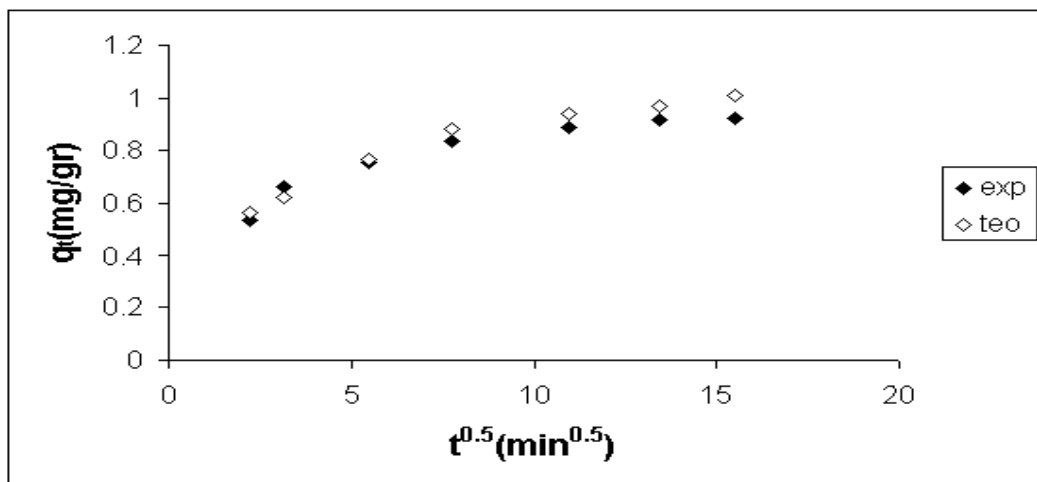
(Continued on next page)



(f)



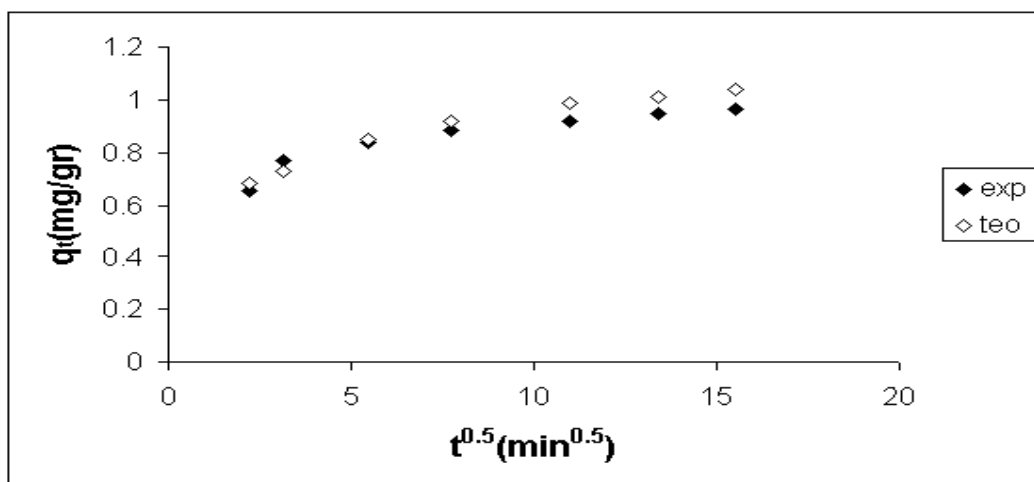
(g)



(h)

Figure 7.144 (cont)

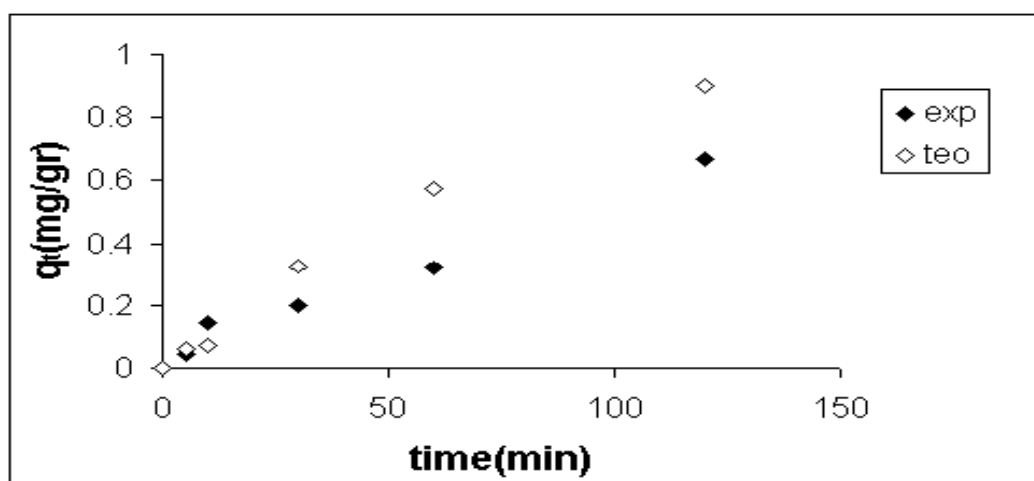
(Continued on next page)



(i)

Figure 7.144 (cont)

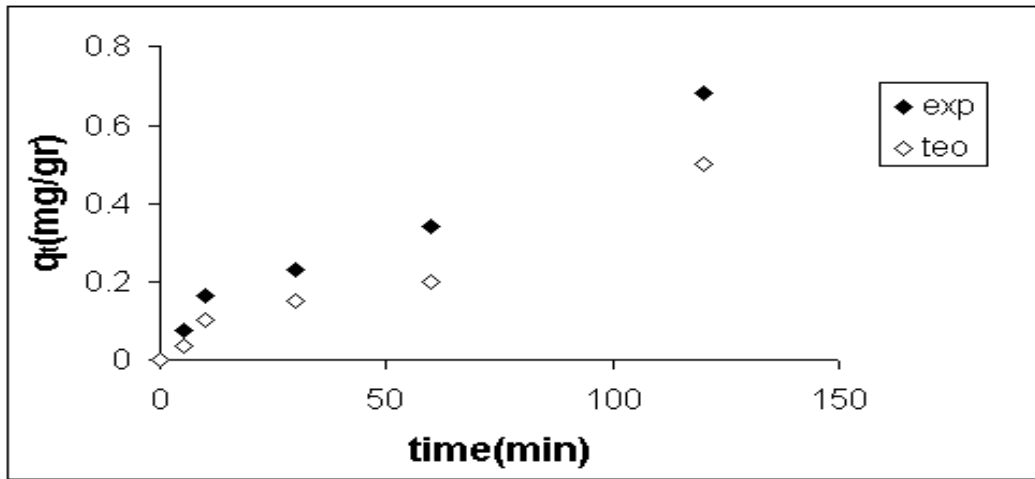
The validity of the pseudo first order kinetic model was checked by the comparison of the experimental and theoretical model results. Figure 7.145 (a)-(i) show the comparison of the both model results. The results indicated that the experimental were much close during the first 5 min. After 5 min, experimental data deviated from theoretical data and noticeable difference was observed. The results indicated that the sorption of Cr (VI) onto sorbents did not follow pseudo first order kinetic model.



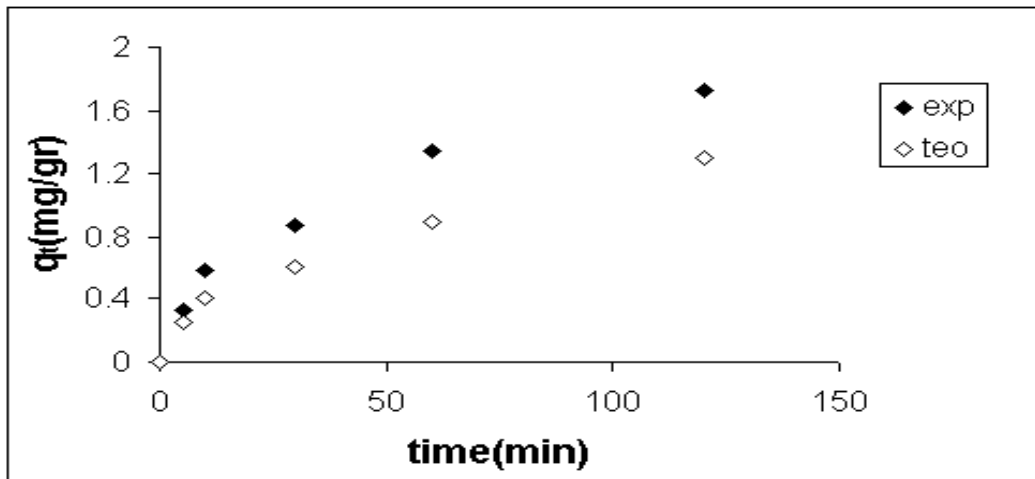
(a)

Figure 7.145. Comparison of theoretical and experimental pseudo first order model results for (a) CLI (b) AMCLI (c) CMCLI (d) ECCLI (e) BSCLI (f) ECAMCLI (g) BSAMCLI (h) ECCMCLI (i) BSCMCLI (Conditions: 50 mg/L, 140 rpm, 25 °C, pH: 3, 25–106  $\mu\text{m}$ )

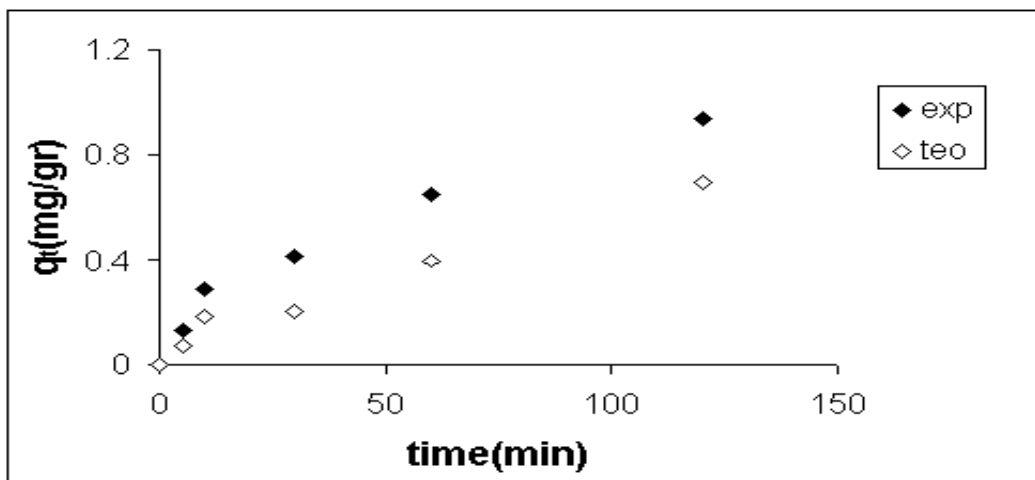




(b)



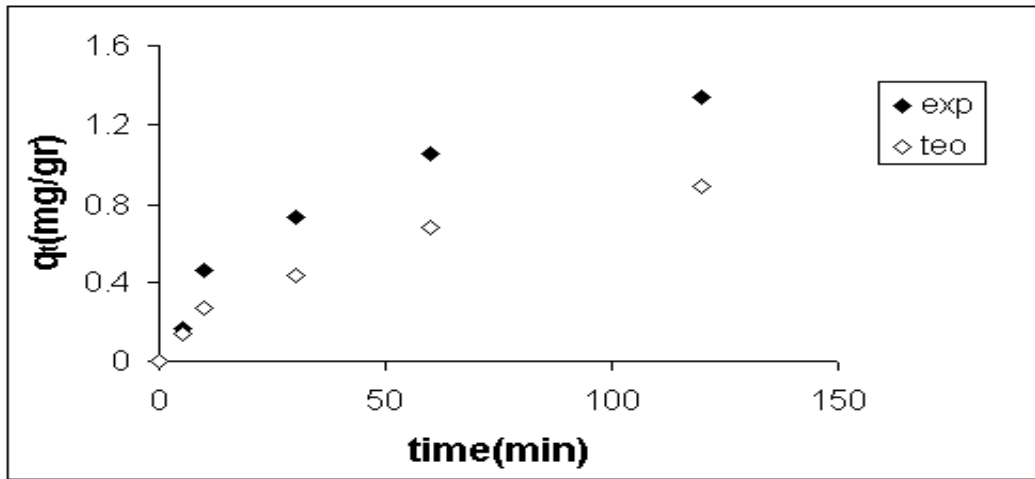
(c)



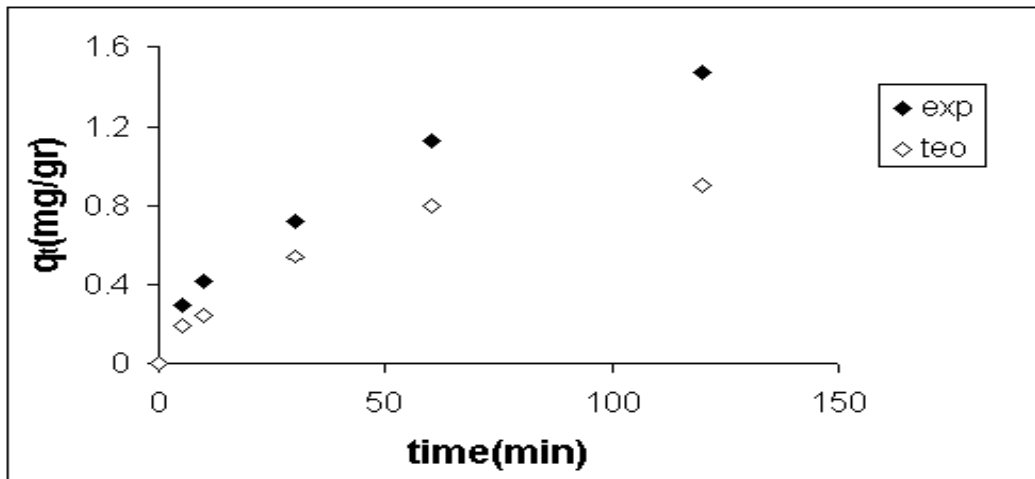
(d)

Figure 7.145 (cont)

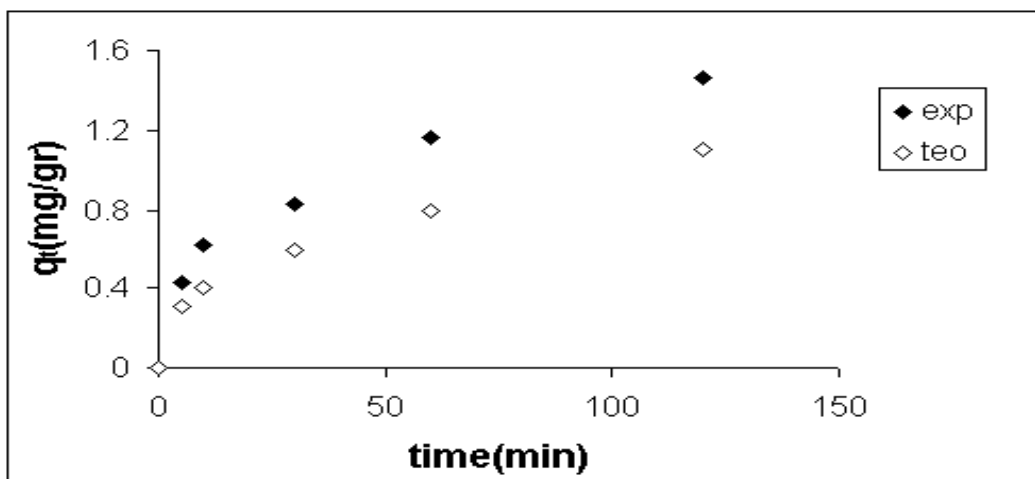
(Continued on next page)



(e)



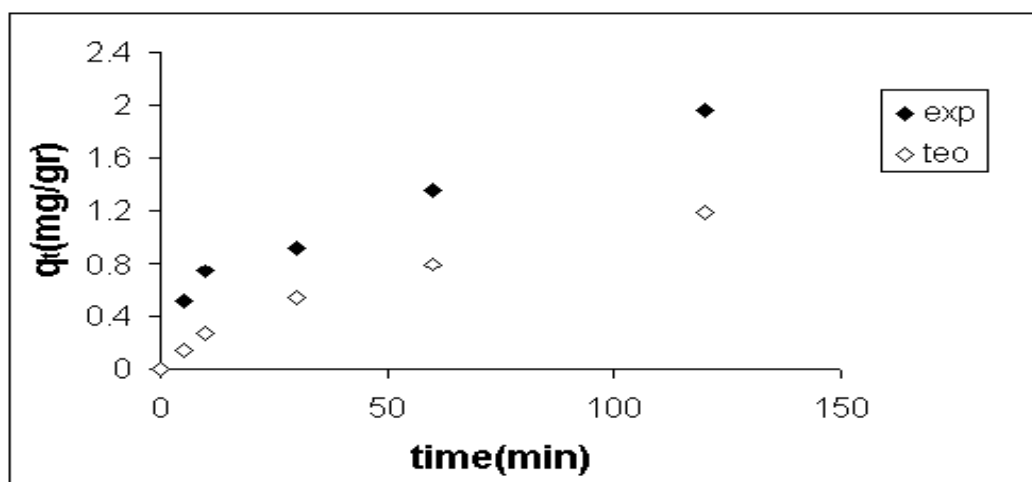
(f)



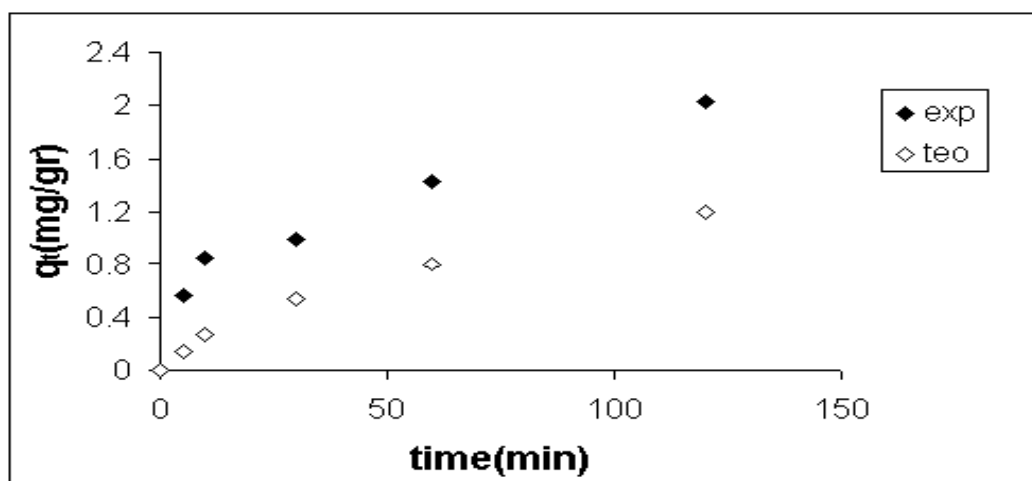
(g)

Figure 7.145 (cont)

(Continued on next page)



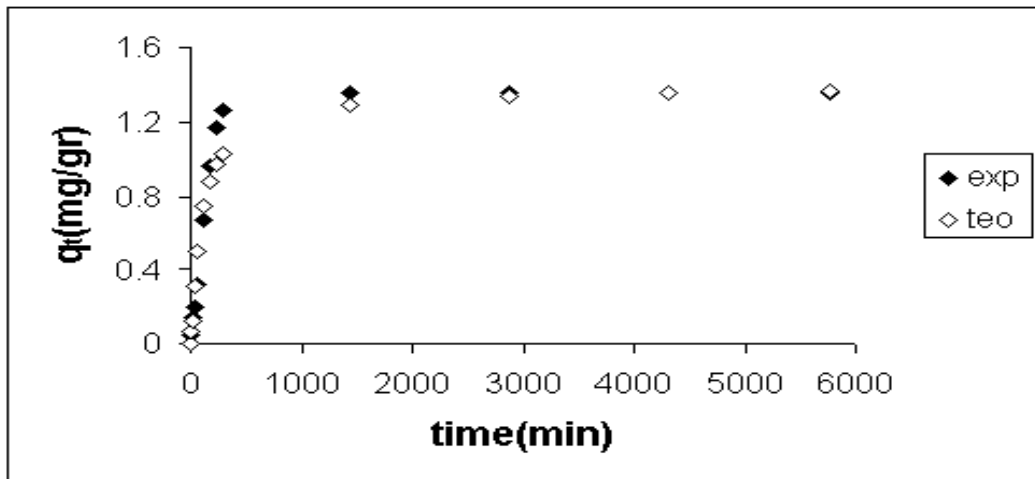
(h)



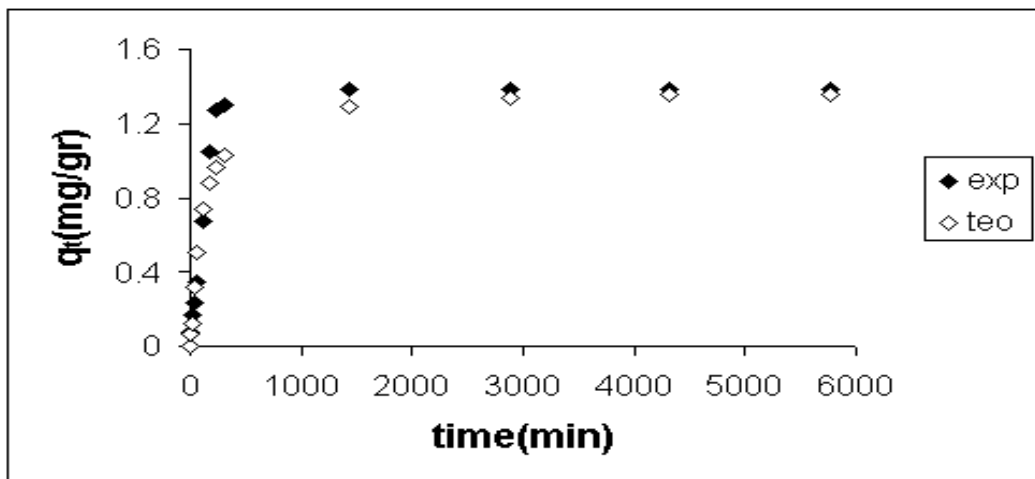
(i)

Figure 7.145 (cont)

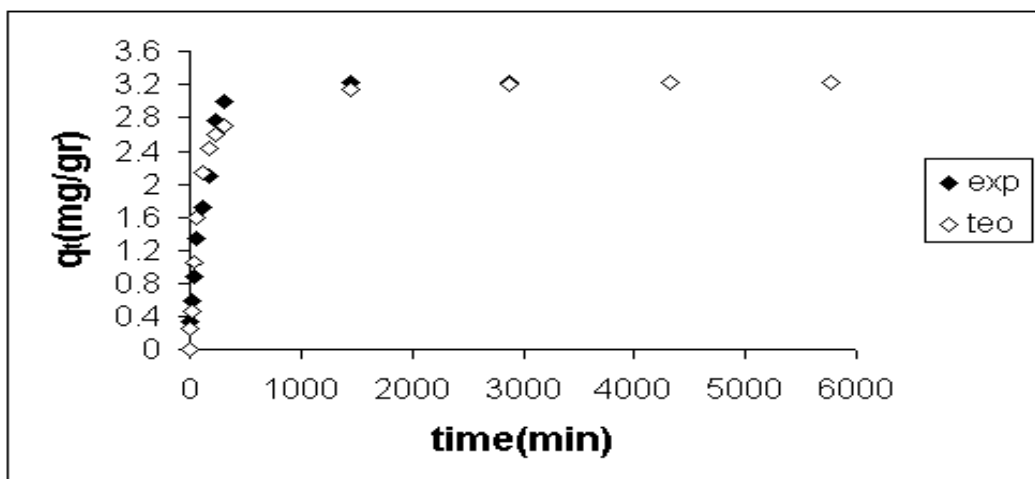
Figure 146 (a)-(i) show the comparison of theoretical and experimental results of pseudo second order model. The results indicated that the experimental and theoretical data were much close during the whole sorption period. Ho and McKay stated that if the chemical sorption was the rate controlling step, the pseudo-second-order model was more likely to predict the behavior over the entire sorption period. The results revealed that the sorption of Cr (VI) onto sorbents was well represented by the pseudo-second order kinetic model.



(a)

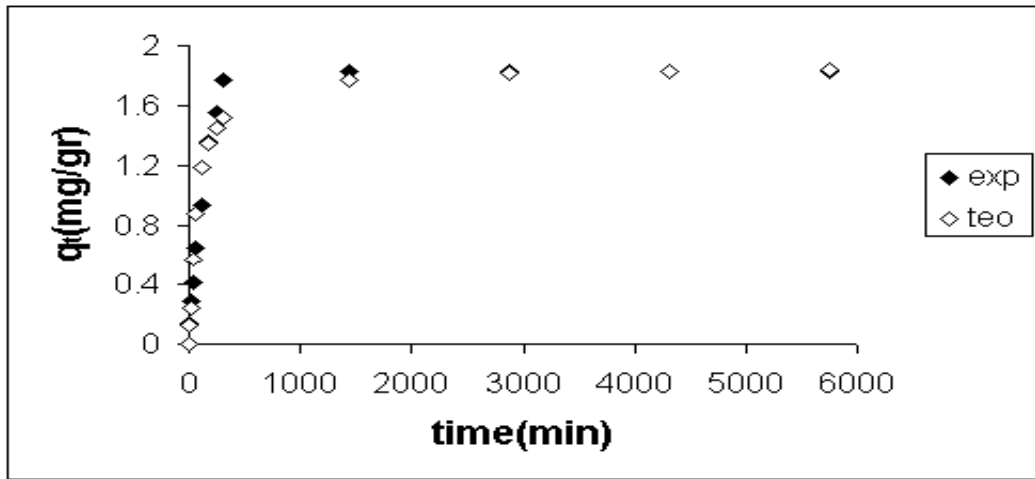


(b)

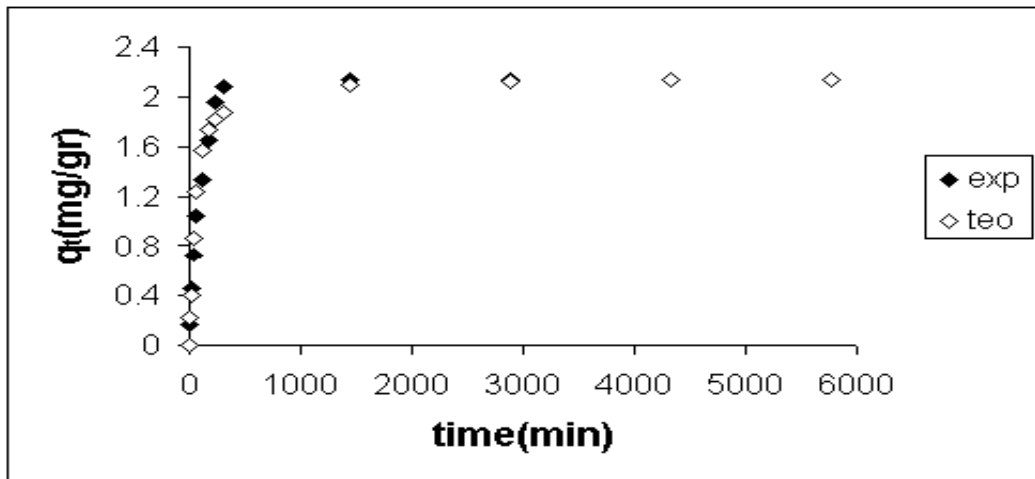


(c)

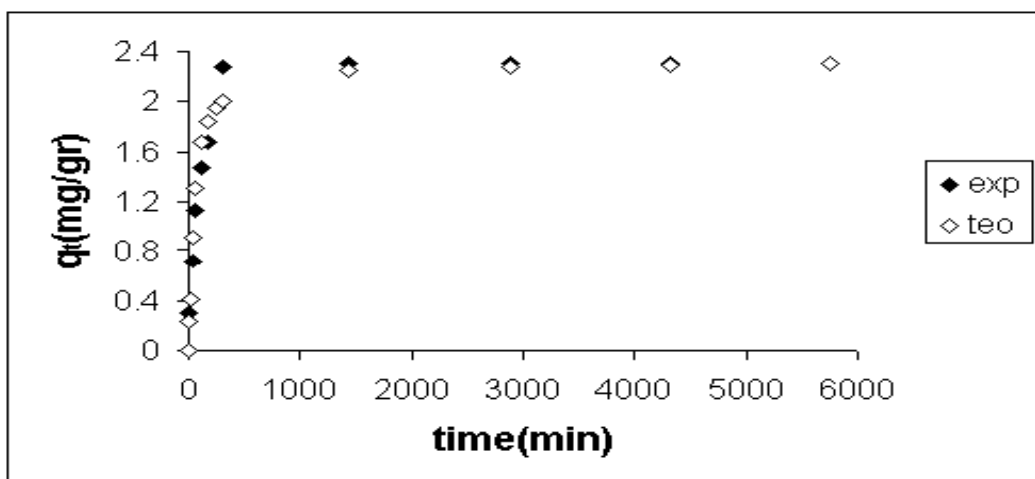
Figure 7.146. Comparison of theoretical and experimental pseudo second order model results for (a) CLI (b) AMCLI (c) CMCLI (d) ECCLI (e) BSCLI (f) ECAMCLI (g) BSAMCLI (h) ECCMCLI (i) BSCMCLI (Conditions: 50 mg/L, 140 rpm, 25 °C, pH: 3, 25–106  $\mu\text{m}$ )



(d)



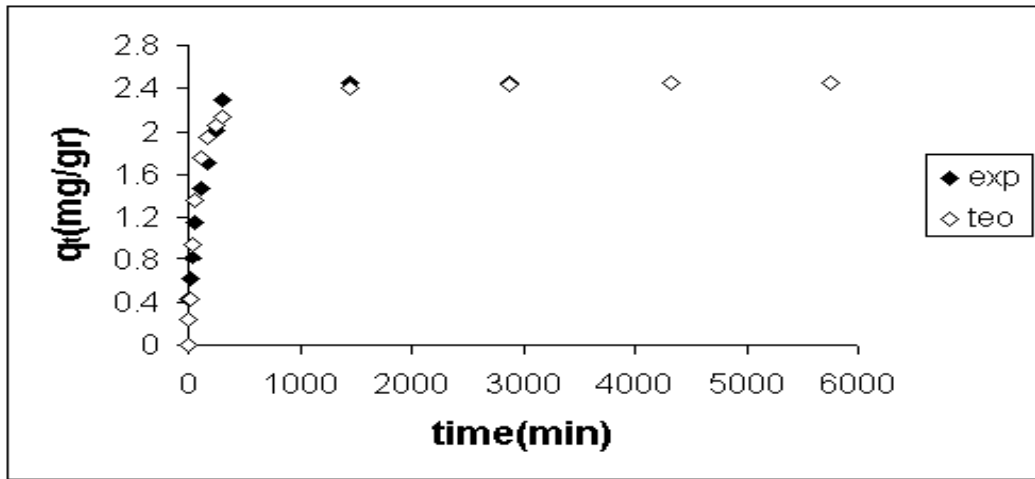
(e)



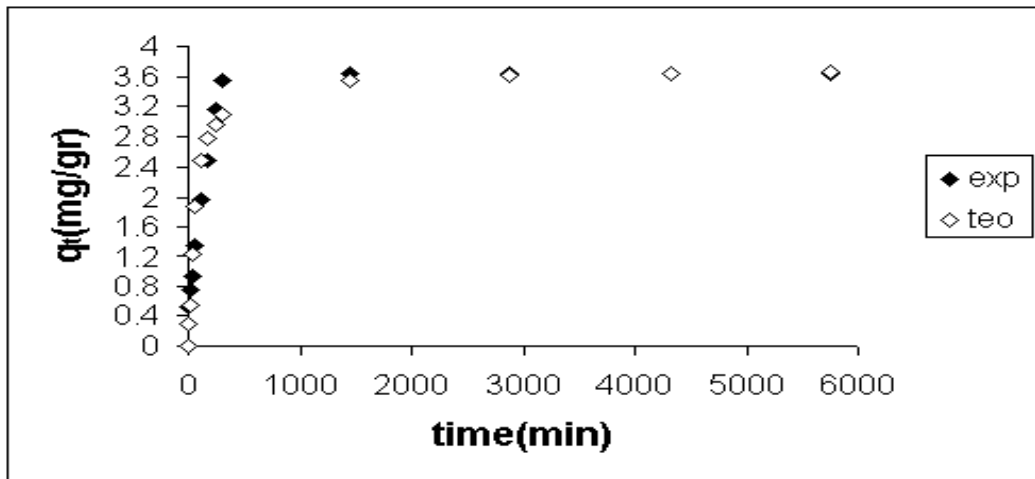
(f)

Figure 7.146 (cont)

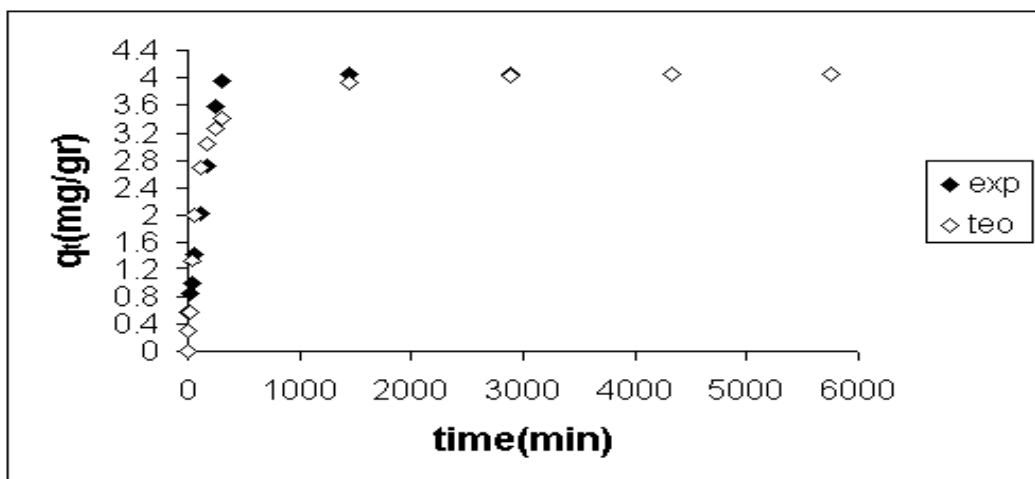
(Continued on next page)



(g)



(h)



(i)

Figure 7.146 (cont)

## 7.6. Comparison of External and Internal Mass Transfer Resistance

Relative importance of internal and external mass resistance was determined by Biot Number. The values of Biot Number at different conditions for all sorbents are tabulated in Table 7.28-7.31. For Biot Number  $\ll 1$ , external mass resistance is the controlling mass transfer step, while for Biot Number  $\gg 100$ , intraparticle diffusion is the predominant mass transfer controlling mechanism. Biot number between 1 and 100 indicate that both mass transfer mechanisms are involved in sorption process (Tragner and Suidan, 1989; Choy et al., 2004). The calculated Biot Number values for all sorbents were greater than 100. The results revealed that Cr (VI) sorption process was mainly controlled by intraparticle diffusion.

Table 7.28. Values of Biot Number for CLI, AMCLI and CMCLI

Parameters		Biot Number CLI	Biot Number AMCLI	Biot Number CMCLI
Initial Concentration (mg/L)	10	375	670	1895
	50	179	209	825
	100	95	115	407
	200	55	75	288
	300	50	75	134
Agitation Speed (rpm)	60	307	333	2337
	100	441	477	4942
	140	375	670	1895
Temperature (°C)	25	375	670	1895
	40	480	494	671
pH	3	375	670	1895
	11	462	500	1017
Particle size (µm)	25-106	375	670	1895
	106-425	509	533	2580

Table 7.29. Values of Biot Number for ECCLI and BSCLI

Parameters		Biot Number ECCLI	Biot Number BSCLI
Initial Concentration (mg/L)	10	1223	1940
	50	378	606
	100	189	283
	200	95	159
	300	70	95
Agitation Speed (rpm)	60	1324	2024
	100	1632	2446
	140	1223	1940
Temperature (°C)	25	1223	1940
	40	432	1285
pH	3	1223	1940
	11	849	894
Particle size (µm)	25-106	1223	1940
	106-425	1589	2102

Table 7.30. Values of Biot Number for ECAMCLI and BSAMCLI

Parameters		Biot Number ECAMCLI	Biot Number BSAMCLI
Initial Concentration (mg/L)	10	1781	2615
	50	586	1079
	100	293	437
	200	154	176
	300	105	122
Agitation Speed (rpm)	60	2213	2327
	100	2511	4898
	140	1781	2615
Temperature (°C)	25	1781	2615
	40	1182	1992
pH	3	1781	2615
	11	923	1567
Particle size (µm)	25-106	1781	2615
	106-425	1719	2213



Table 7.31. Values of Biot Number for ECCMCLI and BSCMCLI

Parameters		Biot Number ECCMCLI	Biot Number BSCMCLI
Initial Concentration (mg/L)	10	2441	3236
	50	1097	1231
	100	442	581
	200	224	293
	300	134	184
Agitation Speed (rpm)	60	5775	5681
	100	3490	3436
	140	2441	3236
Temperature (°C)	25	2441	3236
	40	1364	1638
pH	3	2441	3236
	11	389	1176
Particle size (µm)	25-106	2441	3236
	106-425	2259	2716

## 7.7. Sorption Isotherms

The sorption data for Cr (VI) by clinoptilolite, surfactant modified and bacteria loaded forms at different temperatures were analyzed by a regression analysis to fit the Langmuir and Freundlich isotherm models (Appendix G). Values of Langmuir and Freundlich constants are presented in Table 7.32 and 7.33. The correlation coefficient ( $R^2$ ) values of Langmuir model were higher than 0.99 whereas the correlation coefficient values of Freundlich isotherm models were lower than 0.99. Higher correlation coefficient ( $R^2$ ) values showed that the Langmuir isotherm fitted well with the experimental data.

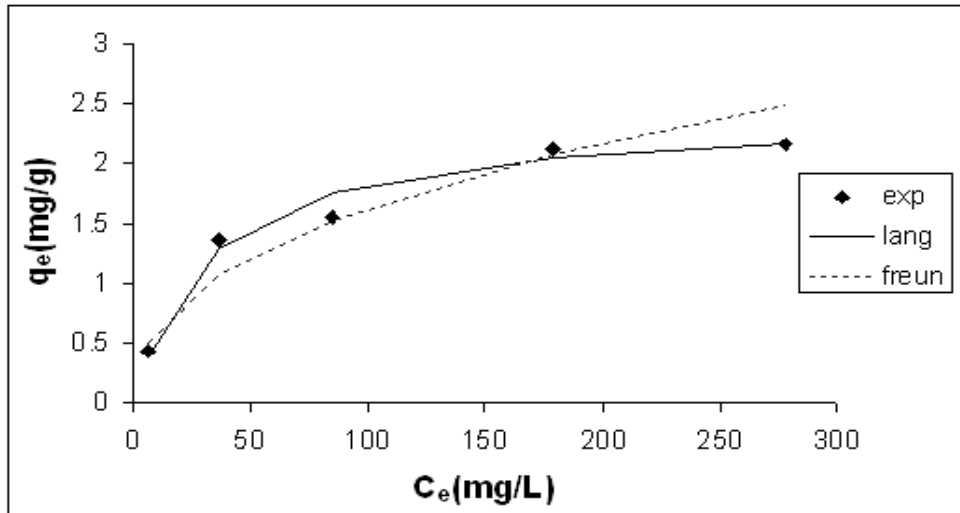
Table 7.32. Parameters of the Langmuir isotherm models

Sorbents	T (°C)	q <sub>m</sub> (mg/gr)	b (L/mg)	R <sup>2</sup>
CLI	25	2.41	0.030	0.994
	40	2.23	0.016	0.974
AMCLI	25	2.43	0.034	0.991
	40	2.11	0.02	0.983
CMCLI	25	3.91	0.219	1
	40	2.52	0.037	0.987
EC-CLI	25	2.51	0.091	0.999
	40	2.48	0.017	0.994
BS-CLI	25	3.59	0.05	0.982
	40	2.54	0.018	0.995
EC-AMCLI	25	2.89	0.117	0.998
	40	2.38	0.017	0.985
BS-AMCLI	25	3.53	0.081	0.995
	40	3.05	0.014	0.978
EC-CMCLI	25	4.52	0.198	0.999
	40	3.93	0.027	0.996
BS-CMCLI	25	4.89	0.21	0.998
	40	4.19	0.028	0.999

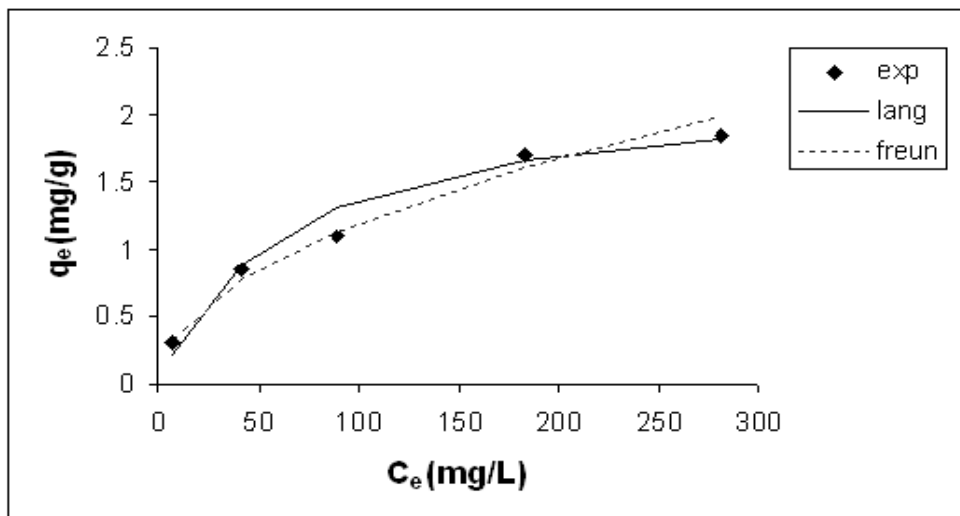
Table 7.33. Parameters of the Freundlich isotherm models

Sorbents	T (°C)	K <sub>f</sub>	n	R <sup>2</sup>
CLI	25	0.237	2.39	0.946
	40	0.127	2.06	0.992
AMCLI	25	0.273	2.54	0.951
	40	0.132	2.06	0.955
CMCLI	25	1	3.62	0.853
	40	0.294	2.55	0.897
EC-CLI	25	0.633	3.87	0.946
	40	0.121	1.89	0.972
BS-CLI	25	0.72	3.49	0.975
	40	0.128	1.91	0.967
EC-AMCLI	25	0.831	4.191	0.923
	40	0.124	1.954	0.971
BS-AMCLI	25	0.990	3.97	0.964
	40	0.127	1.85	0.987
EC-CMCLI	25	1.29	3.94	0.88
	40	0.271	2.06	0.96
BS-CMCLI	25	1.66	4.55	0.883
	40	0.28	2	0.94

Fig. 7.147-7.155 show comparison of the theoretical Langmuir and Freundlich isotherm model with experimental data at 25 and 40 °C. As it is seen from the figures, experimental data was very well represented by Langmuir isotherm model.

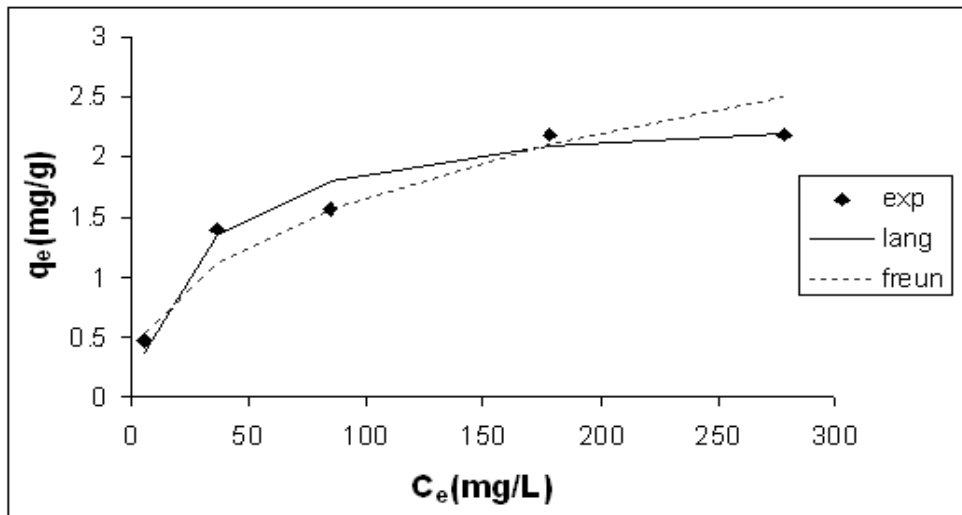


(a)

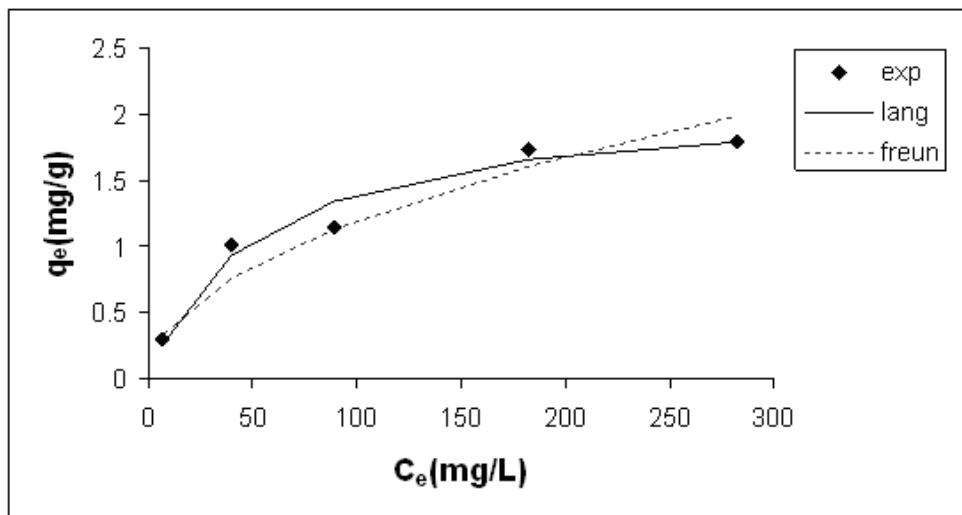


(b)

Figure 7.147. Equilibrium isotherm for Cr (VI) sorption with CLI (a) 25 °C (b) 40 °C

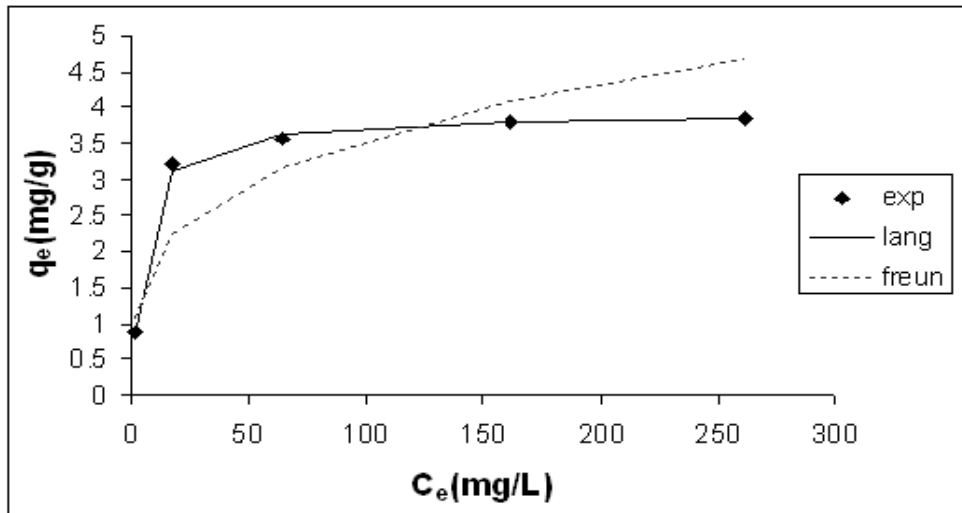


(a)

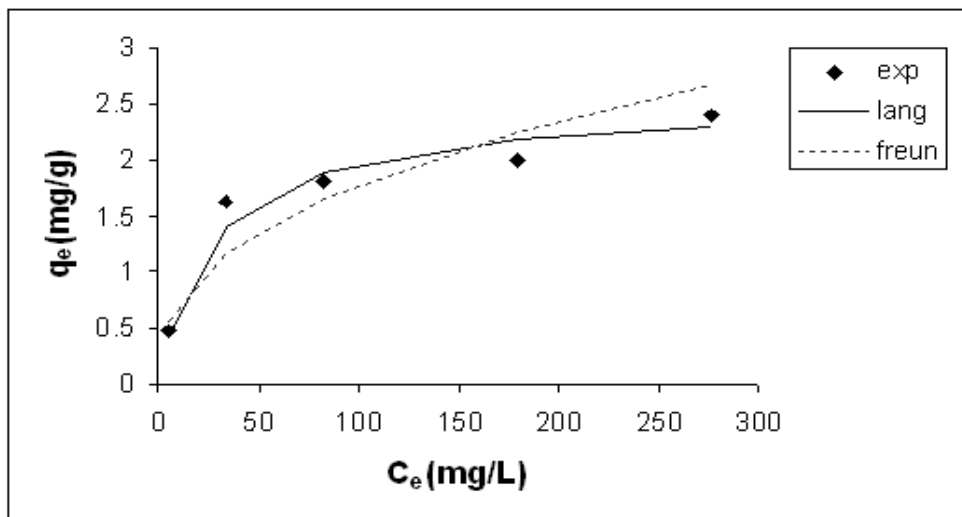


(b)

Figure 7.148. Equilibrium isotherm for Cr (VI) sorption with AMCLI (a) 25 °C  
(b) 40 °C

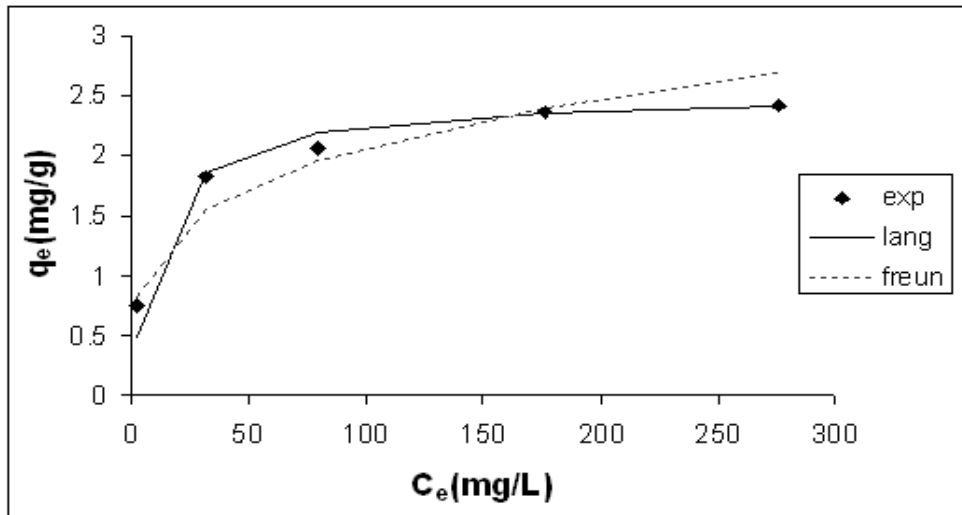


(a)

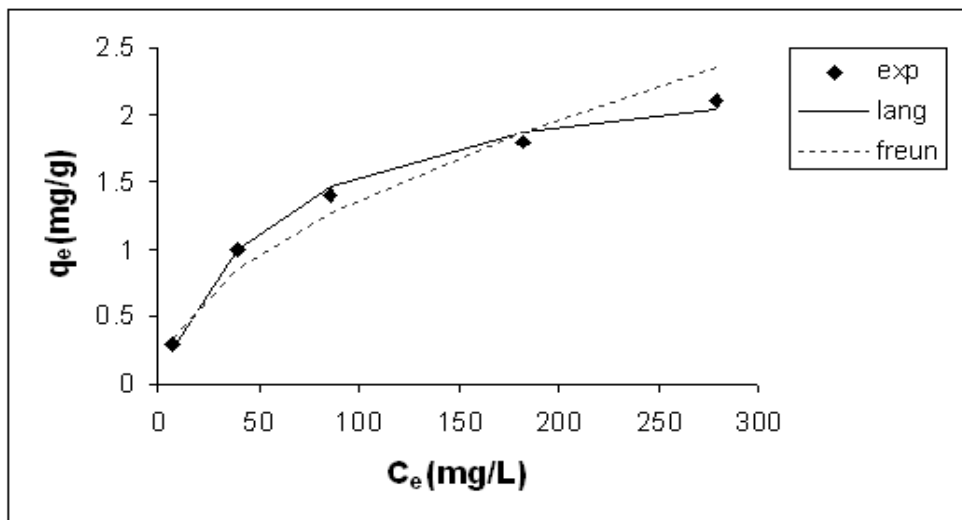


(b)

Figure 7.149. Equilibrium isotherm for Cr (VI) sorption with CMCLI (a) 25 °C  
(b) 40 °C

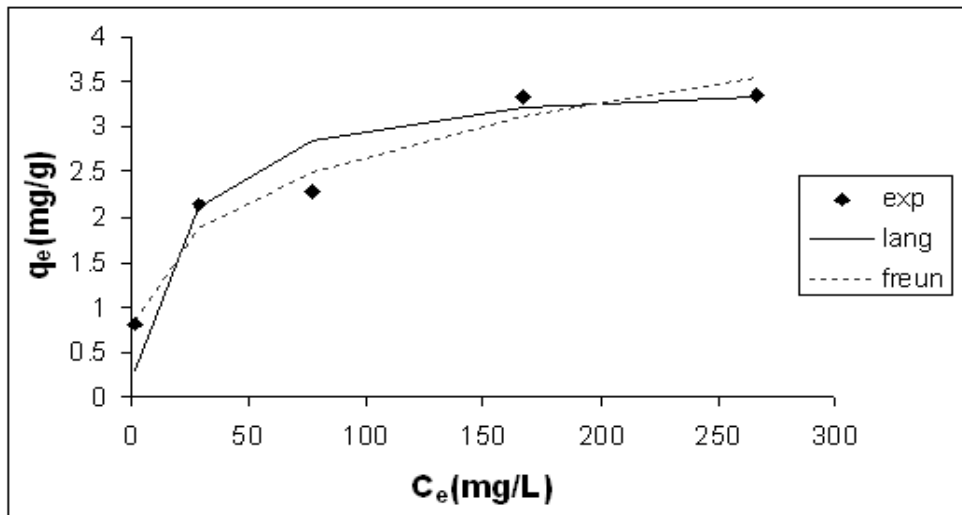


(a)

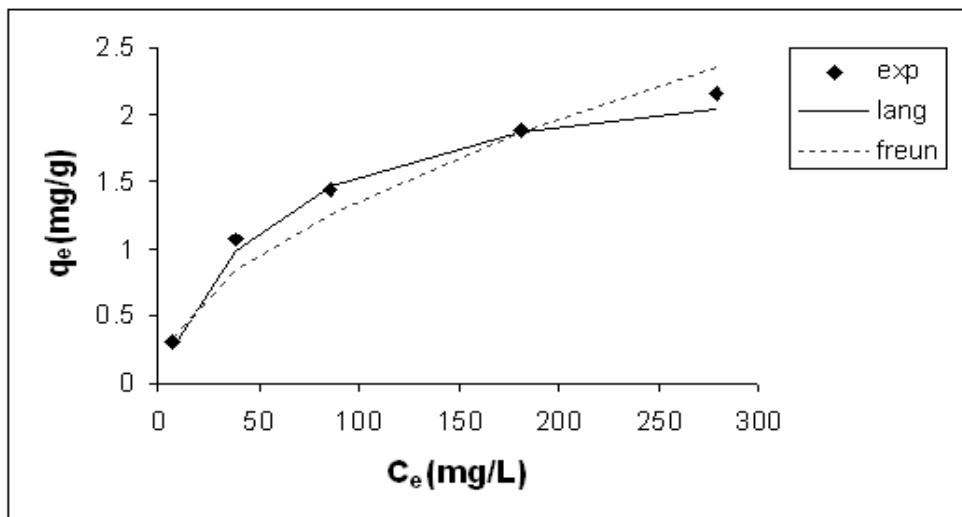


(b)

Figure 7.150. Equilibrium isotherm for Cr (VI) sorption with EC-CLI (a) 25 °C  
(b) 40 °C

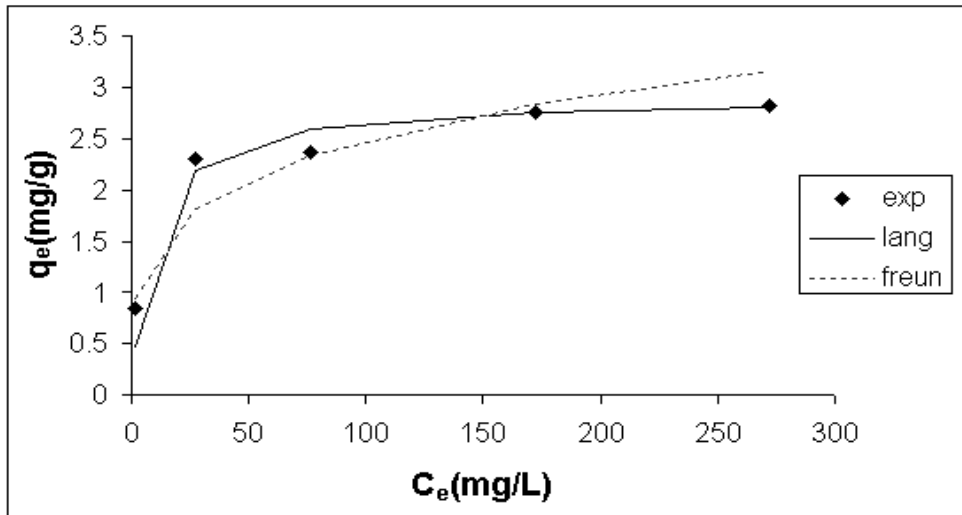


(a)

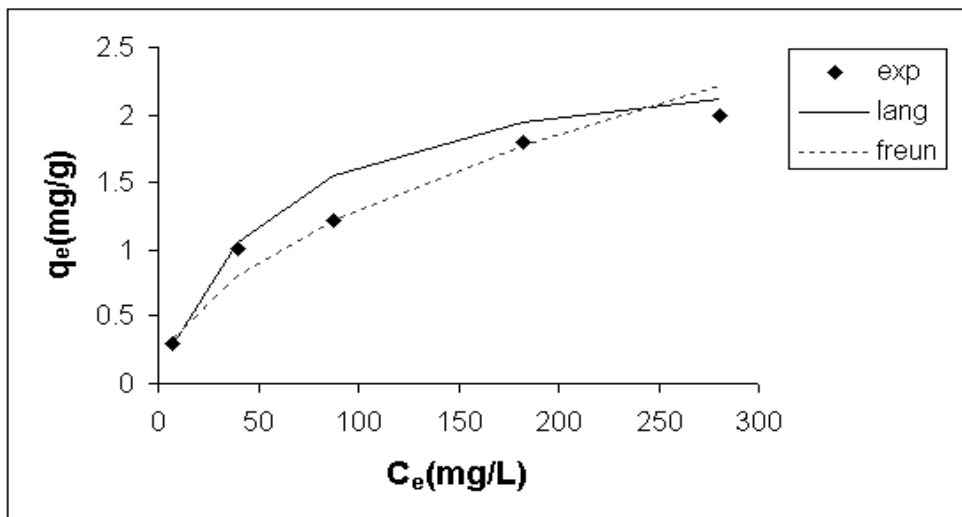


(b)

Figure 7.151. Equilibrium isotherm for Cr (VI) sorption with BS-CLI (a) 25 °C  
(b) 40 °C



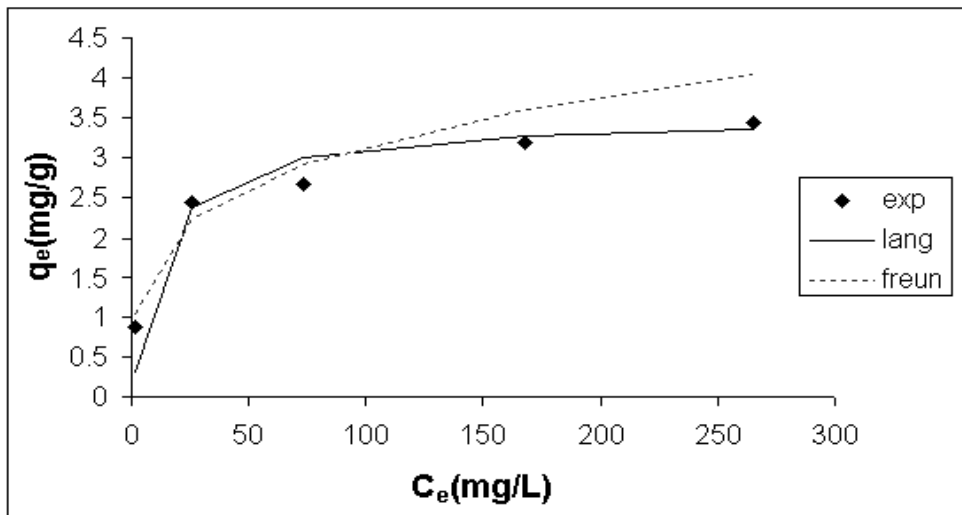
(a)



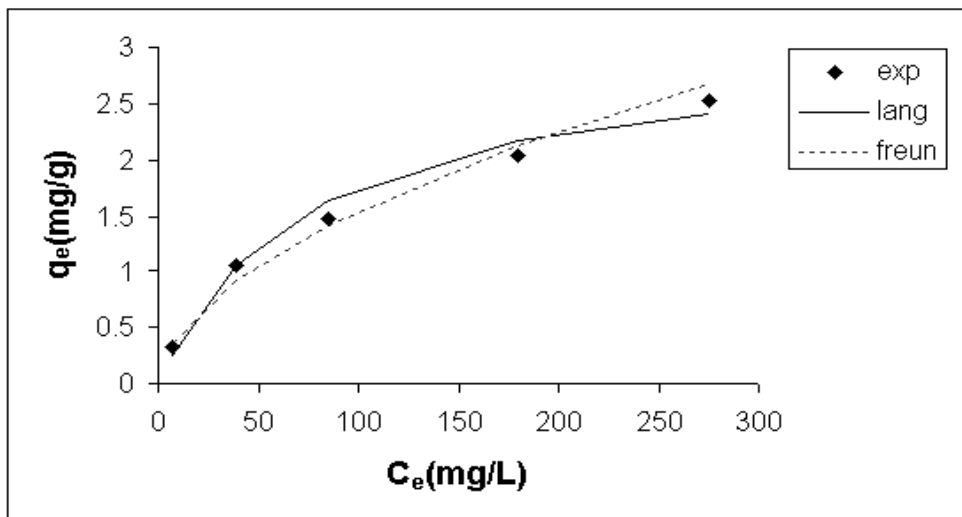
(b)

Figure 7.152. Equilibrium isotherm for Cr (VI) sorption with EC-AMCLI (a) 25 °C  
(b) 40 °C



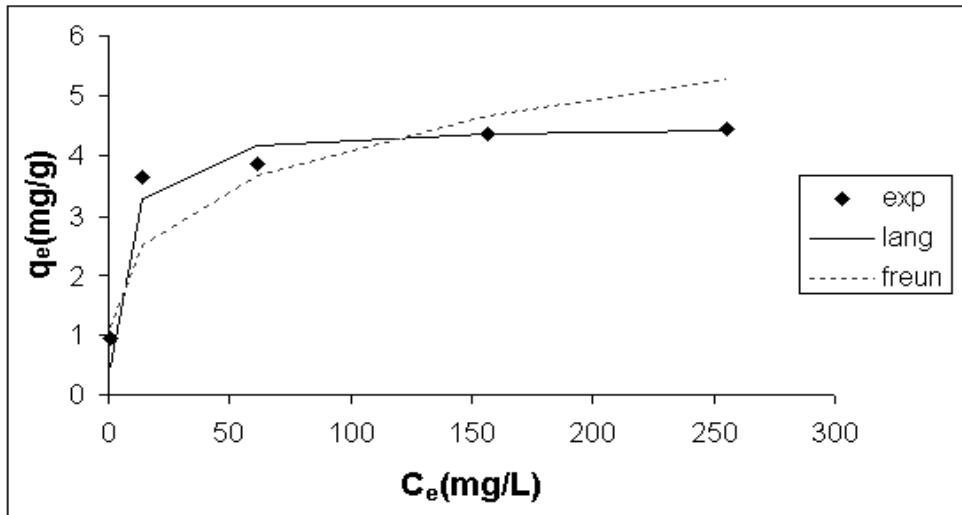


(a)

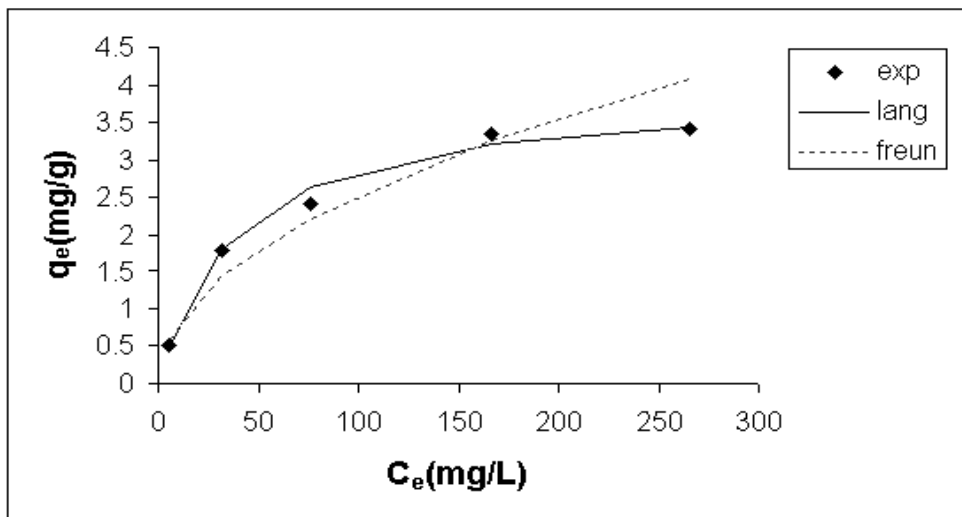


(b)

Figure 7.153. Equilibrium isotherm for Cr (VI) sorption with BS-AMCLI (a) 25 °C  
(b) 40 °C

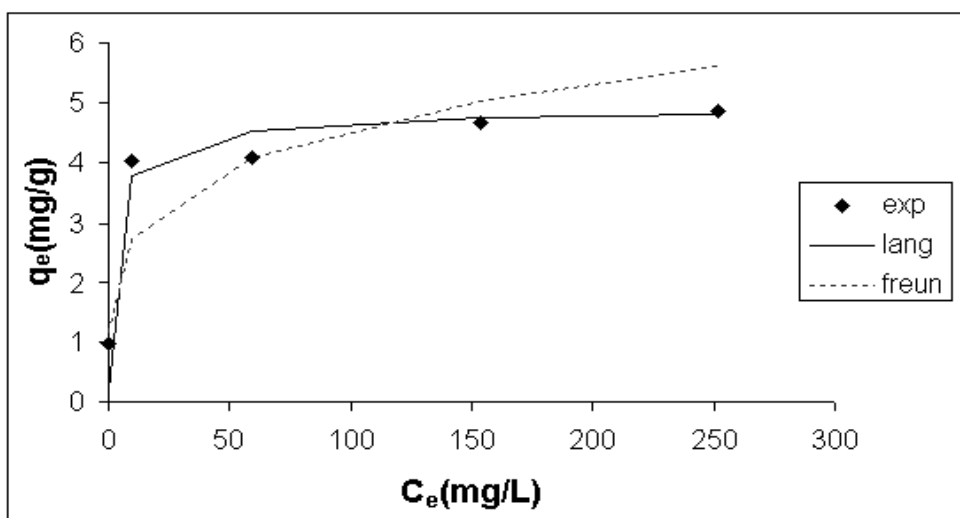


(a)

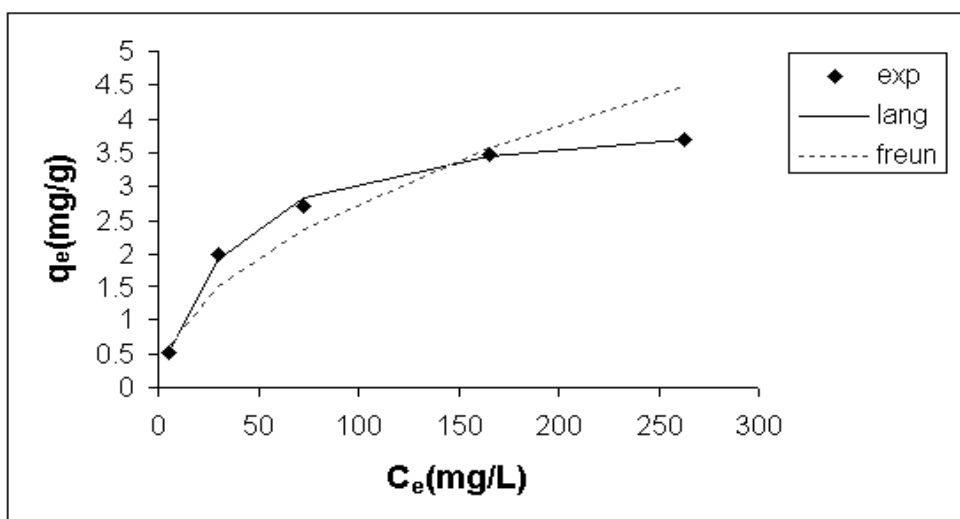


(b)

Figure 7.154. Equilibrium isotherm for Cr (VI) sorption with EC-CMCLI (a) 25 °C  
(b) 40 °C



(a)



(b)

Figure 7.155. Equilibrium isotherm for Cr (VI) sorption with BS-CMCLI (a) 25 °C  
(b) 40 °C

## 7.8. Thermodynamic Parameters

Thermodynamic parameters such as Gibbs free energy ( $\Delta G^\circ$ ), the enthalpy change ( $\Delta H^\circ$ ) and entropy change ( $\Delta S^\circ$ ) for the sorption of Cr (VI) on the sorbents are calculated using the following equations. The values of  $\Delta H^\circ$  and  $\Delta S^\circ$  is determined from the slope and the intercept of the plot between  $\ln b_m$  versus  $1/T$  (Appendix H).

$$\Delta G^0 = -RT \ln b_m \quad (7.8)$$

$$\Delta G^0 = \Delta H^0 - T\Delta S^0 \quad (7.9)$$

$$\ln b_m = \frac{\Delta S^0}{R} - \frac{\Delta H^0}{RT} \quad (7.10)$$

where R is the gas constant (8.314 J/mol.K),  $b_m$  is Langmuir constant (L/mol) and T is temperature (K).

The values of thermodynamic parameters are given in Table 7.34. It is clear from this table that all the values of  $\Delta G^0$  were negative indicating that Cr (VI) sorption process was feasible and spontaneous in nature. The Gibbs free energy values at 25 °C were higher negative values than the values at 40 °C. For that reason, more energetically favorable sorption was occurred at 25 °C. The negative values of  $\Delta H^0$  indicated that the sorption process was exothermic in nature. The negative value of entropy ( $\Delta S$ ) showed the decreased randomness at the solid–liquid interface during the sorption of Cr (VI) onto the sorbents.

It has been reported that  $\Delta G^0$  values up to -20 kJ/mol are consistent with electrostatic interaction between sorption sites and the metal ion (physical sorption), while  $\Delta G^0$  values more negative than -40 kJ/mol involve charge sharing or transfer from the sorbent surface to the metal ion to form a coordinate bond (chemical sorption) (Horsfall et al., 2004). The calculated  $\Delta G^0$  values were found as -20 kJ/mol. The results also indicated that physical sorption was predominant mechanism in Cr (VI) sorption process.

Table 7.34. Thermodynamic parameters for Cr (VI) sorption on the sorbents

Sorbents	T (K)	$\Delta G^\circ$ (kJ/mol)	$\Delta H^\circ$ (kJ/mol)	$\Delta S^\circ$ (kJ/molK)
CLI	298	-18.5	-35.8	-0.058
	313	-17.6		
AMCLI	298	-18.7	-27.4	-0.029
	313	-18.3		
CMCLI	298	-23.6	-91.9	-0.23
	313	-19.9		
EC-CLI	298	-21.1	-86.7	-0.22
	313	-17.8		
BS-CLI	298	-20.1	-52.8	-0.11
	313	-18.4		
EC-AMCLI	298	-22.3	-99.8	-0.26
	313	-18.4		
BS-AMCLI	298	-19.3	-90.8	-0.24
	313	-15.7		
EC-CMCLI	298	-22.5	-103	-0.27
	313	-18.5		
BS-CMCLI	298	-23.6	-104.1	-0.27
	313	-19.6		

## 7.9. Activation Energy

The activation energy of Cr(VI) sorption onto the sorbents is calculated by Arrhenius relationship:

$$\ln K = \ln A - \frac{E_a}{RT} \quad (7.11)$$

where K is the rate constant, A the Arrhenius constant which is a temperature independent factor,  $E_a$  the activation energy (kJ/mol), R the gas constant (8.314 J/mol K) and T is the temperature in Kelvin (K).

Activation energy of sorption process was calculated using the values of rate constant from intraparticle diffusion and pseudo second order equations (Appendix I). The values of activation energy ( $E_a$ ) was determined from a plot of  $\ln K$  versus  $1/T$  and the results are tabulated in Table 7.35.

The magnitude of activation energy gives an idea about the type of sorption which is mainly physical or chemical. Low activation energies (5–40 kJ/mol) are characteristics for physical sorption, while higher activation energies (40–800 kJ/mol) are characteristic for chemical sorption (Ho and McKay, 2000). Activation energy values of Cr (VI) sorption onto the sorbents were lower than 40 kJ/mol. The results revealed that Cr (VI) sorption process was a physical sorption. Therefore, the affinity of Cr (VI) for the sorbents might be ascribed to Van der Waals forces, hydrogen bonding and electrostatic forces between Cr (VI) species and sorbents. The negative value of the activation energy indicated that Cr (VI) sorption did not favor at high temperature.

Table 7.35. The activation energy values of Cr (VI) sorption onto the sorbents

Sorbents	$E_a$ (kJ/mole)	
	( $k_d$ )	( $k_2$ )
CLI	-21.9	-23.5
AMCLI	-17	-18.5
CMCLI	-33.5	-34.6
EC-CLI	-35.3	-36.4
BS-CLI	-25.9	-28.9
EC-AMCLI	-35.4	-38.7
BS-AMCLI	-33.9	-34.8
EC-CMCLI	-31.6	-32.5
BS-CMCLI	-37.8	-39.4

## CHAPTER 8

### CONCLUSION

Considering the characterization studies, the parent mineral is identified as clinoptilolite. The properties of parent and its surfactant modified forms of can be summarized as:

- SEM results indicated that organic layers were formed on the clinoptilolite rich mineral surface after modification.
- In the XRD patterns, although only decrease in the intensities of the major peaks were observed for the cationic surfactant (HDTMA) modified form two new peaks were seen for the anionic surfactant (SDS) modified form.
- FTIR results of the both modified forms revealed new bands ,which are related to the antisymmetric and symmetric C-H stretching of methylene group and – S=O stretching, were formed.
- Zeta potential results showed that both clinoptilolite and anionic modified clinoptilolite rich mineral were negatively charged and they preserved their negative surface charge in the pH range of 2-12. Cationic modified clinoptilolite rich mineral results showed that cationic modified clinoptilolite rich mineral was positively charged at pH<8.2, whereas it was negatively charged at pH>8.2.
- Parking areas for the HDTMA and SDS on the clinoptilolite rich mineral indicated bilayer surfactant configuration.

Gram positive (*B. subtilis*, *S. aureus*, *S. epidermidis*) and negative (*E. coli*, *P. aeruginosa*) bacteria removal results revealed that:

- Cationic and anionic surfactant modified clinoptilolite rich minerals were much more effective than clinoptilolite rich mineral.
- Removal performances of the gram positive bacteria were higher than gram negative bacteria. The reason for higher bacteria removal might be attributed to secondary polymers on the gram positive bacteria cell wall which may enhance the chemical reactivity of the functional groups.
- Hydrogen bonding was significant mechanism in the bacteria removal by clinoptilolite rich mineral and anionic surfactant modified clinoptilolite rich

mineral whereas both attractive electrostatic forces and hydrogen bonding were effective in the bacteria removal by cationic surfactant modified clinoptilolite rich mineral.

Zeta potential and FTIR results revealed that:

- Non electrostatic forces (hydrogen bonding) play a significant role rather than the electrostatic forces in the cases of clinoptilolite, anionic surfactant modified clinoptilolite and their bacteria loaded forms. Both hydrogen bonding and attractive electrostatic forces are responsible in the cases of cationic surfactant modified clinoptilolite rich mineral and its bacteria loaded forms.

Batch Cr (VI) sorption experiments indicated that:

- The initial Cr (VI) uptake rate decreases with increasing pH, initial concentration, temperature, particle size whereas it increases with increasing agitation speed.
- The equilibrium sorption capacity is not affected by agitation speed and particle size.

Sorption kinetic model results and thermodynamic analysis revealed that:

- ✓ Pseudo-second order kinetic model and Weber-Morris model fitted well with the experimental data more accurately than the pseudo first order kinetic model and Mathew-Weber and Furusawa-Smith model.
- ✓ Sorption of Cr (VI) on the sorbents was a multi-step process, involving external and intraparticle diffusion.
- ✓ Cr (VI) sorption process was mainly controlled by intraparticle diffusion.
- ✓ Cr (VI) sorption process was exothermic and spontaneous.
- ✓ The activation energy results revealed that Cr (VI) sorption process was a physical sorption. Therefore, the affinity of Cr (VI) for the sorbents might be ascribed to Van der Waals forces, hydrogen bond and electrostatic forces between Cr (VI) species and the sorbents.

Bacteria removal results indicated that the decrease level in bacteria concentration were found as in the order of  $1-10^2$  for clinoptilolite rich mineral,  $10^2-10^4$  for anionic surfactant modified clinoptilolite rich mineral and  $10^3-10^5$  for cationic surfactant modified clinoptilolite rich mineral. Cr (VI) percentage removal was found as %45 for the parent mineral and this value increased up to 86% for cationic surfactant modified form. Highest Cr (VI) percentage removal (94%) was achieved by *B. subtilis* loaded cationic surfactant modified clinoptilolite rich mineral.



Local clinoptilolite rich mineral and its modified forms have high potential values in Cr (VI) sorption and bacteria removal.

## REFERENCES

- Abbaszadegan, M.; Monteiro, P.; Ouwens, R.N.; Ryu, H.; Alum, A. Removal and Inactivation of Cryptosporidium and Microbial Indicators by a Quaternary Ammonium Chloride (QAC)-Treated Zeolite in Pilot Filters. *Journal of Environmental Science and Health Part A*, **2006**, 41, 1201–1210.
- Abskharon, R.N.N.; Gad El-Rab, S.M.F.; Hassan, S.H.A.; Shoreit, A.A.M. Reduction of Toxic Hexavalent Chromium by *E.Coli*. *Global Journal of Biotechnology and Biochemistry*, **2009**, 4(2), 98-103.
- Ackley, M.; Yang, R.T. Diffusion in Ion Exchanged Clinoptilolites. *AIChE Journal*, **1991**, 37 (11), 1645-1656.
- Ackley, M.; Rege, S.U.; Saxena, H. Application of natural zeolites in the purification and separation of gases. *Microporous and Mesoporous Materials*, **2003**, 61, 25-42.
- Adhiya, J.; Cai, X.; Sayre, R. T.; Traina, S. J. Binding of Aqueous Cadmium by the Lyophilized Biomass of *Chlamydomonas Reinhardtii*. *Colloids and Surfaces A: Physicochemical and Engineering Aspects*, **2002**, 210, 1-11.
- Akar, S.T.; Yetimoğlu, Y.; Gedikbey, T. Removal of Chromium (VI) Ions from Aqueous Solutions by Using Turkish Montmorillonite Clay: Effect of Activation and Modification. *Desalination*, **2009**, 244 (1-3), 97-108.
- Akdeniz, Y. The Effect of Microwaves on Ion Exchange in Zeolites, Izmir Institute of Technology, Izmir, Turkey, 2009.
- Alsoy, S. Natural Zeolites in Wastewater Treatment, Ege University, Izmir, Turkey, 1993.
- Ams, D.A.; Fein, J.B.; Dong, H.; Maurice, P.A. Experimental Measurements of the Adsorption of *Bacillus Subtilis* and *Pseudomonas mendocina* onto Fe-Oxyhydroxide-Coated and Uncoated Quartz Grains. *Geomicrobiology Journal*, **2004**, 21, 511–519.
- Aravindhana, R.; Madhan, B.; Rao, J. R.; Nair, B.U.; Ramasami, T.C. Bioaccumulation of Chromium from Tannery Wastewater: An Approach for Chrome Recovery and Reuse. *Environ Sci Technol.*, **2004**, 38(1), 300-306.
- Arca, M.Y.; Tüzün, İ., Yalçın, E., İnce, Ö.; Bayramoğlu, G. Utilisation of Native, Heat and Acid-Treated Microalgae *Chlamydomonas reinhardtii* Preparations for Biosorption of Cr (VI) Ions. *Process Biochemistry*, **2005**, 40(7), 2351-2358.
- Armağan, B.; Özdemir, O.; Turan, M.; Çelik, M.S. The Removal of Reactive Azo Dyes by Natural and Modified Zeolites. *Journal of Chemical Technology and Biotechnology*, **2003**, 78, 725-732.

- Armenta, G.A; Iglesias, M.E.P.; Ramos, R.L. Adsorption Kinetic Behaviour of Pure CO<sub>2</sub>, N<sub>2</sub> and CH<sub>4</sub> in Natural Clinoptilolite at Different Temperatures. *Adsorption Science and Technology*, **2003**,21(1), 81-91.
- Arslan, G.; Pehlivan, E. Batch Removal of Chromium (VI) from Aqueous Solution by Turkish Brown Coals. *Bioresource Technology*, **2007**, 98, 2836–2845.
- Atakul, S. Synergistic Effect of Zinc Stearate and Natural Zeolite on PVC Thermal Stability, Izmir Institute of Technology, Izmir, Turkey, 2004.
- Attia, A.A.; Khedr, S.A.; Elkholy, S.A. Adsorption of Chromium Ion (VI) by Acid Activated Carbon. *Brazilian Journal of Chemical Engineering*, **2010**, 27 (1), 183-193.
- Babel, S.; Kurniawan, T.A. A Research Study on Cr (VI) Removal from Contaminated Wastewater Using Natural Zeolite. *Ion Exchange*, **2003**, 14, 289-292.
- Banerjee, S.S.; Joshi, M.V.; Jayaram, R.V. Removal of Cr (VI) and Hg (II) from Aqueous Solutions Using Fly Ash and Impregnated Fly Ash. *Separation and Purification Technology*, **2004**, 39 (7), 1611-1629.
- Barakat, M.A. Adsorption of Heavy Metals from Aqueous Solutions on Synthetic Zeolite. *Research Journal of Environmental Sciences*, **2008**, 2(1), 13-22.
- Baup, S.; Jaffre, C.; Wolbert, D.; Laplanche, A. Adsorption of Pesticides onto Granular Activated Carbon: Determination of Surface Diffusivities Using Simple Batch Experiments. *Adsorption*, **2000**, 6, 219-228.
- Bayat, B. Comparative Study of Adsorption Properties of Turkish Fly Ashes II. The Case of Cr (VI) and Cadmium (II). *Journal of Hazardous Materials*, **2002**, 95, 275–290.
- Bayramoğlu, G.; Çelik, G.; Yalçın, E.; Yılmaz, M.; Arıca, M.Y. Modification of Surface Properties of *Lentinus sajor-caju* Mycelia by Physical and Chemical Methods: Evaluation of Their Cr<sup>6+</sup> Removal Efficiencies from Aqueous Medium. *Journal of Hazardous Material*, **2005**, 119 (1–3), 219–229.
- Benkli, Y.E.; Can, M.F.; Turan, M.; Çelik, M.S. Modification of Organo-Zeolite Surface for the Removal of Reactive Azo Dyes in Fixed-Bed Reactors. *Water Research*, **2005**, 39, 487-493.
- Bhattacharya, K.; Venkobachar, C. Removal of Cadmium (II) by Low Cost Adsorbents. *J. Environ. Eng. Diu.* **1984**, 104, 110-122.
- Bhattacharyya, K.G.; Gupta, S.S. Adsorption of Chromium (VI) from Water by Clays. *Ind. Eng. Chem. Res.*, **2006**, 45, 7232–7240.
- Bhattacharya, A.K.; Naiya, T.K.; Mandal, S.N.; Das, S.K. Adsorption, Kinetics and Equilibrium Studies on Removal of Cr (VI) from Aqueous Solutions Using

- Different Low-Cost Adsorbents. *Chemical Engineering Journal*, **2008**, 137, 529-541.
- Bowman, R. Applications of Surfactant-Modified Zeolites to Environmental Remediation. *Microporous and Mesoporous Materials*, **2003**, 61, 43-56.
- Breck, D.W. *Zeolite Molecular Sieves Structure, Chemistry and Use*, Wiley Interscience, New York, 1974.
- Brum, M.C.; Capitaneo, J.L.; Oliveira, J.F. Removal of Hexavalent Chromium from Water by Adsorption onto Surfactant Modified Montmorillonite. *Minerals Engineering*, **2010**, 23(3), 270-272.
- Campos, V.; Morais, L.C.; Buchler, P.M. Removal of Chromate from Aqueous Solution Using Treated Natural Zeolite. *Environmental Geology*, **2007**, 52, 1521-1525.
- Can, Ö. Ion Exchange in Natural Zeolite Packed Column, Izmir Institute of Technology, Izmir, Turkey, 2004
- Cansever, B. Treatment of Domestic Wastewater with Natural Zeolites, Izmir Institute of Technology, Izmir, Turkey, 2004.
- Cao, Y.; Wei, X.; Cai, P.; Huang, Q.; Rong, X.; Liang, W. Preferential adsorption of extracellular polymeric substances from bacteria on clay minerals and iron oxide, *Colloids and Surfaces B: Biointerfaces*, **2011**, 83, 122–127
- Cheng, F.; Wang, Y. Determination of the Copper Oxidation State in a Zeolite Catalyst Through the X-ray Absorption Edge/Self Absorption Effect by Electron Probe Microanalysis. *X-Ray Spectrometry*, **1994**, 23, 272–277.
- Chutia, P.; Kato, S.; Kojima, T.; Satokawa, S. Adsorption of As (V) on Surfactant-Modified Natural Zeolites. *Journal of Hazardous Material*, **2009**, 162, 204-211.
- Choy, K. K.H.; Porter, J. F.; McKay, G. Film–pore diffusion models—analytical and numerical solutions. *Chemical Engineering Science*, **2004**, 59, 501-512.
- Cloete, T.E.; Brözel, V.S.; Holya, V.S. Practical Aspects of Biofouling Control in Industrial Water Systems. *Int. Biodeterior. Biodegradation*, **1992**, 29, 299-341.
- Cloete, T.E.; Jacobs, L. Surfactants and the Attachment of *Pseudomonas Aeruginosa* to 3CR12 Stainless steel and Glass. *Water SA*, **2001**, 27 (1), 21-26.
- Coeuret, F. Percolating Porous Electrode-I. Mass transfer in fixed bed. *Electrochim. Acta*, **1976**, 21, 185-193.
- Cordoves P.; Valde, G.; Fernandez, T.; Luis, P.; Calzo, J.; Garcia, M. Characterization of the Binding Site Affinity Distribution of a Surfactant-Modified Clinoptilolite. *Microporous and Mesoporous Materials*, **2008**, 109, 38-48.

- Deepa , K.K. ; Sathishkumar , M.; Binupriya , A.R.; Murugesan , G.S.; Swaminathan , K. ; Yun, S.E. Sorption of Cr(VI) from Dilute Solutions and Wastewater by Live and Pretreated Biomass of *Aspergillus Flavus*. *Chemosphere*, **2006**, 62, 833–840.
- Demir, H. Synergistic Effect of Natural Zeolites on Flame Retardant Additives Izmir Institute of Technology, Izmir, Turkey, 2004.
- Demir, H.; Sipahioğlu, M.; Balköse, D.; Ülkü, S. Effect of Additives on Flexible PVC Foam Formation. *Journal of Materials Processing Technology*, **2008**, 195 (1-3), 144-153.
- Deo, N.; Natarajan, K.A.; Somasundaran, P. Mechanisms of Adhesion of *Paenibacillus Polymyxa* onto Hematite, Corundum and Quartz. *Int. J. Miner. Process.* **2001**, 62, 27–39.
- Derjaguin BV, Landau L. Theory of the Stability of Strongly Charged Lyophobic Sols and of the Adhesion of Strongly Charged Particles in Solutions of Electrolytes. *Acta Physiocochem. URSS*, **1941**, 14, 628–633.
- Diaz-Nava, C.; Olguin, M.T., Solache-Rios, M., Alarcon-Herrera, M.T., Aguilar-Elguezabal, A. Phenol sorption on surfactant-modified Mexican zeolitic-rich tuff in batch and continuous systems. *Journal of Hazardous Materials*, **2009**, 167, 1063-1069.
- Doula, M.; Ioannou, A. The Effect of Electrolyte Anion on Cu Adsorption–Desorption by Clinoptilolite. *Microporous and Mesoporous Materials*, **2003**, 58, 115-130.
- Dönmez, G.C.; Aksu, Z.; Öztürk, A.; Kutsal, T. A Comparative Study on Heavy Metal Biosorption Characteristics of Some Algae. *Process Biochem.* , **1999**, 34 (9), 885–892.
- Eisenman, G. Cation selective glass electrodes and their mode of operation. *Biophys. J.*, **1962**, 2, 259–323.
- Elangovan, R.; Abhipsa, S.; Rohit B.; Ligy P.; Chandraraj, K. Reduction of Cr(VI) by a *Bacillus sp.* *Biotechnology Letters* , **2006**, 28, 247–252.
- EPA (Environmental Protection Agency) (1990) *Environmental Pollution Control Alternatives*. EPA/625/5-90/025, EPA/625/4-89/023, Cincinnati, US
- Erdoğan, B.C.; Seyhan, A.T.; Ocak, Y.; Tanoğlu, M.; Balköse, D.; Ülkü, S. Cure Kinetics of Epoxy Resin-Natural Zeolite Composites. *Journal of Thermal Analysis and Calorimetry*, **2008**, 94(3), 743–747.
- Faghihian, H.; Bowman, R. Adsorption of Chromate by Clinoptilolite Exchanged with Various Metal Cations. *Water Research*, **2005**, 39, 1099–1104.
- Fang, L.; Cai, P; Li, P.; Wu, H.; Liang, W.; Rong, X.; Chen, W.; Huang, Q. Microcalorimetric and potentiometric titration studies on the adsorption of

- copper by *P. putida* and *B. thuringiensis* and their composites with minerals. *Journal of Hazardous Materials*, **2010**, 181, 1031-1038.
- Farias, T.; Menorval, L.C.; Zajac, J.; Rivera, A. Adsorbilization of drugs onto natural clinoptilolite modified by adsorption of cationic surfactants. *Colloids and Surfaces B: Biointerfaces*, **2010**, 76, 421-426.
- Flemming H.C.; Wingender J. Relevance of Microbial Extracellular Polymeric Substances (EPSs). Part I: Structural and Ecological Aspects. *Water Sci Technol*, **2001**, 43, 1-8.
- Fletcher M. Effects of Culture Concentration and Age, Time, and Temperature on Bacterial Attachment to Polystyrene. *Can J Microbiol*, **1977**, 23, 1-6.
- Fu, Q.; Deng, Y.; Li, H.; Liu, J.; Hu, H.; Chen, S.; Sa, T. Equilibrium, Kinetic and Thermodynamic Studies on the Adsorption of the Toxins of *Bacillus Thuringiensis* Subsp. *Kurstaki* By Clay Minerals. *Applied Surface Science*, **2009**, 255 (8), 4551-4557.
- Gabr, R.M.; Gad El-Rab, S.M.F.; Abskharon, R.N.N.; Hassan, S.H.A.; Shoreit, A.A.M. Biosorption of Hexavalent Chromium Using Biofilm of *E. Coli* Supported on Granulated Activated Carbon. *World J Microbiol Biotechnol*, **2009**, 25, 1695-1703.
- Gaikar, V.G.; Padalkar K.V.; Aswal, V.K. Characterization of Mixed Micelles of Structural Isomers of Sodium Butyl Benzene Sulfonate and Sodium Dodecyl Sulfate by SANS, FTIR Spectroscopy and NMR Spectroscopy. *Journal of Molecular Liquids*, **2008**, 138, 155-167.
- Ganguli, A.; Tripathi, A.K. Survival and Chromate Reducing Ability of *Pseudomonas Aeruginosa* in Industrial Effluents. *Letters in Applied Microbiology*, **1999**, 28, 76-80.
- Gardon AS, Millero FJ. Electrolyte Effects on Attachment of an Estuarine Bacterium. *Appl Environ Microbiol*, **1984**, 47, 495-499.
- Ghiaci, M.; Kiaa, R.; Abbaspur, A.; Seyedeyn-Azad, F. Adsorption of Chromate by Surfactant-Modified Zeolites and MCM-41 Molecular Sieve. *Separation and Purification Technology*, **2004**, 40, 285-295.
- Ghiaci, M; Abbaspur, A.; Kiaa, R; Seyedeyn-Azad, F. Equilibrium Isotherm Studies for the Sorption of Benzene, Toluene, and Phenol onto Organo-Zeolites and as-synthesized MCM-41. *Separation and Purification Technology*, **2004**, 40, 217-229.
- Ghosh, P.K. Hexavalent chromium [Cr (VI)] removal by acid modified waste activated carbons. *Journal of Hazardous Materials*, **2009**, 171, 116-122.
- Gilbert P; Evans D.J.; Evans E; Duguid I.G.; Brown M.R.W. Surface Characteristics and Adhesion of *E. coli* and *S. epidermidis*. *J Appl Bacteriol*, **1991**, 71, 72-77.

- Gode, F.; Pehlivan, E. Chromium (VI) Adsorption by Brown Coals. *Energy Sources, Part A: Recovery, Utilization, and Environmental Effects*, **2006**, 28, 447–457.
- Goldberg, S. Use of Surface Complexation Models in Soil Chemical Systems. *Adv. Agron.* **1992**, 47, 233-329.
- Gupta, V.K.; Rastogi, A. Biosorption of Hexavalent Chromium by Raw and Acid-Treated Green Alga *Oedogonium Hatei* from Aqueous Solutions. *Journal of Hazardous Material*, **2009**, 163, 396–402.
- Haggerty, G. M.; Bowman, R. S. Sorption of Chromate and Other Inorganic Anions by Organo-Zeolite. *Environmental Science and Technology*, **1994**, 28, 452-458
- Hamadi, N.K.; Chen, X.D.; Farid, M.M.; Lu, M.G.Q. Adsorption Kinetics for the Removal of Chromium (VI) from Aqueous Solution by Adsorbents Derived From Used Tyres and Saw Dust. *Chem. Eng. J.*, **2001**, 83, 95–105.
- Ho, Y.S.; McKay, G. Sorption of Dye from Aqueous Solution by Peat. *Chemical Engineering Journal*, **1998**, 70, 115-124.
- Ho, Y.S.; Ng, J.C.Y.; McKay, G. Kinetics of Pollutant Sorption by Biosorbents: Review. *Separation and Purification Methods*, **2000**, 29 (2), 189-232.
- Ho, Y.S.; Ofomaja, A.E. Pseudo-second-order model for lead ion sorption from aqueous solutions onto palm kernel fiber. *Journal of Hazardous Material*, **2006**, 129, 137–142.
- Horsfall, M.; Spiff, A. I.; Abia, A. A. Studies on the Influence of Mercaptoacetic Acid (MAA) Modification of Cassava (*Manihot Sculenta* Cranz), Waste Biomass on the Adsorption of  $\text{Cu}^{2+}$  and  $\text{Cd}^{2+}$  from Aqueous Solution. *Bulletin of the Korean Chemical Society*, **2004**, 25 (7), 969-976
- Hossein, F.; Mousazadeh, M.H. Removal of PAHs from n-Paraffin by Modified Clinoptilolite. *Iran. J. Chem. Chem. Eng.* , **2007**, 26 (3), 121–127.
- Hrenovic, J.; Tibljaš, D.; Orhan, Y.; Büyükgüngör, H. Immobilization of *Acinetobacter calcoacetius* using natural carriers. *Water SA* , **2005**, 31(2),261-266.
- <http://classes.midlandstech.edu>
- Hu, B.; Luo, H. Adsorption of hexavalent chromium onto montmorillonite modified with hydroxyaluminum and cetyltrimethylammonium bromide. *Applied Surface Science*, **2010**, 257, 769–775.
- Huang, H.; Xiao, X.; Yan, B.; Yang, L. Ammonium Removal from Aqueous Solutions by Using Natural Chinese (Chende) Zeolite as Adsorbent. *Journal of Hazardous Material*, **2010**, 175, 247-252.
- Hunter, R. J. *Introduction to Modern Colloid Science*, 1st ed., Oxford Science Publication, UK and USA, 1993.

- Igarashi, H.; Uchida, H.; Sukuzi, M.; Sasaki, Y.; Watanabe; M. Removal of carbon monoxide from hydrogen-rich fuels by selective oxidation over platinum catalyst supported on zeolite. *Applied Catalysis A: General*, **1997**, 159, 159-169.
- İlhan, S; Nourbakhsh, M.N.; Kılıarslan, S.; Özdağ, H. Removal of Chromium, Lead and Copper from Industrial Wastewater by *Staphylococcus saprophiticus*. *Turkish Electronic Journal of Biotechnology*, **2004**, 2, 50-57.
- Inglezakis, V.J.; Diamadis, N.A.; Loizidou, M.D.; Grigoropoulou, H.P. Effect of Pore Clogging on Kinetics of Lead uptake by clinoptilolite. *Journal of Colloid and Interface Science*, **1999**, 215, 54-57.
- Inglezakis V.J.; Loizidou M.D.; Grigoropoulou H.P. Ion Exchange of  $Pb^{2+}$ ,  $Cu^{2+}$ ,  $Fe^{3+}$ , and  $Cr^{3+}$  on Natural Clinoptilolite: Selectivity Determination and Influence of Acidity on Metal Uptake. *Journal of Colloid and Interface Science*, **2003**, 261, 49-54.
- Ivanova, E., Karsheva, M. Ethanol vapours adsorption on natural clinoptilolite-Equilibrium experiments and modeling. *Separation and Purification Technology*, **2010**, 73 (3) 429-431.
- Jia, C.Y; Wei, D.Z.; Li, P.J.; Li, X.J.; Tai, P.D.; Liu, W.; Gong, Z.Q. Selective adsorption of *Mycobacterium Phlei* on pyrite and sphalerite. *Colloids and Surfaces B: Biointerfaces*, **2011**, 83, 214-219.
- Jiang, D.; Huang, Q.; Cai, P.; Rong, X.; Chen, W. Adsorption of *Pseudomonas Putida* on Clay Minerals and Iron Oxide. *Colloids and Surfaces B: Biointerfaces*, **2007**, 54, 217-221
- Jin, X.; Jiang, M.; Shan, X.; Pei, Z.; Chen, Z. Adsorption of Methylene Blue and Orange II onto Unmodified and Surfactant-Modified Zeolite. *Journal of Colloid and Interface Science*, **2008**, 328 (2), 243-247.
- Kallo, D., *Reviews in Mineralogy and Geochemistry, Natural Zeolites: Occurrence, Properties, Applications*, Volume 45, 519-550, 2001.
- Karabelas, A.J.; Wegner, T.H.; Hantratty, T.J. Use of asymptotic relations to correlate mass transfer data in packed beds. *Chemical Engineering Science*, **1971**, 26 (10), 1581-1589.
- Karadağ, D.; Akgül, E.; Tok, S., Erturk; F., Kaya, M.A.; Turan, M. Basic and Reactive Dye Removal Using Natural and Modified Zeolites. *Journal of Chemical and Engineering Data*, **2007**, 52(6), 2436-2441.
- Karapınar, N. Application of Natural Zeolite for Phosphorus and Ammonium Removal from Aqueous Solutions. *Journal of Hazardous Material*, **2009**, 170, 1186-1191.
- Kärger, J.; Ruthven, D. M. *Diffusion in Zeolites and Other Microporous Solids*, John Wiley and Sons: New York; 1992.



- Kataoka, T.; Yoshida, H.; Ueyama, K. Mass transfer in laminar region between liquid and packing material surface in packed bed. *J. Chem. Eng. Japan*, **1972**, 5, 34-38.
- Karthikeyan, T.; Rajgopal, S.; Miranda, L. R. Chromium (VI) Adsorption from Aqueous Solution by Hevea Brasilinesis Sawdust Activated Carbon. *J. Hazardous Material*, **2005**, 124 (1-3), 192-199.
- Khambhaty, Y.; Mody, K.; Basha, S., Jha, B. Biosorption of Cr (VI) onto Marine *Aspergillus Niger*: Experimental Studies and Pseudo-Second Order Kinetics. *World J. Microbiol Biotechnology*, **2009**, 25, 1413-1421.
- Khezami, L.; Capart, R. Removal of Chromium (VI) from Aqueous Solution by Activated Carbons: Kinetic and Equilibrium Studies. *J. Hazardous Material*, **2005**, 123, 223-231.
- Kıvanç, M.; Karakaş, N.; Platin, S. Atık Sulardaki Krom İyonlarının Giderilmesinde “*Bacillus Subtilis*” in Kullanılması. *Ekoloji*, **1996**, 20, 17-20.
- Kinnari, T.J.; Esteban, J.; Martin-de-Hijas, N.Z.; Sanchez-Munoz, O.; Sanchez-Salcedo, S.; Colilla, M.; Vallet-Regi, M.; Gomez-Barrena, E. Influence of Surface Porosity and pH on Bacterial Adherence to Hydroxyapatite and Biphasic Calcium Phosphate Bioceramics. *Journal of Medical Microbiology*, **2009**, 58, 132–137.
- Komiyama, H.; J.M. Smith. Surface Diffusion in Liquid-Filled Pores. *AIChE J.*, **1974**, 20(6), 1110–1117.
- Kotas, J.; Stasicka, Z. Chromium Occurrence in the Environment and Methods of its Speciation, *Environmental Pollution*, **2000**, 107, 263-283.
- Krishna, B.S.; Murty, D.S.R.; Jaiprakash, B.S. Thermodynamics of Chromium (VI) Anionic Species Sorption onto Surfactant-Modified Montmorillonite. *J. Colloid Interf. Sci.*, **2000**, 229, 230–236.
- Kubato, M.; Nakabayashi, T.; Matsumoto, Y.; Shiomi, T.; Yamada, Y.; Ino, K.; Yamanokuchi, H.; Matsui, M.; Tsunoda, T.; Mizukami, F.; Sakaguchi, K. Selective Adsorption of Bacterial Cells Onto Zeolites. *Colloids and Surfaces B: Biointerfaces*, **2008**, 64, 88-97.
- Kuleyin, A. Removal of Phenol and 4-Chlorophenol by Surfactant-Modified Natural Zeolite. *Journal of Hazardous Material*, **2007**, 144, 307-315.
- Kumar, S.; Upadhyay, S. N.; Mathur, V. K. Low Reynolds number mass transfer in packed beds of cylindrical particles. *Industrial and Engineering Chemistry Process Design and Development*, **1977**, 16, 1-8.
- Lakatos, J.; Brown, S. D; Snape, C. E. Coals as Sorbents for the Removal and Reduction of Hexavalent Chromium from Aqueous Waste Streams. *Fuel*, **2002**, 81, 691-698.

- Lam, A.; Rivera, A., Rodriguez-Fuentes, G. Theoretical study of metronidazole adsorption on clinoptilolite. *Microporous and Mesoporous Materials*, **2001**, 49, 157-162.
- Lam, A.; Rivera, A. Theoretical study of the interaction of surfactants and drugs with natural zeolite. *Microporous and Mesoporous Materials*, **2006**, 91, 181-186.
- Lameiras, S.; Quintelas, C.; Tavares, T. Biosorption of Cr (VI) Using a Bacterial Biofilm Supported on Granular Activated Carbon and on Zeolite. *Bioresource Technology*, **2008**, 99, 801–806
- Lee, V.K.C; McKay, G. Comparison of Solutions for the Homogeneous Surface Diffusion model Applied to Adsorption Systems. *Chem. Eng. Journal*, **2004**, 98, 255-264.
- Lehner, T. Removal of Pathogenic Parasites Using Surfactant-modified Zeolite Barriers in a Model Aquifer, The University of Texas At El Paso, USA, 2004.
- Leonard, A.; R.R. Lauwerys. Carcinogenicity and Mutagenicity of Chromium. *Mutat. Res.*, **1980**, 76, 227-239.
- Levenspiel, O., Chemical Reaction Engineering (second ed.), John Wiley, New York, 1972.
- Li, B.; Logan, B.E. Bacterial Adhesion to Glass and Metal Oxide Surfaces, *Colloids and Surfaces B: Biointerfaces*, **2004**, 36, 81-90.
- Li., Z.; Bowman, R. Counterion Effects on the Sorption of Cationic Surfactant and Chromate on Natural Clinoptilolite. *Environmental Science and Technology*, **1997**, 31, 2407-2412.
- Li., Z.; Bowman, R. Sorption of Perchloroethylene by Surfactant-Modified Zeolite as Controlled by Surfactant Loading. *Environmental Science and Technology*, **1998**, 32, 2278-2282.
- Li., Z.; Burt, T.; Bowman, R. Sorption of Ionizable Organic Solutes by Surfactant-Modified Zeolite. *Environmental Science and Technology*, **2000**, 34, 3756-3760.
- Li., Z.; Bowman, R. Retention of Inorganic Oxyanions by Organo-Kaolinite, *Water Research*, **2001**, 35(16), 3771-3776.
- Li, Z; Beachner, R.; McManama, Z, Hanlie, H. Sorption of Arsenic by Surfactant-Modified Zeolite and Kaolinite. *Microporous and Mesoporous Materials*, **2007**, 105, 291-297.
- Lin, Z.; Wu, J.; Xue, R., Yang, Y. Spectroscopic Characterization of Au<sup>3+</sup> Biosorption by Waste Biomass of *Saccharomyces cerevisiae*. *Spectrochim. A Mol Biomol Spectosc*, **2005**, 61 761–765.

- Loukidou, M. X.; Zouboulis, A. I.; Karapantsios, T. D.; Matis, K. A. Equilibrium and Kinetic Modeling of Chromium (VI) Biosorption by *Aeromonas caviae*. *Colloids and Surfaces A: Physicochem. Eng. Aspects*, **2004**, 242, 93-104.
- Majdan, M.; Pikus, S.; Rzacynska, Z.; Uwan, M.; Maryuk, O.; Kwiatkowski, R.; Skrzypek, H. Characteristics of Chabazite Modified by Hexadecyltrimethylammonium Bromide and of its Affinity toward Chromates. *Journal of Molecular Structure*, **2006**, 791, 53-60.
- Mameri, N.; Boudries, N.; Addour, L.; Belhocine, D.; Lounici, H.; Grib, H.; Paus, A. Batch Zinc Biosorption by a Bacterial Nonliving *Streptomyces rimosus* Biomass. *Water Research*, **1999**, 33(6), 1347-1354.
- Marshall K.C.; Stout R., Mitchell R. Mechanisms of the Initial Events in the Sorption of Marine Bacteria to Surfaces. *J Gen Microbiol*, **1971**, 68, 337-348.
- Matthew, A. P.; Weber, W. J. Effects of external mass transfer and intraparticle diffusion on adsorption rates in slurry reactors. *AIChE Symp. Ser.* **1977**, 166, 91-98.
- Mayer, C.; Moritz, R.; Kirschner, C.; Borchard, W.; Maibaum, R.; Wingender, J.; Flemming, H.C. The Role of Intermolecular Interactions: Studies on Model Systems for Bacterial Biofilms. *Int. J. Biol. Macromol.* , **1999**, 26, 3-16.
- McDonnell, G., Russell, A.D. Antiseptics and disinfectants: activity, action, and resistance. *Clin. Microbiol. Rev.* **1999**, 12, 147-179.
- Mckay, G. Solution to the Homogeneous Surface Diffusion Model for Batch Adsorption Using Orthogonal Collocation. *Chemical Engineering Journal*, **2001**, 81, 213-221.
- Mehta, S.K.; Chaudhary, S.; Bhasin, K.K.; Kumar, R.; Aratono, M. Conductometric and Spectroscopic Studies of Sodium Dodecyl Sulfate in Aqueous Media in the Presence of Organic Chalcogen. *Colloids and Surfaces A: Physicochem. Eng. Aspects*, **2007**, 304, 2007, 88-95
- Mei, L.; Busscher, H.J.; Mei, H.C.; Ren, Y. Influence of surface roughness on streptococcal adhesion forces to composite resins, *Dental Materials*, **2011**
- Mier, M.C.; Callejas, R.L.; Gehr, R.; Cisneros, B.J.; Alvares, P.J. Heavy Metal Removal with Mexican Clinoptilolite: Multi-component Ionic Exchange. *Water Research*, **2001**, 35 (2), 373-378.
- Michelson, L.D.; Gideon P.G.; Pace, E.G.; Katal, L.H. Removal of Soluble Mercury from Wastewater by Complexing Techniques, US Department of Industry, Office of Water Res. Technol. Bull. No. 74, 1975.
- Mijangos, F.; Navarro A.; Jodra, Y. Kinetic Analysis of Phenol Adsorption from Aqueous Systems. *Canadian Journal of Chemical Engineering*, **2001**, 79, 737-743.

- Milan, Z.; Pozas, C.L.; Cruz, M.; Borja, R; Sanchez, E; Ilangovan, K.; Espinosa, Y.; Luna, B. The Removal of Bacteria by Modified Natural Zeolites. *Journal of Environmental Science and Health, Part A Toxic/Hazardous Substances and Environmental Engineering*, **2001**, 36(6), 1073-1087
- Miranda, M.G.M.; Olguin, M.T. Arsenic Sorption by Modified Clinoptilolite–Heulandite Rich Tuffs. *Journal of Inclusion Phenomena and Macrocyclic Chemistry*, **2007**, 59,131-142.
- Mistry, K.; Desai, C.; Lal, S.; Patel, K.; Patel, B.Hexavalent Chromium Reduction by *Staphylococcus Sp.* Isolated From Cr (VI) Contaminated Land Fill. *International Journal of Biotechnology and Biochemistry*, **2010**, 6(1), 117-129.
- Mohan, D.; Pittman, C.U. Activated Carbons and Low Cost Adsorbents for Remediation of Tri- and Hexavalent Chromium from Water. *Journal of Hazardous Material*, **2006**, 137 (2), 762-811.
- Motsi, T.; Rowson, N.A.; Simmons, M.J.H. Adsorption of Heavy Metals from Acid Mine Drainage by Natural Zeolite. *International Journal of Mineral Processing*, **2009**, 92, 42-48.
- Mumpton, F.A. *Natural Zeolites: Occurrence, Properties and Use*, Pergamon Press, 1978.
- Mumpton, F.A. La Roca Magica: Uses of Natural Zeolites in Agriculture and Industry. *Proceedings of National Academy of Sciences of the United States of America*, **1999**, 96, 3463-3470.
- Nakamura, T.; Ishikawa, M.; Hiraiwa, T.; Sato, J. X-Ray Diffractometric Determination of Clinoptilolite in Zeolite Tuff using Multiple Analytical Lines. *Anal. Sci.* **1992**, 8, 539-543.
- Narin, G. A Chromatographic Study of Carbon Monoxide Adsorption in Clinoptilolite. Izmir Institute of Technology, Izmir, Turkey, 2001.
- Olive, H.; Lacoste, G. Application of volumetric electrodes to the recuperation of metals in industrial effluents-I. Mass transfer in fixed beds of spherical conductive particles. *Electrochim. Acta.* **1979**, 24, 1109-1114.
- Orhan, Y.; Kocaoba, S. Adsorption of Toxic Metals by Natural and Modified Clinoptilolite. *Annali di Chimica*, **2007**, 97, 781-790.
- Ortega, M.P.; Hagiwara, T.; Watanabe, H.; Sakiyama, T. Adhesion behavior and removability of *Escherichia coli* on stainless steel surface, *Food Control*, **2010**, 21, 573-578.
- Özkan, F.C; Ülkü S. The Effect of HCl Treatment on Water Vapor Adsorption Characteristic of Clinoptilolite Rich Natural Zeolites. *Microporous and Mesoporous Material*, **2005**, 77, 47-53.

- Özkan, F.C; Ülkü S. Diffusion Mechanism of Water Vapour in a Zeolitic Tuff Rich in Clinoptilolite. *Journal of Thermal Analysis and Calorimetry*, **2008**, 94(3), 699-702.
- Parameswari, E.; Lakshmanan, A.; Thilagavathi, T. Biosorption of Chromium (VI) and Nickel (II) by Bacterial Isolates from an Aqueous Solution. *Electronic Journal of Environmental, Agricultural and Food Chemistry*, **2009**, 8(3), 150-156.
- Park, D.; Yun, Y.S; Park, J.M. Use of Dead Fungal Biomass for the Detoxification of Hexavalent Chromium: Screening and Kinetics. *Process Biochem.* **2005**, 40, 2559.
- Park, D.;Yun,Y.S; Park, J.M. Studies on Hexavalent Chromium Biosorption by Chemically-Treated Biomass of *Ecklonia* sp. *Chemosphere*, **2005**, 60 (10), 1356–1364.
- Pavelic, K.; Hadzija, M.; Bedrica, L.; Pavelic, J.; Dikic, I.; Katic, M.; Kralj, M.; Bosnar, M.H.; Kapitanovic, S.; Poljak-Blazi, M.; Krizanac, S.; Stojkovic, R.; Jurin, M.; Subotic, B.; Colic, M. Natural Zeolite Clinoptilolite: New Adjuvant in Anticancer Therapy. *Journal of Molecular Medicine*, **2001**, 78, 708-720.
- Pavelic, K.; Katic, M.; Sverko, V.; Marotti, T.; Bosnjak, B.; Balog, T.; Stojkovic, R.; Radacic, M.; Colic, M.; Poljak-Blazi, M. Immunostimulatory Effect of Natural Clinoptilolite as a Possible Mechanism of its Antimetastatic Ability. *Journal of Cancer Research and Clinical Oncology*, **2002**, 128, 37-44.
- Pellerin C.; Booker SM. Reflections on Hexavalent Chromium. *Environ Health Persp.* **2000**, 108, 402–407.
- Pethkar, A.V.; Kulkarni, S. K.; Paknikar, K.M. Comparative Studies on Metal Biosorption by Two Strains of *Cladosporium Cladosporioide*. *Bioresource Technology*, **2001**, 20, 211-215.
- Pineda, T.B. Bacterial Species Spectroscopic Characterization by FTIR, Normal Raman and Surface Enhanced Raman Scattering. University of Puerto Rico, Puerto Rico, 2006.
- Prakasham, R.S.; Merrie, J.S.; Sheela, R., Saswathi, N.; Ramakrishna, S.V. Biosorption of Chromium (VI) by Free and Immobilized *Rhizopus Arrhizus*. *Environ. Pollut.*, **1999**, 104 (3) 421–427.
- Quintelas, C; Fernandes, B.; Castro J.; Figueiredo, H.; Tavares, T. Biosorption of Cr(VI) by Three Different Bacterial Species Supported on Granular Activated Carbon-a Comparative Study. *Journal of Hazardous Materials*, **2008**, 153, 799–809.
- Quintelas, C; Rocha, Z.; Silva, B.; Fonseca, B.; Figueiredo, H.; Tavares, T. Removal of Cd (II), Cr(VI), Fe(III) and Ni(II) from Aqueous Solutions by an *E. coli* Biofilm Supported on Kaolin. *Chemical Engineering Journal*, **2009**, 149(1-3), 319-324.

- Quintelas, C; Rocha, Z.; Silva, B.; Fonseca, B.; Figueiredo, H.; Tavares, T. Biosorptive Performance of an *Escherichia Coli* Biofilm Supported on Zeolite NaY for the Removal of Cr(VI), Cd(II), Fe(III) and Ni(II). *Chemical Engineering Journal*, **2009**, 152(1), 110-115.
- Ramos, R.L.; Azuara, A.J.; Flores, P.E.D.; Coronado, G.R.M.; Barron, J.M.; Mendoza, M.S.B. Adsorption of Chromium (VI) from an Aqueous Solution on a Surfactant-Modified Zeolite. *Colloids and Surfaces A: Physicochemical Engineering Aspects*, **2008**, 330, 35-41.
- Ranz, W.E.; Marshall, W.R. Evaporation from drops Part I. *Chemical Engineering Progress*, **1952**, 48, 141-146.
- Riveria, A.; Farias, T. Clinoptilolite–surfactant composites as drug support: A new potential application. *Microporous and Mesoporous Materials*, **2005**, 80, 337-346.
- Rivera-Garza, M.; Olguin, M.T; Garcia-Sosa, I.; Alcantara, D.; Rodriguez-Fuentes, G. Silver Supported on Natural Mexican Zeolite as an Antibacterial Material. *Microporous and Mesoporous Materials*, **2000**, 39, 431-444.
- Rodriguez-Fuentes, G.; Barrios, M.A.; Iraizoz, A.; Perdomo, I.; Cedre, B.; Enterex: Antidiarrheic drug based on purified natural clinoptilolite, *Zeolites*, **1997**, 19, 441-448.
- Rodriguez-Fuentes, G.; Denis, A.R.; Barrios, M.A.; Ivarez, A., Colarte, A.I. Antacid drug based on purified natural clinoptilolite. *Microporous and Mesoporous Materials*, **2006**, 94, 200-207.
- Rong, X.; Huang, Q; He, X.; Chen, H.; Cai, P.; Liang, W. Interaction of *Pseudomonas Putida* with Kaolinite and Montmorillonite: A Combination Study by Equilibrium Adsorption, ITC, SEM and FTIR. *Colloids and Surfaces B: Biointerfaces*, **2008**, 64, 49–55.
- Rong, X.; Chen, W.; Huang, Q; Cai, P.; Liang, W. *Pseudomonas Putida* Adhesion to Goethite: Studied by Equilibrium Adsorption, SEM, FTIR and ITC. *Colloids and Surfaces B: Biointerfaces*, **2010**, 80, 79–85.
- Rosenberg, M.; Kjelleberg, S. Hydrophobic interactions in bacterial adhesion. *Advance in Microbial Ecology*, **1986**, 9, 353-393.
- Rozic, M.; Sipusic, D.I.; Sekovanic, L.; Miljanic, S.; Curkovic, L.; Hrenovic, J. Sorption Phenomena of Modification of Clinoptilolite Tuffs by Surfactant Cations. *Journal of Colloid and Interface Science*, **2009**, 331, 295–301.
- Russel A.D. Mechanisms of Bacterial Resistance to Biocides. *Int. Biodeterior*, **1990**, 26, 101-110.
- Rust, C.; Schulze-Makuch, D.; Bowman, R. Removal of the human pathogen *Giardia Intestinalis* from groundwater, Zeolite 06—7 th International Conference on the

Occurrence, Properties, and Utilization of Natural Zeolites , Socorro, New Mexico USA, 16–21 July 2006.

Ruthven, D. M. *Principles of Adsorption and Adsorption Processes*, John Wiley and Sons: New York; 1984.

Ruthven, D. M. Fundamentals of Adsorption Equilibrium and Kinetics in Microporous Solids. In *Adsorption and Diffusion, Molecular Sieves*; Karge, H. G.; Weitkamp, J.; Eds.; Springer-Verlag: Berlin, 2006; Vol. 7; 1.

Scamehorn, J.F.; Schechter, R.S.; Wade, W.H. Adsorption of surfactants on mineral oxide surfaces from aqueous solutions: III. Binary mixtures of anionic and nonionic surfactants. *Journal of Colloid and Interface Science*, **1982**, 85 (2), 494-501.

Scheidegger, A.M., Sparks D.L. A Critical Assessment of Sorption-Desorption Mechanisms at the Soil Mineral/Water Interface. *Soil Science*, **1996**, 161, 813-831.

Schulze, D. Surfactant-Modified Zeolite can Protect Drinking Water Wells from Viruses and Bacteria. *Transactions American Geophysical Union*, **2002**, 83 (18), 193-197.

Selatnia, A.; Bakhti, M.Z., Madani, A., Kertous, L., Mansouri, Y. Biosorption of Cd<sup>2+</sup> from Aqueous Solution by a NaOH-Treated Bacterial Dead *Streptomyces rimosus* Biomass. *Hydrometallurgy*, **2004**, 75, 11– 24

Seler, D.M.; Pivac, N. The Effect of Natural Clinoptilolite on the Serotonergic Receptors in the Brain of Mice with Mammary Marcinoma. *Life Science*, **2003**, 73, 2059-2069.

Selomulya, C; Meeyoo, V.; Amal, R. Mechanisms of Cr (VI) Removal from Water by Various Types of Activated Carbons. *J. Chemical Technol. Biotechnology*, **1999**, 74, 111-122.

Semmens, M.J.; Seyfarth, M. The Selectivity of Clinoptilolite for Certain Heavy Metals. *Environmental Science and Technology*, **1975**, 11, 517-526.

Sheng, P.X.; Ting, Y.P.; Chen, J.P.; Hong, L. Sorption of Lead, Copper, Cadmium, Zinc, and Nickel by Marine Algal Biomass: Characterization of Biosorptive Capacity and Investigation of Mechanisms. *J. Colloid Interf. Sci.*, **2004**, 275, 131–141.

Shichi, A.; Satsuma, A.; Iwase, M.; Shimizu, K., Komai, S., Hattori, T. Catalyst Effectiveness Factor of Cobalt Exchanged Mordenites for the Selective Reduction of NO with Hydrocarbons. *Applied Catalysis B: Environmental*, **1998**, 17, 107-113.

Sirkecioğlu, A.; Altav, Y.; Şenatalar, A.E. Adsorption of H<sub>2</sub>S and SO<sub>2</sub> on Bigadiç Clinoptilolite. *Separation Science and Technology*, **1995**, 30(13), 2747-2762.

- Sphan, H.; Schlunder, E. U. The scale-up of activated carbon columns for water purification based on results from batch tests-1. *Chemical Engineering Science*, **1975**, 30, 529-537.
- Sprynkyy, M.; Ligor, T.; Lebeynets, M.; Buszewski, B. Kinetic and equilibrium studies of phenol adsorption by natural and modified forms of the clinoptilolite. *Journal of Hazardous Materials*, **2009**, 169, 847-854.
- Stanley PM. Factors Affecting the Irreversible Attachment of *Pseudomonas Aeruginosa* to Stainless Steel. *Can J Microbiol*, **1983**, 29, 1493–1499.
- Stasicka, Z.; Kotaś, J. Chromium Occurrence in the Environment and Methods of its Speciation. *Environmental Pollution*, **2000**, 107 (3), 263–283.
- Stevik, T.K.; Aa, K.; Ausland, G., Hanssen, J.F. Retention and Removal of Pathogenic Bacteria in Wastewater Percolating through Porous Media: a Review. *Water Research*, **2004**, 38, 1355-1367.
- Stumm, W.; James, J. Aquatic Chemical Kinetics. In *Reaction Rates of Processes in Natural Waters Environmental Science and Technology*. Wiley-Inter Science Series of Texts and Monographs, 1990.
- Stumm, W. Chemistry of the Solid–Water Interface, J. Wiley & Sons Inc., New York, 1991.
- Sullivan, E. J., Hunter, D. B., and Bowman, R. S. Topological and thermal properties of surfactant-modified clinoptilolite studied by Tapping-Mode™ atomic force microscopy and high-resolution Thermogravimetric analysis. *Clays Clay Miner.*, **1997**, 45, 42–53.
- Suzuki, M.; Takao, F. Concentration Dependence of Surface Diffusion Coefficient of Propionic Acid in Activated Carbon Particles. *AIChE J.*, **1982**, 28, 380-385.
- Şenatalar, A.E.; Sirkecioğlu, A. Removal of Ammonium Ion from Wastewaters by Bigadiç Clinoptilolite. *Turkish Journal of Engineering and Environmental Sciences*, **1995**, 19, 399-405.
- Top, A. Cation Exchange ( $\text{Ag}^+$ ,  $\text{Zn}^{+2}$ ,  $\text{Cu}^{+2}$ ) Behaviour of Natural Zeolite Mineral Clinoptilolite. Izmir Institute of Technology, Izmir, Turkey, 2001.
- Toprak, R.; Girgin, İ. Aktifleştirilmiş Klinoptilolit ile Deri Sanayii Atık Sularından Kromun Giderilmesi. *Turk J Engin Environ Sci*, **2000**, 24, 343-351
- Townsend, R.P. Ion Exchange in Zeolites: Some Recent Developments in Theory and Practice. *Pure & Applied Chemistry*, **1986**, 58 (10), 1359-1366.
- Traegner, U.K.; Suidan, M.T. Parameter Evaluation for Carbon Adsorption. *J. Environ. Eng. Div.*, **1989**, 115 (12), 109–128.
- Tsitsishvili, G.V.; Andronikashvili, T.G.; Kirov, G.N; Filizova, L.D. *Natural Zeolites*, Ellis Horwood, New York, 1992.



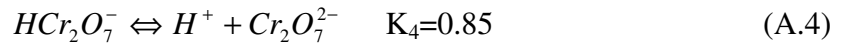
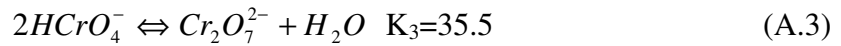
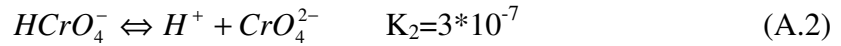
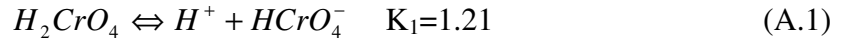
- Tunalı, S.; Kiran, I.; Akar, T. Chromium (VI) Biosorption Characteristics of *Neurospora Crassa* Fungal Biomass. *Min. Eng.*, **2005**, 18 (7), 681–689.
- Türkmen, M. Removal of Heavy Metals from Wastewaters by Use of Natural Zeolites. Izmir Institute of Technology, İzmir, Turkey, 2001.
- Ülkü, S. Application of Natural Zeolites in Water Treatment. Çevre '84-Umwelli '84; V. Deutch- Türkisches Symposium für Umweltingenieurwesen.
- Ülkü, S. Heat and Mass Transfer in Adsorbent Beds. In *Convective Heat and Mass Transfer in Porous Media*; Kakaç, S., Kilkiş, B., Kulakci, F. A., Arınç, F., Eds.; NATO Series; Kluwer Academic Publishers: Dordrecht, 1991;695-725.
- Ülkü, S.A.; Mobedi, M. Adsorption in Energy Storage. In *Energy Storage Systems*; Kakaç, S., Kilkiş, B. Eds.; Kluwer Academic Publishers: Netherlands, 1989; 487-507.
- Verwey E.J.W; Overbeek J.T.G. Theory of the stability of lyophobic colloids. Amsterdam: Elsevier; 1948.
- Villadsen, J.V.; Stewart, W.E. Solution of Boundary-Value Problems by Orthogonal Collocation. *Chemical Engineering Science*, **1967**, 22, 1483-1501.
- Volesky, B. Biosorption and Me. *Water Research*, **2007**, 41, 4017 – 4029
- Wang, J.; Chen, C. Biosorbents for Heavy Metals Removal and Their Future. *Biotechnology Advances*, **2009**, 27, 195-226
- Wang, J.; Li; A.; Xu, L.; Zhou, Y. Adsorption of Tannic and Gallic Acids on a New Polymeric Adsorbent and the Effect of Cu(II) on Their Removal. *Journal of Hazardous Materials*, **2009**, 169, 794-800.
- Warchol, J.; Misaelides, P.; Petrus, R.; Zamboulis, D. Preparation and Application of Organo-Modified Zeolitic Material in the Removal of Chromates and Iodides. *Journal of Hazardous Material*, **2006**, 137, 1410-1416.
- Wei, X.; Fang, L.; Cai, P.; Huang, Q.; Chen, H.; Liang, W.; Rong, X.; Influence of extracellular polymeric substances (EPS) on Cd adsorption by bacteria. *Environmental Pollution*, **2011**, 159, 1369-1374
- Whitekettle W.K. Effects of Surface-Active Chemicals on Microbial Adhesion. *J. Ind. Microbiol*, **1991**, 7, 105-116.
- Yang, X.; Al-Duri, B. Kinetic modeling of liquid-phase adsorption of reactive dyes on activated carbon. *Journal of Colloid and Interface Science*, **2005**, 287, 25–34.
- Yee, N.; Fein, J.B.; Daughney, C.J. Experimental Study of the pH, Ionic Strength, and Reversibility Behavior of Bacteria–Mineral Adsorption. *Geochimica et Cosmochimica Acta*, **2000**, 64 (4), 609-617.

- Yun, Y. S.; Park, D. H.; Park, J. M.; Volesky, B. Biosorption of Trivalent Chromium on the Brown Seaweed Biomass. *Environ. Sci. Technol.*, **2001**, 35, 4353-4358.
- Yusof, A.M.; Malek, N.A.M.N. Removal of Cr (VI) and As(V) from aqueous solutions by HDTMA-modified zeolite Y. *Journal of Hazardous Materials*, **2009**, 162, 1019-1024.
- Zamzow, M.J.; Murphy, J.E. Removal of Metal Cations from Water Using Zeolites. *Separation Science and Technology*, **1992**, 27(14), 1969-1984.
- Zhang, Y.; Zhong, S.; Zhang, M.; Lin, Y. Antibacterial Activity of Silver-Loaded Zeolite Prepared by a Fast Microwave-Loading Method. *Journal of Material Science*, **2009**, 44, 457-462.
- Zhang, H.; Tang, Y.; Cai, D.; Liu, X.; Wang, X.; Huang, Q.; Yu, Z. Hexavalent chromium removal from aqueous solution by algal bloom residue derived activated carbon: Equilibrium and kinetic studies. *Journal of Hazardous Materials*, **2010**, 181, 801-808.
- Zeng, Y.; Woo, H.; Lee, G.; Park, J. Removal of Chromate from Water Using Surfactant Modified Pohang Clinoptilolite and Haruna Chabazite. *Desalination*, **2010**, 257, 102-109.

## APPENDIX A

### HEXA VALENT CHROMIUM SPECIATION DIAGRAM

Total hexavalent chromium is composed of five species which are  $H_2CrO_4$ ,  $HCrO_4^-$ ,  $CrO_4^{2-}$ ,  $Cr_2O_7^{2-}$  and  $HCr_2O_7^-$ . The speciation diagram is calculated by using the reactions between these species and the reaction equilibrium constant (K).



The total chromium concentration is written from the summation of five species which is given in Equation A.5.

$$[Cr] = [H_2CrO_4] + [HCrO_4^-] + [CrO_4^{2-}] + 1/2[Cr_2O_7^{2-}] + 1/2[HCr_2O_7^-] \quad (A.5)$$

Equations A.6- A.9 defines the equilibrium constants for Cr (VI) species:

$$K_1 = \frac{[H^+][HCrO_4^-]}{[H_2CrO_4]} \quad (A.6)$$

$$K_2 = \frac{[H^+][CrO_4^{2-}]}{[HCrO_4^-]} \quad (A.7)$$

$$K_3 = \frac{[Cr_2O_7^{2-}]}{[HCrO_4^-]^2} \quad (A.8)$$

$$K_4 = \frac{[Cr_2O_7^{2-}][H^+]}{[HCr_2O_7^-]} \quad (A.9)$$

In order to calculate amount of each species, Equations A.6-A.9 can be arranged and substituted into A.5.

### A.1. Calculation of Concentration of $H_2CrO_4$

From Eqn A.6:

$$[HCrO_4^-] = \frac{[H_2CrO_4]K_1}{[H^+]} \quad (A.10)$$

From Eqn A.6 and Eqn A.7:

$$[CrO_4^{2-}] = \frac{K_1K_2 [H_2CrO_4]}{[H^+]^2} \quad (A.11)$$

From Eqn A.6 and Eqn A.8:

$$[Cr_2O_7^{2-}] = \frac{K_1^2K_3 [H_2CrO_4]^2}{[H^+]^2} \quad (A.12)$$

From Eqn A.6, Eqn A.8 and Eqn A.9:

$$[HCr_2O_7^-] = \frac{K_1^2K_3 [H_2CrO_4]^2}{K_4[H^+]^2} \quad (A.13)$$

Substituting equations A.10-A.13 into equation A.5 gives the total amount of chromium (VI) as a function of  $[H_2CrO_4]$  and  $[H^+]$ .

$$[Cr] = [H_2CrO_4] + \frac{K_1 [H_2CrO_4]}{[H^+]} + \frac{K_1K_2 [H_2CrO_4]}{[H^+]^2} + \frac{K_1^2K_3 [H_2CrO_4]^2}{2[H^+]^2} + \frac{K_1^2K_3 [H_2CrO_4]^2}{2K_4[H^+]^2} \quad (A.14)$$

Eqn A.14 is a quadratic. In order to solve the quadratic equation, the terms are grouped and the final equation is given in Eqn A.16.

$$\left[ \frac{K_1^2 K_3}{2[H^+]^2} + \frac{K_1^2 K_3}{2K_4[H^+]^2} \right] [H_2CrO_4]^2 + \left[ \frac{K_1}{[H^+]} + \frac{K_1 K_2}{[H^+]^2} + 1 \right] [H_2CrO_4] - [Cr] = 0 \quad (\text{A.15})$$

$$[H_2CrO_4] = \frac{\left[ \frac{K_1}{[H^+]} + \frac{K_1 K_2}{[H^+]^2} + 1 \right] + \sqrt{\left[ \frac{K_1}{[H^+]} + \frac{K_1 K_2}{[H^+]^2} + 1 \right]^2 + 4 \left[ \frac{K_1^2 K_3}{2[H^+]^2} + \frac{K_1^2 K_3}{2K_4[H^+]^2} \right] [Cr]}{2 \left[ \frac{K_1^2 K_3}{2[H^+]^2} + \frac{K_1^2 K_3}{2K_4[H^+]^2} \right]} \quad (\text{A.16})$$

## A.2. Calculation of Concentration of $HCrO_4^-$

From Eqn A.6:

$$[H_2CrO_4] = \frac{[H^+] K_1 [HCrO_4^-]}{K_1} \quad (\text{A.17})$$

From Eqn A.7:

$$[CrO_4^{2-}] = \frac{K_2 [H_2CrO_4]}{[H^+]} \quad (\text{A.18})$$

From Eqn A.8:

$$[Cr_2O_7^{2-}] = K_3 [HCrO_4^-]^2 \quad (\text{A.19})$$

From Eqn A.8 and A.9:

$$[HCr_2O_7^-] = \frac{K_3 [H^+] [HCrO_4^-]^2}{K_4} \quad (A.20)$$

Substituting equations A.17-A.20 into equation A.5 gives the total amount of chromium (VI) as a function of  $[HCrO_4^-]$  and  $[H^+]$ .

$$[Cr] = \frac{[H^+] K_1 [HCrO_4^-]}{K_1} + [HCrO_4^-] + \frac{K_2 [HCrO_4^-]}{[H^+]} + \frac{K_3 [HCrO_4^-]^2}{2} + \frac{K_3 [H^+] [HCrO_4^-]^2}{2K_4} \quad (A.21)$$

Eqn A.21 is a quadratic. In order to solve the quadratic equation, the terms are grouped and the final equation is given in Eqn A.23.

$$\left[ \frac{K_3}{2} + \frac{K_3 [H^+]}{2K_4} \right] [HCrO_4^-]^2 + \left[ \frac{[H^+]}{K_1} + \frac{K_2}{[H^+]} + 1 \right] [HCrO_4^-] - [Cr] = 0 \quad (A.22)$$

$$[HCrO_4^-] = \frac{- \left[ \frac{[H^+]}{K_1} + \frac{K_2}{[H^+]} + 1 \right] + \sqrt{\left[ \frac{[H^+]}{K_1} + \frac{K_2}{[H^+]} + 1 \right]^2 + 4 \left[ \frac{K_3}{2} + \frac{K_3 [H^+]}{2K_4} \right] [Cr]}}{2 \left[ \frac{K_3}{2} + \frac{K_3 [H^+]}{2K_4} \right]} \quad (A.23)$$

### A.3. Calculation of Concentration of $CrO_4^{2-}$

From Eqn A.6 and A.7:

$$[H_2CrO_4] = \frac{[H^+]^2 [CrO_4^{2-}]}{K_1 K_2} \quad (A.24)$$

From Eqn A.7:

$$[HCrO_4^-] = \frac{[H^+]^2 [CrO_4^{2-}]}{K_2} \quad (A.25)$$

From Eqn A.7 and A8:

$$[Cr_2O_7^{2-}] = \frac{K_3 [H^+]^2 [CrO_4^{2-}]^2}{K_2^2} \quad (A.26)$$

From Eqn A.7, A.8 and A.9:

$$[HCr_2O_7^-] = \frac{K_3 [H^+]^3 [CrO_4^{2-}]^2}{K_4 K_2^2} \quad (A.27)$$

Substituting equations A.24-A.27 into equation A.5 gives the total amount of chromium (VI) as a function of  $[CrO_4^{2-}]$  and  $[H^+]$ .

$$[Cr] = \frac{[H^+]^2 [CrO_4^{2-}]}{K_1 K_2} + \frac{[H^+] [CrO_4^{2-}]}{K_2} + [CrO_4^{2-}] + \frac{K_3 [H^+]^2 [CrO_4^{2-}]^2}{2K_2^2} + \frac{K_3 [H^+]^3 [CrO_4^{2-}]^2}{2K_4 K_2^2} \quad (A.28)$$

Eqn A.28 is a quadratic. In order to solve the quadratic equation, the terms are grouped and the final equation is given in Eqn A.30.

$$\left[ \frac{K_3 [H^+]^2}{2K_2^2} + \frac{K_3 [H^+]^3}{2K_4 K_2^2} \right] [CrO_4^{2-}]^2 + \left[ \frac{[H^+]^2}{K_1 K_2} + \frac{K_2 [H^+]}{K_2} + 1 \right] [CrO_4^{2-}] - [Cr] = 0 \quad (A.29)$$

$$[CrO_4^{2-}] = \frac{- \left[ \frac{[H^+]^2}{K_1 K_2} + \frac{[H^+]}{K_2} + 1 \right] + \sqrt{\left[ \frac{[H^+]^2}{K_1 K_2} + \frac{[H^+]}{K_2} + 1 \right]^2 + 4 \left[ \frac{K_3 [H^+]^2}{2K_2^2} + \frac{K_3 [H^+]^3}{2K_4 K_2^2} \right] [Cr]}}{2 \left[ \frac{K_3 [H^+]^2}{2K_2^2} + \frac{K_3 [H^+]^3}{2K_4 K_2^2} \right]} \quad (A.30)$$

#### A.4. Calculation of Concentration of $\text{Cr}_2\text{O}_7^{2-}$

From Eqn A.6 and A.8:

$$[\text{H}_2\text{CrO}_4] = \frac{[\text{H}^+][\text{Cr}_2\text{O}_7^{2-}]^{0.5}}{K_1 K_3^{0.5}} \quad (\text{A.31})$$

From Eqn A.8:

$$[\text{HCrO}_4^-] = \frac{[\text{Cr}_2\text{O}_7^{2-}]^{0.5}}{K_3^{0.5}} \quad (\text{A.32})$$

From Eqn A.7 and A.8:

$$[\text{CrO}_4^{2-}] = \frac{K_2 [\text{Cr}_2\text{O}_7^{2-}]^{0.5}}{K_3^{0.5} [\text{H}^+]} \quad (\text{A.33})$$

From Eqn A.9:

$$[\text{HCr}_2\text{O}_7^-] = \frac{[\text{H}^+][\text{Cr}_2\text{O}_7^{2-}]}{K_4} \quad (\text{A.34})$$

Substituting equations A.31-A.34 into equation A.5 gives the total amount of chromium (VI) as a function of  $[\text{Cr}_2\text{O}_7^{2-}]$  and  $[\text{H}^+]$ .

$$[\text{Cr}] = \frac{[\text{H}^+]^2 [\text{Cr}_2\text{O}_7^{2-}]^{0.5}}{K_1 K_3^{0.5}} + \frac{[\text{Cr}_2\text{O}_7^{2-}]^{0.5}}{K_3^{0.5}} + \frac{K_2 [\text{Cr}_2\text{O}_7^{2-}]^{0.5}}{K_3^{0.5} [\text{H}^+]} + \frac{[\text{Cr}_2\text{O}_7^{2-}]}{2} + \frac{[\text{H}^+][\text{Cr}_2\text{O}_7^{2-}]}{2K_4} \quad (\text{A.35})$$

Eqn A.35 is a quadratic. In order to solve the quadratic equation, the terms are grouped and the final equation is given in Eqn A.37.



$$\left[ \frac{1}{2} + \frac{[H^+]}{2K_4} \right] [Cr_2O_7^{2-}] + \left[ \frac{[H^+]}{K_1K_3^{0.5}} + \frac{1}{K_3^{0.5}} + \frac{K_2}{K_3^{0.5}[H^+]} \right] [Cr_2O_7^{2-}]^{0.5} - [Cr] = 0 \quad (A.36)$$

$$[Cr_2O_7^{2-}] = \frac{\left[ - \left[ \frac{[H^+]}{K_1K_3^{0.5}} + \frac{1}{K_3^{0.5}} + \frac{K_2}{K_3^{0.5}[H^+]} \right] + \sqrt{\left[ \frac{[H^+]}{K_1K_3^{0.5}} + \frac{1}{K_3^{0.5}} + \frac{K_2}{K_3^{0.5}[H^+]} \right]^2 + 4 \left[ \frac{1}{2} + \frac{[H^+]}{2K_4} \right] [Cr]} \right]}{2 \left[ \frac{1}{2} + \frac{[H^+]}{2K_4} \right]} \quad (A.37)$$

### A.5. Calculation of Concentration of $HCr_2O_7^-$

From Eqn A.6, A.8 and A.9:

$$[H_2CrO_4] = \frac{K_4 [H^+]^{0.5} [HCr_2O_7^-]^{0.5}}{K_1 K_3^{0.5}} \quad (A.38)$$

From Eqn A.8 and A.9:

$$[HCrO_4^-] = \frac{K_4^{0.5} [HCr_2O_7^-]^{0.5}}{K_3^{0.5} [H^+]^{0.5}} \quad (A.39)$$

From Eqn A.7 and A.8:

$$[Cr_2O_4^{2-}] = \frac{K_2 K_4^{0.5} [HCr_2O_7^-]^{0.5}}{K_2 [H^+]^{1.5}} \quad (A.40)$$

From Eqn A.9:

$$[Cr_2O_7^{2-}] = \frac{K_4 [HCr_2O_7^-]}{[H^+]} \quad (A.41)$$

Substituting equations A.38-A.41 into equation A.5 gives the total amount of chromium (VI) as a function of  $[HCr_2O_7^-]$  and  $[H^+]$ .

$$[Cr] = \frac{K_4^{0.5}[H^+]^{0.5}[HCr_2O_7^-]^{0.5}}{K_1K_3^{0.5}} + \frac{K_4^{0.5}[HCr_2O_7^-]^{0.5}}{K_3^{0.5}[H^+]^{0.5}} + \frac{K_2K_4^{0.5}[HCr_2O_7^-]^{0.5}}{K_2[H^+]^{1.5}} + \frac{K_4[HCr_2O_7^-]}{2[H^+]} + \frac{[HCr_2O_7^-]}{2} \quad (A.43)$$

Eqn A.43 is a quadratic. In order to solve the quadratic equation, the terms are grouped and the final equation is given in Eqn A.45.

$$\left[ \frac{1}{2} + \frac{K_4}{2[H^+]} \right] [HCr_2O_7^-] + \left[ \frac{K_4^{0.5}[H^+]^{0.5}}{K_1K_3^{0.5}} + \frac{K_4^{0.5}}{K_3^{0.5}[H^+]^{0.5}} + \frac{K_2K_4^{0.5}}{K_2[H^+]^{1.5}} \right] [HCr_2O_7^-]^{0.5} - [Cr] = 0 \quad (A.44)$$

$$[HCr_2O_7^-] = \frac{\left[ - \left[ \frac{K_4^{0.5}[H^+]^{0.5}}{K_1K_3^{0.5}} + \frac{K_4^{0.5}}{K_3^{0.5}[H^+]^{0.5}} + \frac{K_2K_4^{0.5}}{K_2[H^+]^{1.5}} \right] + \sqrt{\left[ \frac{K_4^{0.5}[H^+]^{0.5}}{K_1K_3^{0.5}} + \frac{K_4^{0.5}}{K_3^{0.5}[H^+]^{0.5}} + \frac{K_2K_4^{0.5}}{K_2[H^+]^{1.5}} \right]^2 + 4 \left[ \frac{1}{2} + \frac{K_4}{2[H^+]} \right] [Cr]} \right]}{2 \left[ \frac{1}{2} + \frac{K_4}{2[H^+]} \right]} \quad (A.45)$$

Using the above mentioned equations, Cr (VI) speciation diagram is calculated and shown in Figure 4.1.

## APPENDIX B

### DETERMINATION OF CHROMIUM (VI) CONCENTRATION

Chromium concentrations taken at certain time intervals were analyzed using Inductively Coupled Atomic Emission Spectroscopy (ICP-AES 96, Varian). In ICP analysis, the sample solution which was obtained from the batch experiment was diluted by adding ultra-pure water to the mixture of 1 mL of sample solution and 1 mL HNO<sub>3</sub> which added up to 100 mL. ICP standard solutions were prepared by using 1000 mg/L ICP-multi element solution. Blank sample was prepared in 100 mL flask by using 1 mL HNO<sub>3</sub> and ultra-pure water.

The concentration of Cr (VI) was also determined by measuring the absorbance of the purple complex of Cr (VI) with 1,5-diphenylcarbazide at 540 nm spectrophotometrically.

#### **B.1. Amount of Exchangeable Cations in the Liquid Phase**

ICP-AES was also used to understand the ion exchange mechanism between the Cr (VI) and the exchangeable cations of the clinoptilolite rich mineral. Ion exchange is a stoichiometric reaction. Therefore, in any ion exchange reaction, the equivalent of the major cations released to the solution should be equal to those of the equivalent cations sorbed. For this reason, a balance of equivalent of cations was constructed between the major exchangeable cations released to the solution phase and equivalent of change of Cr (VI) ion in solution. The results are tabulated in B.1-B.10. In tables, equivalent of Cr(VI) ion sorbed by solid phase was determined by the difference in the concentration of Cr(VI) ion in equivalents and also it was calculated by the summation of the equivalents of Na<sup>+</sup>, Mg<sup>+2</sup>, Ca<sup>+2</sup> and K<sup>+</sup> ions released to the solution.

Table B.1. Equivalent of exchangeable cations and Cr (VI) in the sorbents (Conditions: 10 mg/L, 140 rpm, 25 °C, 25–106 μm)

Sorbents	$q_{eq}^a$ (meq /g)	$q_{eq}^b$ (meq /g)	% differences
CLI	0.055	0.040	27.2
AMCLI	0.059	0.042	28.9
CMCLI	0.095	0.063	33.6
EC-CLI	0.062	0.044	29.1
BS-CLI	0.067	0.046	31.3
SA-CLI	0.0638	0.044	31.1
SE-CLI	0.065	0.045	30.8
PA-CLI	0.058	0.041	29.3
EC-AMCLI	0.072	0.047	34.7
BS-AMCLI	0.075	0.049	34.7
SA-AMCLI	0.072	0.049	31.9
SE-AMCLI	0.073	0.049	32.9
PA-AMCLI	0.061	0.045	26.2
EC-CMCLI	0.100	0.065	35.0
BS-CMCLI	0.104	0.064	38.5
SA-CMCLI	0.100	0.065	35.0
SE-CMCLI	0.102	0.066	35.3
PA-CMCLI	0.097	0.065	32.9

a=from Cr (VI) measurements

b=from  $Na^+$  +  $Ca^{2+}$  +  $K^+$  +  $Mg^{2+}$  measurements

Table B.2. Equivalent of exchangeable cations and Cr (VI) in the sorbents (Conditions: 10 mg/L, 140 rpm, 25 °C, pH :3, 25–106 μm)

Sorbents	$q_{eq}^a$ (meq /g)	$q_{eq}^b$ (meq /g)	% differences
CLI	0.05	0.033	34
AMCLI	0.054	0.036	33.3
CMCLI	0.100	0.057	43
EC-CLI	0.084	0.055	34.5
BS-CLI	0.095	0.061	35.8
EC-AMCLI	0.097	0.065	33
BS-AMCLI	0.101	0.068	32.7
EC-CMCLI	0.108	0.07	35.1
BS-CMCLI	0.113	0.074	34.5

a=from Cr (VI) measurements

b=from  $Na^+$  +  $Ca^{2+}$  +  $K^+$  +  $Mg^{2+}$  measurements

Table B.3. Equivalent of exchangeable cations and Cr (VI) in the sorbents (Conditions: 10 mg/L, 140 rpm, 25 °C, pH: 11, 25–106 µm)

Sorbents	$q_{eq}^a$ (meq /g)	$q_{eq}^b$ (meq /g)	% differences
CLI	0.043	0.027	37.2
AMCLI	0.047	0.029	38.3
CMCLI	0.057	0.034	40.3
EC-CLI	0.048	0.030	37.5
BS-CLI	0.049	0.029	40.8
EC-AMCLI	0.047	0.03	36.2
BS-AMCLI	0.048	0.031	35.4
EC-CMCLI	0.049	0.032	34.7
BS-CMCLI	0.051	0.032	37.3

a=from Cr (VI) measurements

b=from  $Na^+ + Ca^{2+} + K^+ + Mg^{2+}$  measurements

Table B.4. Equivalent of exchangeable cations and Cr (VI) in the sorbents (Conditions: 50 mg/L, 140 rpm, 25 °C, pH: 3, 25–106 µm)

Sorbents	$q_{eq}^a$ (meq /g)	$q_{eq}^b$ (meq /g)	% differences
CLI	0.156	0.100	35.9
AMCLI	0.161	0.103	36.1
CMCLI	0.37	0.18	51.3
EC-CLI	0.21	0.142	32.3
BS-CLI	0.25	0.167	33.2
EC-AMCLI	0.27	0.169	37.4
BS-AMCLI	0.28	0.178	36.4
EC-CMCLI	0.42	0.20	52.3
BS-CMCLI	0.47	0.22	53.2

a=from Cr (VI) measurements

b=from  $Na^+ + Ca^{2+} + K^+ + Mg^{2+}$  measurements

Table B.5. Equivalent of exchangeable cations and Cr (VI) in the sorbents (Conditions: 100 mg/L, 140 rpm, 25 °C, pH: 3, 25–106 µm)

Sorbents	$q_{eq}^a$ (meq /g)	$q_{eq}^b$ (meq /g)	% differences
CLI	0.17	0.11	35.3
AMCLI	0.18	0.12	33.3
CMCLI	0.41	0.20	51.2
EC-CLI	0.24	0.16	33.3
BS-CLI	0.26	0.177	31.9
EC-AMCLI	0.27	0.18	33.3
BS-AMCLI	0.31	0.19	38.7
EC-CMCLI	0.44	0.22	50
BS-CMCLI	0.47	0.24	48.9

a=from Cr (VI) measurements

b=from  $Na^+ + Ca^{2+} + K^+ + Mg^{2+}$  measurements

Table B.6. Equivalent of exchangeable cations and Cr (VI) in the sorbents (Conditions: 200 mg/L, 140 rpm, 25 °C, pH: 3, 25–106 μm)

Sorbents	$q_{eq}^a$ (meq /g)	$q_{eq}^b$ (meq /g)	% differences
CLI	0.24	0.14	41.7
AMCLI	0.25	0.15	40
CMCLI	0.44	0.20	54.5
EC-CLI	0.27	0.154	42.9
BS-CLI	0.38	0.22	42.1
EC-AMCLI	0.32	0.22	31.2
BS-AMCLI	0.37	0.23	37.9
EC-CMCLI	0.50	0.28	44
BS-CMCLI	0.54	0.31	42.6

a=from Cr (VI) measurements

b=from  $Na^+ + Ca^{2+} + K^+ + Mg^{2+}$  measurements

Table B.7. Equivalent of exchangeable cations and Cr (VI) in the sorbents (Conditions: 300 mg/L, 140 rpm, 25 °C, pH: 3, 25–106 μm)

Sorbents	$q_{eq}^a$ (meq /g)	$q_{eq}^b$ (meq /g)	% differences
CLI	0.25	0.147	41.2
AMCLI	0.25	0.155	38
CMCLI	0.45	0.23	48.9
EC-CLI	0.28	0.174	37.9
BS-CLI	0.39	0.25	35.9
EC-AMCLI	0.32	0.21	34.4
BS-AMCLI	0.40	0.26	35
EC-CMCLI	0.51	0.28	45.1
BS-CMCLI	0.56	0.30	46.4

a=from Cr (VI) measurements

b=from  $Na^+ + Ca^{2+} + K^+ + Mg^{2+}$  measurements

## APPENDIX C

### ORIENTATION OF SDS MOLECULE ON CLINOPTILOLITE RICH MINERAL

The orientation of SDS molecule on the clinoptilolite rich mineral surface was determined from Bragg's Law.

$$n\lambda = 2d \sin \theta \quad n = 1, 2, \dots$$

where  $\lambda$  (1.546 Å) is the wavelength of the incident beam,  $d$  is the inter-planar distance and  $\theta$  is the angle of the incidence beam.

XRD peaks of SDS molecule were found as 6.621, 7.256, 9.04 and 11.3.  $d/n$  values were determined from Bragg's Law equation.

$$n \cdot 1.546 = 2d \sin \frac{6.621}{2} \quad \frac{d}{n} = 13.385 \quad n=3 \quad d=40.1 \text{ Å}$$

$$n \cdot 1.546 = 2d \sin \frac{7.256}{2} \quad \frac{d}{n} = 12.22 \quad n=3 \quad d=36.7 \text{ Å}$$

$$n \cdot 1.546 = 2d \sin \frac{9.04}{2} \quad \frac{d}{n} = 9.81 \quad n=4 \quad d=39.2 \text{ Å}$$

$$n \cdot 1.546 = 2d \sin \frac{11.3}{2} \quad \frac{d}{n} = 7.85 \quad n=5 \quad d=39.2 \text{ Å}$$

The length of SDS molecule was reported as 21 Å (Gao et al., 2010). For bilayer configuration, the length of SDS molecule was calculated as 42 Å. XRD results revealed that the length of SDS was found as 39.2 Å. The surfactant configuration of SDS molecule is shown in Figure C.1. The results indicated that the angle between SDS molecules was determined as 68.9°.

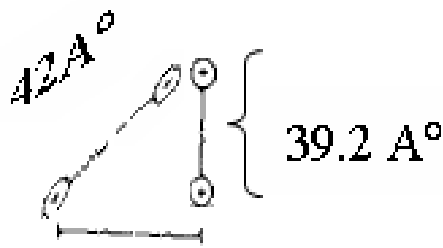


Figure C.1. The surfactant configuration of SDS molecule

In order to determine angle between SDS molecules on the clinoptilolite rich mineral, the similar procedure was applied for anionic modified clinoptilolite rich mineral.

XRD peaks of anionic modified clinoptilolite rich mineral were found as 5.752, 6.621, 8.693 and 11.1.  $d/n$  values were determined from Bragg's Law equation.

$$n \cdot 1.546 = 2d \sin \frac{5.752}{2} \quad \frac{d}{n} = 15.41 \quad n=2 \quad d=30.8 \text{ \AA}$$

$$n \cdot 1.546 = 2d \sin \frac{8.693}{2} \quad \frac{d}{n} = 10.2 \quad n=3 \quad d=30.6 \text{ \AA}$$

$$n \cdot 1.546 = 2d \sin \frac{11.1}{2} \quad \frac{d}{n} = 7.99 \quad n=4 \quad d=31.9 \text{ \AA}$$

The surfactant configuration of SDS molecule on the clinoptilolite rich mineral surface is shown in Figure C.21. The results indicated that the angle between SDS molecules on the clinoptilolite rich mineral was determined as 49.6°.

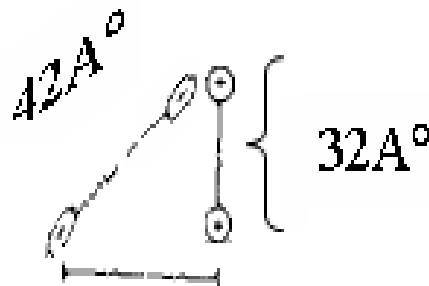


Figure C.2. The surfactant configuration of SDS molecule on clinoptilolite



## APPENDIX D

### PORE SIZE DISTRIBUTIONS OF NATURAL AND SURFACTANT MODIFIED ZEOLITE SAMPLES

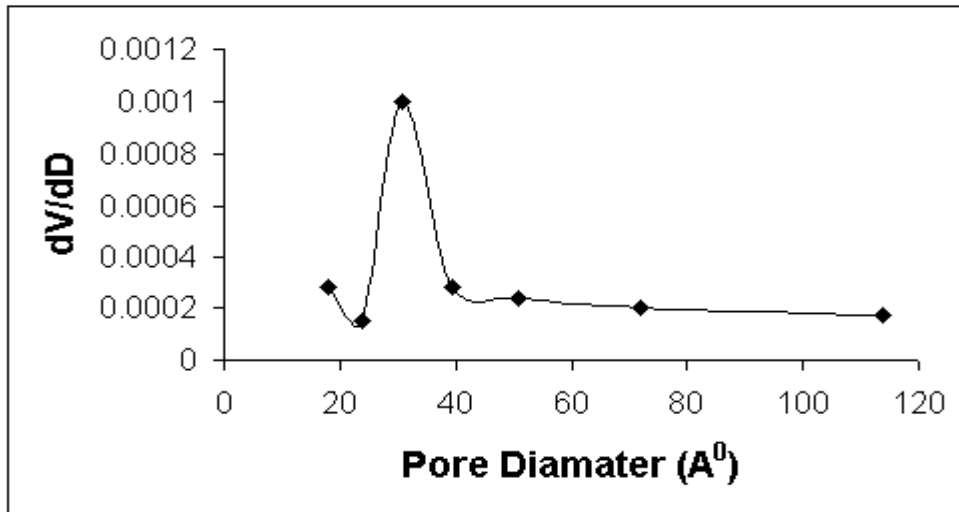


Figure D.1. Pore size distribution of CLI

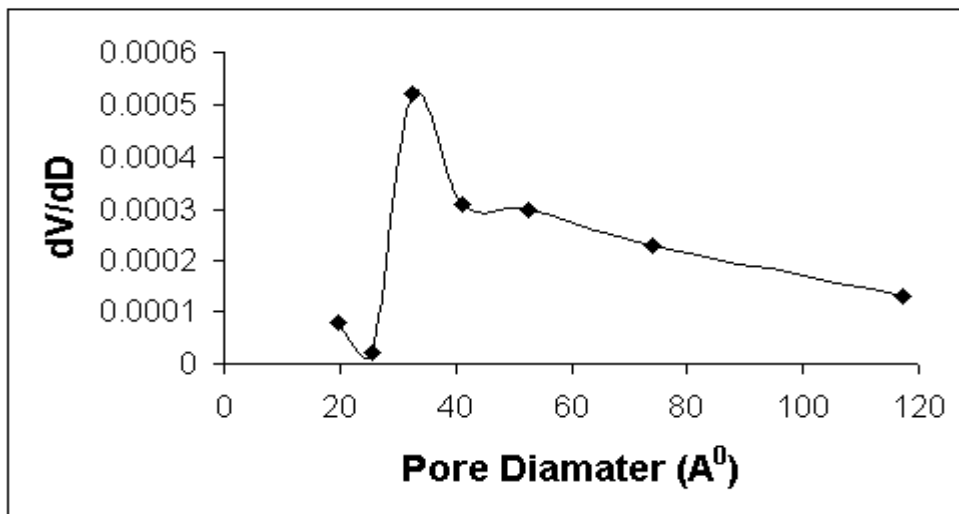


Figure D.2. Pore size distribution of CMCLI

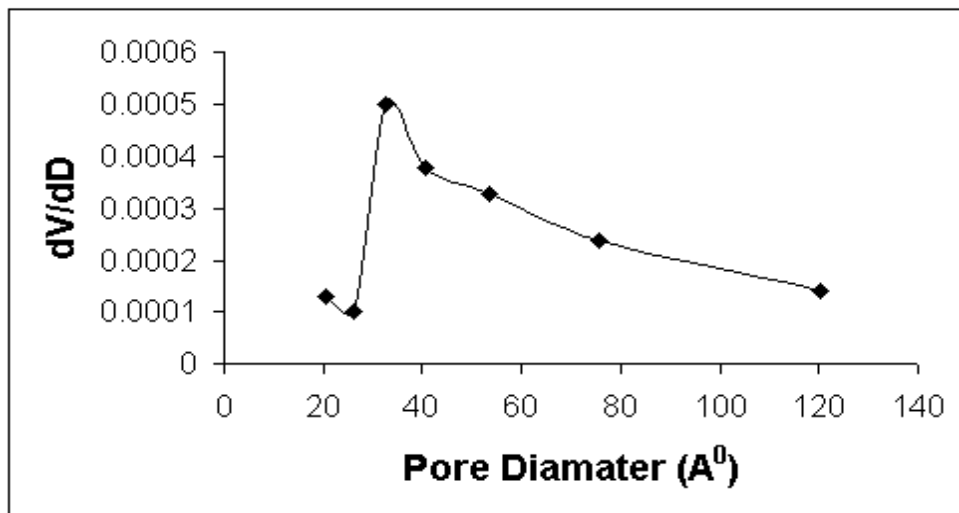


Figure D.3. Pore size distribution of CMCLI

## APPENDIX E

### XRD RESULTS

#### E.1. Natural and Surfactant Modified Zeolites after Bacteria Attachment

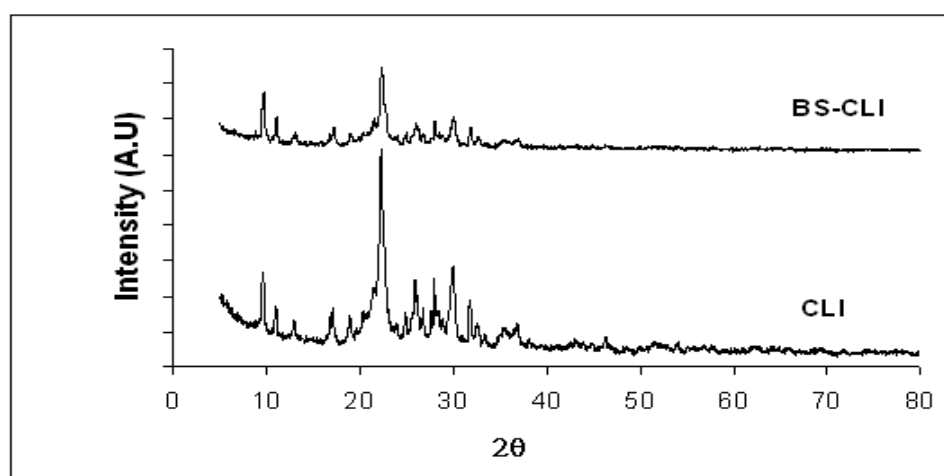


Figure E.1. XRD patterns of clinoptilolite rich mineral after *B. subtilis* attachment

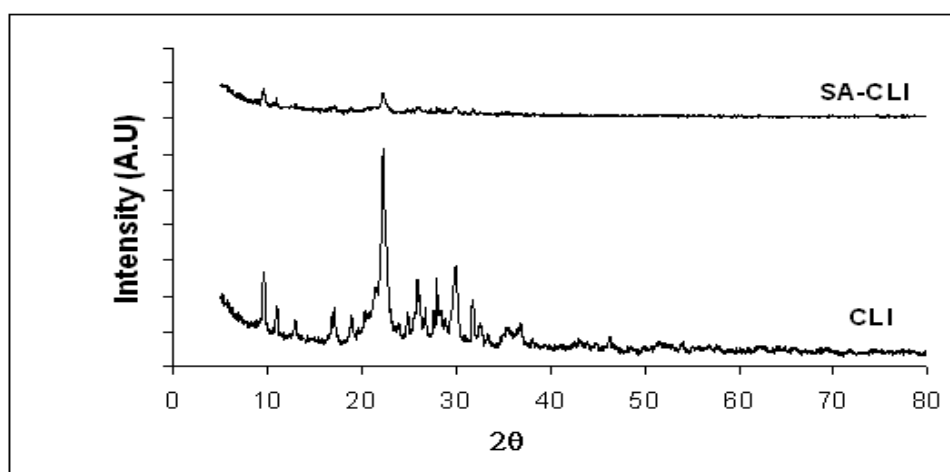


Figure E.2. XRD patterns of clinoptilolite rich mineral after *S. aureus* attachment

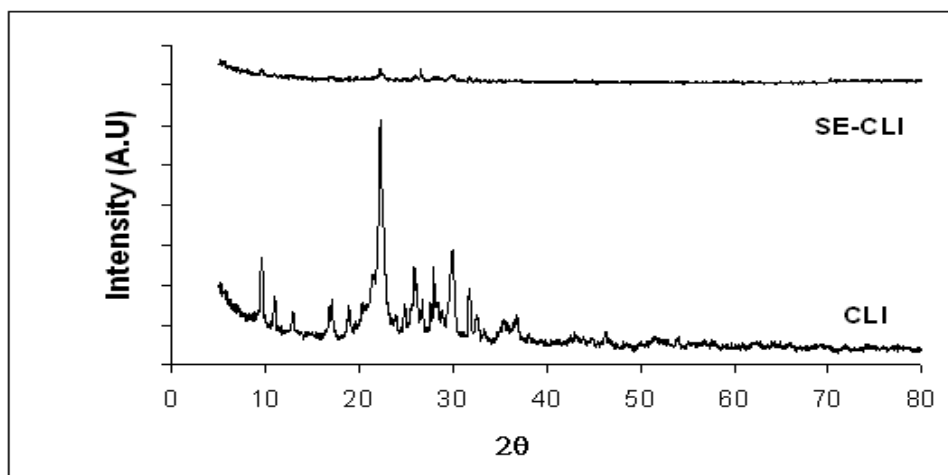


Figure E.3. XRD patterns of clinoptilolite rich mineral after *S. epidermidis* attachment

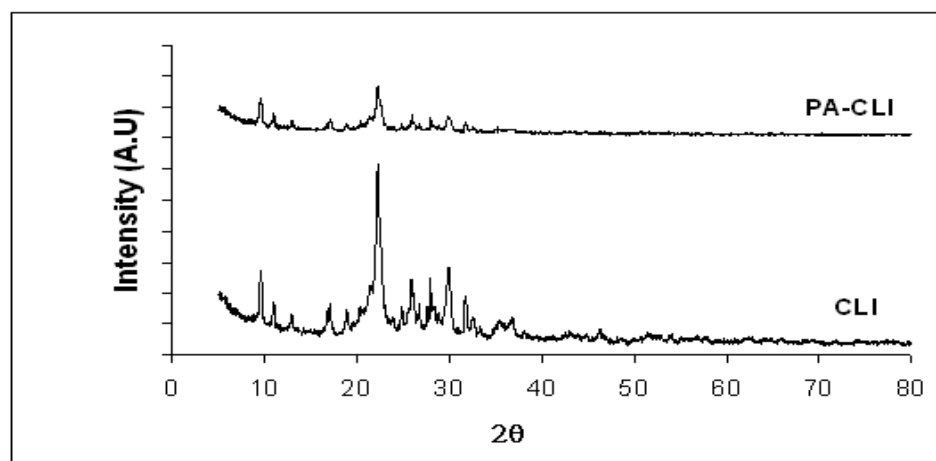


Figure E.4. XRD patterns of clinoptilolite rich mineral after *P. aeruginosa* attachment

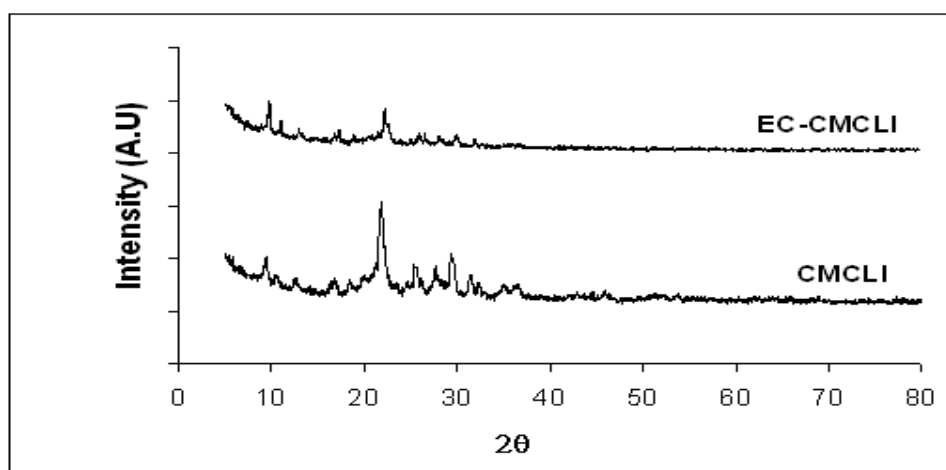


Figure E.5. XRD patterns of cationic modified clinoptilolite rich mineral after *E. coli* attachment

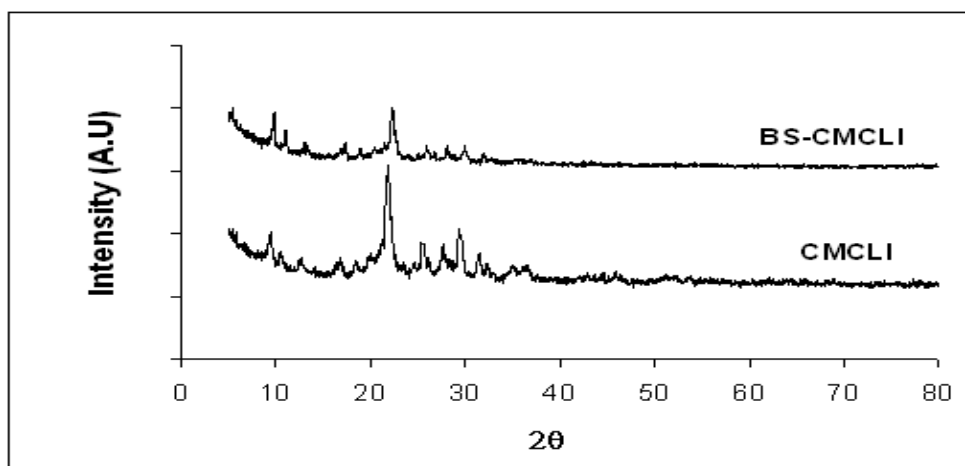


Figure E.6. XRD patterns of cationic modified clinoptilolite rich mineral after *B. subtilis* attachment

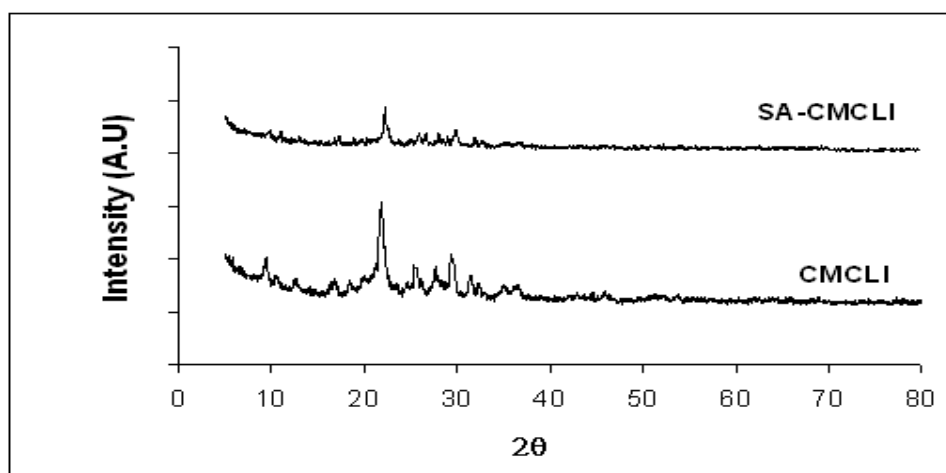


Figure E.7. XRD patterns of cationic modified clinoptilolite rich mineral after *S. Aeurus* attachment

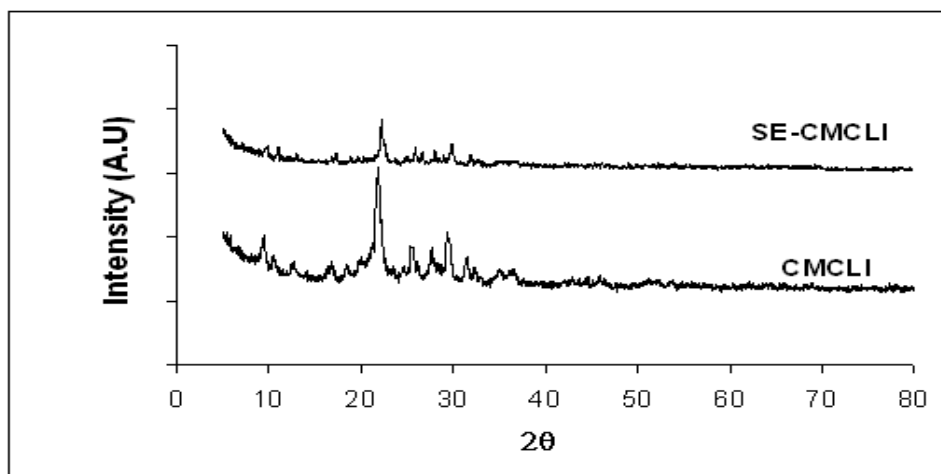


Figure E.8. XRD patterns of cationic modified clinoptilolite rich mineral after *S. epidermidis* attachment

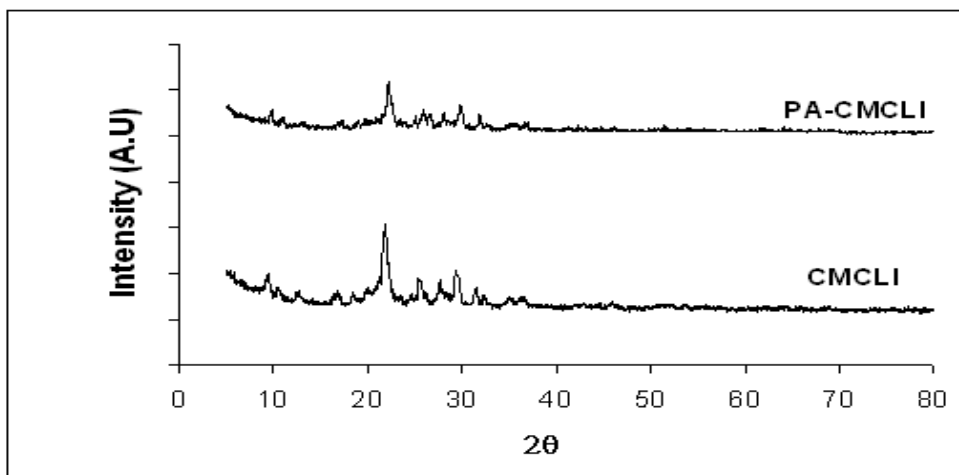


Figure E.9. XRD patterns of cationic modified clinoptilolite rich mineral after *P. aeruginosa* attachment

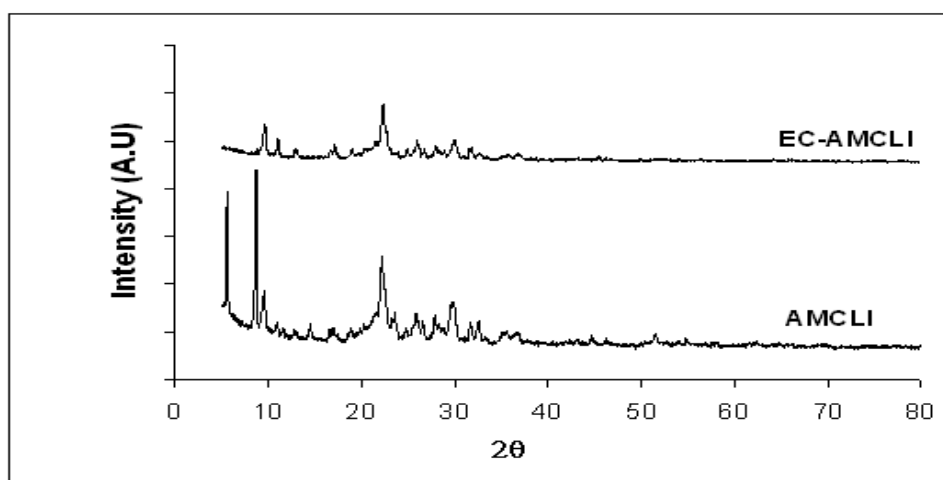


Figure E.10. XRD patterns of anionic modified clinoptilolite rich mineral after *E. coli* attachment

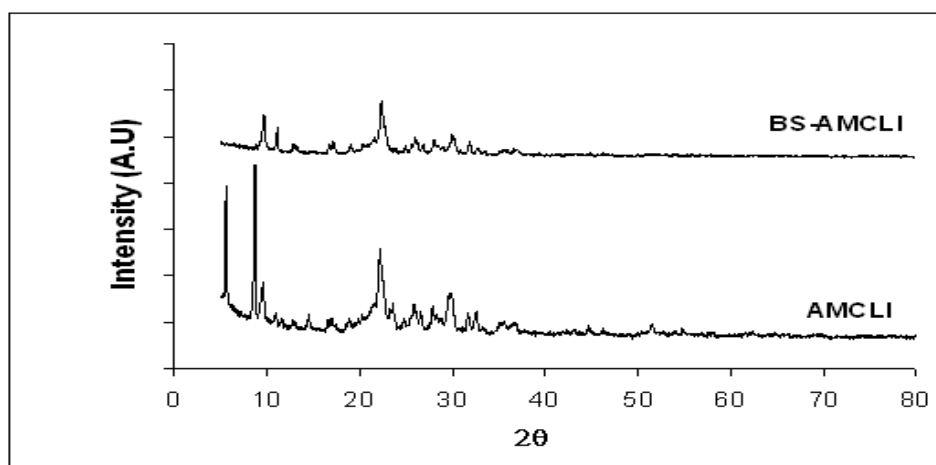


Figure E.11. XRD patterns of anionic modified clinoptilolite rich mineral after *B. subtilis* attachment

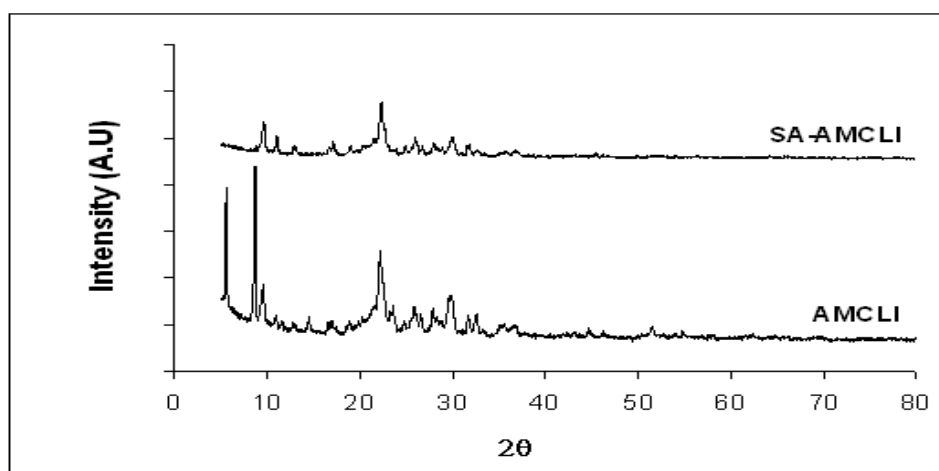


Figure E.12. XRD patterns of anionic modified clinoptilolite rich mineral after *S. aureus* attachment

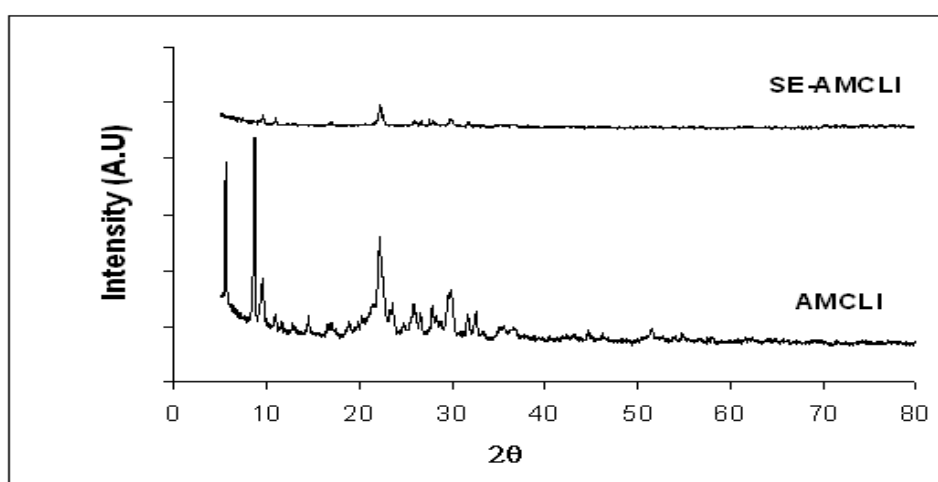


Figure E.13. XRD patterns of anionic modified clinoptilolite rich mineral after *S. epidermidis* attachment

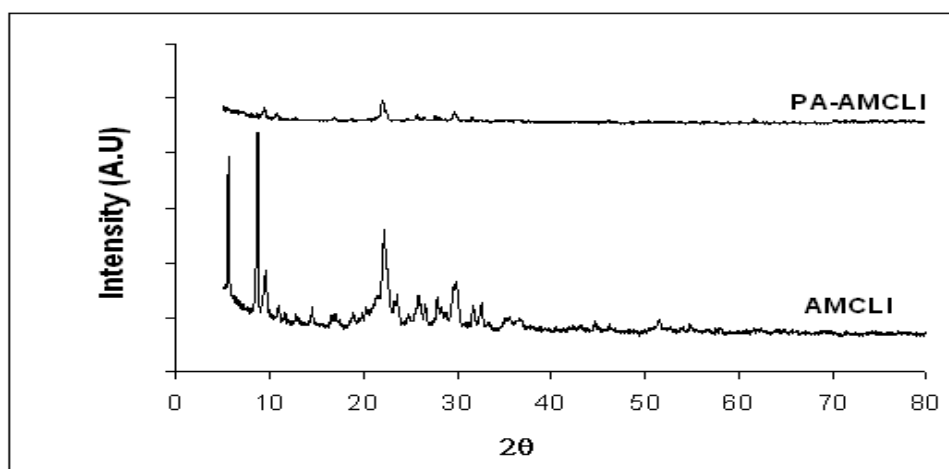
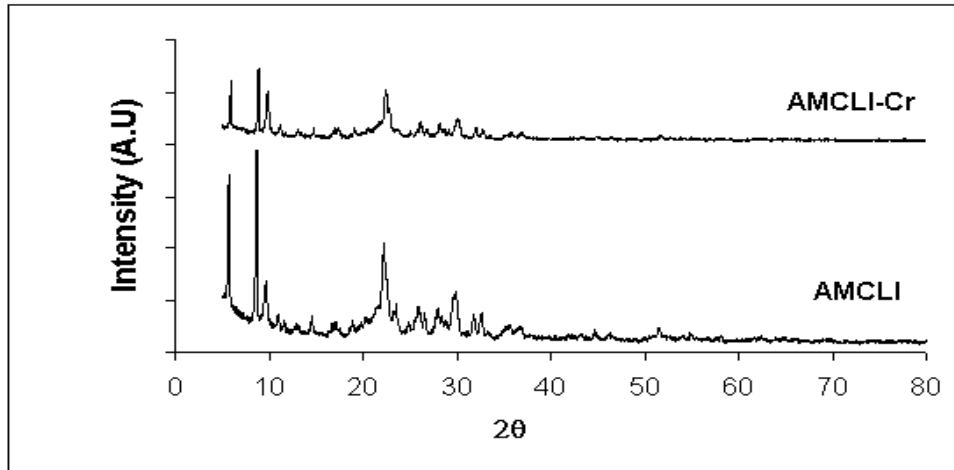


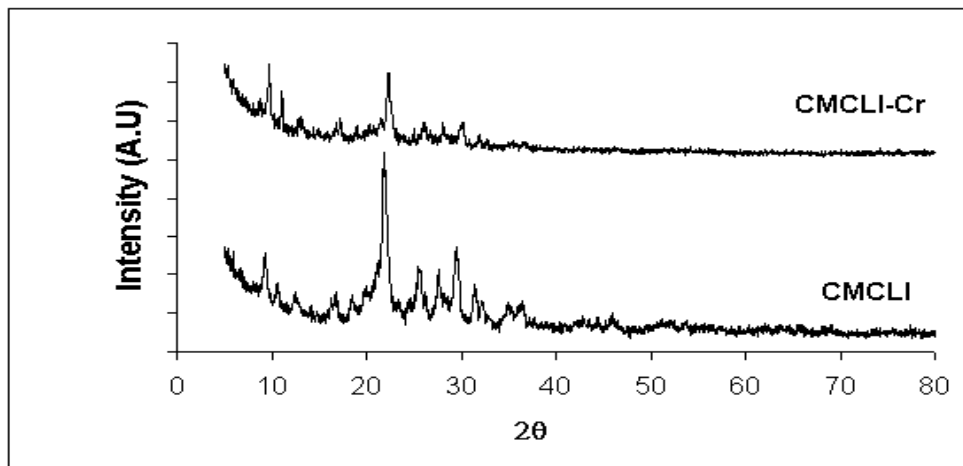
Figure E.14. XRD patterns of anionic modified clinoptilolite rich mineral after *P. aeruginosa* attachment

## E.2. Surfactant Modified and Bacteria Loaded Zeolites after Cr (VI) Sorption

### Sorption

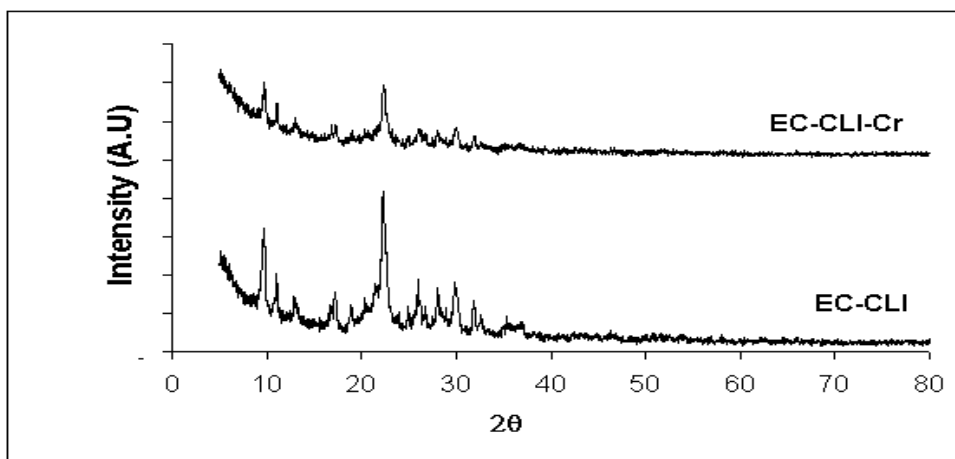


E.15. XRD results of AMCLI after Cr (VI) sorption

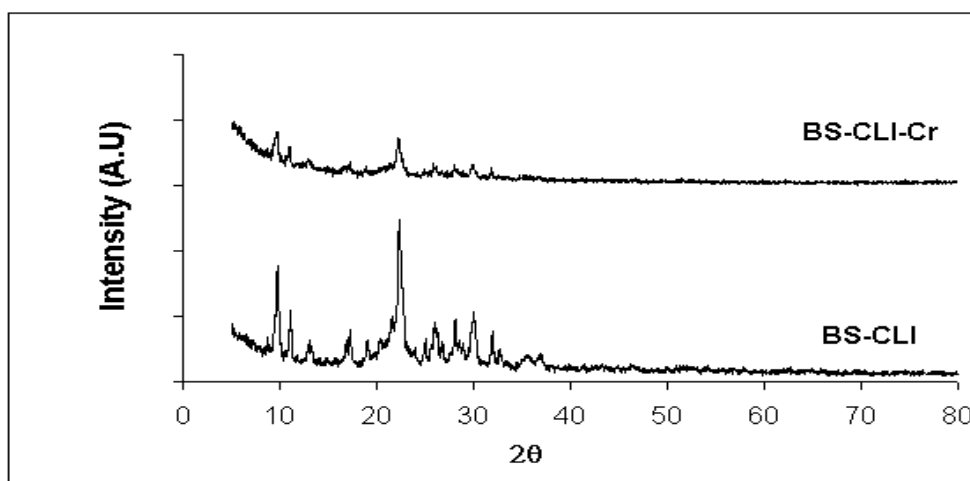


E.16. XRD results of CMCLI after Cr (VI) sorption

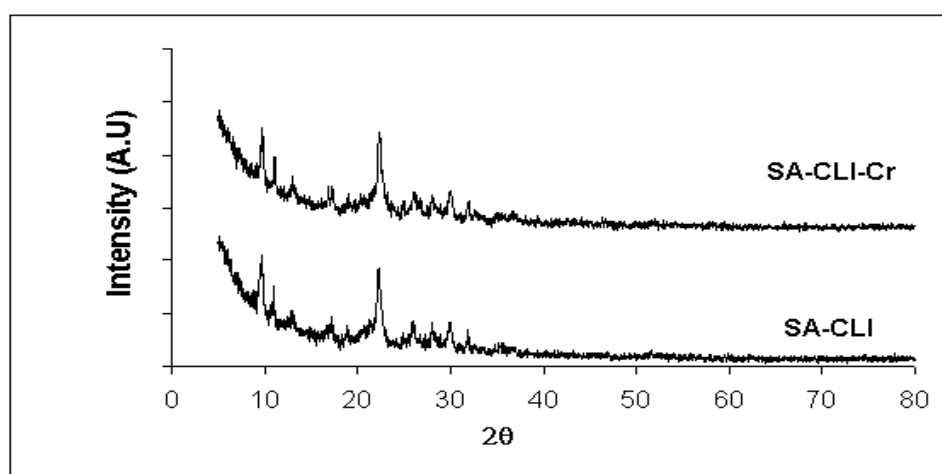




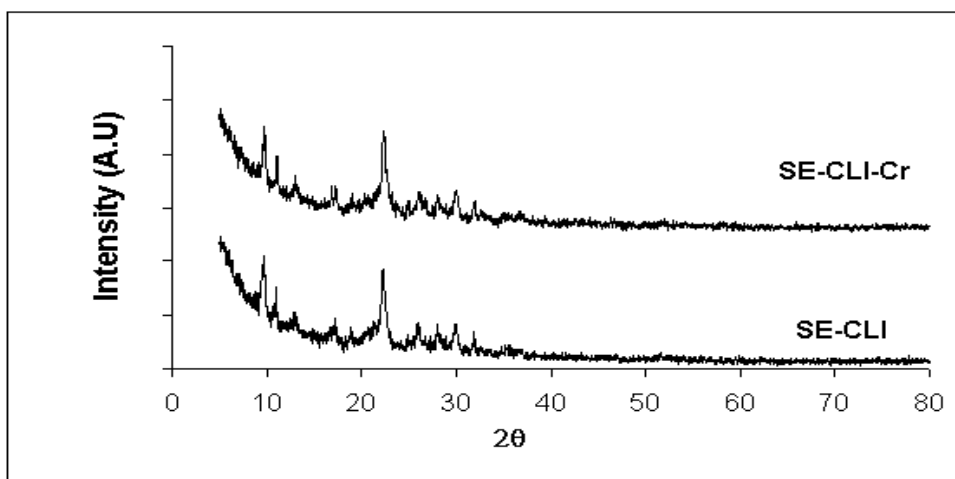
E.17. XRD results of EC-CLI after Cr (VI) sorption



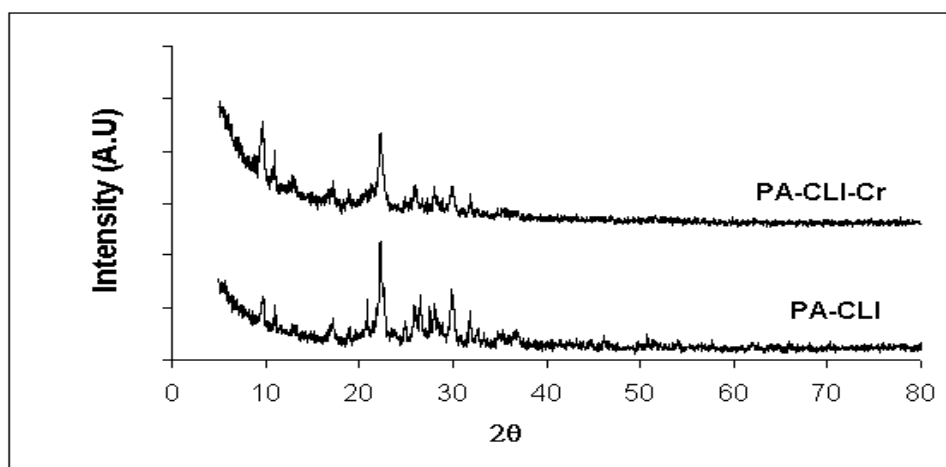
E.18. XRD results of BS-CLI after Cr (VI) sorption



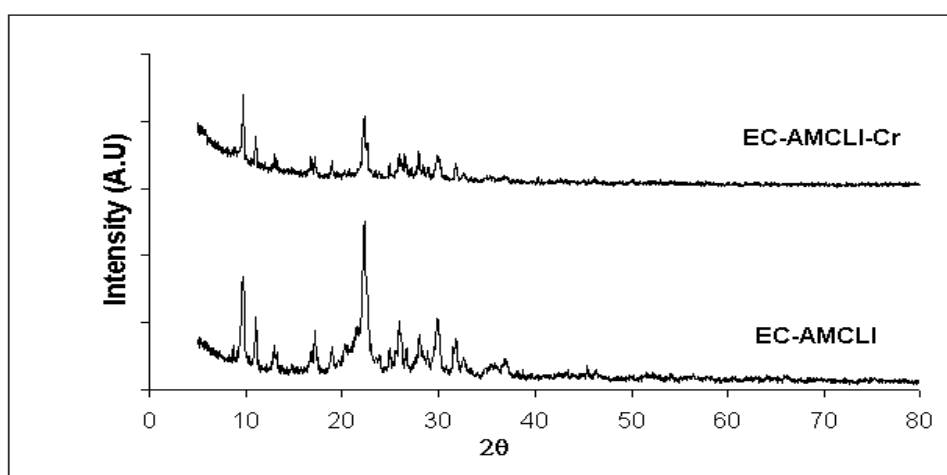
E.19. XRD results of SA-CLI after Cr (VI) sorption



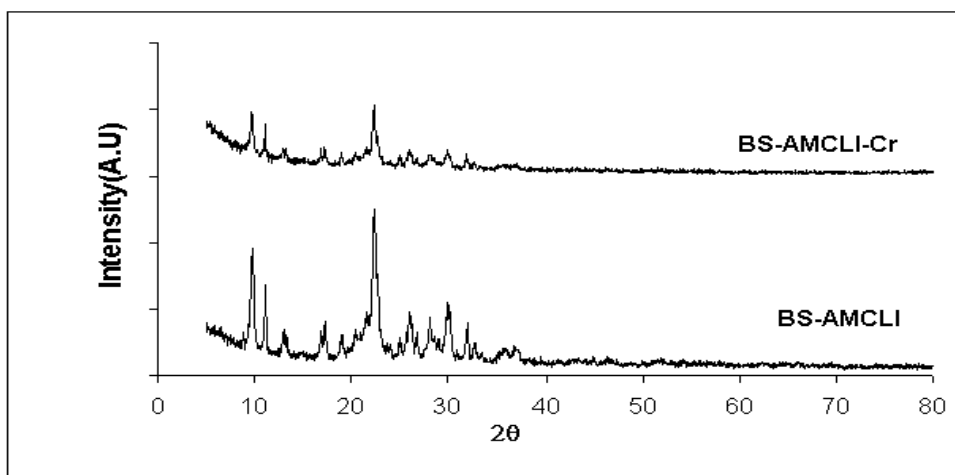
E.20. XRD results of SE-CLI after Cr (VI) sorption



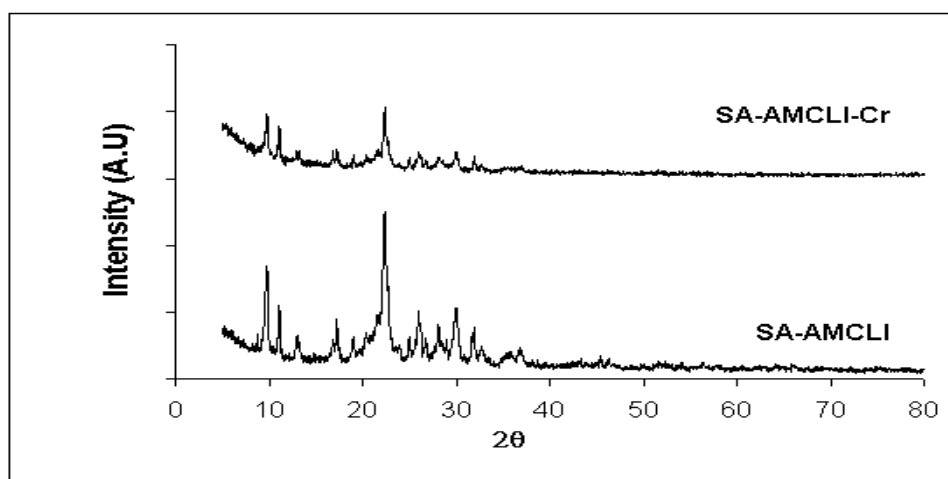
E.21. XRD results of PA-CLI after Cr (VI) sorption



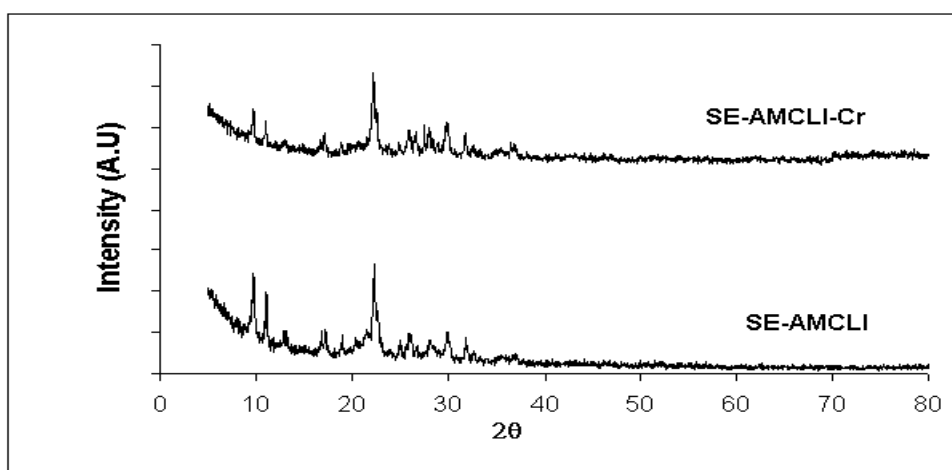
E.22. XRD results of EC-AMCLI after Cr (VI) sorption



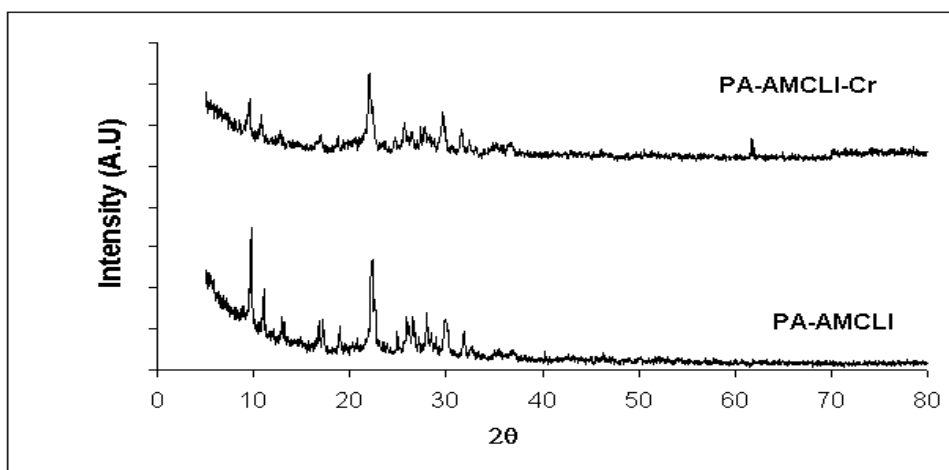
E.23. XRD results of BS-AMCLI after Cr (VI) sorption



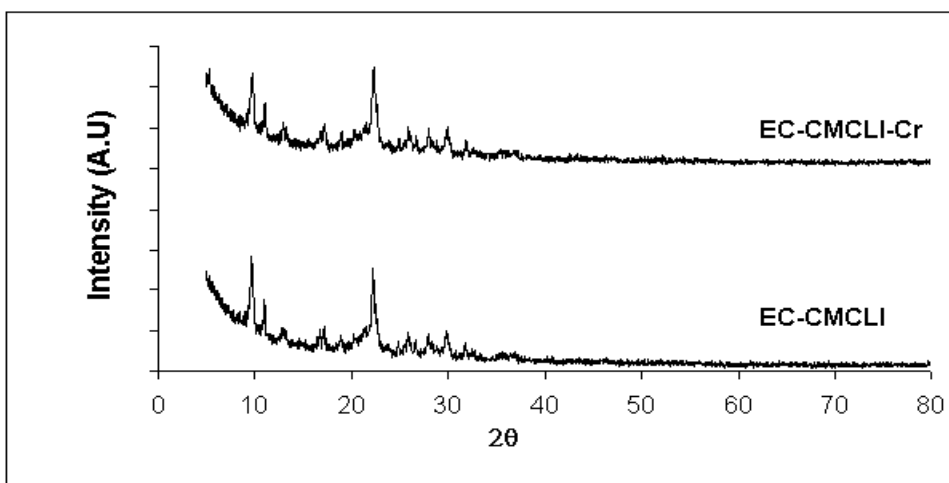
E.24. XRD results of SA-AMCLI after Cr (VI) sorption



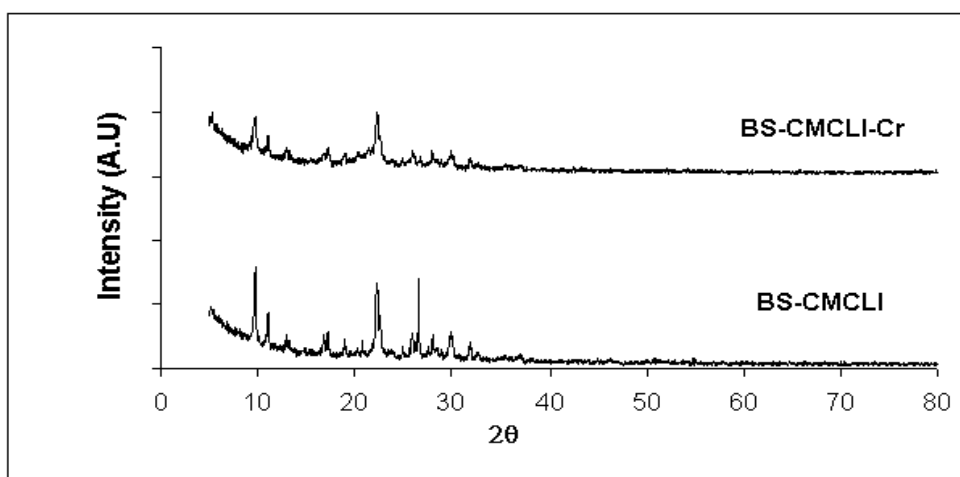
E.25. XRD results of SE-AMCLI after Cr (VI) sorption



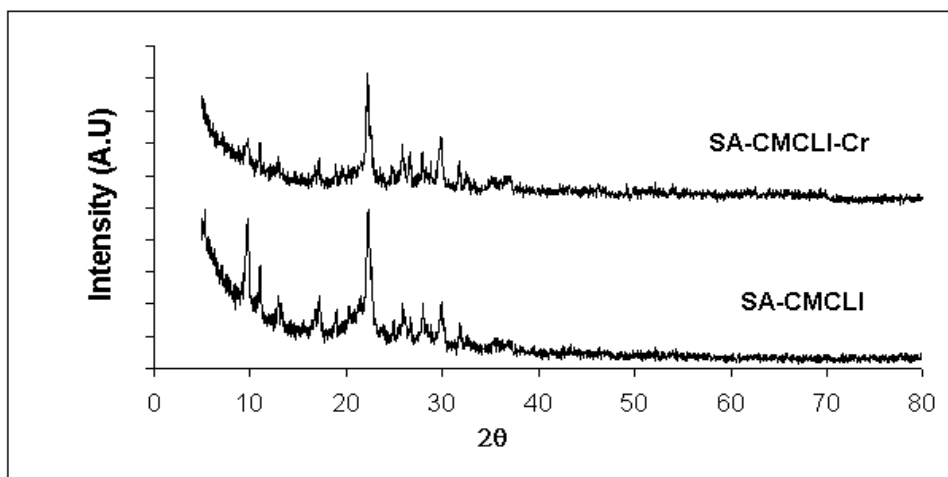
E.26. XRD results of PA-AMCLI after Cr (VI) sorption



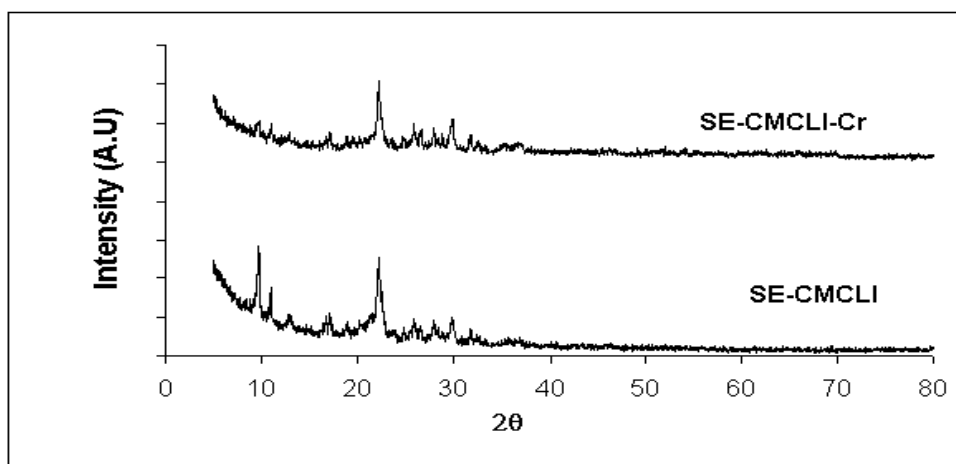
E.27. XRD results of EC-CMCLI after Cr (VI) sorption



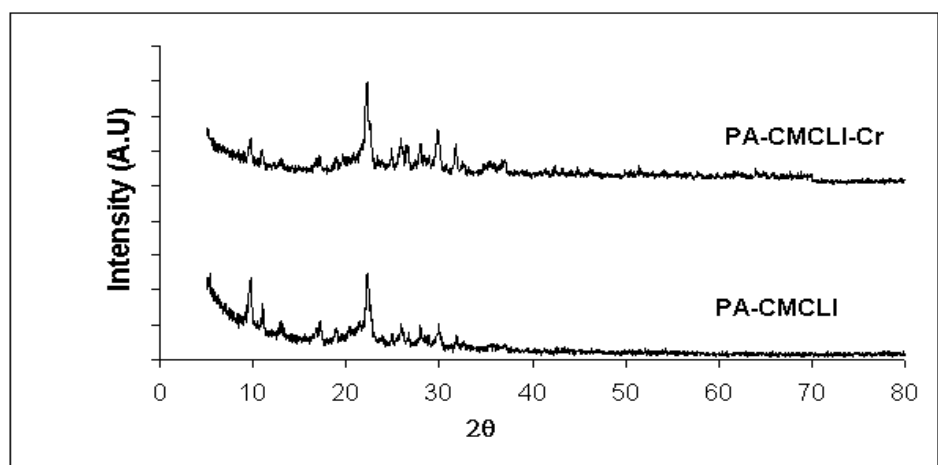
E.28. XRD results of BS-CMCLI after Cr (VI) sorption



E.29. XRD results of SA-CMCLI after Cr (VI) sorption

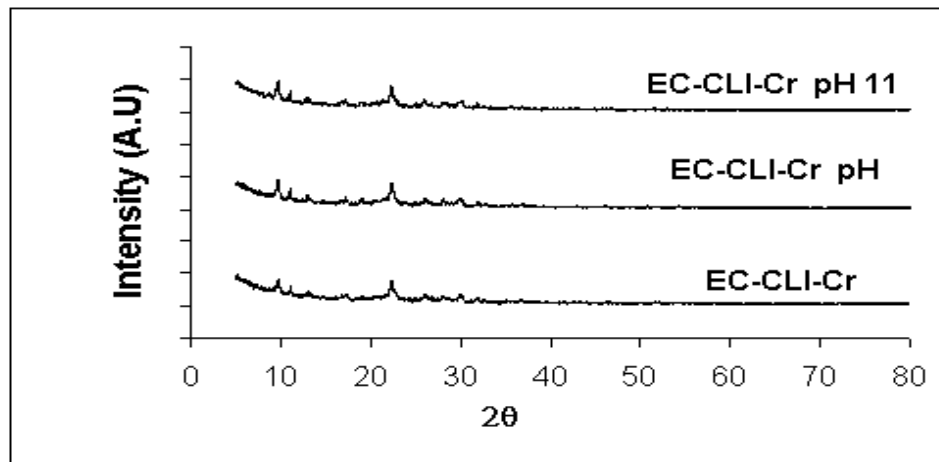


E.30. XRD results of SE-CMCLI after Cr (VI) sorption

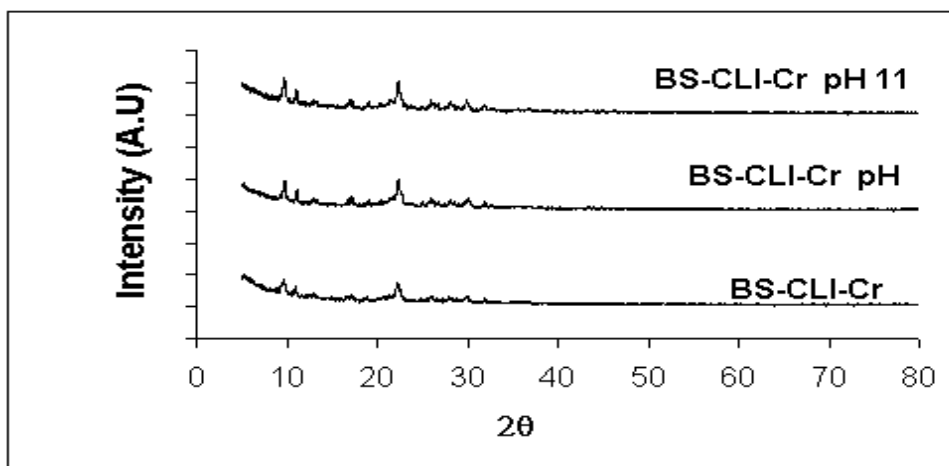


E.31. XRD results of PA-CMCLI after Cr (VI) sorption

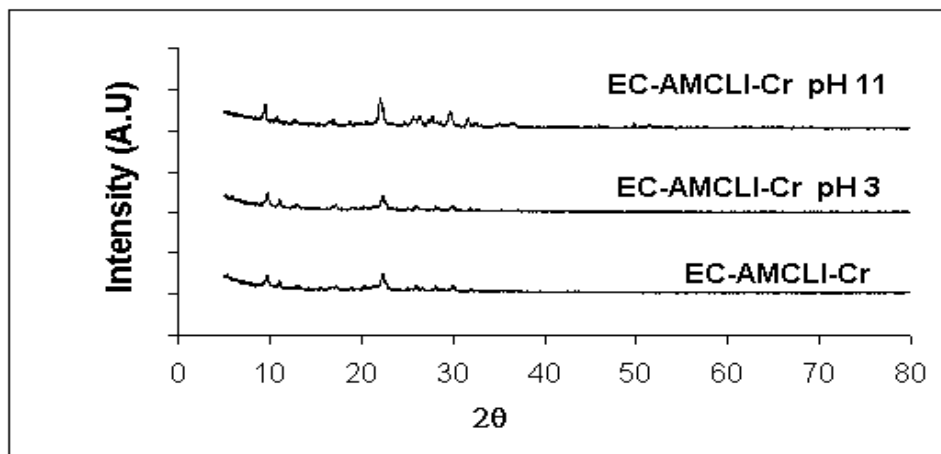
### E.3. Bacteria Loaded Zeolites after Cr (VI) Sorption at pH 3 and 11



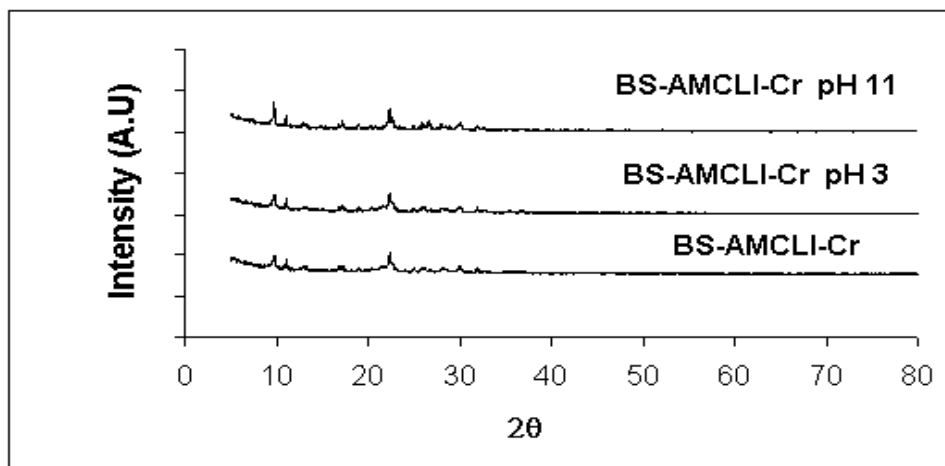
E.32. XRD results of EC-CLI after Cr (VI) sorption at pH 3 and 11



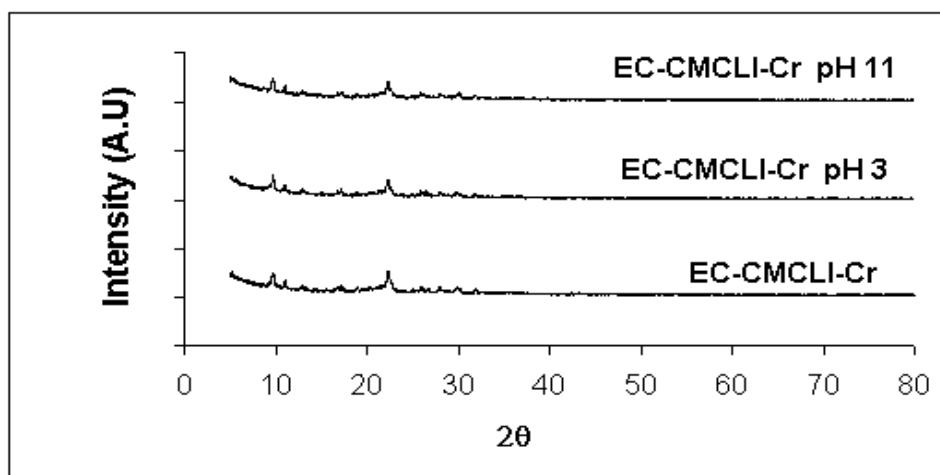
E.33. XRD results of BS-CLI after Cr (VI) sorption at pH 3 and 11



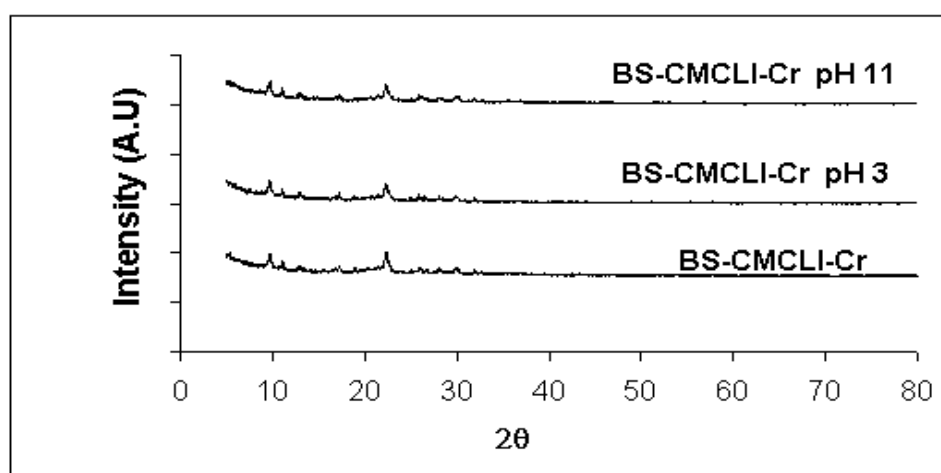
E.34. XRD results of EC-AMCLI after Cr (VI) sorption at pH 3 and 11



E.35. XRD results of BS-AMCLI after Cr (VI) sorption at pH 3 and 11



E.36. XRD results of EC-CMCLI after Cr (VI) sorption at pH 3 and 11



E.37. XRD results of BS-CMCLI after Cr (VI) sorption at pH 3 and 11

## APPENDIX F

### SORPTION KINETIC MODEL CALCULATION

#### F.1. Determination of External Mass Transfer Coefficient

Mathew-Weber and Furusawa Smith models were used to calculate the external mass transfer coefficient ( $k_f$ ). In Mathew-Weber Model, the external mass transfer coefficient is calculated from the slope of plot of  $\ln C/C_0$  versus time.

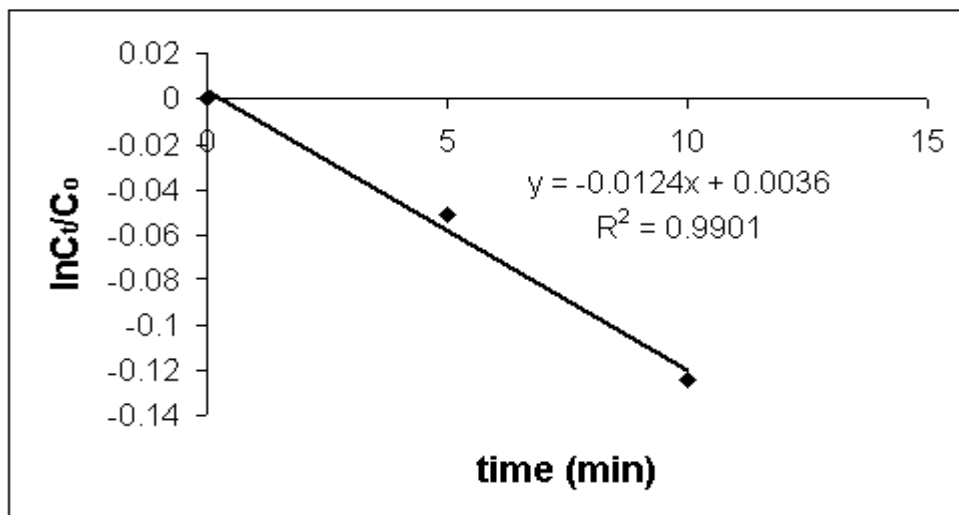


Figure F.1. Mathew and Weber solution of the kinetic data

The slope of the plot was -0.0124, which was equal to the  $-k_f \cdot S$ .  $S$  is determined from following equation:

$$S = \frac{6m/V}{d_p \rho_p (1 - \epsilon_p)}$$

where  $m$  is the mass of adsorbent,  $V$  is the volume of solution,  $d_p$  is the particle diameter,  $\rho_p$  particle density,  $\epsilon_p$  is porosity.

$$S = \frac{6 * (0.5/0.05)}{65.5 * 10^{-6} * 1800(1 - 0.38)} = 821 \text{ m}$$



External mass transfer coefficient value for Mathew and Weber was found as  $15 \cdot 10^{-6}$  m/min.

The external mass transfer coefficient for Furusawa-Smith model is determined

from the slope of  $\left( \frac{1}{1 + \frac{1}{\frac{m}{V}K_L}} \right) \ln \left( \frac{C_t}{C_0} - \frac{1}{\frac{m}{V}K_L} \left( 1 - \frac{C_t}{C_0} \right) \right)$  versus time.

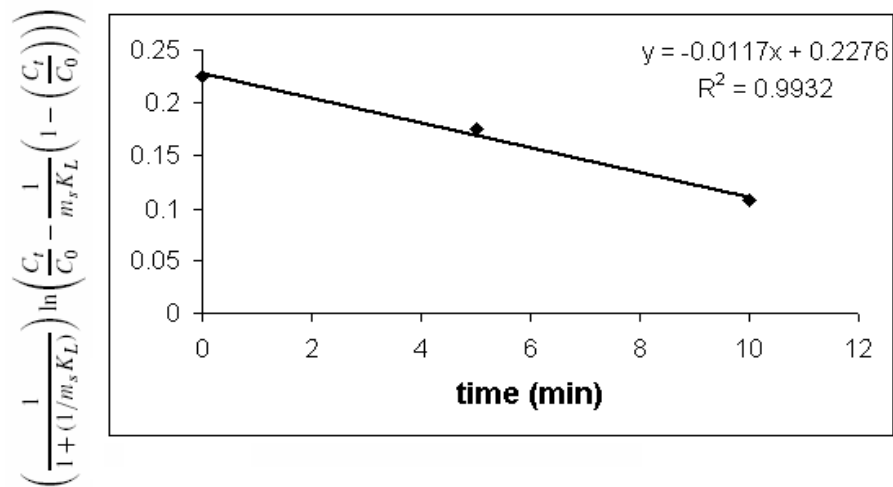


Figure F.2. Furusawa-Smith model solution of the kinetic data

The slope of the plot was -0.0117, which was equal to the  $-k_f \cdot S$ . External mass transfer coefficient value for Furusawa-Smith was found as  $14.2 \cdot 10^{-6}$  m/min.

## F.2. Model Results of Piecewise Linear Regression (PLR) Method

Table F.1. Model results of PLR method for CLI

Parameters		L-L		L-L-L		L-L-L-L	
		AIC	SSE	AIC	SSE	AIC	SSE
<b>Initial Concentration (mg/L)</b>	10	-48.1	0.006	-16.6	0.004	-	0.009
	50	-0.88	1.10	-8.6	0.009	-	0.007
	100	-23.7	0.09	9.07	0.06	-	0.005
	200	20.8	0.12	8.77	0.06	-	0.06
	300	-17.2	0.18	10.3	0.07	-	0.04
<b>Agitation Speed (rpm)</b>	60	-64.8	0.0009	34.4	0.0005	-	0.0005
	100	-66.8	0.0007	-33.5	0.0005	-	0.0004
	140	-48.1	0.006	-16.6	0.004	-	0.009
<b>Temperature (°C)</b>	25	-48.1	0.006	-16.6	0.004	-	0.009
	40	-58.1	0.002	-40.8	0.002	-	0.002
<b>pH</b>	3	-48.1	0.006	-16.6	0.004	-	0.009
	11	-64.1	0.0009	-30.4	0.0007	-	0.0005
<b>Particle size (µm)</b>	25-106	-48.1	0.006	-16.6	0.004	-	0.009
	106-425	-63.2	0.001	-49.9	0.0009	-	0.0004

Table F.2. Model results of PLR method for AMCLI

Parameters		L-L		L-L-L		L-L-L-L	
		AIC	SSE	AIC	SSE	AIC	SSE
<b>Initial Concentration (mg/L)</b>	10	-60.2	0.0015	-30.4	0.007	-	0.009
	50	-27.3	0.059	-0.13	0.022	-	0.021
	100	-23.7	0.09	8.94	0.06	-	0.006
	200	-20.9	0.12	8.97	0.06	-	0.05
	300	-16.9	0.18	-2.5	0.02	-	0.02
<b>Agitation Speed (rpm)</b>	60	-64.8	0.0009	-34.4	0.0005	-	0.0005
	100	-66.7	0.0007	-33.5	0.0006	-	0.0004
	140	-60.2	0.0015	-30.4	0.007	-	0.009
<b>Temperature (°C)</b>	25	-60.2	0.0015	-30.4	0.007	-	0.009
	40	-56.4	0.0003	-33.8	0.0003	-	0.0003
<b>pH</b>	3	-60.2	0.0015	-30.4	0.007	-	0.009
	11	-64.8	0.0009	-34.4	0.0005	-	0.0005
<b>Particle size (µm)</b>	25-106	-60.2	0.0015	-30.4	0.007	-	0.009
	106-425	-63.2	0.002	-49.9	0.0008	-	0.0004

Table F.3. Model results of PLR method for CMCLI

Parameters		L-L		L-L-L		L-L-L-L	
		AIC	SSE	AIC	SSE	AIC	SSE
<b>Initial Concentration (mg/L)</b>	10	-36.8	0.02	-22.1	0.002	-	0.0004
	50	-24.9	0.08	5.4	0.04	-	0.07
	100	-23.8	0.09	-2.71	0.017	-	0.04
	200	-16.7	0.185	5.19	0.04	-	0.035
	300	-34.2	0.03	-0.73	0.02	-	0.02
<b>Agitation Speed (rpm)</b>	60	-63.2	0.001	-32.5	0.0006	-	0.004
	100	-40.7	0.014	-17.7	0.003	-	0.002
	140	-36.8	0.02	-22.1	0.002	-	0.0004
<b>Temperature (°C)</b>	25	-36.8	0.02	-22.1	0.002	-	0.0004
	40	-60.2	0.0015	-31	0.008	-	0.0001
<b>pH</b>	3	-36.8	0.02	-22.1	0.002	-	0.0004
	11	-44.6	0.009	-34.5	0.005	-	0.001
<b>Particle size (µm)</b>	25-106	-36.8	0.02	-22.1	0.002	-	0.0004
	106-425	-44.4	0.009	-23.6	0.02	-	0.0006

Table F.4. Model results of PLR method for ECCLI

Parameters		L-L		L-L-L		L-L-L-L	
		AIC	SSE	AIC	SSE	AIC	SSE
<b>Initial Concentration (mg/L)</b>	10	-43.2	0.01	-30.7	0.0007	-	0.004
	50	-33.9	0.03	-50.5	0.02	-	0.009
	100	-27.2	0.06	-13.4	0.005	-	0.02
	200	-28.1	0.06	-0.39	0.02	-	0.05
	300	-30.2	0.05	-5.29	0.02	-	0.01
<b>Agitation Speed (rpm)</b>	60	-48.7	0.005	-13.5	0.005	-	0.004
	100	-52.1	0.003	-18.4	0.003	-	0.002
	140	-43.2	0.01	-30.7	0.0007	-	0.004
<b>Temperature (°C)</b>	25	-43.2	0.01	-30.7	0.0007	-	0.004
	40	-57.1	0.002	-43.9	0.0002	-	0.0008
<b>pH</b>	3	-43.2	0.01	-30.7	0.0007	-	0.004
	11	-51.5	0.004	-22.8	0.002	-	0.0008
<b>Particle size (µm)</b>	25-106	-43.2	0.01	-30.7	0.0007	-	0.004
	106-425	-47.2	0.007	-13.7	0.005	-	0.003

Table F.5. Model results of PLR method for BSCLI

Parameters		L-L		L-L-L		L-L-L-L	
		AIC	SSE	AIC	SSE	AIC	SSE
Initial Concentration (mg/L)	10	-37.7	0.02	-15.9	0.004	-	0.0002
	50	-31.9	0.04	-8.6	0.009	-	0.008
	100	-35.3	0.03	-11.3	0.006	-	0.006
	200	-17.7	0.17	12.6	0.09	-	0.07
	300	-24.5	0.08	1.98	0.03	-	0.02
Agitation Speed (rpm)	60	-51.7	0.004	-18.2	0.003	-	0.002
	100	-63.2	0.001	-32.5	0.0006	-	0.0004
	140	-37.7	0.02	-15.9	0.004	-	0.0002
Temperature (°C)	25	-37.7	0.02	-15.9	0.004	-	0.0002
	40	-58.1	0.002	-40.9	0.0003	-	0.0002
pH	3	-37.7	0.02	-15.9	0.004	-	0.0002
	11	-51.6	0.004	-25.7	0.002	-	0.0007
Particle size (µm)	25-106	-37.7	0.02	-15.9	0.004	-	0.0002
	106-425	-46.8	0.007	-26.6	0.001	-	0.0007

Table F.6. Model results of PLR method for ECAMCLI

Parameters		L-L		L-L-L		L-L-L-L	
		AIC	SSE	AIC	SSE	AIC	SSE
Initial Concentration (mg/L)	10	-55.2	0.003	-31.7	0.0006	-	0.0005
	50	-35.8	0.03	-3.9	0.01	-	0.01
	100	-35.5	0.02	-0.58	0.02	-	0.02
	200	-18.4	0.16	6.33	0.04	-	0.04
	300	-40.6	0.009	-8.33	0.009	-	0.008
Agitation Speed (rpm)	60	-51.8	0.004	-18.2	0.003	-	0.002
	100	-47.1	0.007	-22.4	0.002	-	0.002
	140	-55.2	0.003	-31.7	0.0006	-	0.0005
Temperature (°C)	25	-55.2	0.003	-31.7	0.0006	-	0.0005
	40	-56.3	0.002	-38.9	0.003	-	0.0003
pH	3	-55.2	0.003	-31.7	0.0006	-	0.0005
	11	-47.5	0.006	-37.7	0.0004	-	0.0004
Particle size (µm)	25-106	-55.2	0.003	-31.7	0.0006	-	0.0005
	106-425	-47.3	0.007	-13.7	0.005	-	0.003

Table F.7. Model results of PLR method for BSAMCLI

Parameters		L-L		L-L-L		L-L-L-L	
		AIC	SSE	AIC	SSE	AIC	SSE
<b>Initial Concentration (mg/L)</b>	10	-44.8	0.009	-27.3	0.002	-	0.00008
	50	-39.5	0.02	-4.6	0.02	-	0.004
	100	-24.8	0.08	10.7	0.07	-	0.03
	200	-18.5	0.16	-10.2	0.008	-	0.005
	300	-21.5	0.11	-0.45	0.02	-	0.02
<b>Agitation Speed (rpm)</b>	60	-63.2	0.001	-27.2	0.001	-	0.0004
	100	-40.6	0.01	-12.4	0.006	-	0.002
	140	-44.8	0.009	-27.3	0.002	-	0.00008
<b>Temperature (°C)</b>	25	-44.8	0.009	-27.3	0.002	-	0.00008
	40	-52.5	0.004	-37.3	0.0003	-	0.002
<b>pH</b>	3	-44.8	0.009	-27.3	0.002	-	0.00008
	11	-56.3	0.002	-31.7	0.0007	-	0.0009
<b>Particle size (µm)</b>	25-106	-44.8	0.009	-27.3	0.002	-	0.00008
	106-425	-46.8	0.007	-23.3	0.002	-	0.001

Table F.8. Model results of PLR method for ECCMCLI

Parameters		L-L		L-L-L		L-L-L-L	
		AIC	SSE	AIC	SSE	AIC	SSE
<b>Initial Concentration (mg/L)</b>	10	-35.9	0.03	-20.3	0.003	-	0.00009
	50	-18.1	0.16	6.1	0.05	-	0.03
	100	-13.9	0.26	0.96	0.02	-	0.02
	200	-23.7	0.09	-026	0.02	-	0.011
	300	-22.1	0.1	10.9	0.08	-	0.06
<b>Agitation Speed (rpm)</b>	60	-36.7	0.02	-19.9	0.003	-	0.0004
	100	-37.6	0.0	-20.8	0.003	-	0.0006
	140	-35.9	0.03	-20.3	0.003	-	0.00009
<b>Temperature (°C)</b>	25	-35.9	0.03	-20.3	0.003	-	0.00009
	40	-60.7	0.002	-30.6	0.0008	-	0.0003
<b>pH</b>	3	-35.9	0.03	-20.3	0.003	-	0.00009
	11	-48.4	0.006	-26.8	0.001	-	0.0006
<b>Particle size (µm)</b>	25-106	-35.9	0.03	-20.3	0.003	-	0.00009
	106-425	-46.8	0.007	-23.4	0.002	-	0.002

Table F.9. Model results of PLR method for BSCMCLI

Parameters		L-L		L-L-L		L-L-L-L	
		AIC	SSE	AIC	SSE	AIC	SSE
Initial Concentration (mg/L)	10	-40.2	0.02	-36.4	0.0005	-	0.0002
	50	-11.1	5.9	5.9	0.05	-	0.05
	100	-13.6	0.27	4.1	0.04	-	0.03
	200	17.4	0.5	-8.3	0.1	-	0.15
	300	-13.3	0.3	7.4	0.06	-	0.02
Agitation Speed (rpm)	60	-36.8	0.02	-28.2	0.0003	-	0.0004
	100	-37.7	0.02	-26.9	0.0004	-	0.0004
	140	-40.2	0.02	-36.4	0.0005	-	0.0002
Temperature (°C)	25	-40.2	0.02	-36.4	0.0005	-	0.0002
	40	-60.7	0.002	-38.8	0.0003	-	0.0003
pH	3	-40.2	0.02	-36.4	0.0005	-	0.0002
	11	-55.2	0.003	-44.1	0.0002	-	0.0002
Particle size (µm)	25-106	-40.2	0.02	-36.4	0.0005	-	0.0002
	106-425	-46.8	0.007	-19.7	0.003	-	0.002

### F.3. Model Graphs of Piecewise Linear Regression (PLR) Method

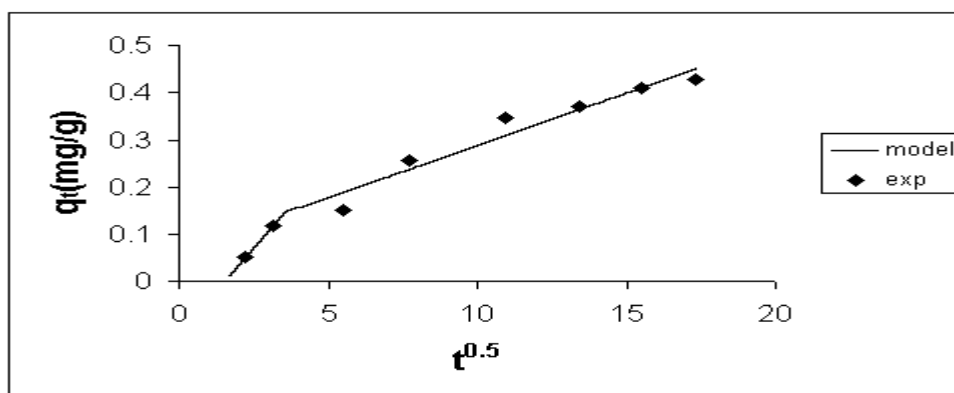


Figure F.3. The comparison of experimental and models with three (L-L-L) linear segments for Cr (VI) sorption with CLI (Conditions: 10 mg/L, 140 rpm, 25 °C, pH: 3, 25–106 µm)

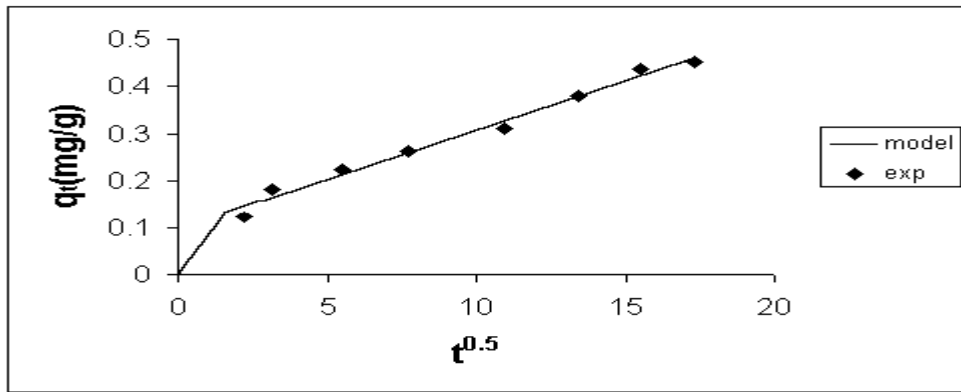


Figure F.4. The comparison of experimental and models with three (L-L-L) linear segments for Cr (VI) sorption with AMCLI (Conditions: 10 mg/L, 140 rpm, 25 °C, pH: 3, 25–106  $\mu\text{m}$ )

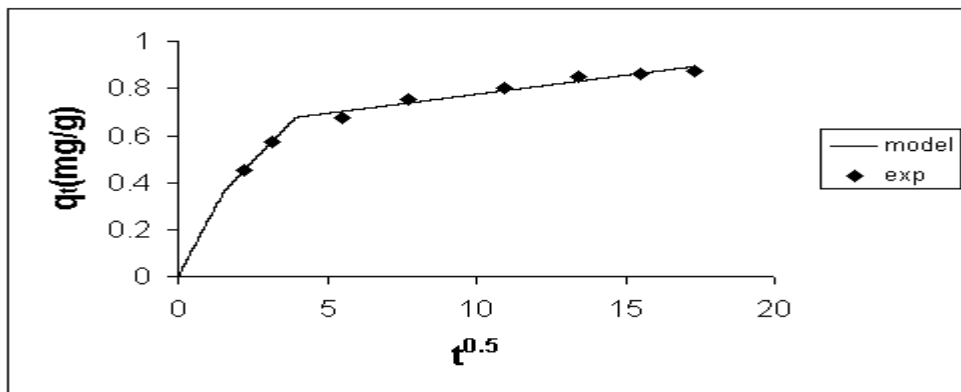


Figure F.5. The comparison of experimental and models with three (L-L-L) linear segments for Cr (VI) sorption with CMCLI (Conditions: 10 mg/L, 140 rpm, 25 °C, pH: 3, 25–106  $\mu\text{m}$ )

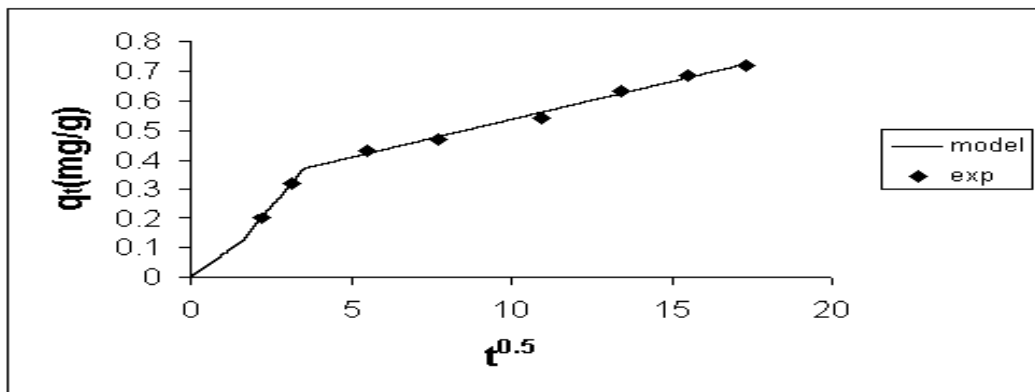


Figure F.6. The comparison of experimental and models with three (L-L-L) linear segments for Cr (VI) sorption with EC-CLI (Conditions: 10 mg/L, 140 rpm, 25 °C, pH: 3, 25–106  $\mu\text{m}$ )

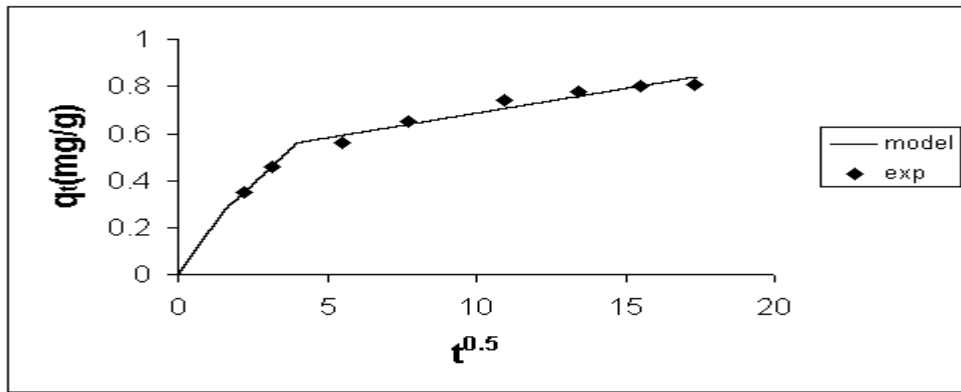


Figure F.7. The comparison of experimental and models with three (L-L-L) linear segments for Cr (VI) sorption with BS-CLI (Conditions: 10 mg/L, 140 rpm, 25 °C, pH: 3, 25–106  $\mu\text{m}$ )

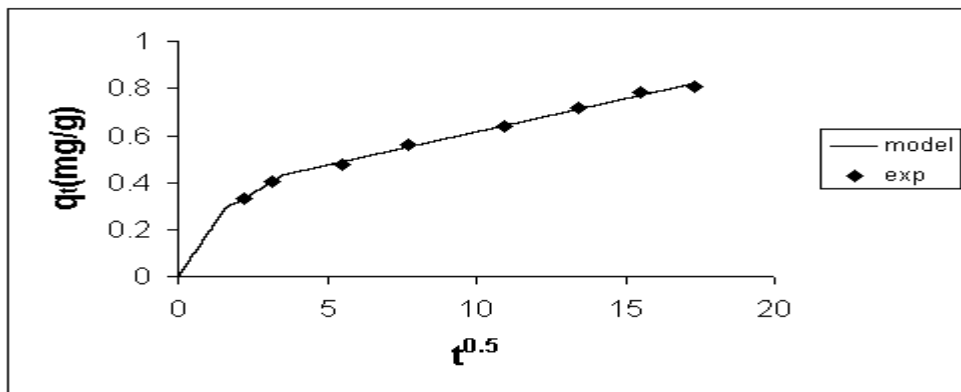


Figure F.8. The comparison of experimental and models with three (L-L-L) linear segments for Cr (VI) sorption with EC-AMCLI (Conditions: 10 mg/L, 140 rpm, 25 °C, pH: 3, 25–106  $\mu\text{m}$ )

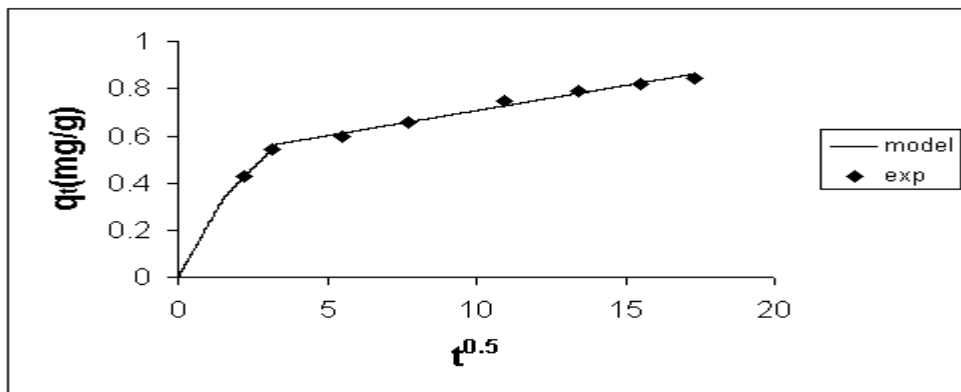


Figure F.9. The comparison of experimental and models with three (L-L-L) linear segments for Cr (VI) sorption with BS-AMCLI (Conditions: 10 mg/L, 140 rpm, 25 °C, pH: 3, 25–106  $\mu\text{m}$ )



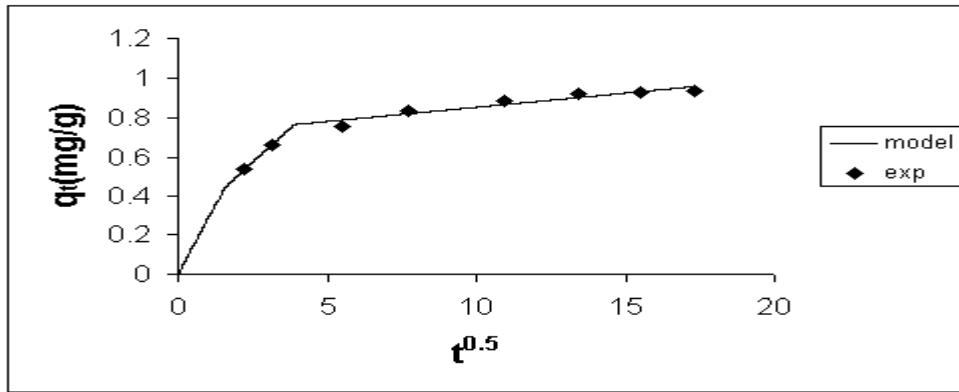


Figure F.10. The comparison of experimental and models with three (L-L-L) linear segments for Cr (VI) sorption with EC-CMCLI (Conditions: 10 mg/L, 140 rpm, 25 °C, pH: 3, 25–106  $\mu\text{m}$ )

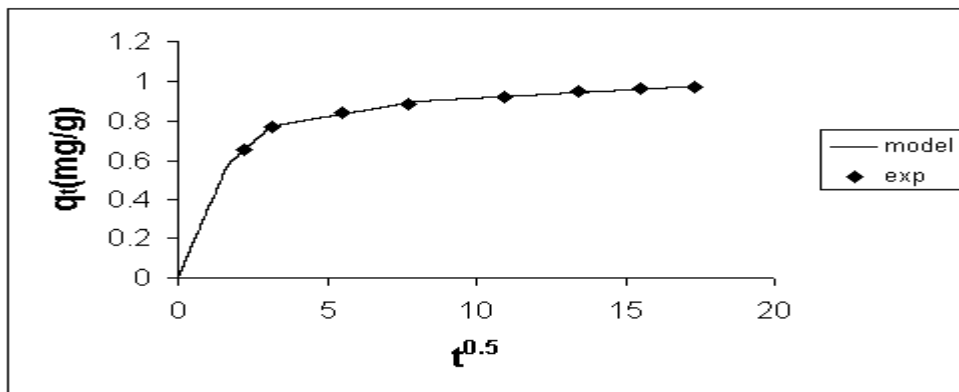


Figure F.11. The comparison of experimental and models with three (L-L-L) linear segments for Cr (VI) sorption with BS-CMCLI (Conditions: 10 mg/L, 140 rpm, 25 °C, pH: 3, 25–106  $\mu\text{m}$ )

#### D.4. Calculation of Effective Diffusion Coefficient for Short and Long Time Period

The effective diffusion coefficient ( $D_{\text{eff}}$ ) for short time period was determined from the slope of the plot of  $q_t/q_e$  versus  $\sqrt{t}$ .

$$\frac{q_t}{q_e} = \frac{6}{\sqrt{\pi}} \left( \frac{D_e \cdot t}{r_p^2} \right)^{1/2} \quad \left( \frac{q_t}{q_\infty} < 0.3 \right)$$

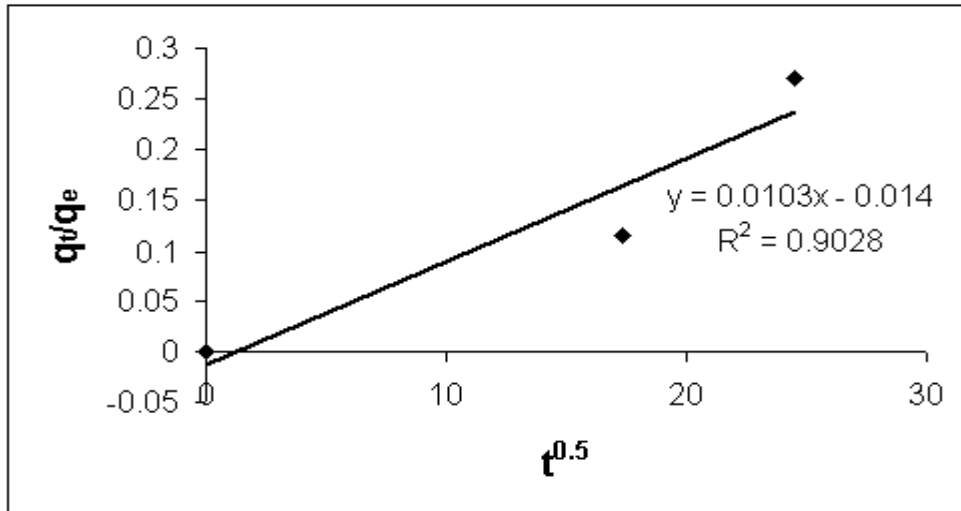


Figure F.12.  $q_t/q_e$  versus  $t^{0.5}$

The slope of the plot was 0.0103, which was equal to  $\frac{6}{\sqrt{\pi}} \frac{D_e^{1/2}}{r_p}$ . Effective diffusion coefficient value for short time period was found as  $0.9 \cdot 10^{-14} \text{ m}^2/\text{sec}$ .

The effective diffusion coefficient ( $D_{\text{eff}}$ ) for long time period was determined from the slope of the plot of  $\ln [1 - \frac{q_t}{q_e}]$  versus time.

$$1 - \frac{q_t}{q_e} = \frac{6}{\pi^2} \exp\left(-\frac{\pi^2 D_e t}{r_p^2}\right) \quad \left(\frac{q_t}{q_e} > 0.7\right)$$

$$\ln\left(1 - \frac{q_t}{q_e}\right) = -\frac{\pi^2 D_e}{r_p^2} t + \ln \frac{6}{\pi^2}$$

$$\ln\left(1 - \frac{q_t}{q_e}\right) = -\frac{\pi^2 D_e}{r_p^2} t - 0.497$$

The slope of the plot was -0.0002, which was equal to  $-\frac{\pi^2 D_e}{r_p^2}$ . Effective diffusion coefficient value for long time period was found as  $2.2 \cdot 10^{-14} \text{ m}^2/\text{sec}$ .

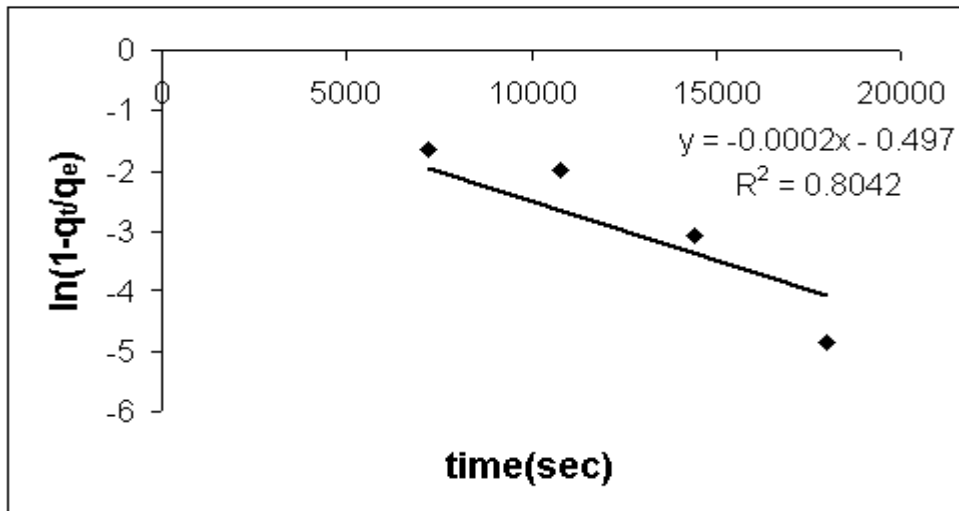


Figure F.13.  $\ln [1 - \frac{q_t}{q_e}]$  versus time

### D.5. Determination of Pseudo-First and Second Order Rate Constant

The pseudo first order rate constant ( $k_1$ ) is determined from the slope of plot of the  $\log (q_e - q_t)$  versus  $t$ .

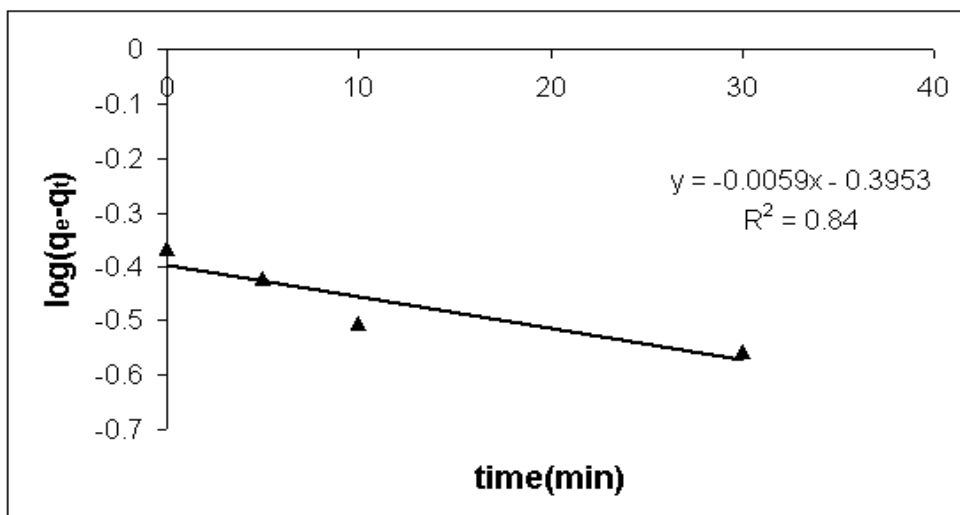


Figure F.14. Lagergren reaction model solution of the kinetic data

The slope of the plot was  $-0.0059$ , which was equal to  $-\frac{k_1}{2.303}$ . Pseudo first order rate constant ( $k_1$ ) value was determined as  $13.6 \times 10^{-3} \text{ min}^{-1}$ .

The pseudo second-order rate constant ( $k_2$ ) values were determined from intercepts of the plots of  $t/q_t$  versus  $t$ .

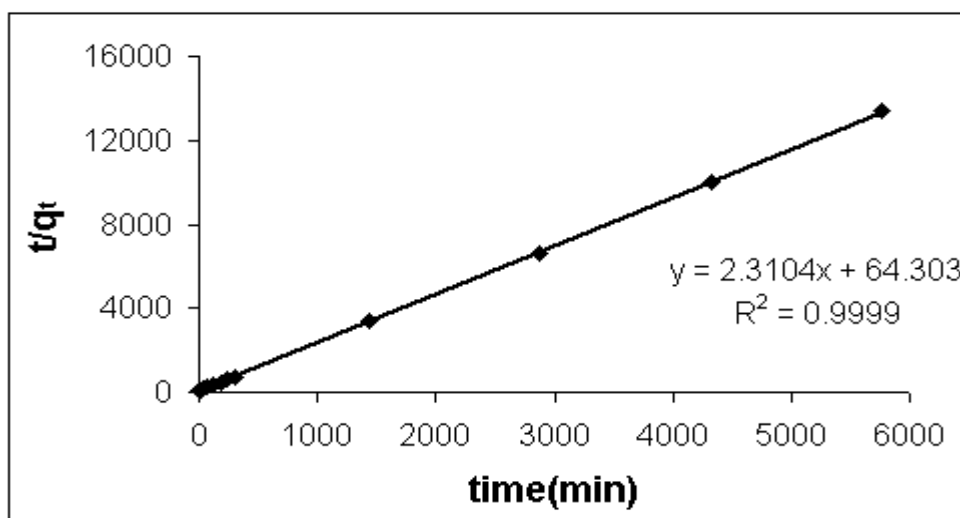


Figure F.15. Pseudo second order model solution of the kinetic data

Pseudo second order rate constant ( $k_2$ ) value was determined as  $82.9 \times 10^{-3}$  gr/mgmin.

#### D.6. Values of Correlation Coefficient ( $R^2$ ) of Models for all Sorbents

The values of correlation coefficient of models for all sorbents are tabulated in Table F.10- F.18.

Table F.10. The values of correlation coefficient ( $R^2$ ) at different conditions for CLI

Parameters		Correlation coefficient ( $R^2$ )					
		MW	FS	WM	PFO	PSO	
<b>Initial Concentration</b> (mg/L)	10	0.99	0.99	0.98	0.84	0.99	
	50	0.96	0.96	0.99	0.85	0.99	
	100	0.90	0.89	0.95	0.94	0.99	
	200	0.98	0.99	0.99	0.94	0.99	
	300	0.99	0.99	0.96	0.91	0.99	
<b>Agitation Speed</b> (rpm)	60	0.99	0.99	0.97	0.91	0.99	
	100	0.99	0.99	0.99	0.92	0.99	
	140	0.99	0.99	0.98	0.84	0.99	
<b>Temperature</b> (°C)	25	0.99	0.99	0.98	0.84	0.99	
	40	0.98	0.97	0.99	0.90	0.99	
<b>pH</b>	3	0.99	0.99	0.98	0.84	0.99	
	11	0.98	0.97	0.99	0.92	0.99	
<b>Particle size</b> ( $\mu\text{m}$ )	25-106	0.99	0.99	0.98	0.84	0.99	
	106-425	0.94	0.95	0.99	0.92	0.99	

MW: Mathew-Weber, FS: Furusawa-Smith, WM: Weber-Morris, PFO: Pseudo-first order model, PSO: Pseudo-second order model

Table F.11. The values of correlation coefficient ( $R^2$ ) at different conditions for AMCLI

Parameters	Correlation coefficient ( $R^2$ )					
	MW	FS	WM	PFO	PSO	
<b>Initial Concentration</b> (mg/L)	10	0.97	0.96	0.99	0.76	0.99
	50	0.99	0.99	0.99	0.86	0.99
	100	0.90	0.89	0.94	0.90	0.99
	200	0.97	0.96	0.99	0.91	0.99
	300	0.99	0.98	0.96	0.92	0.99
<b>Agitation Speed</b> (rpm)	60	0.99	0.99	0.97	0.91	0.99
	100	0.99	0.99	0.99	0.96	0.99
	140	0.97	0.96	0.99	0.76	0.99
<b>Temperature</b> (°C)	25	0.97	0.96	0.99	0.76	0.99
	40	0.98	0.97	0.99	0.91	0.99
<b>pH</b>	3	0.97	0.96	0.99	0.76	0.99
	11	0.97	0.97	0.97	0.94	0.99
<b>Particle size</b> ( $\mu\text{m}$ )	25-106	0.97	0.96	0.99	0.76	0.99
	106-425	0.94	0.95	0.99	0.92	0.99

MW: Mathew-Weber, FS: Furusawa-Smith, WM: Weber-Morris, PFO: Pseudo-first order model, PSO: Pseudo-second order model

Table F.12. The values of correlation coefficient ( $R^2$ ) at different conditions for CMCLI

Parameters	Correlation coefficient ( $R^2$ )					
	MW	FS	WM	PFO	PSO	
<b>Initial Concentration (mg/L)</b>	10	0.95	0.90	1	0.78	1
	50	0.99	0.99	0.99	0.87	0.99
	100	0.99	0.99	0.99	0.90	0.99
	200	0.97	0.98	1	0.91	0.99
	300	0.99	0.99	0.96	0.90	0.99
<b>Agitation Speed (rpm)</b>	60	0.93	0.92	0.97	0.76	0.99
	100	0.97	0.94	0.97	0.70	1
	140	0.95	0.90	1	0.78	1
<b>Temperature (°C)</b>	25	0.95	0.90	1	0.78	0.99
	40	0.97	0.96	0.98	0.75	1
<b>pH</b>	3	0.95	0.90	1	0.78	1
	11	0.99	0.99	0.98	0.76	1
<b>Particle size (µm)</b>	25-106	0.95	0.90	1	0.78	1
	106-425	0.99	0.98	1	0.86	0.99

MW: Mathew-Weber, FS: Furusawa-Smith, WM: Weber-Morris, PFO: Pseudo-first order model, PSO: Pseudo-second order model

Table F.13. The values of correlation coefficient ( $R^2$ ) at different conditions for ECCLI

Parameters	Correlation coefficient ( $R^2$ )					
	MW	FS	WM	PFO	PSO	
Initial Concentration (mg/L)	10	0.98	1	0.87	1	
	50	0.99	1	0.87	0.99	
	100	0.99	0.99	0.88	0.99	
	200	0.95	0.94	0.99	0.91	0.99
	300	0.97	0.96	0.97	0.91	0.99
Agitation Speed (rpm)	60	0.97	1	0.87	0.99	
	100	0.94	1	0.86	0.99	
	140	0.99	1	0.87	1	
Temperature (°C)	25	0.99	1	0.87	1	
	40	0.99	1	0.90	0.99	
pH	3	0.99	1	0.87	1	
	11	0.99	1	0.74	0.99	
Particle size ( $\mu\text{m}$ )	25-106	0.99	1	0.87	1	
	106-425	0.99	1	0.84	0.99	

MW: Mathew-Weber, FS: Furusawa-Smith, WM: Weber-Morris, PFO: Pseudo-first order model, PSO: Pseudo-second order model



Table F.14. The values of correlation coefficient ( $R^2$ ) at different conditions for BSCLI

Parameters	Correlation coefficient ( $R^2$ )					
	MW	FS	WM	PFO	PSO	
<b>Initial Concentration (mg/L)</b>	10	0.95	0.92	0.95	0.78	1
	50	0.97	0.97	1	0.91	0.99
	100	0.98	0.98	1	0.91	0.99
	200	0.98	0.98	0.97	0.91	0.99
	300	0.98	0.98	0.97	0.91	0.99
<b>Agitation Speed (rpm)</b>	60	0.97	0.96	0.98	0.76	0.99
	100	0.93	0.91	0.97	0.76	1
	140	0.95	0.92	0.95	0.78	1
<b>Temperature (°C)</b>	25	0.95	0.92	0.95	0.78	1
	40	0.98	0.97	0.99	0.85	1
<b>pH</b>	3	0.95	0.92	0.95	0.78	1
	11	0.99	0.99	0.94	0.82	1
<b>Particle size (µm)</b>	25-106	0.95	0.92	0.95	0.78	1
	106-425	0.99	0.99	1	0.83	0.99

MW: Mathew-Weber, FS: Furusawa-Smith, WM: Weber-Morris, PFO: Pseudo-first order model, PSO: Pseudo-second order model

Table F.15. The values of correlation coefficient ( $R^2$ ) at different conditions for ECAMCLI

Parameters	Correlation coefficient ( $R^2$ )					
	MW	FS	WM	PFO	PSO	
<b>Initial Concentration</b> (mg/L)	10	0.91	0.90	1	0.70	1
	50	0.95	0.94	1	0.91	0.99
	100	0.98	0.98	1	0.91	0.99
	200	0.99	0.99	1	0.91	0.99
	300	0.99	0.99	0.99	0.91	0.99
<b>Agitation Speed</b> (rpm)	60	0.97	0.96	0.94	0.76	0.99
	100	0.95	0.92	0.94	0.70	1
	140	0.91	0.90	1	0.70	1
<b>Temperature</b> (°C)	25	0.91	0.90	1	0.70	1
	40	0.98	0.99	0.97	0.85	1
<b>pH</b>	3	0.91	0.90	1	0.70	1
	11	0.99	0.99	0.98	0.84	1
<b>Particle size</b> ( $\mu\text{m}$ )	25-106	0.91	0.90	1	0.70	1
	106-425	0.99	0.99	1	0.90	0.99

MW: Mathew-Weber, FS: Furusawa-Smith, WM: Weber-Morris, PFO: Pseudo-first order model, PSO: Pseudo-second order model

Table F.16. The values of correlation coefficient ( $R^2$ ) at different conditions for BSAMCLI

Parameters	Correlation coefficient ( $R^2$ )					
	MW	FS	WM	PFO	PSO	
Initial Concentration (mg/L)	10	0.95	0.91	1	0.70	1
	50	0.96	0.95	1	0.80	0.99
	100	0.95	0.95	1	0.91	0.99
	200	0.97	0.97	0.99	0.91	0.99
	300	0.99	0.99	0.99	0.91	0.99
Agitation Speed (rpm)	60	0.93	0.91	0.99	0.75	0.99
	100	0.95	0.94	1	0.86	1
	140	0.95	0.91	1	0.70	1
Temperature (°C)	25	0.95	0.91	1	0.70	1
	40	0.98	0.99	0.98	0.85	1
pH	3	0.95	0.91	1	0.70	1
	11	0.99	0.99	0.98	0.91	1
Particle size ( $\mu\text{m}$ )	25-106	0.95	0.91	1	0.70	1
	106-425	0.99	0.94	1	0.83	0.99

MW: Mathew-Weber, FS: Furusawa-Smith, WM: Weber-Morris, PFO: Pseudo-first order model, PSO: Pseudo-second order model

Table F.17. The values of correlation coefficient ( $R^2$ ) at different conditions for ECCMCLI

Parameters	Correlation coefficient ( $R^2$ )					
	MW	FS	WM	PFO	PSO	
<b>Initial Concentration</b> (mg/L)	10	0.95	0.89	0.96	0.75	1
	50	0.96	0.96	0.98	0.91	0.99
	100	0.91	0.90	0.99	0.73	0.99
	200	0.99	0.99	1	0.81	0.99
	300	0.99	0.99	0.98	0.91	0.99
<b>Agitation Speed</b> (rpm)	60	0.94	0.96	0.97	0.78	0.99
	100	0.93	0.95	0.97	0.77	1
	140	0.95	0.89	0.96	0.75	1
<b>Temperature</b> (°C)	25	0.95	0.89	0.96	0.75	1
	40	0.97	0.96	0.97	0.75	1
<b>pH</b>	3	0.95	0.89	0.96	0.75	1
	11	0.99	0.96	0.95	0.91	1
<b>Particle size</b> ( $\mu\text{m}$ )	25-106	0.95	0.89	0.96	0.75	1
	106-425	0.95	0.94	1	0.90	0.99

MW: Mathew-Weber, FS: Furusawa-Smith, WM: Weber-Morris, PFO: Pseudo-first order model, PSO: Pseudo-second order model

Table F.18. The values of correlation coefficient ( $R^2$ ) at different conditions for BSCMCLI

Parameters	Correlation coefficient ( $R^2$ )					
	MW	FS	WM	PFO	PSO	
Initial Concentration (mg/L)	10	0.94	0.91	0.96	0.70	1
	50	0.97	0.98	0.97	0.70	0.99
	100	0.98	0.99	1	0.81	0.99
	200	0.98	0.96	1	0.81	0.99
	300	0.99	0.99	1	0.76	0.99
Agitation Speed (rpm)	60	0.95	0.94	0.97	0.78	0.99
	100	0.94	0.95	0.97	0.75	1
	140	0.94	0.91	0.96	0.70	1
Temperature (°C)	25	0.94	0.91	0.96	0.70	1
	40	0.97	0.98	0.97	0.76	1
pH	3	0.94	0.91	0.96	0.70	1
	11	0.98	0.97	0.98	0.86	1
Particle size ( $\mu\text{m}$ )	25-106	0.94	0.91	0.96	0.70	1
	106-425	0.99	0.93	1	0.90	0.99

MW: Mathew-Weber, FS: Furusawa-Smith, WM: Weber-Morris, PFO: Pseudo-first order model, PSO: Pseudo-second order model

## APPENDIX G

### ISOTHERM MODELS

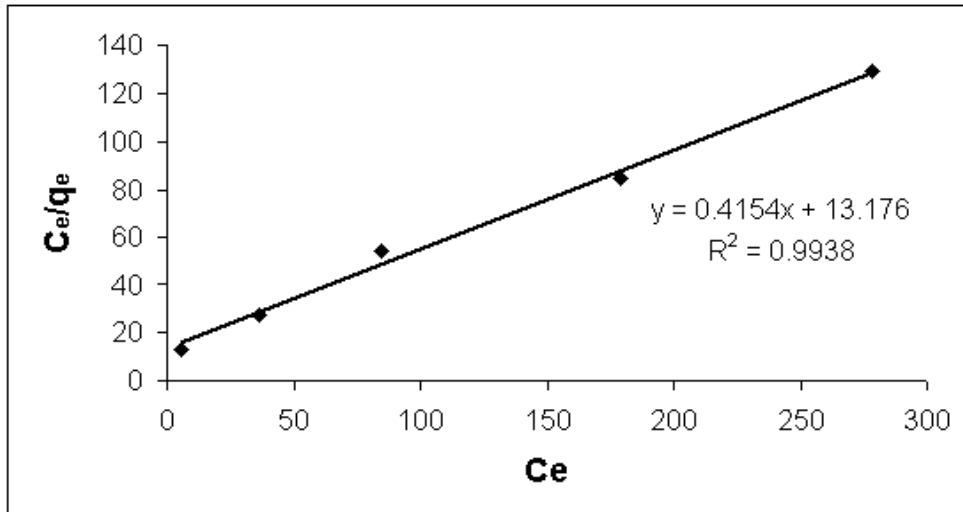


Figure G.1. Langmuir plot for Cr (VI) sorption onto clinoptilolite rich mineral at 25°C

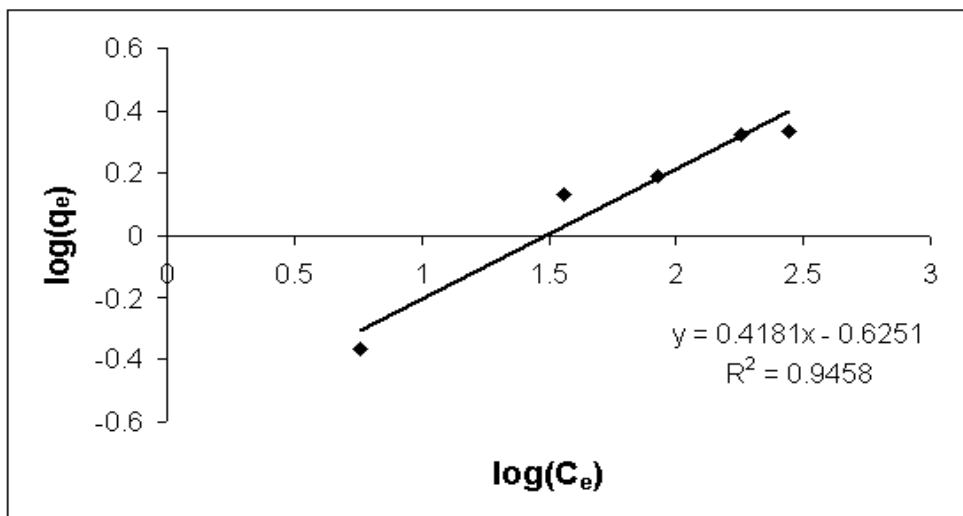


Figure G.2. Freundlich plot for Cr (VI) sorption onto clinoptilolite rich mineral at 25°C

## APPENDIX H

### THERMODYNAMIC PARAMETERS

The values of  $\Delta H^\circ$  and  $\Delta S^\circ$  is determined from the slope and the intercept of the plot between  $\ln b_m$  versus  $1/T$ .

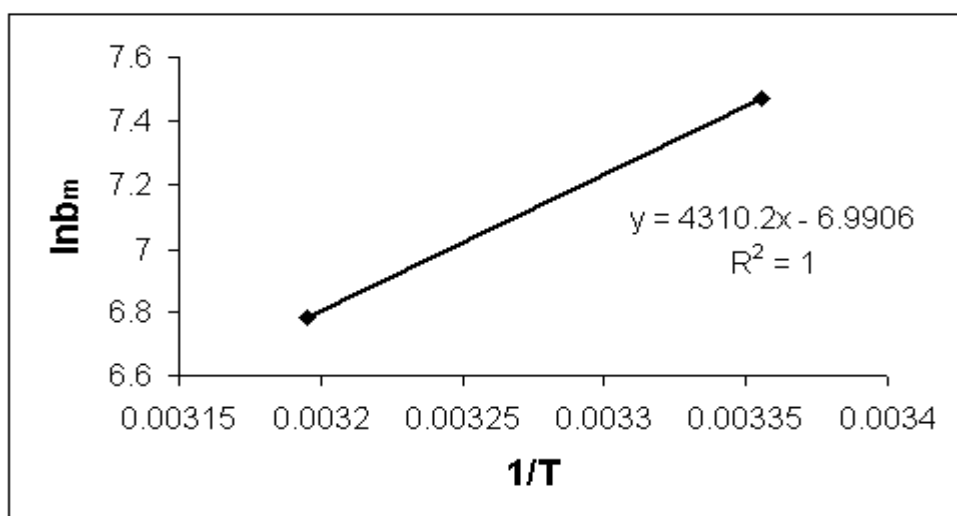


Figure H.1 Van't Hoff plot for Cr (VI)-clinoptilolite rich mineral

$$\Delta H^\circ = -slope * R = -35.8 \frac{kJ}{mol}$$

$$\Delta S^\circ = int * R = -0.058 \frac{kJ}{molK}$$

$$\Delta G^\circ = \Delta H^\circ - T\Delta S^\circ = 18.51 \frac{kJ}{mol} \text{ (at 298K)}$$

## APPENDIX I

### ACTIVATION ENERGY

The values of activation energy ( $E_a$ ) are determined from a plot of  $\ln K$  versus  $1/T$ .

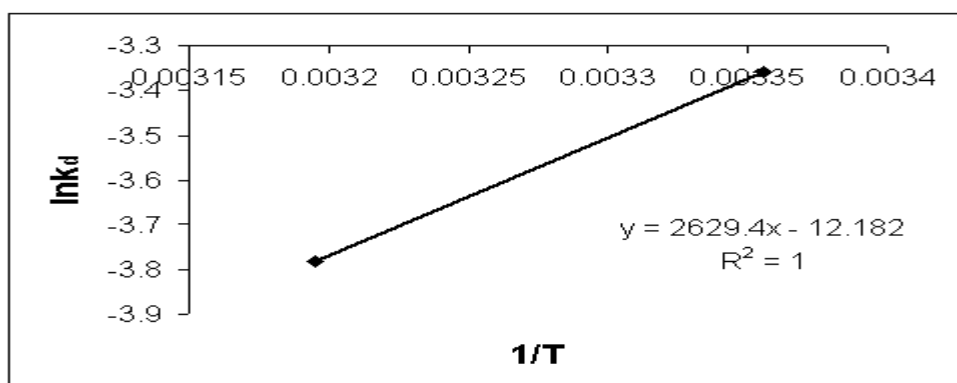


Figure I.1. Arrhenius plot of  $\ln k_d$  vs  $1/T$  for the sorption of Cr (VI) onto CLI

$$E_a = -\text{slope} * R = -2629 * 8.341 \frac{J}{\text{molK}} = -21.8 \frac{kJ}{\text{mol}}$$

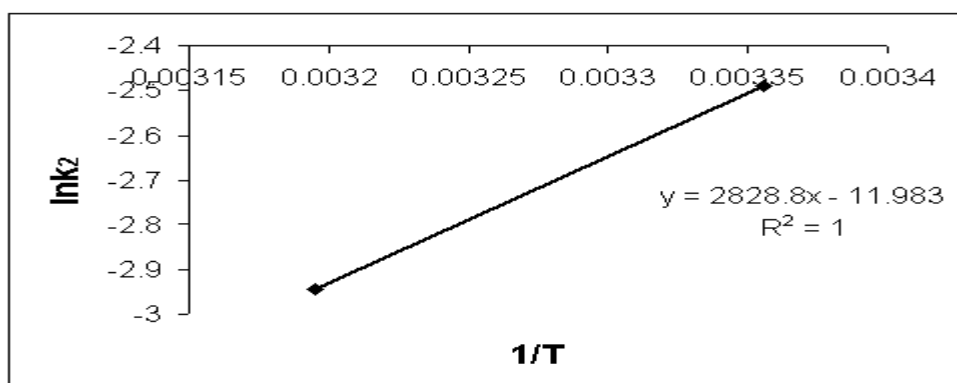


Figure I.2. Arrhenius plot of  $\ln k_2$  vs  $1/T$  for the sorption of Cr (VI) onto CLI

$$E_a = -\text{slope} * R = -2828 * 8.341 \frac{J}{\text{molK}} = -23.5 \frac{kJ}{\text{mol}}$$



## **BEYHAN CANSEVER ERDOĞAN**

**Date of Birth** : 19.09.1977

**Place of Birth** : Turkey

**Citizenship** : Turkish

### **EDUCATION**

**[1995-2001] B.Sc. (Chemical Engineering)**

**Ege University**

Department of Chemical Engineering, Izmir, Turkey

Dissertation: Classification of Volatile Products Evolved From Temperature Programmed Co-Pyrolysis of Turkish Oil Shale with Different Kerogen Types

**[2001-2004] M.Sc. (Chemical Engineering)**

**İzmir Institute of Technology**

Department of Chemical Engineering, Izmir, Turkey

Dissertation: Domestic Wastewater Treatment with Natural Zeolite

**[2004-2011] Ph.D. (Chemical engineering)**

**İzmir Institute of Technology**

Department of Chemical Engineering, İzmir, Turkey

Dissertation: Cr(VI) Removal with Natural, Surfactant Modified and Bacteria Loaded Zeolites

### **PUBLICATIONS**

Erdoğan, B.C.; Seyhan, A.T.; Ocak, Y.; Tanoğlu, M.; Balköse, D.; Ülkü, S. Cure Kinetics of Epoxy Resin-Natural Zeolite Composites. *Journal of Thermal Analysis and Calorimetry*, **2008**, 94(3), 743–747.

Savrik, S.A.; Erdoğan, B.C.; Balköse, D.; Ülkü, S. Statistical Thermal Stability of PVC. *Journal of Applied Polymer Science*, **2010**, 116, 1811-1822.

Erdoğan, B.C.; Ülkü, S. Sorption of ammonium onto Gördes clinoptilolite rich mineral specimens, *Applied Clay Science*, **2011**, (Accepted Manuscript: CLAY3652)

Erdoğan, B.C.; Ülkü, S. Cr (VI) Sorption by Using Clinoptilolite and Bacteria Loaded Clinoptilolite Rich Mineral, *Microporous and Mesoporous Materials*, **2011**, (Accepted Manuscript: MICMAT-D-11-00347)

Erdoğan, B.C.; Ülkü, S. Statistical analysis of ammonium removal with clinoptilolite rich mineral, *Applied Clay Science*, **2011**, (Submitted Manuscript: CLAY3709)